Geothermal exploration and tectonic studies in southwestern Canada using the magnetotelluric method

by

Cedar Hanneson

A thesis submitted in partial fulfillment of the requirements for the degree of

Doctor of Philosophy

in

Geophysics

Department of Physics

University of Alberta

Abstract

Subduction zones are an important class of plate boundaries and are the location of several important geological processes. Significant mineral and geothermal energy resources are also formed by plate convergence. The magnetotelluric (MT) method is a useful tool to study subduction zones, volcanoes, backarc regions, and geothermal systems because measurements of subsurface resistivity are sensitive to the presence of fluids such as brine and partial melt. In this thesis, the following three applications of MT exploration in the Cascadia subduction zone and surrounding areas in southwestern Canada are described.

1) The Mount Meager volcanic complex in southwestern British Columbia (BC) is an active volcano and one of Canada's most promising geothermal prospects. MT data collected at Mount Meager were inverted to create an electrical resistivity model to a depth of 25 km. The model is characterized by high resistivity (> 100 Ωm) in the upper 6–7 km, implying relatively dry, unaltered rock. Within this resistive layer, localized conductors observed in the upper 2 km correspond to clay-rich layers that may act as caprocks and trap geothermal fluids below. Beneath the resistive upper crust, there is a major conductor in the depth range 5–15 km below sea level with an average resistivity of ~3 Ωm. Laboratory experiments of melt resistivity and petrological data from erupted volcanic rocks were used to interpret the resistivity of this feature. The inferred magma body was estimated to have a minimum volume of $\sim 2\times10^{12}$ m^3 comprising 18–32% dacitic-to-trachydacitic melt with 6–8 wt.% H_2O at a temperature of 800–900 °C. The model also shows low resistivity fluid pathways from the northern part of the magma body, that rise toward Mount Meager and nearby fumaroles. Along with other geophysical and geological models produced by the Garibaldi Geothermal

Energy Project, this resistivity model will reduce the exploration risk associated with geothermal energy development.

2) Geothermal exploration with MT is widely used in focused studies such as that described above at Mount Meager. However, MT also has the potential to determine regional-scale controls on the distribution and location of geothermal resources. MT data measured at 331 locations were used to create the first regional-scale 3-D resistivity model of the southern Canadian Cordillera. A number of conductive features were observed in the crust and uppermost mantle of the southeastern Cordillera. The previously reported Canadian Cordilleran regional conductor was modelled as a number of discrete conductors in the depth range 15–55 km beneath the Omineca belt. Temperatures in the range 400–700 °C are inferred at depths of 15–26 km and saline aqueous fluids are likely the cause of the low resistivity. Temperatures in the range 700–1300 °C are expected at depths of 26–55 km and small volumes of partial melt may explain the low resistivity. The Southern Alberta-British Columbia conductor (SABC), Red Deer conductor, and Loverna conductor were imaged as a single connected conductor, whose low resistivity is likely caused by sulphide mineralization. A group of conductors was imaged near the southern Rocky Mountain Trench in the depth range 10–70 km and their low resistivity is likely caused by interconnected saline fluids and possibly interconnected graphite films.

3) MT data were used in southwestern Canada to study changes in lithospheric thickness. Previous geophysical studies have shown that the lithosphere-asthenosphere boundary (LAB) is at a depth of 60–70 km beneath the Cascadia backarc, increasing to more than 150 km beneath the craton in Alberta. MT can also image the depth of the LAB and the model derived in the previous study was used to map the depth of the LAB. A subvertical backarc-craton lithosphere step (BCLS) occurs between 117 °W

and 119 °W in southern BC. The vertical projection of the BCLS at the surface of the Earth is located between the Kootenay Arc and a line marking granitic rocks with an initial $^{87}Sr/^{86}Sr$ ratio of 0.706. The cratonic lithosphere thickens to the north, from 150 km in southern Alberta to 250–300 km in central Alberta. The transition from a subhorizontal LAB in southern Alberta to a northward dipping LAB occurs below the SABC.

The results of these studies could aid further geothermal exploration and tectonic studies in southwestern Canada.

Preface

The research presented in this thesis is original work by Cedar Hanneson. It has been written to fulfill the requirements for the degree of Doctor of Philosophy at the University of Alberta. This research was carried out under the supervision of Dr. Martyn Unsworth in the Department of Physics.

A version of Chapter 4 has been published as Hanneson, C. and Unsworth, M.J. (2023a) Magnetotelluric imaging of the magmatic and geothermal systems beneath Mount Meager, southwestern Canada. *Canadian Journal of Earth Sciences*, Canadian Cordilleran Volcanism special issue, 1-19, doi:10.1139/cjes-2022-0136. This publication included a "Supplementary Materials" document, which has been reproduced as Appendix B of this thesis. Cedar Hanneson and Martyn Unsworth collected MT data with the help of Andrew Williamson and Zoë Vestrum. Cedar Hanneson processed the MT data, created a resistivity model, interpreted the results, made the figures, wrote the original manuscript, revised the manuscript, and is the corresponding author. Dr. Martyn Unsworth provided guidance during modelling and interpretation, provided feedback on the original manuscript, and provided feedback on revised versions of the manuscript.

A version of Chapter 5 has been published as Hanneson, C. and Unsworth, M.J. (2023b) Regional-scale resistivity structure of the middle and lower crust and uppermost mantle beneath the southeastern Canadian Cordillera and insights into its causes. *Geophysical Journal International*, 234, 2032-2052, doi:10.1093/gji/ggad183. This publication included a "Supporting Information" document, which has been reproduced as Appendix C of this thesis. Cedar Hanneson collected MT data with the help of Darcy Cordell, Ben Lee, Sean Bettac, and Ray Wang. Cedar Hanneson processed the MT data, created a resistivity model, interpreted the results, made the figures, wrote the original manuscript, revised the manuscript, and is the corresponding author. Dr. Martyn Unsworth provided guidance during modelling and interpretation, provided feedback on the original manuscript, and provided feedback on revised versions of the manuscript.

Chapter 6 will be submitted to *Journal of Geophysical Research: Solid Earth* as a manuscript titled "Lithospheric thickness and the backarc-craton lithosphere step in southwestern Canada determined from a 3-D electrical resistivity model" by Hanneson, C. and Unsworth, M.J. The

supplemental material that will be submitted with this manuscript has been reproduced as Appendix D of this thesis. Cedar Hanneson designed the analyses, interpreted the results, made the figures, and wrote the original manuscript. Dr. Martyn Unsworth provided feedback on the original manuscript.

While a graduate student at the University of Alberta, Cedar Hanneson published two additional peer-reviewed scientific journal articles, one as the lead author and one as a co-author. They are not included in this PhD thesis, but are mentioned here for completeness. The first was published as Hanneson, C., Johnson, C.L., Mittelholz, A.M., Al Asad, M.M., and Goldblatt, C. (2020) Dependence of the interplanetary magnetic field on heliocentric distance at 0.3-1.7 AU: A six-spacecraft study. *Journal of Geophysical Research: Space Physics*, 125, 1-12, doi:10.1029/2019JA027139. The second was published as Cordell, D., Unsworth, M.J., Lee, B., Hanneson, C., Milling, D.K., and Mann, I.R. (2021) Estimating the geoelectric field and electric power transmission line voltage during a geomagnetic storm in Alberta, Canada using measured magnetotelluric impedance data: The influence of three-dimensional electrical structures in the lithosphere. *Space Weather*, 19, 1-20, doi:10.1029/2021SW002803.

Acknowledgments

I would like to thank my supervisor, Dr. Martyn Unsworth, for teaching me most of what I know about the magnetotelluric (MT) method and other electromagnetic geophysical methods. We worked together to collect MT data in Peru, British Columbia (at Mount Meager and Mount Cayley), and the Yukon. We installed MT stations by truck, boat, and helicopter. I learned a lot from him about MT deployments and fieldwork in general. I am very grateful for these experiences and the knowledge that I gained from them.

I thank my supervisory committee members, Dr. Claire Currie and Dr. Stephen Johnston. They provided support and guidance during my graduate studies. I thank my PhD thesis examiners, Dr. Thomas Chacko and Dr. Ian Ferguson, for their helpful comments and suggestions. I would also like to thank Dr. Catherine Johnson for providing my first scientific research opportunity, and for helping me write and publish my first peer-reviewed scientific journal article.

During my graduate studies, I participated in 182 days of fieldwork. This involved digging many holes and driving many kilometres, both in a variety of conditions. My graduate studies also involved an exchange of knowledge and ideas with other students, as well as a lot of writing and proofreading. I thank all of these students who did fieldwork with me and/or provided assistance in the lab/office: Dr. Enci Wang, Dr. Darcy Cordell, Dr. Benjamin Lee, Sean Bettac, Theron Finley, Zoë Vestrum, Brandon Chase, Erich Slobodian, Megan Caston, Javier Gonzalez, Keytash Moshtaghian, Andrew Williamson, and Ray Wang.

I wholeheartedly thank my partner, Nicole Barker, for her much-needed advice and support throughout my PhD program, as well as my step-daughter, Lily, and our pets (Kipo, Yumyan, and Mandu) for their companionship and stress relief (most of the time). I would also like to thank my grandparents, parents, and sisters, who all believed in me when I made the difficult decision to end my old career, go to university in my thirties, and get a PhD in my forties. Finally, I would like to recognize Jamie Yates and Chris Springbett, close friends who died while I was in grad school, as well as my brother, Shanti Hanneson, who died before I went back to school. You will be forever remembered, loved, and missed.

Table of Contents

List of Tables

List of Figures

List of Common Symbols and Abbreviations

1-D	one-dimensional
2-D	two-dimensional
3-D	three-dimensional
AMT	audio magnetotelluric
BBMT	broadband magnetotelluric
BC	British Columbia
BCLS	backarc-craton lithosphere step
CCRC	Canadian Cordilleran regional conductor
EM	electromagnetic
Ga	giga-annum (billion years)
GPa	gigapascal (billion pascals)
GVB	Garibaldi volcanic belt
Hz	hertz
ka	kiloannum (thousand years)
km	kilometre (thousand metres)
LAB	lithosphere-asthenosphere boundary
LMT	long-period magnetotelluric
Ma	mega-annum (million years)
MMVC	Mount Meager volcanic complex
MT	magnetotelluric
MW	megawatt (million watts)
MWe	megawatt of electric power
R.M.S.	root-mean-square
SABC	southern Alberta-British Columbia conductor
SRMT	southern Rocky Mountain Trench
vol.%	volume per cent
WCSB	Western Canada Sedimentary Basin
wt.%	weight per cent
Ωm	ohm·metre

1. Introduction

The research presented in this thesis was motivated by a desire to advance the development of geothermal energy resources in Canada. This has the potential to reduce the environmental effects of Canada's current method of energy production, which is contributing to carbon emissions and has had an impact on global climate. To develop geothermal energy in an effective way, it is important to first understand the energy landscape of Canada, especially the western provinces where much of the country's geothermal energy potential is found. In this chapter, recent energy production and energy consumption in Canada are described and used to motivate a discussion of geothermal energy, geothermal systems, and geothermal exploration. Finally, the research that will be presented in Chapters 4-6 is introduced.

1.1. Energy consumption and energy production in Canada

Canada has a relatively high per capita energy consumption compared with the global average (Figure 1.1). Factors such as cold winters and low population density contribute to this high level of energy consumption. Canada's provinces and territories vary greatly when in comes to the sources of the energy they consume. Hydroelectricity is the most common form of electricity in Canada, accounting for 59.5% of the country's electricity generation in 2019, but the main sources of electricity generation vary considerably among different regions (Figure 1.2). In the western provinces of British Columbia (BC), Alberta and Saskatchewan, there is a stark contrast between hydroelectricity in BC (87.2% in 2019) and electricity generated by burning coal and natural gas in Alberta (89.3% combined in 2019) and Saskatchewan (81.5% combined in 2019).

The burning of fossil fuels has significantly increased the atmospheric concentration of carbon dioxide and is a major contributor to a warming planet with a changing climate (Prentice et al., 2001; Solomon et al., 2009). In 2015, only 22% of Canada's total energy consumption was from renewable sources (United Nations Development Programme, 2019). However, the total renewable energy potential in Canada has been estimated to be 150% of the 2010 energy demand, implying that renewable energy could meet our future energy needs (Barrington-Leigh & Ouliaris, 2017).

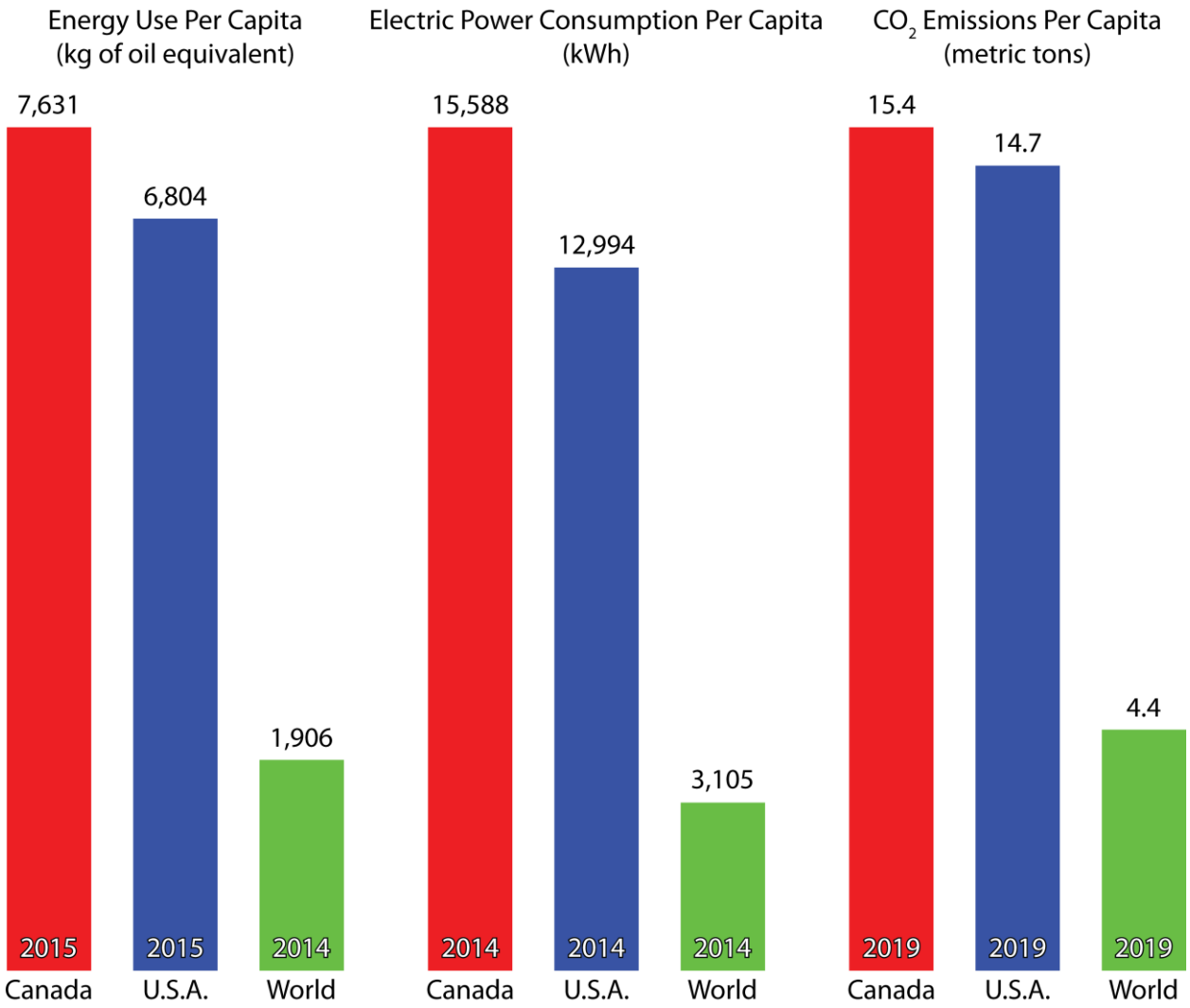

Figure 1.1*: Per capita energy use, electric power consumption and CO_2 emissions in Canada (red), the United States (blue) and the world (green), for the year shown in white at the bottom of each bar. Data is from The World Bank (https://data.worldbank.org/indicator, accessed 2023/01/20).*

Societal, economic and environmental concerns necessitate that Canada plan for the future by diversifying its energy portfolio, and adding renewables such as wind and solar. Geothermal energy is a good renewable option to include because of its potential to provide consistent baseload power with a relatively low carbon footprint (Grasby et al., 2012). Unlike some other sources of renewable energy, geothermal power plants can generate electricity throughout the day and year. In contrast, solar can only generate electricity during the daytime, which is longer in the spring and summer; and wind power is only viable when there are sufficient wind speeds to generate electricity. Northern Canada in particular has limited daylight in the winter and fall, as well as low temperatures.

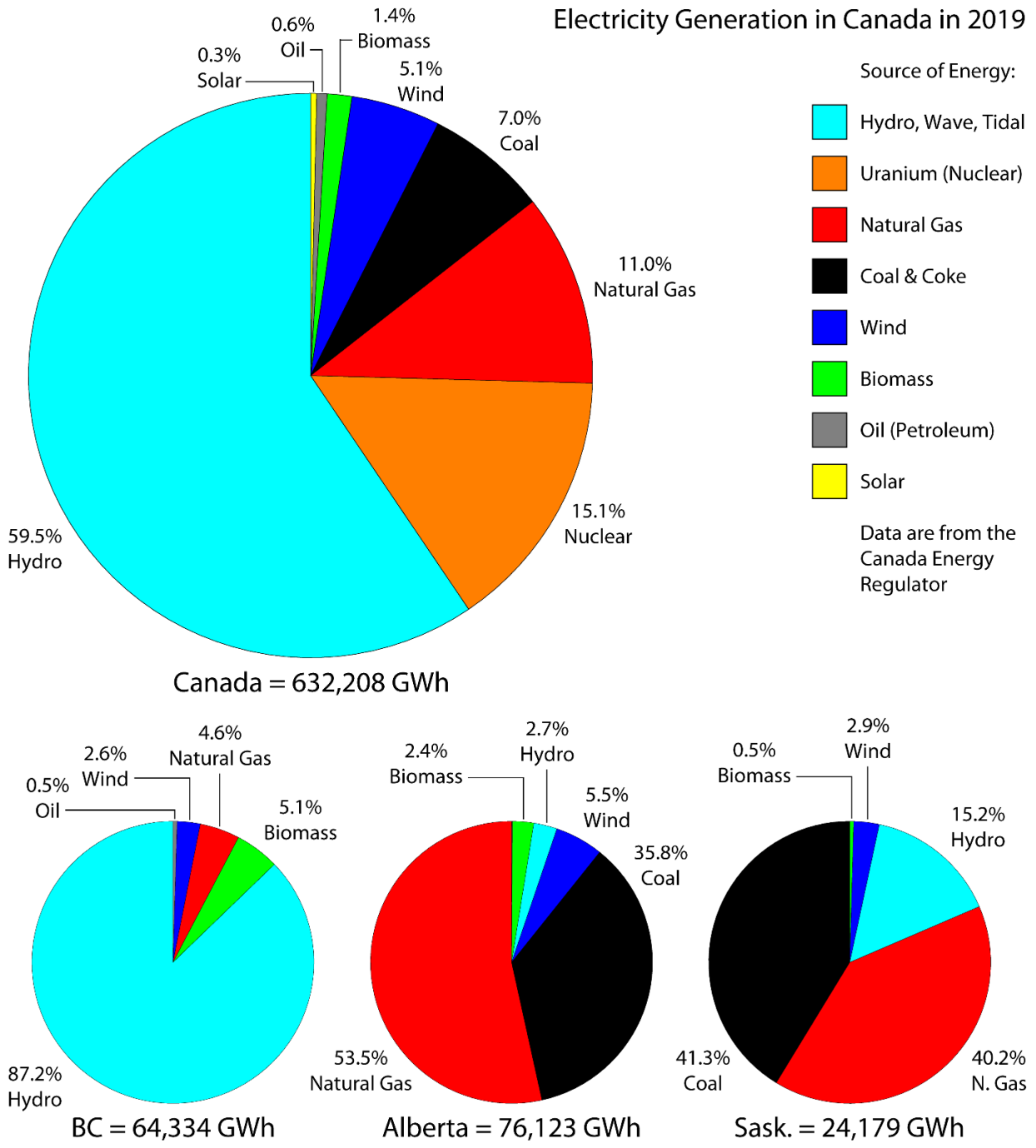

***Figure 1.2**: Electricity generation in Canada, British Columbia (BC), Alberta, and Saskatchewan (Sask.) in 2019, divided by source. Data are from the Canada Energy Regulator (https://www.cer-rec.gc.ca, accessed 2023/03/27).*

Secondary energy is that which is used directly by end users and it includes energy used to heat and cool buildings, run vehicles, and run machinery. Electricity only accounted for 20% of Canada's secondary energy use in 2018 (Natural Resources Canada, 2022). Natural gas, motor gasoline, oil, and other oil products accounted for 71% (Figure 1.3 a). Space heating

and water heating accounted for 82% of Canada's residential energy use in 2018 and only 25% of that used electricity (Figure 1.3 b-d). The majority of residential space heating (53%) and water heating (70%) used natural gas (Figure 1.3 c-d). Space heating and water heating also accounted for 59% of Canada's commercial and institutional energy use in 2018 (Figure 1.3 e). Primary energy includes energy used to transform one form of energy into another, transport energy supplies to consumers, and feed industrial production processes (Natural Resources Canada, 2022). It also includes secondary energy.

Decarbonisation of space heating and water heating will therefore be necessary to meet Canada's goal of net-zero greenhouse gas emissions by 2050. Geothermal energy is uniquely qualified to help with this challenge because heat from the Earth can be used directly for heating buildings and water, without the need to generate electricity. Direct-use geothermal applications also include agricultural processes such as heating greenhouses, drying crops, and industrial composting. There are also some great urban applications such as melting snow and ice on roads, parking lots and sidewalks, heating swimming pools, and brewing beer. Examples of direct-use applications can be found at https://nea.is/geothermal/direct-utilization/ and geothermal-powered breweries include Riff Raff Brewing Co. in Colorado, Ölverk Brewery in Iceland, Akatsuki Brewery in Japan, and Vapori di Birra in Italy. Unlike electric power generation, which requires higher temperatures, direct-use heat applications can utilize low-temperature geothermal systems (Grasby et al., 2012).

1.2. Geothermal energy resources

Geothermal resources are often categorized by temperature. Grasby et al. (2012) suggested the following classification scheme: high-temperature (e.g., > 150 °C), medium-temperature (e.g., 80–150 °C), and low-temperature (e.g., < 80 °C). High-temperature and medium-temperature resources can be used to efficiently generate electricity, while low-temperature resources can only be used to produce heat. High-temperature resources may be further categorized by the geological context: hydrothermal systems, magmatic systems, and hot dry rock (Grasby et al., 2012). These types of resources are shown schematically in Figure 1.4. Conventional geothermal systems (Figure 1.4 a-b) have three key requirements: (1) heat, (2) porosity containing fluid, and (3) permeability allowing fluid flow. Unconventional geothermal systems (Figure 1.4 c-d) require heat to be present, but technology is used to replace the other two requirements.

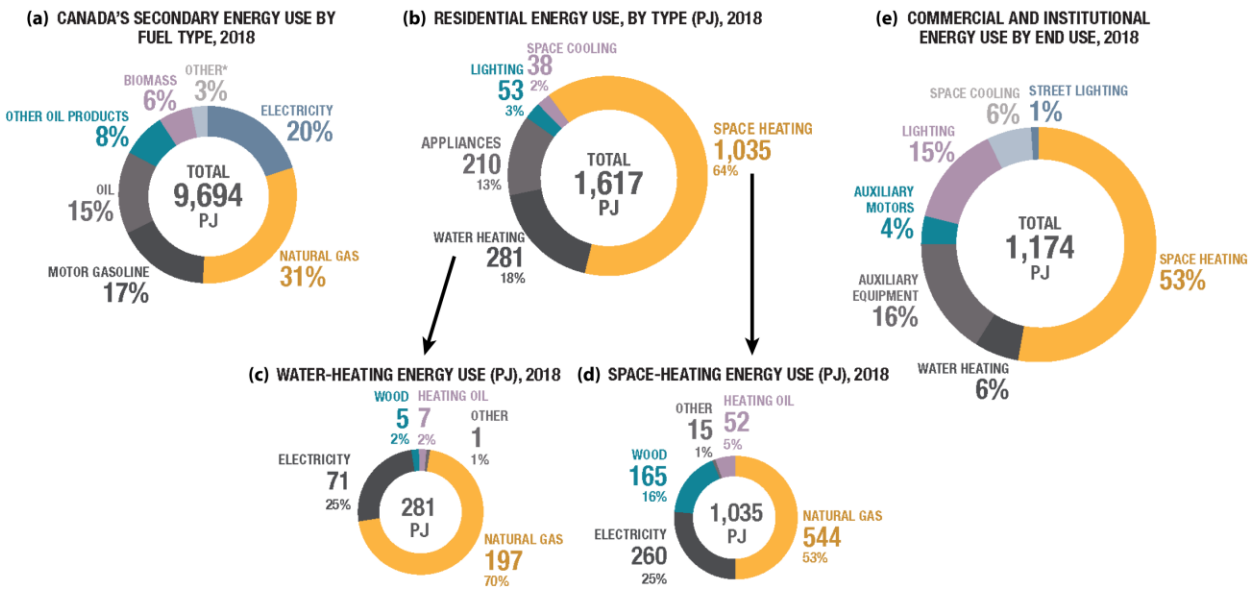

***Figure 1.3**: Secondary energy use in Canada in 2018. (a) All secondary energy use, divided by fuel type. (b) Residential energy use, divided by use. (c) Residential water-heating energy use, divided by fuel type. (d) Residential space-heating energy use, divided by fuel type. (e) Commercial and institutional energy use, divided by use. These figures were reproduced from the National Resources Canada (NRCan) Energy Fact Book 2021-2022, pages 43-46 (Natural Resources Canada, 2022). This thesis is not affiliated with nor endorsed by NRCan.*

Convective hydrothermal systems typically contain a geothermal reservoir overlain by a clay cap, as illustrated in panel (a) of Figure 1.5 (Pellerin et al., 1996). Near the surface, temperatures are usually too low for hydrothermal alteration to take place and a high-resistivity layer of unaltered rock is present. Temperature increases with depth and clay alteration begins in the range 50–100 °C. Smectite is formed at the lowest temperatures, a layer with a mixture of illite and other clays is formed at moderate temperatures (e.g., 150–200 °C), then chlorite and epidote around 230 °C (Hersir et al., 2013). The protolith can also have an effect; for example, Chang-Bock et al. (2002) found that chlorite formed at lower temperatures in basalt than in granite or rhyolite. The high-temperature chlorite-type mineral assemblage is more resistive than the low-temperature clay assemblage; however, these alteration products will persist after cooling has occurred, therefore electrical resistivity can only provide an upper bound on reservoir temperature (Hersir et al., 2013).

Hersir et al. (2013) presented a 3-D resistivity model from inversion of magnetotelluric (MT) data from the Krýsuvík high-temperature geothermal area in Iceland (Figure 1.5 b). Boreholes confirmed that smectite-zeolite alteration caused very low resistivity and chlorite alteration caused slightly higher resistivity (see KR-06 and KR-05 in Figure 1.5 b). At greater depths, the high-temperature reservoir was even more resistive.

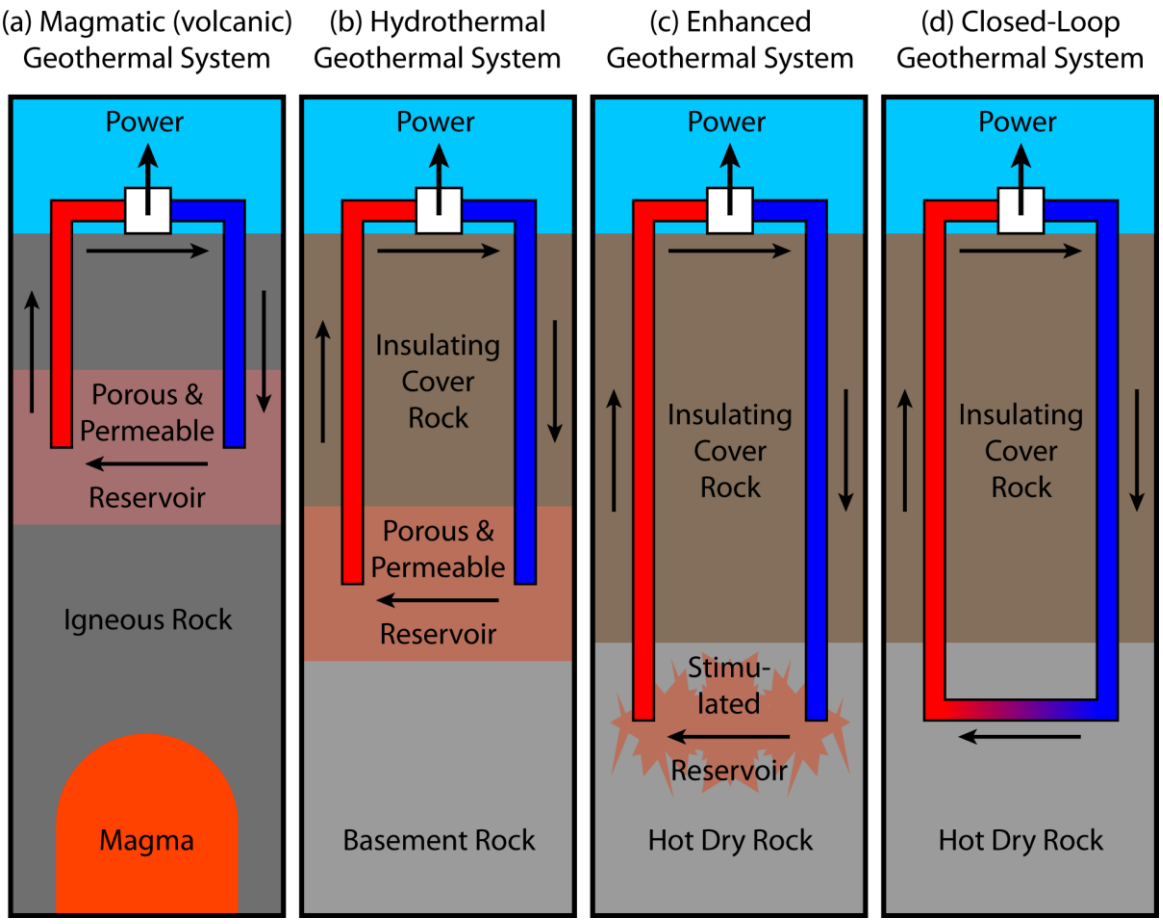

***Figure 1.4**: Schematic diagrams of different types of high-temperature geothermal resources.*

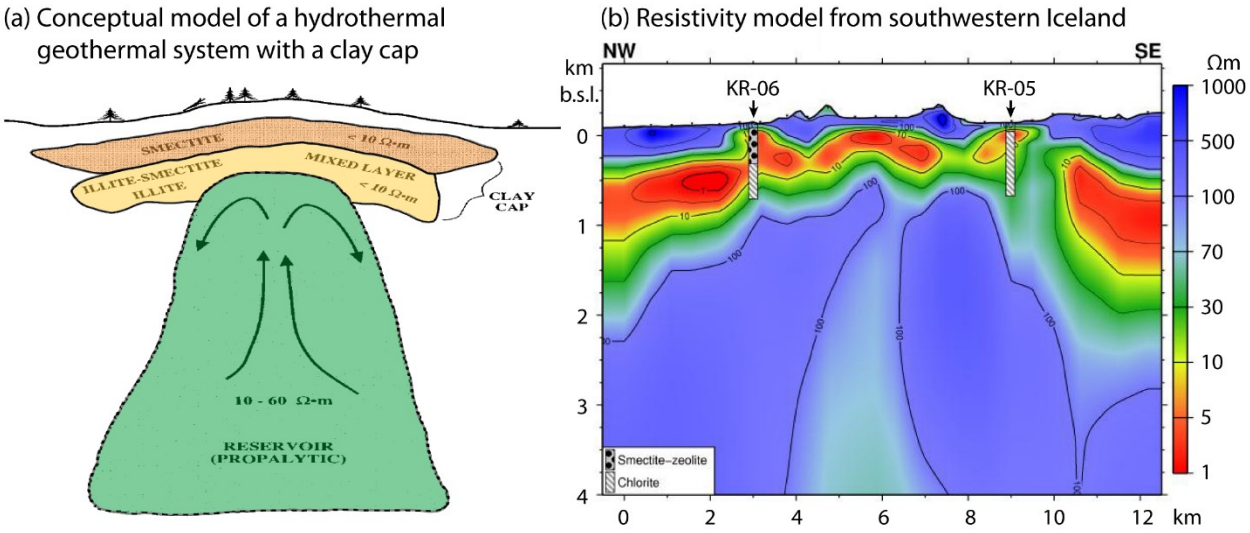

***Figure 1.5**: (a) Conceptual model of a hydrothermal geothermal system with a clay cap, modified from Pellerin et al. (1996). (b) Resistivity model of the Krýsuvík high-temperature geothermal area in southwestern Iceland, modified from Hersir et al. (2013).*

Magmatic (volcanic) geothermal systems exist near tectonic plate boundaries and mantle hot spots. Countries that produce geothermal energy near plate boundaries include Indonesia, the Philippines, New Zealand, Kenya, and Iceland. Magmatic geothermal systems have higher geothermal gradients than intraplate hydrothermal systems, so high-temperature resources can be found at shallower depths. A typical geothermal gradient in continental lithosphere is approximately 25-30 °C/km in the upper 3 km (Limberger et al., 2018). Northwest of Edmonton, near Grande Prairie, a geothermal gradient of ~24 °C/km has been measured (Huang et al., 2021). Estimated geothermal gradients in the sedimentary rocks of Alberta span a wide range, but the average is greater than 30 °C/km (Grasby et al., 2012). In contrast, the geothermal gradient at Mount Meager, a volcano in southwestern BC, is ~90 °C/km (see Chapter 4 for details). In the Canadian Shield, geothermal gradients are lower than the global average. For example, a value of approximately 12-15 °C/km has been estimated in eastern Ontario (Lorencak et al., 2004).

Supercritical water occurs at high temperatures and high pressures, when both parameters are greater than the critical point. Under supercritical conditions, water vapour and liquid water can no longer coexist, and they are replaced by a single supercritical fluid phase. In some magmatic geothermal systems, supercritical reservoirs may be found and they have a higher energy density than reservoirs containing liquid and/or vapour. For example, exploitation of supercritical fluids at 430–550 °C could increase geothermal energy production by an order of magnitude, compared with liquid water and steam at a temperature less than 300 °C (Kummerow et al., 2020).

Hydrothermal and magmatic systems are only found in very specific geographic locations. Many of these have already been developed for geothermal energy production. In each, the three factors of heat, porosity, and permeability allow energy extraction. However, heat is found everywhere in the Earth away from plate boundaries and volcanoes. For example, deep crystalline basement rocks often contain economically useful heat, but the porosity and permeability can be low, making it difficult to extract the heat.

Hot dry rocks can be exploited for geothermal power generation by (1) creating a stimulated reservoir with artificially created porosity and permeability and (2) adding fluids to transport heat. This is called an enhanced geothermal system (EGS) and is shown in panel (c) of Figure 1.5. Closed-loop geothermal systems (Figure 1.5 d) can also be used to extract heat energy from hot dry rocks, and they avoid the potential problems associated with fluid loss and H_2S

(sour gas). One limitation of this method is the reduced surface area when replacing a reservoir with a borehole or a series of boreholes. Closed-loop technologies are being developed by Eavor Technologies Inc., GreenFire Energy Inc., and Novus Earth Energy Operations Inc., among others.

1.3. Exploration for geothermal energy resources

The effective and economic utilization of geothermal resources for energy production requires several stages of exploration, analysis, and development (Figure 1.6). It requires understanding of the regional controls on the locations of geothermal reservoirs and their quality and long-term viability. Geological studies can provide some information about subsurface resources. For example, they can map geological units and faults, and determine mineralogical properties at the surface. However, geophysical studies are key because they can provide direct information about subsurface structures at depth that cannot be obtained from surface observations alone.

Seismic methods are used to determine the velocity of seismic waves (both pressure waves and shear waves) within the Earth. Gravity methods use spatial variations in the strength of gravity to determine density variations within the Earth. Magnetic methods measure magnetic fields to determine the magnetization and/or magnetic permeability of rocks. Electrical and electromagnetic methods use electric current and electromagnetic waves to determine the electrical chargeability and electrical conductivity (or its reciprocal, electrical resistivity) within the Earth (Chapter 3).

The research presented in this thesis used electromagnetic (EM) geophysical methods to identify and characterize geothermal targets in western Canada and their regional surroundings, thereby reducing the risk for future investment in this important renewable energy resource. Electrical and EM methods are valuable tools during geothermal exploration because they can measure electrical resistivity (Chapter 3). This is a physical rock property which is particularly sensitive to the presence of brines, molten rock, and clay, which produce low-resistivity anomalies, and is therefore useful in the search for hydrothermal geothermal systems (Ussher et al., 2000). A variety of EM and electrical techniques have been developed over the years and can be divided into those using natural (passive source) and man-made (controlled source) signals (Pellerin et al., 1996).

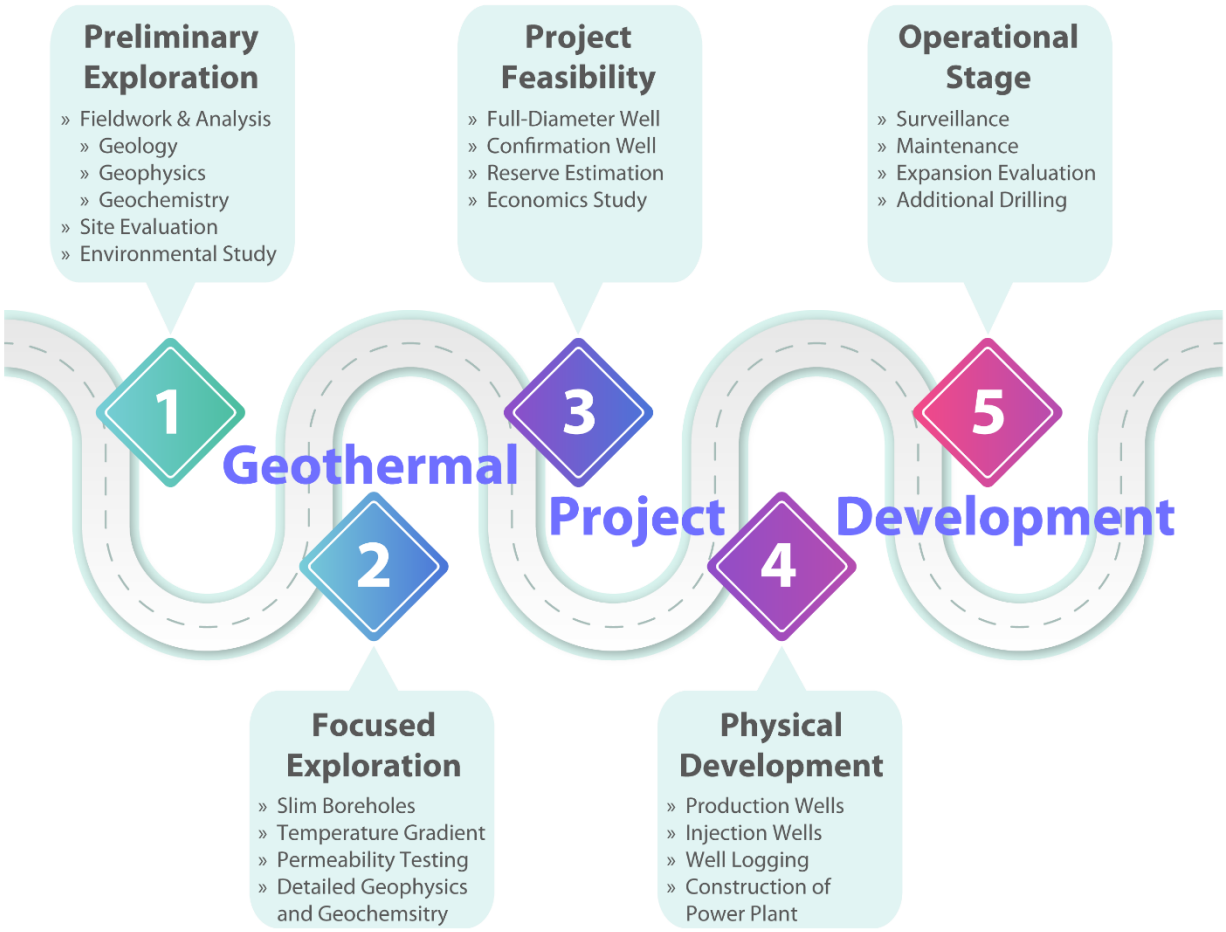

***Figure 1.6**: Stages of geothermal power project development. Geophysics is important for stages 1 and 2. This figure was created by modifying a template from freepik.com.*

For near surface imaging, methods that use man-made signals are preferred. DC resistivity uses electric current that is injected directly into the Earth, but investigation is limited by the size of the electrode array. Resistivity can also be imaged with controlled-source EM methods that include time-domain EM and frequency-domain EM, which use frequency as a proxy for depth. These methods have been used for geothermal exploration in the past (Muñoz, 2014; Pellerin et al., 1996).

For deeper imaging, beyond a few km, the MT method (Chapter 3) is the only practical approach. It is an EM geophysical method that allows subsurface resistivity structure to be mapped using surface measurements of the Earth's natural electric and magnetic fields. Modern MT exploration with a grid of stations can produce reliable 3-D models of subsurface resistivity. The frequencies measured control the depth of investigation, which can range from hundreds of metres to hundreds of kilometres.

MT has been successfully used to delineate many geothermal systems (e.g., Arango et al., 2009; Bibby et al., 2009; Heise et al., 2008; Hersir et al., 2013; Muñoz, 2014) and can greatly reduce the uncertainty and cost of exploratory drilling. Therefore, mapping subsurface resistivity structure with EM geophysics is an integral part of an economically viable development plan. Integration with other data types (e.g., seismic, gravity, structural, and geochemical) can constrain and aid in the interpretation of these resistivity models, providing even greater subsurface knowledge and certainty prior to drilling.

1.4. Geothermal energy in Canada

Western North America has high geothermal potential (Jones, 2019) and geothermal power production is well-established in the western U.S.A., which includes the Cascadia subduction zone and the Basin and Range Province. In fact, the U.S.A. is the country with the greatest installed geothermal power generation capacity in the world (Figure 1.7). Despite its similar tectonic setting and geology, Canada is unfortunately lagging behind when it comes to geothermal development.

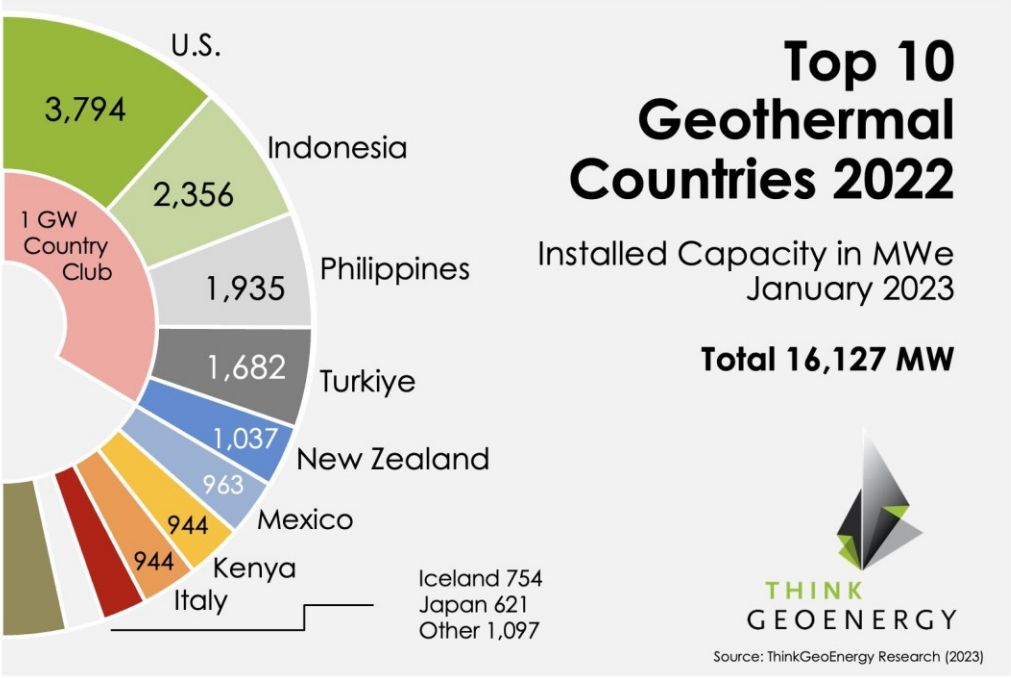

***Figure 1.7**: Installed geothermal power generation capacity at the end of 2022. Figure © ThinkGeoEnergy. (https://www.thinkgeoenergy.com/thinkgeoenergys-top-10-geothermal-countries-2022-power-generation-capacity-mw, accessed 2023/03/29).*

In March 2023, FutEra Power Corp., a wholly owned subsidiary of Razor Energy Corp., began operation of its co-produced geothermal and natural gas power plant in Swan Hills, Alberta. This is the only Canadian project to date to provide geothermal power to the electrical grid. There are currently no fully geothermal power plants operating in Canada; however, there are some in research and development stages in western Canada. For example, the Clarke Lake geothermal project is located near Fort Nelson, BC; the Alberta No. 1 geothermal project is located in the Municipal District of Greenview, near Grande Prairie, Alberta; and the Deep Earth Energy Production (DEEP) geothermal project is located near Estevan, Saskatchewan.

Western Canada has significant, yet currently unexploited, geothermal resources (Grasby et al., 2012), which could play a significant role in the future energy portfolio of this country. The total geothermal power potential in BC and Yukon has been estimated at 3,000-5,000 MWe (Ghomshei, 2010). It has long been recognized that British Columbia has a range of significant geothermal resources including fault-hosted systems, volcanic hydrothermal systems, and hot dry rock (Jessop, 1998). Volcanic systems are found in the Garibaldi Volcanic Belt (GVB) and fault-hosted systems are found in the southern Rocky Mountain Trench. Both fault-hosted systems and hot dry rock resources are found in the Columbia Mountains.

1.5. Thesis objectives

To help move geothermal development forward in Canada, improved exploration is needed to lower the economic risks to developers. This thesis uses geophysical exploration to address this in southwestern Canada. The research presented in this thesis was centred on two areas of southern BC: (1) Mount Meager in the Garibaldi Volcanic Belt (Chapter 4) and (2) southeastern BC in the Canadian Cordillera (Chapters 5 and 6). Study Area #1 is characterized by a volcanic geothermal system. Study Area #2 is characterized by fault-hosted hydrothermal systems and hot dry rock resources.

The research objectives of these three studies are:

1) Chapter 4:
    - Determine the size, location, and physical properties of the deep heat source (magma body) beneath Mount Meager.
    - Image fluid pathways that may connect the heat source with near surface geothermal manifestations and reservoirs.
    - Provide a regional context for the South Meager geothermal reservoir, which has been studied at a local scale over the past several decades.

2) Chapter 5:
    - Determine the spatial extent, distribution, and physical cause of the low-resistivity crust beneath the southern Omineca belt.
    - Estimate the water content of the upper mantle beneath the southeastern Canadian Cordillera.
    - Determine if resistivity features in the crust and upper mantle of southeastern BC are statistically correlated with surface geothermal manifestations.
3) Chapter 6:
    - Determine the depth of the electrical lithosphere-asthenosphere boundary (LAB) in southwestern Canada.
    - Investigate how the depth of the electrical LAB varies between the backarc region and the adjacent craton, i.e., in the east-west direction.
    - Investigate how the depth of the electrical LAB varies within the North American craton in Alberta, i.e., in the north-south direction.

1.6. Thesis outline

The geology and tectonic setting of the study areas (Figure 1.8) are discussed in Chapter 2. Expanding on the material presented in Section 1.3, Chapter 3 provides a discussion of the electrical resistivity of Earth materials and electromagnetic geophysical methods. It describes the physics and mathematics that underpin the MT method, providing a foundation for the original research presented in Chapters 4-6.

Chapter 4 presents and discusses a resistivity model centred on Mount Meager (Study Area #1 in Figure 1.8). This chapter was published in *Canadian Journal of Earth Sciences* (Hanneson & Unsworth, 2023a) and the associated supplemental material can be found in Appendix B. Additional details about this publication were given in the Preface.

Chapter 5 presents and discusses the upper 100 km of a resistivity model centred on southeastern BC (Study Area #2 in Figure 1.8). This chapter was published in *Geophysical Journal International* (Hanneson & Unsworth, 2023b) and the associated supplemental material can be found in Appendix C. Additional details about this publication were given in the Preface.

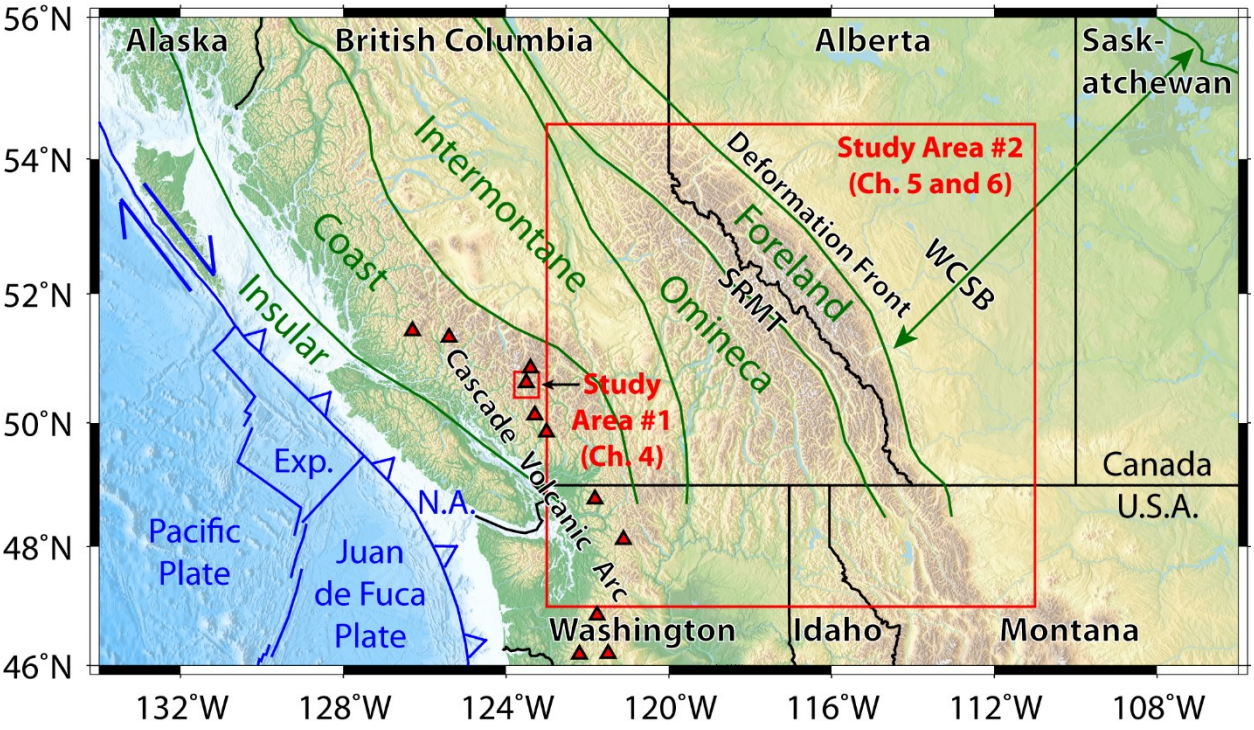

***Figure 1.8**: Map of southwestern Canada and northwestern U.S.A. Study Area #1 is centred on Mount Meager and described in Chapter 4. Study Area #2 is centred on southeastern BC and described in Chapters 5 and 6. Political boundaries (black lines), morphogeological boundaries (blue lines), tectonic plate boundaries (red lines), and volcanoes (triangles) are shown. Exp. = Explorer plate, N.A. = North American plate, SRMT = southern Rocky Mountain Trench, and WCSB = Western Canada Sedimentary Basin.*

Chapter 6 presents and discusses the upper 400 km of the resistivity model centred on southeastern BC. This chapter focusses on the lithosphere-asthenosphere boundary and the Cordillera-craton boundary, whereas Chapter 5 focusses on the crust and uppermost mantle. Chapter 6 was written as a draft manuscript for a scientific journal and it will be submitted to *Journal of Geophysical Research: Solid Earth* in the near future. The supplemental material that will accompany this submission can be found in Appendix D.

The resistivity models presented in these chapters are the culmination of many inversions, of both measured datasets and synthetic datasets. These inversions were performed on parallel computing clusters provided by the Digital Research Alliance of Canada, formerly known as Compute Canada, and they used more than 500 core years in total. See Table A.1 in Appendix A for details.

Most geothermal exploration to date, worldwide, has focused on identifying specific geothermal reservoirs. A more regional approach is also useful, allowing an understanding of

the factors that control the spatial distribution of geothermal resources (e.g., Peacock & Siler, 2021). Chapter 4 explores a specific geothermal reservoir and associated heat source, whereas Chapter 5 explores crustal-scale features over a relatively large geographic region. The geophysical models and interpretations presented in this thesis can aid the exploration and development of geothermal energy resources in southwestern Canada.

Lastly, Chapter 7 provides a summary of this thesis and suggestions for future research.

2. Tectonic setting and geology

The Earth's lithosphere is broken into seven main tectonic plates, as well as numerous smaller plates (Fowler, 2005). Over geologic time scales, plate tectonics has been a primary factor controlling the distribution of mineral resources and energy resources. Oceanic crust is generated at tectonic spreading centres, such as the mid-Atlantic ridge, and the vast majority of it eventually returns to the Earth's asthenosphere in subduction zones, along with the underlying oceanic mantle lithosphere. As an oceanic plate subducts, dehydration reactions in the crust release water and other volatiles into the mantle of the overriding plate. This lowers the melting point of the mantle rocks producing buoyant magma that ascends, some of which eventually erupts at the surface creating a volcanic arc. This process also brings energy in the form of heat to the upper crust, resulting in volcanic geothermal systems. In addition to volcanic eruptions, subduction zones can host megathrust earthquakes; therefore, hazard assessment and mitigation are key drivers of subduction zone research.

2.1. Cascadia subduction zone

Western North America has been shaped by subduction since the Middle Devonian when plate convergence initiated ~390 million years ago (Monger & Price, 2002). The Cascadia subduction zone is located west of the study areas (Figure 1.8). Adjacent to the subduction zone are the Juan de Fuca and Explorer plates, which are two of the small tectonic plates that resulted from the breakup of the Farallon plate over the past 20-30 million years (Irwin, 1990). The Juan de Fuca and Explorer ridges are seafloor spreading centres that separate these plates from the Pacific plate to the west. The Cascadia subduction zone is where the Juan de Fuca and Explorer plates are subducting beneath the North American plate. The tectonic convergence rate between the Juan de Fuca and North American plates is ~40 mm/year (Kreemer et al., 2014). In contrast, the Explorer plate is subducting at a rate of only 5-20 mm/year (Hutchinson et al., 2020). The chain of volcanoes associated with the Cascadia subduction zone is called the Cascade volcanic arc and discussed in Section 2.2. North of the Explorer plate, the plate boundary changes from convergent to transform at the Queen Charlotte Triple Junction, and the Cascade volcanic arc ends.

The Juan de Fuca plate is 0-11 million years old at the Cascadia subduction zone, in contrast to the 120-145 million-year-old Pacific plate at the Tohoku subduction zone, east of Japan (Jones, 2019). There is presently significant along-strike variability in subduction zone

geometry, inter-plate coupling, and mantle wedge characteristics. This 3-D structure makes the Cascadia subduction zone a complex and interesting area to study. Since it is a young, warm end-member, the subducting plate in the forearc is 300-600 °C hotter than an old, cool end-member such as the Okhotsk plate of Japan, and this facilitates eclogitization at shallow depths of 40-90 km (Kirby et al., 1996; Peacock & Wang, 1999; Savard et al., 2018). The location of the main fluid flux within a given subduction zone is related to the age and temperature of the subducting plate. In Cascadia, the dominant release of water occurs at shallow depths in the forearc, contrasted with greater depths in the backarc in Japan (Savard et al., 2018).

The Cascadia backarc, east of the volcanic arc, also has spatially variable structure. It is unusual in that it has thin lithosphere and high heat flow, both of which extend far inland. The transition from young accreted material to old cratonic lithosphere occurs 750-850 km east of the subduction zone (Currie, Cassidy, et al., 2004). At this location, the transition from thin to thick lithosphere is one of the most dramatic on Earth. However, the exact location and geometry of this transition is still a topic of debate and is discussed in more detail in Chapter 6.

Understanding of subduction zone and backarc structure benefits from multiple types of geophysical measurement. Electrical resistivity, measured with electromagnetic methods, is important because it can help determine the fluid content and temperature of the crust and upper mantle. The backarc has previously been studied with 2-D transects of magnetotelluric measurements, showing low resistivity beneath the volcanic arc and within the mantle wedge (Rippe et al., 2013).

Many studies have advanced our understanding of subduction-related processes since the turn of the century (e.g., Hyndman & Peacock, 2003; Jones et al., 2018; Kelemen et al., 2003; Schellart & Rawlinson, 2013; Syracuse et al., 2010; Wilson et al., 2014). Subduction zones often host economically viable high-enthalpy geothermal resources, e.g., New Zealand, Japan and Central America (Moeck, 2014). This thesis studies one such resource in southwestern Canada (Chapter 4).

2.2. Cascade volcanic arc

The Cascade Volcanic Arc is a direct consequence of the subduction described in Section 2.1 and it extends from western BC to northern California (Figure 2.1). The northern portion of

the arc, from Silverthrone caldera to Glacier Peak, is called the Garibaldi Volcanic Belt (GVB). The southern portion, from Mount Lassen in northern California up to but excluding Glacier Peak, is called the High Cascades. The GVB trends northwest and is 300-400 km inboard of the Cascadia subduction zone trench, whereas the High Cascades trend north and are 250-300 km inboard of the trench (Hickson, 1994). This implies that the subducted tectonic plates dip more steeply in the south than the north. The volcanic arc occurs where the subducted plate is at a depth of 60-120 km (Figure 2.2).

The GVB is a Quaternary-aged glaciovolcanic arc and it includes the Mount Meager volcanic complex which has had at least two explosive volcanic eruptions in the past 25,000 years (Hickson, 1994; Russell et al., 2021; Venugopal et al., 2020). The most voluminous volcanic complex in the GVB is Mount Baker and the most recent eruption in the GVB occurred at Glacier Peak in the mid-1700s (Hickson, 1994). In the Canadian segment of the GVB, Mount Meager is the largest stratovolcano and the most recently active volcano, with a volume of 20 km^3 and a Plinian-to-Pelean eruption ~2,400 years ago (Hickson, 1994). Mount Meager is one of Canada's most promising opportunities for geothermal development and the subject of Chapter 4.

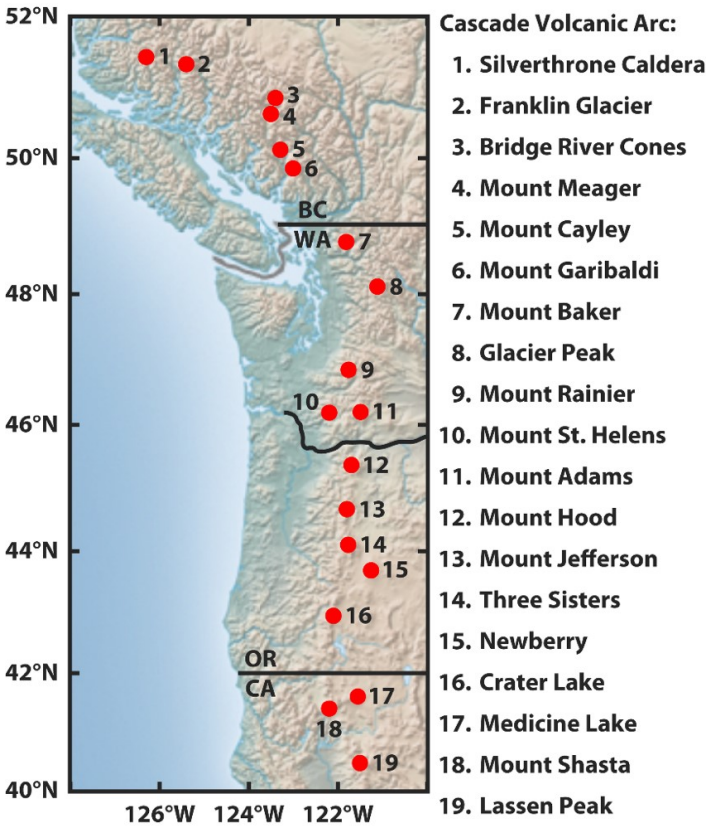

***Figure 2.1**: Map of the Cascade volcanic arc. Black lines are provincial and state boundaries. BC = British Columbia, WA = Washington, OR = Oregon, and CA = California.*

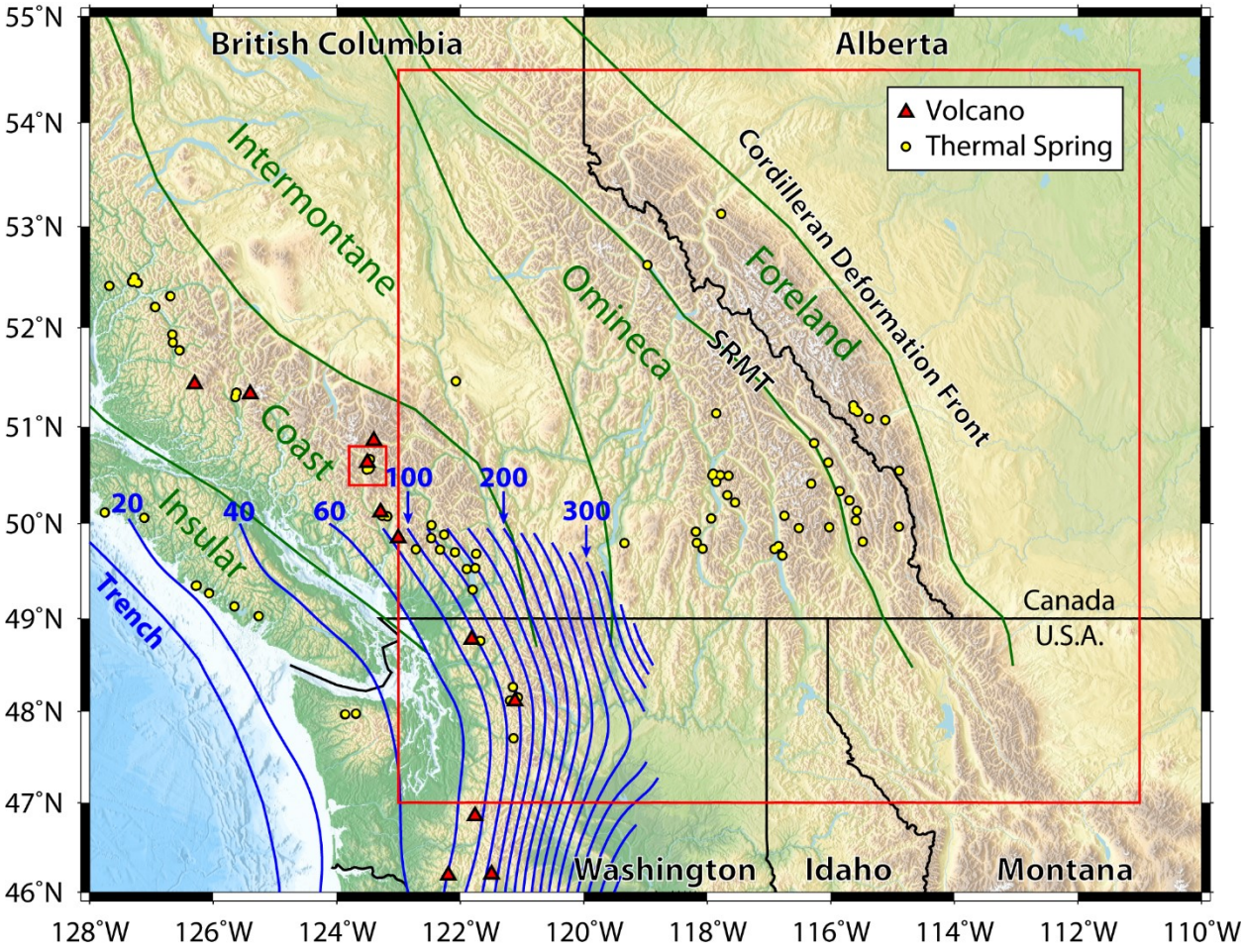

***Figure 2.2**: Map of southwestern Canada and northwestern U.S.A. Blue lines are contours of depth to the top of the subducted plate, in increments of 20 km (Hayes, 2018). Red triangles are volcanoes and yellow dots are thermal springs. Political boundaries (black lines), morphogeological boundaries (green lines), and study areas (red boxes) are also shown. SRMT = southern Rocky Mountain Trench.*

2.3. Canadian Cordillera

The Canadian Cordillera is an ~800 km wide and ~2,500 km long orogenic belt that covers much of BC and the Yukon, as well as some western parts of Alberta and the Northwest Territories. The Cordillera is widely regarded as an accretionary orogen, made up of several distinct terranes that were added to the North American margin throughout the Mesozoic and early Cenozoic. For simplicity, the Cordillera is often divided into five morphogeological belts based on bedrock type and geomorphology (Gabrielse et al., 1991). From west to east, they are: (1) the Insular belt, (2) the Coast belt, (3) the Intermontane belt, (4) the Omineca belt, and (5) the Foreland belt, as shown in Figure 1.8. Study Area #1 is in the Coast belt. Study Area #2 extends from the Coast belt to the Foreland belt and beyond.

The Insular belt is a region of moderate topography that encompasses Vancouver Island, Haida Gwaii, and the westernmost mainland of BC. Its bedrock is largely igneous, including extensive basalt flows and granitic intrusions. The Coast belt encompasses the high-elevation, extensively glaciated mountain range that runs the length of western BC and is dominantly made up of large plutonic complexes associated with the subduction that led to the Cretaceous to Eocene accretion of the Insular belt terranes. Modern continental arc volcanoes associated with the Cascadia subduction zone have developed on top of the Mesozoic plutonic complex. The Intermontane belt is an elevated plateau with subdued relief and is dominantly made up of island arc volcanic rocks and associated sedimentary sequences. The Omineca belt is a mountainous region dominantly composed of mid- to high-grade meta-sedimentary rocks, as well as numerous continental arc-type plutonic suites. The Foreland belt encompasses the rugged Canadian Rocky Mountains, which are composed of the largely unmetamorphosed but highly deformed sedimentary rocks that once formed the Laurentian (ancient North American) passive margin. The information in this paragraph was summarized from Gabrielse et al. (1991).

Accretion of the various exotic island-arc terranes of the Intermontane and Insular belts resulted in contractional deformation from the Jurassic to the Eocene, giving rise to the Canadian Cordillera. Following the cessation of orogenesis, the southern Cordillera underwent widespread crustal extension in the Eocene, which was accommodated on an array of normal faults, many of which run through Study Area #2 in southeastern BC (Parrish et al., 1988). Some of these Eocene-aged normal faults have been reactivated as dextral strike-slip faults in response to far-field stress from the active Cascadia subduction zone (Finley, 2020; Finley et al., 2022). The present-day deformation is especially relevant for understanding geothermal systems for two reasons: (1) extension provides a mechanism for crustal thinning and an increased geothermal gradient, and (2) recently active faults are more likely to be permeable conduits allowing convection of thermal water from depth to the surface. The southeastern Canadian Cordillera is the subject of Chapter 5.

2.4. Southern Rocky Mountain Trench

The study in Chapter 5 is centred on the Southern Rocky Mountain Trench (SRMT), and the faults that occur within and adjacent to it. These faults include: the SRMT fault, Purcell Thrust fault, Redwall fault, and Lussier fault. The SRMT fault occupies the SRMT for much of its length, though there are limited outcrop exposures of the fault itself. The fault dips steeply west and estimates of normal dip-slip displacement range from 2-10 km (Gal & Ghent, 1990;

McDonough & Simony, 1988; van der Velden & Cook, 1996). The across-fault continuity of several transverse features, both structural and stratigraphic, indicate that it does not exhibit significant strike-slip offset (McMechan & Thompson, 1989), though Finley (2020) suggested the possibility of post-Eocene dextral offset on the order of tens of kilometers. The Purcell Thrust fault is located within the SRMT from 51.5 °N (north of Golden, BC) to 50.5 °N (near Invermere, BC). This fault is regarded as an out-of-sequence thrust fault that developed during the last stages of Mesozoic compression. Notably, no thermal springs occur along SRMT where the Purcell Thrust occurs, suggesting this structure may not be conducive to fluid circulation. The Redwall and Lussier faults run parallel with and to the east of the SRMT, between the towns of Radium and Cranbrook, BC. These faults are not well-studied, and have variably been interpreted as dextral, sinistral, or thrust faults (Charlesworth, 1959; Foo, 1979; North & Henderson, 1954). Many thermal springs along the southern SRMT in fact coincide with these faults rather than the main SRMT fault, hence their inclusion in Chapter 5.

Thermal springs in the study area (Figure 2.2) include the Wolfenden, Radium, Fairmont, Red Rock, Lussier, Ram Creek, and Wildhorse hot springs near the SRMT (Allen et al., 2006; Grasby & Hutcheon, 2001). Aqueous geothermometry has indicated that the spring water reaches temperatures of ~40-100 °C, implying circulation depths of ~2-5 km (Grasby & Hutcheon, 2001). While these temperatures are on the lower limit of what can be used to efficiently produce electricity, there is interest in using these systems for direct-use geothermal heating (Tuya Terra Geo Corp., 2016).

Advancements have been made in our understanding of fault-hosted geothermal systems in the southeastern Canadian Cordillera (Finley, 2020); however, correlations with crustal-scale structures have yet to be made. Geophysical methods are needed to image tens of kilometers below the surface and electromagnetic methods are particularly useful because of their sensitivity to the presence of fluids.

2.5. The Mohorovičić discontinuity (Moho) and lithosphere-asthenosphere boundary (LAB)

The deeper lithospheric structure in Study Area #2 has previously been investigated using a variety of geophysical techniques, e.g., 2-D inversion of MT data (Rippe et al., 2013), multimode seismic waveform inversion (Schaeffer & Lebedev, 2014), Rayleigh wave tomography (Bao & Eaton, 2015), and finite-frequency seismic tomography (Chen et al.,

2018). Hyndman and Lewis (1999) summarized that the Moho is at 32-34 km depth in the southern Canadian Cordillera and 40-50 km depth in the adjacent craton. Bennett et al. (1975) modelled the Moho at 51-58 km depth near the SRMT. The Moho marks a sharp increase in seismic wave velocity with depth, but the contrast in composition and density do not necessarily lead to a coincident change in electric properties. Hence, electromagnetic methods are usually insensitive to the Moho. However, a large gradient in electrical resistivity was observed near the Moho beneath the Slave craton, a region with especially resistive crust (Jones & Ferguson, 2001).

If fluids are bounded by the Moho, its location may be inferred using electromagnetic methods. Deep crustal aqueous fluids tend to occur in the 400-700 °C temperature range (Hyndman & Shearer, 1989) and in the southern Canadian Cordillera, Moho temperatures are approximately 800-1000 °C (Currie & Hyndman, 2006); therefore, deep water is most likely to occur in the crust in the 10-30 km depth range. However, fluids in geothermal systems in the southern Canadian Cordillera have been interpreted to be meteoric in origin, circulating to depths less than 5 km (Grasby & Hutcheon, 2001). Water in the lower crust may be derived from dehydration of oceanic crust and sediments in subduction zones, and devolatilization of upwelling mantle (Hyndman & Shearer, 1989, and references therein).

The Cordilleran lithosphere is relatively thin, which is due, in part, to crustal extension and thinning in the Eocene. The lithosphere-asthenosphere boundary (LAB) in this region is at a depth of 60-70 km (Currie et al., 2023) as illustrated in Figure 2.3. Based on observed thermal conditions, such as high surface heat flow (~75 mW/m^2), vigorous convection in the asthenosphere is believed to occur (Currie, Wang, et al., 2004; Hyndman et al., 2005). A map of heat flow is shown in Figure 2.4. In southern BC, heat flow is lower (~40 mW/m^2) in the forearc, higher (~75 mW/m^2) in the backarc, and lower (~40 mW/m^2) above the adjacent craton (Currie, Wang, et al., 2004). In southwestern Alberta, the depth of the LAB increases to more than 180 km (Bao & Eaton, 2015), which is approximately three times the value observed in the backarc region. This thick lithosphere is part of the North American craton.

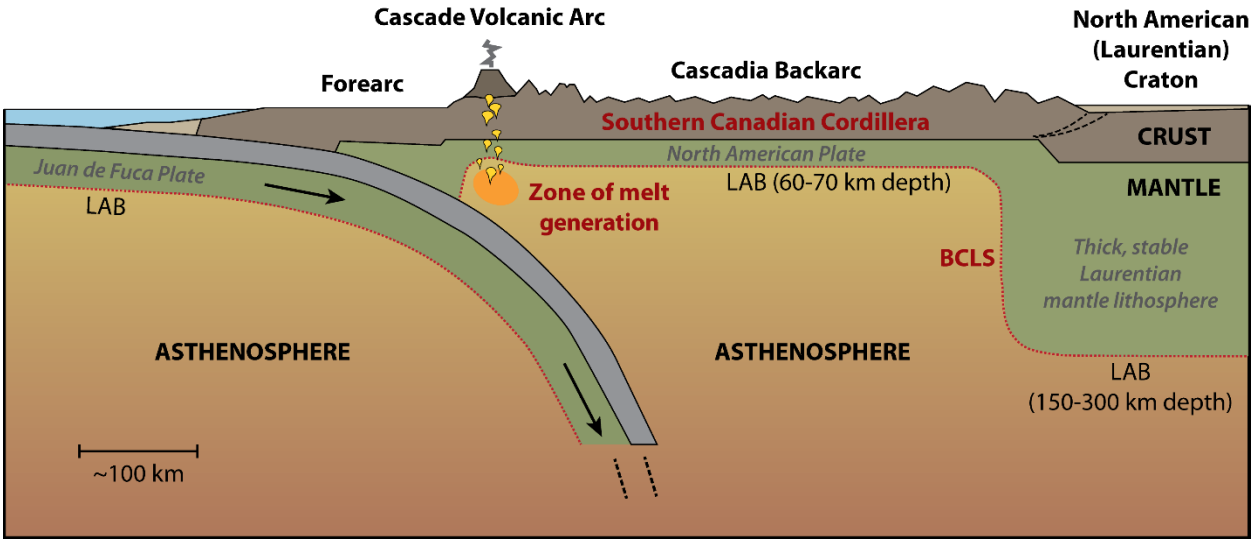

***Figure 2.3**: Schematic cross-section of southwestern Canada, modified from Hyndman et al. (2005). LAB = lithosphere-asthenosphere boundary and BCLS = backarc-craton lithosphere step. The LAB and BCLS are discussed in Chapter 6. The mantle lithosphere below the Cordillera (labelled North American plate) includes both Laurentian and Cordilleran lithosphere. The exact location and geometry (including faulting and deformation) of the mantle lithosphere transition is uncertain and beyond the scope of this thesis.*

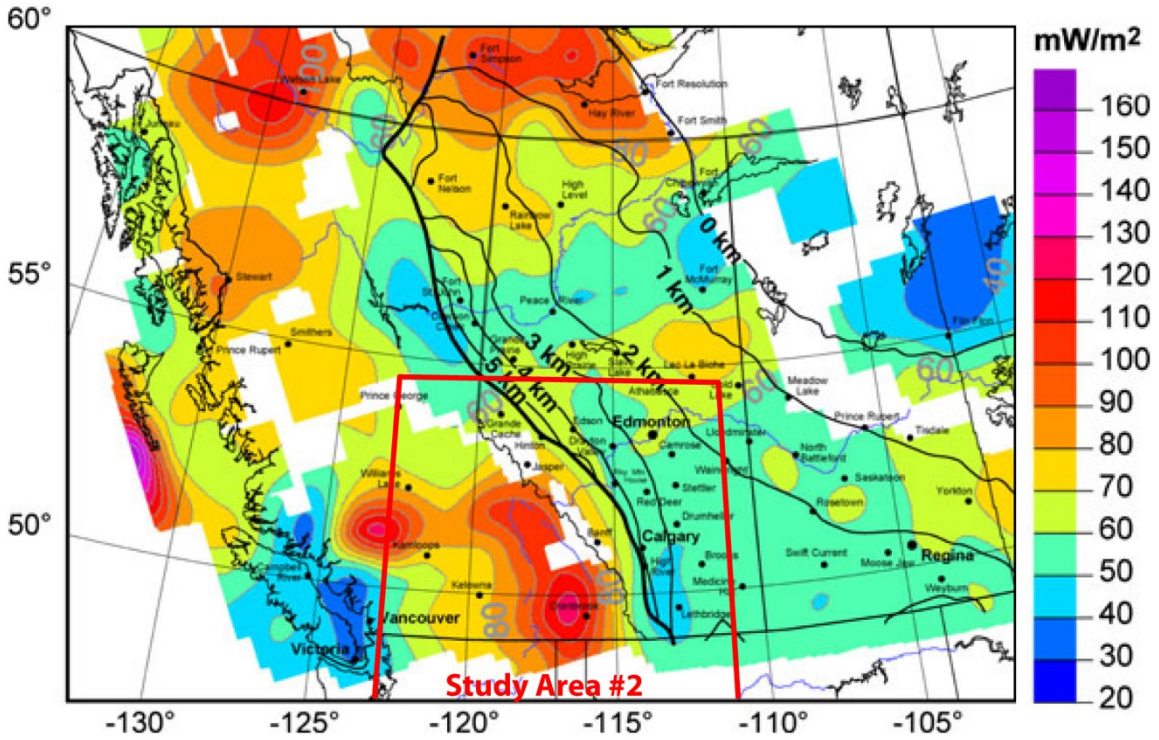

***Figure 2.4**: Averaged heat flow in western Canada, modified from Majorowicz and Grasby (2010b). Black contours indicate thickness of the Western Canada Sedimentary Basin (WCSB). Red lines show the location of Study Area #2. Within this study area, there is high heat flow in the Cordilleran region and lower heat flow in the WCSB region.*

2.6. The Western Canada Sedimentary Basin

The Western Canada Sedimentary Basin (WCSB) is a wedge of sedimentary rocks that thickens in a southwesterly direction from the Canadian shield to the Cordilleran foreland, where its thickness can exceed 6 km (Porter et al., 1982). In southern Alberta, it is ~6.5 km thick in the west and ~3.1 km in the east; and the general stratigraphy is Mesozoic to early Cenozoic siliciclastic rocks underlain by Paleozoic carbonate rocks (Lemieux, 1999).

Study Area #2 is centered on the Omineca belt with the Foreland belt to the east and the Intermontane belt to the west. There are many thermal springs in the southern Omineca belt, especially near the Purcell Thrust, Redwall, Rocky Mountain Trench, Purcell Trench and Columbia River faults (Grasby & Hutcheon, 2001). This prospective geothermal area is of interest, as is the regional tectonic framework of the entire study area, as discussed in Chapters 5 and 6.

2.7. Study areas

Study Area #1 surrounds Mount Meager in the Coast belt and is the subject of Chapter 4 (in the depth range 0-25 km). Study Area #2 spans an area of approximately 700 km × 700 km in southwestern Canada and is the subject of Chapter 5 (in the depth range 0-100 km) and Chapter 6 (in the depth range 0-400 km).

During my graduate program at the University of Alberta, I performed 48 days of fieldwork near Mount Meager (Study Area #1), 37 days of fieldwork in southeastern BC (Study Area #2), and 97 days of fieldwork at other locations not directly related to my PhD research, totalling 182 days. See Table A.2 in Appendix A for more details.

3. Electrical resistivity of Earth materials and electromagnetic geophysical methods

Electromagnetic (EM) geophysical methods provide information about subsurface electrical resistivity and related properties, such as electrical chargeability and magnetic permeability. Electrical resistivity is an important rock property that is often investigated during geothermal exploration, as well as in studies of volcanic systems and subduction zones. Resistivity is useful for these applications because of its sensitivity to the presence of fluids such as saline water and partial melt. This chapter introduces the concept of electrical resistivity and describes how it varies among common Earth materials, then provides a high-level discussion of classical electromagnetism. Frequency-domain EM geophysical methods are discussed, with a focus on the magnetotelluric (MT) method. Finally, this chapter concludes with a brief description of geophysical inverse theory and non-uniqueness.

3.1. Electrical resistivity of Earth materials

The propagation of EM signals in the Earth depends on electrical resistivity, electrical chargeability, dielectric permittivity, and magnetic permeability. Resistivity has the greatest effect and is the focus of this section.

3.1.1. Definition of electrical resistivity

To describe the movement of electric charge within a continuous medium, Ohm's law can be written in vector form as

$$\boldsymbol{J} = \sigma \boldsymbol{E} \tag{1}$$

where $\boldsymbol{J}$ is the current density in A/m^2, σ is the electrical conductivity in S/m, and $\boldsymbol{E}$ is the electric field strength in V/m. Electrical resistivity, ρ, is simply the reciprocal of electrical conductivity,

$$\rho = \frac{1}{\sigma} = \frac{\boldsymbol{E}}{\boldsymbol{J}} \tag{2}$$

and is measured in Ωm. Current flows in the direction of the electric field, so when the medium is isotropic, the resistivity is a scalar quantity. Throughout this thesis, vector quantities are written as bold symbols and scalar quantities as light (non-bold) symbols.

Electric charge is carried through Earth materials by electrons, ions, and electron holes (positively charged quasiparticles). In brine and molten rock, the charge carriers are ions. In igneous rocks, all three types of charge carrier may be present and minerals such as sulphides act as semiconductors. In sedimentary rocks, the grains have high resistivity and charge is carried by ions moving through pore fluids between grains and clay minerals along grain boundaries.

Electric current is defined as the amount of electric charge passing a given point in space per unit time, $I = \Delta q/\Delta t$. The ability of electric current to flow through a conductive medium is related to the mobility of the charge carriers, defined as the drift velocity per unit electric field, $\boldsymbol{\mu} = v/\boldsymbol{E}$. If a conductive pathway with cross-sectional area A contains n charge carriers per unit volume, each having charge q, then the current will be

$$I = \frac{\Delta q}{\Delta t} = \frac{nqAv\Delta t}{\Delta t} = nqAv \tag{3}$$

and the current density will be

$$\boldsymbol{J} = \frac{I}{A} = \frac{nqAv}{A} = nqv = nq\boldsymbol{\mu}\boldsymbol{E} \tag{4}$$

Therefore, the electrical conductivity is $\sigma = nq\mu$ and the electrical resistivity is $\rho = 1/nq\mu$. This is as expected since an increase in mobile charge carriers will increase the conductivity (and decrease the resistivity).

3.1.2. Single-phase systems

Materials with only one phase will be considered first as they are simple, and then multi-phase systems will be considered in Section 3.1.5. The resistivity values of a selection of common materials, in their pure forms, are listed in Table 3.1.

Copper and the other metals listed in Table 3.1 are conductors, with resistivity values in the range 10^{-8}-10^{-7} Ωm. Modern humans interact with electric current on a near-continuous basis, from the lights and appliances in our homes to the phones in our pockets and the computers that underpin much of present-day society. When it comes to the electrical systems that connect and sustain our civilization, copper is ubiquitous. This is because it is relatively affordable and has low resistivity.

Carbon in the form of graphite is also a conductor, with resistivities in the range 10^{-6}-10^{-2} Ωm. Carbon in the form of diamond, however, has very high resistivity, around 10^{16} Ωm. In

graphite, each carbon atom bonds to three other carbon atoms in a sheet-like structure, leaving one valence electron free and these electrons can move across the sheets. In diamond, on the other hand, each carbon atom bonds to four other carbon atoms in a tetrahedral structure, leaving no free valence electrons. This causes graphite to be soft and electrically conductive, and diamond to be hard and electrically resistive.

Common rock-forming minerals are also resistive. For example, pure silicon dioxide (quartz) has a resistivity around 10^{15} Ωm. When other oxides are added (e.g., Al_2O_3, Na_2O, K_2O, etc.) to form feldspars, the resistivity is lower, around 10^9-10^{11} Ωm. These crystalline minerals have strong lattice structures with very few charge carriers, and these limited charge carriers have low mobility. Resistivity typically decreases as temperature increases because the additional kinetic energy can increase the mobility of the charge carriers.

Pure water is also a resistor, with a resistivity around 10^5 Ωm. H_2O molecules are electrically neutral, so pure water has no net charge and no charge carriers. However, H_2O is a polar molecule, giving water a high dielectric permittivity. With the addition of dissolved salts, ionic conduction causes water to become electrically conductive. This is described in detail in the following section.

Table 3.1*: Electrical resistivity of some pure materials at 20°C, along with quartz at 25°C and a range of feldspars.*

Pure Material at 20°C (unless stated otherwise)	**Resistivity (Ωm)**	**Reference**
Silver	1.62×10^{-8}	Halliday and Resnick (2014)
Copper	1.69×10^{-8}	Halliday and Resnick (2014)
Gold	2.35×10^{-8}	Halliday and Resnick (2014)
Aluminum	2.75×10^{-8}	Halliday and Resnick (2014)
Iron	9.68×10^{-8}	Halliday and Resnick (2014)
Graphite (Carbon) parallel to basal plane	$2.5\text{-}5.0 \times 10^{-6}$	Pierson (1993)
Graphite (Carbon) perpendicular to basal plane	3×10^{-3}	Pierson (1993)
Water	2.385×10^5	Light et al. (2004)
Feldspars (62.7-66.5% SiO_2 + 16.9-21.9% Al_2O_3)	10^9-10^{11} (approximate)	Bakhterev (2008)
Quartz (Silicon Dioxide) at 25°C	$2.0\text{-}3.6 \times 10^{15}$	Srivastava et al. (1985)
Diamond (Carbon)	10^{16} (approximate)	Halliday and Resnick (2014)

3.1.3. Resistivity of saline aqueous fluids

Saline aqueous fluids, also known as brines, are common in the Earth's crust and they are usually electrically conductive. Sinmyo and Keppler (2017) used empirical and theoretical considerations to derive an equation for the electrical conductivity of NaCl-bearing aqueous fluids,

$$\log(\sigma) = -1.7060 - \frac{93.78}{T} + 0.8075\log(c) + 3.0781\log(d) + \log(\Lambda_0) \quad (5)$$

where σ is the conductivity in S/m, T is the temperature in K, c is the NaCl concentration in wt.%, d is the density of pure water in g/cm^3 at a given temperature and pressure, P, and

$$\Lambda_0 = 1{,}573 - 1{,}212\,d + \frac{537{,}062}{T} - \frac{208{,}122{,}721}{T^2} \quad (6)$$

is the molar conductivity of NaCl in water at infinite dilution in S·cm^2/mol. This equation is valid for 100 °C ≤ T ≤ 800 °C, P ≤ 1 GPa, and 0.3 ≤ d < ~1.3 g/cm^3. Guo and Keppler (2019) derived a high-pressure version of equation (5),

$$\log(\sigma) = -0.919 - \frac{872.5}{T} + 0.852\log(c) + 7.61\log(d) + \log(\Lambda_0) \quad (7)$$

which is valid for 300 °C ≤ T ≤ 900 °C, 1 GPa < P ≤ 5 GPa, and 0.3 ≤ d < ~1.4 g/cm^3. The resistivity is therefore a function of temperature and salinity, as well as either density or pressure. The most abundant dissolved salt in fluid inclusions is usually NaCl, and KCl produces similar resistivity values (Nesbitt, 1993); therefore, these relationships are good approximations for typical crustal fluids. Acidity can also affect resistivity; however, metamorphic crustal fluids are usually restricted to a small range of pH values (Nesbitt, 1993).

The density of pure water (d in the equations above) can be found using an equation of state (e.g., Zhang and Duan, 2005) or tabulated values (e.g., Anderson et al., 1991). At common subsurface conditions, it increases with increasing pressure due to compression and decreases with increasing temperature due to expansion (Figure 3.1). Temperature and pressure both increase with depth in the Earth, which has a moderating effect on the density variation of water with depth, since one causes expansion and the other causes compression.

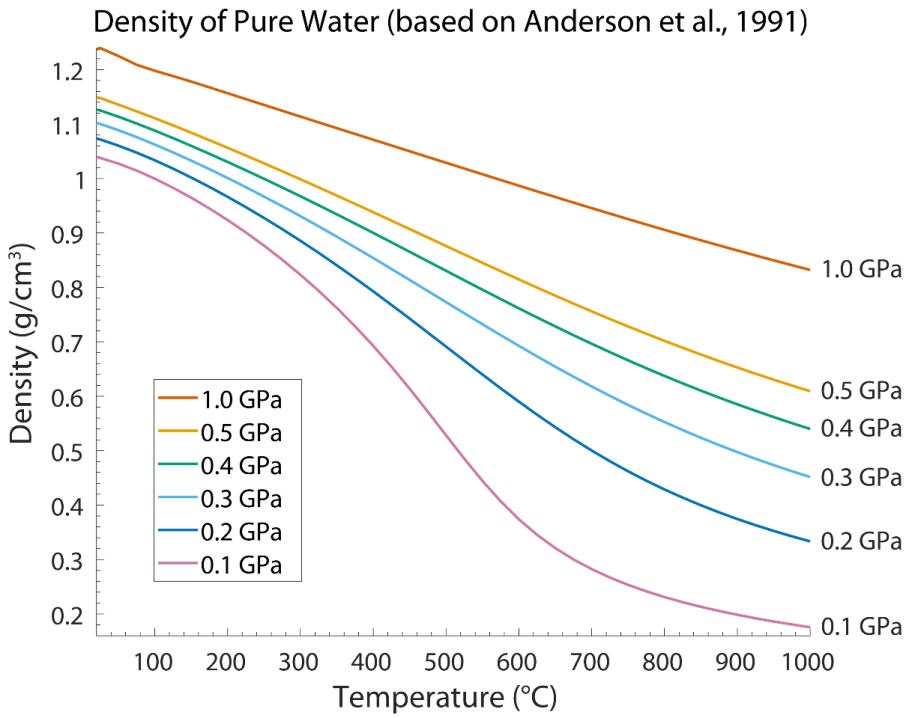

Figure 3.1*: The density of pure water as a function of temperature at six pressures, from the tabulated values of Anderson et al. (1991).*

The resistivity of NaCl-bearing aqueous fluids as a function of temperature and NaCl concentration, according to equation (5) at either constant density or constant pressure, is shown in Figure 3.2. At constant density, the resistivity decreases with increasing salinity and with increasing temperature. At constant pressure, the resistivity decreases with increasing salinity; however, it only decreases with increasing temperature up to a certain point, then it increases. This threshold temperature is ~250 °C at 0.1 GPa, ~350 °C at 0.5 GPa, and ~450 °C at 1.0 GPa. This behaviour occurs because if the temperature is increased without increasing the pressure, the corresponding decrease in density causes an increase in resistivity. Beyond the threshold temperature, this increase is greater than the decrease in resistivity associated with the increase in temperature, i.e., the increase in molecular kinetic energy and ion mobility.

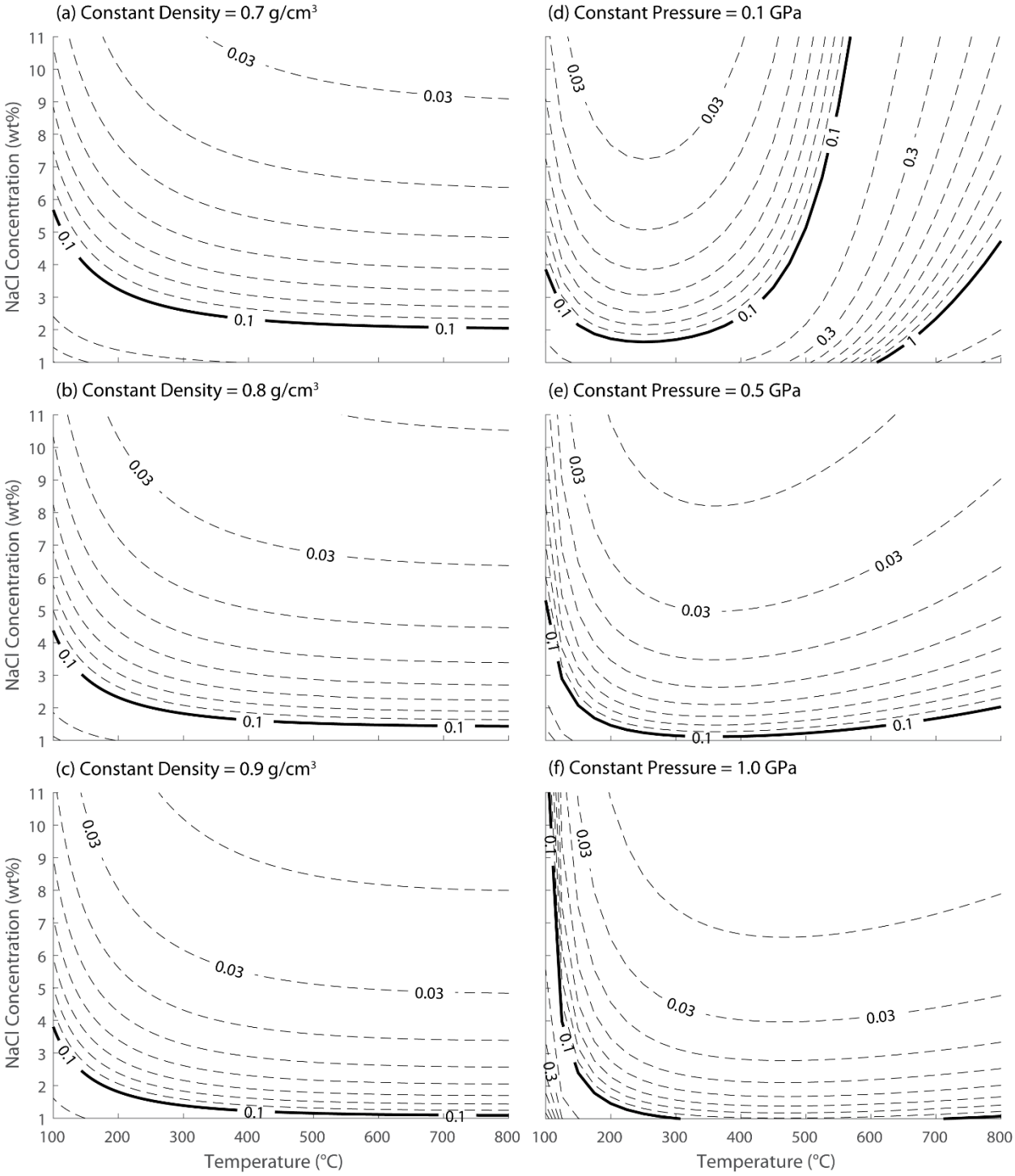

***Figure 3.2**: Resistivity (contours in Ωm) of NaCl-bearing aqueous fluids (brines) at 100-800 °C (Sinmyo & Keppler, 2017). (a-c) Calculations at constant density. (d-f) Calculations at constant pressure.*

3.1.4. Resistivity of silicate melts

Magma is a mixture of conductive melt and resistive grains, and the melt portion is the focus of this section. The concentration and mobility of ions is the primary factor affecting the resistivity of silicate melts, and one or two ionic species, those with the highest mobility, e.g., Na^+, dominate the electrical conductivity (Zhang et al., 2021). Melt resistivity decreases with increasing temperature and with increasing water content, due to the increased mobility of charge carriers (Zhang et al., 2021). In anhydrous melts, Na^+ is the dominant charge carrier; in hydrous melts, the mobility of K^+, Mg^{2+} and Ca^{2+} is increased, and they have a more significant charge carrying role (Zhang et al., 2021). Melt resistivity increases with increasing pressure, but this is often a relatively small effect; the strongest pressure dependence occurs in highly polymerized melts (Zhang et al., 2021).

The resistivity of silicate melts has been measured in laboratories for a range of compositions and experimental conditions (Gaillard, 2004; Guo et al., 2016, 2017; Laumonier et al., 2015, 2017, 2019; Li et al., 2020; Ni et al., 2011). The melt compositions used in these experiments are shown in Figure 3.3, and the resulting mathematical models are shown in Figure 3.4, for a range of temperatures, pressures, and water contents. Temperature and water content both have a significant effect on melt resistivity, as does the alkali content (Na_2O+K_2O). Silica content (SiO_2) has a less pronounced effect, and pressure has the weakest effect.

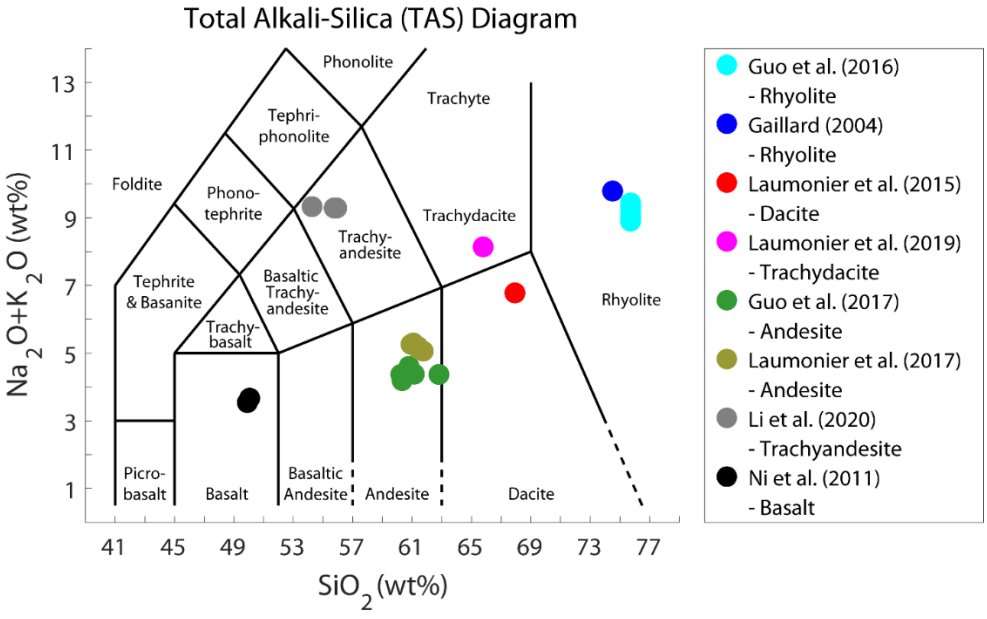

***Figure 3.3**: Total alkali-silica diagram with the chemical classification of Le Bas et al. (1986, 1992) and the chemical composition of rocks used in the melt conductivity experiments of Guo et al. (2016, 2017), Gaillard (2004), Laumonier et al. (2015, 2017, 2019), Li et al. (2020), and Ni et al. (2011).*

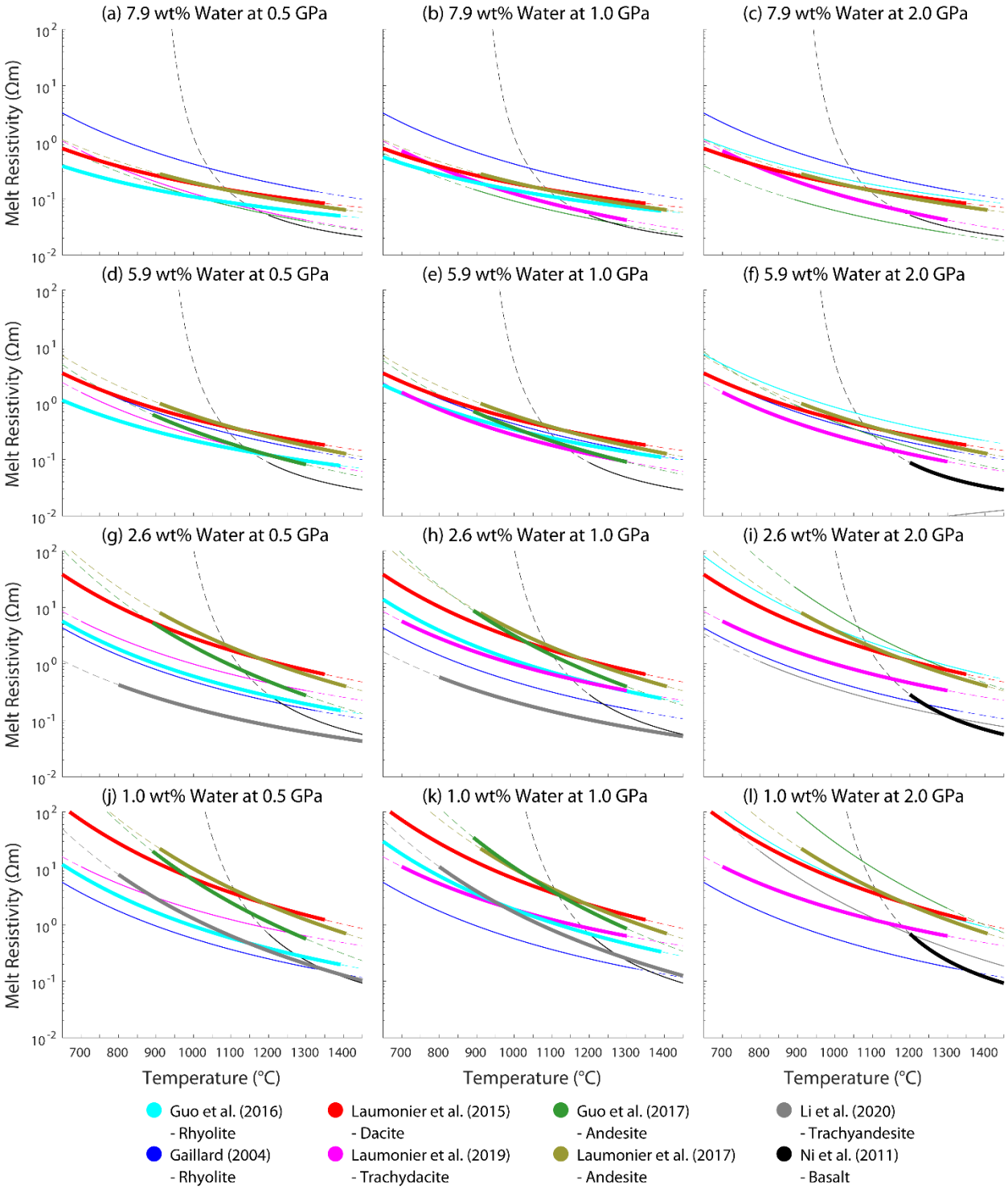

***Figure 3.4**: Resistivity of hydrous silicate melts (Gaillard, 2004; Guo et al., 2016, 2017; Laumonier et al., 2015, 2017, 2019; Li et al., 2020; Ni et al., 2011) using the colour scheme from Figure 3.3. Thick lines indicate that the temperature, pressure and water content are all within the experimental ranges. Thin lines indicate that the pressure and/or water content are outside the experimental range. Dashed lines indicate that the temperature is outside the experimental range.*

3.1.5. Mixing laws and multi-phase systems

Many important Earth materials are a mixture of a high resistivity phase and a low resistivity phase, e.g., magma bodies and geothermal reservoirs. A mixing law is a way of calculating the average (bulk) resistivity of the various phases and a number have been developed over the years. They can be used to estimate the bulk resistivity of a material containing multiple phases, each having a different resistivity. For example, it is often useful to model a rock as a simple system of two components: (1) a solid phase with high resistivity and (2) a fluid phase with low resistivity.

Archie's law (Archie, 1942) describes an ideal system where rock grains are assumed to have infinite resistivity and pores contain a conductive fluid. Its general form may be written as

$$\rho = \rho_w S^{-n} \phi^{-m} \tag{8}$$

where ρ is the bulk resistivity of the rock, ρ_w is the resistivity of the pore fluid, S is the fluid saturation, n is the saturation exponent, ϕ is the porosity, and m is the cementation exponent. S and ϕ have values in the range 0-1. The exponents, m and n, are empirically derived and typically have values in the range 1-2.

Glover et al. (2000) modified Archie's law to include two conducting phases:

$$\sigma = \sigma_1 (1 - \phi_2)^{(\ln(1-\phi_2^m)/\ln(1-\phi_2))} + \sigma_2 \phi_2^m \tag{9}$$

where σ is the bulk conductivity of the rock, σ_1 is the conductivity of the first phase, σ_2 is the conductivity of the second phase, ϕ_2 is the volume fraction of the second phase, and m is the cementation exponent of the second phase. In the limit $\sigma_1 \to 0$, i.e., infinite resistivity, equation (9) becomes the classic Archie's law (equation (8)) with $\rho_w = 1/\sigma_2$ and S = 1.

The Hashin-Shtrikman upper and lower bounds are

$$\sigma_+ = \sigma_2 \left[1 - \frac{3(1-\phi_2)(\sigma_2 - \sigma_1)}{3\sigma_2 - \phi_2(\sigma_2 - \sigma_1)} \right] \tag{10}$$

and

$$\sigma_- = \sigma_1 \left[1 + \frac{3\phi_2(\sigma_2 - \sigma_1)}{3\sigma_1 + (1-\phi_2)(\sigma_2 - \sigma_1)} \right] \tag{11}$$

respectively (Glover et al., 2000; Hashin & Shtrikman, 1962). The lower bound of bulk resistivity is $\rho_- = 1/\sigma_+$ and is denoted HS−. The upper bound of bulk resistivity is $\rho_+ = 1/\sigma_-$ and is denoted HS+. HS− is similar to resistors connected in parallel and HS+ is similar to

resistors connected in series (Figure 3.5). Equations (8), (9), (10), and (11) are plotted in Figure 3.6.

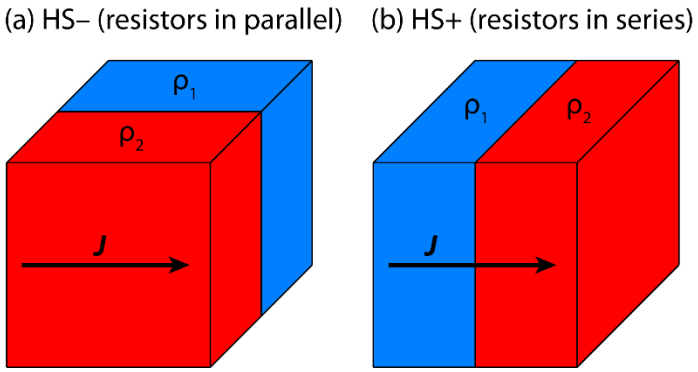

***Figure 3.5**: (a) Resistors connected in parallel. (b) Resistors connected in series.*

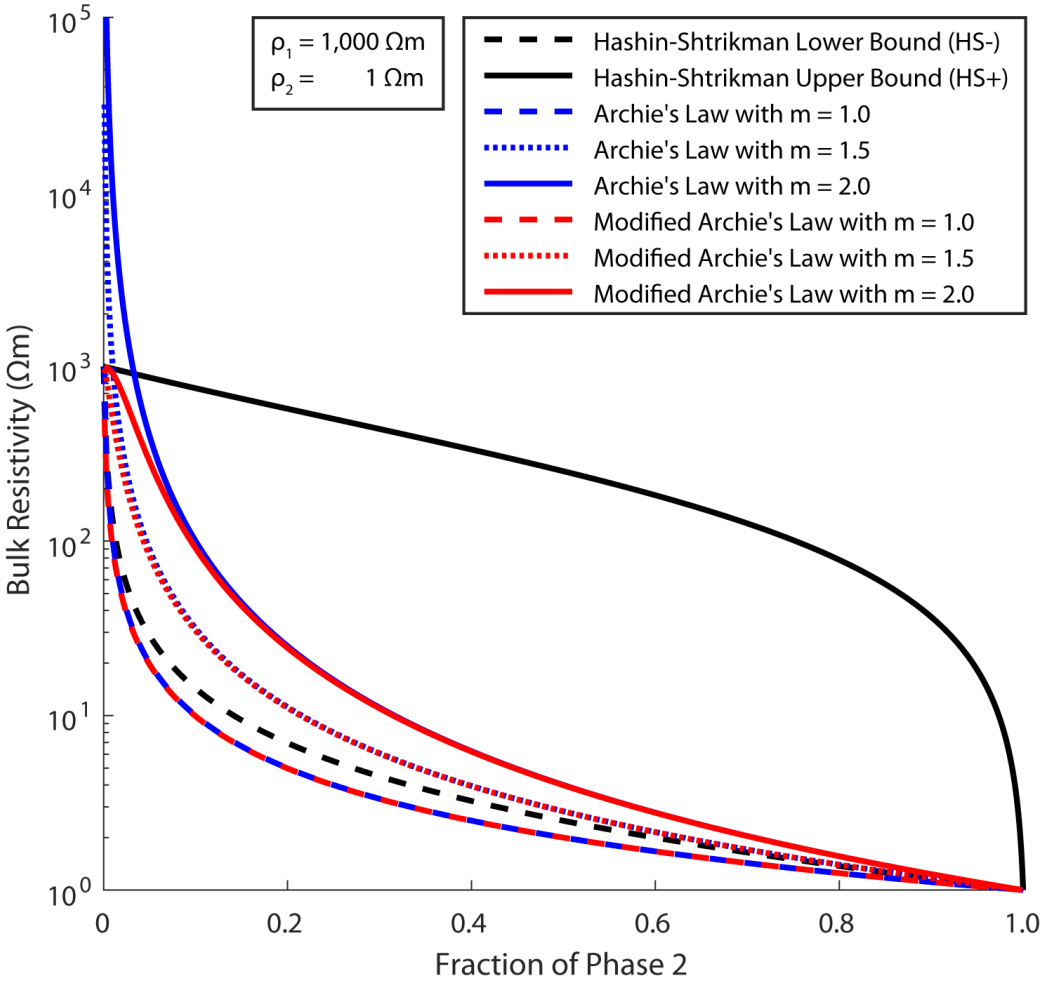

***Figure 3.6**: Theoretical bulk resistivity of a two-phase system, calculated using different mixing laws. Phase 1 has a resistivity of 1,000 Ωm and phase 2 has a resistivity of 1 Ωm. Archie's Law gives an unphysical bulk resistivity at low fractions when m > 1.*

In Chapters 4 and 5, equations (5) and (9) are used to calculate the bulk resistivity of brine-containing crustal rocks. These rocks include upper-crustal rocks in a volcanic setting (Chapter 4) and mid- and lower-crustal rocks in a backarc setting (Chapter 5). Calculations such as these, made possible by recent advancements such as the results of Sinmyo and Keppler (2017), are key to interpreting resistivity models in tectonic, volcanic and geothermal research. In Chapters 4 and 5, the melt resistivity values described in Section 3.1.4 are used to calculate the bulk resistivity of partial melts, using equation (9).

3.2. Maxwell's equations and the propagation of electromagnetic fields

Before EM geophysical methods are discussed, a brief overview of classical electromagnetism is required. In this section, Maxwell's equations are presented and the propagation of EM fields in conductive media is discussed. This is important because the Earth is electrically conductive. It is also important to note that Section 3.2 assumes a uniform, isotropic medium. In Section 3.4, additional assumptions and boundary conditions are used to derive the equations of the magnetotelluric method. Anisotropic media are not considered in this chapter.

3.2.1. Maxwell's equations

Classical electromagnetism was developed in the 19th century as a series of physical laws, which were eventually combined into a unified set of equations by Maxwell (1873). They describe the relationships between electric charge, magnetism, and electromagnetic fields.

Gauss's law describes the divergence of an electric field,

$$\nabla \cdot \boldsymbol{E} = \frac{Q}{\varepsilon_0} \tag{12}$$

where $\boldsymbol{E}$ is the electric field strength in V/m, Q is the charge density in C/m^3 and ε_0 is the dielectric permittivity of free space in F/m. This law quantifies how static electric charges generate electric fields.

Gauss's law for magnetism describes the divergence of a magnetic field,

$$\nabla \cdot \boldsymbol{B} = 0 \tag{13}$$

where $\boldsymbol{B}$ is the magnetic flux density in T. The magnetic field strength, $\boldsymbol{H}$ in A/m, is equal to the magnetic flux density divided by the magnetic permeability, $\boldsymbol{B}/\mu$. This law states that

magnetic monopoles, the magnetic analog of electric charges, do not exist. North and south magnetic poles exist only as dipoles, never in isolation.

The Maxwell-Faraday equation, derived from Faraday's law of induction, describes the curl of an electric field,

$$\nabla \times \boldsymbol{E} = -\frac{\partial \boldsymbol{B}}{\partial t} \tag{14}$$

where $\partial/\partial t$ is the partial derivative with respect to time. This law states that a time-varying magnetic field will generate an electric field, and most of our electricity is generated using this principle.

Ampère's law describes the curl of a magnetic field,

$$\nabla \times \boldsymbol{B} = \mu_0 \boldsymbol{J} \tag{15}$$

where μ_0 is the magnetic permeability of free space. This law quantifies how moving electric charges (electric current) generate magnetic fields.

Maxwell added a displacement current term to Ampère's law,

$$\nabla \times \boldsymbol{B} = \mu_0 \left(\boldsymbol{J} + \varepsilon_0 \frac{\partial \boldsymbol{E}}{\partial t} \right) \tag{16}$$

then, using equation (1), equation (16) becomes

$$\nabla \times \boldsymbol{B} = \mu_0 \sigma \boldsymbol{E} + \mu_0 \varepsilon_0 \frac{\partial \boldsymbol{E}}{\partial t} \tag{17}$$

where the first term on the right-hand side represents the conduction current and the second term represents the displacement current. The addition of a displacement current term to Ampère's law made it consistent with charge conservation, and it helped unify the separate phenomena of electricity and magnetism into a unified explanation of electromagnetism.

Quantum electrodynamics (QED), the relativistic quantum field theory of electrodynamics, was developed in the 20th century by Paul Dirac, Richard Feynman, and many others. QED and classical electromagnetism together provide a complete description of the interactions between light (EM waves) and matter. Although QED is a significant and important achievement, it is not necessary for the derivation or use of electromagnetic geophysical methods. Only classical electromagnetism is considered in this thesis.

3.2.2. Propagation of electromagnetic fields in a conductive medium such as the Earth

Maxwell's equations can be used to describe the propagation of an EM field in a medium with conductivity σ, magnetic permeability μ, and dielectric permittivity ε. If we assume these three properties are time invariant, and that there are no free electric charges (i.e., $Q = 0$), equations (14) and (17) can be used to derive the Laplacian of the electric field,

$$\nabla^2 \boldsymbol{E} = \mu\sigma\frac{\partial \boldsymbol{E}}{\partial t} + \mu\varepsilon\frac{\partial^2 \boldsymbol{E}}{\partial t^2} \tag{18}$$

where the first term on the right-hand side represents the conduction current and the second term represents the displacement current. If the conduction current is much larger than the displacement current (i.e., $\sigma >> \omega\varepsilon$), equation (18) becomes a diffusion equation,

$$\nabla^2 \boldsymbol{E} = \mu\sigma\frac{\partial \boldsymbol{E}}{\partial t} \tag{19}$$

and if the displacement current is much larger than the conduction current (i.e., $\omega\varepsilon >> \sigma$), equation (18) becomes a wave equation,

$$\nabla^2 \boldsymbol{E} = \mu\varepsilon\frac{\partial^2 \boldsymbol{E}}{\partial t^2} \tag{20}$$

where the wave speed is $\sqrt{\mu\varepsilon}$. For $\mu = \mu_0 = 1.256637\times10^{-6}$ N/A^2 and $\varepsilon = \varepsilon_0 = 8.854188\times10^{-12}$ F/m, the wave speed is 2.997925×10^{8} m/s, which is the speed of light in vacuum.

3.2.3. Electromagnetic fields in the frequency domain

If we assume EM fields with a harmonic time variation at an angular frequency, $\omega = 2\pi f$, we can apply the separation of variables technique to the electric field,

$$\boldsymbol{E}(x,y,z,t) = \boldsymbol{E}_0(x,y,z)e^{i\omega t} \tag{21}$$

where e is Euler's number and i is the unit imaginary number. If we use this electric field, equation (18) becomes

$$\nabla^2 \boldsymbol{E}_0 e^{i\omega t} = \mu\sigma(i\omega)\boldsymbol{E}_0 e^{i\omega t} + \mu\varepsilon(i\omega)^2 \boldsymbol{E}_0 e^{i\omega t} \tag{22}$$

and simplifies to an equation without temporal dependence,

$$\nabla^2 \boldsymbol{E}_0(x,y,z) = i\omega\mu\sigma\boldsymbol{E}_0(x,y,z) - \omega^2\mu\varepsilon\boldsymbol{E}_0(x,y,z) \tag{23}$$

where the first term on the right-hand side represents the conduction current and the second term represents the displacement current. The ratio of displacement current to conduction current is

$$\frac{I_{disp}}{I_{cond}} = \frac{\omega^2 \mu \varepsilon E_0}{\omega \mu \sigma E_0} = \frac{\omega \varepsilon}{\sigma} = 2\pi f \varepsilon \rho \tag{24}$$

and it can be used to illustrate which type of current is dominant at different frequencies and resistivities, as shown in Figure 3.7. Displacement current is dominant when frequency is in the MHz and GHz ranges, and resistivity is relatively high. Conduction current is dominant at lower frequency and lower resistivity values, covering a large fraction of Figure 3.7.

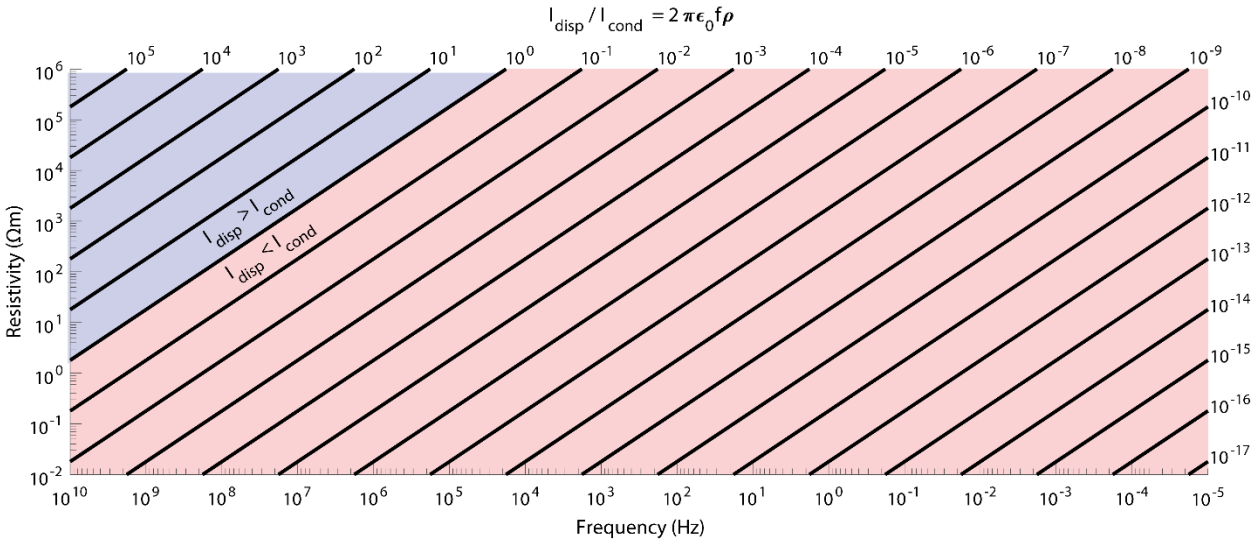

Figure 3.7*: Black lines are contours of the ratio of displacement current to conduction current, as a function of frequency and resistivity. In the blue region, $I_{disp} > I_{cond}$. In the red region, $I_{cond} > I_{disp}$..*

3.3. Frequency-domain electromagnetic geophysical methods

When a time-varying signal is measured, the resulting data are called a time series. This time series is a function of time, $s(t)$, and one can say that $s(t)$ is the measured signal in the time domain. This function can be represented as a sum of sinusoidal functions called a Fourier series,

$$s(t) = a_1 s_1(t) + a_2 s_2(t) + \cdots + a_n s_n(t) = \sum_{i=1}^{n} a_i s_i(t) \tag{25}$$

where each term has a Fourier coefficient, a_i, and a sine or cosine function, s_i. Each term represents a single frequency, f, so you can transform the time series into a function of frequency, $s(f)$. One can say that $s(f)$ is the measured signal in the frequency domain.

Frequency-domain EM geophysical methods use low-frequency EM signals (radio waves) to image subsurface resistivity. Ground-penetrating radar (GPR) uses the highest frequencies

among these methods, typically radio waves in the 10^6-10^9 Hz frequency band (Figure 3.8). At these frequencies, most of the signal energy propagates according to an EM wave equation, especially when the shallow subsurface is resistive (Figure 3.7 and Figure 3.8). Consequently, this method relies on reflection and refraction of radio waves at material interfaces, similar to the seismic waves used in seismic geophysical methods. GPR is particularly useful in studies of glaciers, ice sheets, fresh groundwater, soils, and archaeological sites (Jol, 2009).

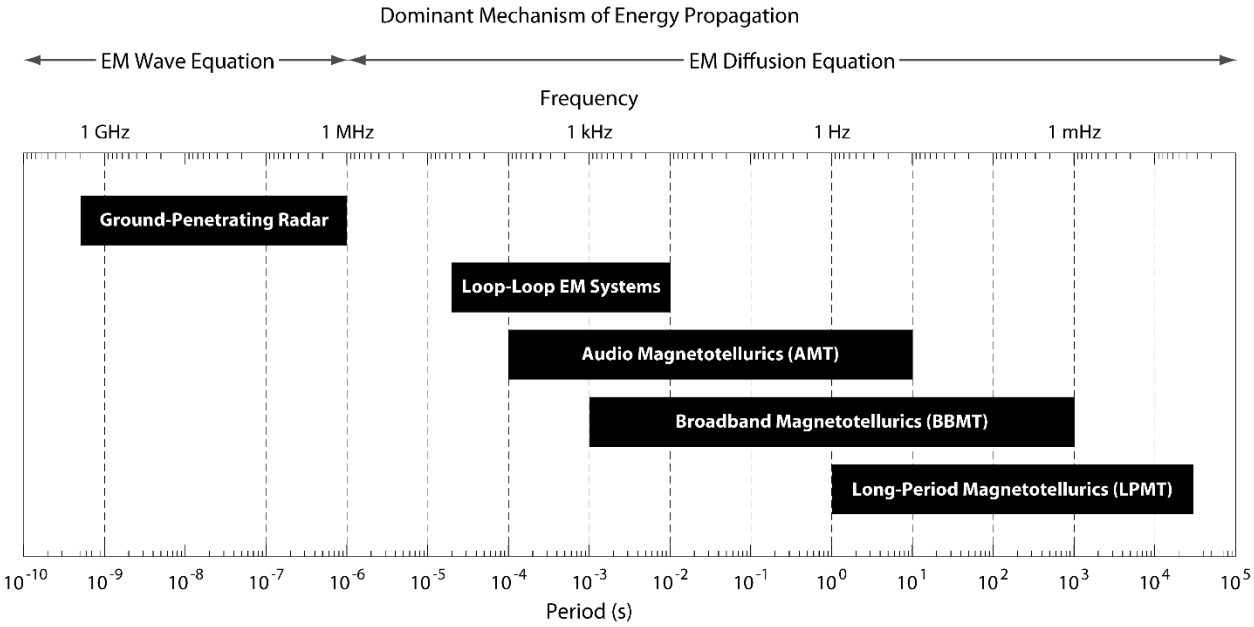

Figure 3.8*: Frequency ranges of common frequency-domain electromagnetic geophysical methods.*

Other common frequency-domain EM methods use radio waves in the 10^{-5}-10^5 Hz frequency range (Figure 3.8). At these frequencies, most of the signal energy propagates in the Earth according to an EM diffusion equation (Figure 3.7 and Figure 3.8). Loop-loop EM systems use an EM transmitter and an EM receiver, and they can be ground-based or airborne. The transmitter consists of a current-carrying loop which generates a primary magnetic field, according to Ampère's law. The primary magnetic field induces electric (eddy) currents in the conductive subsurface, according to Faraday's law, which in turn generate secondary magnetic fields. The receiver is a second loop, in which time variations of the total magnetic field induce an electromotive force (voltage). The induced current carries information about the secondary magnetic field, which in turn carries information about the resistivity of the subsurface. A cartoon illustrating this process is shown in Figure 3.9. This method is used to image the upper 100–1,000 m and is particularly useful in mineral exploration, geotechnical surveys, groundwater studies, and permafrost studies.

The magnetotelluric (MT) method uses natural electromagnetic signals to image the resistivity of the subsurface. It is categorized into three types based on the frequency range used: audio magnetotellurics (AMT), broadband magnetotellurics (BBMT), and long-period magnetotellurics (LMT), as illustrated in Figure 3.8. The theoretical foundations of the MT method were developed by Rikitake (1948), Tikhonov (1950), and Cagniard (1953). Detailed descriptions of the method were given by Simpson and Bahr (2005) and Chave and Jones (2012). The following section provides a condensed description of the MT method.

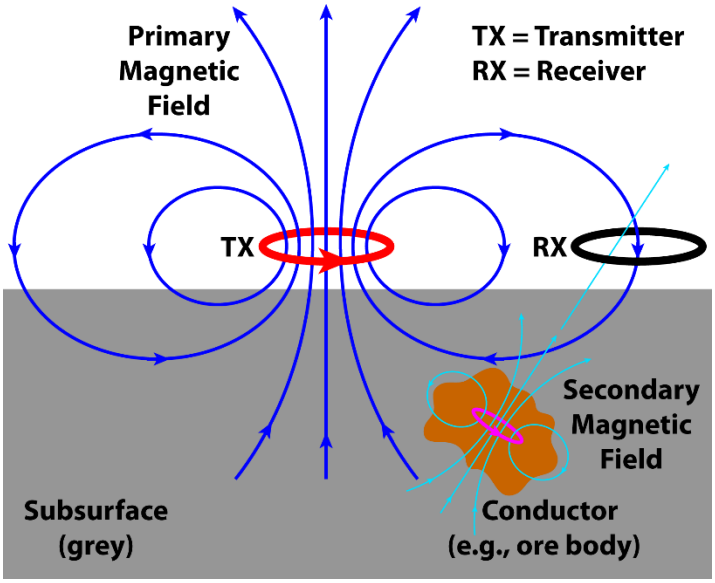

***Figure 3.9**: Cartoon schematic of a loop-loop EM system showing the primary current (red), primary magnetic field (blue), induced current (magenta), secondary magnetic field (cyan), and receiver loop (black).*

3.4. The magnetotelluric method

3.4.1. General concepts and one-dimensional resistivity structure

The MT method measures electric field strength (***E***) and magnetic field strength (***H***) time series at the surface of the Earth. These time series data are converted using Fourier analysis to frequency-domain responses which describe the impedance of the Earth. This thesis uses a coordinate system where the x-direction is north, the y-direction is east, and the z-direction is down.

Since MT uses low frequencies (Figure 3.8), we can ignore the displacement current (Figure 3.7). Therefore, equation (23) becomes

$$\nabla^2 \boldsymbol{E}_0(x,y,z) = i\omega\mu\sigma \boldsymbol{E}_0(x,y,z) \tag{26}$$

If we assume an electric field that is polarized in the *x*-direction (i.e., $\boldsymbol{E}_0 = E_x$), we can further simplify this equation to

$$\nabla^2 E_x - i\omega\mu\sigma E_x = \frac{\partial^2 E_x}{\partial x^2} + \frac{\partial^2 E_x}{\partial y^2} + \frac{\partial^2 E_x}{\partial z^2} - i\omega\mu\sigma E_x = 0 \tag{27}$$

which is a second-order partial differential equation. Now, if we also assume the signal is planar (i.e., only varies in the *z*-direction), equation (27) simplifies to an ordinary differential equation (ODE):

$$\frac{d^2 E_x}{dz^2} - i\omega\mu\sigma E_x = 0 \tag{28}$$

If we let $E_x(z) = Ae^{kz}$, a trial solution with an exponential form, equation (28) becomes

$$\frac{d^2 Ae^{kz}}{dz^2} - i\omega\mu\sigma Ae^{kz} = k^2 Ae^{kz} - i\omega\mu\sigma Ae^{kz} = 0 \tag{29}$$

where *A* is a constant and

$$k = \sqrt{i\omega\mu\sigma} = \pm(1-i)\sqrt{\frac{\omega\mu\sigma}{2}} \tag{30}$$

Therefore, a general solution to the ODE (equation (28)) is

$$\begin{aligned} E_x(z) &= A_1 e^{(1-i)\sqrt{\frac{\omega\mu\sigma}{2}}z} + A_2 e^{-(1-i)\sqrt{\frac{\omega\mu\sigma}{2}}z} \\ &= A_1 e^{\sqrt{\frac{\omega\mu\sigma}{2}}z} e^{-i\sqrt{\frac{\omega\mu\sigma}{2}}z} + A_2 e^{-\sqrt{\frac{\omega\mu\sigma}{2}}z} e^{i\sqrt{\frac{\omega\mu\sigma}{2}}z} \end{aligned} \tag{31}$$

E_x must tend to a real limit as *z* tends to infinity, where the source of the signal is at z < 0, therefore A_1 must be zero. At *z* = 0, $E_x = A_2 e^0 = A_2$. This is the electric field strength at the surface, so let us call it E_s. Given these two boundary conditions, there is now a specific solution to the ODE (equation (28)):

$$\begin{aligned} E_x(z) &= E_s e^{-\sqrt{\frac{\omega\mu\sigma}{2}}z} e^{i\sqrt{\frac{\omega\mu\sigma}{2}}z} \\ &= E_s e^{-\sqrt{\frac{\omega\mu\sigma}{2}}z} \left[\cos\left(\sqrt{\frac{\omega\mu\sigma}{2}}z\right) + i\sin\left(\sqrt{\frac{\omega\mu\sigma}{2}}z\right)\right] \end{aligned} \tag{32}$$

where the real and imaginary parts are both valid solutions.

Now, consider the magnitude of the electric field strength as a function of depth:

$$|E_x(z)| = |E_s|e^{-\sqrt{\frac{\omega\mu\sigma}{2}}z} \tag{33}$$

which decreases monotonically as z increases. The depth at which the magnitude of the electric field strength has decreased by a factor of $1/e$ from its surface value is called the skin depth, δ. Given equation (33), we see that

$$\frac{|E_x(\delta)|}{|E_s|} = \frac{1}{e} = e^{-1} = e^{-\sqrt{\frac{\omega\mu\sigma}{2}}\delta} \tag{34}$$

and

$$\delta = \frac{1}{\sqrt{\frac{\omega\mu\sigma}{2}}} = \sqrt{\frac{2}{\omega\mu\sigma}} = \sqrt{\frac{2}{2\pi f\mu\sigma}} = \sqrt{\frac{\rho T}{\pi\mu}} \tag{35}$$

For $\mu = \mu_0 = 4\pi\cdot10^{-7}$ H/m, the skin depth measured in metres is

$$\delta = \sqrt{\frac{\rho T}{\pi\mu_0}} = \sqrt{\frac{\rho T}{4\pi^2\cdot10^{-7}}} = 503.3\sqrt{\rho T} \tag{36}$$

and is typically considered the penetration depth of the MT method at a specific period, T. From this equation, we see that shorter periods sample the shallower Earth and longer periods sample the deeper Earth. Hence, AMT is used for upper-crustal exploration, BBMT is used for crustal exploration, and LMT is used for lithospheric and upper-mantle exploration.

Consider the simple case of a plane wave, with the electric field polarized in the x-direction, incident on the interface between an insulator (air) and a uniform conductor (halfspace Earth model). An incoming wave with amplitude E_i will be split into a reflected wave with amplitude E_r and a transmitted wave with amplitude E_t (Figure 3.10). At the low frequencies associated with the MT method, the transmitted signal will propagate by diffusion, as discussed in Section 3.3.

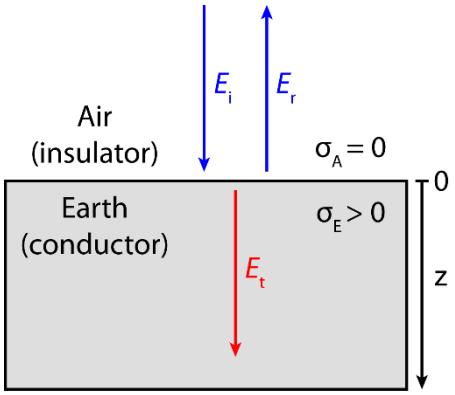

***Figure 3.10**: A polarized plane wave incident on a conductive halfspace.*

Assuming the conductivity of the air, σ_A, is zero, the incoming wave and reflected wave will both have the wave number

$$k_0 = \omega\sqrt{\mu_0\varepsilon_0} \tag{37}$$

The incoming wave is therefore described by

$$\boldsymbol{E}_i(z,t) = E_i e^{-ik_0 z} e^{i\omega t} \tag{38}$$

travelling in the *z*-direction, and the reflected wave is described by

$$\boldsymbol{E}_r(z,t) = E_r e^{ik_0 z} e^{i\omega t} \tag{39}$$

travelling in the –*z*-direction. The transmitted signal, on the other hand, will be described by

$$\boldsymbol{E}_t(z,t) = E_t e^{-k_1 z} e^{i\omega t} \tag{40}$$

travelling in the *z*-direction, and will have the wave number

$$k_1 = (1-i)\sqrt{\frac{\omega\mu\sigma_E}{2}} \tag{41}$$

where σ_E is the conductivity of the halfspace Earth model.

This plane wave will have a magnetic field orthogonal to the electric field, i.e., polarized in the *y*-direction, given by

$$\boldsymbol{H}_y(z,t) = \frac{1}{i\omega\mu}\frac{\partial \boldsymbol{E}_x(z,t)}{\partial z} \tag{42}$$

and both $\boldsymbol{E}_x$ and $\boldsymbol{H}_y$ will be continuous at $z = 0$. The transmitted magnetic field will be described by

$$\begin{aligned}\boldsymbol{H}_t(z,t) &= \frac{1}{i\omega\mu}\frac{\partial \boldsymbol{E}_t}{\partial z} = \frac{1}{i\omega\mu}\frac{\partial (E_t e^{-k_1 z} e^{i\omega t})}{\partial z} \\ &= \frac{-k_1}{i\omega\mu} E_t e^{-k_1 z} e^{i\omega t}\end{aligned} \tag{43}$$

and the impedance of the Earth can be defined as

$$\boldsymbol{Z}_{xy}(\omega) = \frac{\boldsymbol{E}_x(\omega)}{\boldsymbol{H}_y(\omega)} = \frac{\boldsymbol{E}_t}{\boldsymbol{H}_t} = -\frac{i\omega\mu}{k_1} = -\frac{i\omega\mu}{1-i}\sqrt{\frac{2}{\omega\mu\sigma_E}} = \frac{\sqrt{2}}{1+i}\sqrt{\frac{\omega\mu}{\sigma_E}} \tag{44}$$

which, importantly, is independent of σ_A, $|\boldsymbol{E}_x|$ and $|\boldsymbol{H}_y|$. Having removed any dependence on the signal amplitude or properties of the atmosphere, we can determine the conductivity of the Earth:

$$\sigma_E = \frac{\omega\mu}{|\boldsymbol{Z}_{xy}|^2} = \frac{\omega\mu}{\left|\frac{\boldsymbol{E}_x}{\boldsymbol{H}_y}\right|^2} \tag{45}$$

Recall that resistivity is simply the reciprocal of conductivity (equation (2)); therefore

$$\rho_E = \frac{1}{\sigma_E} = \frac{\left|\boldsymbol{Z}_{xy}\right|^2}{\omega\mu} = \frac{1}{\omega\mu}\left|\frac{\boldsymbol{E}_x}{\boldsymbol{H}_y}\right|^2 \tag{46}$$

which is how the MT method uses surface measurements of electric field strength (***E***) and magnetic field strength (***H***) to determine the resistivity of the subsurface.

If the subsurface is not a uniform halfspace, it is useful to define a quantity called the apparent resistivity:

$$\rho_a(\omega) = \frac{1}{\omega\mu_0}\left|\frac{\boldsymbol{E}_x(\omega)}{\boldsymbol{H}_y(\omega)}\right|^2 \tag{47}$$

where the magnetic permeability of the Earth is assumed to be the permeability of free space. The apparent resistivity is the average resistivity of the volume sampled, which is often approximated as a hemisphere with a radius of one skin depth around the measurement point.

In the general 3-D case, the impedance is a complex-valued full-rank second-order tensor,

$$\boldsymbol{Z}(\omega) = \begin{bmatrix} Z_{xx}(\omega) & Z_{xy}(\omega) \\ Z_{yx}(\omega) & Z_{yy}(\omega) \end{bmatrix} \tag{48}$$

where

$$Z_{ij}(\omega) = \frac{E_i(\omega)}{H_j(\omega)} \tag{49}$$

for orthogonal horizontal directions *x* and *y*, typically geographic north and east as in this thesis. The apparent resistivity and phase, respectively, are calculated from the impedance as

$$\rho_{a\,ij}(\omega) = \frac{1}{\omega\mu_0}\left|Z_{ij}(\omega)\right|^2 \tag{50}$$

and

$$\phi_{ij}(\omega) = Arg[Z_{ij}(\omega)] = \tan^{-1}\left[\frac{Im[Z_{ij}(\omega)]}{Re[Z_{ij}(\omega)]}\right] \tag{51}$$

which is usually between 0 and 90 degrees.

If resistivity only varies in the vertical direction (1-D structure), the impedance will have the same magnitude for any pair of orthogonal horizontal directions. This simplifies equation (48) to

$$\boldsymbol{Z}(\omega) = \begin{bmatrix} 0 & Z(\omega) \\ -Z(\omega) & 0 \end{bmatrix} \tag{52}$$

When this antisymmetric impedance tensor is input into equation (50), the negative sign is cancelled by the square and the apparent resistivity becomes a scalar quantity,

$$\rho_a(\omega) = \frac{1}{\omega\mu_0}|Z(\omega)|^2 \tag{53}$$

For a half-space, the phase will be 45° at all frequencies. For a 1-D resistivity structure, the phase will be in the range 0-45° when the resistivity increases with depth, and it will be in the range 45-90° when the resistivity decreases with depth. This fact can be useful for visually checking that the apparent resistivity and phase curves are consistent with each other.

A simple 1-D resistivity model (3 Ωm at 10-20 km depth and 100 Ωm elsewhere) is shown in Figure 3.11, along with the corresponding apparent resistivity and phase. Since the apparent resistivity is an average over the depth range sampled, it does not reach a minimum of 3 Ωm. Instead, it reaches a minimum of 8 Ωm at a period of 400 s, which corresponds to a phase of 45°. If we use these values in equation (36), we get a skin depth of

$$\delta = 503.3\sqrt{\rho T} = 503.3\sqrt{(8)(400)} = 28.5 \text{ km} \tag{54}$$

and a skin depth of 20 km at the same period is given by

$$\delta = 503.3\sqrt{\rho T} = 503.3\sqrt{(4)(400)} = 20.0 \text{ km} \tag{55}$$

where the resistivity is 4 Ωm.

It can also be seen that there is a small increase in apparent resistivity with a maximum at a period of 3 s, along with a corresponding decrease in phase. This is a resonance phenomenon that occurs when the layer thickness (10 km) is comparable in value to the skin depth (δ = 8.7 km when ρ = 100 Ωm and T = 3 s, and δ = 10 km when ρ = 100 Ωm and T = 4 s). However, this effect is rarely seen in measured MT data.

Pseudo-depth profiles of apparent resistivity and phase, where increasing period corresponds to increasing depth, are shown in Figure 3.12. This alternate way of viewing the MT data makes it very clear to see that the phase is greater than 45° when the apparent resistivity is decreasing with depth, and less than 45° when the apparent resistivity is increasing with depth.

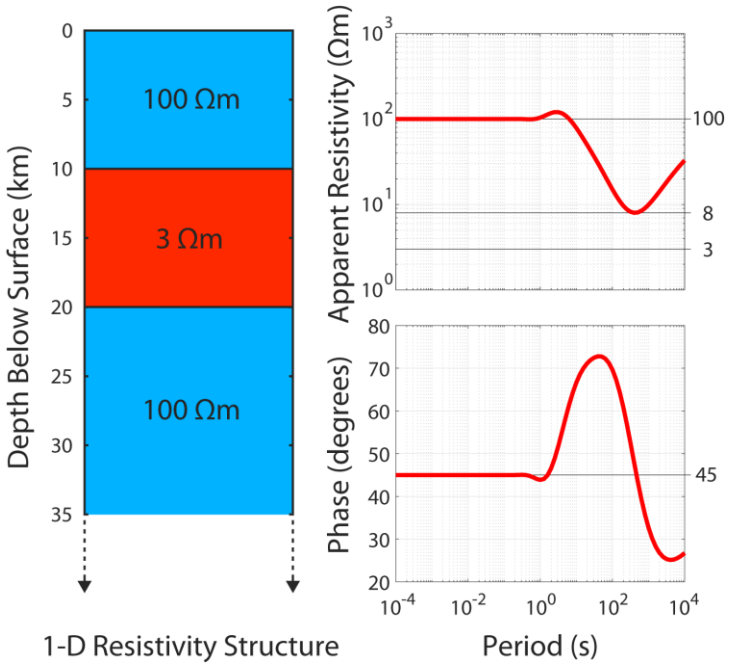

***Figure 3.11**: One-dimensional resistivity structure and corresponding MT responses.*

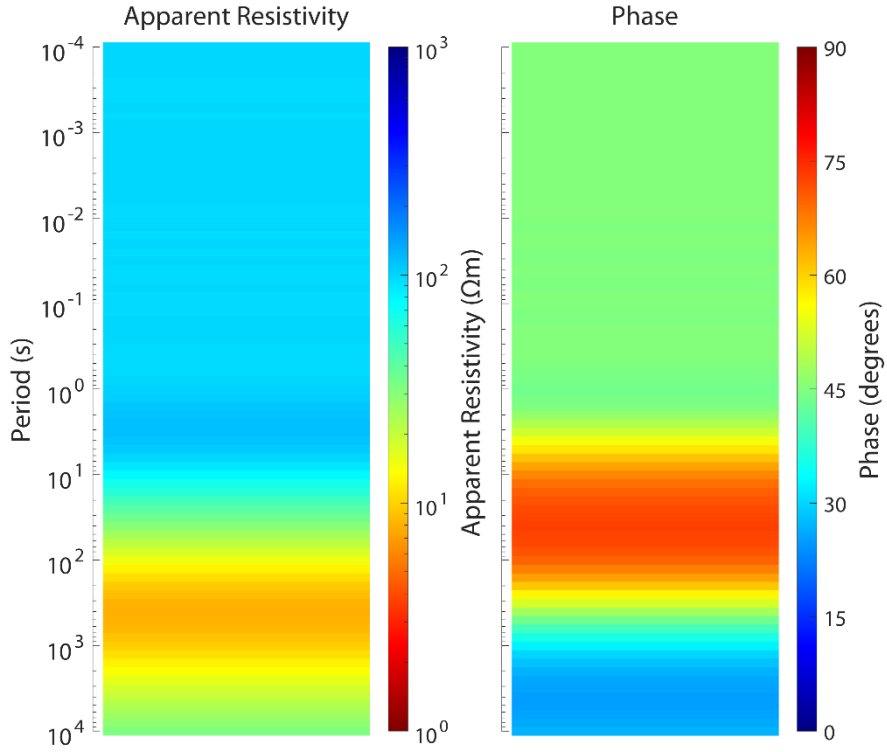

***Figure 3.12**: Apparent resistivity and phase pseudo-depth profiles of the MT response in Figure 3.11.*

3.4.2. Two-dimensional resistivity structure

A second transfer function, the vertical magnetic transfer function, can be computed using just the magnetic field components,

$$\boldsymbol{T}(\omega) = [T_{zx}(\omega) \quad T_{zy}(\omega)] = \begin{bmatrix} \frac{H_z(\omega)}{H_x(\omega)} & \frac{H_z(\omega)}{H_y(\omega)} \end{bmatrix} \tag{56}$$

where z is the vertical direction, pointing downwards in a conventional right-handed coordinate system. The vertical magnetic transfer function is often called the tipper, since it measures how much the magnetic field is tipped away from being horizontal, and it is referred to as such throughout this thesis. If resistivity only varies in the vertical direction (1-D structure), the tipper will be zero at all frequencies.

If resistivity only varies in the vertical direction and one horizontal direction (2-D structure), you can assume two simple source configurations (modes):

1) The electric field is polarized parallel to the strike direction. This is called the E-polarization or the transverse electric (TE) mode. In this case, the magnetic field is confined to the plane orthogonal to the strike direction. For example, $\boldsymbol{E} = E_x\hat{x}$ and $\boldsymbol{B} = B_y\hat{y} + B_z\hat{z}$, as illustrated in panel (a) of Figure 3.13.
2) The magnetic field is polarized parallel to the strike direction. This is called the B-polarization or the transverse magnetic (TM) mode. In this case, the electric field is confined to the plane orthogonal to the strike direction. For example, $\boldsymbol{B} = B_x\hat{x}$ and $\boldsymbol{E} = E_y\hat{y} + E_z\hat{z}$, as illustrated in panel (b) of Figure 3.13.

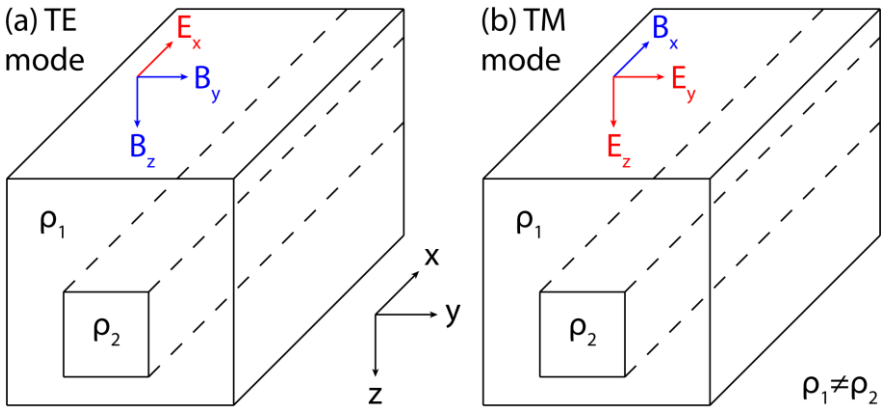

***Figure 3.13**: Two-dimensional resistivity structure with MT modes: (a) transverse electric (TE) mode and (b) transverse magnetic (TM) mode.*

The magnetic flux density, $\boldsymbol{B}$, is simply the magnetic field strength scaled by the magnetic permeability, $\mu\boldsymbol{H}$. In both 2-D modes, $\boldsymbol{E}$ is orthogonal to $\boldsymbol{H}$; therefore, the diagonal elements of the impedance tensor are zero, provided one chooses a coordinate system parallel/orthogonal to the strike direction. Hence, equation (48) becomes

$$\boldsymbol{Z}(\omega) = \begin{bmatrix} 0 & Z_{xy}(\omega) \\ Z_{yx}(\omega) & 0 \end{bmatrix} \tag{57}$$

In the TM mode, the electric field is orthogonal to the strike direction. Therefore, electric currents are induced orthogonal to strike, and the boundaries between regions with different resistivity can develop electric charges on the surfaces. Note that this violates the assumption that there are no free charges (Section 3.2.2) and is called a galvanic effect. The TM mode includes both inductive and galvanic effects, and it can resolve both conductors and resistors.

In the TE mode, the electric field is parallel to the strike direction. Therefore, electric currents are induced parallel to strike, and there are no galvanic effects. The tipper is part of the TE mode (see B_z in Figure 3.13 a), where an electric current along strike induces a magnetic field in the plane orthogonal to strike. The TE mode can resolve conductors, but not resistors.

A simple 2-D resistivity model with a 3 Ωm prism at 10-20 km depth embedded in a 100 Ωm halfspace is shown in Figure 3.14. This figure also shows the corresponding apparent resistivity and phase calculated at six locations. At the shortest periods, the apparent resistivity is slightly greater than 100 Ωm and the phase is slightly greater than 45°. This is an artifact arising from the model cell size being similar to the skin depth at these periods, and it can be ignored for the purposes of this exercise. The same type of behaviour in Section 3.4.3 can likewise be ignored. We can instead assume halfspace behaviour (ρ_a = 100 Ωm and φ = 45°) at the shortest periods.

The TE mode (red curves) has a strong inductive effect, resulting in a significant decrease in apparent resistivity and corresponding increase in phase. The amplitude of these changes increases as the measurement location moves toward the conductive prism, i.e., from west to centre in Figure 3.14.

The TM mode (blue curves) has a less significant decrease in apparent resistivity and corresponding increase in phase, compared with the TE mode. Most of the variations in apparent resistivity are accompanied by a significant phase response, suggesting a primarily

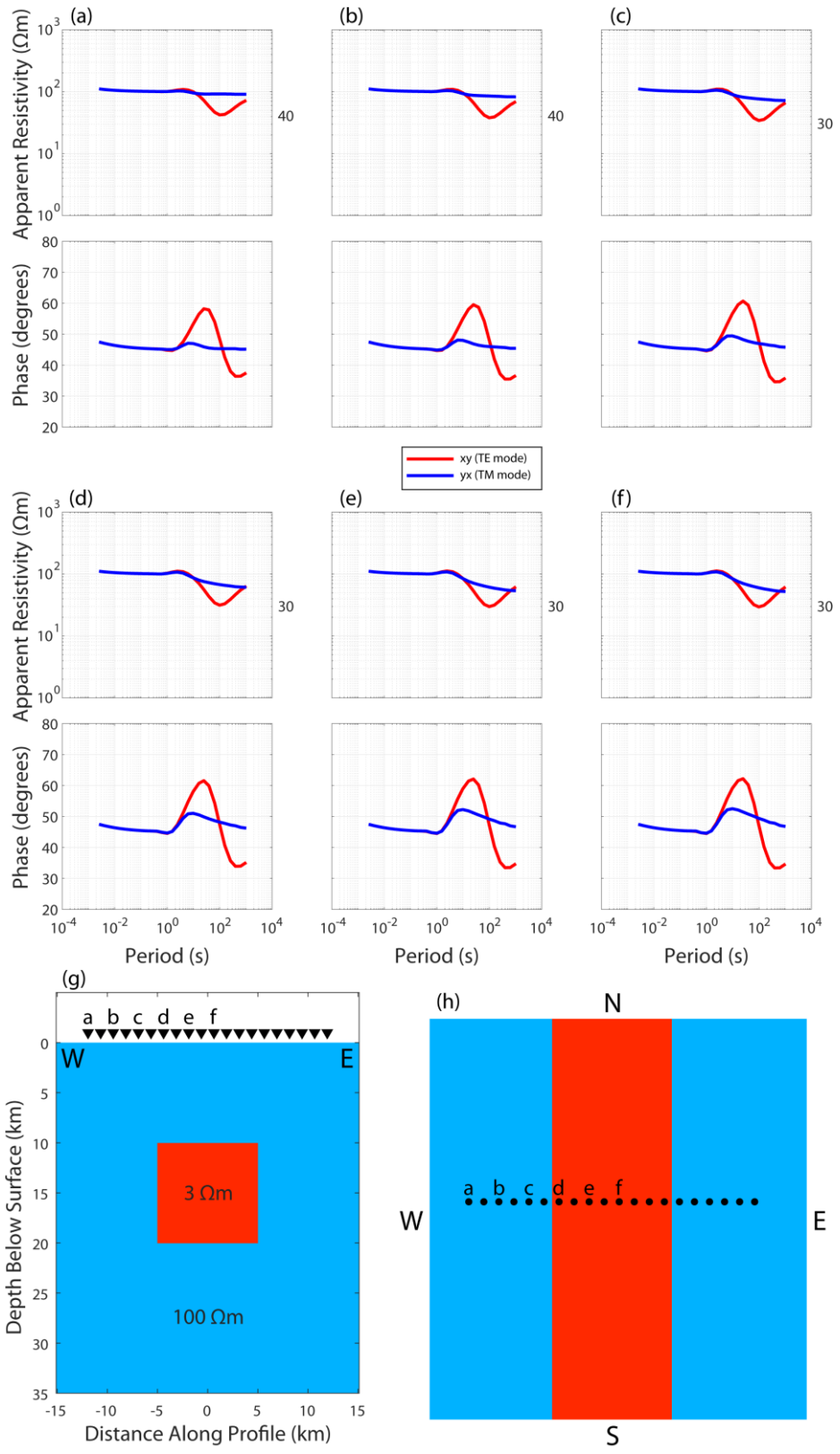

Figure 3.14*: Two-dimensional resistivity structure and corresponding MT responses. MT data were calculated at 20 locations, six of which are shown in panels a-f. Pseudo-sections using all 20 locations are shown in Figure 3.15.*

inductive response. The amplitude of these changes increases as the measurement location moves toward the conductive prism, but the apparent resistivity does not reach a local minimum as it did for the TE mode. Away from the prism, the TM response is close to a halfspace response (Figure 3.14 a). The weak TM responses may be due to the fact that the conductor is relatively deep, i.e., the depth is comparable to the scale of the conductor.

Apparent resistivity and phase pseudo-sections are shown in Figure 3.15. This is another way to visualize MT data. It can be clearly seen that the TE mode resolves the conductor better than the TM mode, and that the response becomes stronger as you move toward the conductor. In the TE mode, it can also be seen that the phase is near 45° when the apparent resistivity is near its minimum value, which occurs at periods around 100 s. The phase is greater above this point and less below it.

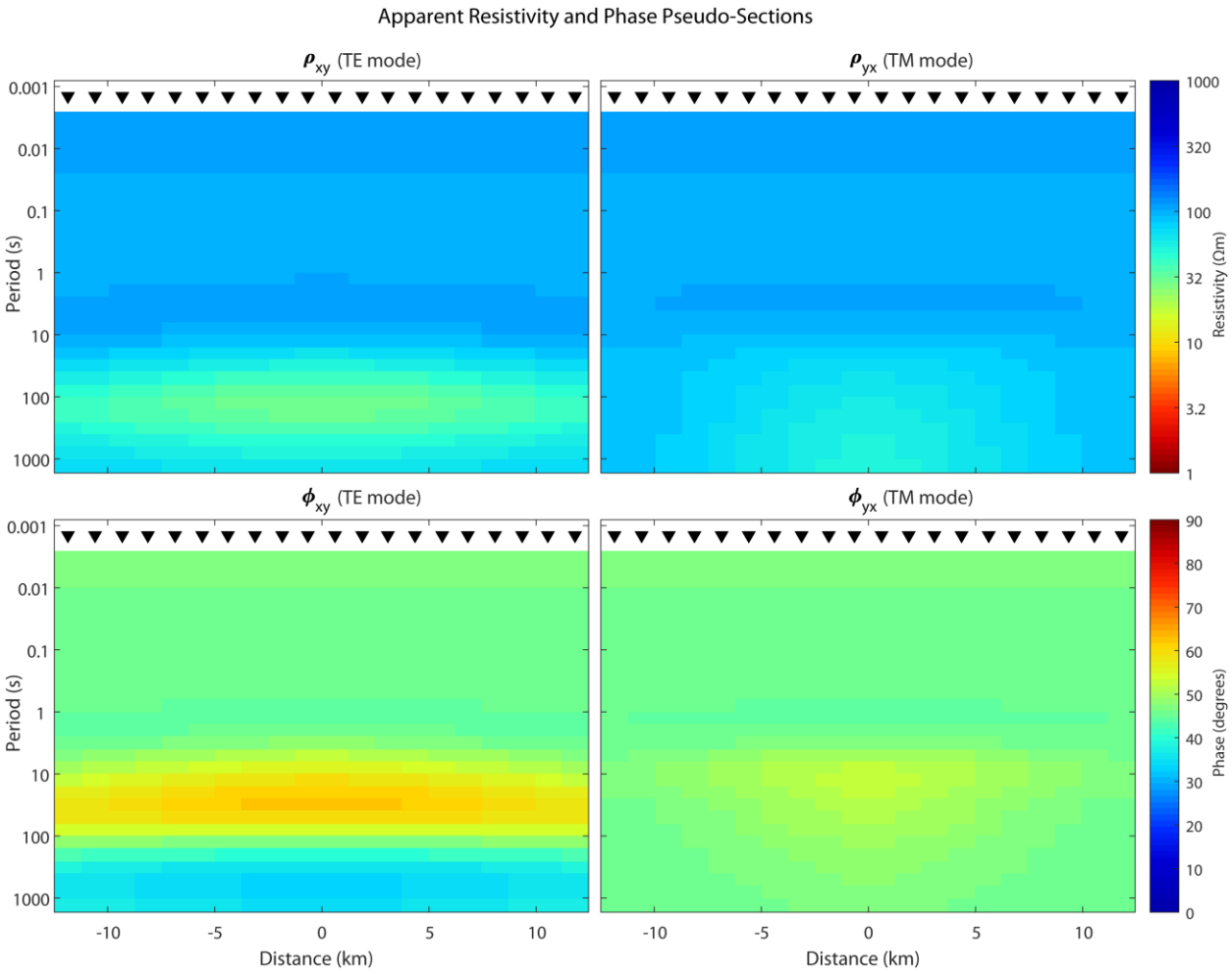

***Figure 3.15**: Apparent resistivity and phase pseudo-sections of the MT responses in Figure 3.14.*

3.4.3. Three-dimensional resistivity structure

A simple 3-D resistivity model with a 3 Ωm cube at 10-20 km depth embedded in a 100 Ωm halfspace is shown in Figure 3.16. This figure also shows the corresponding apparent resistivity and phase calculated at six locations. When MT data are calculated above the cube, the *xy* and *yx* responses are almost identical, similar to a 1-D response. At data locations away from the cube, there is a slight split between *xy* and *yx* at long periods. In general, we see that TE and TM behaviour is absent when the resistivity structure is 3-D.

Apparent resistivity and phase pseudo-sections are shown in Figure 3.17 and it can be clearly seen that the *xy* and *yx* responses are very similar. Due to the simplicity of this 3-D resistivity model, the MT responses are similar to 1-D responses. The 3-D response is much weaker than the 2-D response because the conductor is smaller, being a cube instead of a prism spanning the model domain. Also, the size of the conductor is comparable to its depth, potentially making it more difficult to image.

A more complex 3-D resistivity model representing a hydrothermal geothermal system (e.g., Figure 1.5) embedded in a 1,000 Ωm halfspace is shown in Figure 3.18. This 3-D model has a 60 Ωm reservoir measuring 3.5 km × 3.5 km × 5.0 km, overlain by a clay cap measuring 7.0 km × 7.0 km × 2.1 km. This clay cap is comprised of a 1.5 km thick 3 Ωm layer sandwiched between two 0.3 km thick 30 Ωm layers, all overlain by 1.0 km of 1,000 Ωm host rock.

The MT response is similar to a halfspace response when the data location is away from the conductors (Figure 3.18 a). As the data location moves toward the conductors, the two data components split with ρ_{xy} (red) decreasing and ρ_{yx} (blue) increasing (Figure 3.18 b-d). When the data location is above the clay cap, ρ_{xy} and ρ_{yx} both decrease greatly with increasing period (Figure 3.18 e-f). When the data location is near the centre of the grid, the MT response is similar to a 1-D response (Figure 3.18 f). The conductor is shallower than the one in the previous 3-D example, resulting in a stronger response.

Apparent resistivity and phase pseudo-sections are shown in Figure 3.19. At data locations above the hydrothermal system, low apparent resistivity and high phase are observed at a range of periods.

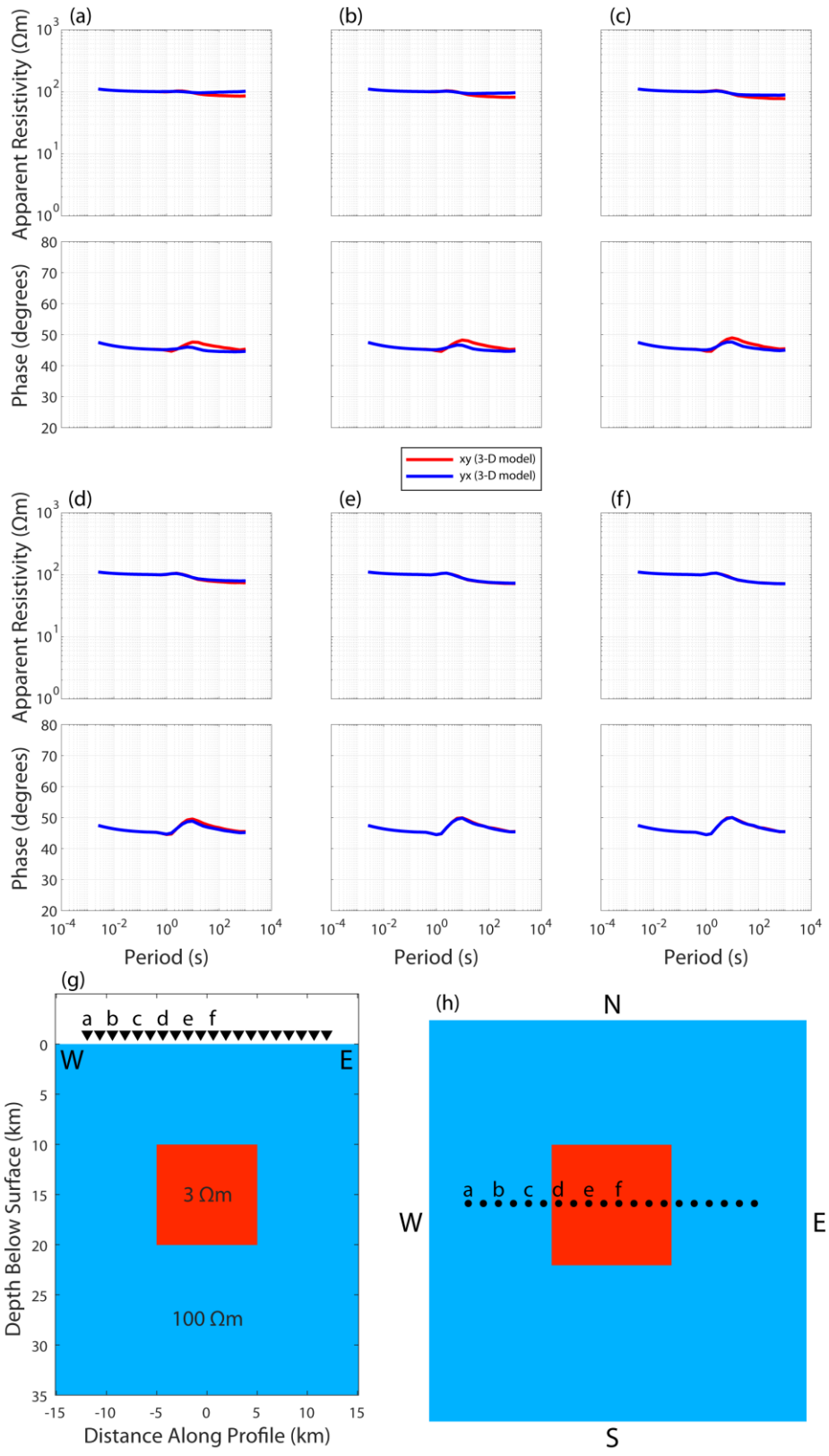

***Figure 3.16**: Three-dimensional resistivity structure and corresponding MT responses. MT data were calculated at 20 locations, six of which are shown in panels a-f. Pseudo-sections using all 20 locations are shown in Figure 3.17.*

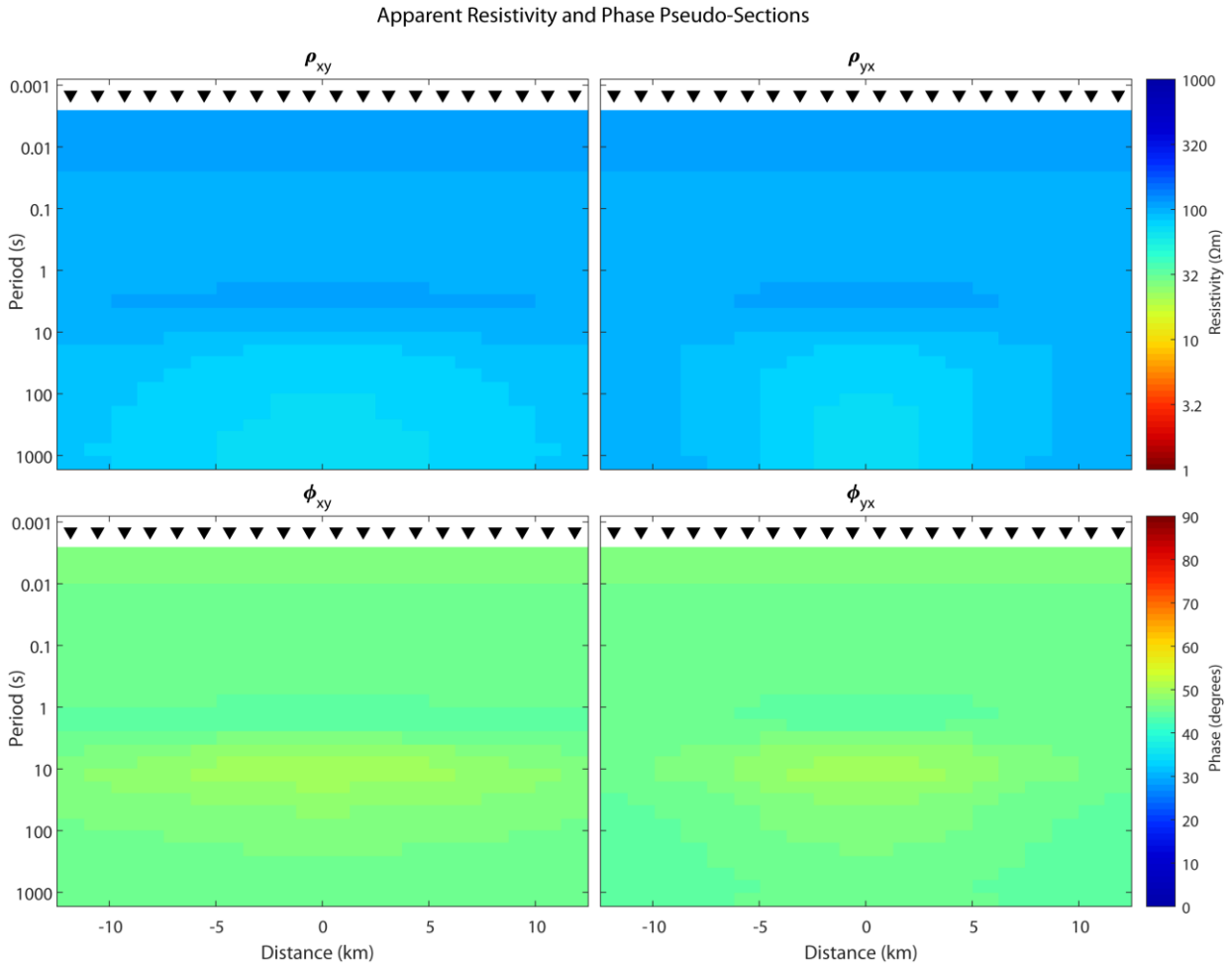

***Figure 3.17**: Apparent resistivity and phase pseudo-sections of the MT responses in Figure 3.16.*

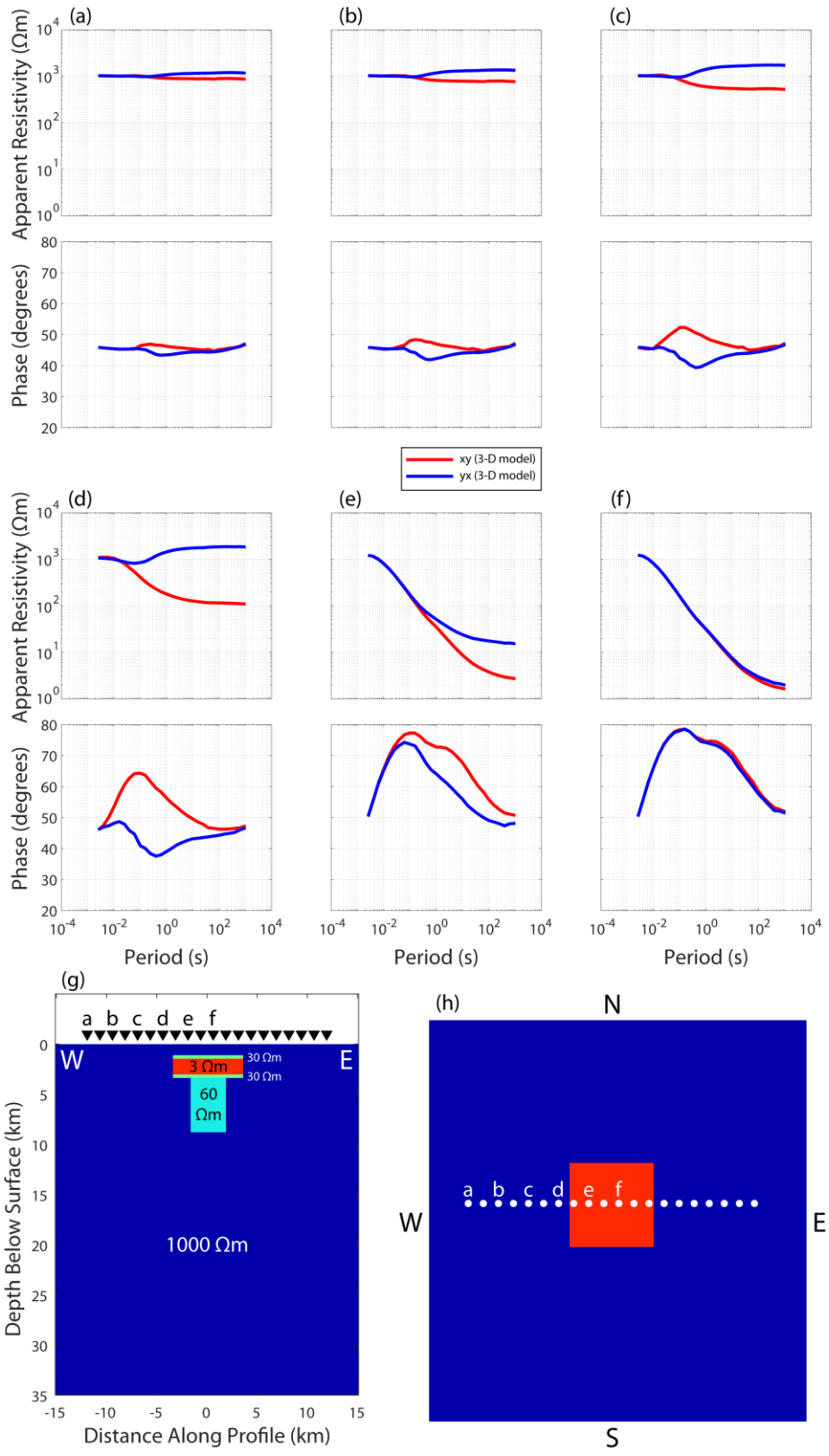

***Figure 3.18**: Three-dimensional resistivity structure and corresponding MT responses. MT data were calculated at 20 locations, six of which are shown in panels a-f. Pseudo-sections using all 20 locations are shown in Figure 3.19.*

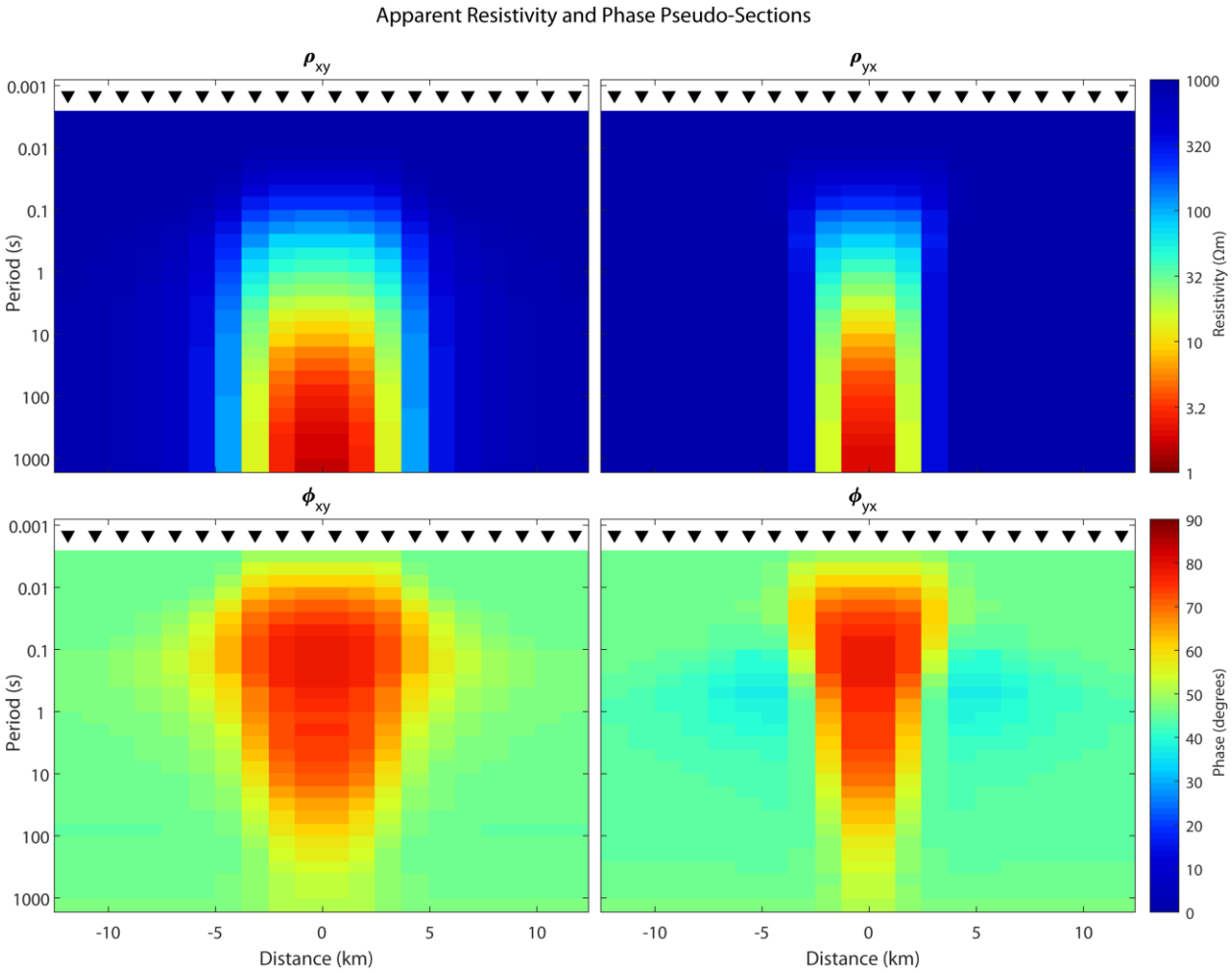

***Figure 3.19**: Apparent resistivity and phase pseudo-sections of the MT responses in Figure 3.18.*

3.4.4. Examples from Mount Meager, southwestern Canada

To illustrate the complexity of real-world 3-D MT data, apparent resistivity and phase data measured at Mount Meager (Chapter 4) are shown in Figure 3.20, along with corresponding pseudo-sections in Figure 3.21. MGR110, MGR210 and mt13 (Figure 3.20 b,c,e) are good examples of high quality MT data. The curves are smooth and the phase is in the range 0-90°. Good quality data is also observed at site mt24 (Figure 3.20 f) but there are two outliers in the *yx* mode at the longest periods.

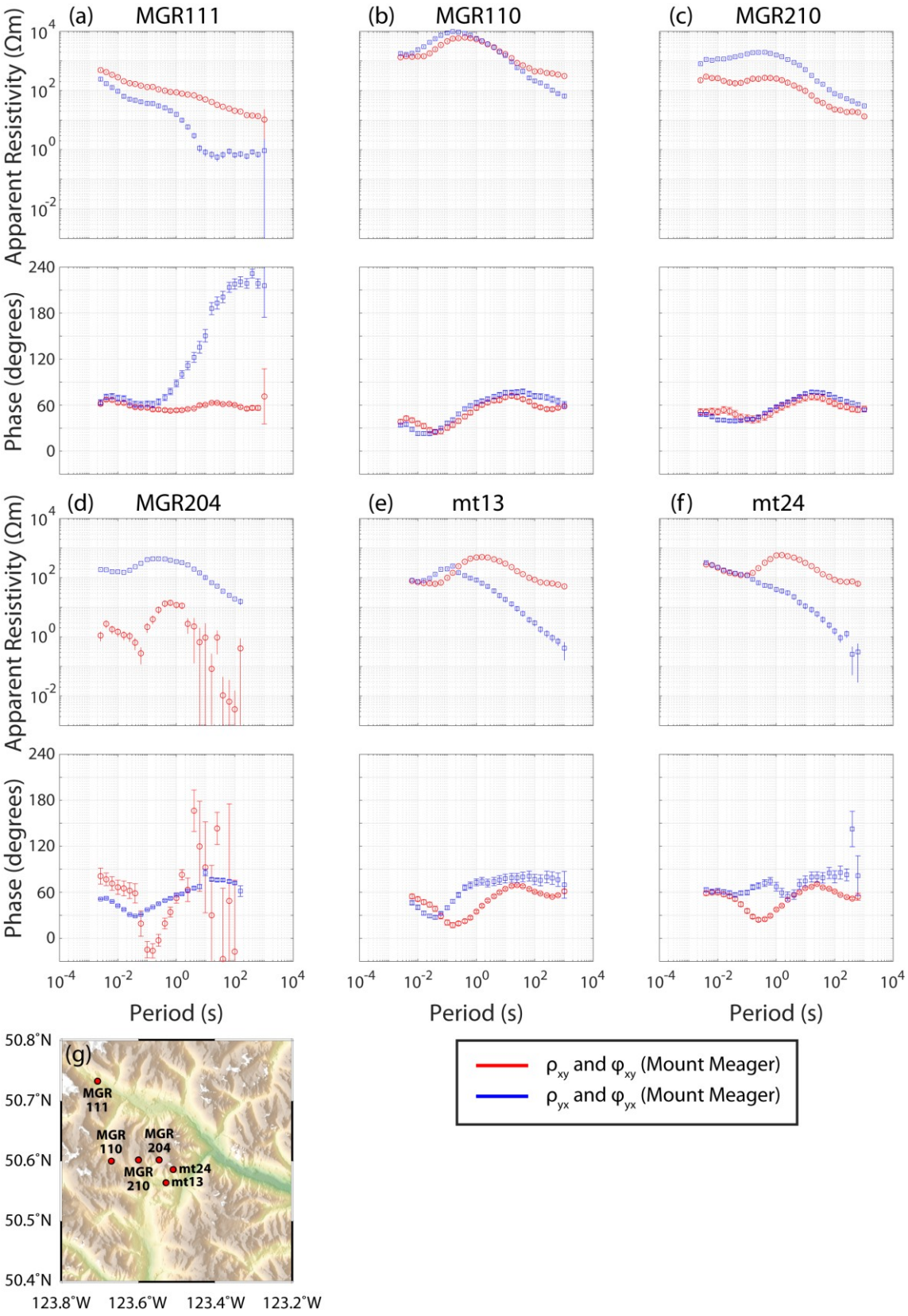

***Figure 3.20**: (a-f) Apparent resistivity and phase data measured at Mount Meager (Chapter 4). (g) Map of station locations.*

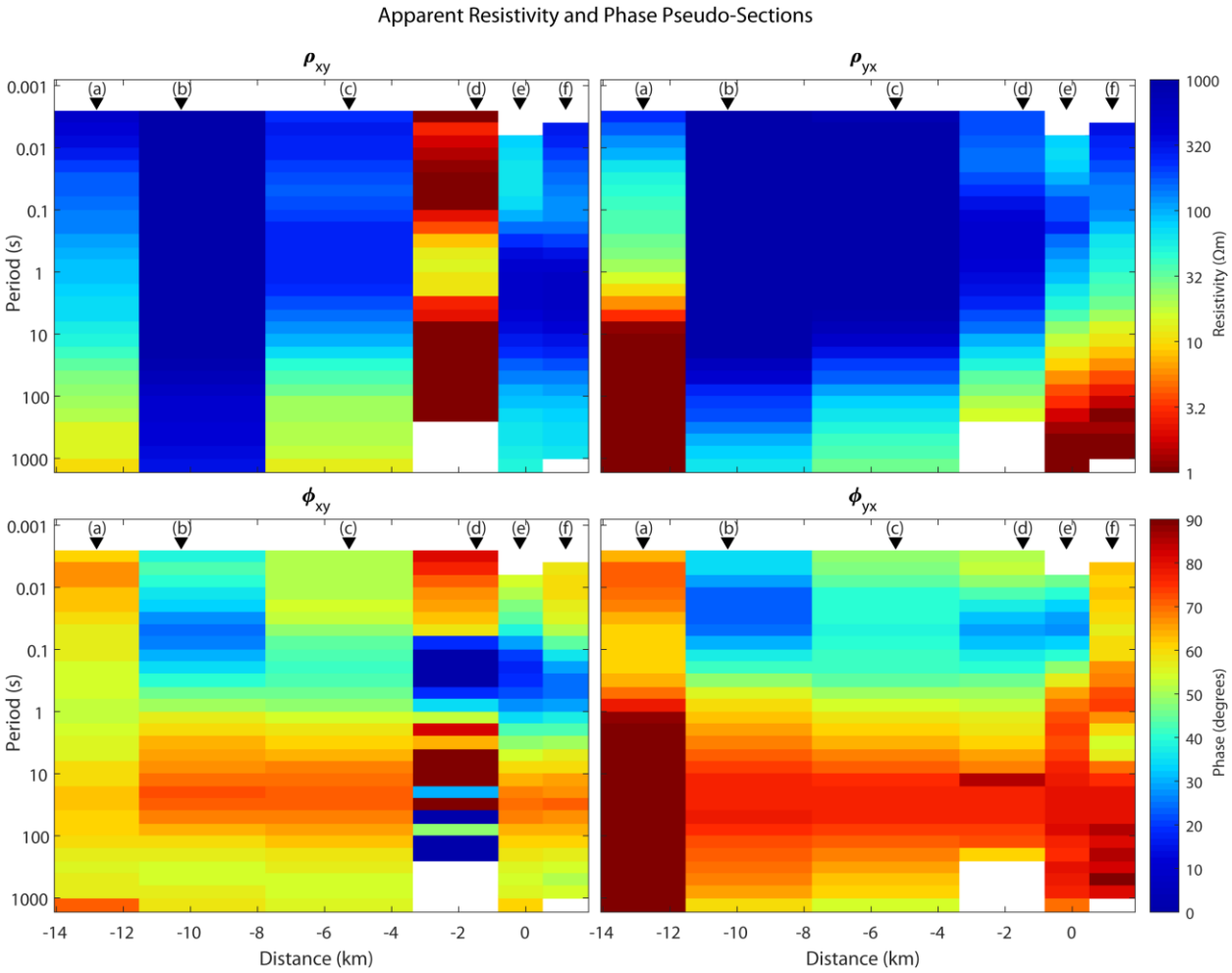

***Figure 3.21**: Apparent resistivity and phase pseudo-sections of the MT data in Figure 3.20.*

MGR111 (Figure 3.20 a) has high quality data except at the longest period. The phase at long periods at this site is significantly greater than 90° but this is a 3-D effect and these data were well fit by the inversion model (Chapter 4). MGR204 (Figure 3.20 d) has good quality data in the *yx* mode; however, the *xy* mode is an example of poor quality MT data. This indicates that there was noise in the E_x and/or H_y time series. In this case, visual inspection of the time series revealed that E_x was noisy.

As a comparison, the spatial distribution and frequency distribution of these six sites were used to investigate the simple 2-D resistivity model from Section 3.4.2. As before, apparent resistivity and phase curves (Figure 3.22) and pseudo-sections (Figure 3.23) are plotted. As expected, these data are very similar to the ones shown in Figure 3.14 and Figure 3.15.

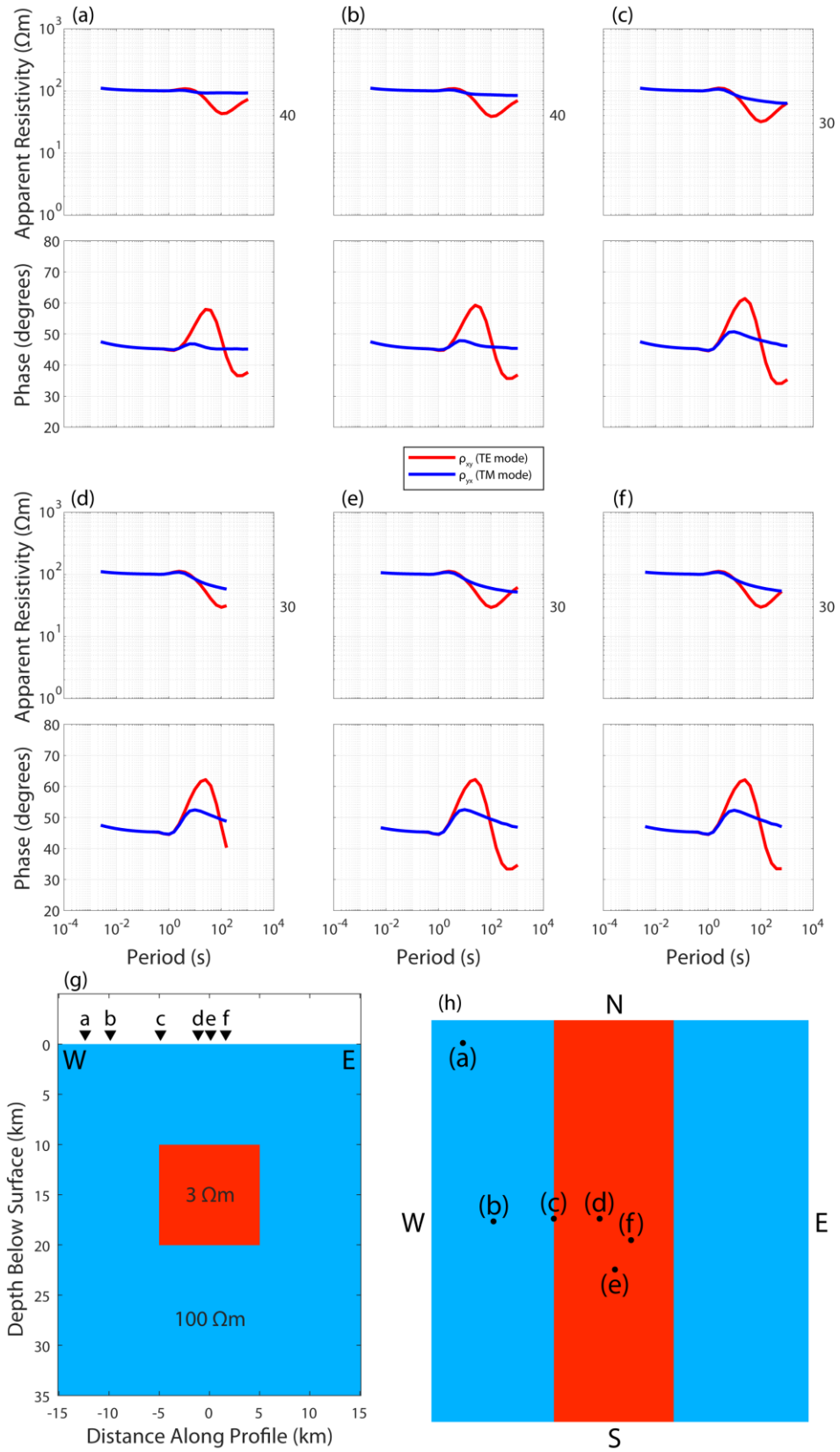

***Figure 3.22**: Two-dimensional resistivity structure and corresponding MT responses, calculated at locations and periods based on the Mount Meager dataset (as discussed on the previous page).*

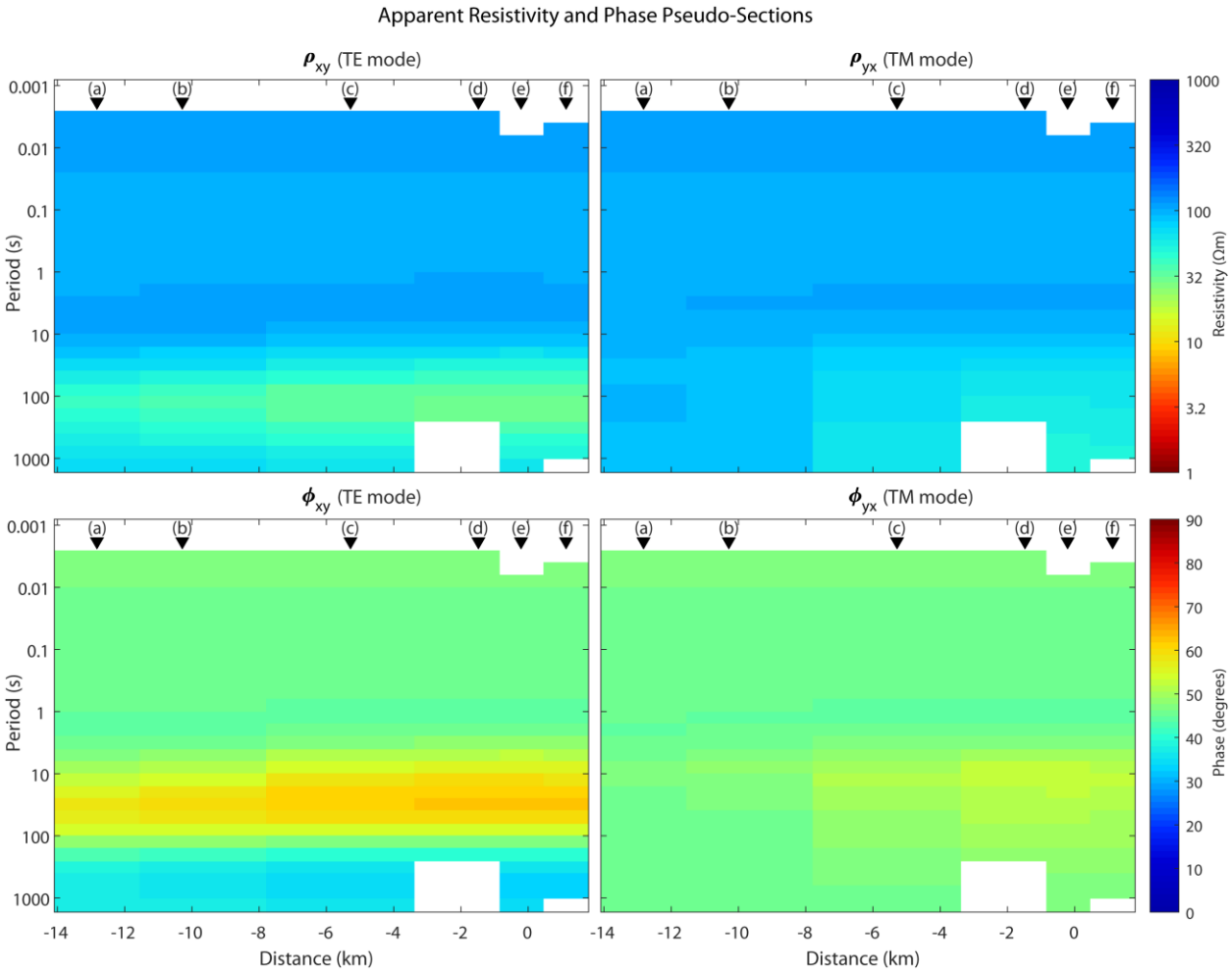

***Figure 3.23**: Apparent resistivity and phase pseudo-sections of the MT responses in Figure 3.14. The white regions indicate periods at which the MT stations mentioned in Section 3.4.2 did not have data.*

The spatial distribution and frequency distribution of these six sites were also used to investigate the simple 3-D resistivity model from Section 3.4.3. As before, apparent resistivity and phase curves (Figure 3.24) and pseudo-sections (Figure 3.25) are plotted.

At three of the data locations (a, d and f), the *xy* and *yx* responses are almost perfectly aligned with each other, similar to a 1-D response. At the other three locations, there is a slight split between *xy* and *yx* at long periods. Directly east of the cube (b and c), ρ_{xy} is a little bit lower than ρ_{yx}, due to an inductive effect in the *x*-direction. Directly south of the cube (e), ρ_{yx} is a little bit lower than ρ_{xy}, due to an inductive effect in the *y*-direction. In general, we see that TE and TM behaviour is absent when the resistivity structure is 3-D.

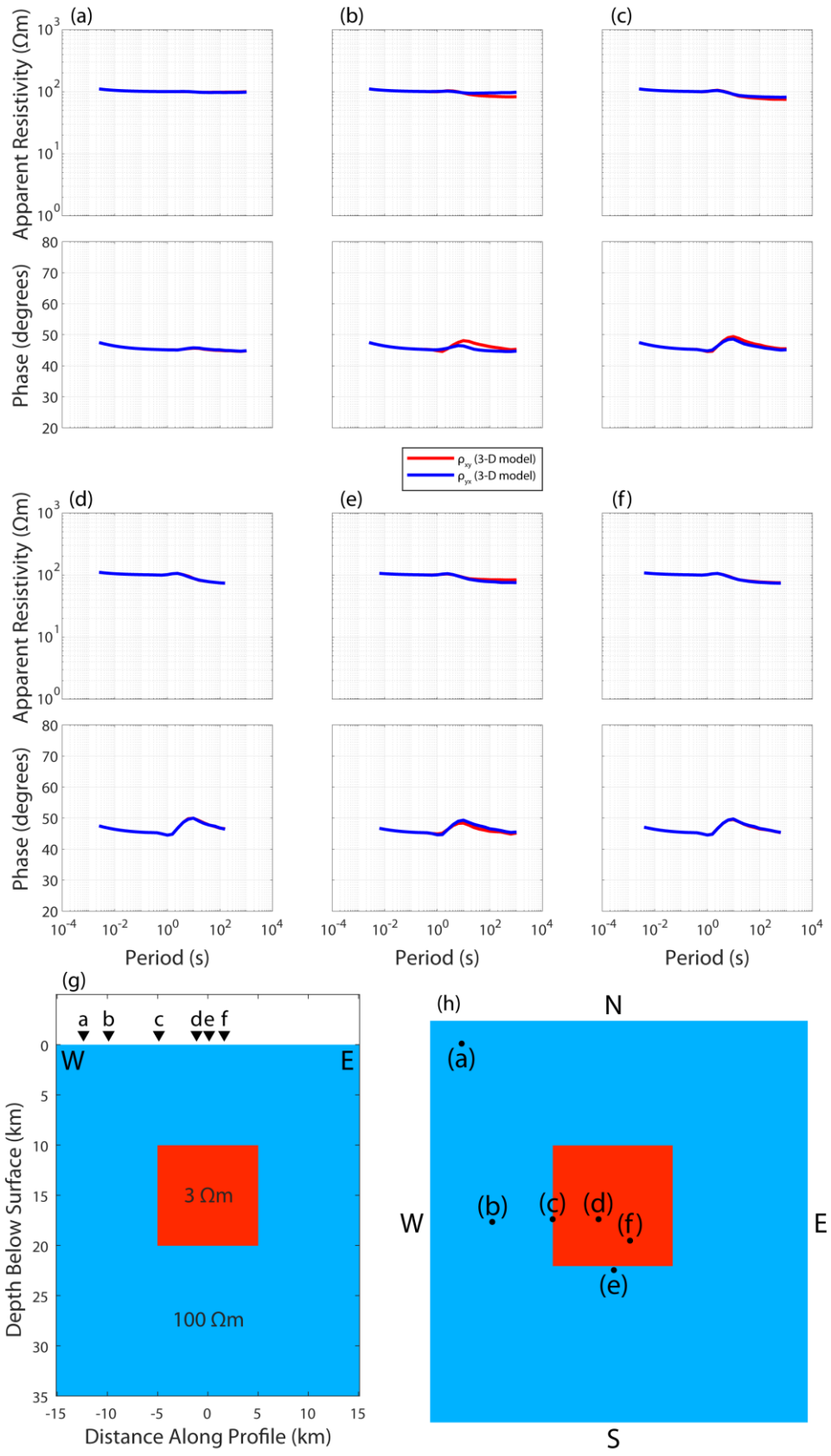

***Figure 3.24**: Three-dimensional resistivity structure and corresponding MT responses.*

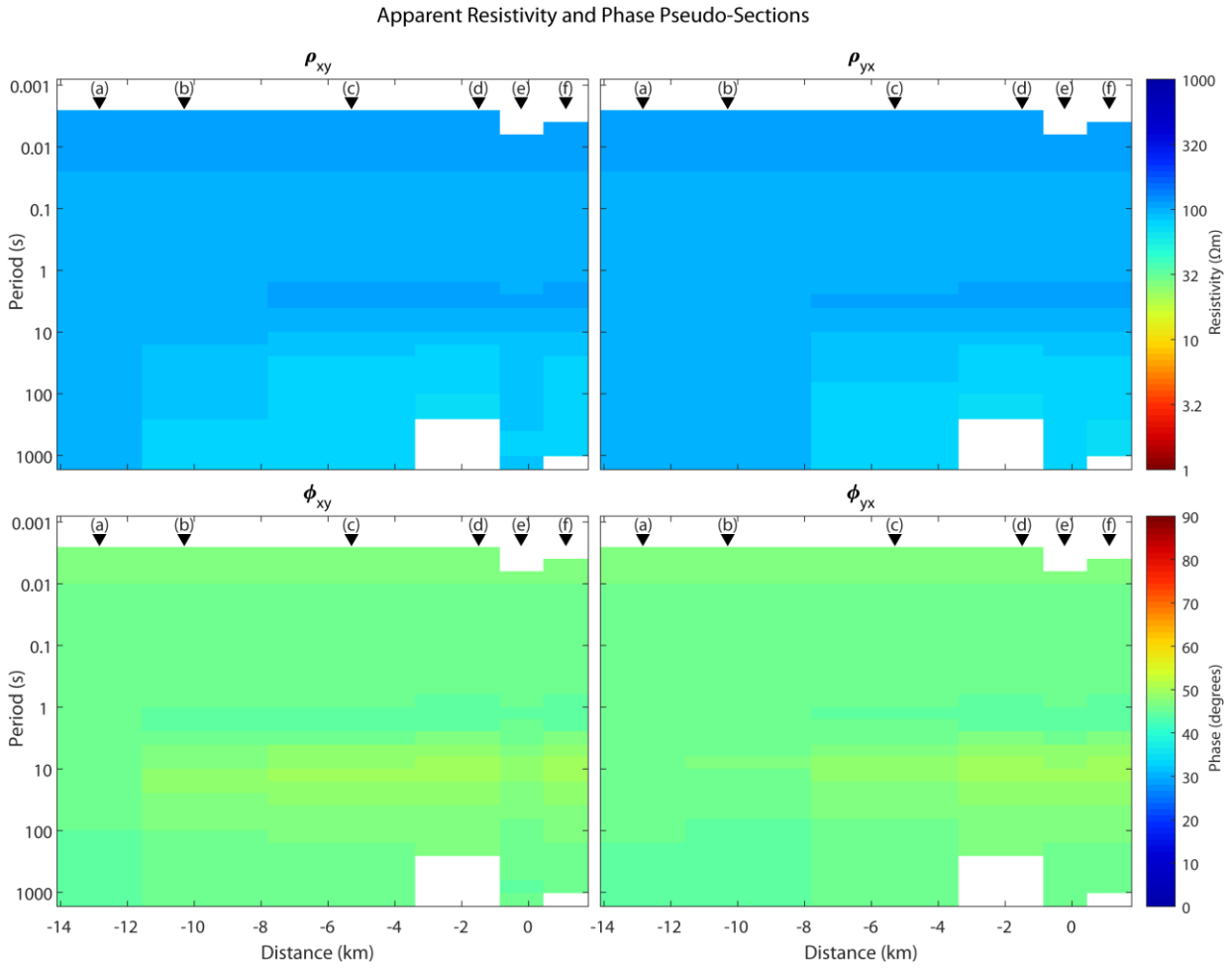

***Figure 3.25**: Apparent resistivity and phase pseudo-sections of the MT responses in Figure 3.15. The white regions indicate periods at which the MT stations mentioned in Section 3.4.2 did not have data.*

3.4.5. Dimensionality and directionality of magnetotelluric impedance data

3.4.5.1. Polar diagrams and impedance tensor skew

It was shown in the previous section that the impedance tensor has different characteristics when the subsurface resistivity structure is 1-D, 2-D or 3-D (equations (52), (57) and (48), respectively). This knowledge can be used to infer dimensionality and directionality of MT data by rotating the impedance tensor, mathematically, and observing the results. One way to do this is to plot polar diagrams of impedance magnitude as a function of rotation angle, θ. This only needs to be done for $|Z_{xx}(\theta)|$ and $|Z_{xy}(\theta)|$ because $|Z_{yy}(\theta)| = |Z_{xx}(\theta+90°)|$ and $|Z_{yx}(\theta)| = |Z_{xy}(\theta+90°)|$.

When the subsurface resistivity structure is 1-D, $|Z_{xx}(\theta)| = 0$ for all θ and $|Z_{xy}(\theta)|$ is constant for all θ, as shown in equation (52). In this case, the polar diagrams of Z_{xx} and Z_{xy} are a point at the origin and a circle of radius Z, respectively. Static shifts can cause the polar diagrams of a 1-D resistivity structure to look like those of a 2-D resistivity structure (described in the next paragraph) so caution should always be employed.

When the subsurface resistivity structure is 2-D, $|Z_{xx}(\theta)| = 0$ when θ is parallel or perpendicular to strike, as shown in equation (57). In this case, the polar diagram of Z_{xx} is a quadrifolium (Weisstein, 2023b), i.e., a four-leaf clover pattern. $|Z_{xy}(\theta)| = |Z_{xy}|$ when θ is 0° or 180° and $|Z_{xy}(\theta)| = |Z_{yx}|$ when θ is 90° or 270°. Therefore, the polar diagram of Z_{xy} has 2-fold rotational symmetry; it is a hippopede (Weisstein, 2023a), i.e., a peanut-shaped pattern. The major and minor axes will be parallel or perpendicular to strike, lining up with the zero points of the Z_{xx} polar diagram; they are usually plotted together on the same axes. Additional information (e.g., geological knowledge) is needed to choose one of the two possible (orthogonal) strike directions.

When the subsurface resistivity structure is 3-D, $|Z_{xx}(\theta)|$ and $|Z_{xy}(\theta)|$ are both non-zero for all θ, as shown in equation (48). In this case, the polar diagrams of Z_{xx} and Z_{xy} are both hippopedes and neither plots at the origin.

In measured MT data, even if the geoelectric structure is predominantly 2-D, the impedance tensor will always have non-zero diagonal elements. If 2-D resistivity structure is suspected, the two possible (orthogonal) strike directions can be determined by finding the rotation angle that minimizes the sum of the squares of the diagonal elements. This angle is called the Swift angle, α.

To estimate the degree to which the impedance tensor can be considered 2-D or 3-D, you can use a rotationally invariant quantity called the skew,

$$\kappa = \frac{|Z_{xx} + Z_{yy}|}{|Z_{xy} - Z_{yx}|} \tag{58}$$

where low values ($\kappa < 0.3$) suggest 2-D structure and high values ($\kappa > 0.3$) suggest 3-D structure. In any case, caution should be used and all other available information considered.

3.4.5.2. The magnetotelluric phase tensor

Localized near-surface conductors can distort the MT response produced by the larger-scale resistivity structure of interest, and this distortion is usually confined to the horizontal electric field, with the horizontal magnetic field being nearly undistorted (Caldwell et al., 2004). Furthermore, these distortions are independent of frequency below a maximum value, which is usually relatively high, and these frequency-independent electric field distortions are called galvanic distortions (Caldwell et al., 2004). Near-surface heterogeneity may drastically distort the amplitude of the electric field, but the phase (equation (51)) is virtually unaffected by galvanic distortion and the regional phase tensor can be recovered from the observed impedance tensor (Caldwell et al., 2004).

The galvanic distortion can be represented by a distortion tensor,

$$\boldsymbol{D} = \begin{bmatrix} d_{xx} & d_{xy} \\ d_{yx} & d_{yy} \end{bmatrix} \tag{59}$$

such that the observed (distorted) electric field is

$$\boldsymbol{E}(\omega) = \boldsymbol{D}\boldsymbol{E}_{\boldsymbol{R}}(\omega) = [\boldsymbol{D}\boldsymbol{Z}_{\boldsymbol{R}}(\omega)]\boldsymbol{H}(\omega) \tag{60}$$

where $\boldsymbol{E_R}$ and $\boldsymbol{Z_R}$ are the regional electric field and impedance tensor, respectively, that we want to recover. The magnetic field is assumed to be undistorted.

For a complex impedance tensor, $\boldsymbol{Z} = \boldsymbol{X} + i\boldsymbol{Y}$, where $\boldsymbol{X}$ = Re($\boldsymbol{Z}$) and $\boldsymbol{Y}$ = Im($\boldsymbol{Z}$), we can define a phase tensor,

$$\boldsymbol{\Phi} = \boldsymbol{X}^{-1}\boldsymbol{Y} = \boldsymbol{X}_{\boldsymbol{R}}^{-1}\boldsymbol{Y}_{\boldsymbol{R}} = \boldsymbol{\Phi}_{\boldsymbol{R}} \tag{61}$$

which is independent of the distortion tensor. Note that the upper case phi ($\boldsymbol{\Phi}$) in equation (61) is not the same as the lower case phi (φ) in equation (51). In component form, equation (61) is

$$\boldsymbol{\Phi} = \begin{bmatrix} \Phi_{xx} & \Phi_{xy} \\ \Phi_{yx} & \Phi_{yy} \end{bmatrix} = \frac{1}{\det(\boldsymbol{X})} \begin{bmatrix} X_{yy}Y_{xx} - X_{xy}Y_{yx} & X_{yy}Y_{xy} - X_{xy}Y_{yy} \\ X_{xx}Y_{yx} - X_{yx}Y_{xx} & X_{xx}Y_{yy} - X_{yx}Y_{xy} \end{bmatrix} \tag{62}$$

where det ($\boldsymbol{X}$) = $X_{xx}X_{yy} - X_{yx}X_{xy}$ is the determinant of $\boldsymbol{X}$. In component form, equation (51) is

$$\boldsymbol{\phi} = \begin{bmatrix} \phi_{xx} & \phi_{xy} \\ \phi_{yx} & \phi_{yy} \end{bmatrix} = \begin{bmatrix} \tan^{-1}\left(\frac{Y_{xx}}{X_{xx}}\right) & \tan^{-1}\left(\frac{Y_{xy}}{X_{xy}}\right) \\ \tan^{-1}\left(\frac{Y_{yx}}{X_{yx}}\right) & \tan^{-1}\left(\frac{Y_{yy}}{X_{yy}}\right) \end{bmatrix} \tag{63}$$

and in general the components of $\boldsymbol{\Phi}$ are not functions of the components of $\boldsymbol{\phi}$.

The phase tensor is characterized by three coordinate invariants (Caldwell et al., 2004). They are the minimum and maximum tensor values (Φ_{min} and Φ_{max}) and the phase tensor skew angle,

$$\beta = \frac{1}{2}\tan^{-1}\left[\frac{\Phi_{xy} - \Phi_{yx}}{\Phi_{xx} + \Phi_{yy}}\right] \tag{64}$$

not to be confused with the impedance tensor skew (equation (58)). Given the rotation matrix,

$$\boldsymbol{R}(\alpha + \beta) = \begin{bmatrix} \cos(\alpha + \beta) & \sin(\alpha + \beta) \\ -\sin(\alpha + \beta) & \cos(\alpha + \beta) \end{bmatrix} \tag{65}$$

another angle, which represents the phase tensor's dependence on the coordinate system,

$$\alpha = \frac{1}{2}\tan^{-1}\left[\frac{\Phi_{xy} + \Phi_{yx}}{\Phi_{xx} - \Phi_{yy}}\right] \tag{66}$$

completes a set of four values that completely define the phase tensor (Caldwell et al., 2004). These values can be represented graphically by an ellipse, as shown in Figure 3.26.

When the subsurface resistivity structure is 1-D, the phase tensor diagram is a circle and β is zero. When the subsurface resistivity structure is 2-D, the phase tensor diagram is an ellipse with Φ_{max} in the strike direction and β is zero. When the subsurface is 3-D, the phase tensor diagram is an ellipse with Φ_{max} in the dominant strike direction, if there is one, and β is usually non-zero. Phase tensor diagrams are often plotted as ellipses filled with colours according to their β values. This provides another graphical tool for determining the dimensionality of MT data, and the strike direction when a 2-D approximation is valid.

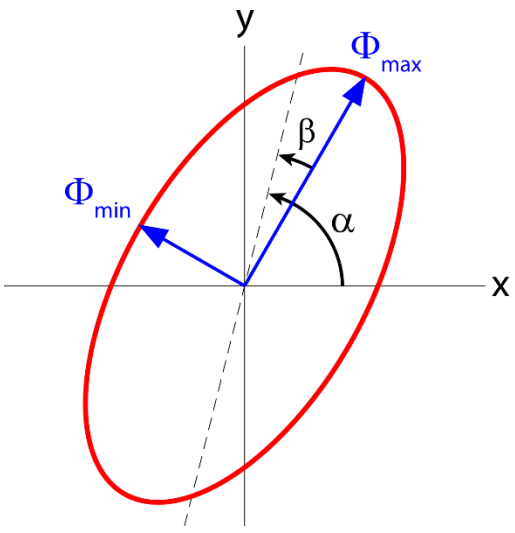

***Figure 3.26**: Graphical representation of the phase tensor in which four values (Φ_{min}, Φ_{max}, α and β) completely define the phase tensor.*

The phase tensor ellipse corresponding to the simple 1-D resistivity model (Section 3.4.1) is shown in Figure 3.27. Because the data are 1-D, the ellipse is identical at all frequencies.

Phase tensor ellipses corresponding to the simple 2-D resistivity model (Section 3.4.2) are shown in Figure 3.28. β is approximately zero at all sites and all frequencies. At periods around 10-100 s, the major axis of the ellipses is in the *x*-direction, corresponding to the strike direction. At these periods, the TE mode phase is greater than 45° (Figure 3.15). At periods around 100-1000 s, the major axis of the ellipses is in the *y*-direction, which is orthogonal to the strike direction. At these periods, the TE mode phase is less than 45° (Figure 3.15).

Phase tensor ellipses corresponding to the simple 3-D resistivity model (Section 3.4.3) are shown in Figure 3.29. The ellipticity is close to one at all sites and all frequencies. β is approximately zero at all sites and all frequencies. As mentioned in Section 3.4.3, these synthetic MT data are similar to 1-D data.

Phase tensor ellipses corresponding to the more complex 3-D resistivity model (Section 3.4.3) are shown in Figure 3.30. At the sides and centre of the section, the phase tensors are similar to 1-D data (ellipticity ≈ 1 and β ≈ 0). To either side of centre, the major axis of the ellipses is in the *x*-direction at a majority of periods, but β is still approximately zero.

Finally, phase tensor ellipses corresponding to the MT data measured at Mount Meager (Section 3.4.4) are shown in Figure 3.31. There is a large range of β values. There is also a large range of ellipticities and no preferred strike direction. These characteristics are common of real-world 3-D MT data.

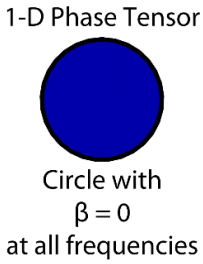

Figure 3.27*: Phase tensor ellipse of the MT response in Figure 3.11. The ellipse is identical at all frequencies.*

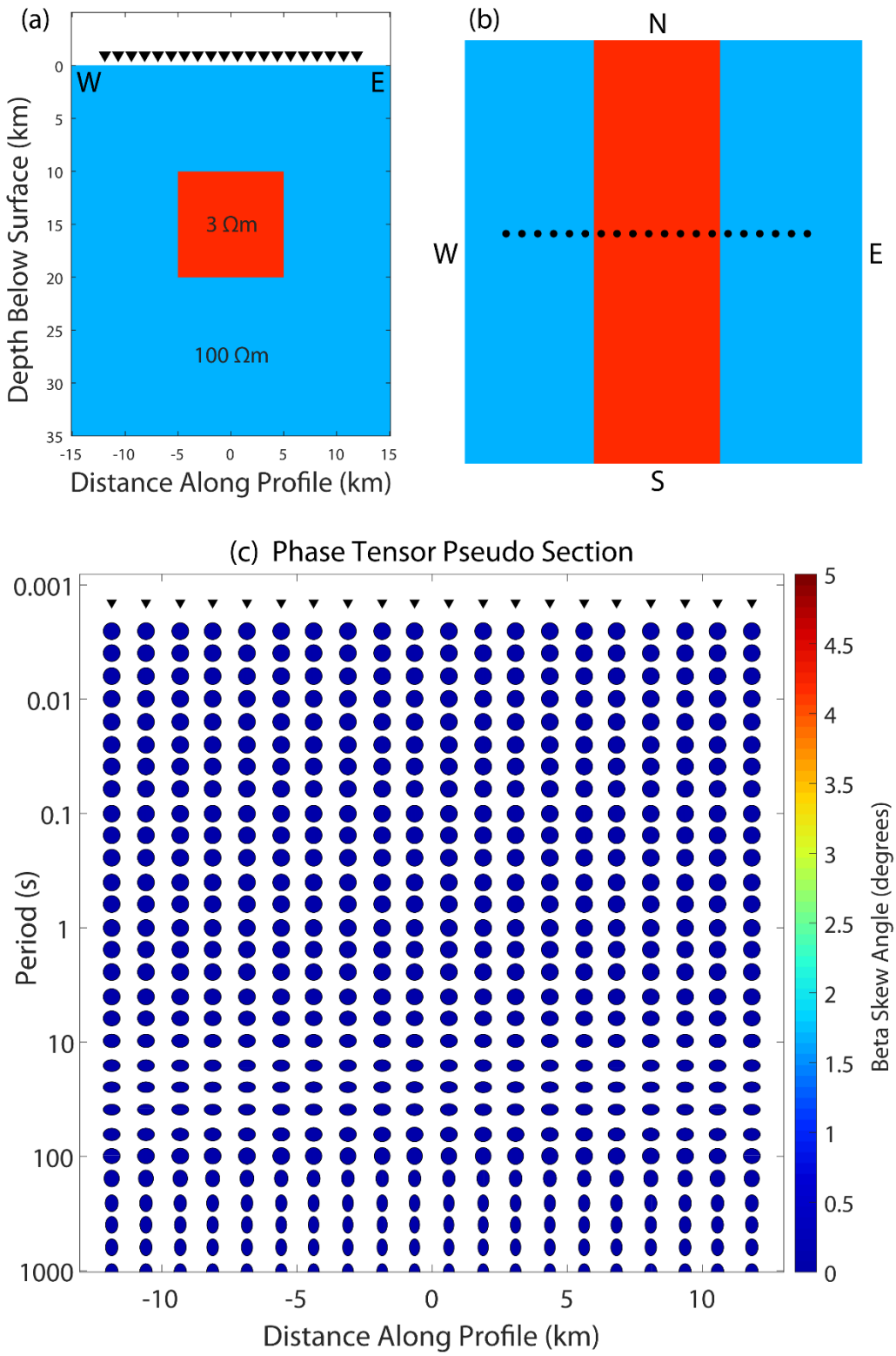

***Figure 3.28**: (a) Cross-section of 2-D model. (b) Depth slice of 2-D model. (c) Phase tensor ellipse pseudo-section of the MT responses, as shown in Figure 3.14.*

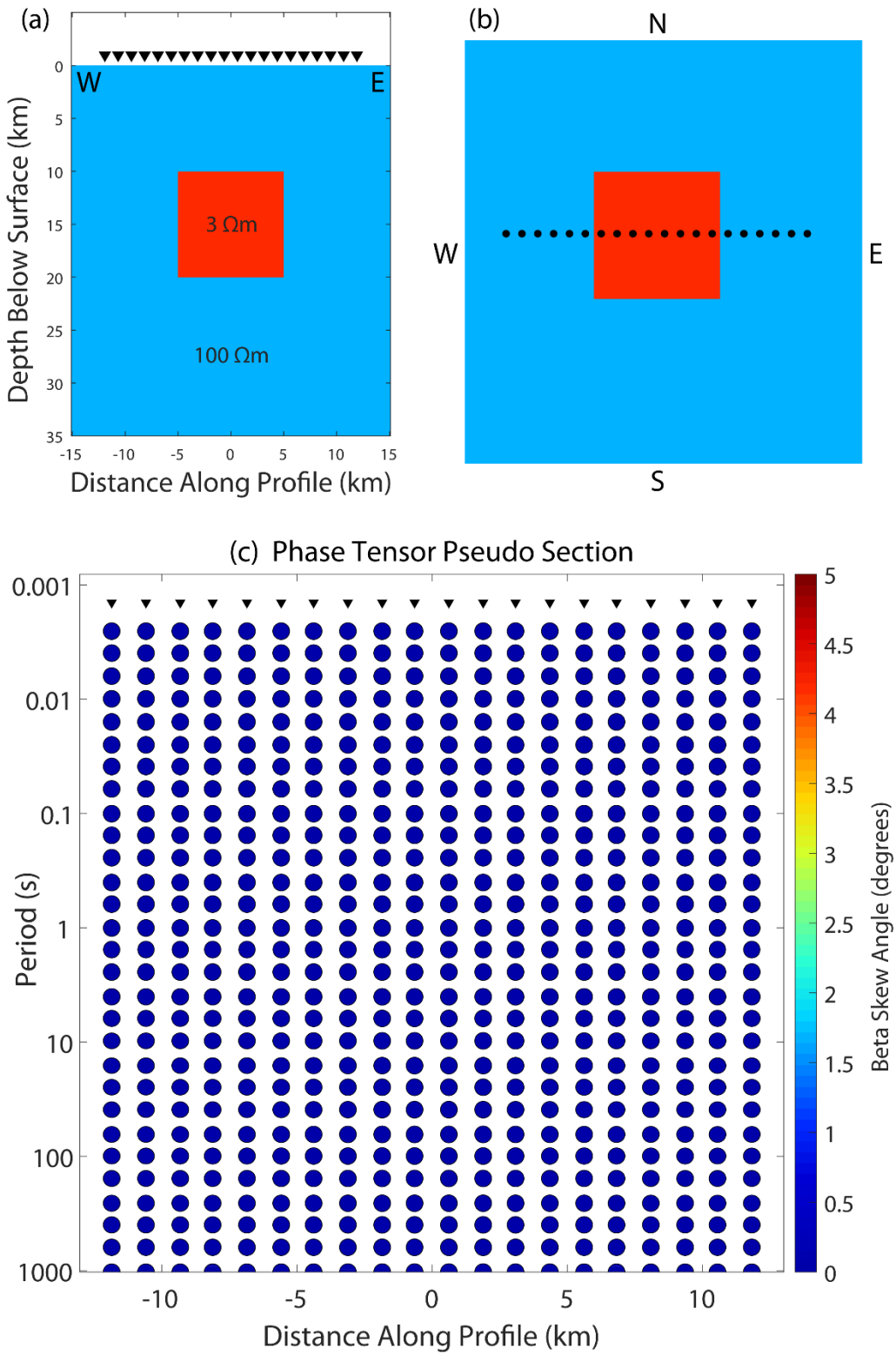

***Figure 3.29**: (a) Cross-section of simple 3-D model. (b) Depth slice of simple 3-D model. (c) Phase tensor ellipse pseudo-section of the MT responses, as shown in Figure 3.16.*

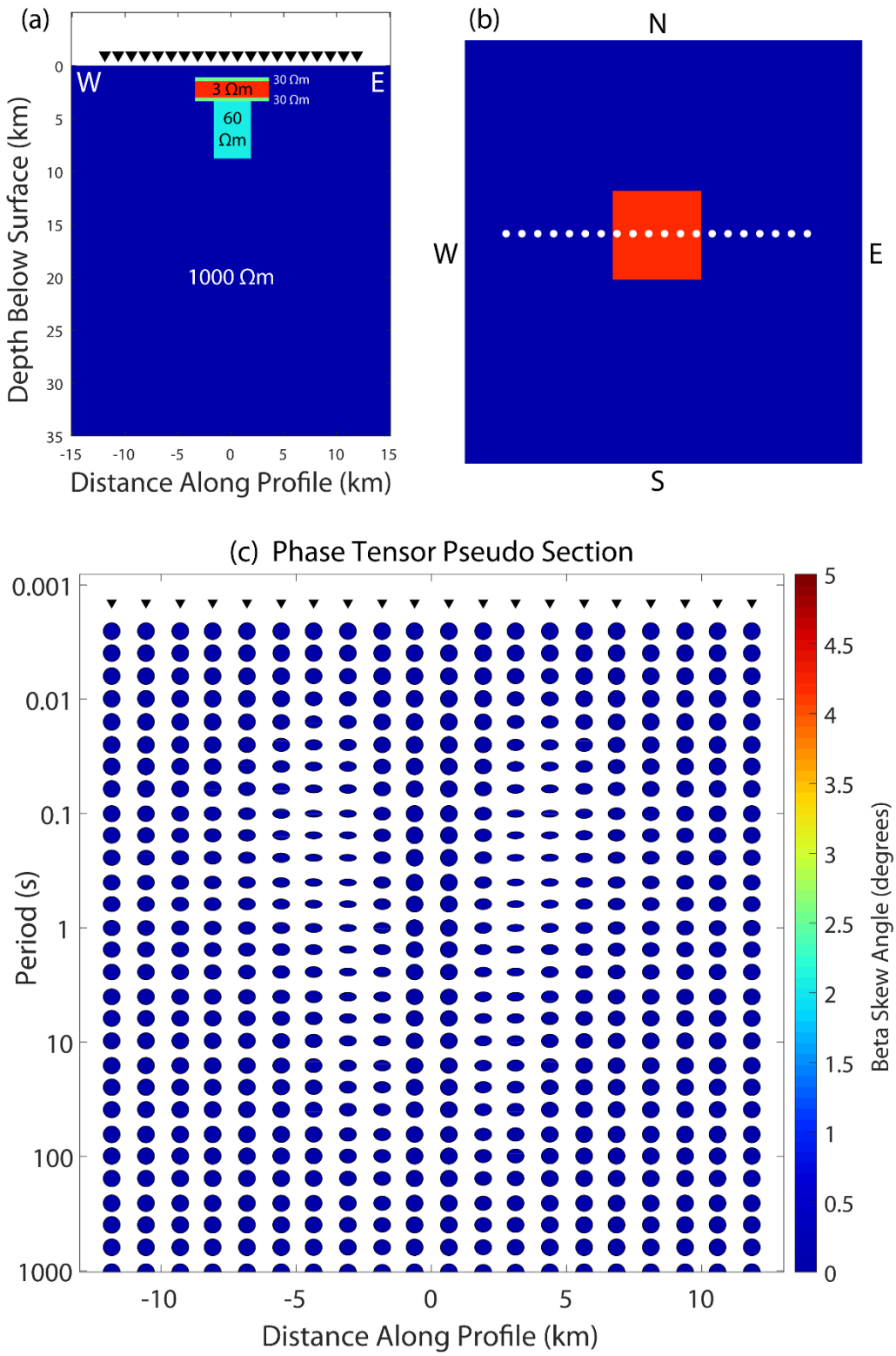

***Figure 3.30**: (a) Cross-section of 3-D model. (b) Depth slice of 3-D model. (c) Phase tensor ellipse pseudo-section of the MT responses, as shown in Figure 3.18.*

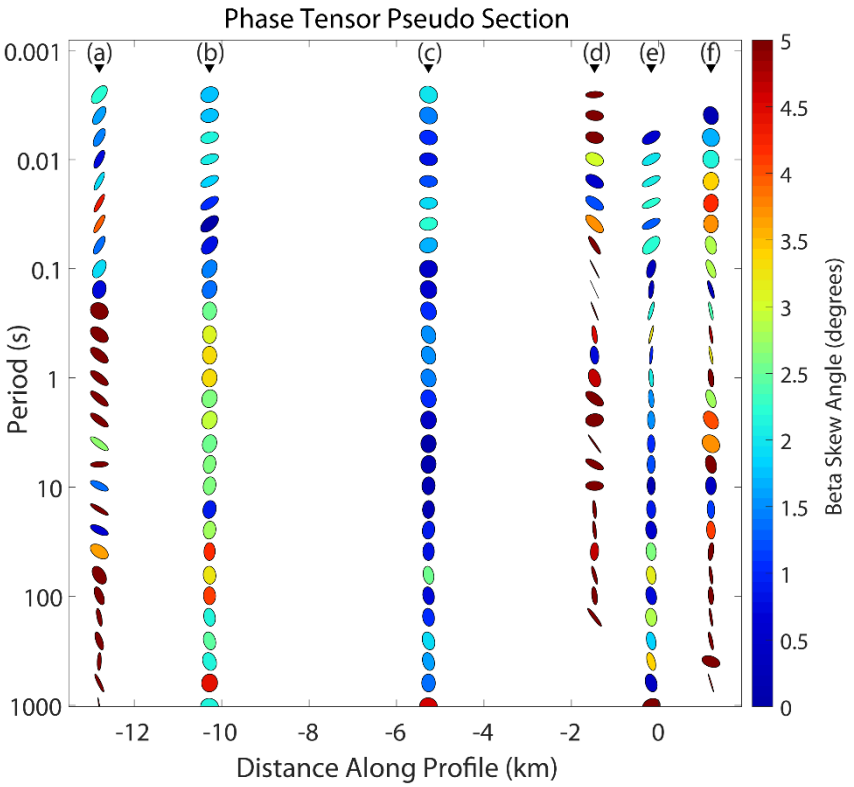

***Figure 3.31**: Phase tensor ellipse pseudo-section of the MT data in Figure 3.20.*

3.5. Practical aspects of the magnetotelluric method

3.5.1. Magnetotelluric data recording and instrumentation

To collect high-quality data at shorter periods (i.e., higher frequencies), shorter recordings are adequate; however, longer recordings are needed to collect sufficient data at longer periods (i.e., lower frequencies). Hence, AMT time series are typically 1-4 hours (3,600-14,440 s), BBMT time series are typically 12-48 hours (43,200-172,800 s), and LMT time series are typically 1-3 weeks (604,800-1,814,400 s). AMT is used to explore the upper 1-4 km, BBMT is used to explore the upper 10-40 km (e.g., Chapter 4), and LMT is used to explore the upper 100-400 km (e.g., Chapters 5 and 6).

The sampling rate must be at least twice the frequency of the highest frequency data desired, and an order of magnitude higher is better. For high-frequency bands, discontinuous sampling can be used, e.g., recording for two seconds every minute. The MT data quality will also depend on a number of other factors including the strength of the signal (recall that MT is a

natural-source method), proximity to noise sources (e.g., anthropogenic radio waves), and surface conditions (e.g., temperature and humidity/aridity).

AMT uses metal stakes or porous pot electrodes to measure the electric field in two orthogonal horizontal directions. BBMT and LMT use porous pot electrodes because electric charge can accumulate on metal stakes during relatively long recordings. The electric field is taken to be the electric potential difference between two electrodes divided by the distance between the two electrodes. AMT and BBMT use search coil magnetometers, also known as induction magnetometers, to measure the magnetic field in three orthogonal directions (two horizontal and one vertical). The vertical search coil can be omitted if you do not require tipper data. LMT uses a fluxgate magnetometer because it has a higher signal-to-noise ratio at long periods, and it measures the 3-D vector field. A schematic diagram of a typical MT installation is shown in Figure 3.32.

The research presented in this thesis used BBMT and LMT data. BBMT data were collected using the Phoenix MTU-V5-2000 and Phoenix MTU-5C systems. LMT data were collected using the Narod Intelligent Magnetotelluric System (NIMS). Photos of the MTU-5C and NIMS are shown in Figure 3.33.

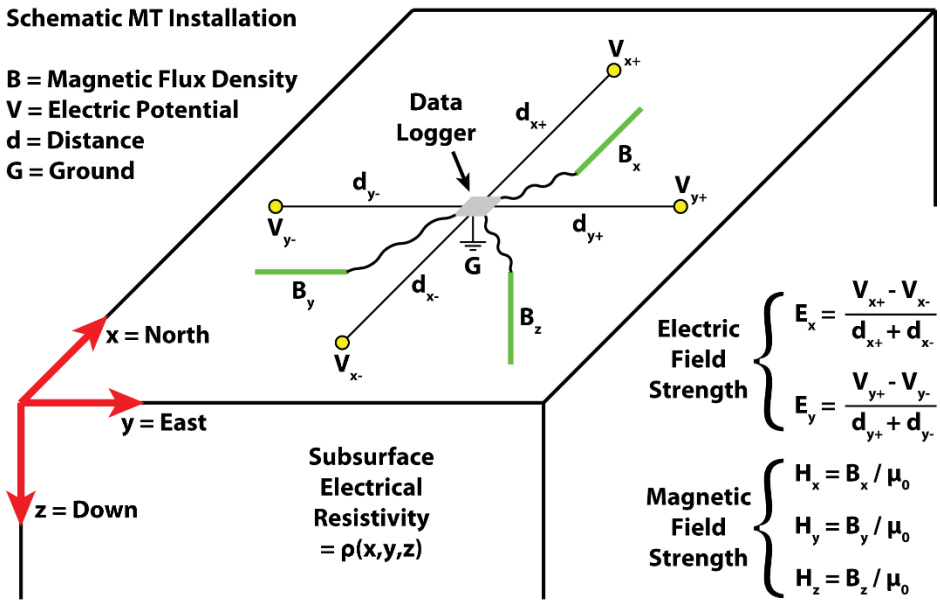

***Figure 3.32**: Schematic diagram of a typical magnetotelluric station. Yellow dots are electrodes and green lines are search coil magnetometers. To collect long-period MT data, the induction coils are replaced with a fluxgate magnetometer.*

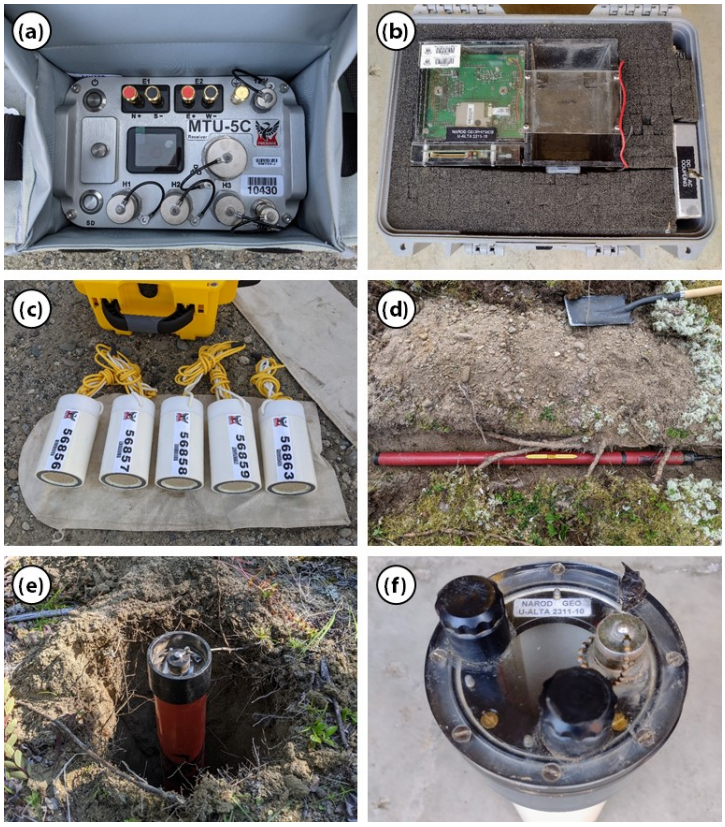

***Figure 3.33**: (a) Phoenix MTU-5C data logger. (b) NIMS data logger. (c) Porous pot electrodes. (d) Search coil magnetometer measuring the horizontal magnetic field. (e) Search coil magnetometer measuring the vertical magnetic field. (f) Narod Geophysics fluxgate magnetometer.*

3.5.2. Magnetotelluric time series processing

MT data are typically viewed and interpreted in the frequency domain; therefore, spectral analysis is performed on the raw time series. Subsets of data are chosen such that the spectral energy is negligible at frequencies greater than the Nyquist frequency (Hermance, 1973). These new time series are transformed into the frequency domain by Fourier harmonic analysis, usually the Fast-Fourier Transform (FFT). This assumes a fundamental period and a finite number of harmonics, so the sum of a Fourier series is used (Hermance, 1973). This early stage of processing results in a set of complex coefficients for each frequency and each MT field channel, e.g., E_x, E_y, H_x, H_y, and H_z (Smaï & Wawrzyniak, 2020).

By the early 1960's, it was common to calculate auto-correlation and cross-correlation time series, which were then Fourier transformed. This is usually referred to as power spectral analysis and the exact technique employed should reflect whether the dominant signal is transient or stationary (Hermance, 1973). From the Fourier transformed (frequency domain)

data, the impedance tensor elements must be estimated. Finally, the tensor impedance estimates should be rotated to the principal directions.

Egbert and Booker (1986) showed that the assumptions of a uniform source field and uncorrelated Gaussian-distributed errors were violated at long periods at geomagnetic mid-latitudes. Since the method of simple least squares can fail under these circumstances, they described a weighted least squares procedure and formulated a robust alternative to least squares.

For long-period geomagnetic depth sounding (GDS) data, it is essential to use weighted least squares, and most likely for MT data as well. At periods less than 300 s, error variance is independent of signal power, therefore Egbert and Booker (1986) proposed that ordinary least squares would be justified.

There is strong evidence to support the assumption that robust estimates of geomagnetic transfer functions are superior to least squares estimates. Proper windowing is important and Egbert and Booker (1986) suggested keeping windows as short as possible (relative to the target frequency), and that even if some poor quality data is included, the estimates will not be affected.

Simpson and Bahr (2005) summarized the methods of MT data processing. Time series are analyzed in the frequency domain after performing a discrete Fourier transformation. Logarithmically-spaced evaluation frequencies (ideally 6-10 per decade) are chosen, then spectral analysis is performed. When choosing bandwidths (spectral window sizes), there is a trade-off between resolution and data errors. Use of a Parzen window is a possibility, but it is one of many possible choices (Simpson & Bahr, 2005).

The remote reference method compares magnetic field components at nearby MT stations and it may be used to remove uncorrelated noise (Gamble et al., 1979). Least squares processing may be used to remove correlated noise with a Gaussian distribution. Robust processing methods should be used to remove correlated noise with a non-Gaussian distribution. In certain situations, correlated noise (between the electric and magnetic channels) may be removed with a two-source processing technique (Larsen et al., 1996; Simpson & Bahr, 2005).

MT data noise is often correlated, therefore robust processing methods are widespread (and arguably integral) tools for MT analysis (Chave et al., 1987; Chave & Thomson, 1989; Egbert & Booker, 1986; Larsen et al., 1996; Simpson & Bahr, 2005). The steps involved in MT data processing are summarized in a flowchart (Figure 3.34).

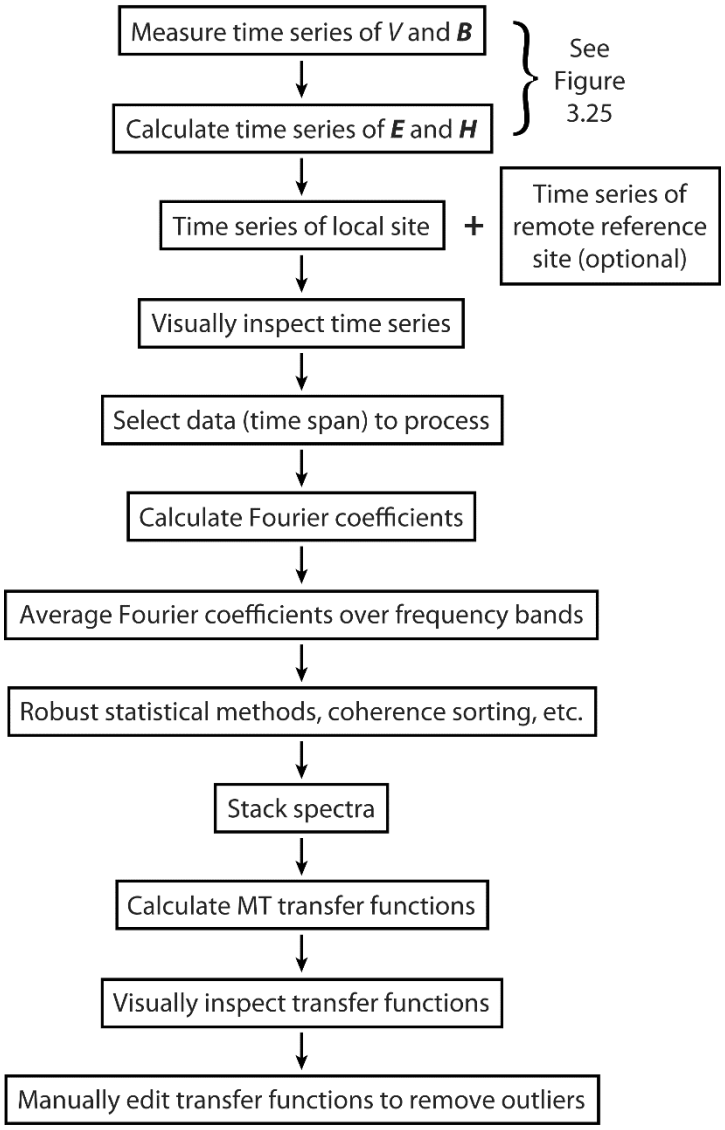

Figure 3.34*: MT data processing work flow.*

After MT time series are processed, MT data are generally viewed as apparently resistivity, phase, and tipper curves in the frequency domain. MT data may also be viewed as determinant apparent resistivity and determinant phase, where the impedance in equations (50) and (51) is replaced with the square root of the determinant of the impedance tensor,

$$Z_{det}(\omega) = det\begin{bmatrix} Z_{xx}(\omega) & Z_{xy}(\omega) \\ Z_{yx}(\omega) & Z_{yy}(\omega) \end{bmatrix}^{\frac{1}{2}} = \left[Z_{xx}(\omega) * Z_{yy}(\omega) - Z_{xy}(\omega) * Z_{yx}(\omega)\right]^{1/2} \quad (67)$$

which is a single complex number. This quantity incorporates all four of the impedance components and it is rotationally invariant.

Tipper data are often viewed in map view as induction vectors,

$$\boldsymbol{I}(\omega) = T_{zx}(\omega)\,\hat{x} + T_{zy}(\omega)\,\hat{y} \quad (68)$$

which point away from conductive regions, known as the Wiese convention, when the real part is plotted. If equation (68) is multiplied by -1, the induction vectors point toward conductive regions, known as the Parkinson convention. Some examples of these quantities are shown and discussed in Chapters 4-6, all of which assume 3-D resistivity structure.

3.6. Geophysical inverse theory and non-uniqueness

The transfer functions described in this chapter are functions of frequency, which is a proxy for depth. To convert these MT data into a model of subsurface resistivity, a mathematical process called inversion is needed. A forward problem uses physics to calculate the data that would be observed given a specified Earth model, for example,

$$\boldsymbol{d}_{\mathrm{p}} = F[\boldsymbol{m}_0] \quad (69)$$

where $\boldsymbol{d}_{\mathrm{p}}$ is the predicted data and $\boldsymbol{m}_0$ is the input model. Conversely, an inverse problem uses physics to calculate an Earth model ($\boldsymbol{m}$) that satisfies a set of observed data ($\boldsymbol{d}$), for example,

$$\boldsymbol{m} = F^{-1}[\boldsymbol{d}] \quad (70)$$

where the inverse function, F^{-1}, contains the physics of the problem along with any assumptions and approximations that were made. In practice, there are fewer data than model parameters and the inverse problem is underdetermined; therefore, an infinite number of solutions exist. This is in contrast to the forward problem, which has a unique solution.

In addition to the non-uniqueness of an underdetermined problem, inevitable noise in the data creates further non-uniqueness. In the case of magnetotellurics, the physics itself adds inherent non-uniqueness to the model, due to the diffusive nature of the electromagnetic signals in the Earth. Ideal MT responses generate smooth transfer functions, so a smooth resistivity model is usually sought; however, this may not be the most realistic model and

other constraints, both geophysical and geological, should be considered during inversion and interpretation.

A range of inversion algorithms have been developed to convert MT data into a model of the subsurface structure and this has included approaches using 1-D, 2-D, or 3-D resistivity models (Siripunvaraporn, 2012). Given the significant variations in geology over the study areas, a 3-D approach was used for the inversions described in Chapters 4-6. They all used the ModEM inversion algorithm, which iteratively updates the resistivity model using the non-linear conjugate gradients (NLCG) method until the model responses fit the measured MT data to within the specified statistical tolerance (Kelbert et al., 2014).

4. Magnetotelluric imaging of the magmatic and geothermal systems beneath Mount Meager, southwestern Canada

Hanneson, C. and Unsworth, M.J. (2023a)
Canadian Journal of Earth Sciences, Canadian Cordilleran Volcanism special issue, 1-19
doi:10.1139/cjes-2022-0136

Abstract

Magnetotelluric data were collected on and around the Mount Meager volcanic complex, an active volcanic complex with eruptions ~2,400 and ~24,300 years ago. Three-dimensional inversion was used to create an electrical resistivity model to a depth of > 20 km. The model is characterized by high resistivity (> 100 Ωm) in the upper 6–7 km, implying relatively dry, unaltered rock. Within this resistive layer, localized conductors are observed in the upper 2 km beneath Pylon Peak and Fish Creek, corresponding to low-permeability, clay-rich layers, acting as caprocks to geothermal fluids below. Beneath the resistive upper crust, there is a large conductor at ~5–15 km below sea level with an average resistivity of ~3 Ωm. Laboratory experiments of melt resistivity and petrological data from erupted volcanic rocks were used to interpret the model. The magma body (deep conductor) is inferred to have a minimum volume of ~2 × 10^{12} m^3 comprising ~18–32% dacitic-to-trachydacitic melt with ~6–8 wt.% H_2O at a temperature of ~800–900 °C. This is below the melt fraction of an eruptible magma body. Resolution tests suggest it might be regional in extent, not localized beneath Mount Meager. There are fluid pathways from the northern part of the magma body, up toward Mount Meager and nearby fumaroles. This model is a significant advancement from its predecessors, created 20–40 years ago, providing the first deep 3-D image of this volcanic system. Along with other geophysical and geological models of the Garibaldi Geothermal Energy Project, it will reduce the exploration risk associated with geothermal energy development.

4.1. Introduction

The tectonics of southwestern British Columbia (BC) is dominated by the subduction of the Juan de Fuca plate beneath North America in the Cascadia Subduction zone (Figure 4.1). The Garibaldi Volcanic Belt (GVB) at the northern end of this subduction zone is a Quaternary-

aged glaciovolcanic arc extending from northern Washington into southwestern BC (Venugopal et al., 2020). The GVB includes the Mount Meager volcanic complex (MMVC), an active calc-alkaline volcanic complex which has had at least two recent explosive volcanic eruptions, ~2,400 and ~24,300 years ago (Hickson, 1994; Russell et al., 2021).

Mount Meager has been studied for nearly 50 years and it is one of Canada's most promising opportunities for geothermal development. Extensive geological and geophysical information make it one of Canada's most thoroughly investigated volcanic geothermal systems (Ghomshei et al., 2004; Grasby et al., 2021; Witter, 2019). Canada's largest recorded landslide occurred at Mount Meager in 2010, and volcanic hazards including landslides are an important and current area of research at Mount Meager (Roberti et al., 2021; Warwick et al., 2022).

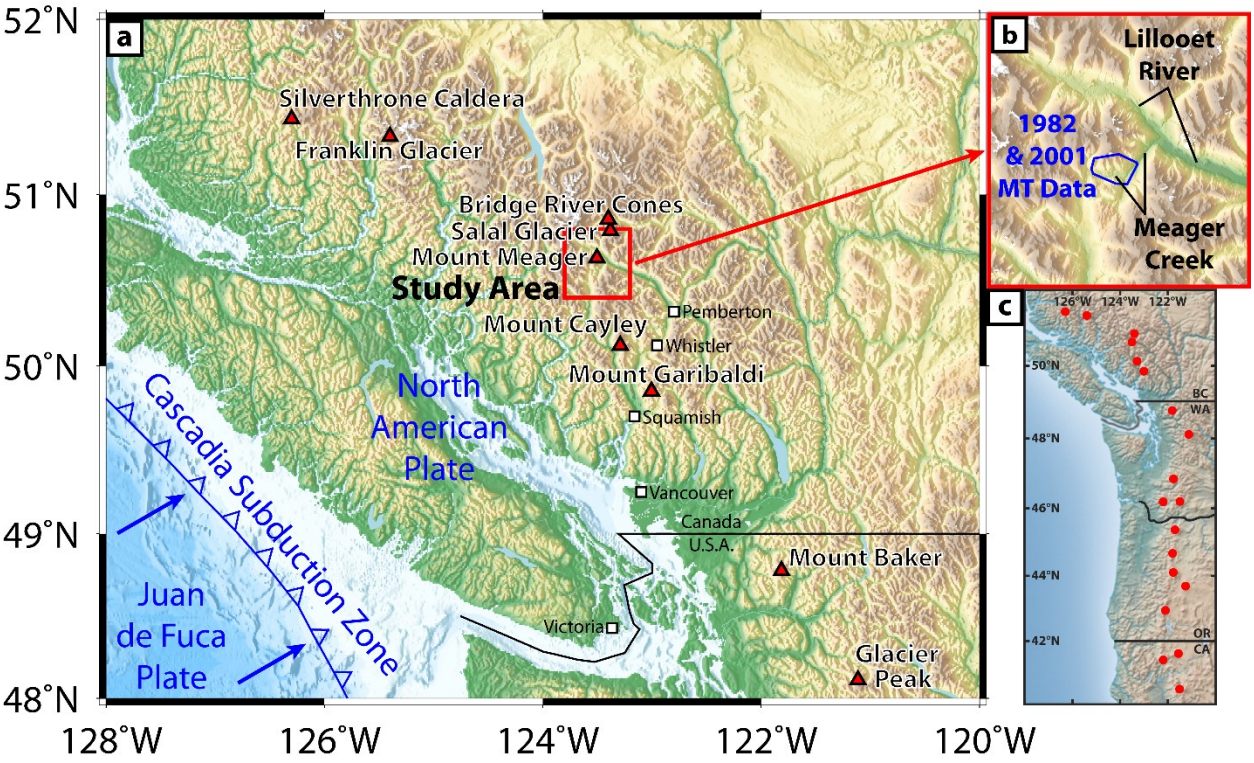

***Figure 4.1**: (a) Map of southwestern BC and northwestern Washington. Cities and towns are shown as squares. Volcanic centres of the Garibaldi Volcanic Belt are shown as triangles. From north to south, they are the Silverthrone caldera complex, the Franklin Glacier volcanic complex, the Bridge River Cones volcanic field, the Salal Glacier volcanic complex, the Mount Meager volcanic complex, the Mount Cayley stratovolcano, the Mount Garibaldi stratovolcano, the Mount Baker stratovolcano, and the Glacier Peak stratovolcano. (b) Study area with the area covered by the 1982 and 2001 magnetotelluric data (blue polygon). (c) Map of western North America showing the Cascade Volcanic Arc (red dots). These maps were plotted in latitude and longitude coordinates using the Mercator projection. The topography data are from the Shuttle Radar Topography Mission (SRTM) and were made publicly available by the United States Geological Survey (USGS).*

Despite decades of research, the structure of Mount Meager at depths greater than a few kilometres had not been imaged in 3-D. Questions that remain unanswered involve the nature or existence of a magma body and related hydrothermal system. To address these shortcomings, the Garibaldi Geothermal Energy Project was initiated in 2019. This was a multidisciplinary research program that included broadband magnetotelluric (MT), audio-magnetotelluric (AMT), passive seismic and gravity surveys, as well as bedrock mapping, fracture analysis, and thermal-spring geochemistry (Grasby et al., 2021). This paper describes the analysis of broadband magnetotelluric (BBMT) data, collected in 2019 and 2020, that were used to image the magmatic and hydrothermal systems in the upper- and middle-crust.

4.2. Background and motivation

4.2.1. Tectonic setting

The Juan de Fuca plate subducts beneath the North American plate at the Cascadia subduction zone at a rate of ~40 mm/year (Kreemer et al., 2014). Dehydration reactions in the subducting slab release volatiles into the overlying mantle, lowering its melting point and creating a region of partial melt, which leads to volcanism at the surface (Stern, 2002).

The chain of volcanoes resulting from this subduction process is called the Cascade volcanic arc (Figure 4.1 c). In the United States, the volcanic arc trends north and is called the High Cascades, extending from Mount Lassen in northern California to Washington state. The northernmost segment of the arc trends roughly northwest from Glacier Peak to the Silverthrone caldera, and is called the Garibaldi Volcanic Belt (Mullen et al., 2017; Venugopal et al., 2020). The GVB is 300–400 km inboard of the trench, whereas the High Cascades are 250–300 km inboard (Hickson, 1994). This implies that the subducted plate dips more steeply in the south than it does in the north.

4.2.2. Volcanic history of the Garibaldi Volcanic Belt

Volcanic centres of the GVB are shown in panel (a) of Figure 4.1. Mount Baker is the most voluminous volcanic complex in the GVB, with an estimated volume of 72 km^3 (Hickson, 1994). The most recent eruption in the GVB occurred at Glacier Peak in northern Washington in the mid-1700s, although Mount Baker experienced increased hydrothermal activity in 1975–1977 (Hickson, 1994). In the Canadian segment of the GVB, Mount Meager is the

largest stratovolcano and the most recently active volcano, with a volume of 20 km^3 and a Plinian-to-Pelean eruption ~2,400 years ago (Hickson, 1994).

Recent volcanism across the GVB has been dacitic-to-rhyolitic at Mount Meager, dacitic at Mount Cayley and Mount Garibaldi, and andesitic at Mount Baker and Glacier Peak (Hickson, 1994) illustrating a change from felsic composition in the north to intermediate silica content in the south. Mullen and Weis (2015) analyzed samples derived from more primitive magmas, i.e., rocks with more mafic compositions, and found them to be alkalic in the north and calc-alkaline in the south, due to mixing with melts from the depleted mantle wedge. They asserted that this was evidence for trench-parallel mantle flow and mixing beneath the GVB. This mantle flow was assumed to be northward below the Juan de Fuca plate and southward above it, with upward flow through the Nootka Fault slab window. Along-margin variations in seismic shear wave anisotropy are also observed and they could be indicative of complex mantle flow near the Queen Charlotte triple junction, where subduction transitions to strike-slip motion (Currie, Cassidy, et al., 2004).

The MMVC includes basaltic rocks of the Cracked Mountain Assemblage and Mosaic Assemblage, andesitic-to-dacitic rocks of the Plinth Assemblage and Capricorn Assemblage, and dacitic rocks of the Plinth Pyroclastic Deposit and Pebble Creek Formation (PCF). This 400 ka eruptive history follows a trend of increasing silica content. The chemistry of the MMVC is discussed in more detail in Section 4.5.1.

Hot springs occur near Mount Meager, Mount Cayley, Mount Baker, and Glacier Peak (Hickson, 1994) implying there is a significant heat source beneath the GVB. Elevated thermal gradients measured in drill holes at Mount Meager give additional evidence for the nature of the geothermal resource, as described below.

4.2.3. Geothermal exploration at Mount Meager

The Mount Meager area drew attention as a geothermal target in the 1970s because of two thermal spring systems: Meager Creek hot springs and Pebble Creek hot spring, also known as Keyhole hot spring (Souther, 1981). Early exploration work included geothermometry, direct current (DC) resistivity surveys, and diamond drilling (Fairbank et al., 1981). Lewis and Jessop (1981) measured heat flow of 132 mW/m^2 in a drill hole near Mount Meager, compared with a mean of 79mW/m^2 in three drill holes each more than 10 km from Mount Meager.

In 1980 and 1982, three large-diameter exploration holes (MC1, MC2, and MC3) were drilled to depths in excess of 3 km and fluid temperatures as high as 270 °C were encountered; however, these deep exploration holes were not drilled into high-permeability zones (Ghomshei et al., 2004; Ghomshei & Stauder, 1989). In 1984, MC1 produced fluids at 200–210 °C and supplied a 20 kW demonstration plant (Ghomshei et al., 2004). The geothermal reservoir was estimated to be 6×10^9 m^3 with an electric power capacity of 220 MWe for 30 years (Ghomshei & Stauder, 1989). Two subsequent wells (MC6 and MC8) had temperatures in excess of 230 °C and flow testing demonstrated a hydraulic connection between them (Witter, 2019).

Based on these studies, Mount Meager is recognized as one of the most promising high-temperature geothermal resources in Canada. However, barriers to development have been identified and need to be addressed. One challenge has been its distance to the power grid. This has improved in recent years because Innergex Renewable Energy Inc. has been operating two run-of-river hydroelectric plants near Mount Meager since 2017, as part of their Upper Lillooet River Hydro Project. Electricity generated at these two facilities is transmitted to the BC Hydro transmission system by a 230 kV transmission line. The proximity of this high-voltage line to Meager Creek has increased the economic feasibility of a geothermal power plant in the area. An alternative method of energy production is being pursued by Meager Creek Development Corporation, which is planning to produce green hydrogen from water by electrolysis using geothermally generated electricity.

Another challenge to geothermal development comes from landslide hazards. A large rockslide and debris flow occurred at Mount Meager on 6 August 2010, that displaced 53 million cubic metres of material (Allstadt, 2013; Guthrie et al., 2012; Roberti et al., 2018). Meager Creek was temporarily dammed and the flood risk led to the evacuation of 1500 Pemberton residents (Guthrie et al., 2012). Therefore, hazard assessment is also an important consideration for ongoing geothermal development at Mount Meager.

4.2.4. Previous electrical and electromagnetic geophysical studies at Mount Meager

Geophysical methods are widely used in geothermal exploration (Hersir et al., 2022) and studies of magma plumbing systems (Magee et al., 2018). Methods that measure electrical resistivity are key to delineating geothermal resources because the resistivity of rocks is controlled by important parameters such as temperature, porosity, fluid salinity, and the

presence of clay alteration minerals (Hersir et al., 2022). These methods are also powerful tools in volcanic studies because magma and magmatic hydrothermal fluids are usually much less resistive than solid rock (Magee et al., 2018).

DC methods measure electric potentials at the surface while electric current is being injected into the ground, and the penetration depth is proportionate to the electrode spacing (Burger et al., 2006; Hersir et al., 2022). These methods are typically used in geothermal exploration to image the resistivity of the shallowest 1–2 km (Hersir et al., 2022).

Induced polarization (IP) methods measure the response of the subsurface after current injection ceases; these methods can use DC and time-domain measurements, or alternating current and frequency-domain measurements (Burger et al., 2006). IP methods are used to image the electrical chargeability, a physical property related to electrical conductivity that allows a build-up of electric charge. These methods are widely used in mineral exploration. Clays and brines also have a high chargeability, making it a useful property to map during geothermal exploration. These IP methods can be used to image the upper 3–4 km of the subsurface (Gross et al., 2021).

In addition to DC and IP methods, direct measurements of resistivity can be made by well-logging if drilling has taken place. However, well-logging is typically restricted to temperatures below a few hundred degrees, with the cost of instrumentation being higher when high-temperature functionality is required.

In 1974 and 1975, dipole–dipole IP surveys were conducted at Mount Meager, using frequency-domain and time-domain equipment (Shore, 1978). Shore (1978) estimated the resistivity of the South Meager anomaly to be 25–30 Ωm, embedded in a background resistivity of 200–1200 Ωm. Based on the geophysical method used, subsurface resistivity was likely imaged to a depth of several kilometres. This anomaly corresponds to the south reservoir, also known as the Meager Creek reservoir (Nevin et al., 1978; Shore, 1978).

Electromagnetic (EM) methods measure time variations of EM fields at the surface, which are affected by the resistivity of the subsurface. They include both controlled-source and passive-source methods (Hersir et al., 2022; Magee et al., 2018). EM methods are particularly useful because the depth of investigation is controlled by the frequency of the signal, a significant advantage over DC methods where depth is controlled by the offset between the receiver and

transmitter dipoles. Passive-source ground-based EM methods include the MT method and the higher frequency AMT method. Controlled-source EM methods include the controlled-source AMT method and the transient EM method. AMT can image the resistivity of the upper several kilometres, whereas BBMT can image tens of kilometres. AMT and BBMT are suitable methods to use in environmentally sensitive and culturally significant areas because they have a minimal environmental footprint and the equipment is only installed for a short amount of time, ranging from a couple of hours to a few days.

MT has been applied at Mount Meager since exploration began in the 1970s. During three surveys in 1976–1979, MT soundings were measured at 17 sites near Mount Meager, Meager Creek, and the Lillooet River (Pham Van Ngoc, 1977, 1978, 1980). Pham Van Ngoc (1980) used data from 11 sites surrounding Mount Meager to infer the presence of a high temperature zone a few kilometres below Mount Meager and suggested that it could be related to a magma body.

In 1982, seven MT soundings were measured near Meager Creek along an east–west traverse crossing the South Meager thermal anomaly (Flores et al., 1985; Flores-Luna, 1986). A set of four-layer models were created using 1-D inversion and they inferred the presence of a conductor (10–60 Ωm) with its top at 80–380 m depth and its base at 330–660 m depth (Flores-Luna, 1986). The bottom layer (half-space) had a resistivity of 5–140 Ωm beginning at a depth of 5–27 km. The results of Flores-Luna (1986) did not support the conclusion of Pham Van Ngoc (1980) that there might be partial melt a few kilometres below the surface.

The data from 1982 were re-analyzed by Jones and Dumas (1993) using 1-D inversion, 2-D forward modelling, and 2-D inversion of a reduced data set. They imaged a conductor (20–80 Ωm) less than 200 m below the surface that was 6 km wide and 500 m thick, which they interpreted as a clay cap. They also imaged a region of low resistivity (10 Ωm) below 14.5 km depth and interpreted it as a magma body.

In 2001, 31 MT soundings were measured near Meager Creek during a commercial survey, mostly on the south slope of the Mount Meager massif (Candy, 2001). These MT data, along with the data from 1982, were analyzed using 2-D inversion and 3-D inversion. The resulting models showed a conductive region (30–100 Ωm) in the upper 1–2 km and moderate resistivity (<500 Ωm) at depths of ~8 km (Candy, 2001). However, the models presented did not extend deep enough to image the inferred magma body.

4.2.5. Motivation for the current broadband MT study

There are still uncertainties in (1) the permeability and porosity of the rocks in the geothermal reservoir, (2) the size and location of the deep heat source, (3) fluid pathways upward from the heat source, and (4) the pattern of regional groundwater flow. These uncertainties are being addressed with new geological and geophysical studies that are part of the Garibaldi Geothermal Energy Project (Grasby et al., 2021). This project included an AMT study to model the shallow structure of the geothermal reservoir (Hormozzade Ghalati et al., 2022). It also included the BBMT study described in this paper that is focused on the deeper structure and magma body.

Prior MT studies, described in the previous section, focused on the South Meager anomaly, below Meager Creek and the south side of the Mount Meager massif (Figure 4.1 b). Jones and Dumas (1993) imaged a potential magma body below 14.5 km depth, along a profile near Meager Creek. To image the 3-D geometry and spatial extent of a magma body such as this, a grid of BBMT stations extending beyond the MMVC was required. MT surveys were conducted in 2019 and 2020 to serve this purpose, as described in the following section.

4.3. Data and methods

4.3.1. The magnetotelluric method

The MT method measures electric field strength (***E***) and magnetic field strength (***H***) time series at the surface of the Earth. These time series data are converted into frequency domain responses which describe the impedance of the Earth. The impedance is a complex-valued tensor,

$$\boldsymbol{Z}(\omega) = \begin{bmatrix} Z_{xx}(\omega) & Z_{xy}(\omega) \\ Z_{yx}(\omega) & Z_{yy}(\omega) \end{bmatrix} \tag{71}$$

where

$$Z_{ij}(\omega) = \frac{E_i(\omega)}{H_j(\omega)} \tag{72}$$

for orthogonal horizontal directions *x* and *y*, representing geographic north and east, respectively. The apparent resistivity and phase, respectively, are calculated from the impedance as

$$\rho_{a\,ij}(\omega) = \frac{1}{\omega\mu_0}\left|Z_{ij}(\omega)\right|^2 \tag{73}$$

and

$$\phi_{ij}(\omega) = Arg[Z_{ij}(\omega)] = \tan^{-1}\left[\frac{Im[Z_{ij}(\omega)]}{Re[Z_{ij}(\omega)]}\right] \quad (74)$$

which is usually in the range 0–90°. A second transfer function, the vertical magnetic transfer function, can be computed using just the magnetic field components,

$$\boldsymbol{T}(\omega) = [T_{zx}(\omega) \quad T_{zy}(\omega)] = \left[\frac{H_z(\omega)}{H_x(\omega)} \quad \frac{H_z(\omega)}{H_y(\omega)}\right] \quad (75)$$

where *z* is the vertical direction, pointing downwards in a conventional right-handed coordinate system. The vertical magnetic transfer function is referred to as the tipper. Tipper data are often viewed in map view as induction vectors,

$$\boldsymbol{I}(\omega) = T_{zx}(\omega)\,\hat{x} + T_{zy}(\omega)\,\hat{y} \quad (76)$$

which point away from conductive regions, known as the Wiese convention, when the real part is plotted. For a more detailed description of the MT method, please see Hanneson and Unsworth (2023b) and references therein.

4.3.2. Magnetotelluric data

As part of the Garibaldi Geothermal Energy Project, BBMT data were measured at 35 locations in 2019 and 2020 (Figure 4.2). MT data do not need to be collected simultaneously, so the data collected in this study were combined with data collected in 1982 and 2001 for analysis (Table B.1). This approach assumes that the subsurface resistivity structure has not changed significantly over the time frame of the surveys. For example, 20–40 years is a relatively short amount of time when considering the evolution of a magma body and its associated hydrothermal systems (Arnórsson, 2014; Karakas et al., 2017).

MT data at all 29 frequencies, from six representative stations, are shown in geographic coordinates in Fig. 3. Stations mt14 and mt22 were located above the South Meager anomaly (Figure 4.2) and the *yx* component of apparent resistivity, which is proportional to $|\mathrm{E_y/H_x}|^2$, decreases significantly with decreasing frequency (Figure 4.3 a-b). This implies a deep conductor with electric current flowing in the east–west direction.

Stations MGR114 and MGR119 were located north and south, respectively, of the South Meager anomaly (Figure 4.2) and the apparent resistivity decreases with decreasing frequency, but not as much as at mt14 and mt22 (Figure 4.3 c-d). This implies that the deep conductor extends beyond the South Meager area. Both components of the tipper data from

MGR114 are noisy at low frequencies, likely due to movement of the vertical induction coil during recording.

Stations MGR121 and MGR207 were located at the northeastern and western edges, respectively, of the MT station grid (Figure 4.2) and the apparent resistivity is higher than at the other four sites (Figure 4.3 e-f). This implies that the deep conductor does not extend below the northeastern and western edges of the grid.

Figure 4.4 and Figure 4.5 show the measured data in map view at six of the 29 frequencies in the MT data set. The apparent resistivity and phase were approximated by using the determinant impedance, $Z_{det}(\omega) = [Z_{xx}(\omega)Z_{yy}(\omega) - Z_{xy}(\omega)Z_{yx}(\omega)]^{1/2}$, where ω is the angular frequency. This quantity incorporates all four of the impedance components and is rotationally invariant. The induction vectors are plotted using the Wiese convention; therefore, the arrows point away from conductive regions. Skin depth increases with decreasing frequency, so frequency is a proxy for depth, as illustrated in Table B.2 and Figure B.1.

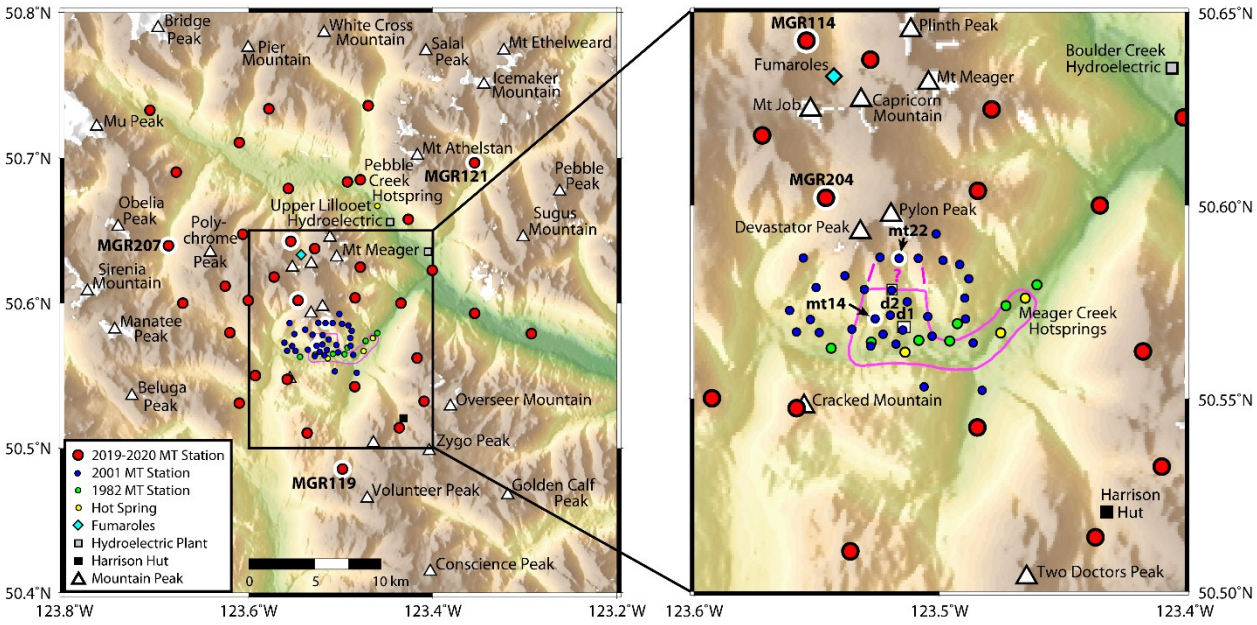

Figure 4.2*: Map of the study area with locations of broadband MT stations and other points of interest. MT stations mentioned in the paper are outlined in white and labelled: (left) MGR119, MGR121, MGR207; (right) MGR114, MGR204, mt14, mt22. The pink line represents the South Meager anomaly, the northern extent of which is uncertain (approximated after Nevin et al., 1978). This anomaly was also mentioned by Shore (1978) and others. The white rectangle labelled d1 is centred on the locations of drill holes MC-1, MC-2, and MC-3. The white rectangle labelled d2 is centred on the locations of drill holes MC-6 and MC-8. These maps were plotted in latitude and longitude coordinates using the Mercator projection. The topography data are from the Shuttle Radar Topography Mission (SRTM) and were made publicly available by the United States Geological Survey (USGS).*

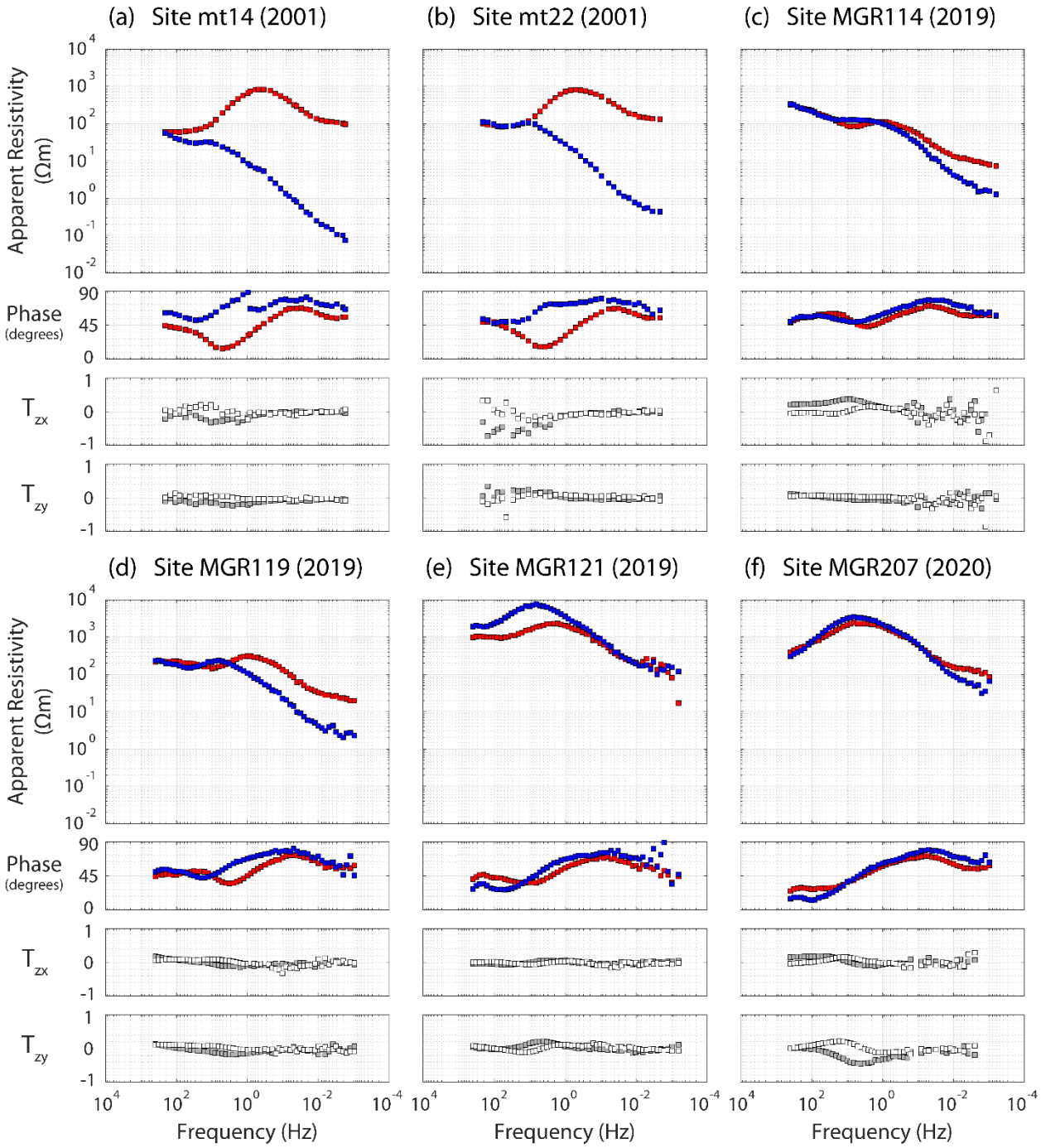

***Figure 4.3**: Apparent resistivity, phase, and tipper data from six MT stations. Red squares are xy components (calculated using the north–south electric field and east–west magnetic field), blue squares are yx components (calculated using the east–west electric field and north–south magnetic field), grey squares are real components, and white squares are imaginary components. These MT stations are highlighted and labelled in Figure 4.2: (a) mt14 near the middle of the 2001 grid, (b) mt22 south of Pylon Peak, (c) MGR114 northwest of the fumaroles, (d) MGR119 at the southern edge of the grid, (e) MGR121 at the northeastern edge of the grid, east of Mt. Athelstan, and (f) MGR207 at the western edge of the grid, west of Polychrome Peak.*

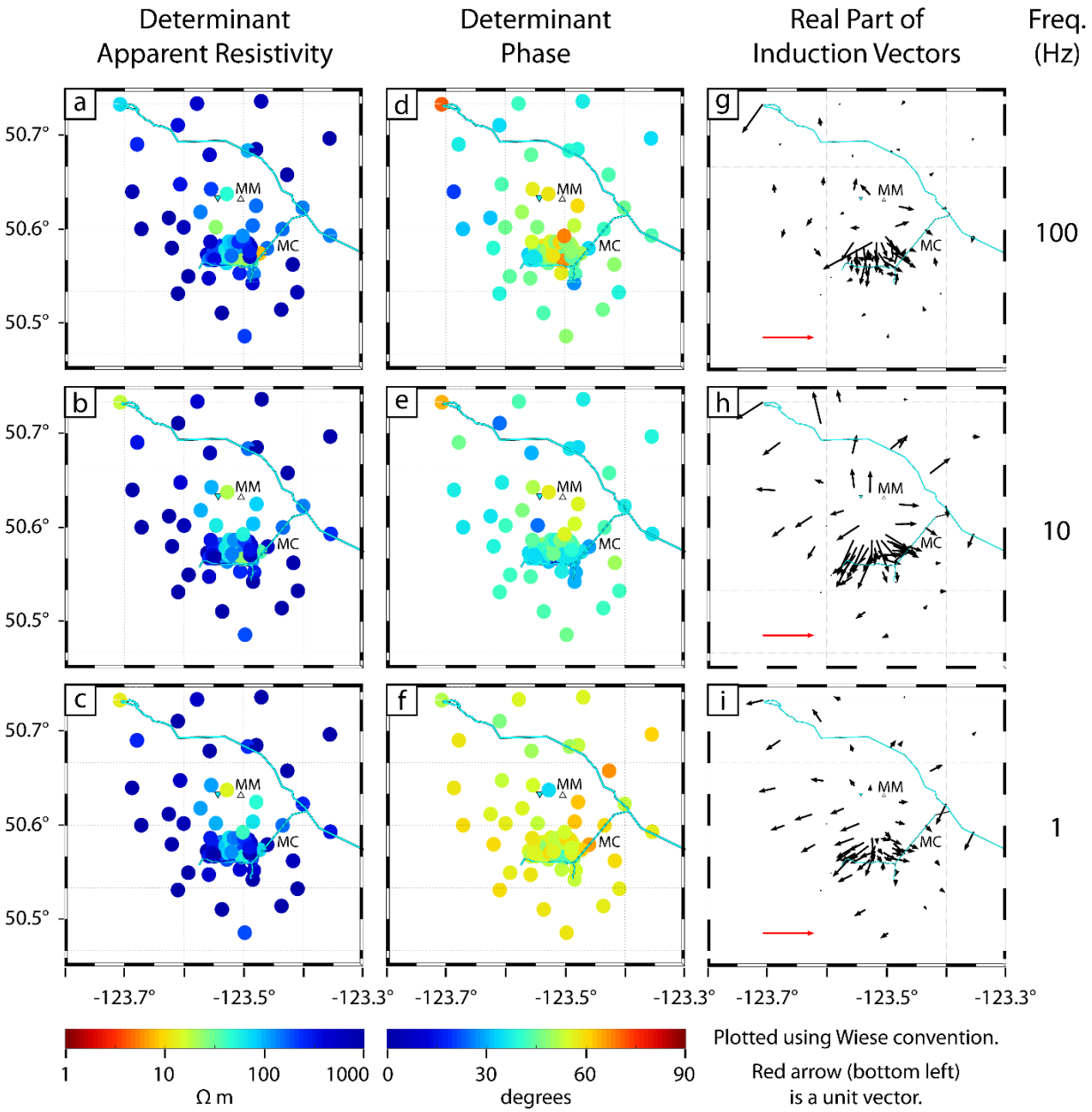

***Figure 4.4**: Determinant apparent resistivity (a–c), determinant phase (d–f), and real part of induction vectors using the Wiese convention (g–i) at three logarithmically spaced frequencies, representative of the high frequencies in the data set. Abbreviations: MC, Meager Creek; MM, Mount Meager.*

In the frequency range 1–100 Hz, the apparent resistivity is high (> 100 Ωm) at most of the MT sites. This indicates that the upper several kilometres are resistive, except for some small conductive features. In the frequency range 10–100 Hz, the phase is around 45°, indicating that at shallow depths the resistivity does not vary significantly with depth. An exception to this is higher phase between Mount Meager and Meager Creek, indicating a shallow conductor in this area which corresponds to the South Meager anomaly mentioned in Section 4.2.4. At

a frequency of 1 Hz, the phase is greater than 45° at most of the MT sites, indicating that resistivity is decreasing with depth. In the frequency range 1–100 Hz, induction vectors generally point radially outward, suggesting a conductive central region in the volcanic core. Surface elevation differs by ~2 km over the survey area and a topographic effect was believed to be partially responsible for the pattern of induction vectors observed, as discussed in Section 4.4.2.3.

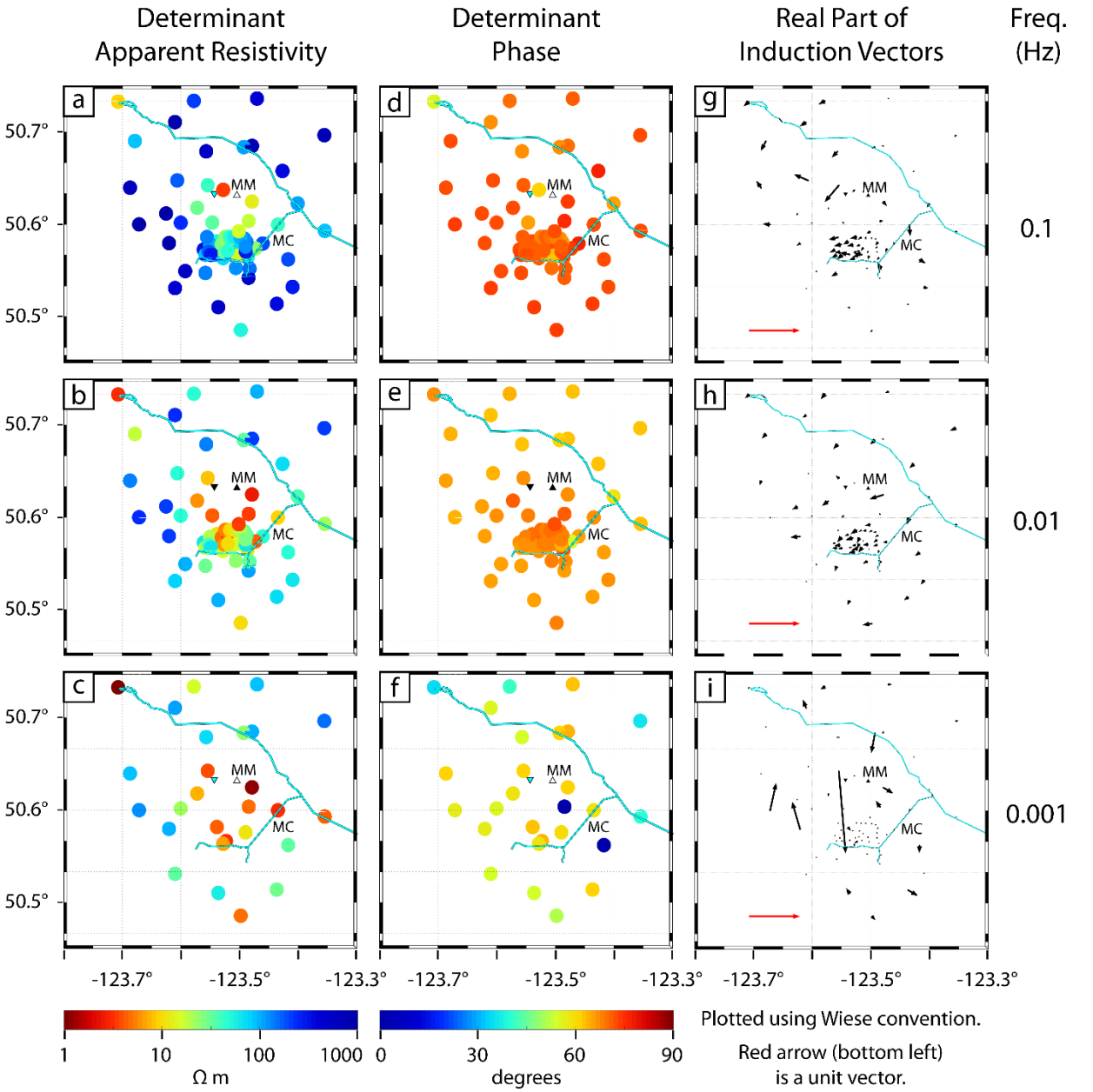

***Figure 4.5**: Determinant apparent resistivity (a–c), determinant phase (d–f), and real part of induction vectors using the Wiese convention (g–i) at three logarithmically spaced frequencies, representative of the low frequencies in the data set. Abbreviations: MC, Meager Creek; MM, Mount Meager.*

In the frequency range 0.001–0.1 Hz, the apparent resistivity is low at many of the MT sites, especially below the massif. This indicates that there is a deep conductor beneath the massif. In the frequency range 0.01–0.1 Hz, the phase is 60–90° at most of the MT sites, indicating that resistivity is decreasing rapidly with depth. Signals at these frequencies are penetrating into the deep conductor. At a frequency of 0.001 Hz, the phase is only slightly greater than 45°, indicating that the signals have likely reached the base of the deep conductor. In the frequency range 0.001–0.1 Hz, the induction vectors are small, except for some outliers. In the frequency range 0.01–0.1 Hz, induction vectors on the south flank of the massif point west, suggesting that the deep conductor might deepen to the east or extend further to the east.

A range of inversion algorithms have been developed to convert MT data into a model of the subsurface structure and this has included approaches using 1-D, 2-D, or 3-D resistivity models (Siripunvaraporn, 2012). Given the significant variations in geology over the study area, and inherently 3-D nature of a volcanic system, a 3-D approach was used for the inversion of the MT data. This used the ModEM inversion algorithm that iteratively updates the resistivity model using the nonlinear conjugate gradients method until the model responses fit the measured MT data to within the specified statistical tolerance (Kelbert et al., 2014). The inversion data, model mesh, and inversion parameters are described in the following sections.

4.3.3. MT data selection and inversion model

The inversion used MT data at 29 frequencies, logarithmically spaced between 0.001 and 400 Hz, measured at 66 locations (Figure 4.6). The median distance between a station and its nearest neighbour was 1.1 km; the mean distance between a station and its nearest neighbour was 1.9 km. The data were measured in geomagnetic coordinates: magnetic north and east for x and y, respectively. For the inversion, they were rotated to a geographic coordinate system: geographic north and east for x and y, respectively. The following error floors were applied to the impedance ($\boldsymbol{Z}$) and tipper ($\boldsymbol{T}$) data: 5% of $\sqrt{|Z_{xy}||Z_{yx}|}$ to $\boldsymbol{Z}$ and 0.03 to $\boldsymbol{T}$. This was done to avoid skewed weighting if the errors at some sites and frequencies were estimated to be unreasonably low.

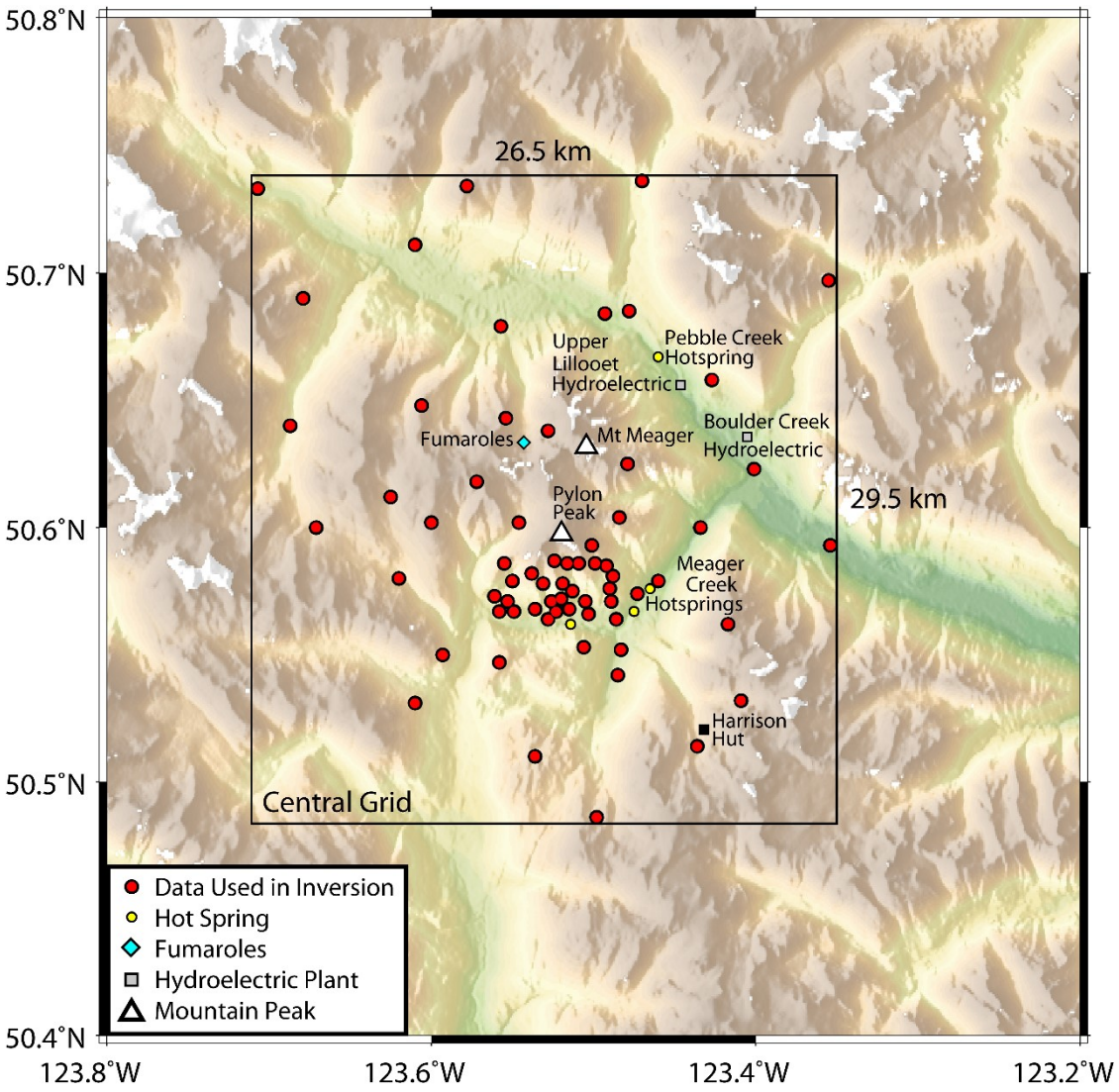

***Figure 4.6**: Map of the study area with locations of MT data used in the inversion, as well as other points of interest. This map was plotted in latitude and longitude coordinates using the Mercator projection. The topography data are from the Shuttle Radar Topography Mission (SRTM) and were made publicly available by the United States Geological Survey (USGS).*

The central grid of the model, containing all MT stations, was 29.5 × 26.5 km. The model cells had a horizontal extent of 250 × 250 m in the region where MT data were defined, with 15 padding cells increasing geometrically by a factor of 1.35 away from this central grid. In the vertical direction, the upper layers were 50 m thick, and layer thickness increased geometrically by a factor of 1.1 below the base of topography. The top 12 layers, higher than all the MT sites, were removed to decrease the total model size and computing resources needed. The final model had dimensions of 201, 198, and 298 km in the north–south, east–west, and vertical directions, respectively (148 × 136 × 105 cells).

4.3.4. Inversion parameters and data misfit

The inversion of geophysical data is inherently non-unique, i.e., it can be shown that many models can fit a given data set to within a specified statistical tolerance (Parker & Whaler, 1981). This was investigated by undertaking a significant number of inversions that explored different data subsets, initial model configurations, model covariances, and regularization parameters. The ModEM inversion algorithm of Kelbert et al. (2014) was used in all cases and the inversions are listed in Table B.3.

One important factor to investigate is the degree of spatial smoothing imposed on the resistivity model. In ModEM, this is imposed through the model covariance length scale, γ, which is a measure of model smoothing applied across cell boundaries, where a higher number corresponds to more smoothing. The preferred inversion used γ = 0.4 in the horizontal and vertical directions. These values were chosen after a series of sensitivity tests were performed, as described in Section 4.4.2.

A second parameter that controls the smoothing is the regularization parameter, λ. This parameter was systematically reduced during the inversions until it reached a minimum value of 10^{-8}. If the inversion begins with a high value, such as λ = 10, the inversion produces a spatially smooth resistivity model. With a low value, such as λ = 10^{-4}, the inversion produces a rougher model with a lower data misfit.

Twenty-seven 3-D inversions were run to examine how the choice of data and control parameters influenced the final 3-D resistivity model (Table B.3). The preferred inversion (Table B.3, inversion 15) began with λ = 10 and a root mean square (R.M.S.) misfit of 11.7, then after 450 iterations, the inversion converged to an R.M.S. misfit of 1.77 with λ = 10^{-8}. The model did not change significantly during the last third of the iterations and the preferred model is from iteration 323, at λ = 10^{-6}, with a misfit of 1.92. The final iteration was not used because λ = 10^{-8} was an arbitrary end point; the inversion would have continued if a lower value of λ had been chosen. Figure B.2 shows inversion parameters for all iterations. The preferred model was chosen for a balance between data misfit and model smoothness, taking into consideration the sensitivity tests discussed in Section 4.4.2.

The station-by-station data misfit is shown in Figure 4.7. The highest misfit is from the site between Mount Meager and the fumaroles; this station was installed on a rock glacier and the MT data were noisy, likely due to ground motion. All other sites have a misfit of 2.7 or less.

The six different data components had similar misfit at all frequencies (Figure B.3), showing that the joint inversion was able to successfully fit the full impedance tensor and the tipper data.

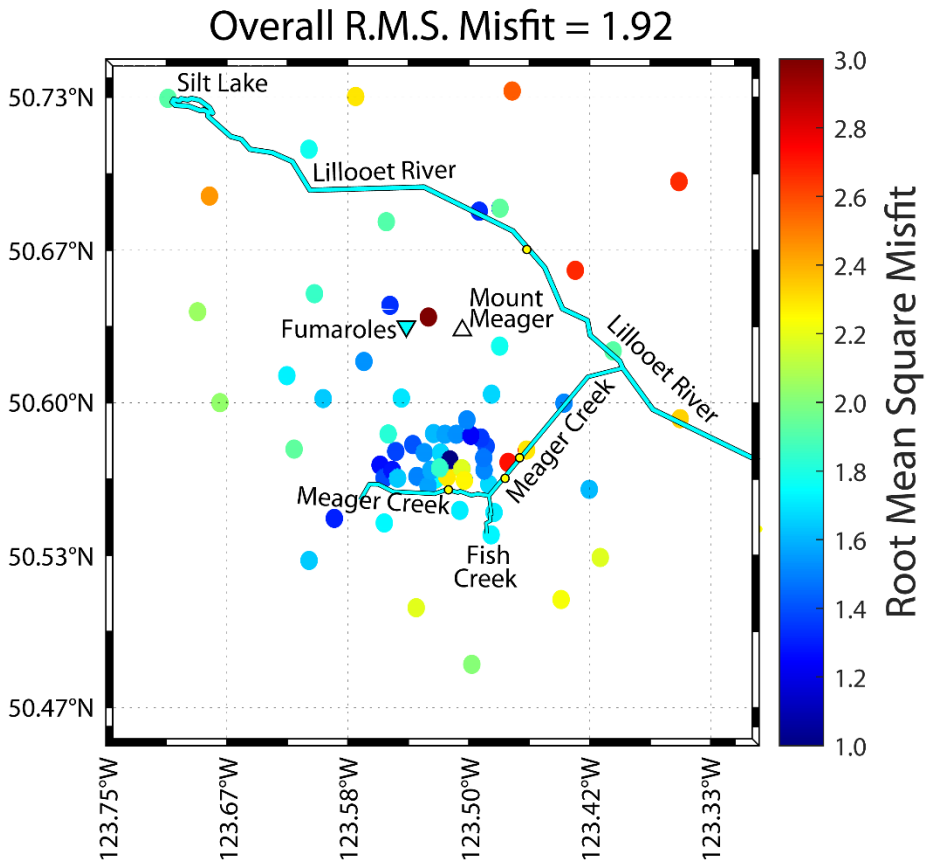

***Figure 4.7**: R.M.S. misfit of each MT sounding, plotted in map view.*

4.4. Resistivity model

A preliminary 3-D resistivity model was presented in two Geoscience BC reports (Hanneson & Unsworth, 2022; Unsworth et al., 2021). The preferred resistivity model presented below supersedes the one presented in these reports. This new model differs from the preliminary one in a few ways: (1) the near surface conductors extend slightly deeper, (2) there is a conductor around sea level beneath MT station MGR204, in between Meager Creek and the fumaroles, and (3) the deep conductor is slightly larger and has a slightly different shape. These differences are small, but the authors believe they better represent the true subsurface resistivity structure.

4.4.1. Description of the preferred resistivity model

The preferred 3-D resistivity model is presented in Figure 4.8 and Figure **4.9**. A 1–1,000 Ωm colour scale was used because it accounts for 98.6% of the model cells; 0.1% are < 1 Ωm and 1.3% are > 1,000 Ωm. The upper 6–7 km are generally resistive, with a number of small near surface conductors. These conductors are located in the central part of the model, near Mount Meager and Meager Creek. Specifically, there are significant conductors in the upper 2 km beneath Pylon Peak and Fish Creek.

Below the resistive upper crust, there is a large conductor in the depth range 5–15 km below sea level. It has a resistivity of 0.3–30 Ωm and an average resistivity of ~3 Ωm (Figure B.4). This 10 km thick conductor spans 20 km in the north–south direction and 20 km in the east–west direction. As an approximation, an ellipsoid with these distances as axes has a volume of 2,100 km^3. Above the northern part of this deep conductor, there is a conductive zone extending up toward Mount Meager and the fumaroles (Figure 4.9 a–c). In this zone, the resistivity is 20–90 Ωm (Figure B.5). Below the deep conductor, the resistivity increases until it becomes uniformly 90–100 Ωm below a depth of approximately 40 km, approaching the 100 Ωm resistivity of the starting model.

4.4.2. Sensitivity tests

4.4.2.1. Multiple inversions and exploration of parameters

Before a resistivity model is interpreted, it is important to carefully evaluate the various features present in the model. A key part of this process was described in the previous section where a range of inversions were undertaken and summarized in Table B.3. To investigate the effect of varying the model covariance length scale, γ, nine different configurations were used (Table B.3, inversions 9–17). The final R.M.S. misfit, when $\lambda = 10^{-8}$, ranged from 1.77 to 3.77 and the lowest occurred when γ = 0.4 in all three directions (Figure B.6).

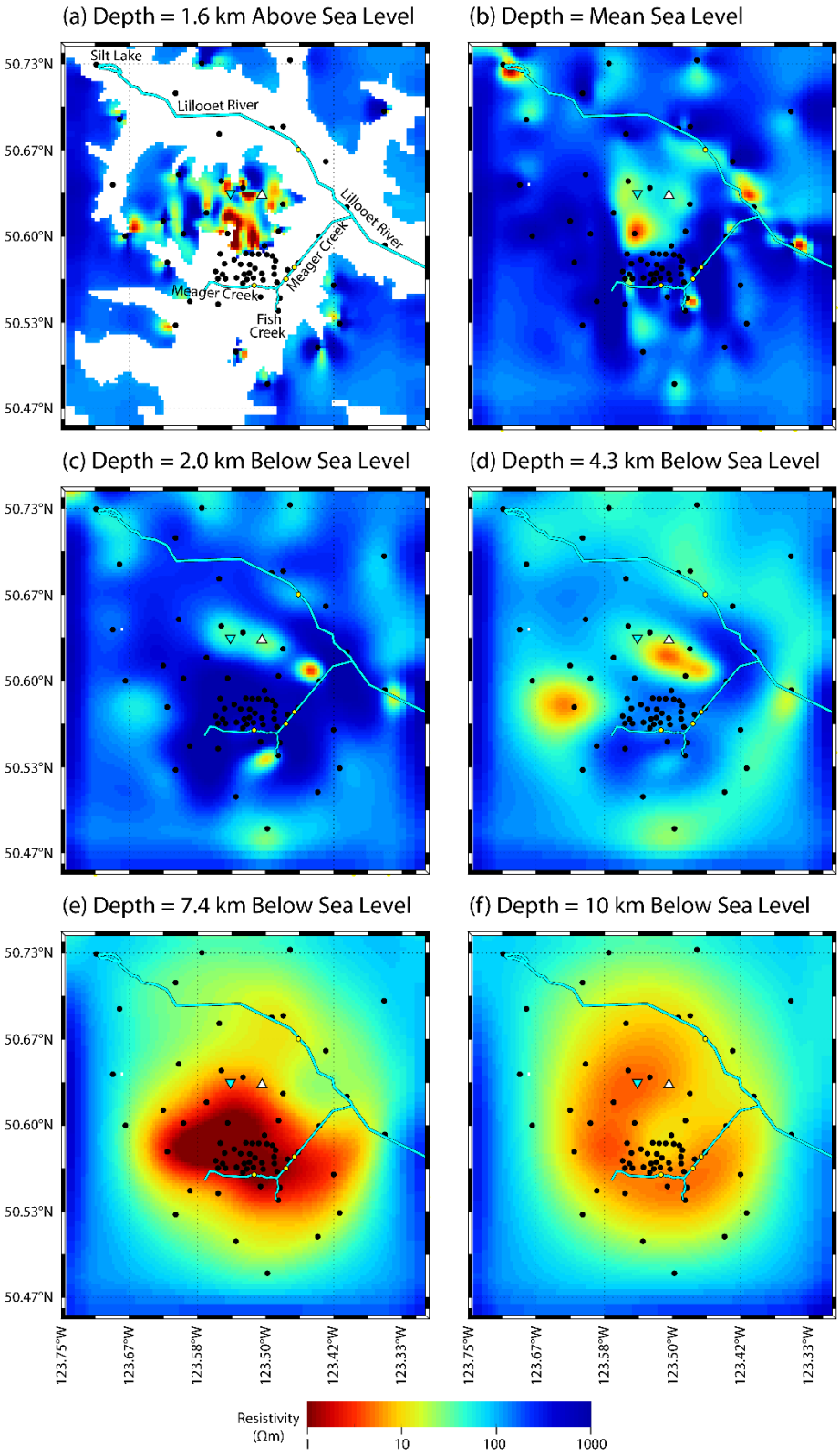

***Figure 4.8**: (a-f) Depth slices from the preferred 3-D resistivity model. Cyan lines represent the surface locations of Silt Lake, Lillooet River, Meager Creek, and Fish Creek, as labelled in panel (a). White and cyan triangles are the locations of Mount Meager and the fumaroles, respectively. Black dots are MT data locations and yellow dots are hot spring locations.*

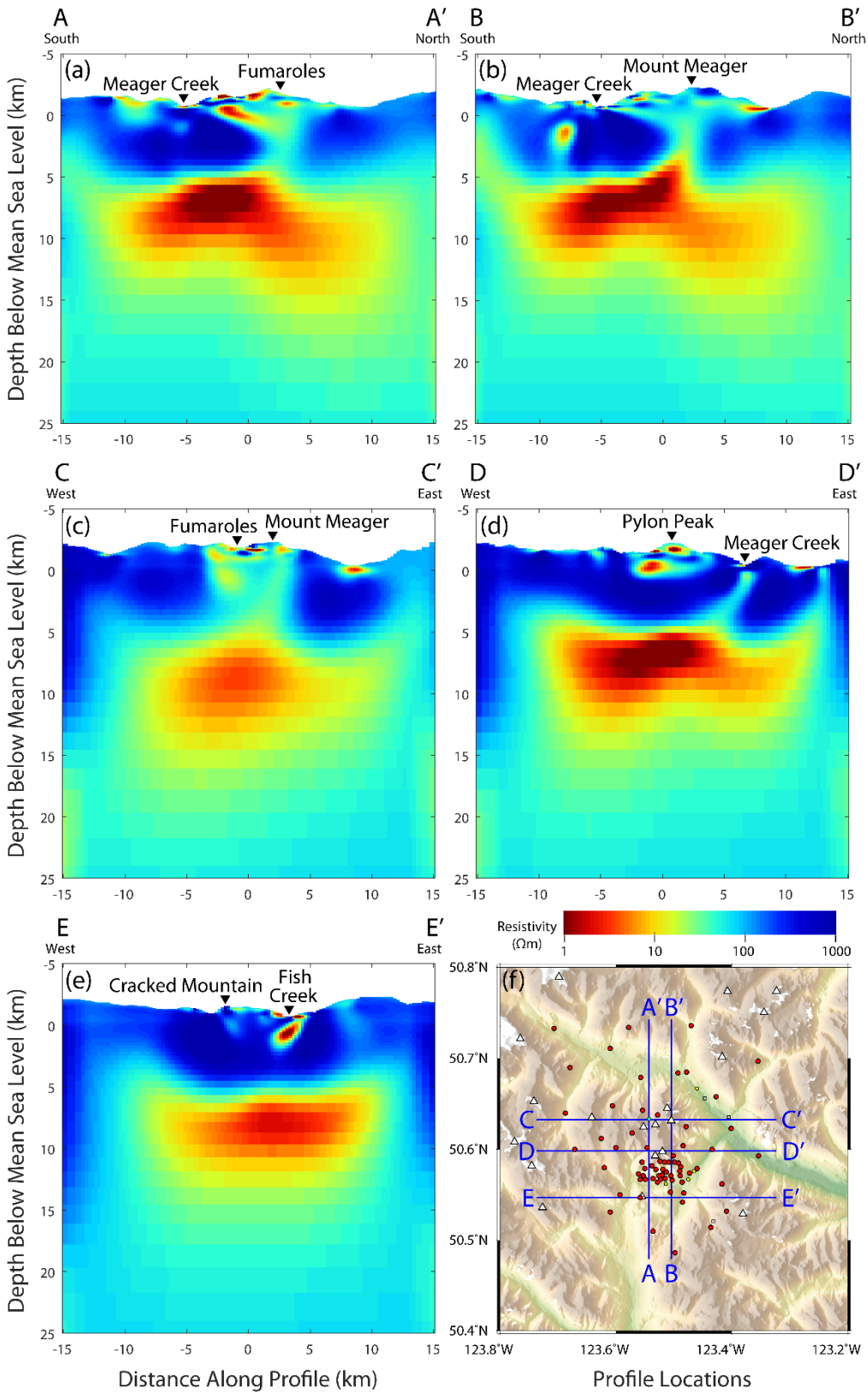

***Figure 4.9**: (a–e) Cross-sections from the preferred 3-D resistivity model. Black triangles indicate landmarks at the surface. (f) Topographic map with cross-section locations. Red dots are MT data locations and yellow dots are hot spring locations.*

4.4.2.2. Model editing

4.4.2.2.1 Deep conductor in the depth range 5–15 km below sea level

Another approach to investigating model sensitivity is to edit the model and calculate the change in misfit. If part of the model can be changed without changing the data misfit, it is not well resolved by the data. This approach was used to address a particular aspect of the model, the low resistivity layer at 5–15 km below sea level, which appears to have an unusually low resistivity (down to 0.3 Ωm). This test was implemented by taking models from inversions 4 and 15 (i4 and i15) and editing the models so that cells with a resistivity below a certain threshold value were assigned that value. Thresholds in the range 1–10 Ωm were considered. Then the edited models were used as starting models for inversion of the original data set, which is referred to as "reinversion" throughout this section. The unedited models were also used as starting models for reinversion, to provide a baseline for comparison. See Table B.3 (inversions 5–8 and 19–23) for details.

When the unedited models were used, reinversion led to small decreases in R.M.S. misfit: (i4) 0.02 and (i15) 0.19. When the edited models were used, reinversion also led to small decreases in R.M.S. misfit: (i4) 0.09–0.29 and (i15) 0.11–0.17. The greatest decrease occurred when the threshold was (i4) 3 Ωm and (i15) 2 Ωm. For these two cases, the minimum resistivity after reinversion was (i4) 0.008 Ωm, cf. 0.0002 Ωm (unedited starting model), and (i15) 0.07 Ωm, cf. 0.007 Ωm (unedited starting model). The mean resistivity after reinversion was (i4) 196 Ωm, cf. 172 Ωm (unedited starting model), and (i15) 202 Ωm, cf. 183 Ωm (unedited starting model).

Resistivity cross-sections for i15, its 2 Ωm threshold inversion, and the 2 Ωm threshold starting model are shown in Figure B.7. MT responses at three MT sites, for i15 and its 2 Ωm threshold inversion, are shown in Figure B.8. The responses are very similar. Reinversion using edited starting models resulted in an order of magnitude increase in minimum resistivity, but only small increases in mean resistivity and small decreases in R.M.S. misfit. Statistical tests (F-tests and Kolmogorov–Smirnov (KS) tests) were used to compare six resistivity models: (1) i4, (2) i4 reinversion, named i4gt0, (3) i4 3 Ωm threshold inversion, named i4gt3, (4) i15, (5) i15 reinversion, named i15gt0, and (6) i15 2 Ωm threshold inversion, named i15gt2. The results are shown in Table B.4 and Table B**.5**, along with written explanations. Notably, i15gt0 and i15gt2 are not statistically significantly different; therefore, i15 is considered the preferred resistivity model (Table B.3, inversion 15).

4.4.2.2.2 Conductive zone extending up toward Mount Meager and the fumaroles

To test the sensitivity of the MT data to the conductive zone extending upward from the northern part of the deep conductor toward Mount Meager and the fumaroles, this region was replaced with a 500 Ωm block measuring 5 km × 8 km × 5 km in the x, y, and z-directions, respectively (Figure B.9). The MT response of the preferred resistivity model was then compared with the response of this edited model. The overall R.M.S. misfit increased from 1.92 to 2.01.

The apparent resistivity and phase, measured at two sites above the resistive block, are shown in Figure B.10, along with the corresponding model responses. When the 500 Ωm block was added, the misfit at MGR114 increased from 1.34 to 1.78 and the misfit at MGR118 increased from 1.78 to 3.02. This analysis showed that the conductive zone imaged in the preferred resistivity model is a reliable feature.

4.4.2.2.3 Maximum depth of data sensitivity

Model editing and KS tests were also used to determine the maximum depth at which the MT data were sensitive to resistivity variations, and the results are shown in Table B.6. When the preferred resistivity model was edited to be very resistive (10,000 Ωm) below a depth of 100 km or shallower, the residuals were statistically significantly different at a 97% confidence level. This was true for the full data set as well as the impedance data separately and the tipper data separately.

When the preferred resistivity model was edited to be very conductive (0.01 Ωm) below a depth of 85 km or shallower, the residuals were statistically significantly different at a 98% confidence level. This was true for the full data set and the impedance data separately. However, the tipper data separately had residuals that were statistically significantly different at a 95% confidence level when the model was edited to be very conductive below a depth of 20 km or shallower.

The base of the deep conductor is at a depth of approximately 15 km below sea level, and the resistivity increases below (Figure 4.9). The preferred resistivity model is presented to a maximum depth of 25 km below sea level, which is 25–28 km below the surface. When the preferred resistivity model was altered below a depth of 26.5 km, the KS test p value for the

full data set was close to zero (10^{-15} for a conductor and 10^{-41} for a resistor); therefore, there is high confidence that the MT data were sensitive to resistivity variations at the depths shown in Figure 4.8 and Figure **4.9**.

4.4.2.3. Effect of topography on MT data and inversion results

To investigate the effect of topography on the tipper data, the MT response was calculated for a model with a uniform 10 Ωm resistivity and the same spatial discretization as the preferred resistivity model. The real part of the synthetic induction vectors, plotted using the Wiese convention, is shown in Figure B.11. At high frequencies (1–100 Hz) vectors point away from the massif; at low frequencies (0.001–0.1 Hz) the vector magnitudes are near zero. A uniform half-space, without topography, would result in magnitudes of zero at all frequencies; therefore, the nonzero induction vectors are primarily due to topography, specifically the Earth–air interface with a very large horizontal resistivity gradient, from 10 Ωm (Earth) to 10^{17} Ωm (air).

To further investigate the influence of the tipper data on the final resistivity model, an impedance-only inversion was undertaken and compared with the impedance–tipper joint inversion, where all other parameters remained the same (Table B.3, inversions 15 and 18). Figure B.12 shows a comparison of model slices, and the differences are small. When the tipper data are excluded, the deep conductor extends slightly farther to the south and less to the east. There are also some small changes to the shallow resistivity structure, but nothing that would significantly change the interpretations. The preferred resistivity model is from joint inversion of impedance and tipper data.

To investigate the effect of topography on the inversion model, the 66-site impedance–tipper data set was reinverted using a model mesh with (1) the elevation of the padding cells reduced to sea level and (2) no topography included, i.e., the entire surface at sea level. To investigate the effect of the spatial distribution and density of MT data on the inversion model, a 34-site impedance–tipper data set was inverted, using models with and without topography. This reduced data set included only 2019–2020 data; all legacy data were removed. These four models are compared with the preferred resistivity model in Figure B.13 and the spatial distribution of the 66-site and 34-site data sets are compared in Figure B.14.

The topography only had a small effect on the deep conductor. The horizontal extent of the deep conductor was slightly reduced when topography was not included, but the depth and

thickness remained similar. When the legacy data were omitted, the deep conductor had a greater horizontal extent and a slightly higher resistivity, but the depth and thickness remained similar.

To investigate the effect of topography on apparent resistivity and phase data, a series of simple layered models were created. MT responses were calculated at six locations and compared with corresponding 1-D responses (Figure B.15–Figure B**.17**). At some sites, the 3-D response is similar to the 1-D response; at others, there is a significant difference between the *xy* and *yx* modes. The inversion algorithm can successfully fit the measured data at these sites (Figure 4.7).

4.4.2.4. Synthetic inversions

To investigate the ability of the MT data to resolve the lateral extent of the deep conductor, two synthetic models were created: (1) a 0.1 Ωm layer at 5.1–7.8 km below sea level, embedded in a 1000 Ωm half-space (Figure B.18); and (2) a 0.1 Ωm block at 5.1–14.6 km below sea level and spanning 19 × 19 km horizontally, embedded in a 1000 Ωm half-space (Figure B.19). Synthetic MT data were generated for these two resistivity models, then Gaussian noise was added (5% for impedance data and 0.03 for tipper data). These synthetic MT data were then inverted using (1) impedance and tipper data jointly and (2) impedance data only.

In all four cases, the inversion modelled conductor was shallower than in the true model (its top at 1–3 km below sea level instead of 5 km), and the spatial extent of the conductor was reduced. The conductive layer was not recovered beyond the grid of MT stations and was instead imaged as a conductor near the middle of the grid (Figure B.18). These results revealed the need for further sensitivity testing.

To more thoroughly investigate the ability of the MT data to resolve the lateral extent of the deep conductor, six additional synthetic models were created: (1) a 3 Ωm layer at 5.7–16.1 km below sea level, embedded in a 100 Ωm half-space (Figure B.20), (2) a 3 Ωm layer at 9.7–19.7 km below sea level, embedded in a 100 Ωm half-space (Figure B.20), (3) model #1 with the elevation of the padding cells reduced to sea level (Figure B.21), (4) model #2 with the elevation of the padding cells reduced to sea level (Figure B.21), (5) a 3 Ωm layer at 6.7–16.5 km below the surface (topography not included), embedded in a 100 Ωm half-space (Figure B.22), and (6) a 3 Ωm layer at 10.0–20.0 km below the surface (topography not

included), embedded in a 100 Ωm half-space (Figure B.22). Synthetic impedance and tipper data were generated as before, then they were jointly inverted.

In these six cases, the imaged conductor was still restricted to the area covered by the grid of MT stations. The depth to the top of the conductor was resolved much more accurately, although the true thickness of the layer was not. Also, note that the resistive upper layer is often imaged as having a bowl-like geometry. This is most likely an artifact associated with the limited areal extent of the MT grid. The MT method can determine the distance from an MT station to a conductor. When the horizontal extent of an MT grid is limited, a conductive layer can be imaged as being deeper below the centre of the array and shallower near the edges of the array, resulting in a bowl-shaped conductor.

These synthetic inversion results highlight the limitations of the data set and inversion algorithm to recover the true resistivity distribution given the MT grid, topography, and model mesh used. It was found that the topography modelling did not cause any significant resistivity modelling errors. It was found that errors in the depth estimation of the deep conductor, especially near the edges of the MT array, were likely due to the limited areal extent of the array. Considering these results, the deep conductor observed in the preferred resistivity model may actually represent a conductive layer with greater lateral extent.

4.5. Interpretation

4.5.1. Deep conductor (magma body)

The low resistivity observed in the depth range 5–15 km below sea level may be caused by the presence of a magma body. To investigate this possibility, this section discusses the chemistry of the MMVC, laboratory experiments measuring the resistivity of silicate melts, and calculations of bulk resistivity assuming partial melt.

Early eruptions that contributed to the MMVC have ages of 120,000–440,000 years and were basaltic in composition; more recent eruptions within the past 30,000 years were dacitic in composition (Figure 4.10). Eruptions around 100,000 years ago were bimodal in composition, including the mafic Mosaic assemblage as well as the felsic Plinth and Capricorn assemblages. This suggests the possibility of two magma sources, a higher density basaltic magma and a lower density dacitic magma.

Approximately 10,000–100,000 years of mafic magmatism at a given volcanic centre are required to generate andesites and dacites, through the processes of crystal fractionation and crustal melting, and the length of time required for magma differentiation increases significantly with increasing SiO_2 concentration (Reagan et al., 2003). Therefore, the bulk resistivity calculations described in this section assumed a composition similar to that of the most recent eruption.

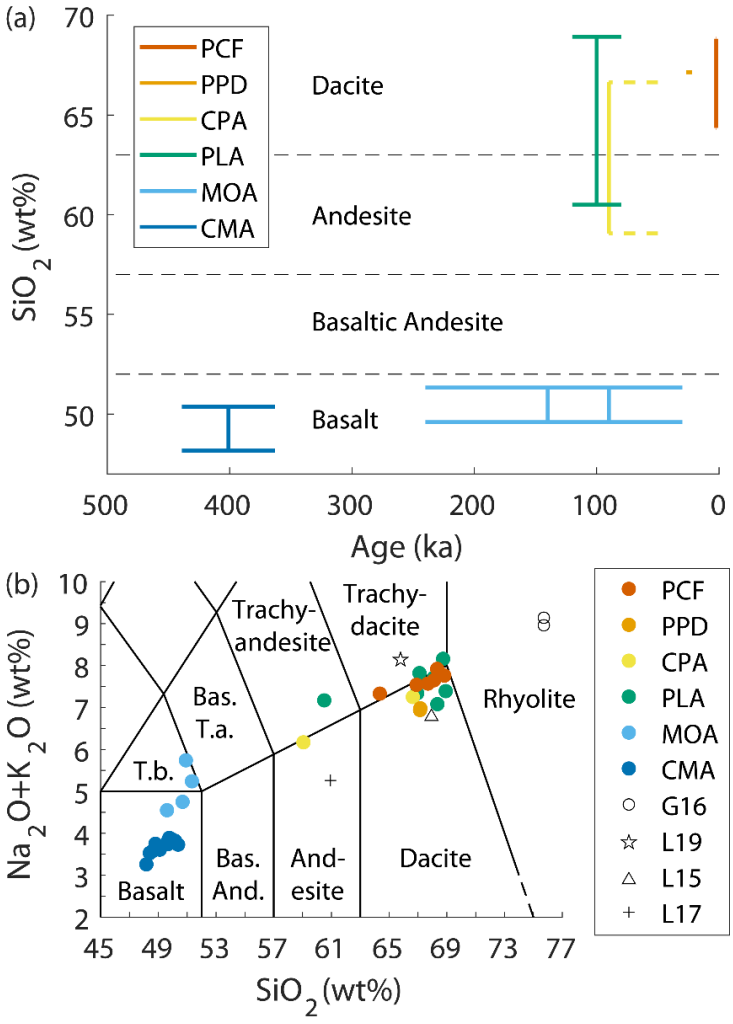

***Figure 4.10**: (a) Age and SiO_2 content of the Mount Meager volcanic complex. Abbreviations: CMA, Cracked Mountain Assemblage; CPA, Capricorn Assemblage; MOA, Mosaic Assemblage; PCF, Pebble Creek Formation; PLA, Plinth Assemblage; PPD, Plinth Pyroclastic Deposit. Vertical lines are published ages and SiO2 contents. Horizontal lines are age uncertainties: PCF = 2.37 ± 0.05 ka (Read, 1990); PPD = 24.3 ± 2.3 ka (Russell et al., 2021); CPA < 90 ka (Read, 1990); PLA = 100 ± 20 ka (Read, 1990); MOA = (90 ± 60 ka, 140 ± 100 ka) (Read, 1990); and CMA = 401 ± 38 ka (Harris et al., 2022). (b) Total alkali silica (TAS) diagram with the chemical classification of Le Bas et al. (1986, 1992). Whole rock chemistry of PCF, CPA, PLA, and MOA are from Stasiuk et al. (1996); PPD are from Russell et al. (2021); and CMA are from Harris et al. (2022). Black symbols are chemical compositions of rocks used in melt conductivity experiments: G16, Guo et al. (2016); L19, Laumonier et al. (2019); L15, Laumonier et al. (2015); L17, Laumonier et al. (2017). Numerical values are listed in Table S7. Abbreviations: Bas. And., Basaltic Andesite; Bas. T.a., Basaltic Trachyandesite; T.b., Trachybasalt.*

The youngest rocks (2,370 ± 50 years old) of the MMVC belong to the PCF. The alkali-silica content of these rocks (Table B.7) places them near the dacite–trachydacite boundary, with some samples near the rhyolite boundary (Figure 4.10 b). The resistivity of molten rocks with this composition can be estimated based on laboratory experiments (Guo et al., 2016; Laumonier et al., 2015, 2019). Variations in melt resistivity are illustrated in Figure 4.11, where it can be seen that at a given temperature, there is a decrease in resistivity due to composition, from dacite to trachydacite to rhyolite. Due to the fact that the composition of the PCF is between the compositions of laboratory experiments involving these three rock types, the bulk resistivity calculations assumed a trachydacitic melt composition. There is also a decrease in resistivity as water content increases. At the highest water content shown (8 wt.%), the dacite curve crosses the trachydacite curve (Figure 4.11 c). At 700–1,000 °C, trachydacitic melt with 4–8 wt.% H_2O has a resistivity in the range 0.1–3 Ωm.

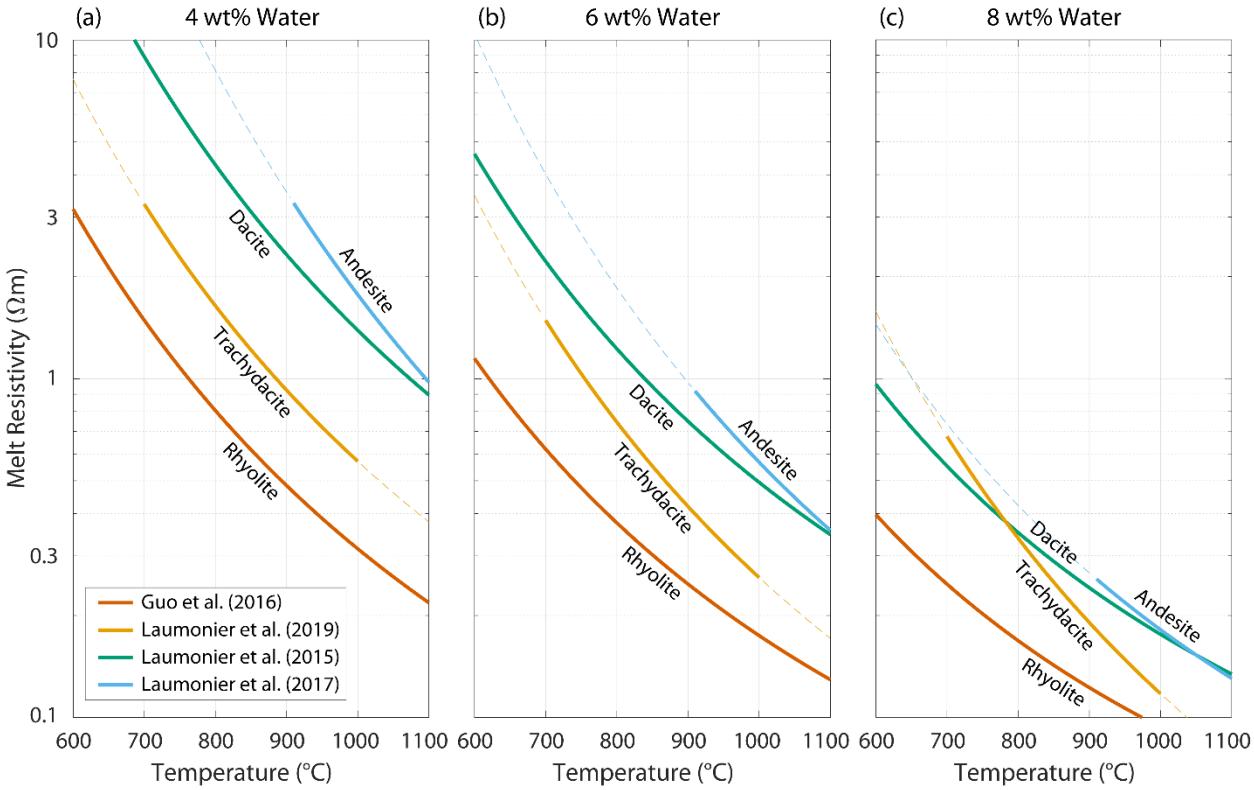

***Figure 4.11**: Resistivity of hydrous silicate melts at a pressure of 0.3 GPa, with three water contents: (a) 4 wt.%, (b) 6 wt.%, and (c) 8 wt.%. Empirically derived models were obtained from Laumonier et al. (2015, 2017, 2019) and Guo et al. (2016). Experimental water content ranges were 1.7–9.0 wt.%, 1.7–9.0 wt.%, 0–8.1 wt.%, and 0.1–7.9 wt.%, respectively. Dashed lines are outside the experimental temperature ranges.*

To interpret the resistivity of the deep conductor, it is necessary to calculate the bulk resistivity of a partial melt. Three factors must be considered in this calculation.

1) Resistivity of mineral grains: The resistivity of the grains is high. The PCF has an average composition of 68 wt.% SiO_2 and 7.7 wt.% $Na_2O + K_2O$ (Table B.7). Dai et al. (2014) measured the resistivity of dry oligoclase granite (68 wt.% SiO_2 and 8.0 wt.% $Na_2O + K_2O$) as ~1,000 Ωm at a temperature of ~850 °C. This is in agreement with the dry granite results of Olhoeft (1981).

2) Resistivity of melt: The resistivity of the melt is low. The formula of Laumonier et al. (2019) was used to calculate the resistivity of hydrous silicate melt with a trachydacitic composition (66 wt.% SiO_2 and 8.1 wt.% $Na_2O + K_2O$) in the temperature range 700–1,000 °C with 4–8 wt.% H_2O. The calculated melt resistivity was in the range 0.1–3 Ωm.

3) Distribution of melt within the matrix: The modified Archie's law of Glover et al. (2000) was used to calculate the bulk resistivity as a function of melt fraction, using 1,000 Ωm as the solid phase resistivity and the trachydacite melt resistivity as the fluid phase resistivity (Figure 4.12). The value used for the Archie cementation exponent, *m*, was coupled to the melt fraction, following the methods of Samrock et al. (2021). The melt phase was assumed to be fully connected with $m = 1$ for melt fractions greater than 40%. As melt fraction decreased, the cementation exponent was increased linearly to a maximum value of 2.1 for a melt fraction of 0%. Experiments have shown that $m = 1.73$ for crystalline mush, and that *m* increases from 1.81 to 2.1 as saline water freezes in permafrost soil (Samrock et al., 2021, and references therein).

As expected, a given bulk resistivity can be caused by many combinations of the three factors listed above. Consider the case where the bulk resistivity is 3 Ωm. High temperature (1,000 °C) and high water content (8 wt.%) would require 15% melt to explain the bulk resistivity. With lower temperature (900 °C) and lower water content (6 wt.%), 25% melt would be required. With even lower temperatures (< 800 °C) and even lower water contents (< 4 wt.%), more than 50% melt would be required. Figure 4.12 shows a dozen different combinations of temperature and water content, illustrating the trade-off between these parameters and the necessity of additional constraints.

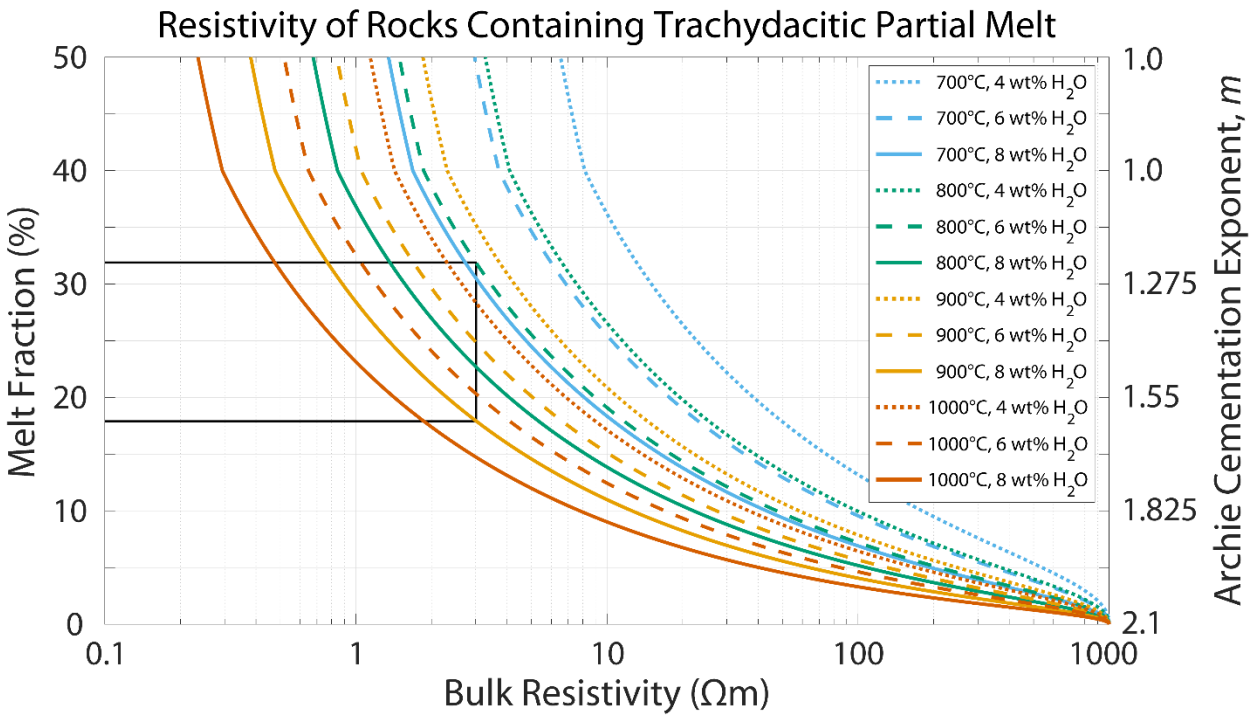

***Figure 4.12**: Bulk resistivity of rocks containing trachydacitic partial melt. The modified Archie's law of Glover et al. (2000) was used with a solid phase resistivity of 1,000 Ωm and a fluid phase resistivity based on the empirically derived model of Laumonier et al. (2019). The Archie cementation exponent, m, was varied linearly with melt fraction, φ, as m = 2.1–2.75φ for 0 < φ < 0.4, and m was held constant at 1 for φ > 0.4, following the methods of Samrock et al. (2021).*

The rock sample analyzed by Laumonier et al. (2019) was from Ciomadul, a volcano in Romania that last erupted 32,000 years ago (Harangi et al., 2015). Laumonier et al. (2019) used resistivity measurements to infer a magma body, at depths of approximately 5–18 km below Ciomadul, containing 20–58% dacitic-to-rhyolitic melt with 6.0–7.7 wt.% H_2O. Amphibole and biotite, which are hydrous phases, are common in the Ciomadul dacites; this implies a minimum water content of 4 wt.% (Harangi et al., 2015). A seismic low-velocity zone provided additional evidence of a magma body, in the depth range 8–20 km below Ciomadul (Popa et al., 2012). The large conductor beneath Mount Meager is at a similar depth (5–15 km below sea level plus 0.4–2.7 km above sea level) and the PCF also contains amphibole and biotite (Hickson et al., 1999); therefore, Ciomadul is a relevant comparison. Mount Meager was active more recently (2,370 years cf. 32,000 years), has higher heat flow (132 mW/m^2 cf. 85–120 mW/m^2), and has a larger geothermal gradient near the surface (270 °C at a depth of 3 km cf. 78 °C at a depth of 1.14 km), compared with Ciomadul (Ghomshei et al., 2004; Harangi et al., 2015; Lewis & Jessop, 1981). Based on these considerations, the Mount Meager magma body is likely hotter than the Ciomadul magma body, which was estimated to be 700–750 °C near the centre (Laumonier et al., 2019). At a temperature of

900 °C and a pressure of 0.4 GPa, dacitic melt is saturated at 9 wt.% H_2O; this saturation fraction increases with increasing pressure (Prouteau & Scaillet, 2003).

The Mount Meager magma body could be 800–900 °C with 6–8 wt.% H_2O, based on the presence of hydrous phases in the PCF and the saturation limit of dacitic melt, as discussed above. This equates to 18–32% well-connected melt (*m* in the range 1.2–1.6) given a bulk resistivity of 3 Ωm (black lines in Figure 4.12). This is below the melt fraction of an eruptible magma body, ~45% (Laumonier et al., 2019). However, the estimated melt fraction would increase if (1) the temperature was decreased, (2) the water content was decreased, (3) the bulk resistivity was decreased, (4) the melt resistivity was decreased, e.g., by increasing the alkali content, and to a lesser extent the SiO_2 content, or (5) the cementation exponent, *m*, was increased.

4.5.2. Possibility of saline aqueous fluids

Assuming a geothermal gradient of 90–100 °C/km, a fluid density of 700–800 kg/m^3, and a granodiorite density of 2,700–2,800 kg/m^3, the temperature, hydrostatic pressure, and lithostatic pressure at a depth of 6 km are 540–600 °C, 41–47 MPa, and 159–165 MPa, respectively. At all of these conditions, aqueous fluids would be in a supercritical state (Nono et al., 2020). At these temperatures, the bulk resistivity of a supercritical brine-saturated geothermal reservoir would be similar to the resistivity of dry rock (Nono et al., 2020). Therefore, saline aqueous fluids cannot explain the observed resistivity of the deep conductor. The fluid density range considered above is a crude estimation, but it serves the purposes of this exercise. Reasonable changes to this density estimation should still result in supercritical conditions.

A small amount of supercritical brine may be present, but it would not significantly affect the melt fraction estimation. Above the deep conductor, where the resistivity is 100–1,000 Ωm, there may be a more significant amount of supercritical brine. Exploitation of supercritical fluids at 430–550 °C could increase geothermal energy production by an order of magnitude, compared with liquid and steam at less than 300 °C (Kummerow et al., 2020). This could be considered at Mount Meager; however, porosity and permeability estimates are beyond the scope of this study.

4.5.3. Shallow conductors (clay alteration minerals)

The AMT study at Mount Meager resulted in a resistivity model of the upper 5 km, surrounding the South Meager anomaly (Hormozzade Ghalati et al., 2022). This model used a finer horizontal grid than the one presented here, 75 m cf. 250 m, and the higher frequency data were more sensitive to near surface resistivity variations. For detailed interpretations of the upper 5 km, readers are directed to the results of Hormozzade Ghalati et al. (2022).

The regional resistivity model, from inversion of BBMT data, is consistent with the interpretations of Hormozzade Ghalati et al. (2022) that the shallow conductive zones correspond to low-permeability, clay-rich layers, which act as caprocks to the geothermal fluids below. Future research could jointly invert the AMT and BBMT data, to create a unified resistivity model. This would require a multiscale approach with a fine model mesh covering the geothermal reservoir, and a coarser model mesh covering the magma body and surrounding areas.

The conductors that Hormozzade Ghalati et al. (2022) called C1 and C2, covering most of the near surface area between Pylon Peak and Meager Creek, are also present in the regional resistivity model. Figure B.23 compares these two models and there are two notable differences: (1) the near surface conductors are approximately twice as thick in the AMT model, compared with the BBMT model and (2) the shallow basement beneath these conductors is more resistive in the AMT model than the BBMT model. The model presented by Hormozzade Ghalati et al. (2022) extended to a depth of only 3.5 km below sea level, therefore the deep conductor (magma body) was not imaged.

4.5.4. Conductive pathways from the deep conductor to the surface

Above the northern part of the magma body, there is a conductive zone extending up toward Mount Meager and the fumaroles (Figure 4.9 a–c). In this zone, the resistivity is 20–90 Ωm (Figure B.5). The fumaroles were first observed in 2016, but they were probably active for a long time before that, hidden beneath Job Glacier (Roberti et al., 2018). The MMVC has lost 1.3 km^3 of ice since 1987, and the ice has recently become thin enough for hot volcanic gases to reach the surface (Roberti et al., 2018).

Fumaroles are a surface expression of a hydrothermal system, and their existence is related to permeable conduits that bring fluids from depth toward the surface (Müller et al., 2021).

They are associated with extensive mineral precipitation, and this hydrothermal alteration can extend deep below the surface expression (Müller et al., 2021). The low resistivity zone beneath Mount Meager and the fumaroles is likely correlated with hydrothermal alteration minerals, indicating fluid pathways from a degassing magma body to the surface.

The MT grid is not dense in this region, but the conductive zone is a robust feature that was imaged by a wide range of inversion parameters. It is contrasted with the high resistivity imaged above the central and southern parts of the deep conductor, e.g., below the Pylon Peak and Fish Creek conductors (Figure 4.9 d-e).

4.6. Discussion

A temperature of 800–900 °C at a depth of 8–9 km (i.e., the centre of the magma body) implies an average geothermal gradient of ~100 °C/km. This value is similar to the near surface geothermal gradient of ~90 °C/km that was measured in boreholes at Mount Meager, i.e., ~270 °C at depths of ~3 km (Ghomshei et al., 2004). This information could potentially be used to estimate the depth of higher temperature geothermal resources where supercritical fluids may be present. In making these estimates, a couple of factors must be recognized. The first is that the temperatures below Mount Meager are likely not in a steady state. The magma body may be in the process of cooling and the thermal gradient may be changing over time. The second is that while heat is transferred by conduction in solid rocks, hydrothermal fluids and magma will transport heat by advection. These two factors mean that the present-day thermal structure beneath Mount Meager is likely to be 3-D and varying with time. The 3-D resistivity model presented in this study can provide constraints for developing a new thermal model of the deeper parts of the geothermal resource where the fluids have a significantly higher temperature than in the shallow parts of the reservoir that are currently being developed.

It would also be beneficial to undertake additional research into the composition of the magma body and how this causes the low resistivity. This could include consideration of the volatile phase in determining the bulk resistivity, using the multiphase Archie's law of Glover (2010), following the methods of Samrock et al. (2021). More detailed thermal and geochemical analyses could better constrain the temperature and water content of the magma body, allowing a refined estimate of the melt fraction. Density and seismic velocity models of the Garibaldi Geothermal Energy Project (Calahorrano-Di Patre & Williams-Jones, 2021; Gilbert et al., 2021) could also help constrain the location and properties of the magma body.

Improving estimates of the thickness of the magma layer is important because the synthetic inversion results presented above suggested that the MT inversion could be underestimating the thickness.

In addition to jointly inverting the AMT and MT data, future work could include inverting the BBMT data used in this study using a different inversion algorithm, perhaps one that uses an unstructured and/or adaptive, tetrahedral mesh, to better model the rugged topography (e.g., Kordy et al., 2016; Usui et al., 2017). Furthermore, additional BBMT data were collected in 2021 and 2022 at Mount Cayley and Mount Garibaldi (Grasby et al., 2022). These new data along with legacy data, including long-period MT data, will facilitate regional resistivity modelling of the central GVB (Figure 4.1 a). This will help distinguish between a large (regional) magma layer and a number of smaller (local) magma bodies beneath individual volcanic centres.

Meteoric water may enter the hydrothermal system in the Lillooet Valley, on the north side of the MMVC, and emerge along Meager Creek, on the south side of the MMVC. The preferred resistivity model shown in panel (b) of Figure 4.9 does not provide definitive answers to questions regarding regional groundwater flow. Further research utilizing collectively the BBMT model (this study), the AMT model (Hormozzade Ghalati et al., 2022), and the structural geology study (Muhammad et al., 2021) would be better equipped to answer such questions.

4.7. Conclusions

Recent 3-D inversion of BBMT data confirmed the existence of a magma body beneath Mount Meager, as suggested by Jones and Dumas (1993) using 2-D methods. Due to the rugged topography (~2 km of elevation variation over the survey area), rectilinear model mesh (250 m horizontal resolution), and spatial distribution of MT stations, it could not be determined whether the magma body is restricted to the volume modelled in this study (Figure 4.8 and Figure 4.9) or part of a larger magma layer, as shown to be possible by synthetic inversions (Figure B.18–Figure B.22). It is also possible that the magma body is thicker than modelled by the inversion (see Section 4.4.2.4).

Based on the resistivity model presented here, the Mount Meager magma body has a volume of at least 2×10^{12} m^3 and contains 18–32% dacitic-to-trachydacitic melt with 6–8 wt.% H_2O at a temperature in the range 800–900 °C. Additional research is needed to refine these parameter estimates and confirm the geometry of this magma body. While precise details

cannot be concluded definitively, there is clearly a deep heat source beneath Mount Meager which provides the thermal energy found in the overlying hydrothermal systems. This 3-D resistivity model is a significant advancement from its predecessors (created 20–40 years ago) and it has provided the first deep 3-D image of this volcanic system. Along with the other geophysical and geological models of the Garibaldi Geothermal Energy Project, it will reduce the exploration risk associated with geothermal energy development.

4.8. Acknowledgments

Steve Grasby is thanked for his leadership in all aspects of the Garibaldi Geothermal Energy Project. The study area is located in the unceded territory of the Lil'wat Nation and the authors are grateful for their support of this project. The 2001 MT data were collected by Geosystem Canada Inc., under contract to Frontier Geosciences Inc., and the authors thank Cliff Candy for sharing them. The 1982 MT data were acquired by Ron Kurtz and Jon DeLaurier from the Pacific Geoscience Centre, funded by the Federal Geothermal Energy Program. The authors thank Andrew Williamson and Zoë Vestrum for their help during fieldwork; Fateme Hormozzade Ghalati and Jim Craven for their comments and suggestions; Alexander Grayver and an anonymous reviewer for their detailed and thoughtful reviews; Gary Egbert, Anna Kelbert, and Naser Meqbel for use of the ModEM inversion algorithm; the Digital Research Alliance of Canada (formerly Compute Canada) for access to high-performance cluster computing; and the great pilots at No Limits Heli Adventures for their helicopter services.

Funding was provided by NSERC Discovery Grant RGPIN-2020-04240 to Martyn J. Unsworth and an award from the Future Energy Systems program at the University of Alberta. A Geoscience BC scholarship was awarded to Cedar Hanneson in 2021. Additional funding for the Garibaldi Geothermal Energy Project, including access to helicopters, was provided by Natural Resources Canada and Geoscience BC.

5. Regional-scale resistivity structure of the middle and lower crust and uppermost mantle beneath the southeastern Canadian Cordillera and insights into its causes

Hanneson, C. and Unsworth, M.J. (2023b)
Geophysical Journal International, 234, 2032-2052
doi:10.1093/gji/ggad183

Summary

Subduction zones are recognized as an important class of plate boundaries and are the location of a number of important geological processes. They are also important because of the mineral and geothermal energy resources formed by plate convergence. While subduction zones around the world have a number of common features, there are also significant differences among them. The Cascadia subduction zone in southern British Columbia is characterized by a relatively hot subducting plate, and a broad backarc region that is believed to exhibit a shallow, convecting asthenosphere.

The magnetotelluric (MT) method is a useful tool to study subduction zones and backarc regions because measurements of subsurface resistivity are sensitive to the presence of fluids. A number of previous MT studies have taken place in this region, but they were limited to a 2-D approach to data analysis. As the MT method has developed, it has become clear that there is a significant advantage to using a 3-D approach to data analysis.

This paper presents the first regional-scale 3-D resistivity model of the southern Canadian Cordillera and provides new insights into the lithospheric structure and the distribution of fluids. The southeastern Canadian Cordillera has high heat flow and numerous thermal springs, the locations of which are often controlled by faults. However, the deeper thermal structure and origin of the fluids are poorly understood. To develop an improved understanding of the structure of this area, MT data measured at 331 locations were used to create a 3-D model of subsurface electrical resistivity.

This study is primarily focused on the Omineca and Foreland morphogeological belts in southeastern British Columbia, which are separated by the southern Rocky Mountain Trench.

The resistivity model is presented to a depth of 100 km and a number of conductive features are observed in the crust and uppermost mantle of the southeastern Cordillera. The locations of these conductors broadly matched previously reported conductors, but the 3-D inversion revealed new details of their geometry.

The previously reported Canadian Cordilleran Regional conductor was modelled as a number of discrete conductors in the depth range 15–55 km beneath the Omineca belt. Temperatures approximately in the range 400–700 °C are expected at depths of 15–26 km and saline aqueous fluids are likely the cause of the low resistivity. Temperatures approximately in the range 700–1,300 °C are expected at depths of 26–55 km and small volumes of partial melt may explain the low resistivity.

The Southern Alberta–British Columbia conductor, Red Deer conductor and Loverna conductor were imaged as a single connected conductor, whose low resistivity is likely caused by sulphide mineralization. A group of conductors was imaged near the southern Rocky Mountain Trench in the depth range 10–70 km and their low resistivity is likely caused by interconnected saline fluids and possibly interconnected graphite films.

To understand if the distribution of thermal springs was correlated with the 3-D resistivity model, a statistical study was undertaken. This showed no clear correlation between crustal conductance and the distribution of thermal springs.

5.1. Introduction

For the past 400 million years, the tectonics of western North America has been dominated by subduction (Monger & Price, 2002). Compared with other subduction zones, the present-day Cascadia subduction zone has a number of unusual features. The young age of the subducting Juan de Fuca plate makes this one of the warmest subduction zones, with the Juan de Fuca plate in the forearc being 300–600 °C hotter than the Okhotsk plate beneath Japan (Savard et al., 2018). In addition, the backarc of the Cascadia subduction zone is unusual in that it has thin lithosphere and high heat flow that extend far into the North American continent (Currie, Wang, et al., 2004). There is evidence that crustal extension has occurred in this region. The transition from young accreted material to old cratonic lithosphere occurs 750–850 km east of the subduction zone (Currie, Cassidy, et al., 2004).

The tectonics of the Canadian Cordillera were investigated as part of the Lithoprobe project in the 1980s and 1990s. These studies used extensive magnetotelluric (MT) exploration to study the distribution of crustal fluids (Jones et al., 2014). Studies of this area are important because it contains significant geothermal energy potential. Geothermal exploration has made extensive use of MT exploration on the reservoir scale (Muñoz, 2014) and is also able to assist geothermal exploration at the regional scale by imaging to lower-crustal depths (J. R. Peacock & Siler, 2021).

This early MT exploration was limited to profiles and 2-D inversion of the data could not constrain the crustal resistivity structure in 3-D. Since 2003, the University of Alberta has systematically extended MT data coverage in the southern Canadian Cordillera. This paper presents the first regional-scale 3-D resistivity model of the southern Canadian Cordillera.

5.2. Background and motivation

5.2.1. Tectonic setting

The regional tectonics are dominated by the subduction of the Juan de Fuca plate beneath the North American plate at the Cascadia subduction zone (Figure 5.1). Dehydration of the subducting slab releases volatiles into the overlying mantle, and generates melt that forms the Cascade volcanic arc (Stern, 2002). East of the volcanic arc, the Cascadia backarc is characterized by unusually thin lithosphere and high heat flow, which extend far into North America (Figure 5.2). The crustal structure varies spatially both along strike and across strike, with variations partially due to crustal extension in the Eocene. The lithosphere–asthenosphere boundary (LAB) in this region is at a depth of 50–60 km based on seismic, mantle xenolith and thermal studies (Currie & Hyndman, 2006). Based on observed thermal conditions, such as high surface heat flow (~75 mW/m^2), vigorous convection in the asthenosphere is believed to occur (Currie, Wang, et al., 2004; Hyndman et al., 2005).

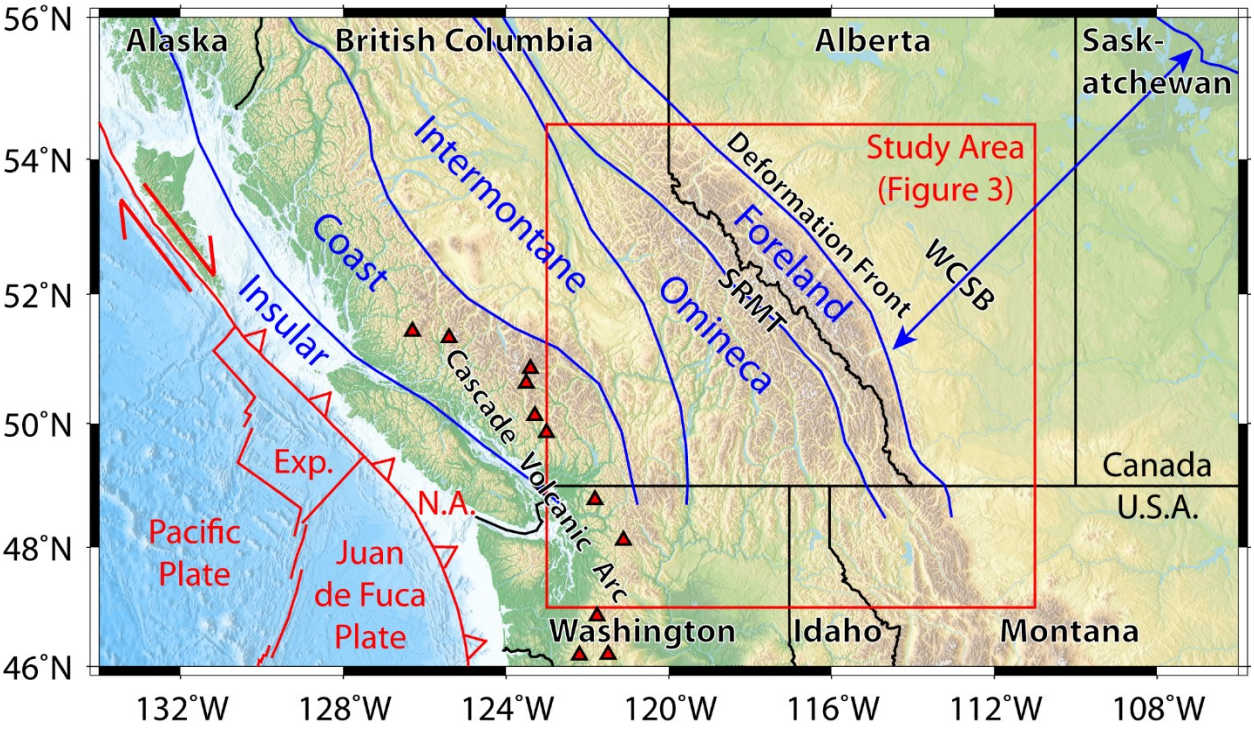

***Figure 5.1**: Map of southwestern Canada and northwestern USA. Political boundaries (black lines), morphogeological boundaries (blue lines), tectonic plate boundaries (red lines) and volcanoes (triangles) are shown. The red box indicates the location of Figure 5.3. Exp. = Explorer plate, N.A. = North American plate, SRMT = southern Rocky Mountain Trench and WCSB = Western Canada Sedimentary Basin.*

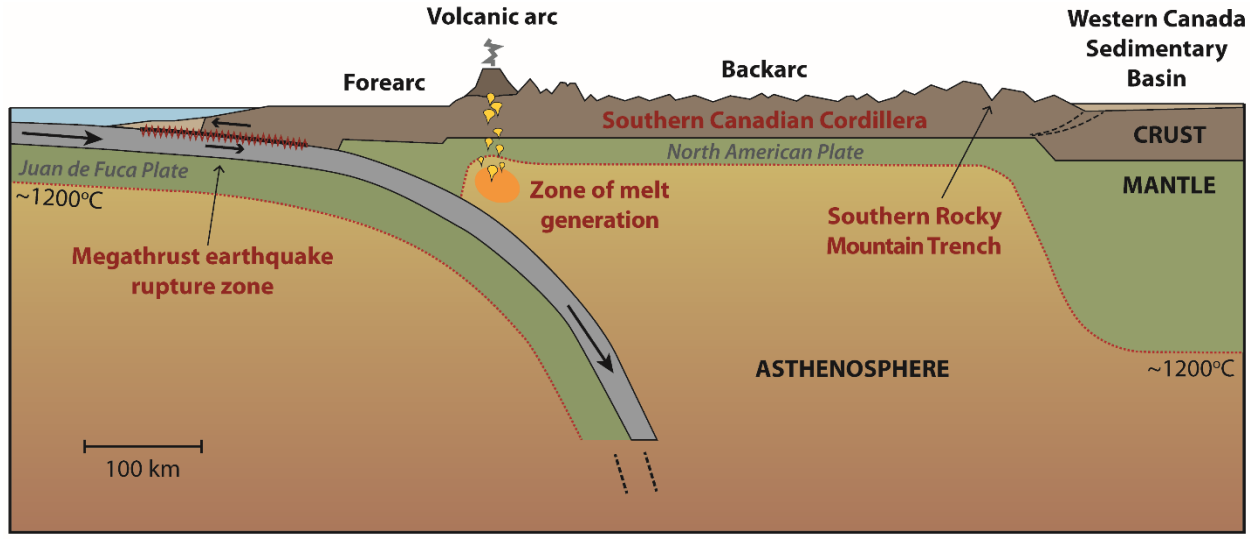

***Figure 5.2**: Schematic cross-section of the Cascadia subduction zone and the southern Canadian Cordillera.*

5.2.2. Crustal structure

The Canadian Cordillera is an accretionary orogen, comprised of distinct terranes that were added to the North American margin throughout the Mesozoic and early Cenozoic (Monger & Price, 2002). For simplicity, the Cordillera is often divided into five morphogeological belts based on bedrock type and geomorphology (Gabrielse et al., 1991). From west to east, they are the Insular, Coast, Intermontane, Omineca and Foreland belts (Figure 5.1). The study area is comprised of:

1) The Intermontane belt, whose accretion resulted in compressional deformation from the Jurassic to the Eocene, giving rise to mountain building. Continued convergence between the North American plate and the oceanic plates to the west allowed this extended period of compression.
2) The Omineca belt, which is a mountainous region dominantly composed of mid- to high-grade meta-sedimentary rocks, as well as numerous continental arc-type plutonic suites (Gabrielse et al., 1991). The present-day deformation is especially relevant for under- standing geothermal systems for two reasons: (1) extension provides a mechanism for crustal thinning and an increased geothermal gradient, and (2) recently active faults are more likely to be permeable conduits allowing convection of hot water from depth to the surface.
3) The Foreland belt, which encompasses the rugged Canadian Rocky Mountains, which are composed of the largely unmetamorphosed but highly deformed sedimentary rocks of the former passive margin (Gabrielse et al., 1991).
4) The Western Canada Sedimentary Basin (WCSB), which is a wedge of sedimentary rocks that thickens in a southwesterly direction from the Canadian shield to the Cordilleran foreland (Porter et al., 1982).

This study is primarily focused on the southern Omineca and Foreland belts, which are separated by the southern Rocky Mountain Trench (SRMT). Faults that occur within and adjacent to the SRMT include the SRMT fault, Purcell Thrust fault, Redwall fault and Lussier River fault. Notably, no thermal springs occur along the SRMT where the Purcell Thrust occurs, suggesting this fault may not be conducive to fluid circulation. The Redwall and Lussier River faults run parallel with and to the east of the SRMT, around 50 °N. Many thermal springs along the southern SRMT in fact coincide with these faults rather than the main SRMT fault.

Hyndman and Lewis (1999) placed the Moho at 32–34 km depth in the southern Canadian Cordillera and 40–50 km depth in the craton to the east, based on various seismic studies.

Deep crustal aqueous fluids tend to occur in the 400–700 °C temperature range (Hyndman & Shearer, 1989). Moho temperatures are approximately 800–1,000 °C beneath the southern Cordillera (Currie & Hyndman, 2006); therefore, deep crustal water is most likely to occur in the 15–30 km depth range. Water in the lower crust may be derived from dehydration of oceanic crust and sediments in subduction zones, as well as the devolatilization of upwelling mantle (Hyndman & Shearer, 1989, and references therein). However, fluids in geothermal systems in the southern Canadian Cordillera have been interpreted to be meteoric in origin, circulating to depths less than 5 km (Grasby & Hutcheon, 2001).

5.2.3. Geothermal conditions

Western North America has high geothermal potential (Jones, 2019). In western Canada, the total geothermal power potential in British Columbia (BC) and Yukon has been estimated at 3,000–5,000 MWe (Ghomshei, 2010), yet there are currently no commercial geothermal power plants operating in Canada. Geothermal resources in BC are found in volcanic systems, fault-hosted systems and hot dry rock (Grasby et al., 2012). Volcanic systems are found in the Cascade volcanic arc and fault-hosted systems are found near the SRMT. Both fault-hosted geothermal systems and hot dry rock resources are found in the Columbia Mountains.

In the southeastern Cordillera, heat flow is anomalously high, 70–120 mW/m^2 compared with the Canadian average of 48−80 mW/m^2 (Majorowicz & Grasby, 2010a). For comparison, an average of 85–90 mW/m^2 is observed in the Basin and Range, which hosts many of the United States' high-temperature (> 150 °C) geothermal systems (Wisian & Blackwell, 2004). The presence of more than 40 thermal springs within the study area is suggestive of the region's geothermal potential. It has previously been suggested that the locations of these thermal springs are controlled by faults that allow deep circulation and consequent heating of meteoric water (Grasby & Hutcheon, 2001).

Advancements have been made in the understanding of fault- hosted geothermal systems in the southeastern Canadian Cordillera (Finley, 2020; Finley et al., 2022); however, correlations between upper-crustal fault systems and lower-crustal geophysical anomalies have yet to be made in this region, as they have been elsewhere (e.g., Peacock & Siler, 2021). Geophysical methods are needed to image tens of kilometres below the surface. Electromagnetic (EM) methods are particularly useful because of their sensitivity to the presence of fluids.

5.2.4. Prior magnetotelluric exploration in the Canadian Cordillera

The Canadian Cordillera was one of the first regions where detailed MT exploration was used to study the tectonic processes at work. The locations of several vintages of Canadian MT data are shown in Figure C.1. A conductive layer in the middle-to-lower crust was discovered beneath most of the Intermontane and Omineca belts of southern BC, and was named the Canadian Cordilleran Regional (CCR) conductor (Caner et al., 1969; Gough, 1986). Jones, Gough, et al. (1992) extended this work with the Lithoprobe Southern Cordilleran Transect (transects *ewn* and *ews*, north and south of 50 °N, respectively) and showed that the CCR conductor was laterally heterogeneous. Majorowicz and Gough (1994) analysed MT data from the Intermontane and Omineca belts around 52–53 °N and concluded that a continuous mid-crustal conductor was not consistent with the data, thereby showing that the CCR conductor was not continuous at these latitudes.

Jones and Gough (1995) presented a synthesis of more than 400 MT soundings from the Canadian Cordillera in the latitude range 49–53.5 °N and inferred that the top of the CCR conductor was deeper below the Intermontane belt than the Omineca belt. They interpreted this conductor as being due to the presence of saline fluids. Marquis et al. (1995) further analysed Lithoprobe data across the Intermontane–Omineca boundary at 50 °N and determined that the top of the conductive layer was 15–17 km deep in the Intermontane belt and 8–10 km deep in the Omineca belt, and coincident with an increase in seismic reflectivity. They proposed mid-crustal fluids trapped by a ductile shear zone as a common cause of these two geophysical anomalies.

Ledo and Jones (2001) analysed more than 150 MT soundings along five profiles in central and southern BC and presented 2-D models extending to 50 km depth. Their interpretation used seismic data to infer that the southern Omineca belt had a conductive (10–46 Ωm) lower crust which they interpreted as interconnected saline fluids, and possibly partial melt below 25 km depth.

The studies mentioned above used broadband MT data that were not capable of imaging beneath the crustal conductors. This was because the relatively short-period EM signals were attenuated by the low resistivity material. To image the upper mantle, long-period MT data were first collected by Soyer and Unsworth (2006) with a profile that extended from the Pacific Ocean to the Intermontane belt. A 2-D inversion revealed low resistivity in the upper mantle that was interpreted as being due to hydrated olivine and/or a small amount of partial melt.

Long-period MT data coverage was improved by (1) extension of the ABC-South profile to the east and (2) collection of the parallel ABC-North profile (Rippe et al., 2013). A 2-D in version showed that the ABC-S profile was characterized by a crustal conductor beneath the Intermontane and Omineca belts at a depth of 20 km. ABC-N had a similar but weaker conductor. These lower-crustal conductors were interpreted as saline fluids and/or partial melt. The difference between the crustal conductors on the ABC-N and ABC-S profiles was interpreted as being due to different amounts of Eocene crustal extension. The mantle below these conductors also had relatively low resistivity, indicative of a shallow asthenosphere in the backarc.

The study area of this paper extends into the North American craton beneath the WCSB. A number of prior MT surveys have taken place in this region. Nieuwenhuis et al. (2014) performed 3-D inversion of long-period MT data collected in southern Alberta. The resulting resistivity model showed a number of crustal and upper-mantle conductors that had been previously reported by prior studies, and included the crustal Red Deer conductor (RDC) and a larger conductor that was called the southern Alberta conductivity anomaly by Gough et al. (1982) and later the Southern Alberta–British Columbia conductor (SABC) by Gough (1986). More recently, a 3-D inversion of the whole of Alberta was undertaken and revealed a similar structure (Wang & Unsworth, 2022).

Related MT studies of the Cascadia subduction zone, backarc region and craton took place in the USA during the EarthScope project. Meqbel et al. (2014) inverted long-period MT data measured at 325 sites in northwestern USA with ~70 km station spacing. The resulting 3-D resistivity model imaged the SABC in the depth range 31–65 km, as well as a mantle conductor north of the Idaho-BC border; however, this latitude (49 °N) is beyond the extent of their grid and connectivity between the two could not be shown. Their northernmost cross-section, at 48.5 °N, showed low resistivity beneath Mount Baker and an east-dipping resistor to the east that extended below the SABC. They interpreted this resistor as the Siletzia curtain of Schmandt and Humphreys (2011), a seismic anomaly thought to be a relict slab of the Farallon plate.

5.2.5. Motivation for the current MT study

Despite extensive research in western Canada with MT, a number of questions remain unanswered about the structure of the crust and upper mantle in the southern Canadian Cordillera. Prior studies used a 2-D inversion approach and this revealed significant

differences in structure along strike (Ledo & Jones, 2001; Rippe et al., 2013). Following the success of the 3-D approach elsewhere (e.g., Meqbel et al., 2014), a 3-D approach has been applied in this region for the first time and is described in this paper. Questions that still need to be answered, and that motivated this study, include:

1) What is the spatial extent, distribution, and physical cause of the low-resistivity crust beneath the southern Omineca belt, previously described by Ledo and Jones (2001) and others?
2) What is the water content of the upper mantle? A previous MT study revealed elevated water content in the upper mantle (Rippe et al., 2013) which supported the hypothesis of a rapidly convecting Cordilleran upper mantle with high temperature and water content. However, previous studies used a 2-D approach that was inherently limited.
3) Are resistivity features in the crust and upper mantle of this region correlated with surface geothermal manifestations? Historically, the search for geothermal resources has focused on locating reservoirs in the upper few kilometres of the crust. However, deeper geophysical exploration has the potential to give an understanding of the factors that may control the distribution of geothermal resources. This approach has been used in mineral exploration through the so-called mineral systems approach (McCuaig et al., 2010) and the MT method has been used in recent years to investigate such mineral systems (e.g., Comeau et al., 2022; Heinson et al., 2018; Wise & Thiel, 2020). A recent study has shown that this approach may be applicable to geothermal exploration (Peacock & Siler, 2021).

5.3. Data and methods

5.3.1. The magnetotelluric method

The MT method uses natural, low-frequency EM signals to image the electrical resistivity of the subsurface and is widely used in both studies of crustal structure and geothermal exploration (e.g., Muñoz, 2014). The MT method measures time variations of the electric and magnetic fields at the surface of the Earth. The ratio of electric to magnetic fields produces estimates of a transfer function called the impedance that determines the electrical resistivity of the Earth. The ratio of vertical to horizontal magnetic fields produces estimates of a transfer function called the tipper that defines horizontal variations in resistivity. Apparent resistivity is computed from impedance and can be considered an average resistivity over the depth range sampled at a specific frequency. Phase is related to changes in apparent resistivity with frequency and phases greater than 45° indicate a decrease in resistivity with depth. By

observing a range of frequencies, these transfer functions can be used to calculate the electrical resistivity as a function of depth. A full description of the MT method was given by Chave and Jones (2012).

The MT method has two main advantages that make it suitable for studies of crustal fluids, and specifically for geothermal exploration:

1) It can effectively image aqueous and magmatic fluids. The electrical resistivity of the crust varies over several orders of magnitude: dry crystalline rock has a resistivity in excess of 1,000 Ωm, whereas the presence of aqueous fluids or partial melt can lower this to values less than 10 Ωm. Thus, MT data can determine the location and content of fluid-rich zones.
2) It can resolve crustal features over a broad range of depths allowing for investigation of both fine-scale crustal structure and deeper resistivity anomalies. The frequency of the passive EM signals controls the depth of exploration according to the skin depth (δ) which is defined in metres as: $\delta \cong 500\sqrt{\rho T}$, where ρ is the bulk resistivity in Ωm and T is the period of the signal in seconds. Therefore, longer periods give information about deeper resistivity structures and signals are more attenuated in lower resistivity materials. This broad depth range is a distinct advantage over other EM methods that are more limited in scale.

5.3.2. Magnetotelluric data

To undertake an effective 3-D inversion, a grid of MT stations is preferred. This study used data from 331 MT stations in the region 47.7 to 54 °N and 112 to 122 °W, as shown in Figure 5.3. These data included 110 Lithoprobe sites, 22 EarthScope USArray sites, and 19 sites from other studies. The additional 180 MT soundings were collected by the University of Alberta between 2003 and 2018. See Table C.1 for a full list of MT stations and panel (a) of Figure C.2 for the frequency distribution of the data set. The time-series data were processed using the statistically robust algorithms of Egbert and Eisel (1998). The resulting frequency-domain transfer functions were used in conjunction with the other available MT data, and they were edited manually to remove outliers.

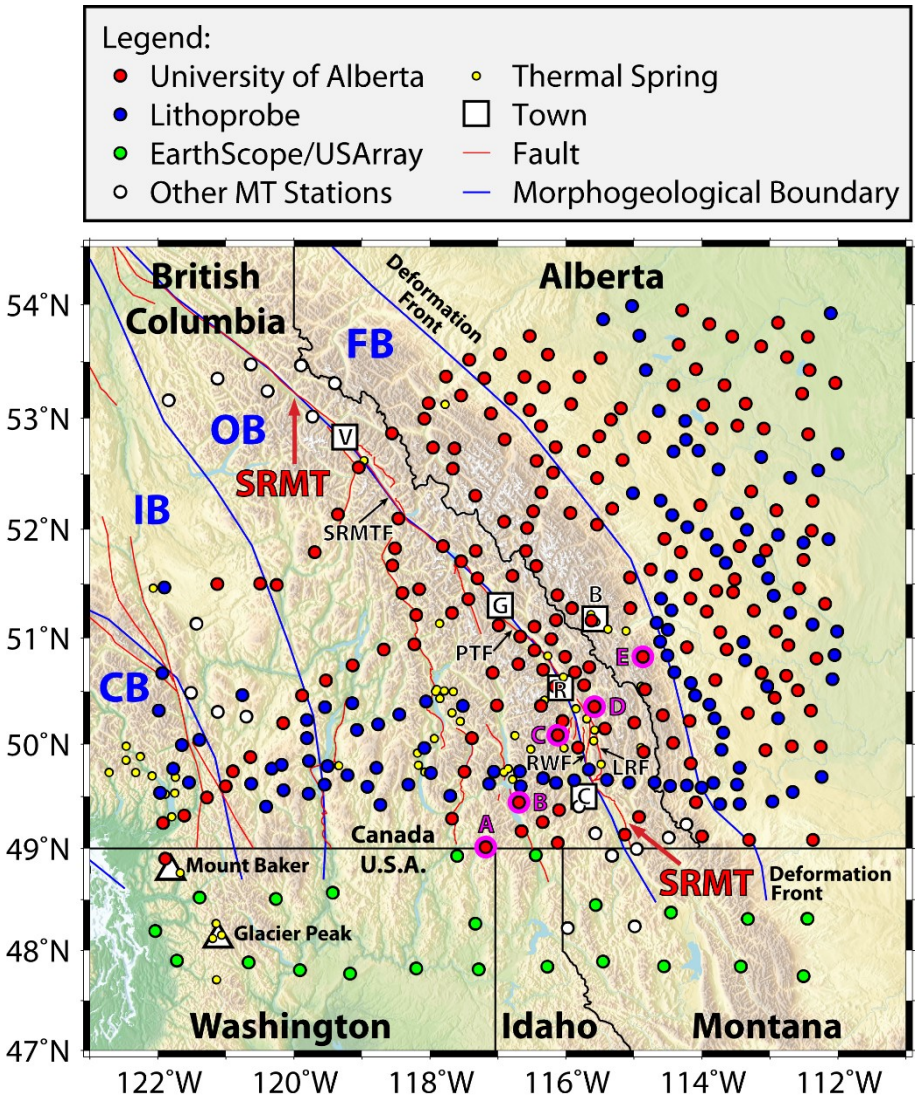

***Figure 5.3**: MT stations (large dots) used in the inversion to generate the resistivity model. MT data were collected by/for the University of Alberta (red dots), Lithoprobe (blue dots), EarthScope/USArray (green dots) and other projects (white dots). Political boundaries (black lines), morphogeological boundaries (blue lines), major faults (red lines), thermal springs (yellow dots), major volcanic centres (white triangles) and towns mentioned in the paper (white squares) are also shown. Data from the MT stations circled and labelled in pink are shown in Figure C.12. CB = Coast belt; IB = Intermontane belt; OB = Omineca belt; FB = Foreland belt; SRMT = southern Rocky Mountain Trench; SRMTF = southern Rocky Mountain Trench fault; PTF = Purcell Thrust fault; RWF = Redwall fault; LRF = Lussier River fault; V = Valemount, BC; G = Golden, BC; B = Banff, Alberta; R = Radium, BC and C = Cranbrook, BC.*

Before inverting MT data, it is important to review them and understand their characteristics. The data are shown in map view at four representative periods in Figure 5.4 and Figure 5.5. The quantities plotted in Figure 5.4 and Figure 5.5 are defined in Section C.1 of Appendix C. The induction vectors are plotted using the Wiese (1962) convention; therefore, the vectors point away from conductive regions. Skin depth increases with increasing period, so period can be considered as a proxy for depth (Table C.6). At the shortest periods, there is limited

data south of the Canada–USA border. At long periods, data coverage in BC becomes sparse, with the ABC-S profile being the notable exception. There are few data points in the northwest, largely due to inaccessible terrain; and this area has been omitted from the interpretation and discussion.

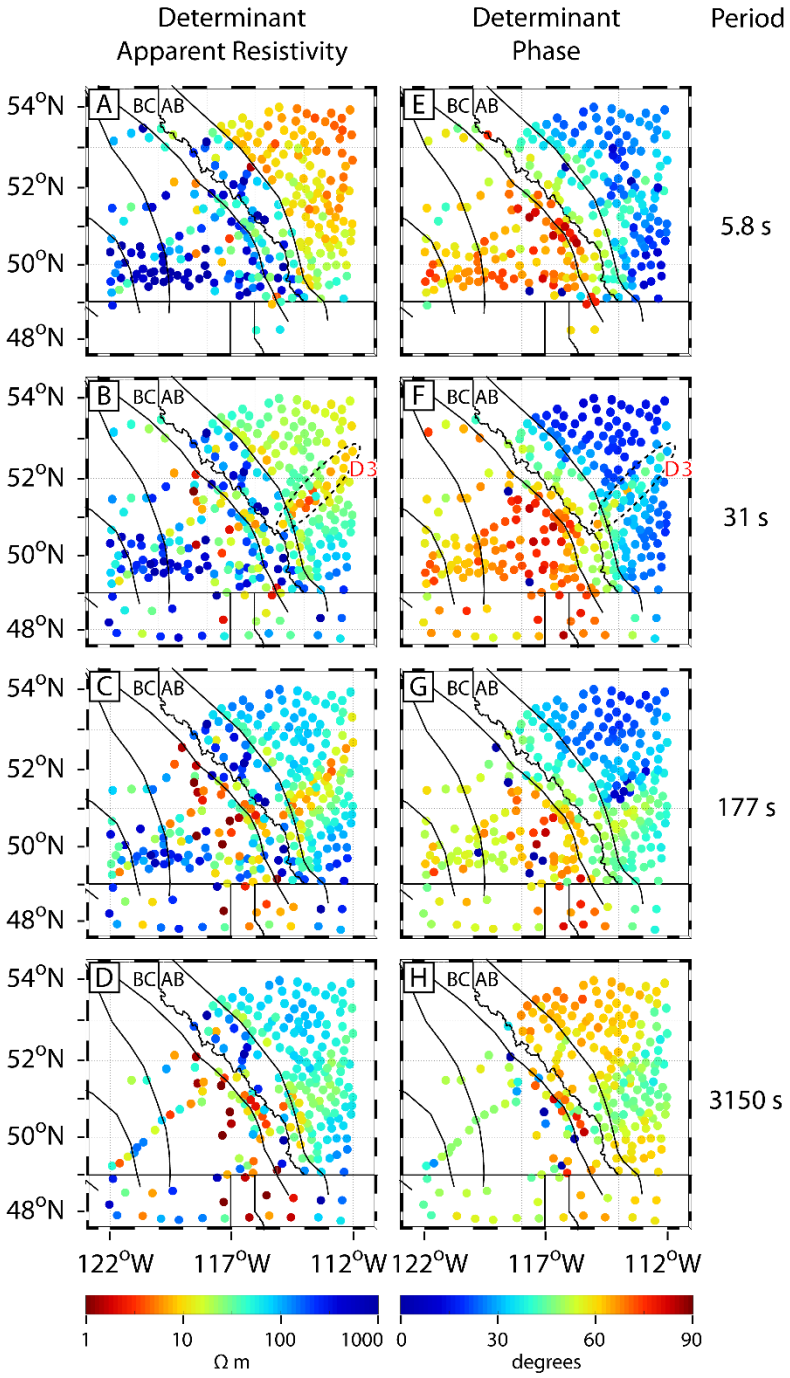

***Figure 5.4**: (a)–(d) Determinant apparent resistivity and (e)–(h) determinant phase at four representative periods. D3 (black dashed oval) is discussed in the text. BC = British Columbia and AB = Alberta.*

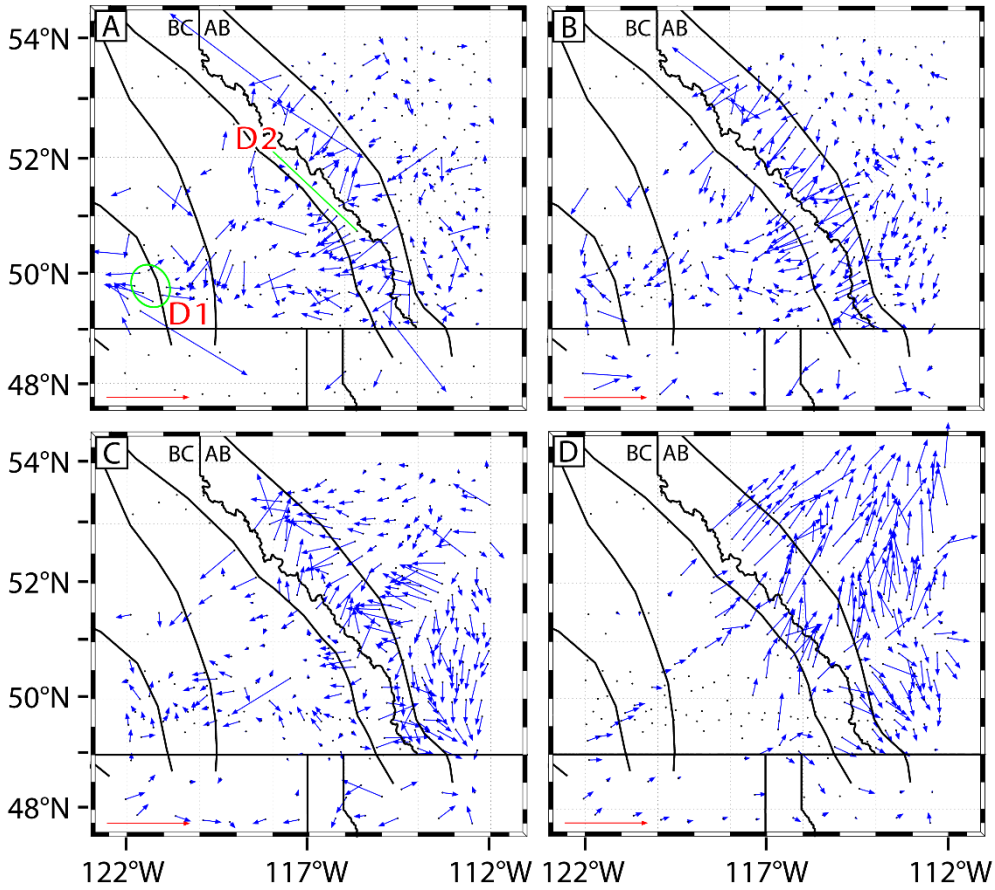

***Figure 5.5**: Real part of induction vectors using the Wiese convention at four representative periods: (a) 5.8 s, (b) 31 s, (c) 177 s and (d) 3,150 s. Red arrow (bottom left) is a unit vector. D1 (green oval) and D2 (green line) are discussed in the text. BC = British Columbia and AB = Alberta.*

At a period of 5.8 s, there is high apparent resistivity west of the Cordilleran deformation front, contrasted with low apparent resistivity to the east. This change can be associated with the presence of low resistivity clastic sedimentary rocks in the WCSB, contrasted with high resistivity rocks in the upper crust of the Rocky Mountains (e.g., limestone, shale, and sandstone; Thompson et al., 2006) and crystalline rocks in the ranges to the west. The determinant phase is mostly greater than 45° in the Cordillera, indicating that resistivity is decreasing with depth; and mostly less than 45° in the WCSB, indicating that resistivity is increasing with depth. In the southwest, induction vectors point away from the Fraser River fault, near the Coast-Intermontane boundary (D1 in Figure 5.5). This indicates shallow current flow, subparallel to the fault, in a zone of low resistivity, consistent with the results of Jones, Kurtz, et al. (1992). There is also a set of oppositely pointing induction vectors in the western Foreland belt (D2 in Figure 5.5), implying another shallow zone of low resistivity. Finally, induction vectors point westward near the Cordilleran deformation front, providing further evidence of a conductive upper crust in the WCSB.

At a period of 31 s, the apparent resistivity in the eastern Omineca belt and western Foreland belt has decreased, relative to the shorter period discussed above, and there are high phases west of the BC–Alberta border. This suggests the presence of a conductive middle- to-lower crust in the southeastern Cordillera. There is a northeast trending feature east of the deformation front with low apparent resistivity and ~45° phase (D3 in Figure 5.4). It is likely associated with the RDC or SABC. As with the data at shorter periods, the induction vectors point away from the WCSB and western Foreland belt, indicating that low resistivity persists at greater depths.

At a period of 177 s, the apparent resistivity in the southeastern Cordillera has further decreased, relative to shorter periods; and the phase is lower, but still generally greater than 45°. This indicates that resistivity is still decreasing with depth, but more slowly than at shorter periods. In Alberta, the north (51–54 °N) has lower phase than the south, suggesting that the north is more resistive than the south in this region. The conductive anomaly in the east is still present, but there is higher resistivity to the north and south of it. The induction vector map is dominated by vectors pointing away from this feature.

At a period of 3,150 s, there is reduced data coverage west of the deformation front and the apparent resistivity is variable. East of the deformation front, the resistivity is more uniform; and the phase is moderate near the SABC and high elsewhere. This indicates that resistivity is decreasing with depth, suggesting that the signals have penetrated beyond the base of the resistive craton. East of the SRMT and north of the SABC, the induction vectors consistently point north-to-northeast. South of the SABC, they point to the southeast.

5.3.3. MT data selection and 3-D inversion setup

The inversion used MT data at 18 periods, logarithmically spaced between 1 and 18,000 s, measured at 331 locations. The sites were chosen from a total of more than 700 for the high quality of their data and to ensure that the station distribution was as spatially uniform as possible. The median distance between a station and its nearest neighbour was 22 km; the mean was 25 km. Panel (a) of Figure C.2 shows how many stations had impedance and tipper data defined at each of the 18 periods. Panel (b) of Figure C.2 shows the skin depth at the same periods for six half-spaces between 0.1 and 10,000 Ωm. Fourteen of these periods, between 6 and 10,000 s, had impedance and tipper data at more than 200 stations. For a moderately valued 100 Ωm half-space, these periods correspond to a range of skin depths

between 12 and 500 km. For more conductive regions, the skin depths are less; and for more resistive regions, the skin depths are greater.

The data were measured in geomagnetic coordinates: magnetic north and east for *x* and *y*, respectively. For the inversion, they were rotated to a geographic coordinate system: geographic north and east for *x* and *y*, respectively. The following error floors were applied to the impedance (***Z***) and tipper (***T***) data: 5% of $\sqrt{|Z_{xy}||Z_{yx}|}$ to Z_{xy} and Z_{yx}, 10% of $\sqrt{|Z_{xy}||Z_{yx}|}$ to Z_{xx} and Z_{yy}, and 0.03 to T_{zx} and T_{zy}.

The study area had a horizontal extent of approximately 700 × 700 km; therefore, a relatively coarse mesh was used, as explained below. The model cells were 5 × 5 km in the horizontal plane, with 12 padding cells increasing geometrically by a factor of 1.4 away from the central part of the grid which encompasses the MT stations. Given the areal extent of the study area, this was the finest grid that could be modelled using a reasonable amount of memory on the parallel computing cluster used for the inversions. The final inversion required ~500 GB of memory and ran for 23 days. It was one of 20 inversions run for this study, not including synthetics. During MT data selection, locations were chosen to ensure that a minimum of two vacant grid cells separated any two MT sites. The uppermost layer was 50 m thick, and the layer thickness increased geometrically by a factor of 1.15 downward. The total model had dimensions of 2689, 2709 and 1105 km in the NS, EW and vertical directions respectively (172 × 176 × 58 cells). At the longest period in our data set, the skin depth in a 100 Ωm half-space is 679 km; therefore, the model extended approximately 1.5 skin depths in all directions.

Due to the coarseness of the mesh and the computing resources needed, topography and bathymetry were not included in the model. Topography is often omitted from regional-scale long-period MT studies. In these studies, the interstation spacing is larger than the horizontal scale of the topography. In addition, the depth of investigation is an order of magnitude greater than the differences in elevation across the study area. Modelling the topography would greatly increase the computational cost. Previous studies using a similar approach have all ignored topography (Bedrosian & Feucht, 2014; Meqbel et al., 2014; Wang & Unsworth, 2022; Yang et al., 2021). The effect of the Pacific Ocean was addressed with a forward calculation that added seawater to a uniform 100 Ωm earth. The presence of seawater had minimal effect on apparent resistivity, phase or induction vectors at the array of MT stations. This is illustrated in Figure C.3–Figure C**.7**.

5.3.4. Inversion parameters and data misfit

Before discussing and interpreting the 3-D inversion model, it is important to note that the non-uniqueness inherent in the inversion process was addressed by undertaking many inversions (Table C.2). These inversions explored different data sets, regularization parameters, model covariances and initial model configurations. The ModEM inversion algorithm of Kelbert et al. (2014) was used in all cases.

Model covariance length scale, γ, is a measure of model smoothing applied across cell boundaries, where a higher number corresponds to more smoothing. The preferred inversion used γ= 0.5 in the horizontal directions and γ= 0.3 in the vertical direction. These values were chosen after a series of sensitivity tests were performed, as described in Section 5.4.2. The model has a tear halfway through the sedimentary basins of the upper crust, as determined by the CRUST 1.0 model (Laske et al., 2013), meaning that γ was reduced to zero at model cell interfaces corresponding to half of the sedimentary layer thickness, hence no smoothing was imposed across the tear. It allowed for sharp resistivity transitions as might be expected from the layered structure of the WCSB. Typical sedimentary strata in this region are siliciclastic rocks overlying carbonate rocks (Lemieux, 1999) and since the latter are more resistive, it was reasonable to place a tear within the sedimentary layer. This initial condition had little effect on the resistivity structure beneath the Cordillera, but it was used because it did affect the resistivity structure beneath the WCSB. The inversion started with a regularization parameter (λ) of 1 and this value decreased, one order of magnitude at a time, to a minimum value of 10^{-8} at the end of the in version. With high values of λ, the inversion produced a spatially smooth resistivity model; with low values of λ, the inversion produced a rougher model with lower data misfit. This resulted in spatially smooth resistivity models at early iterations, then allowed more complex structures to emerge as the inversion progressed.

Twenty 3-D inversions w ere run to examine the effect of different choices of the available MT data and model dependence on the control parameters (Table C.2). The preferred inversion used a starting model with a resistivity of 10 Ωm above the tear in the sedimentary basins and 100 Ωm everywhere else. The inversion began with λ= 1 and an RMS misfit of 15.8, then after 382 iterations, the in version con verged to an RMS misfit of 1.94 with λ= 10^{-8}. The error floors defined in Section 5.3.3 were used.

During the last 100 iterations or more, the model did not change in ways that would affect the interpretations. The preferred model is from iteration 313, with λ= 10^{-3} and a misfit of

2.08. The final iteration was not used because $\lambda = 10^{-8}$ was an arbitrary end point; the inversion would have continued if a lower value of λ had been chosen. The preferred model has a good balance between smoothness and misfit. Figure C.8 shows inversion parameters for all iterations. The plot of model norm as a function of misfit has an inflection point at iteration 234, where model norm = 2.96, misfit = 2.22 and λ = 1. This model only differs from the preferred model in subtle ways and its selection would not significantly alter the interpretations.

To investigate the effects of different starting models, four initial model configurations were used: (1) a 100 Ωm half-space, (2) a 100 Ωm half-space with a tear at the boundary between basement and sedimentary rocks at depths less than ~4 km, (3) 100 Ωm below the aforementioned tear and 10 Ωm above it and (4) a tear halfway through the sedimentary rocks, with 100 Ωm below it and 10 Ωm above it. These four starting models correspond to inversions 12–15 in Table C.2 and are illustrated in Figure C.9. To investigate the effects of different data sets, starting model 1 was used to invert the impedance data only (all tipper data were ignored) and starting model 4 was used to invert a data set without tipper at the two longest periods. These two data sets correspond to inversions 16 and 17 in Table C.2.

The impedance-only inversion failed to adequately image the conductor in Alberta implied by the data (D3 in Figure 5.4); therefore, this resistivity model was disregarded. The inversion model starting from configuration 2 had unreasonably low conductivity concentrated near the base of the sedimentary layer and the RDC was not present; therefore, this resistivity model was disregarded. The inversion starting from configuration 3 did not image the RDC either. Instead, it produced a swath of low resistivity in the sedimentary layer above where the RDC was presumed to be; therefore, this resistivity model was disregarded. The RDC and SABC are prominent features in the other models. The inversion models using starting model configurations 1 and 4 are very similar away from the WCSB.

The resistivity model with a tear halfway through the sedimentary layer, from inversion of the data set without tipper data at the two longest periods, was chosen as the preferred model (Table C.2, inversion 20). When the long period tipper data were included, they resulted in the highest misfit of any single-component single-period misfit. Meqbel et al. (2014) found a similar challenge and omitted tipper data at periods longer than 6,500 s to avoid non-plane wave effects in the MT signals.

The single-station data RMS misfit at four selected periods is shown in Figure 5.6. Overall, this shows that the data are being well fitted by the inversion. Many of the locations with high misfit are in the eastern Omineca belt and western Foreland belt, a region where previous studies have inferred the presence of anisotropy, which cannot be represented in the isotropic 3-D inversion (Lee, 2020). Sites west of and in the western Omineca belt generally had low misfits. Sites in the WCSB had low misfit except at the shortest and longest periods. The data misfit was greatest at the three shortest and three longest periods (Figure C.10 a), which were also the six periods with the least data (Figure C.2 a). In general, the six different data components had similar misfit (Figure C.10 b–d), hence the joint inversion was able to successfully fit both the impedance and tipper data.

The predicted responses of the inversion model are shown in Figure C.11 for comparison with Figure 5.4 and Figure 5.5. The data fit is generally good. As is usual in inversion, some phase outliers were not fit, for example, the three blue dots in the southern- most Omineca belt at a period of 177 s in Figure 5.4. Apparent resistivity, phase and tipper curves, for both observed and predicted data at five MT sites, are also shown in Figure C.12.

5.4. Preferred resistivity model (iteration 313 of inversion 20)

In this section, the 3-D resistivity model is described, then sensitivity test results are presented. All model slices have been plotted with two resistivity contours: 25 and 400 Ωm. These values are equidistant, on a logarithmic scale, from the initial resistivity of 100 Ωm; and 25 Ωm is a local minimum of a histogram of model cell resistivity in the upper 100 km, excluding padding cells (Figure C.13).

Inversion of MT data with the ModEM algorithm produces spatially smooth resistivity models, so the definition of the edge of a conductive anomaly is some what arbitrary. A value of 25 Ωm was chosen to coincide with a local minimum of the model cell resistivity histogram (Figure C.13). This ensured that the bulk of the conductive anomalies was contained within the 25 Ωm resistivity contours.

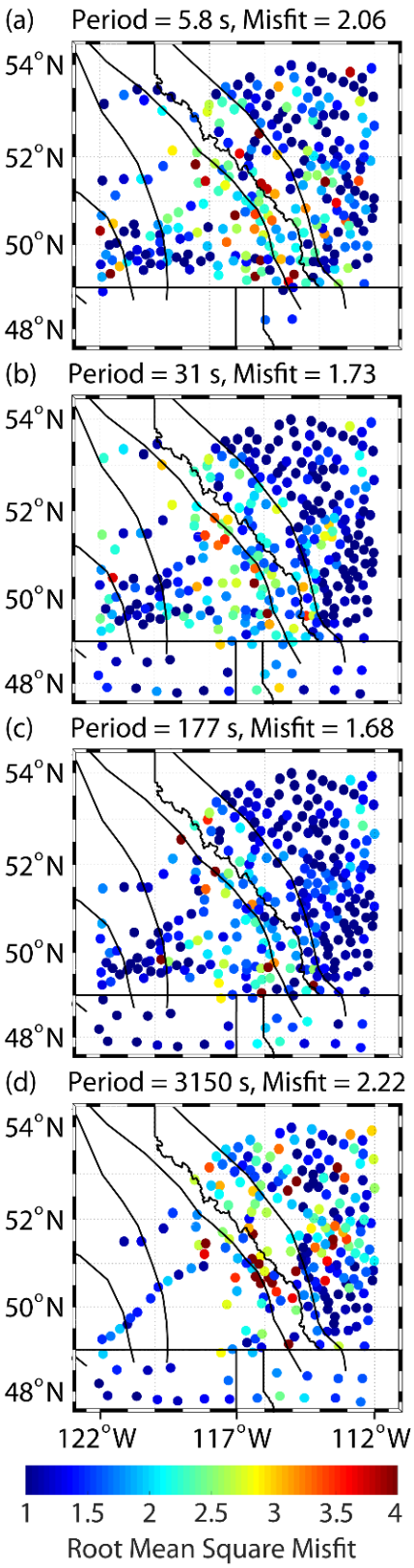

***Figure 5.6**: RMS misfit of observed data to predicted data from the preferred model at four representative periods. Coloured dots are individual station misfits and the overall period misfit is written above each panel.*

5.4.1. Description of the preferred 3-D resistivity model

A preliminary 3-D resistivity model was presented in a Geoscience BC report by Hanneson and Unsworth (2022). The preferred resistivity model presented in this paper supersedes the model presented in this report. Figure 5.7–Figure **5.9** show the preferred resistivity model. Key features are described in this section, then they are interpreted in Section 5.6.

The resistivity structure shown in these figures is relatively complicated and contains several low resistivity features (conductors). These are grouped into four main areas and depth ranges. Each zone is composed of multiple conductors that are discussed in the interpretation section.

C1 group: there is a prominent belt of low resistivity extending southwest across the Alberta Basin of the WCSB and beneath the Canadian Cordillera, labelled C1a and C1b. The minimum resistivity is below 1 Ωm and these structures extend from the crust to upper-mantle depths of 70 km or more. This conductive belt can be identified as the SABC (C1a) of Gough (1986) and the Loverna conductor (C1b) of Nieuwenhuis et al. (2014). These two conductors are connected in the preferred resistivity model (Figure 5.8 b). Another conductor (C1c) occurs at 51–52 °N in the eastern Foreland belt at depths of 30–70 km and is named the Banff conductor in this paper.

C2 group: the second group of conductors is located in the crust near the SRMT, with a minimum resistivity less than 1 Ωm. In this paper, C2a and C2b are named the Valemount conductor and the Golden conductor, respectively. These features extend to lower-crustal depths with a northwest dip.

C3 group: the third group (C3a, C3b and C3c) is located in the Omineca Belt, west of the SRMT, in the middle and lower crust. This is identified as the Canadian Cordilleran Regional conductor (CCRC) reported in prior studies (e.g., Gough, 1986; Ledo & Jones, 2001). However, now with 3-D coverage and inversion, it can be seen that this feature is composed of multiple discrete conductors.

C4: the fourth feature is the low resistivity upper mantle (C4) beneath the Canadian Cordillera (Figure 5.8). This was imaged in previous studies, but only sampled on a limited number of profiles (Ledo & Jones, 2001; Rippe et al., 2013). The new model presented in this paper

gives a 3-D image of this feature; however, the model resolution in this region is reduced because it is beneath another conductor (C3).

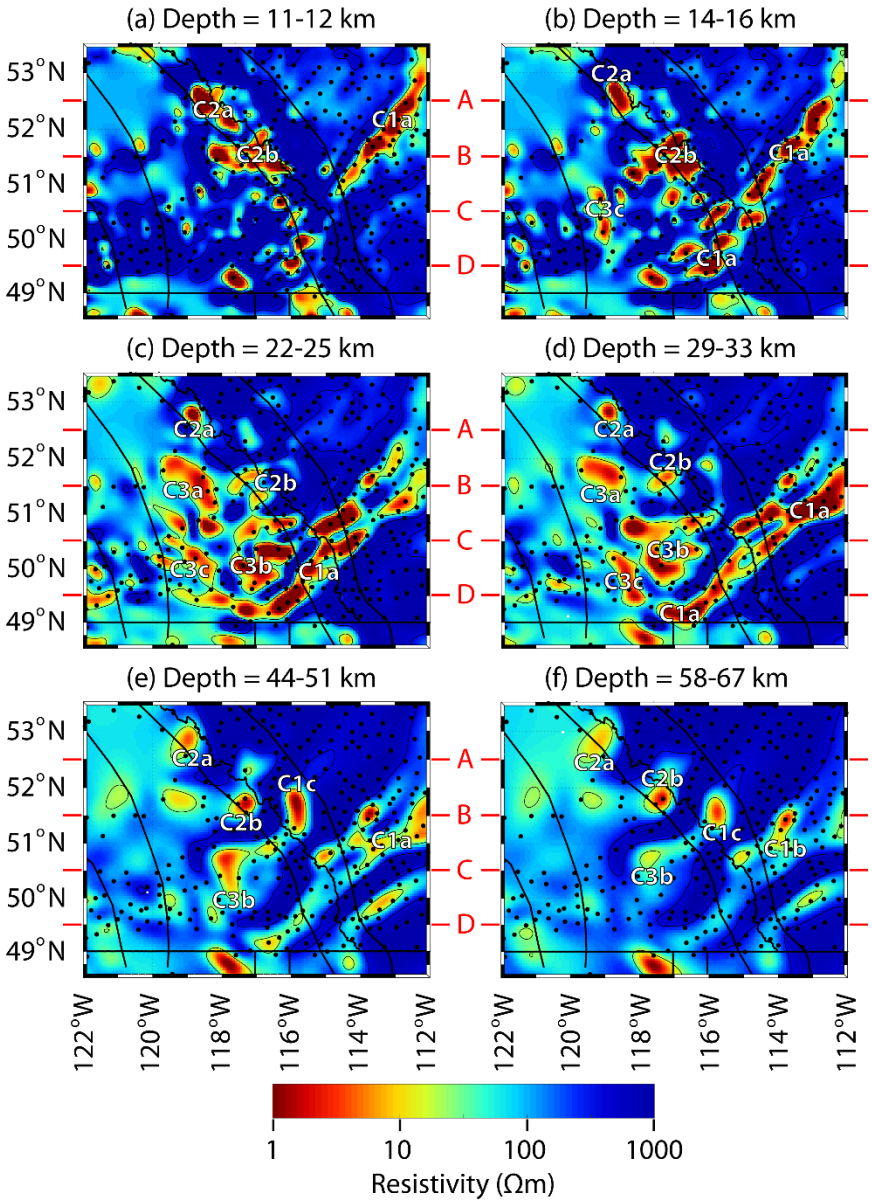

Figure 5.7*: Six depth slices from the preferred 3-D resistivity model. Thin black lines are resistivity contours at 25 and 400 Ωm. Thick black lines are political and morphogeological boundaries. Black dots are MT data locations. Red lines labelled A–D indicate the latitudes of the cross-sections shown in Figure 5.8. Conductors mentioned in the text are labelled C1–C3.*

The new 3-D model is compared with the 2-D models of Rippe et al. (2013) in Figure C.14. Both the 2-D and 3-D models show (1) a region of high crustal resistivity beneath the Omineca Belt and (2) a southward decrease in crustal resistivity along strike. The broad similarity of

the 2-D and 3-D models support the previous interpretations. The use of a 3-D inversion allows the along strike variation in crustal structure of this region to be modelled for the first time and reveals that previously reported conductors may actually be composed of multiple conductors.

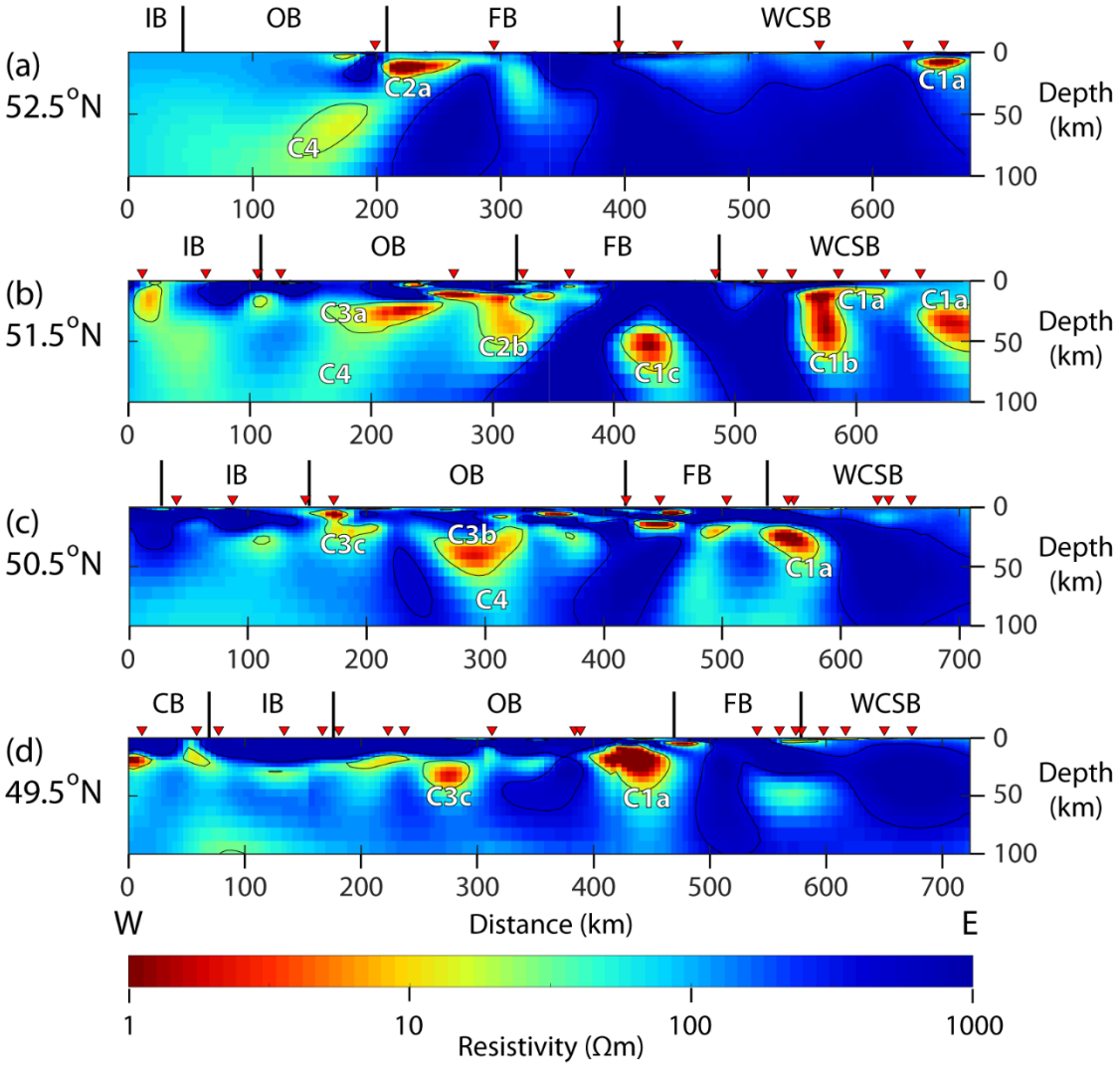

***Figure 5.8**: Cross-sections from the preferred 3-D resistivity model, from west (122 °W) to east (112 °W) at four selected latitudes: (a) 52.5 °N, (b) 51.5 °N, (c) 50.5 °N and (d) 49.5 °N. Thin black lines are resistivity contours at 25 and 400 Ωm. Conductors mentioned in the text are labelled C1–C4. MT sites within 10 km of the profiles are projected onto the cross-sections as red triangles. CB = Coast belt, IB = Intermontane belt, OB = Omineca belt, FB = Foreland belt and WCSB = Western Canada Sedimentary Basin.*

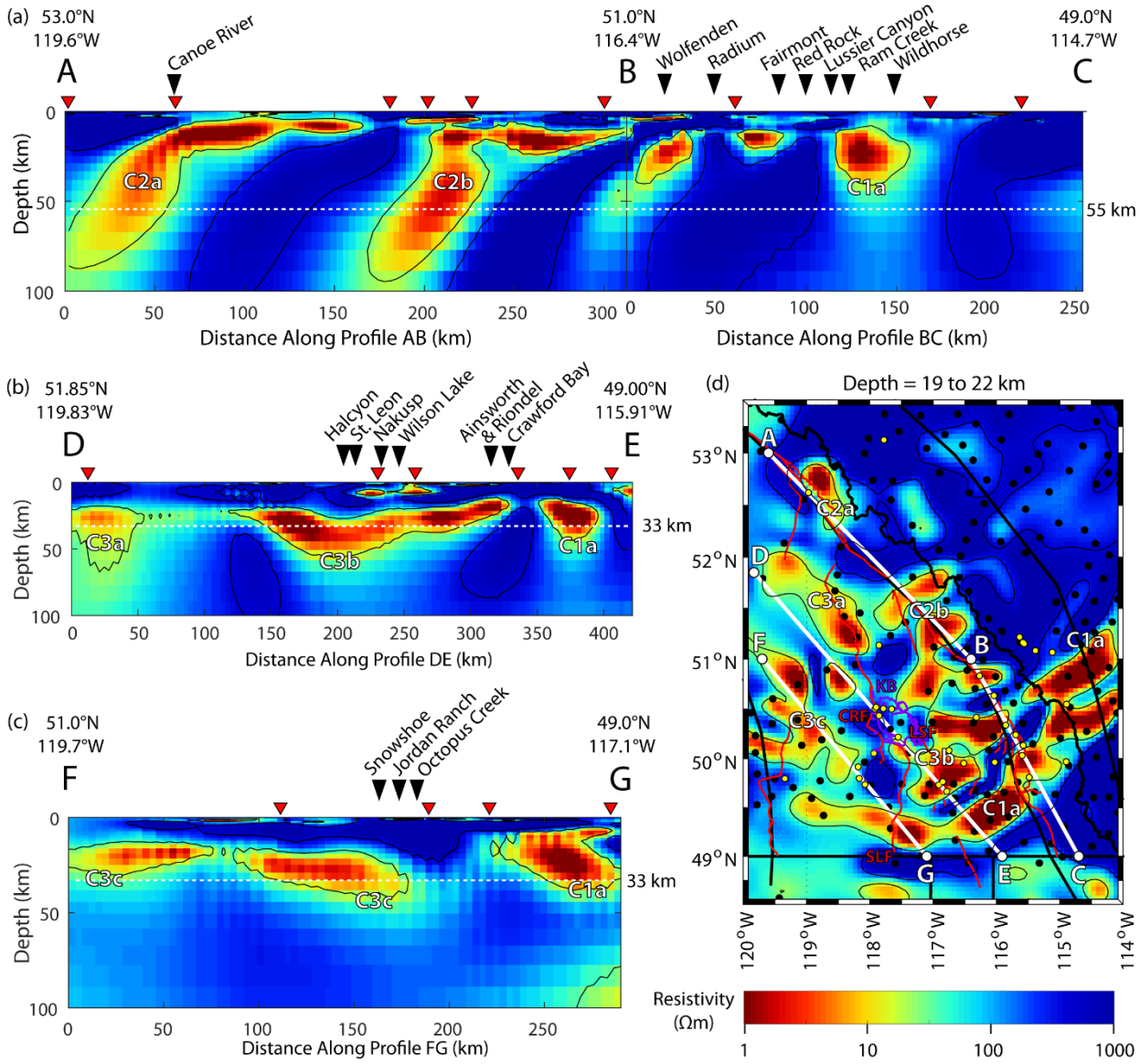

***Figure 5.9**: (a) Cross-section A–B–C near the SRMT. The Moho (approximate) is plotted within the layer at 51–58 km depth, in accordance with the seismic refraction results of Bennett et al. (1975). (b) Cross-section D–E in the southcentral Omineca belt. The Moho (approximate) is plotted on the layer interface at 33 km depth, in accordance with the summary of Hyndman and Lewis (1999). (c) Cross-section F–G in the southwestern Omineca belt. Nearby thermal springs are projected onto the three profiles, as shown by the black triangles. MT sites within 10 km of the profiles are projected onto the cross-sections as red triangles. (d) Horizontal model slice showing the locations of cross-sections A–B–C, D–E and F–G. Political and morphogeological boundaries (black lines), surface traces of major faults (red lines), surface trace of the Kuskanax batholith (purple lines), MT sites (black dots) and thermal springs (yellow dots) are overlaid. KB = Kuskanax batholith, CRF = Columbia River fault, LSF = Lakeshore fault and SLF = Slocan Lake fault.*

5.4.2. Sensitivity tests and resolution tests

The depth range of data sensitivity is investigated and discussed in detail in Section C.2.1 of Appendix C. Model editing and Kolmogorov–Smirnov (KS) tests (Massey, 1951) were used to determine the maximum depth at which the MT data were sensitive to resistivity variations, found to be 415 km (Table C.3). This paper interprets upper-mantle structure to a depth of 100 km and this part of the resistivity model is well resolved by the MT data. The minimum depth at which the MT data were sensitive to resistivity variations was investigated using the skin depth equation (Section 5.3.1) and the average resistivity of the upper crust (Figure C.15). Taking this analysis into account, it was decided to reduce interpretation of structure in the upper 10 km of the model.

Synthetic inversions were used to investigate model resolution (Figure C.16–Figure C**.30** and Table C.4–Table C**.5**). They are discussed in detail in Section C.2.2 of Appendix C. Two key points are (1) caution must be employed when interpreting the resistivity model in an area with spatially sparse MT data and (2) resistivity anomalies should not be considered robust unless they are at least 30 km (six model cells) wide.

5.5. Factors affecting resistivity

5.5.1. Temperature and pressure beneath the southern Canadian Cordillera and adjacent craton

Knowledge of temperature and pressure as functions of depth is key to making informed interpretations of crustal and upper-mantle resistivity models. Temperature–depth profiles and pressure–depth profiles are shown in Figure 5.10. The methods used to calculate them are described in Section C.3 of Appendix C.

These temperature and pressure profiles were utilized when determining parameter ranges for calculations in Section 5.5.2 and when interpreting the resistivity model. The minimum melting point of continental crust is ~700 °C; this may also be the upper temperature limit for the persistence of aqueous fluids in the crust, based on evidence for granulite facies conditions being dry (Hyndman & Shearer, 1989). Note that 700 °C is above the Moho in the southern Canadian Cordillera and below the Moho in the adjacent craton. In the following section, aqueous fluids at temperatures ≤ 700 °C and partially melted rocks at temperatures ≥ 800 °C are considered.

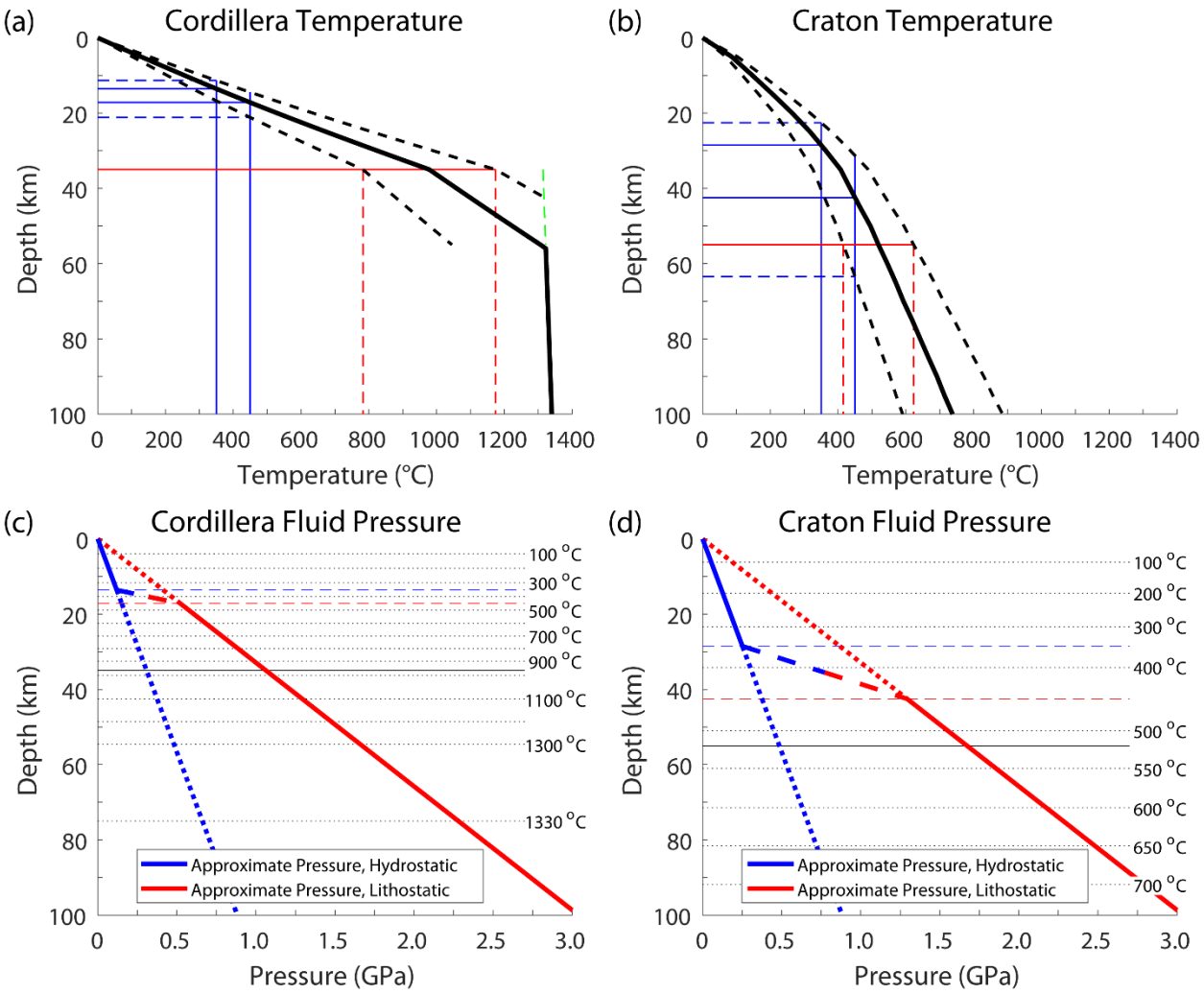

***Figure 5.10**: (a) and (b) Geotherms (black lines) to 100 km depth in the Cascadia backarc in southern BC (Currie & Hyndman, 2006) and the adjacent craton (Hyndman, 2010; Hyndman et al., 2009) with temperature ±20% (black dashes). Mantle adiabat (green dashes) and brittle-ductile transition at 350–450 °C (blue lines) are also shown. Moho depths (red lines) and Moho temperature ranges (red dashes) are approximated at 35 km depth in the Cascadia backarc and 55 km depth in the adjacent craton. (c) and (d) Hydrostatic pressure (blue lines) based on a uniform density of 0.9 g/cm^3 and lithostatic pressure (red lines) based on a uniform density of 3.1 g/cm^3. Fluid pressure is assumed to be hydrostatic in the brittle regime (< 350 ◦C) and lithostatic in the ductile regime (> 450 °C) with less certainty in the 350–450 °C temperature range (dashes). Isotherms (black dots) are shown along with approximate Moho depths (black lines) of 35 km in the Cascadia backarc and 55 km in the adjacent craton.*

5.5.2. Causes of low resistivity in the crust and upper mantle

5.5.2.1. Saline fluids

Sinmyo and Keppler (2017) empirically derived a numerical model of the electrical conductivity of NaCl-bearing aqueous fluids and calibrated it over the temperature range 100–800 °C. This model is a function of fluid density and a constant density of 0.9 g/cm^3 was used

in the following calculations, as justified in Section C.3 of Appendix C. At constant density, the resistivity of aqueous NaCl decreases with increasing temperature and with increasing salinity (Figure C.31). It should be noted that at constant pressure, the resistivity of aqueous NaCl decreases with increasing salinity; however, it only decreases with increasing temperature up to a certain point, then it increases. This threshold temperature is ~250 °C at 0.1 GPa and ~350 °C at 0.5 GPa. Salinities of 1–6 equivalent wt.% NaCl are typical of sedimentary and metamorphic fluids from oceanic environments, higher salinities may be found in rocks deposited in continental environments, and very high salinities may be found in high-grade metamorphic settings, with melt inclusion data showing fluid salinities of 1–15 wt.% NaCl and clustering near 5 wt.% (Sinmyo & Keppler, 2017).

To test if saline fluids can explain bulk resistivity values less than 10 Ωm, the modified Archie's law of Glover et al. (2000) was used to calculate the bulk resistivity of rocks containing NaCl-bearing aqueous fluids. Figure C.32 shows the bulk resistivity as a function of porosity and fluid connectivity, for temperatures of 200–700 °C and NaCl concentrations of 2–10 wt.%. With m = 1, the brine is fully connected and as m increases, connectivity decreases. Bulk resistivity is controlled by salinity, porosity and fluid connectivity; temperature has a minor effect. In upper crustal basins, sedimentary rocks containing saline aqueous fluids commonly have values of $1.5 < m < 2.5$ (Glover et al., 2000). Assuming a temperature greater than 200 °C, a salinity less than 10 wt.%, a porosity less than 3% and a cementation exponent, *m*, greater than 1.5, saline fluids can explain bulk resistivity values less than 10 Ωm if the salinity is greater than 3 wt.% and *m* is less than 1.8, as illustrated by the red polygons in Figure C.32.

5.5.2.2. Silicate melts

Ni et al. (2011) measured the electrical conductivity of hydrous basaltic melts at 1,200–1,650 °C, Guo et al. (2017) measured the electrical conductivity of hydrous andesitic melts at 891–1,300 °C, and Li et al. (2020) measured the electrical conductivity of hydrous shoshonitic melts at 800–1,550 °C. The resistivity of these melts, as a function of temperature and water content, is shown in Figure C.33. Li et al. (2020) and Guo et al. (2017) modelled their results with the Arrhenius equation, while Ni et al. (2011) observed non-Arrhenian behaviour and modelled their results with the Vogel–Fulcher–Tammann (VFT) equation. In the Arrhenius equation, logarithmic conductivity is linear with inverse temperature; in the VFT equation, it is not. This explains why the contours in panel (c) of Figure C.33 behave differently, compared with those in panels (a) and (b).

The resistivity of basaltic melt is lower than that of andesitic melt and the resistivity of shoshonitic melt is lower than that of the other two. To test if hydrous melt can explain bulk resistivity values less than 10 Ωm, the modified Archie's law of Glover et al. (2000) was used to calculate the bulk resistivity of rocks containing partial melt. A shoshonitic composition was considered for temperatures of 800–1,200 °C. Andesitic and basaltic compositions were considered for a temperature of 1,200 °C. For all three chemical compositions, water contents of 2–4 wt.% were considered (Figure C.34). Assuming a temperature less than 1,200 °C, a melt fraction less than 4%, and a cementation exponent, *m*, greater than 1.3, andesitic and basaltic partial melts cannot explain bulk resistivity values less than 10 Ωm. Recall that with $m = 1$, the melt is fully connected, and as *m* increases, connectivity decreases. With the same assumptions, shoshonitic partial melt can explain bulk resistivity values as low as 2 Ωm. With high temperature and water content, shoshonitic partial melt can explain bulk resistivity values less than 10 Ωm with as little as 1–2% melt, as illustrated by the red polygons in Figure C.34.

Melt resistivity decreases with decreasing silica content, from andesite to basalt, primarily because of the increase in temperature required to produce these melts. There is a small decrease in melt resistivity, from andesite to basalt, at constant temperature (Figure C.33). Melt resistivity also decreases with increasing alkali content. Mafic composition alone cannot explain very low bulk resistivity given small, non-eruptible, melt fractions. An alkali-rich composition, as opposed to calc-alkaline, is necessary to explain very low bulk resistivity with small melt fractions. Chemical compositions of the rocks used in the melt conductivity experiments (Guo et al., 2017; Li et al., 2020; Ni et al., 2011) are plotted on a total alkali-silica (TAS) diagram in Figure C.35, using the classification scheme of Le Bas et al. (1986, 1992). Compositions of a selection of alkali-rich Eocene volcanic rocks from the southern Canadian Cordillera (Adams et al., 2005; Dostal et al., 2003, 2019, 2021) are also plotted. This is done for illustrative purposes; it is not suggested that Eocene magmas have persisted until the present. Further discussion of alkali-rich magmatism is presented in Section 5.7.2.

5.5.2.3. Sulphide mineralization

Sulphide minerals can form during chemical interactions between magma and adjacent rock, crystallization of mafic melt and hydrothermal alteration (DeLucia et al., 2019). However, sulphides may be unstable at depths greater than the uppermost mantle (Selway, 2014). Laboratory experiments showed that olivine containing 1 vol.% (~1.4 wt.%) iron sulphide had

a bulk resistivity that was up to several orders of magnitude lower than olivine without impurities, particularly at temperatures above 750 °C (Watson et al., 2010).

Furthermore, basaltic melt mixed with a small amount of sulphide melt has a much lower resistivity than pure basaltic melt. For example, an upper-mantle resistivity of 10–20 Ωm at depths of 40–70 km in the southern Sierra Nevada was explained by 2–5% partial melt without sulphides (Park et al., 1996) or less than 1% partial melt with at least 0.25% sulphide melt (Ducea & Park, 2000). Sulphide melt is denser than silicate melt and separation could lead to a concentration of sulphides over time (Ducea & Park, 2000). Grain-boundary sulphide mineralization and small fractions of sulphide melt could contribute to low resistivity in the middle- to lower-crust and uppermost mantle.

5.5.2.4. Graphite in the lower continental crust

Graphite is approximately 10 orders of magnitude more conductive than common crustal rock-forming minerals (Glover, 1996), so small interconnected amounts can cause a low bulk resistivity. For example, a bulk resistivity of 30 Ωm can be explained by 1–100 ppm graphite, depending on the interconnection (Hyndman et al., 1993).

Glover (1996) concluded that interconnected graphite films were a possible cause of low resistivity in the lower continental crust, but cautioned that their extent was still unknown. Hyndman et al. (1993) concluded that saline fluids were more likely than graphite to be the most common cause of widespread low resistivity in the lower continental crust.

Yoshino and Noritake (2011) studied graphite films on synthetic grain boundaries of quartz to simulate silicate minerals under lower crustal conditions. They concluded that a thick (~1 mm) interconnected layer of graphite might survive over geological time, but thin graphite films are unlikely to be a cause of low resistivity in the lower continental crust because disconnection of the films is probable. They determined that interconnected graphite precipitated at high temperatures (above 727 °C) is unstable; and that interconnected graphite precipitated at low temperatures (below 727 °C) is transient, with a 100 nm film remaining interconnected for < 200 years at 427 °C and < 20,000 years at 327 °C. Recall that 400 °C occurs at ~15 km depth in the southern Canadian Cordillera and ~34 km depth in the adjacent craton (Figure 5.10). Reduction of CO_2 in metamorphic rocks is the most likely source of carbon in the lower continental crust (Hyndman et al., 1993).

5.5.2.5. Summary

A bulk resistivity of 3–10 Ωm could be explained by interconnected saline fluids with sufficient salinity in rocks with sufficient porosity; however, a bulk resistivity of less than 3 Ωm would require more than 10 equivalent wt.% NaCl and/or more than 3% porosity if saline fluids were the primary cause (Figure C.32). A conductive solid phase, such as grain-boundary graphite or sulphide mineralization, is a probable cause of very low resistivity; however, thin graphite films are only likely at low temperatures (less than 400 °C). Where high temperatures (greater than 800 °C) exist, the low resistivity could also be explained by a small fraction of hydrous alkali-rich partial melt (Figure C.34), or a small fraction of hydrous basaltic partial melt containing sulphide melt.

5.6. Interpretation

5.6.1. Conductors in the craton (C1)

Conductors in the cratonic basement beneath the WCSB in Alberta have been discussed previously. Nieuwenhuis et al. (2014) imaged the SABC, Red Deer and Loverna conductors. These conductors are connected in the preferred resistivity model presented in this paper (C1a and C1b). The SABC extends beneath the Foreland belt and southeastern Omineca belt, implying that the Precambrian basement in this region is largely intact. Reactivation of transverse structures in the cratonic basement beneath the southeastern Canadian Cordillera played an important role in the formation of major mineral deposits in the region (McMechan, 2012). The Banff conductor (C1c) is also located in the cratonic basement, beneath the Foreland belt.

The resistivity of these conductors is too low to be explained by interconnected saline fluids (Figure C.32) and temperatures in the craton are too low to allow partial melting. Laboratory studies have shown that graphite films are likely only stable at temperatures below ~400 °C (Yoshino & Noritake, 2011). This corresponds to depths less than 34 km in the craton and 15 km beneath the Cordillera. Therefore, sulphide mineralization is the most probable cause of low resistivity below these depths, and both graphite films and sulphide mineralization are possible causes above these depths.

5.6.2. Conductors near the SRMT (C2)

C2a and C2b are in the depth range 10–70 km (Figure 5.9 a), which correspond to temperatures of approximately 150–600 °C in the craton (Figure 5.10 b). These temperatures are below the solidus of common crustal rocks. Interconnected saline fluids and interconnected graphite films are possible explanations for the low resistivity. Melt emplaced from hotter regions at greater depth could be present in this depth range; however, it would solidify over time and recharge would be needed to maintain the molten region.

5.6.3. Canadian Cordilleran Regional conductor (C3)

Zones of low resistivity are common globally in the lower continental crust. This study area in the southern Cordillera is one where a conductive layer was first seen and the debate about their origin began. Previous interpretations considered partial melt, graphite, and aqueous fluids (Glover, 1996; Hyndman et al., 1993). This debate has not yet been resolved. In this section, we consider the cause of the layer based on the fact that (1) additional laboratory studies are now available compared to the 1990s and (2) a 3-D resistivity model of the subsurface structure is available, in contrast to previous 2-D models.

5.6.3.1. Causes of low resistivity based on temperature and rheology

The CCRC is observed in the depth range 15–55 km in the southern Omineca belt, corresponding to temperatures of approximately 400–1,300 °C in the backarc (Figure 5.10 a). Deep crustal aqueous fluids tend to occur in the 400–700 °C temperature range (Hyndman & Shearer, 1989), corresponding to depths of approximately 15–26 km. Partial melt is possible at higher temperatures, i.e. 700–1,300 °C, corresponding to depths of approximately 26–55 km. The observed bulk resistivity can be explained by interconnected saline fluids and/or sulphide mineralization at mid-crustal depths, and hydrous partial melt and/or sulphide mineralization at lower-crustal depths and upper-mantle depths.

If aqueous fluids are the cause of the low resistivity, then it is important to understand why they form a layer. Aqueous fluids may stagnate below the brittle–ductile transition (BDT) in a depth range characterized by an inverted pressure gradient (Connolly & Podladchikov, 2004). The depth of neutral buoyancy, approximately 2–4 km below the BDT, acts as a barrier to upward fluid flow, and fluid flow above the BDT may be directed downward to the depth of neutral buoyancy (Connolly & Podladchikov, 2004). The fluid in this stagnant zone is

overpressured and can cause hydrofracturing, leading to a thickening of the stagnant layer up to 2–5 km (Connolly & Podladchikov, 2004). Geological heterogeneity could give rise to multiple stagnation zones at different depths (Connolly & Podladchikov, 2004). The MT method may image a series of thin conductors as a single conductor because the top of the upper conductor would be best resolved, and the other interfaces would be less well resolved due to attenuation of the magnetic field.

This phenomenon was considered in the analysis of MT data from Mongolia that revealed low-resistivity zones in the lower crust at a depth of approximately 30–40 km, and 5–15 km below the BDT (Comeau et al., 2020). These zones, which were less than 10 km thick, could represent localization and stagnation of metamorphic fluids (Comeau et al., 2020). Fluid inclusions in metamorphic minerals and metasomatic changes in rock compositions provide evidence of a lower-crustal fluid phase (Manning, 2018).

The studies above give valuable context for the Canadian Cordillera. The BDT occurs at a temperature of 400 °C ±50 °C (Nesbitt & Muehlenbachs, 1995) corresponding to a depth range of ~14–17 km in the backarc region of the southern Canadian Cordillera (Figure 5.10 a). The fact that the top of the CCRC is around the depth of the BDT strengthens the interpretation that the upper parts of the CCRC, at depths of approximately 15–26 km, are related to saline fluids. These fluids are likely to be produced from crystallizing melts or metamorphic reactions as proposed by Manning (2018).

5.6.3.2. Geometry of conductors

The CCRC appears to be a group of discrete conductors rather than a single continuous conductor. This observation is supported by the extensive sensitivity tests, discussed in Section 5.4.2 and Appendix C.

Isotropic inversion of MT data due to anisotropic resistivity structure can result in a pattern of subparallel conductors (Heise & Pous, 2001). The synthetic models with 17 conductive prisms, each 10 km wide, separated by 10 km gaps (Figure C.21) can be used as an example of macro-anisotropy. When synthetic MT data from these resistivity models were inverted, the resulting resistivity models contained an incorrect number of subparallel conductors, that is, 6 or 7, not 17.

Electrical anisotropy may have played a role in producing the conductivity pattern observed in the preferred resistivity model. For example, Lee (2020) performed isotropic and anisotropic 3-D inversions of MT data collected near the SRMT fault at Kinbasket Lake, and preferred the anisotropic resistivity model to the isotropic resistivity model, based on geological considerations. Some MT sites in the eastern Omineca belt and western Foreland belt had higher than average RMS misfit (Figure 5.6); this area may exhibit electrical anisotropy.

An anisotropic version of ModEM was recently developed (Kong et al., 2021); however, it requires significantly greater computing resources than the isotropic version and has not yet been successfully applied to a large data set such as the one described in this paper. Due to resource constraints, anisotropic inversions were not performed; they are recommended for future research. Given the large study area, covering many different geological units, there could be some areas and depths that exhibit electrical anisotropy, while the majority of the modelled volume could be isotropic.

5.6.4. Upper mantle

High heat flow and geodynamic modelling have suggested that the asthenosphere beneath the southern Cordillera is shallow and likely undergoing convection (Currie, Wang, et al., 2004; Hyndman et al., 2005). The low viscosity necessary for this is inferred to be due to high temperature and elevated water content in the asthenosphere. Previous MT studies have supported this hypothesis. Beneath the Intermontane and Omineca belts, low upper-mantle resistivity was interpreted as due to elevated H^+ concentrations with an estimated water content of 50 ppm at 50 km depth and 100–300 ppm at 150 km depth (Rippe et al., 2013). These prior studies were restricted to 2-D transects and inherently limited in their ability to model the resistivity structure off profile. The new 3-D resistivity model gives the opportunity to extend these studies of the upper mantle to 3-D.

The method of Rippe et al. (2013) was applied to the 3-D resistivity model to estimate water contents in the upper-mantle west of the SRMT and results are shown in Figure 5.11. The estimated water contents were in the range 0.03–334 ppm with a mean of 37 ppm and a median of 22 ppm. These estimates used a geotherm with a temperature of 1,340 °C at a depth of 100 km. The geotherm used by Rippe et al. (2013) had a temperature of 1,320 °C at a depth of 100 km. The MT data have good areal coverage at periods up to 1,000 s (Figure

C.2). A skin depth of 100 km at a period of 1,000 s corresponds to an average resistivity of 40 Ωm, therefore the MT data should be sensitive to the water content at this depth.
The temperature at a depth of 100 km could be as low as 1,200 °C (Hyndman et al., 2009) and as high as 1,475 °C (Canil et al., 2021), as described in Section C.3 of Appendix C. Lower temperatures would require a higher water content as conduction by H^+ is thermally activated (Gardés et al., 2014). Note that resolution is inherently limited beneath the CCRC, as shown by the synthetic inversions in Figure C.19 and Figure C**.20**. Downward smoothing of the conductor will produce a lower value of resistivity and an overestimate of the water content.

Fourier transform infrared spectroscopy measurements of water content in mantle peridotites originating above the spinel–garnet transition, around 72 km depth, beneath arc and backarc regions resulted in values of 22–90 ppm (Canil et al., 2021). Mantle water content was predicted to be less than 150 ppm above the LAB and ~300 ppm in the asthenosphere where Canadian Cordilleran lavas originated (Canil et al., 2021). The estimated water contents in Figure 5.11 are relatively low, suggesting that the mantle beneath the southern Canadian Cordillera may have a lower temperature, in better agreement with Hyndman et al. (2009).

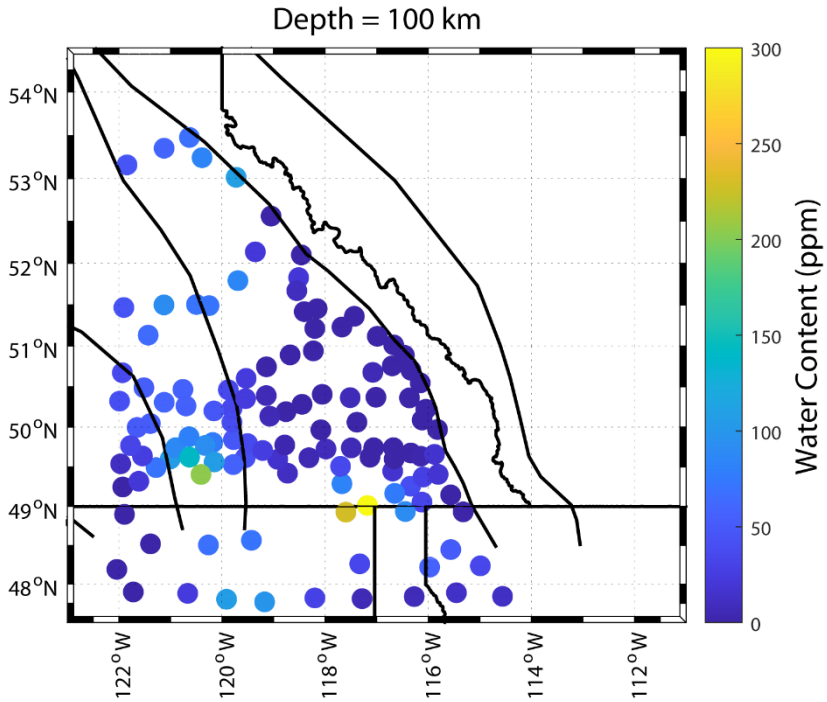

Figure 5.11*: Estimated water content of the mantle at a depth of 100 km, calculated using the results of Gardes et al. (2014) following the method of Rippe et al. (2013). The geotherm of Currie and Hyndman (2006) was used, which has a temperature of 1,340 °C at a depth of 100 km.*

5.6.5. Correlation with spatial distribution of geothermal manifestations

There are more than 40 thermal springs within the study area and the regional heat flow is significantly higher than the Canadian average. Historically, the search for geothermal resources has focused on locating reservoirs in the upper few kilometres of the crust, and one of the motivating questions of this study was whether crustal-scale resistivity features could be correlated with surface geothermal manifestations.

Fluids in geothermal systems in the southern Canadian Cordillera are believed to be primarily meteoric in origin and circulate to depths less than 5 km (Grasby & Hutcheon, 2001). It is possible that there is a connection between the deep saline fluids, interpreted to occur at depths greater than 10 km, and the surface; however, there is currently no evidence that this is the case. This type of connection is significant in geothermal exploration, as shown by Peacock and Siler (2021) who presented a conceptual model for hydrothermal systems in western Nevada. Their model had an accumulation of hot saline fluids at the BDT at a depth of ~15 km and a temperature of ~500 °C. They suggested that episodic release of these trapped fluids could transport heat to shallow geothermal systems driven by meteoric water.

To determine if there was a relationship between the distribution of thermal springs and the mid- or lower-crustal conductors, a statistical analysis was undertaken. MT gives a reliable estimate of conductance, which is the product of conductivity and thickness, measured in Siemens (S). To test for a statistical correlation, the conductance was calculated over the depth range 9.2–38 km for each model column in the area 49–53 °N and 114–120 °W, which encloses 39 thermal springs. The distribution of these values is shown in Figure C.37, along with the distribution of the model columns corresponding to the 39 thermal springs. The median conductance of all model columns in the area was 332 S, with a standard deviation of 21,800 S. The median conductance of the model columns with thermal springs was 1,090 S, with a standard deviation of 3,060 S. These values were calculated for a variety of depth ranges and there was no statistically significant correlation in any of the cases. The long-period MT data used in this study had reduced sensitivity to upper crustal resistivity, making definitive statements regarding these correlations difficult to justify.

5.7. Discussion

5.7.1. Cause of Canadian Cordilleran Regional conductor

The CCRC has been known to geophysicists for decades (Gough, 1986). Ledo and Jones (2001) reported that the southern Omineca belt had a conductive (10–46 Ωm) lower crust. The models presented in this paper have provided an improved understanding of the geometry of the CCRC. These have been combined with recent laboratory studies to investigate the cause of the low resistivity.

Laboratory experiments measuring electrical conductivity of rocks and relevant fluids have been critical to making these new interpretations. Results published over the previous decade (Section 5.5.2) have allowed detailed calculations that were not available to earlier researchers. The primary cause of low resistivity is likely interconnected saline fluids and/or conductive mineralization on grain boundaries. A small fraction of partial melt could be a cause in the lower most crust and upper most mantle, particularly in the west of the study area where temperatures are expected to be higher. However, the melt would have to be hydrous and alkali-rich, or contain a small amount of sulphide melt, to explain the low observed bulk resistivity.

The CCRC is located in the southern Omineca belt, a region that experienced crustal extension during the Eocene. The northern extent of this extension is thought to be around 52 °N. The lack of MT data at 52–53 °N in the Omineca belt prevents determination of the northern extent of the CCRC. There is also evidence of lithospheric delamination at the beginning of the Eocene, as discussed in the following section.

5.7.2. Lithospheric delamination and potassium enrichment

The bulk resistivity modelled, and temperature predicted, in the lowermost crust and uppermost mantle of the southeastern Canadian Cordillera are consistent with small fractions of alkali-rich partial melt. For this to be the case, there would need to be a source of alkali-enriched magma. To investigate this hypothesis, lithospheric delamination is considered as a possible cause of potassium enrichment.

Lithospheric delamination occurs when the lower lithosphere becomes denser than the underlying asthenosphere, detaches from the upper lithosphere, and sinks into the

asthenosphere. Upward advection of hot asthenosphere heats the lower lithosphere and it can decrease the density of the asthenosphere, both by the addition of water to and freezing of peridotite (Kay & Kay, 1993). After a critical amount of compressional shortening, the lithosphere becomes unstable and rapid delamination can occur if necessary lithospheric rheological conditions are met (Kay & Kay, 1993). Regional extension sometimes follows delamination and can result in delamination magmatism, including small volumes of shoshonitic lavas (Kay & Kay, 1993).

Shoshonite is defined as potassic basaltic trachyandesite (Le Bas et al., 1986, 1992) as illustrated in Figure C.36 using the same examples as Figure C.35. Using this classification, the samples analysed by Li et al. (2020) were latite, not shoshonite, because they were potassic trachyandesite. Prior to 1986, the term basaltic trachyandesite was not defined and such compositions were classified as trachyandesite (Le Bas et al., 1992), and the shoshonite association was not precisely defined (e.g., Joplin et al., 1972; Morrison, 1980).

Bao et al. (2014) used Rayleigh-wave tomographic and thermochronological data to argue that large-scale lithospheric delamination occurred in the southern Canadian Cordillera ~55 million years ago, creating an abrupt change in lithospheric thickness beneath the SRMT. This event was followed by regional extension and small-volume potassic magmatism in southern BC, including the rocks shown in Figure C.35 and Figure C.36 that were all dated in the range 50–53 Ma (Adams et al., 2005; Dostal et al., 2003, 2019, 2021). Delamination and subsequent potassic magmatism have also been inferred for the Sierra Nevada in eastern California 3–4 million years ago (Manley et al., 2000), the central Andes in Argentina 2–3 million years ago (Kay & Kay, 1993), and the Tibetan plateau 10–13 million years ago (Turner et al., 1993).

Metasomatism, potassium-enrichment and small-degree partial melting of subcontinental lithospheric mantle, in response to lithospheric delamination and asthenospheric advection, have been proposed to explain potassic delamination magmatism (Manley et al., 2000; Turner et al., 1993). Slab break-off, foundering of subducted lithosphere, upwelling asthenosphere and metasomatised lithospheric mantle have similarly been used to explain potassic magmatism in the Absaroka volcanic province in Wyoming (Feeley, 2003) and the northeast Aegean shoshonite belt in Greece (Pe-Piper et al., 2009). If upwelling asthenosphere and metasomatised lithospheric mantle are currently present beneath the southern Canadian

Cordillera, there may be small, non-eruptible, volumes of alkali-rich partial melt in the lower crust and uppermost mantle, causing a low bulk resistivity.

5.7.3. Red Deer conductor and Southern Alberta–British Columbia conductor

The RDC and SABC are connected in the 3-D resistivity model presented here. They have a resistivity of 1–5 Ωm, interpreted as resulting from the presence of sulphide minerals and possibly interconnected graphite films at shallow depths, that is, at temperatures less than 400 °C.

This conductor also includes the Loverna conductor, that was interpreted as graphite films or sulphides on grain boundaries, caused by enrichment of the upper mantle during north-dipping subduction (Nieuwenhuis et al., 2014). The SABC will be discussed in greater detail in a future publication presenting the resistivity model to a depth of 400 km. This future publication will also consider the transition in lithospheric structure from the Canadian Cordillera to the North American craton, which is a topic of debate and subject of contemporary research (Chen et al., 2018, 2019; DiCaprio et al., 2020; Zaporozan et al., 2018).

Chapter 6 was written as a manuscript to be submitted as the future publication mentioned above.

5.8. Conclusions

The region of low resistivity in the middle and lower crust of the southeastern Canadian Cordillera that was observed by Ledo and Jones (2001), Rippe et al. (2013) and others was modelled as a number of discrete conductors. Synthetic MT inversions suggested that a single continuous conductor was not consistent with the MT data; however, they also suggested that the exact geometry of the conductors may not have been recovered reliably. Given the coarse model mesh (5 km wide cells) and the possibility of electrical anisotropy, readers should focus on the interpretations, which were intentionally generalized, not the exact geometry of the individual conductors. These conductors were interpreted as interconnected saline fluids and/or conductive mineralization on grain boundaries. Where temperatures are high, the CCRC could also be caused by a small fraction of partial melt that either: (1) is hydrous and alkali-rich or (2) contains a small amount of sulphide melt. These interpretations were possible

because of new laboratory experiments published over the past decade, and have advanced the interpretations made in previous studies.

The Loverna conductor, described by Nieuwenhuis et al. (2014), and the SABC and Red Deer conductors, imaged by Wang (2019), were modelled as a single connected conductor. The low resistivities were interpreted as being due to interconnected sulphide mineralization. Where temperatures are relatively low, the low resistivity could also be due to interconnected graphite films on grain boundaries.

This paper presented the first regional-scale 3-D resistivity model of the southern Canadian Cordillera. It focused on the depth range from 10 to 100 km. Further research, including broadband MT data collection and a higher spatial density of data in areas of interest, is needed to relate the crustal resistivity structure to the distribution of thermal springs. Potential geographical areas for future research are (1) an area encompassing the Kuskanax batholith, southern Columbia River fault, and northern Slocan Lake fault (Figure 5.9 d and Figure C.38); and (2) an area encompassing the thermal springs along profile B–C (Figure 5.9). Furthermore, 3-D anisotropic inversion of MT data has recently become possible and can address some of the limitations of previous analyses (Kong et al., 2021; Lee, 2020). The southeastern Canadian Cordillera, particularly near the SRMT, may exhibit electrical anisotropy and future research could include a 3-D anisotropic inversion.

5.9. Acknowledgments

Funding was provided by NSERC Discovery grant RGPIN-2020–04240 to Martyn Unsworth and an award from the Future Energy Systems program at the University of Alberta. A Geoscience BC scholarship was awarded to Cedar Hanneson in 2021. The broadband MT data used in this paper were collected by Phoenix Geophysics with funding from Lithoprobe. Alan Jones undertook quality control and processed the data with funding from the Geological Survey of Canada. We thank all those involved in collecting these data. Their hard work and attention to detail resulted in a very high-quality MT data set. We also thank Theron Finley and Zoë Vestrum for providing invaluable feedback and discussions; four anonymous reviewers for their helpful comments and suggestions; Gary Egbert, Anna Kelbert and Naser Meqbel for use of ModEM; and the Digital Research Alliance of Canada (formerly Compute Canada) for access to high-performance cluster computing.

6. Lithospheric thickness and the backarc-craton lithosphere step in southwestern Canada determined from a 3-D electrical resistivity model

Hanneson, C. and Unsworth, M.J.
written as a manuscript to be submitted to
Journal of Geophysical Research: Solid Earth

6.1. Introduction

In southern British Columbia (BC), lithospheric thickness increases dramatically eastward from the northern Cascadia backarc in the southern Canadian Cordillera to the North American craton (e.g., Bao et al., 2014; Bao & Eaton, 2015; Chen et al., 2018; Zaporozan et al., 2018). It increases eastward from 60-70 km to more than 150 km over a short horizontal distance, forming a step-like geometry referred to as the backarc-craton lithosphere step (BCLS). Bao et al. (2014) described this subvertical boundary as "remarkably sharp."

Lithosphere steps are important for a number of reasons. A lithosphere step may cause a type of mantle flow called edge-driven convection, which can erode the craton edge (Hardebol et al., 2012). If a steep lithosphere step resists this type of erosion, it implies that the craton mantle lithosphere is likely dry and chemically depleted (Currie et al., 2023; Currie & van Wijk, 2016). Dry mantle lithosphere will likely have a high electrical resistivity, hence the magnetotelluric (MT) method is useful for imaging these changes in lithospheric thickness.

This study follows that of Hanneson and Unsworth (2023b) and utilized the same 3-D electrical resistivity model that was obtained from the 3-D inversion of MT data measured at 331 locations. The previous study focused on the upper 100 km of the model and investigated the crustal conductors that were imaged beneath the southern Canadian Cordillera. This study analyzed the upper 400 km of the same model in order to investigate the change in lithospheric thickness and geometry of the lithosphere step.

6.2. Background

6.2.1. Tectonic setting and geologic structure

The Juan de Fuca plate is situated offshore southwestern BC and northwestern Washington, and subducts beneath the North American plate at the Cascadia subduction zone (Figure 6.1). Several distinct terranes were added to the Laurentian margin during the Mesozoic and early Cenozoic, leading to deformation and mountain building as far east as the present-day Rocky Mountains.

East of the plate boundary, the Canadian Cordillera is an orogenic belt comprised of five morphogeological belts. From west to east, they are the Insular, Coast, Intermontane, Omineca, and Foreland belts. The southern Rocky Mountain Trench (SRMT) is located near the boundary between the Omineca and Foreland belts. The Canadian segment of the Cascade Volcanic Arc is located in the Coast belt. East of the volcanic arc, the backarc region extends to the BCLS, the location of which is a main topic of this paper. East of the Cordilleran deformation front, the Western Canada Sedimentary Basin (WCSB) extends across Alberta and into Saskatchewan (Figure 6.1 a).

Aeromagnetic data have been used by Pilkington et al. (2000) and others to delineate Precambrian basement domains beneath the WCSB and Foreland belt (Figure 6.2 a). In southwestern Alberta, three domains of the Archean Hearne province have been reported within the study area. From north to south, they are the Loverna Block (1.78-2.71 Ga), Matzhiwin High (2.59 Ga) and Vulcan Low (2.63 Ga) where the ages in parentheses are from Ross et al. (1991). South of the Hearne province, the Medicine Hat Block (2.61-3.28 Ga) straddles the Canada-U.S.A. border. Northwest of the Hearne province, there are the Lacombe Domain (not dated), Rimbey High (1.80-1.86 Ga), Thorsby Low (1.91-2.38 Ga), and Wabamun High (2.32 Ga).

The Thorsby Low is associated with the Snowbird tectonic zone, a series of linear magnetic and gravity anomalies that extend from Hudson Bay to the Canadian Cordilleran foothills (Ross, 2002). The Rimbey High has been interpreted as a magmatic arc, resulting from southeast-dipping subduction beneath the Hearne province (Ross, 2002). It has been suggested that the Wabamun High is a tectonic escape wedge, resulting from transpression along the Snowbird tectonic zone (Ross et al., 1991). The Vulcan Low has been interpreted as the axial zone of a continental collisional belt, between the Loverna Block and Medicine Hat Block (Eaton et al., 1999). Eaton et al. (1999) interpreted the Matzhiwin High as belonging to the Loverna Block and Vulcan Low, not a separate domain. To the south, the Great Falls

tectonic zone separates the Medicine Hat Block from the Wyoming craton in the U.S.A. (Ross et al., 1991).

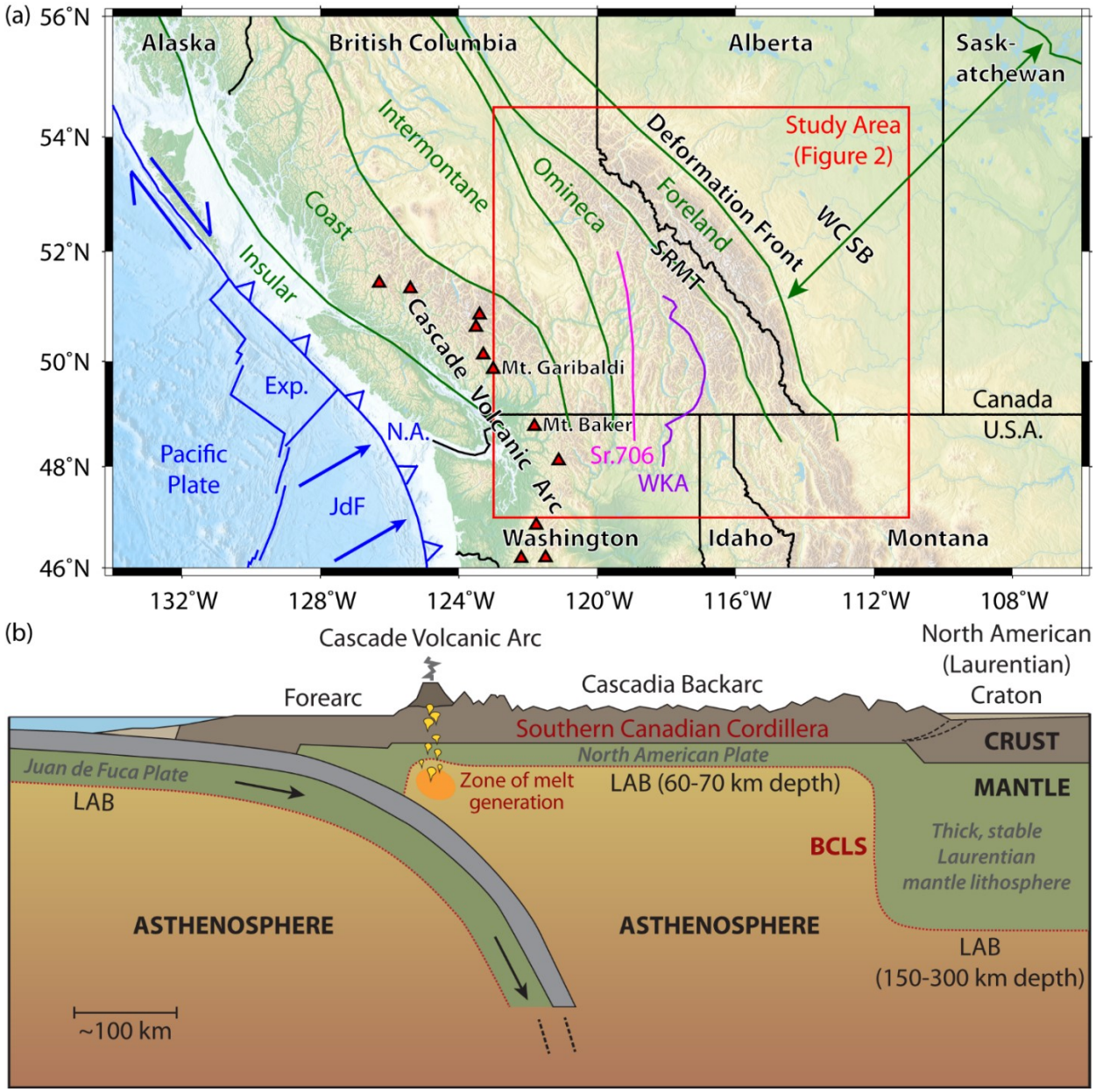

Figure 6.1*: (a) Map of southwestern Canada and northwestern U.S.A. Political boundaries (black lines), morphogeological boundaries (green lines), tectonic plate boundaries (blue lines), and volcanoes (triangles) are shown. The pink line labelled Sr.706 is the approximate location of the $^{87}Sr/^{86}Sr = 0.706$ isopleth. The purple line labelled WKA is the western boundary of the Kootenay Arc (Archibald et al., 1983). The red box indicates the location of Figure 6.2. Exp. = Explorer plate, JdF = Juan de Fuca plate, N.A. = North American plate, SRMT = southern Rocky Mountain Trench, and WCSB = Western Canada Sedimentary Basin. (b) Schematic cross-section of southwestern Canada, modified from Hyndman et al. (2005). LAB = lithosphere-asthenosphere boundary and BCLS = backarc-craton lithosphere step. The mantle lithosphere below the Cordillera (labelled North American plate) includes both Laurentian and Cordilleran lithosphere. The exact location and geometry (including faulting and deformation) of the mantle lithosphere transition west of the BCLS is uncertain.*

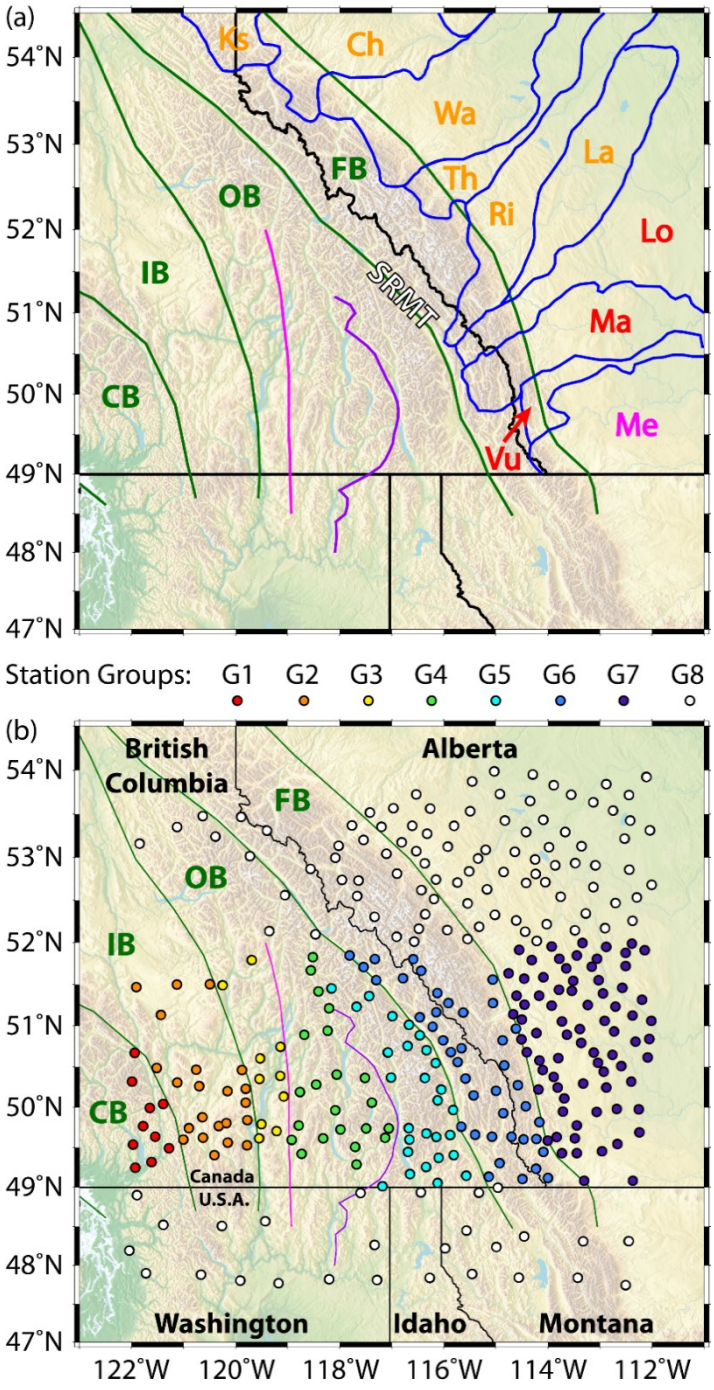

***Figure 6.2**: The study area designated in Figure 6.1. CB = Coast belt, IB = Intermontane belt, OB = Omineca belt, and FB = Foreland belt. (a) Blue lines delineate Precambrian basement domains (Pilkington et al., 2000). The Medicine Hat Block is labelled in pink, domains of the Hearne province are labelled in red, and other domains are labelled in orange. From northwest to southeast, they are: Ks = Ksituan, Ch = Chinchaga, Wa = Wabamun, Th = Thorsby, Ri = Rimbey, La = Lacombe, Lo = Loverna, Ma = Matzhiwin, Vu = Vulcan, and Me = Medicine Hat. (b) MT stations (dots) used in the 3-D inversion to create the resistivity model, colour coded by geographic group. G1 (red): CB at 49-52 °N. G2 (orange): IB at 49-52 °N. G3 (yellow): OB at 49-52 °N west of the Sr isopleth. G4 (green): OB at 49-52 °N east of the Sr isopleth and west of the Kootenay Arc. G5 (cyan): OB at 49-52 °N east of the western boundary of the Kootenay Arc. G6 (blue): FB at 49-52 °N. G7 (purple) 49-52 °N east of the FB. G8 (white): south of 49 °N or north of 52 °N.*

In the southeastern Canadian Cordillera, the Foreland belt contains three major east-verging thrust systems with thin-skinned geometry. From west to east, they are: (1) Lewis-Bourgeau, (2) McConnell, and (3) Foothills. They root into the Rocky Mountain basal décollement and accommodated ~180 km of shortening among them: (1) ~100 km, (2) ~50 km, and (3) ~30 km (Simony & Carr, 2011). The Rocky Mountain basal décollement extends westward past the SRMT, then continues as the Monashee décollement past the Kootenay Arc (Simony & Carr, 2011). Caution should be employed when correlating shallow features with deeper structures, as discussed in Section 6.2.3.

6.2.2. Lithospheric thickness

The lithosphere-asthenosphere boundary (LAB) is a rheological boundary layer between the rigid lithosphere above and the mechanically weak asthenosphere below (Rychert et al., 2020). The rigid lithosphere of the Earth is divided into a number of tectonic plates. A typical oceanic plate has a lithospheric thickness of approximately 60-80 km and a typical continental plate has a lithospheric thickness of approximately 200-250 km (Gung et al., 2003). This estimate of typical continental lithospheric thickness may be high. Long-lived, stable cratons are approximately 150-250 km thick (Pearson et al., 2021).

The LAB is traditionally defined thermally, as the intersection of the lithosphere geotherm and the mantle adiabat (Rychert et al., 2020). The LAB is not a sharp transition and has a finite thickness that can vary from less than 20 km for wet mantle to more than 50 km for dry mantle (Eaton et al., 2009). For the purposes of this study, the LAB is considered a thin layer at a single depth.

A range of datasets can be used to infer the depth of the LAB including seismic velocity, seismic anisotropy, electrical resistivity, heat flow, and xenolith composition (Rychert et al., 2020). Geophysical imaging is a common method of imaging the LAB and different techniques can be used, sometimes giving differing answers.

In seismic studies, the LAB is detected as a decrease in seismic velocity, at the base of a high-velocity layer, and sometimes by an abrupt change in seismic anisotropy (Eaton et al., 2009). At the base of the lithosphere, shear wave velocity typically decreases by 7-9% over a depth interval of 14-52 km in continental settings, and 4-15% over 0-22 km in oceanic settings (Rychert et al., 2020). There are two classes of seismic anisotropy: (1) radial anisotropy, which is a difference between horizontal wave speed and vertical wave speed, and (2)

azimuthal anisotropy, which is a difference in wave speed with azimuth. At the base of the lithosphere, there may be an increase in radial anisotropy with the horizontal shear wave speed being greater than the vertical shear wave speed, or a change in azimuthal anisotropy with the fast direction changing from a fossil direction to one aligned with present-day absolute plate motion (Eaton et al., 2009; Rychert et al., 2020).

In magnetotelluric studies, the LAB is detected as a decrease in electrical resistivity, occurring around 50-400 km depth in continental settings (Rychert et al., 2020). One of the main objectives of this study is to improve knowledge of the electrical LAB beneath the southern Canadian Cordillera and adjacent craton.

The lithosphere is 60-70 km thick in the Cascadia backarc of southern BC, based on geophysical observations including surface heat flow and seismic tomography (Currie et al., 2023). In southwestern Alberta, lithospheric thickness varies from ~170 km to more than 230 km, based on an S-wave velocity model (Bao & Eaton, 2015). Chen et al. (2017) used the maximum negative velocity gradient of their P-wave velocity model, accounting for vertical smearing, to estimate the lithospheric thickness of the Medicine Hat Block (~190 km), Lacombe Domain (~200 km), and southern Hearne province in between (~330 km).

A 3-D resistivity model imaged the electrical LAB at a depth of ~250 km beneath the Medicine Hat Block (Nieuwenhuis et al., 2014). This is considerably deeper than the reported seismic LAB at a depth of ~190 km (Chen et al., 2017). However, a more recent 3-D resistivity model imaged the electrical LAB at a depth of 150-180 km beneath the Medicine Hat Block (Wang & Unsworth, 2022). Nieuwenhuis et al. (2014) and Wang and Unsworth (2022) estimated the location of the LAB using a 100 Ωm contour because it tended to agree with synthetic inversion results and seismic tomography results in Alberta.

6.2.3. Proposed locations of the backarc-craton lithosphere step (BCLS)

The change in lithospheric thickness is believed to occur over a short horizontal distance (Bao et al., 2014); however, the exact location of the BCLS is still debated. Three possible locations have been suggested: (1) the $^{87}Sr/^{86}Sr$ = 0.706 isopleth, (2) the western boundary of the Kootenay Arc, and (3) the SRMT. The first two were originally suggested based on geological considerations, and the third was based on geophysical considerations. At this point, it is important to recognize a fundamental limitation in linking lithospheric structure with surface geology. Mountain building can result in significant horizontal crustal motion, resulting in

features being offset. In the study area, the lithosphere step marks the edge of the Laurentian craton at depth, to which terranes were accreted. At the surface, however, a fold-and-thrust belt overlies the western margin of Laurentia. Crustal deformation during the Laramide and other orogenies has moved the crust to the east. Hence, the Cordilleran deformation front is east of all three suggested locations of the lithosphere step. There has also been significant vertical displacement in some areas; for example, the Monashee décollement was down thrown approximately 20 km (Simony & Carr, 2011).

Granitic rocks with an initial Sr^{87}/Sr^{86} ratio of 0.706 approximate the location of the boundary between shallow marine sedimentary rocks and deep marine sedimentary rocks, deposited along the Laurentian passive continental margin (Kistler & Peterman, 1973). In western Idaho, this ratio changes abruptly across a boundary with ~0.706 or greater to the east and ~0.704 or less to the west, marking the boundary between Precambrian crust and Phanerozoic marine sedimentary rocks (Armstrong et al., 1977). A ratio of 0.706 or greater generally infers that igneous rocks are underlain by Precambrian basement; however, the Sr^{87}/Sr^{86} = 0.706 isopleth may be spatially and temporally variable, and may not correspond universally to the edge of the continental basement (Ross, 1991). In the southern Canadian Cordillera, the 0.706 isopleth is subparallel to lower Paleozoic passive continental margin facies boundaries, suggesting a correlation between the edge of the continental crust and the edge of the rifted shelf (Ross, 1991).

Archibald et al. (1983) claimed that the Kootenay Arc marks the transition from ancestral North America to accreted terranes, where the continental margin wedge was displaced and stacked on the craton margin. Examination of detrital zircons provided evidence that eugeoclinal strata of the Kootenay Arc have a North American affinity (Ross, 1991, and references therein). The western boundary of the Kootenay Arc (WKA) is located in the region 48.0-51.2 °N and 116.9-118.1 °W (purple line in Figure 6.1). Palinspastic restoration provided an estimate of the location of the platform margin of western Laurentia, and this restored hinge line was located east of the strontium isopleth and west of the SRMT, placing it near the WKA (DiCaprio et al., 2020, and references therein).

Seismic geophysical methods have been used to infer a lithosphere step near the SRMT (Bao et al., 2014; Bao & Eaton, 2015; Chen et al., 2018; Zaporozan et al., 2018). The results of these studies are summarized in the following section.

The top of the BCLS is 60-70 km below the surface of the Earth; however, the three suggested locations are all based on upper-crustal geological features. The strontium isopleth, Kootenay Arc, and SRMT at the surface will not necessarily be correlated with mantle features at the depths associated with the BCLS. Recall that basal décollements underlie much of the southern Omineca and Foreland belts, and they accommodated ~180 km of shortening (Section 6.2.1). There may also be a wedge of Laurentian crust in the lithosphere beneath the southern Omineca belt (Colpron et al., 1998; Price, 1986).

6.2.4. Geophysical studies capable of imaging the backarc-craton lithosphere step

Geophysical imaging is needed to determine the location of the BCLS since it is located deep underground. Seismic methods and the MT method are best suited to this task because they are capable of imaging the upper 400 km of the Earth. Heat flow measurements can be used to estimate the depth at which the lithosphere geotherm intersects the mantle adiabat (i.e., the LAB) provided that radiogenic heat production is accounted for (Rychert et al., 2020). This is often achieved by using xenolith data as a calibration (Rychert et al., 2020).

6.2.4.1. Seismic studies

Recall that seismic methods can be used to image the LAB as a decrease in seismic velocity or a change in seismic anisotropic properties (Eaton et al., 2009; Rychert et al., 2020). For example, this can be seen as a decrease in shear wave velocity (7-9% in continental settings), an increase in radial anisotropy (horizontal shear wave speed > vertical shear wave speed), or a change in azimuthal anisotropy with the fast direction becoming aligned with present-day absolute plate motion (Eaton et al., 2009; Rychert et al., 2020).

A shear-wave velocity model from Rayleigh-wave tomography imaged an abrupt craton edge, with low velocities beneath the Cordillera and high velocities within the craton, and this change occurred near the SRMT (Bao & Eaton, 2015). Low Rayleigh-wave phase velocities have been observed beneath the Cordillera, with the edge of the low-velocity region occurring near the SRMT (Zaporozan et al., 2018). Inversion of Rayleigh-wave dispersion curves resulted in a shear wave velocity model with a sharp boundary dipping approximately 30° to the southwest (Zaporozan et al., 2018).

Finite-frequency seismic tomography was used to define a sharp seismic boundary near the SRMT, with both P and S wave velocities increasing eastward (Chen et al., 2018). Chen et al.

(2018) showed a steeply westward dipping BCLS near the SRMT in southeastern BC. Chen et al. (2019) argued that the collisional model of North American Cordillera formation (Johnston, 2008) is more compatible with these seismic observations, from the southern Canadian Cordillera, than is the more-popular accretionary model (Monger et al., 1982). Bao et al. (2014) showed a sharp vertical craton edge beneath the SRMT in their shear-wave velocity model. They also imaged a high-velocity layer beneath the Cordillera below ~150 km depth and interpreted it as delaminated lithosphere. The presence of a detached lithospheric block would support the accretionary hypothesis (Chen et al., 2019).

The shear-wave tomography model of Schaeffer and Lebedev (2014) was used to infer a lithospheric mantle keel at 120-200 km depth extending westward to ~118 °W at ~49.0 °N and ~116 °W at ~48.4 °N (DiCaprio et al., 2020). For comparison, the WKA is located near 117.5 °W at 49.0 °N and near 118.1 °W at 48.4 °N.

6.2.4.2. Magnetotelluric and magnetovariational studies

Recall that the MT method can be used to image the LAB as a decrease in electrical resistivity with depth, typically observed in the depth range 50-400 km below the surface in continental settings (Rychert et al., 2020). A number of prior studies have used the MT method to investigate the North American Cordillera and the adjacent North American craton, with horizontal model resolution ranging from 5 km to 30 km (Table D.2). An overview of the MT method was presented by Hanneson and Unsworth (2023b), and detailed descriptions of the method were given by Simpson and Bahr (2005) and Chave and Jones (2012).

6.2.4.2.1 Previous 3-D MT studies in southwestern Canada

Nieuwenhuis et al. (2014) presented a 3-D resistivity model of southern Alberta, then Wang and Unsworth (2022) built on this research by presenting a 3-D resistivity model of the entire province of Alberta. Nieuwenhuis et al. (2014) tentatively suggested a lithospheric thickness of ~250 km in southern Alberta. Wang and Unsworth (2022) subsequently inferred a lithospheric thickness of 150-180 km in southern Alberta, and 200-300 km in central Alberta. These two studies extended westward to 115 °W and 120 °W, respectively, and neither investigated the lithosphere step in detail.

The 3-D resistivity model presented in Section 6.4 extends to a maximum depth of 400 km and was presented to a depth of 100 km by Hanneson and Unsworth (2023b). This study

extended westward to 122 °W, ~140 km farther west than the study of Wang and Unsworth (2022). Hanneson and Unsworth (2023b) focused on the structure of the crust and uppermost mantle, whereas the current study is concerned with imaging the electrical LAB and the BCLS.

6.2.4.2.2 Previous 3-D MT studies in the northwestern U.S.A.

Similar studies have taken place in the U.S.A. highlighting the ability of the MT method to image up to 400 km below the surface with long-period data. Patro and Egbert (2008) presented a 3-D resistivity model of the northwestern U.S.A. from inversion of EarthScope USArray MT data collected in 2006 and 2007. Then, Bedrosian and Feucht (2014) and Meqbel et al. (2014) utilized EarthScope USArray MT data collected in 2006-2011, and presented 3-D resistivity models extending farther south and farther east than that of Patro and Egbert (2008). Yang et al. (2021) presented a 3-D resistivity model from inversion of EarthScope USArray MT data collected in 2006-2018, covering much of the continental U.S.A. Recently, Munch and Grayver (2023) presented a 3-D resistivity model in spherical coordinates from inversion of EarthScope USArray MT data, covering ~80% of the contiguous United States.

6.2.4.2.3 The Southern Alberta British Columbia conductor

There is a low-resistivity anomaly that strikes northeast-southwest across southern Alberta and southeastern BC. It was detected in the 1970s by magnetovariation studies, then named the Southern Alberta British Columbia conductor (SABC) by Gough (1986) and shown to extend from around 53 °N and 111 °W, beneath the WCSB, to around 49 °N and 116 °W, east of the Kootenay Arc. Wang (1988) inverted magnetovariation field data, concluding that the SABC is caused by a channelled current in a narrow conductor (~80 km wide) surrounded by highly resistive rocks. The SABC is discussed further in Section 6.5.2.

6.2.4.3. Geodynamic modeling

Insights into dynamic processes that could be occurring beneath the southern Canadian Cordillera have been made possible by geodynamic models (Currie et al., 2023; Currie & van Wijk, 2016; Hardebol et al., 2012). Some key findings of these studies are summarized below and illustrate the importance of improving the understanding of lithosphere steps.

Edge-driven convection may have eroded a low-viscosity wet upper mantle beneath the Canadian Cordillera, migrating the lithosphere step cratonward (eastward) until it

encountered a high-viscosity dry upper mantle to resist erosion (Hardebol et al., 2012). The height of the vertical step influences the amount of edge-driven convection and a larger step increases the tendency of cratonward migration (Hardebol et al., 2012). A steep lithosphere step (dip > 45°) is only stable if the craton is significantly stronger (5-50 times) than a damp olivine reference material, and the geometry of the BCLS in southwestern Canada has been inferred to be at least 50-100 million years old (Currie & van Wijk, 2016). Maintenance of a subvertical lithosphere step for more than 50 million years requires a dry and moderately chemically depleted lowermost craton mantle lithosphere (Currie et al., 2023).

6.2.4.4. Motivation for the current study

To better understand the geoelectric structure of the southern Canadian Cordillera and adjacent craton, a regional-scale 3-D resistivity model was needed. A model extending westward from those of Nieuwenhuis et al. (2014) and Wang and Unsworth (2022), and northward from that of Meqbel et al. (2014), was required to answer the questions that motivated the current study. They are: (1) What is the depth of the electrical LAB within the study area? (2) How does it vary between the backarc region and the adjacent craton, i.e., in the east-west direction? (3) How does it vary within the craton, i.e., in the north-south direction?

6.3. Magnetotelluric data and 3-D resistivity model

6.3.1. Magnetotelluric data, inversion parameters, and data misfit

The MT dataset used in this study was comprised of data collected at 331 locations by various groups: 180 by University of Alberta researchers, 110 as part of the Lithoprobe program, 22 by the EarthScope USArray program, and 19 from other studies. The details of these 331 MT sites are listed in Table D.1 and their locations are shown in panel (b) of Figure 6.2.

Impedance data at 18 periods, logarithmically spaced in the range 1–18,000 s, and tipper data at 16 periods, logarithmically spaced in the range 1–5,500 s (Figure D.1 a), were jointly inverted using ModEM (Kelbert et al., 2014). Model smoothing was applied by using a model covariance length scale of 0.5 in the horizontal directions and 0.3 in the vertical direction. The inversion started with a regularization parameter of 1 and an R.M.S. misfit of 15.8. The preferred resistivity model is from iteration 313 with a regularization parameter of 0.001 and

an R.M.S. misfit of 2.08. Additional details of the inversion procedure were given by Hanneson and Unsworth (2023b).

The R.M.S. misfit in map view is shown at four periods in Figure 6.3. At the shorter periods (10–1,000 s), the misfit is lower (1.68–1.96). At the longer period (10,000 s), the misfit is higher (3.03). Fewer sites have data at longer periods, a fact that is seen clearly in panel (d) of Figure 6.3. Of the 331 MT sites used, 313, 314, 283 and 215 had data at 10 s, 100 s, 1,000 s and 10,000 s, respectively (Figure D.1 a).

To advance the results of Hanneson and Unsworth (2023b) for the purposes of this study, the MT sites were divided into eight groups based on geography. They are named G1-G8 in Table D.1 and colour coded in panel (b) of Figure 6.2. The MT method utilizes diffusive physics and MT inversions are usually designed to create smooth resistivity models. Also, there is better model sensitivity below the MT stations, and the poorest sensitivity in regions with limited MT data. Dividing the study area into geographic regions allowed averaging in an attempt to mitigate these concerns by analyzing the 3-D resistivity model beneath the MT stations in each of the groups.

6.3.2. Description of the 3-D resistivity model

Hanneson and Unsworth (2023b) described the upper 100 km of the resistivity model in detail. This section provides further description of the same model, as relevant to this study. Horizontal slices of the 3-D resistivity model are shown in Figure 6.4. The Canadian Cordilleran Regional conductor is located in the depth range 15-55 km beneath the southern Omineca belt (Hanneson & Unsworth, 2023b) and between the vertical projections of the strontium isopleth and SRMT (Figure 6.4 a). The SABC extends from the eastern side of the study area, in a southwesterly direction, to the BC-Idaho border and the vertical projection of the WKA (Figure 6.4 a).

The depth range 100-120 km is certainly below the LAB in the backarc region and above the LAB in the adjacent craton, i.e., a depth at which one would expect to see the lithosphere step. At these depths, there is a strong resistivity gradient from west to east around 119 °W (Figure 6.4 d). This boundary, from light blue to dark blue, has a resistivity of approximately 100 Ωm, a value often associated with the LAB in resistivity models (e.g., Nieuwenhuis et al., 2014; Wang & Unsworth, 2022). Deeper in the resistivity model, there is a strong contrast

east of 119°W between high resistivity in the north and low resistivity in the south (Figure 6.4 e-f), implying a cratonic root that thickens to the north.

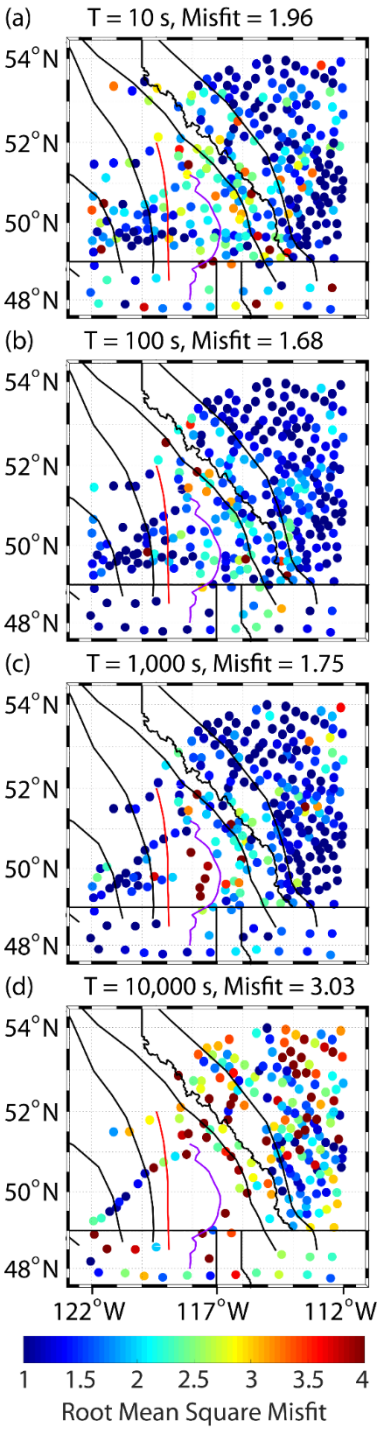

***Figure 6.3**: R.M.S. misfit in map view at four periods. (a) 313/331 MT sites had data at a period of 10 s. (b) 314/331 MT sites had data at a period of 100 s. (c) 283/331 MT sites had data at a period of 1,000 s. (d) 215/331 MT sites had data at a period of 10,000 s.*

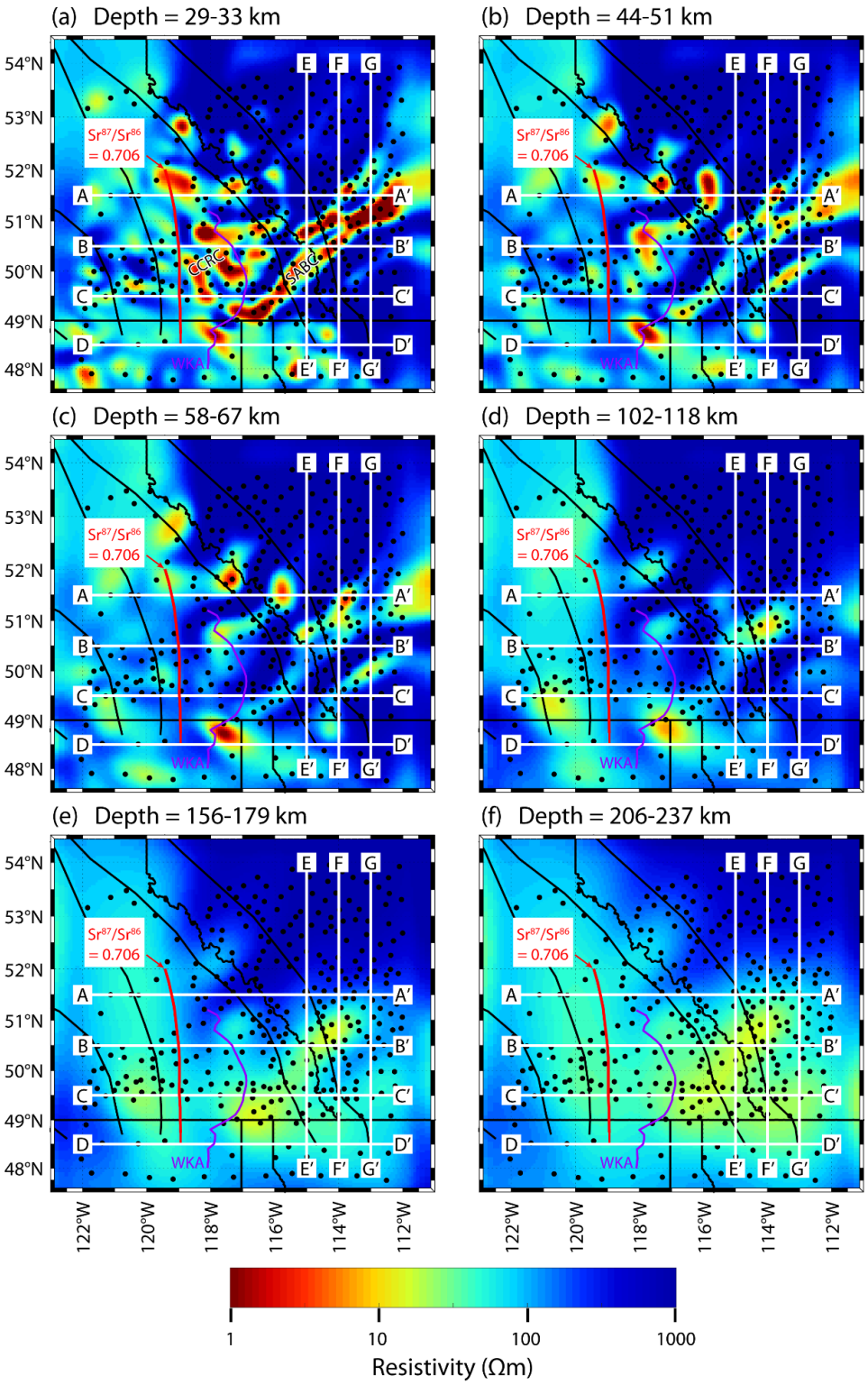

***Figure 6.4**: Six horizontal slices of the 3-D resistivity model. Black lines are political and morphogeological boundaries. The red line is the approximate location of the $^{87}Sr/^{86}Sr = 0.706$ isopleth. The purple line is the western boundary of the Kootenay Arc. Black dots are MT data locations. White lines labelled A-D and E-G indicate the locations of the cross-sections shown in Figure 6.5 and Figure 6.6, respectively. CCRC = Canadian Cordilleran Regional conductor and SABC = Southern Alberta British Columbia conductor.*

Vertical slices of the 3-D resistivity model, plotted from west to east, are shown in Figure 6.5. The base of the cratonic lithosphere is approximated by a horizontal dashed line at a resistivity of ~100 Ωm. At 48.5 °N and 49.5 °N, this boundary is at a depth around 150 km. At 50.5 °N, it is around 170 km, and at 51.5 °N, it is around 220 km, further implying a cratonic root that thickens to the north.

The electrical LAB is less well defined beneath the backarc. Figure 6.5 includes horizontal dashed lines at 65 km depth, based on the estimation of Currie et al. (2023). The two southern cross-sections (Figure 6.5 c-d) also include the top of the subducting Juan de Fuca plate (white lines) estimated from Meqbel et al. (2014) and McCrory et al. (2012). The lithosphere step is difficult to define in these resistivity cross-sections, but it appears to be subvertical and near the vertical projection of the strontium isopleth. Its approximate location is labelled BCLS in Figure 6.5.

Vertical slices of the 3-D resistivity model, plotted from north to south, are shown in Figure 6.6. The LAB is again approximated by dashed lines at a resistivity of ~100 Ωm. In the southern half of the cross-sections, from 48 °N to ~51 °N, this boundary is subhorizontal and occurs at a depth around 150 km. North of ~51 °N, the boundary dips to the north at an angle of 35-45° and extends to the base of the cross-sections at a depth of 400 km.

6.3.3. Sensitivity tests and resolution tests

At longitudes of 114 °W and 115 °W, there is a region of low resistivity between the asthenosphere and the SABC (Figure 6.6 a-b). The MT method is most sensitive to the top of a conductor and its conductance, which is the product of conductivity and thickness. It is less sensitive to the bottom of a conductor and low resistivity regions are sometimes smeared downward in resistivity models. This section addresses the limitations of the resistivity modelling procedure.

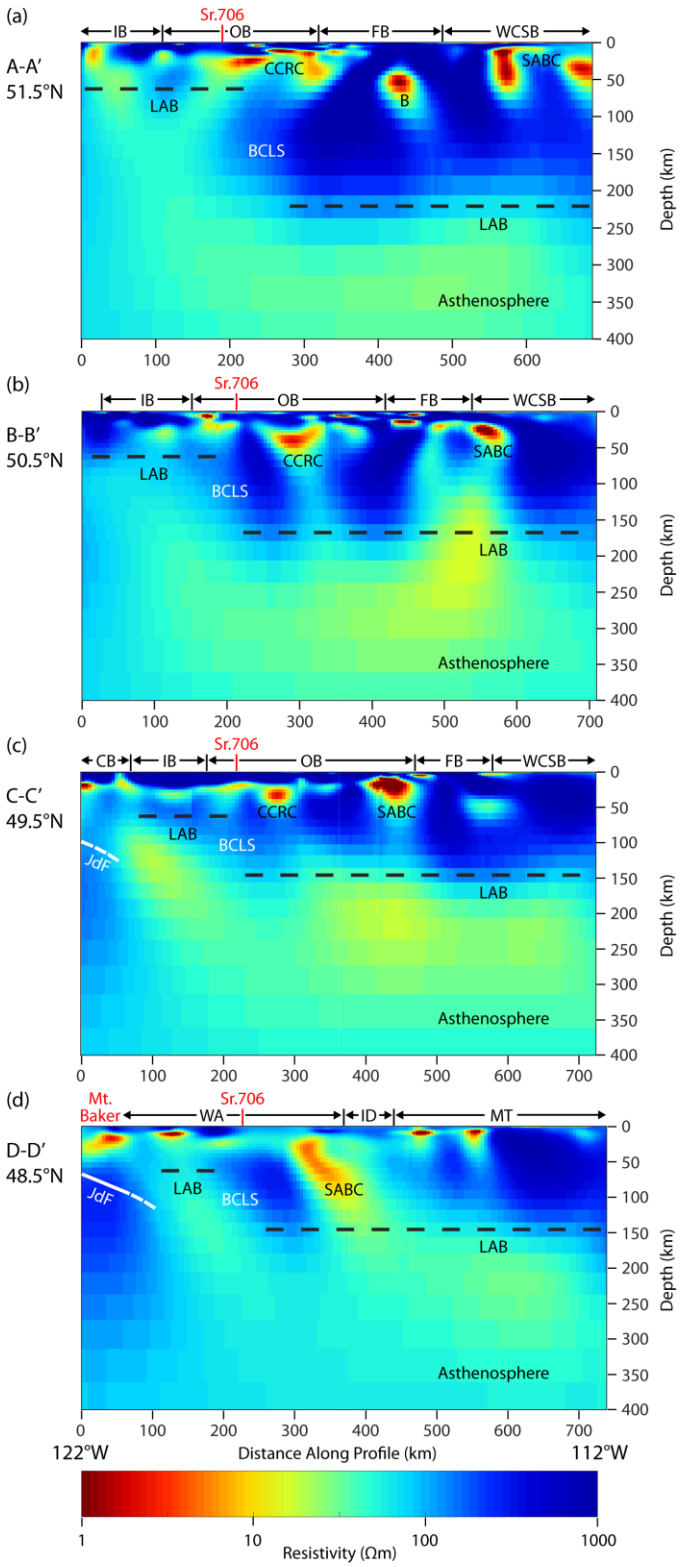

Figure 6.5*: Cross-sections from the 3-D resistivity model, at the locations shown in Figure 6.4. CB = Coast belt, IB = Intermontane belt, OB = Omineca belt, FB = Foreland belt, WCSB = Western Canada Sedimentary Basin, WA = Washington, ID = Idaho, MT = Montana, CCRC = Canadian Cordilleran Regional conductor, B = Banff conductor, SABC = Southern Alberta British Columbia conductor, LAB = lithosphere-asthenosphere boundary, and BCLS = backarc-craton lithosphere step.*

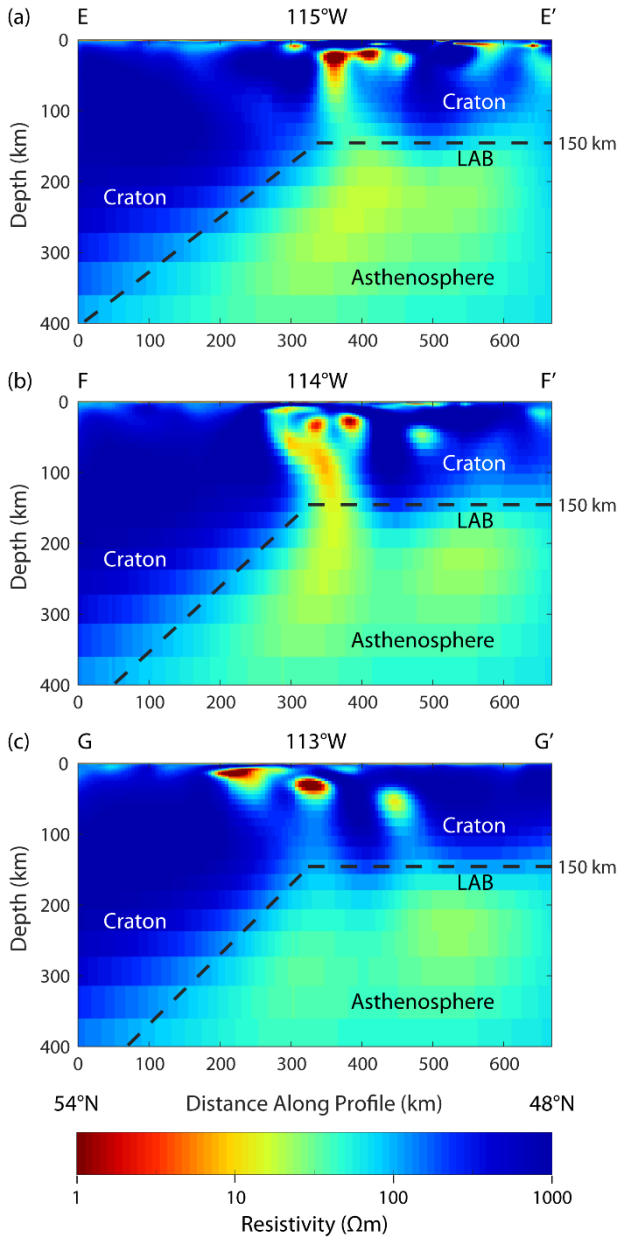

***Figure 6.6**: Cross-sections from the 3-D resistivity model, at the locations shown in Figure 6.4. The black dashed lines indicate the approximate location of the lithosphere-asthenosphere boundary (LAB), based on a resistivity of 100 Ωm.*

6.3.3.1. Model editing to investigate the depth of resolution

The results of sensitivity tests are presented in Section D.2 of Appendix D and summarized here. The resistivity model was edited to be 1 Ωm below a certain depth, ranging from 51 km to 477 km (Table D.3), then the forward response was computed and the change in R.M.S. misfit was calculated. The change in the residuals was then assessed statistically and Kolmogorov-Smirnov (KS) tests were used to infer that the MT dataset was insensitive to

resistivity variations below a depth of 415 km. Hence, the resistivity model was presented to a maximum depth of 400 km.

Due to attenuation of EM signals in conductive media, the MT dataset had sensitivity to greater depths in regions of high resistivity than regions of low resistivity. The skin depth in a 35 Ωm halfspace is 400 km at the longest period in the dataset. In regions where the average resistivity is greater than 35 Ωm, the skin depth at the longest period will be greater than 400 km. However, in regions where the average resistivity is less than 35 Ωm, the skin depth at the longest period will be less than 400 km. This is illustrated in panel (b) of Figure D.1.

Conductance is the product of electrical conductivity and length, measured in Siemens (S), and the MT method is particularly sensitive to this quantity. The conductance of the preferred resistivity model, calculated for three depth ranges, is shown in Figure D.2. The average resistivity is calculated as the depth interval (thickness) divided by the conductance. This is a depth-averaged quantity, not a volume-averaged quantity, but it still provides a useful reference.

In Figure D.2, regions coloured blue or white indicate high sensitivity of the MT dataset at those depths, except where there are no MT stations present. Regions coloured red indicate lower sensitivity of the MT dataset at those depths. The MT data were sensitive to resistivity variations in the upper 200 km across most of the study area. At greater depths, up to 400 km, there was lower sensitivity below the SABC and parts of southeastern BC (Figure D.2 c).

6.3.3.2. Synthetic inversions

To further investigate sensitivity of the MT dataset to resistivity variations in the upper 400 km, fourteen simplified 3-D resistivity models were created (Table D.4 and Figure D.3-Figure D**.16**) and three are shown in Figure 6.7. Synthetic MT data were generated by performing forward calculations, then normally distributed noise was added to the impedance and tipper data. Sensitivity to the electrical LAB and BCLS was investigated using 3-D inversion of these synthetic data.

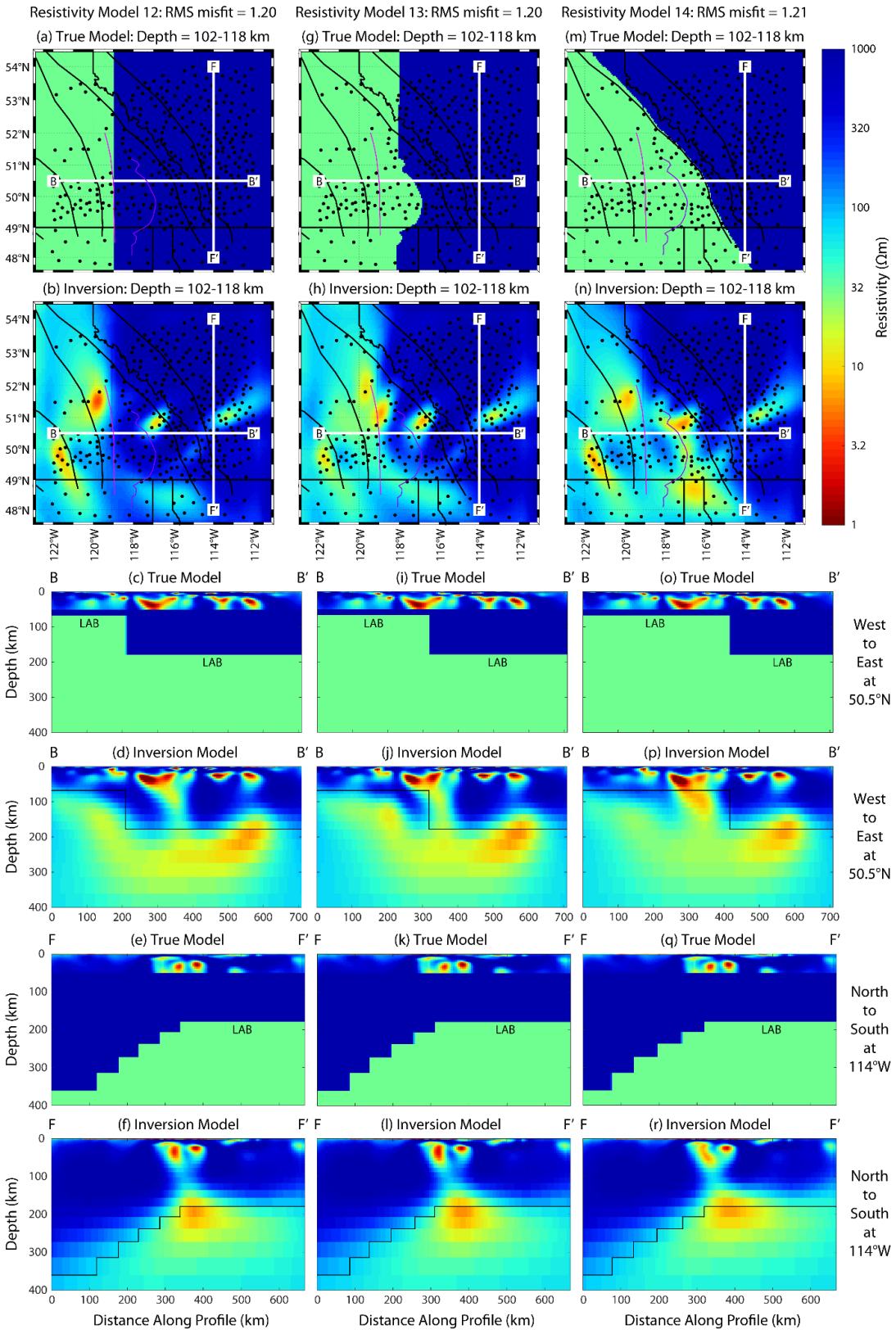

Figure 6.7*: Model slices from three of the synthetic inversions (Table D.4 and Figure D.3-Figure D**.16**) representing the lithosphere-asthenosphere boundary (LAB). (a-f) BCLS near the strontium isopleth. (g-l) BCLS near the WKA. (m-r) BCLS near the SRMT.*

The LAB was placed at various depths, including a model with a north-dipping LAB geometry beneath the WCSB. The three locations discussed in Section 6.2.4 were used as locations of the BCLS. The upper 50 km of these models were either simple (polygons) or complex (the resistivity model from actual 3-D inversion of the measured MT data). Accounting for the error floor, the R.M.S. misfit was in the range 0.966-0.986 for the simple models and 1.20-1.24 for the complex models (Table D.4). Several conclusions can be made by viewing Figure D.3-Figure D**.16**, as discussed in the following paragraphs.

When the lithosphere is resistive (1000 Ωm), the LAB depth is recovered very well. The minimum resistivity is located at the true LAB location, but low resistivity is also observed in one or two model layers (8-67 km) above the true LAB. When the vertical BCLS is shorter (121 km), it is recovered fairly well as a subvertical boundary. When the vertical BCLS is taller (215 km), it is typically recovered as convex toward the craton, with the upper corner occurring near its true position.
When conductors are placed in the upper lithosphere, they are recovered very well, but they are sometimes connected to the LAB by a zone of moderate-to-low resistivity. When the upper lithospheric structure is complex, the BCLS is sometimes recovered poorly or shifted away from the craton. The north-dipping LAB was recovered very well by the inversion. These results were taken into consideration when developing the interpretations and discussion in the following sections.

6.4. Analysis and interpretation

Detailed analysis of the 3-D resistivity model of Hanneson and Unsworth (2023b) was undertaken with the goal of creating a conceptual model of the electrical LAB and BCLS in southwestern Canada. This required interpretation of not only the preferred resistivity model, but also the sensitivity results and comparisons with other geophysical studies.

6.4.1. Average resistivity

The conductance of the preferred resistivity model was calculated beneath the MT station locations over four depth ranges: (1) 0-75 km, (2) 75-150 km, (3) 150-250 km, and (4) 250-400 km. The average conductance was calculated for seven groups of MT stations (coloured dots in Figure 6.2 b) for each of the depth ranges. The depth interval (thickness) was divided by the average conductance to give an average resistivity for each of the 28 sets. The resistivity range of each set is given in Table D.5, along with the average values.

Resistivity profiles beneath each of the seven groups of MT stations are shown in Figure 6.8 and LAB depth ranges are estimated. These LAB depths are shown in panel (a) of Figure 6.9, along with additional LAB depth estimates (Figure 6.9 b) that will be discussed in Section 6.4.3. The average resistivity values (Table D.5) are shown graphically as a cross-section in panel (d) of Figure 6.9. The LAB depth was not estimated for group G1 because the Coast belt, where subduction processes have created a volcanic arc, is beyond the scope of this study. Other studies have used magnetotellurics to study volcanoes in the Coast belt (Hanneson & Unsworth, 2023a; Jones & Dumas, 1993).

The depth range 75-150 km is expected to be below the LAB in the backarc region and above the LAB in the adjacent craton, i.e., where one would expect to see the BCLS. For this reason, it was recently used as a depth range of investigation in another geophysical study in southwestern Canada (Yu et al., 2022). In the latitude range 49-52°N, there is an eastward increase in average resistivity around 119°W, from 78 Ωm to 127 Ωm, in this depth range (Figure 6.9). This agrees with the qualitative description given in Section 6.4.2 and is suggestive of a BCLS near the vertical projection of the strontium isopleth.

Resistivity profiles for synthetic inversion 13 (Figure 6.7) are shown in Figure D.17, for comparison with Figure 6.8, and the corresponding plots are similar. The true LAB depth was recovered by using the 100 Ωm range for groups G1-G3 and G6-G7. In synthetic model 13, the true BCLS location is in between G4 and G5. The inversion overestimated the LAB depth for G4 and underestimated the LAB depth for G5. This further illustrates the point made in Section 6.3.3.2 that the BCLS is sometimes shifted away from the craton in inversion models.

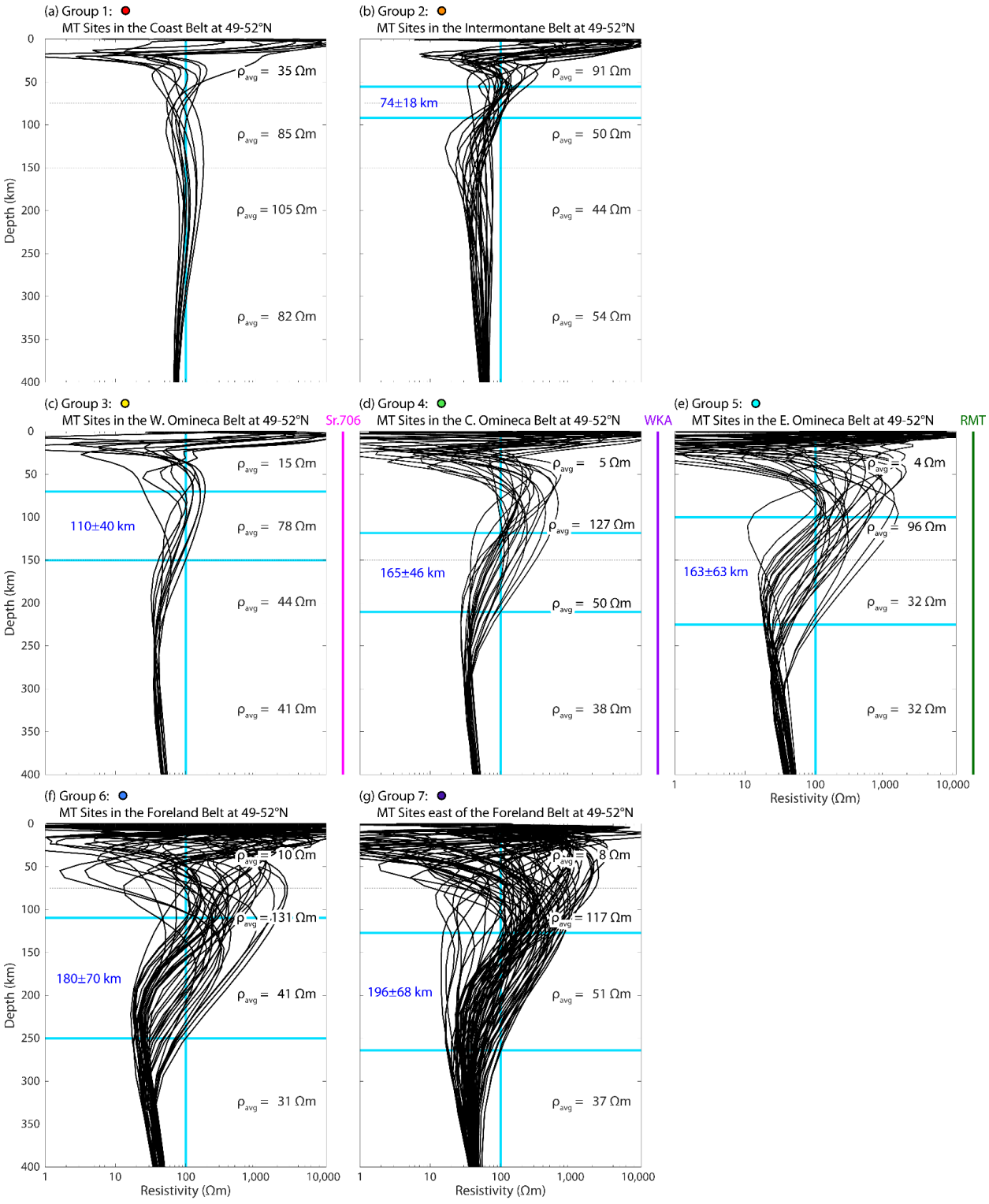

***Figure 6.8**: Resistivity-depth profiles beneath the MT stations in groups G1-G7. The average resistivity values listed on each panel are shown as a cross-section in Figure 6.9. Resistivity ranges are listed in Table D.5. Blue lines indicate the depths at which the resistivity is 100 Ωm. These depth ranges (blue numbers) provide estimates of LAB depth (e.g., Nieuwenhuis et al. 2014; Wang & Unsworth 2022).*

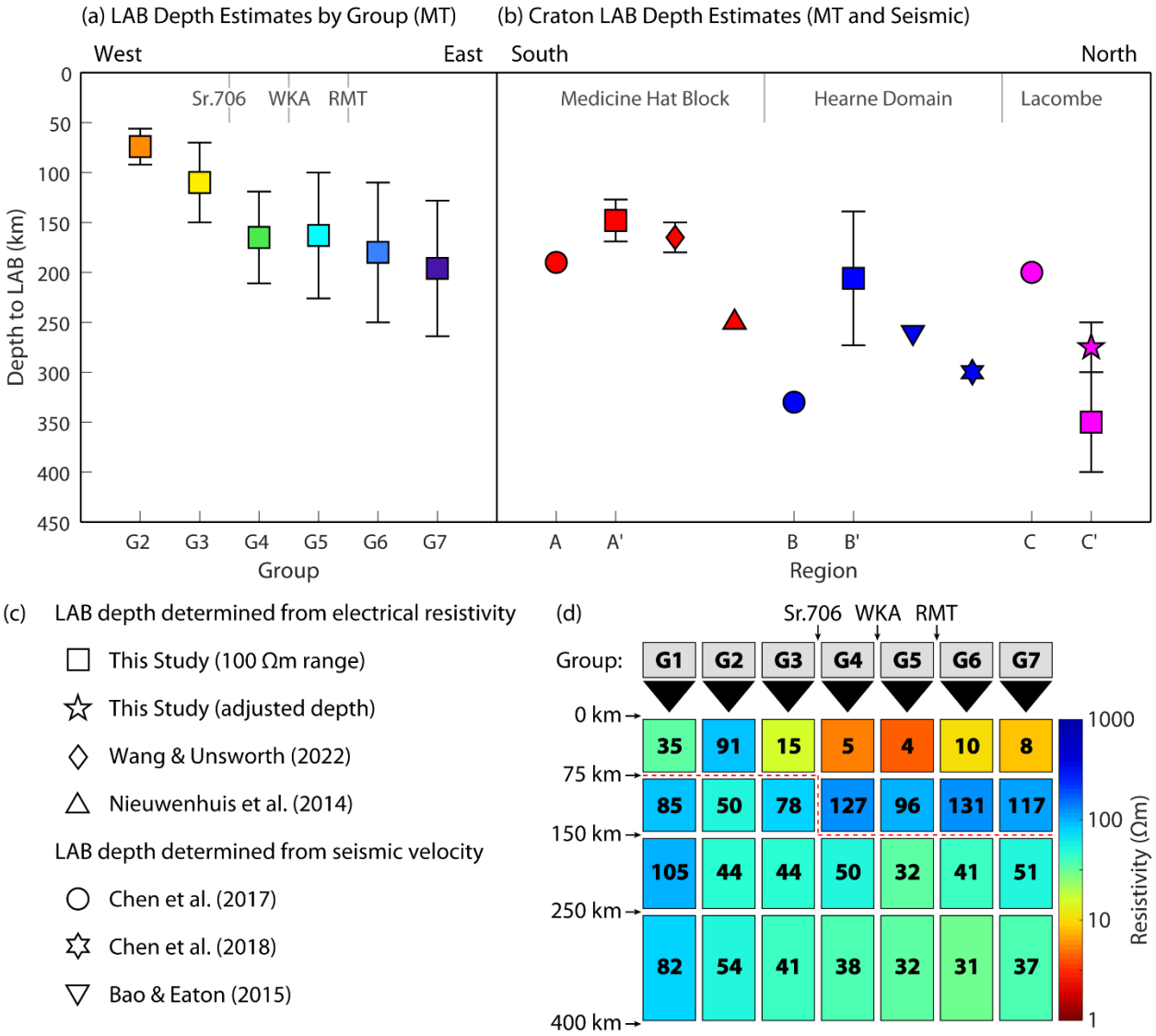

Figure 6.9*: (a) LAB depth estimates from west to east. These values and ranges correspond to the blue lines and numbers in Figure 6.8. (b) LAB depth estimates for the Medicine Hat Block, Hearne Domain, and Lacombe Domain. Regions A-C (Chen et al., 2017) are shown in Figure D.20. Regions A'-C' are sub-regions where the regions of Chen et al. (2017) overlap with the MT station grid. (c) Legend of the symbols used in panels a and b. (d) Average resistivity cross-section calculated using seven geographic groups (G1-G7) and four depth ranges. The groups are shown in panel (b) of Figure 6.2 and listed in Table D.1. The white numbers are average resistivity values in Ωm. Resistivity ranges are listed in Table D.5. The red line (horizontal at 75 km, vertical in between G3 and G4, and horizontal at 150 km) is a schematic representation of the electrical LAB and BCLS in the latitude range 49-52 °N.*

6.4.2. The Southern Alberta British Columbia conductor

The preferred resistivity model in the depth range 16-38 km is shown in Figure D.18 and the conductance in that range is shown in Figure D.19. As mentioned in Section 6.4.2, the SABC extends from the eastern side of the study area, in a southwesterly direction, to the BC-Idaho

border and the vertical projection of the WKA. Figure D.17 and Figure D**.18** reinforce that fact and illustrate it in more detail.

In map view, the SABC is coincident with much of the Loverna Block and Matzhiwin High (Figure D.19). Eaton et al. (1999) interpreted the Matzhiwin High as belonging in part to the Loverna Block and in part to the Vulcan Low, called the Vulcan structure. This reclassification places the SABC in the Loverna Block, bounded by the Rimbey High and Lacombe Domain to the north and the Vulcan structure to the south.

The Vulcan structure has been interpreted as a collisional suture zone between the Loverna Block and the Medicine Hat Block, with delamination and southward subduction of the lower crust of the Loverna Block (Eaton et al., 1999). Nieuwenhuis et al. (2014) imaged an upper-mantle conductor called the Loverna Conductor, which was coincident with the Loverna Block. Hanneson and Unsworth (2023b) imaged the Loverna Conductor as part of the SABC.

Since the SABC is likely related to the collision of two Archean blocks during continental assembly, the western extent of Laurentia should be at least that of the western extent of the SABC. This would put the western edge of the North American craton in southern BC at or westward of 117 °W.

6.4.3. Comparison of the resistivity model with seismic velocity models

P-wave velocity models of the study area have been created using finite-frequency tomography (Chen et al., 2017, 2018, 2019) and absolute P-wave arrival-time inversion (Boyce et al., 2023). S-wave velocity models of the study area have been created using multimode waveform inversion (Schaeffer & Lebedev, 2014), Rayleigh-wave tomography (Bao et al., 2014; Bao & Eaton, 2015), Rayleigh-wave phase velocity inversion (Zaporozan et al., 2018), and finite-frequency tomography (Chen et al., 2018, 2019). In this section, these models are compared with the 3-D resistivity model of Hanneson and Unsworth (2023b).

6.4.3.1. P-wave velocity models

Chen et al. (2017) used the maximum negative velocity gradient of their P-wave velocity model, accounting for vertical smearing, to estimate the lithospheric thickness in three regions. Region A (47-50 °N and 109-114 °W), representing the Medicine Hat Block, was ~190 km. Region B (50.25-52.25 °N and 110-114 °W), representing the southern Hearne

province, was ~330 km. Region C (52.5-53.5 °N and 111.5-114 °W), representing the Lacombe Domain, was ~200 km.

The P-wave velocity perturbation model of Chen et al. (2017) is compared with the preferred resistivity model in Figure D.20. Where MT data were included in the dataset, i.e., west of 112 °W, the depth of the electrical LAB was estimated in regions A, B, and C. Based on a resistivity of 100 Ωm (e.g., Nieuwenhuis et al., 2014; Wang & Unsworth, 2022), these depths are 148 ± 21 km, 206 ± 67 km, and 350 ± 50 km, respectively (Figure 6.9 b and Figure D.20 c).

The inflection point of a resistivity-depth profile can also be used to estimate the depth of the electrical LAB (Bettac et al., 2023). In region A, the inflection point is very well correlated with the 100 Ωm depth range. In region B, the inflection point is in the upper half of the 100 Ωm depth range. In region C, the inflection point is above the 100 Ωm depth range (Figure D.20 c).

Taking this analysis into consideration, the following inferences can be made in regards to the resistivity model. The lithosphere is ~150 km thick in the western half of region A, which is shallower than the ~190 km estimate of Chen et al. (2017). The lithosphere is ~200 km thick in the western half of region B, which is considerably shallower than the ~330 km estimate of Chen et al. (2017). The lithosphere is ~250-300 km thick in region C, which is deeper than the ~200 km estimate of Chen et al. (2017).

In the latitude range 49-52 °N, the P-wave velocity perturbation model of Chen et al. (2019) placed the BCLS within 40-50 km west of the SRMT, with a westward dip. North of ~52 °N, the BCLS was directly beneath the SRMT, with a subvertical to eastward dip. In southwestern Canada, Boyce et al. (2023) imaged this slow-to-fast wavespeed boundary beneath the SRMT, with a steep westward dip.

6.4.3.2. S-wave velocity models

Two S-wave velocity perturbation models are compared with the preferred resistivity model in Figure D.21. These models show the western edge of the high-velocity North American craton in southwestern Canada below the SRMT (Bao et al., 2014) or below the Cordilleran deformation front (Schaeffer & Lebedev, 2014). Zaporozan et al. (2018) imaged the craton edge below the deformation front, with a southwestward dip. Chen et al. (2019) placed the

S-wave boundary near the SRMT, in agreement with their P-wave boundary (Section 6.5.3.1). The SRMT and deformation front both trend approximately northwest (Figure 6.1). In contrast, the western edge of the high-resistivity region in southwestern Canada trends approximately north, and it occurs around 119 °W.

Beneath the Hearne domain, the seismic LAB was imaged at a depth of ~260 km (Bao & Eaton, 2015) or ~300 km (Chen et al., 2018). This is deeper than the electrical LAB estimated at a depth of ~200 km, but still close to the lower bound (273 km) of the 100 Ωm depth range for region B (Figure D.20 c).

6.5. Conclusions and conceptual model

Based on the preferred resistivity model and the average resistivity analysis, the BCLS in southern BC occurs around 119 °W, near the vertical projection of the strontium isopleth. However, inversions of synthetic MT data suggested that the BCLS imaged in the resistivity model could be shifted away from the craton by as much as 50-100 km. This implies that the BCLS in southern BC might actually occur east of 119 °W. The westward extent of the SABC provided evidence that the western edge of the North American craton in southern BC is at or westward of 117 °W. These two lines of evidence lead to the conclusion that the BCLS in southern BC occurs somewhere between 119 °W and 117 °W, a distance of ~140 km. This places the BCLS between the vertical projections of the strontium isopleth and WKA at the surface. Seismic tomography studies have suggested that the transition between thin and thick lithosphere spans a horizontal distance of 50-100 km (Currie et al., 2023).

The electrical LAB was imaged at a depth of ~150 km in southern Alberta and ~250-300 km in central Alberta, in agreement with the results of Wang and Unsworth (2022), and it was imaged as northward dipping in between. The transition from subhorizontal at a depth of ~150 km to northward dipping occurs below the SABC, which coincides with the Loverna Block. These conclusions were used to create a conceptual model of the electrical LAB in southwestern Canada (Figure 6.10).

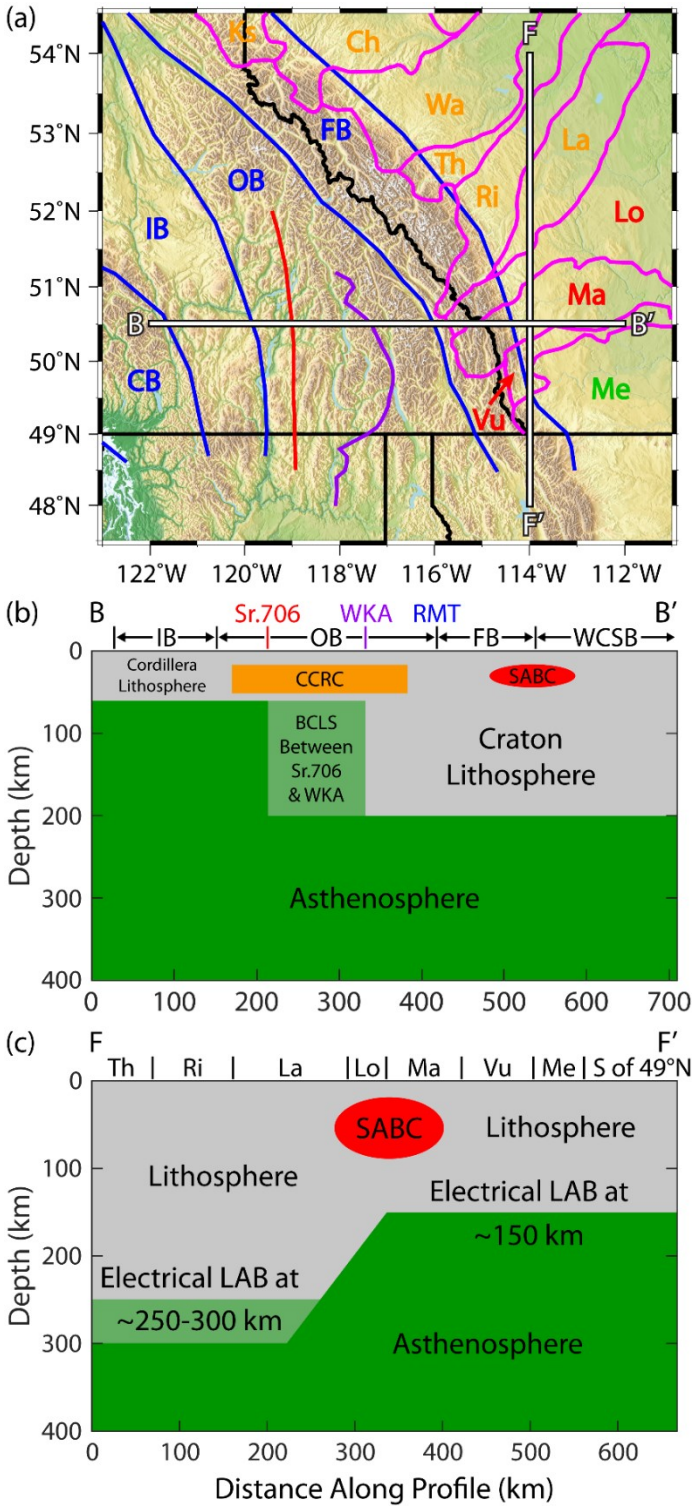

***Figure 6.10**: Schematic diagrams of the lithosphere-asthenosphere boundary in southwestern Canada. (a) Map with locations of cross-sections B-B′ and F′F′. The red line is the approximate location of the $^{87}Sr/^{86}Sr$ = 0.706 isopleth. The purple line is the western boundary of the Kootenay Arc. Political boundaries (black lines), morphogeological boundaries (blue lines), and Precambrian basement domains (pink lines) are also shown. (b) Schematic cross-section along profile B-B′ corresponding to the resistivity model shown in Figure 6.5b. (c) Schematic cross-section along profile F-F′ corresponding to the resistivity model shown in Figure 6.6b.*

The BCLS is subvertical and likely stable; therefore, the lowermost mantle lithosphere of the North American craton in southwestern Canada is likely dry and moderately chemically depleted. The BCLS in southeastern BC occurs below the Canadian Cordilleran Regional conductor (CCRC in Figure 6.10 b). Attenuation of the electric field in the low-resistivity CCRC makes it difficult to image the BCLS below. Therefore, the dip of the BCLS cannot be estimated from this resistivity model, beyond saying that it is subvertical.

6.6. Acknowledgments

Funding was provided by NSERC Discovery Grant RGPIN-2020-04240 to Martyn Unsworth and an award from the Future Energy Systems program at the University of Alberta. A Geoscience BC scholarship was awarded to Cedar Hanneson in 2021. The broadband MT data used in this paper were collected by Phoenix Geophysics with funding from Lithoprobe. Alan Jones undertook quality control and processed the data with funding from the Geological Survey of Canada. We thank all those involved in collecting these data. Their hard work and attention to detail resulted in a very high quality MT data set. We also thank Claire Currie and Stephen Johnston for providing feedback; Gary Egbert, Anna Kelbert, and Naser Meqbel for use of ModEM; and the Digital Research Alliance of Canada (formerly Compute Canada) for access to high-performance cluster computing.

7. Summary

This thesis has applied magnetotelluric studies to research in both geothermal energy and tectonics, at a variety of spatial scales in southwestern Canada. Chapter 4 explored a specific geothermal reservoir and associated heat source at Mount Meager. Chapter 5 explored crustal-scale features within a large geographic region of the southern Canadian Cordillera. Chapter 6 explored lithosphere-scale features within that same region of the Canadian Cordillera. The electrical resistivity models and interpretations presented in this thesis can aid the exploration and development of geothermal energy resources in southwestern Canada, and provide insights into the tectonics of the study areas.

7.1. The magmatic and geothermal systems beneath Mount Meager

Three-dimensional inversion of broadband MT data confirmed the existence of a magma body beneath Mount Meager, as suggested by Jones and Dumas (1993) using 2-D methods for MT data analysis. This magma body could be part of a larger magma layer, as shown to be possible by the inversions of synthetic MT data. It is also possible that the magma body/layer is thicker than modelled in the preferred electrical resistivity model.

Based on this published resistivity model, the Mount Meager magma body has a volume of at least 2×10^{12} m^3 and contains 18–32% dacitic-to-trachydacitic melt with 6–8 wt.% H_2O at a temperature in the range 800–900 °C. This deep heat source beneath Mount Meager provides thermal energy to the overlying hydrothermal systems. Volcanic eruptions generally require a melt fraction greater than ~45%, therefore, an eruption at Mount Meager in the near future is unlikely.

A geothermal gradient of approximately 90–100 °C/km makes the Mount Meager geothermal resource a promising location for the development and production of renewable, low-carbon energy. There is also a possibility that supercritical fluids could be found in between the magma body and the conventional, shallow geothermal reservoir. Supercritical geothermal resources have the potential to provide more energy than conventional geothermal resources.

The 3-D resistivity model presented in Chapter 4 and published in *Canadian Journal of Earth Sciences* is a significant advancement from previous resistivity models, created 20–40 years ago, and it has provided the first deep 3-D image of this volcanic system. Along with the other

geophysical and geological models of the Garibaldi Geothermal Energy Project, it will help reduce the exploration risk associated with geothermal energy development.

7.2. The middle and lower crust beneath the southern Canadian Cordillera

A region of low resistivity in the middle and lower crust was observed beneath the southeastern Canadian Cordillera by Gough (1986), Ledo and Jones (2001), Rippe et al. (2013), and others. This region of low resistivity, the Canadian Cordilleran regional conductor, was modelled as a number of discrete conductors in a new 3-D resistivity model. This model was presented in Chapter 5 and published in *Geophysical Journal International* in 2023.

Synthetic MT inversions suggested that a single continuous conductor was not consistent with the MT data. The various conductors of the CCRC were interpreted as interconnected saline fluids and/or conductive mineralization on grain boundaries. Where temperatures are high, the CCRC could also be caused by a small fraction of partial melt that either: (1) is hydrous and alkali-rich or (2) contains a small amount of sulphide melt. These interpretations were made possible by new laboratory experiments published over the past decade, and have advanced the interpretations made in previous studies.

The Loverna conductor described by Nieuwenhuis et al. (2014), along with the SABC and Red Deer conductors imaged by Wang (2019), were modelled as a single connected conductor. The low resistivity of this feature was interpreted as being due to interconnected sulphide mineralization. Where temperatures are relatively low (< 400 °C), the low resistivity could also be due to interconnected graphite films on grain boundaries.

This published resistivity model is the first regional-scale 3-D resistivity model of the southern Canadian Cordillera, providing new insights into the lithospheric structure and tectonic history of the region. Chapter 5 focused on the depth range 10–100 km, while Chapter 6 focused on the lithosphere-asthenosphere boundary and depths up to 400 km.

7.3. Lithospheric thickness and lithosphere step in southwestern Canada

Based on the published resistivity model mentioned above and the average resistivity analysis described in Chapter 6, the backarc-craton lithosphere step in southern BC occurs around longitude 119 °W, near the vertical projection of the $^{87}Sr/^{86}Sr = 0.706$ isopleth. Inversions of synthetic MT data suggested that the backarc-craton lithosphere step imaged in the resistivity

model could be shifted away from the craton by as much as 50-100 km. This implied that the lithosphere step in southern BC might actually occur east of 119 °W.

The westward extent of the SABC provided evidence that the western edge of the North American craton in southern BC is at or westward of 117 °W. These two lines of evidence lead to the conclusion that the lithosphere step in southern BC occurs somewhere between 119 °W and 117 °W, a horizontal distance of ~140 km. This places it between the vertical projections of the strontium isopleth and the western boundary of the Kootenay Arc at the surface. Seismic tomography studies have suggested that the transition between thin and thick lithosphere spans a horizontal distance of 50-100 km (Currie et al., 2023).

The electrical LAB was imaged at a depth of ~150 km in southern Alberta and ~250-300 km in central Alberta, in agreement with the results of Wang and Unsworth (2022), and it was imaged as northward dipping in between. The transition from subhorizontal at a depth of ~150 km to northward dipping occurs below the SABC, which coincides with the Loverna Block. These conclusions were used to create a conceptual model of the electrical LAB in southwestern Canada (Figure 6.10).

The backarc-craton lithosphere step is subvertical and likely stable over geological time; therefore, the lowermost mantle lithosphere of the North American craton in southwestern Canada is likely dry and moderately chemically depleted. This lithosphere step in southeastern BC occurs below the Canadian Cordilleran Regional conductor and attenuation of the electric field in this low-resistivity feature makes it difficult to image the LAB below. Therefore, the dip of the lithosphere step cannot be estimated from the published resistivity model, beyond determining that it is subvertical.

7.4. Suggestions for future research

7.4.1. Mount Meager and the Garibaldi Volcanic Belt

It would be beneficial to undertake additional research into the composition of the magma body beneath Mount Meager and how it causes the observed low resistivity anomaly. This could include consideration of a volatile phase in determining the bulk resistivity, using the multiphase Archie's law of Glover (2010), following the methods of Samrock et al. (2021). More detailed thermal and geochemical analyses could better constrain the temperature and water content of the magma body, allowing a refined estimate of the melt fraction.

Density and seismic velocity models, such as those being developed by Calahorrano-Di Patre and Williams-Jones (2021) and Gilbert et al. (2021) as part of the Garibaldi Geothermal Energy Project, could also help constrain the location and properties of the magma body. Improving estimates of the thickness of the magma layer is important because the synthetic inversion results presented in Chapter 4 and Appendix B suggested that the MT inversion could be underestimating the thickness.

Future research could include inverting the broadband MT data described in Chapter 4 using a different inversion algorithm, such as one that uses an unstructured and/or adaptive, tetrahedral mesh, to better model the rugged topography (e.g., Kordy et al., 2016; Usui et al., 2017). Furthermore, additional broadband MT data were collected in 2021 and 2022 at Mount Cayley and Mount Garibaldi (Grasby et al., 2022). These new MT data along with legacy data, including long-period MT data, could facilitate regional resistivity modelling of the central Garibaldi Volcanic Belt. This would help distinguish between a large (regional) magma layer and a number of smaller (local) magma bodies beneath individual volcanic centres.

Joint inversions could also be a fruitful area of future research. A joint inversion of broadband MT data and AMT data using a multi-scale model mesh would unify the results of Hanneson and Unsworth (2023a) and Hormozzade Ghalati et al. (2022). A joint inversion of broadband MT data and gravity data is currently in a very preliminary stage and it might provide new insights into the location, geometry, and composition of the Mount Meager magma body (Calahorrano-Di Patre et al., 2023).

Meteoric water may enter the hydrothermal system in the Lillooet Valley, on the north side of the MMVC, and emerge along Meager Creek, on the south side of the MMVC. The published resistivity model shown in Figure 4.9 could not provide definitive answers to questions regarding regional groundwater flow. Collaborative research utilizing the broadband MT model (Hanneson & Unsworth, 2023a), the AMT model (Hormozzade Ghalati et al., 2022), and the structural geology study (Muhammad et al., 2021) would be better equipped to answer such questions.

7.4.2. The Canadian Cordillera in southeastern BC

Further research in southeastern BC, including additional broadband MT data collection and a higher spatial density of MT data in areas of interest, would be needed to better relate the crustal resistivity structure to the distribution of thermal springs. Potential geographical areas

for future research are (1) an area encompassing the Kuskanax batholith, southern Columbia River fault, and northern Slocan Lake fault; and (2) an area encompassing the thermal springs along profile B–C in Figure 5.9.

Recently, 3-D anisotropic inversion of MT data has become possible and could address some of the limitations of previous analyses (Kong et al., 2021; Lee, 2020). The southeastern Canadian Cordillera, particularly near the SRMT, may exhibit electrical anisotropy and future research could include a 3-D anisotropic inversion. However, significant computing resources would be required.

Furthermore, the structural geology of the southern Canadian Cordillera could be investigated using 3-D inversion of gravity data, following the methods of Hayward (2019) that were applied to the northern Canadian Cordillera.

7.4.3. Lithospheric thickness in southwestern Canada

The backarc-craton lithosphere step in southern BC (49–52 °N) occurs around 117–119 °W. Future research would benefit from additional long-period MT data within this region. A dedicated inversion of long-period MT data in the region 49–52 °N and 116–120 °W (an area of approximately 330 km × 280 km) could potentially image the lithosphere step more reliably. However, the Canadian Cordilleran regional conductor would still pose a challenge. Such research could use an isotropic approach and/or an anisotropic approach.

A northward dipping lithosphere-asthenosphere boundary beneath the Loverna Block and SABC in Alberta has not been imaged in seismic tomography studies as it was in Chapter 6. Further research into the geometry of the LAB in central and southern Alberta would be beneficial. Such research could involve joint inversion of long-period MT data and seismic tomography data.

References

Adams, M. G., Lentz, D. R., Shaw, C. S., Williams, P. F., Archibald, D. A., & Cousens, B. (2005). Eocene shoshonitic mafic dykes intruding the Monashee Complex, British Columbia: A petrogenetic relationship with the Kamloops Group volcanic sequence? *Canadian Journal of Earth Sciences*, *42*(1), 11–24. https://doi.org/10.1139/e04-091

Allen, D. M., Grasby, S. E., & Voormeij, D. A. (2006). Determining the circulation depth of thermal springs in the southern Rocky Mountain Trench, south-eastern British Columbia, Canada using geothermometry and borehole temperature logs. *Hydrogeology Journal*, *14*(1–2), 159–172. https://doi.org/10.1007/s10040-004-0428-z

Allstadt, K. (2013). Extracting source characteristics and dynamics of the August 2010 Mount Meager landslide from broadband seismograms: Seismic Inversion of Mount Meager Landslide. *Journal of Geophysical Research: Earth Surface*, *118*(3), 1472–1490. https://doi.org/10.1002/jgrf.20110

Anderson, G. M., Castet, S., Schott, J., & Mesmer, R. E. (1991). The density model for estimation of thermodynamic parameters of reactions at high temperatures and pressures. *Geochimica et Cosmochimica Acta*, *55*(7), 1769–1779. https://doi.org/10.1016/0016-7037(91)90022-W

Arango, C., Marcuello, A., Ledo, J., & Queralt, P. (2009). 3D magnetotelluric characterization of the geothermal anomaly in the Llucmajor aquifer system (Majorca, Spain). *Journal of Applied Geophysics*, *68*(4), 479–488. https://doi.org/10.1016/j.jappgeo.2008.05.006

Archibald, D. A., Glover, J. K., Price, R. A., Farrar, E., & Carmichael, D. M. (1983). Geochronology and tectonic implications of magmatism and metamorphism, southern Kootenay Arc and neighbouring regions, southeastern British Columbia. Part I: Jurassic to mid-Cretaceous. *Canadian Journal of Earth Sciences*, *20*(12), 1891–1913. https://doi.org/10.1139/e83-178

Archie, G. E. (1942). The Electrical Resistivity Log as an Aid in Determining Some Reservoir Characteristics. *Transactions of the AIME*, *146*(01), 54–62. https://doi.org/10.2118/942054-G

Armstrong, R. L., Taubeneck, W. H., & Hales, P. O. (1977). Rb-Sr and K-Ar geochronometry of Mesozoic granitic rocks and their Sr isotopic composition, Oregon, Washington, and

Idaho. *GSA Bulletin*, *88*(3), 397–411. https://doi.org/10.1130/0016-7606(1977)88<397:RAKGOM>2.0.CO;2

Arnórsson, S. (2014). The roots of volcanic geothermal systems—Their birth, evolution and extinction. *Proceedings 5th African Rift Geothermal Conference, Arusha, Tanzania, 29-31 October 2014*. http://theargeo.org/fullpapers/fullpaper/The%20roots%20of%20volcanic%20geothermal%20systems.pdf

Bakhterev, V. V. (2008). High-temperature electric conductivity of some feldspars. *Doklady Earth Sciences*, *420*(1), 554–557. https://doi.org/10.1134/S1028334X08040065

Bao, X., & Eaton, D. W. (2015). Large variations in lithospheric thickness of western Laurentia: Tectonic inheritance or collisional reworking? *Precambrian Research*, *266*, 579–586. https://doi.org/10.1016/j.precamres.2015.05.010

Bao, X., Eaton, D. W., & Guest, B. (2014). Plateau uplift in western Canada caused by lithospheric delamination along a craton edge. *Nature Geoscience*, *7*(11), 830–833. https://doi.org/10.1038/ngeo2270

Barrington-Leigh, C., & Ouliaris, M. (2017). The renewable energy landscape in Canada: A spatial analysis. *Renewable and Sustainable Energy Reviews*, *75*, 809–819. https://doi.org/10.1016/j.rser.2016.11.061

Bedrosian, P. A., & Feucht, D. W. (2014). Structure and tectonics of the northwestern United States from EarthScope USArray magnetotelluric data. *Earth and Planetary Science Letters*, *402*, 275–289. https://doi.org/10.1016/j.epsl.2013.07.035

Bennett, G. T., Clowes, R. M., & Ellis, R. M. (1975). A seismic refraction survey along the southern Rocky Mountain Trench, Canada. *Bulletin of the Seismological Society of America*, *65*(1), 37–54. https://doi.org/10.1785/BSSA0650010037

Bettac, S. P., Unsworth, M. J., Pearson, D. G., & Craven, J. (2023). New constraints on the structure and composition of the lithospheric mantle beneath the Slave craton, NW Canada from 3-D magnetotelluric data – Origin of the Central Slave Mantle Conductor and possible evidence for lithospheric scale fluid flow. *Tectonophysics*, *851*, 229760. https://doi.org/10.1016/j.tecto.2023.229760

Bibby, H. M., Risk, G. F., Grant Caldwell, T., & Heise, W. (2009). Investigations of deep resistivity structures at the Wairakei geothermal field. *Geothermics*, *38*(1), 98–107. https://doi.org/10.1016/j.geothermics.2008.07.002

Boyce, A., Liddell, M. V., Pugh, S., Brown, J., McMurchie, E., Parsons, A., Estève, C., Burdick, S., Darbyshire, F. A., Cottaar, S., Bastow, I. D., Schaeffer, A. J., Audet, P., Schutt, D. L., & Aster, R. C. (2023). A New P-Wave Tomographic Model (CAP22) for North America: Implications for the Subduction and Cratonic Metasomatic Modification History of Western Canada and Alaska. *Journal of Geophysical Research: Solid Earth*, *128*(3), e2022JB025745. https://doi.org/10.1029/2022JB025745

Burger, H. R., Sheehan, A. F., & Jones, C. H. (2006). *Introduction to Applied Geophysics: Exploring the shallow subsurface* (L. Wiegman, Ed.). W. W. Norton & Company.

Cagniard, L. (1953). Basic theory of the magneto-telluric method of geophysical prospecting. *Geophysics*, *18*(3), 605–635. https://doi.org/10.1190/1.1437915

Calahorrano-Di Patre, A. E., & Williams-Jones, G. (2021). *Gravity Survey at Mt. Meager Volcanic Complex: 2019-2020* (Report 2021–08; Chapter 4, pp. 49–78). Geoscience BC.

Calahorrano-Di Patre, A., Pearce, R. K., Williams-Jones, G., Moorkamp, M., Hanneson, C., & Unsworth, M. (2023). Peeking into a Hot Resource: Geophysical Imaging of the Mount Meager Volcanic Complex and its Active Geothermal System. *AGU Fall Meeting Abstracts*, *2023*.

Caldwell, T. G., Bibby, H. M., & Brown, C. (2004). The magnetotelluric phase tensor. *Geophysical Journal International*, *158*(2), 457–469. https://doi.org/10.1111/j.1365-246X.2004.02281.x

Candy, C. (2001). *Crew Development Corporation Report on a Magnetotelluric Survey, South Meager Geothermal Project, Pemberton, British Columbia* (Project FGI-581; p. 168). Frontier Geosciences Inc.

Caner, B., Camfield, P. A., Andersen, F., & Niblett, E. R. (1969). A large-scale magnetotelluric survey in Western Canada. *Canadian Journal of Earth Sciences*, *6*(5), 1245–1261. https://doi.org/10.1139/e69-125

Canil, D., Hyndman, R. D., & Fode, D. (2021). Hygrometric Control on the Lithosphere-Asthenosphere Boundary: A 28 Million Year Record From the Canadian Cordillera. *Geophysical Research Letters*, *48*(9), e2020GL091957. https://doi.org/10.1029/2020GL091957

Chang-Bock, I., Sang-Mo, K., Ho-Wan, C., & Tetsuichi, T. (2002). The geochemical behavior of altered igneous rocks in the Tertiary Gampo Basin, Kyongsang Province, South Korea. *GEOCHEMICAL JOURNAL*, *36*(5), 391–407. https://doi.org/10.2343/geochemj.36.391

Charlesworth, H. A. K. (1959). Some suggestions on the structural development of the Rocky Mountains of Canada. *Journal of the Alberta Society of Petroleum Geologists*, *7*(11), 249–256.

Chave, A. D., & Jones, A. G. (2012). *The Magnetotelluric Method: Theory and Practice*. Cambridge University Press.

Chave, A. D., & Thomson, D. J. (1989). Some comments on magnetotelluric response function estimation. *Journal of Geophysical Research: Solid Earth*, *94*(B10), 14215–14225. https://doi.org/10.1029/JB094iB10p14215

Chave, A. D., Thomson, D. J., & Ander, M. E. (1987). On the robust estimation of power spectra, coherences, and transfer functions. *Journal of Geophysical Research*, *92*(B1), 633. https://doi.org/10.1029/JB092iB01p00633

Chen, Y., Gu, Y. J., Currie, C. A., Johnston, S. T., Hung, S.-H., Schaeffer, A. J., & Audet, P. (2019). Seismic evidence for a mantle suture and implications for the origin of the Canadian Cordillera. *Nature Communications*, *10*(1), 2249. https://doi.org/10.1038/s41467-019-09804-8

Chen, Y., Gu, Y. J., & Hung, S. (2018). A New Appraisal of Lithospheric Structures of the Cordillera-Craton Boundary Region in Western Canada. *Tectonics*, *37*(9), 3207–3228. https://doi.org/10.1029/2018TC004956

Chen, Y., Gu, Y. J., & Hung, S.-H. (2017). Finite-frequency P-wave tomography of the Western Canada Sedimentary Basin: Implications for the lithospheric evolution in Western Laurentia. *Tectonophysics*, *698*, 79–90. https://doi.org/10.1016/j.tecto.2017.01.006

Colpron, M., Warren, M. J., & Price, R. A. (1998). Selkirk fan structure, southeastern Canadian Cordillera: Tectonic wedging against an inherited basement ramp. *GSA Bulletin*, *110*(8), 1060–1074. https://doi.org/10.1130/0016-7606(1998)110<1060:SFSSCC>2.3.CO;2

Comeau, M. J., Becken, M., Connolly, J. A. D., Grayver, A. V., & Kuvshinov, A. V. (2020). Compaction-Driven Fluid Localization as an Explanation for Lower Crustal Electrical Conductors in an Intracontinental Setting. *Geophysical Research Letters*, *47*(19), e2020GL088455. https://doi.org/10.1029/2020GL088455

Comeau, M. J., Becken, M., & Kuvshinov, A. V. (2022). Imaging the Whole-Lithosphere Architecture of a Mineral System—Geophysical Signatures of the Sources and Pathways of Ore-Forming Fluids. *Geochemistry, Geophysics, Geosystems*, *23*(8), e2022GC010379. https://doi.org/10.1029/2022GC010379

Connolly, J. a. D., & Podladchikov, Y. Y. (2004). Fluid flow in compressive tectonic settings: Implications for midcrustal seismic reflectors and downward fluid migration. *Journal of Geophysical Research: Solid Earth*, *109*(B4). https://doi.org/10.1029/2003JB002822

Cordell, D., Unsworth, M. J., Lee, B., Hanneson, C., Milling, D. K., & Mann, I. R. (2021). Estimating the geoelectric field and electric power transmission line voltage during a geomagnetic storm in Alberta, Canada using measured magnetotelluric impedance data: The influence of three-dimensional electrical structures in the lithosphere. *Space Weather*, *19*, e2021SW002803. https://doi.org/10.1029/2021SW002803

Currie, C. A., Cassidy, J. F., Hyndman, R. D., & Bostock, M. G. (2004). Shear wave anisotropy beneath the Cascadia subduction zone and western North American craton. *Geophysical Journal International*, *157*(1), 341–353. https://doi.org/10.1111/j.1365-246X.2004.02175.x

Currie, C. A., & Hyndman, R. D. (2006). The thermal structure of subduction zone back arcs. *Journal of Geophysical Research: Solid Earth*, *111*(B8). https://doi.org/10.1029/2005JB004024

Currie, C. A., Mallyon, D. A., Yu, T.-C., Chen, Y., Schaeffer, A. J., Audet, P., & Gu, Y. J. (2023). Mantle structure and dynamics at the eastern boundary of the northern Cascadia backarc. *Journal of Geodynamics*, *155*, 101958. https://doi.org/10.1016/j.jog.2022.101958

Currie, C. A., & van Wijk, J. (2016). How craton margins are preserved: Insights from geodynamic models. *Journal of Geodynamics*, *100*, 144–158. https://doi.org/10.1016/j.jog.2016.03.015

Currie, C. A., Wang, K., Hyndman, R. D., & He, J. (2004). The thermal effects of steady-state slab-driven mantle flow above a subducting plate: The Cascadia subduction zone and backarc. *Earth and Planetary Science Letters*, *223*(1–2), 35–48. https://doi.org/10.1016/j.epsl.2004.04.020

Dai, L., Hu, H., Li, H., Jiang, J., & Hui, K. (2014). Influence of temperature, pressure, and chemical composition on the electrical conductivity of granite. *American Mineralogist*, *99*(7), 1420–1428. https://doi.org/10.2138/am.2014.4692

DeLucia, M. S., Murphy, B. S., Marshak, S., & Egbert, G. D. (2019). The Missouri High-Conductivity Belt, revealed by magnetotelluric imaging: Evidence of a trans-lithospheric shear zone beneath the Ozark Plateau, Midcontinent USA? *Tectonophysics*, *753*, 111–123. https://doi.org/10.1016/j.tecto.2019.01.011

DiCaprio, L., Maiti, T., Dettmer, J., & Eaton, D. W. (2020). Moho Structure Across the Backarc-Craton Transition in the Northern U.S. Cordillera. *Tectonics*, *39*(2). https://doi.org/10.1029/2019TC005489

Dostal, J., Breitsprecher, K., Church, B. N., Thorkelson, D., & Hamilton, T. S. (2003). Eocene melting of Precambrian lithospheric mantle: Analcime-bearing volcanic rocks from the Challis–Kamloops belt of south central British Columbia. *Journal of Volcanology and Geothermal Research*, *126*(3), 303–326. https://doi.org/10.1016/S0377-0273(03)00153-7

Dostal, J., Corney, R., Church, B. N., & Connolly, R. M. (2021). Petrogenesis of Eocene shoshonitic rocks from South-Central British Columbia: Melting of Proterozoic lithospheric mantle. *Lithos*, *398–399*, 106289. https://doi.org/10.1016/j.lithos.2021.106289

Dostal, J., Shellnutt, J. G., & Church, B. N. (2019). Petrogenesis of an Eocene syenitic intrusion from south-central British Columbia: Evidence for increasing influence of cratonic Laurentia on alkaline magmatism of western North America. *Lithos*, *332–333*, 67–82. https://doi.org/10.1016/j.lithos.2019.01.023

Ducea, M. N., & Park, S. K. (2000). Enhanced Mantle Conductivity from Sulfide Minerals, Southern Sierra Nevada, California. *Geophysical Research Letters*, *27*(16), 2405–2408. https://doi.org/10.1029/2000GL011565

Eaton, D. W., Darbyshire, F., Evans, R. L., Grütter, H., Jones, A. G., & Yuan, X. (2009). The elusive lithosphere–asthenosphere boundary (LAB) beneath cratons. *Lithos*, *109*(1), 1–22. https://doi.org/10.1016/j.lithos.2008.05.009

Eaton, D. W., Ross, G. M., & Clowes, R. M. (1999). Seismic-reflection and potential-field studies of the Vulcan structure, western Canada: A Paleoproterozoic Pyrenees? *Journal of Geophysical Research: Solid Earth*, *104*(B10), 23255–23269. https://doi.org/10.1029/1999JB900204

Egbert, G. D., & Booker, J. R. (1986). Robust estimation of geomagnetic transfer functions. *Geophysical Journal International*, *87*(1), 173–194. https://doi.org/10.1111/j.1365-246X.1986.tb04552.x

Egbert, G. D., & Eisel, M. (1998). *EMTF: Programs for Robust Single Station and Remote Reference Analysis of Magnetotelluric Data: UNIX (and PC) Version* [Computer software].

Fairbank, B. D., Openshaw, R. E., Souther, J. G., & Stauder, J. J. (1981). Meager Creek Geothermal Project: An exploration case history. *Geothermal Resources Council Bulletin*, 1–7. https://doi.org/10.4095/103409

Feeley, T. C. (2003). Origin and Tectonic Implications of Across-Strike Geochemical Variations in the Eocene Absaroka Volcanic Province, United States. *Journal of Geology*, *111*(3), 329–346. https://doi.org/10.1086/373972

Finley, T. D. (2020). *Fault-hosted geothermal systems in southeastern British Columbia* [Master of Science]. University of Alberta.

Finley, T. D., Johnston, S. T., Unsworth, M. J., Banks, J., & Jonathan, D.-I. (2022). Modern dextral strain controls active hydrothermal systems in the southeastern Canadian Cordillera. *GSA Bulletin*. https://doi.org/10.1130/B36500.1

Flores, C., Kurtz, R. D., & DeLaurier, J. (1985). Magnetotelluric exploration in the Meager Mountain geothermal area, Canada. *Acta Geodaetica, Geophysica et Montanistica Hungarica*, *20*(1), 165–171.

Flores-Luna, C. F. (1986). *Electromagnetic induction studies over the Meager Creek geothermal area, British Columbia* [PhD]. University of Toronto.

Foo, W. K. (1979). *Evolution of transverse structures linking the Purcell Anticlinorium to the western Rocky Mountains near Canal Flats, British Columbia* [PhD]. Queens University.

Fowler, C. M. R. (2005). *The Solid Earth: An Introduction to Global Geophysics* (Second). Cambridge University Press.

Gabrielse, H., Monger, J. W. H., Wheeler, J. O., Yorath, C. J., Carter, E. S., Orchard, M. J., Ross, C. A., Ross, J. R. P., Smith, P. L., Tipper, H. W., Sweeney, J. F., Stephenson, R. A., Currie, R. G., & DeLaurier, J. M. (1991). Tectonic framework. In *Geology of the Cordilleran Orogen in Canada* (Vol. 4, pp. 15–59). Geological Survey of Canada.

Gaillard, F. (2004). Laboratory measurements of electrical conductivity of hydrous and dry silicic melts under pressure. *Earth and Planetary Science Letters*, *218*(1), 215–228. https://doi.org/10.1016/S0012-821X(03)00639-3

Gal, L. P., & Ghent, E. D. (1990). Metamorphism in the Solitude Range, southwestern Rocky Mountains, British Columbia: Comparison with adjacent Omineca Belt rocks and tectonometamorphic implications for the Purcell Thrust. *Canadian Journal of Earth Sciences*. https://doi.org/10.1139/e90-161

Gamble, T. D., Goubau, W. M., & Clarke, J. (1979). Magnetotellurics with a remote magnetic reference. *GEOPHYSICS*, *44*(1), 53–68. https://doi.org/10.1190/1.1440923

Gardés, E., Gaillard, F., & Tarits, P. (2014). Toward a unified hydrous olivine electrical conductivity law. *Geochemistry, Geophysics, Geosystems*, *15*(12), 4984–5000. https://doi.org/10.1002/2014GC005496

Ghomshei, M. M. (2010). Canadian Geothermal Power Prospects. *World Geothermal Congress 2010*, 5.

Ghomshei, M. M., Sanyal, S., MacLeod, K., Henneberger, R., Ryder, A., Meech, J., & Fainbank, B. (2004). Status of the South Meager Geothermal Project British Columbia, Canada: Resource Evaluation and Plans for Development. *Geothermal Resources Council Transactions*, *28*, 6.

Ghomshei, M. M., & Stauder, J. J. (1989). Brief Review of the Meager Creek Geothermal Project: A Second Look at the Data. *Geothermal Resources Council Bulletin*, 3–7.

Gilbert, H., Dettmer, J., Savard, G., Klaasen, S., Fichtner, A., & Su, H. (2021). *Mount Meager Passive Seismic Monitoring* (Report 2021–08; Chapter 7, pp. 167–176). Geoscience BC.

Glover, P. W. J. (1996). Graphite and electrical conductivity in the lower continental crust: A review. *Physics and Chemistry of the Earth*, *21*(4), 279–287. https://doi.org/10.1016/S0079-1946(97)00049-9

Glover, P. W. J. (2010). A generalized Archie's law for n phases. *GEOPHYSICS*, *75*(6), E247–E265. https://doi.org/10.1190/1.3509781

Glover, P. W. J., Hole, M. J., & Pous, J. (2000). A modified Archie's law for two conducting phases. *Earth and Planetary Science Letters*, *180*(3), 369–383. https://doi.org/10.1016/S0012-821X(00)00168-0

Gough, D. I. (1986). Mantle upflow tectonics in the Canadian Cordillera. *Journal of Geophysical Research*, *91*(B2), 1909. https://doi.org/10.1029/JB091iB02p01909

Gough, D. I., Bingham, D. K., Ingham, M. R., & Alabi, A. O. (1982). Conductive structures in southwestern Canada: A regional magnetometer array study. *Canadian Journal of Earth Sciences*, *19*(8), 1680–1690. https://doi.org/10.1139/e82-143

Grasby, S. E., Allen, D. M., Bell, S., Chen, Z., Ferguson, G., Jessop, A., Kelman, M., Ko, M., Majorowicz, J., Moore, M., Raymond, J., & Therrien, R. (2012). *Geothermal energy resource potential of Canada* (Open File 6914). Geological Survey of Canada. https://doi.org/10.4095/291488

Grasby, S. E., Ansari, S. M., Barendregt, R. W., Borch, A., Calahorrano-DiPatre, A., Chen, Z., Craven, J. A., Dettmer, J., Gilbert, H., Hanneson, C., Harris, M., Hormozzade, F., Leiter, S., Liu, J., Muhammad, M., Quane, S. L., Russell, J. K., Salvage, R. O., Savard, G., … Vestrum, Z. E. (2021). *Garibaldi Geothermal Energy Project—Phase 1 Final Report* (Report 2021–08; pp. 1–265). Geoscience BC.

Grasby, S. E., Calahorrano-Di Patre, A., Chen, Z., Dettmer, J., Gilbert, H., Hanneson, C., Harris, M., Leiter, S., Liu, J., Muhammad, M., Russell, K., Unsworth, M. J., Williams-Jones, G., & Yuan, W. (2022). *Geothermal Resource Potential of the Garibaldi Volcanic Belt, Southwestern*

British Columbia (Part of NTS 092J): Phase 2 (2022–02; Summary of Activities 2021: Energy and Water, pp. 75–80). Geoscience BC.

Grasby, S. E., & Hutcheon, I. (2001). Controls on the distribution of thermal springs in the southern Canadian Cordillera. *Canadian Journal of Earth Sciences*, *38*, 427–440. https://doi.org/10.1139/e00-091

Grayver, A. V. (2015). Parallel three-dimensional magnetotelluric inversion using adaptive finite-element method. Part I: Theory and synthetic study. *Geophysical Journal International*, *202*(1), 584–603. https://doi.org/10.1093/gji/ggv165

Grayver, A. V., & Kolev, T. V. (2015). Large-scale 3D geoelectromagnetic modeling using parallel adaptive high-order finite element method. *Geophysics*, *80*(6), E277–E291. https://doi.org/10.1190/geo2015-0013.1

Grayver, A. V., van Driel, M., & Kuvshinov, A. V. (2019). Three-dimensional magnetotelluric modelling in spherical Earth. *Geophysical Journal International*, *217*(1), 532–557. https://doi.org/10.1093/gji/ggz030

Gross, L., Soueid Ahmed, A., & Revil, A. (2021). Induced polarization of volcanic rocks. 4. Large-scale induced polarization imaging. *Geophysical Journal International*, *225*(2), 950–967. https://doi.org/10.1093/gji/ggab018

Gung, Y., Panning, M., & Romanowicz, B. (2003). Global anisotropy and the thickness of continents. *Nature*, *422*(6933), Article 6933. https://doi.org/10.1038/nature01559

Guo, H., & Keppler, H. (2019). Electrical Conductivity of NaCl-Bearing Aqueous Fluids to 900 °C and 5 GPa. *Journal of Geophysical Research: Solid Earth*, *124*(2), 1397–1411. https://doi.org/10.1029/2018JB016658

Guo, X., Li, B., Ni, H., & Mao, Z. (2017). Electrical conductivity of hydrous andesitic melts pertinent to subduction zones. *Journal of Geophysical Research: Solid Earth*, *122*(3), 1777–1788. https://doi.org/10.1002/2016JB013524

Guo, X., Zhang, L., Behrens, H., & Ni, H. (2016). Probing the status of felsic magma reservoirs: Constraints from the P–T–H2O dependences of electrical conductivity of rhyolitic melt. *Earth and Planetary Science Letters*, *433*, 54–62. https://doi.org/10.1016/j.epsl.2015.10.036

Guthrie, R. H., Friele, P., Allstadt, K., Roberts, N., Evans, S. G., Delaney, K. B., Roche, D., Clague, J. J., & Jakob, M. (2012). The 6 August 2010 Mount Meager rock slide-debris flow, Coast Mountains, British Columbia: Characteristics, dynamics, and implications for hazard and risk assessment. *Natural Hazards and Earth System Sciences*, *12*(5), 1277–1294. https://doi.org/10.5194/nhess-12-1277-2012

Halliday, D., & Resnick, R. (2014). *Fundamentals of Physics* (Tenth Edition). Jearl Walker.

Hanneson, C., Johnson, C. L., Mittelholz, A., Al Asad, M. M., & Goldblatt, C. (2020). Dependence of the Interplanetary Magnetic Field on Heliocentric Distance at 0.3–1.7 AU: A Six-Spacecraft Study. *Journal of Geophysical Research: Space Physics*, *125*(3). https://doi.org/10.1029/2019JA027139

Hanneson, C., & Unsworth, M. J. (2022). *Magnetotelluric investigations of geothermal systems centred in southern British Columbia (parts of NTS 082, 083, 092, 093)* (Summary of Activities 2022–02; Summary of Activities 2021: Energy and Water, pp. 81–94). Geoscience BC.

Hanneson, C., & Unsworth, M. J. (2023a). Magnetotelluric imaging of the magmatic and geothermal systems beneath Mount Meager, southwestern Canada. *Canadian Journal of Earth Sciences*. https://doi.org/10.1139/cjes-2022-0136

Hanneson, C., & Unsworth, M. J. (2023b). Regional-scale resistivity structure of the middle and lower crust and uppermost mantle beneath the southeastern Canadian Cordillera and insights into its causes. *Geophysical Journal International*, *234*(3), 2032–2052. https://doi.org/10.1093/gji/ggad183

Harangi, S., Novák, A., Kiss, B., Seghedi, I., Lukács, R., Szarka, L., Wesztergom, V., Metwaly, M., & Gribovszki, K. (2015). Combined magnetotelluric and petrologic constrains for the nature of the magma storage system beneath the Late Pleistocene Ciomadul volcano (SE Carpathians). *Journal of Volcanology and Geothermal Research*, *290*, 82–96. https://doi.org/10.1016/j.jvolgeores.2014.12.006

Hardebol, N. J., Pysklywec, R. N., & Stephenson, R. (2012). Small-scale convection at a continental back-arc to craton transition: Application to the southern Canadian Cordillera. *Journal of Geophysical Research: Solid Earth*, *117*(B1). https://doi.org/10.1029/2011JB008431

Harris, M. A., Russell, J. K., Barendregt, R., Porritt, L. A., & Wilson, A. (2022). Explosive glaciovolcanism at Cracked Mountain Volcano, Garibaldi Volcanic Belt, Canada. *Journal of Volcanology and Geothermal Research*, *423*, 107477. https://doi.org/10.1016/j.jvolgeores.2022.107477

Hashim, L., Gaillard, F., Champallier, R., Le Breton, N., Arbaret, L., & Scaillet, B. (2013). Experimental assessment of the relationships between electrical resistivity, crustal melting and strain localization beneath the Himalayan–Tibetan Belt. *Earth and Planetary Science Letters*, *373*, 20–30. https://doi.org/10.1016/j.epsl.2013.04.026

Hashin, Z., & Shtrikman, S. (1962). A Variational Approach to the Theory of the Effective Magnetic Permeability of Multiphase Materials. *Journal of Applied Physics*, *33*(10), 3125–3131. https://doi.org/10.1063/1.1728579

Hayes, G. (2018). *Slab2—A Comprehensive Subduction Zone Geometry Model* [dataset]. U.S. Geological Survey. https://doi.org/10.5066/F7PV6JNV

Hayward, N. (2019). The 3D Geophysical Investigation of a Middle Cretaceous to Paleocene Regional Décollement in the Cordillera of Northern Canada and Alaska. *Tectonics*, *38*(1), 307–334. https://doi.org/10.1029/2018TC005295

Heinson, G., Didana, Y., Soeffky, P., Thiel, S., & Wise, T. (2018). The crustal geophysical signature of a world-class magmatic mineral system. *Scientific Reports*, *8*(1), 10608. https://doi.org/10.1038/s41598-018-29016-2

Heise, W., Caldwell, T. G., Bibby, H. M., & Bannister, S. C. (2008). Three-dimensional modelling of magnetotelluric data from the Rotokawa geothermal field, Taupo Volcanic Zone, New Zealand. *Geophysical Journal International*, *173*(2), 740–750. https://doi.org/10.1111/j.1365-246X.2008.03737.x

Heise, W., & Pous, J. (2001). Effects of anisotropy on the two-dimensional inversion procedure. *Geophysical Journal International*, *147*(3), 610–621. https://doi.org/10.1046/j.0956-540x.2001.01560.x

Hermance, J. F. (1973). Processing of magnetotelluric data. *Physics of the Earth and Planetary Interiors*, *7*(3), 349–364. https://doi.org/10.1016/0031-9201(73)90060-5

Hersir, G. P., Árnason, K., & Vilhjálmsson, A. M. (2013). *3D inversion of magnetotelluric (MT) resistivity data from Krýsuvík high temperature geothermal area in SW Iceland*. 1–14.

Hersir, G. P., Guðnason, E. Á., & Flóvenz, Ó. G. (2022). 7.04—Geophysical Exploration Techniques. In T. M. Letcher (Ed.), *Comprehensive Renewable Energy (Second Edition)* (pp. 26–79). Elsevier. https://doi.org/10.1016/B978-0-12-819727-1.00128-X

Hickson, C. J. (1994). *Character of volcanism, volcanic hazards, and risk, northern end of the Cascade magmatic arc, British Columbia and Washington State* (481; Geological Survey of Canada Bulletin, pp. 231–250). https://doi.org/10.4095/203253

Hickson, C. J., Russell, J. K., & Stasiuk, M. V. (1999). Volcanology of the 2350 B.P. Eruption of Mount Meager Volcanic Complex, British Columbia, Canada: Implications for Hazards from Eruptions in Topographically Complex Terrain. *Bulletin of Volcanology*, *60*(7), 489–507. https://doi.org/10.1007/s004450050247

Hormozzade Ghalati, F., Craven, J. A., Motazedian, D., Grasby, S. E., & Tschirhart, V. (2022). Modeling a fractured geothermal reservoir using 3-D AMT data inversion: Insights from Garibaldi Volcanic Belt, British Columbia, Canada. *Geothermics*, *105*, 102528. https://doi.org/10.1016/j.geothermics.2022.102528

Huang, K. Y., Hickson, C. J., Cotterill, D., & Champollion, Y. (2021). Geothermal Assessment of Target Formations Using Recorded Temperature Measurements for the Alberta No. 1 Geothermal Project. *Applied Sciences*, *11*(608). https://doi.org/10.3390/app11020608

Hutchinson, J., Kao, H., Riedel, M., Obana, K., Wang, K., Kodaira, S., Takahashi, T., & Yamamoto, Y. (2020). Significant geometric variation of the subducted plate beneath the northernmost Cascadia subduction zone and its tectonic implications as revealed by the 2014 MW 6.4 earthquake sequence. *Earth and Planetary Science Letters*, *551*, 116569. https://doi.org/10.1016/j.epsl.2020.116569

Hyndman, R. D. (2010). The consequences of Canadian Cordillera thermal regime in recent tectonics and elevation: A review. *Canadian Journal of Earth Sciences*, *47*(5), 621–632. https://doi.org/10.1139/E10-016

Hyndman, R. D., Currie, C. A., Mazzotti, S., & Frederiksen, A. (2009). Temperature control of continental lithosphere elastic thickness, Te vs Vs. *Earth and Planetary Science Letters*, *277*(3), 539–548. https://doi.org/10.1016/j.epsl.2008.11.023

Hyndman, R. D., Currie, C. A., & Mazzotti, S. P. (2005). Subduction zone backarcs, mobile belts, and orogenic heat. *GSA TODAY*, *15*, 4–10.

Hyndman, R. D., & Lewis, T. J. (1999). Geophysical consequences of the Cordillera–Craton thermal transition in southwestern Canada. *Tectonophysics*, *306*(3–4), 397–422. https://doi.org/10.1016/S0040-1951(99)00068-2

Hyndman, R. D., & Peacock, S. M. (2003). Serpentinization of the forearc mantle. *Earth and Planetary Science Letters*, *212*(3–4), 417–432. https://doi.org/10.1016/S0012-821X(03)00263-2

Hyndman, R. D., & Shearer, P. M. (1989). Water in the lower continental crust: Modelling magnetotelluric and seismic reflection results. *Geophysical Journal International*, *98*(2), 343–365. https://doi.org/10.1111/j.1365-246X.1989.tb03357.x

Hyndman, R. D., Vanyan, L. L., Marquis, G., & Law, L. K. (1993). The origin of electrically conductive lower continental crust: Saline water or graphite? *Physics of the Earth and Planetary Interiors*, *81*(1), 325–345. https://doi.org/10.1016/0031-9201(93)90139-Z

Irwin, W. (1990). Geology and plate-tectonic development. In *The San Andreas fault system, California.* (pp. 61–80). U.S. Government Printing Office.

Jessop, A. M. (1998). Geothermal Energy in Canada. *Geoscience Canada*, *25*(1), 33–41.

Johnston, S. T. (2008). The Cordilleran Ribbon Continent of North America. *Annual Review of Earth and Planetary Sciences*, *36*(1), 495–530. https://doi.org/10.1146/annurev.earth.36.031207.124331

Jol, H. M. (Ed.). (2009). *Ground Penetrating Radar: Theory and Applications* (First). Elsevier.

Jones, A. (2019). Geothermal Abundance in the Cascade Range (Washington / Oregon / N. California). *IOP Conference Series: Earth and Environmental Science*, *249*(012012), 1–9. https://doi.org/10.1088/1755-1315/249/1/012012

Jones, A. G., & Dumas, I. (1993). Electromagnetic images of a volcanic zone. *Physics of the Earth and Planetary Interiors*, *81*(1–4), 289–314. https://doi.org/10.1016/0031-9201(93)90137-X

Jones, A. G., & Ferguson, I. J. (2001). The electric moho. *Nature*, *409*(6818), 331–333.

Jones, A. G., & Gough, D. I. (1995). Electromagnetic images of crustal structures in southern and central Canadian Cordillera. *Canadian Journal of Earth Sciences*, *32*(10), 1541–1563. https://doi.org/10.1139/e95-126

Jones, A. G., Gough, D. I., Kurtz, R. D., DeLaurier, J. M., Boerner, D. E., Craven, J. A., Ellis, R. G., & McNeice, G. W. (1992). Electromagnetic images of regional structure in the southern Canadian Cordillera. *Geophysical Research Letters*, *19*(24), 2373–2376. https://doi.org/10.1029/92GL01457

Jones, A. G., Kurtz, R. D., Boerner, D. E., Craven, J. A., McNeice, G. W., Gough, D. I., DeLaurier, J. M., & Ellis, R. G. (1992). Electromagnetic constraints on strike-slip fault geometry—The Fraser River fault system. *Geology*, *20*(6), 561–564. https://doi.org/10.1130/0091-7613(1992)020<0561:ECOSSF>2.3.CO;2

Jones, A. G., Ledo, J., Ferguson, I. J., Craven, J. A., Unsworth, M. J., Chouteau, M., & Spratt, J. E. (2014). The electrical resistivity of Canada's lithosphere and correlation with other parameters: Contributions from Lithoprobe and other programmes. *Canadian Journal of Earth Sciences*, *51*(6), 573–617. https://doi.org/10.1139/cjes-2013-0151

Jones, D. W. R., Katz, R. F., Tian, M., & Rudge, J. F. (2018). Thermal impact of magmatism in subduction zones. *Earth and Planetary Science Letters*, *481*, 73–79. https://doi.org/10.1016/j.epsl.2017.10.015

Joplin, G. A., Kiss, E., Ware, N. G., & Widdowson, J. R. (1972). Some chemical data on members of the shoshonite association. *Mineralogical Magazine*, *38*(300), 936–945. https://doi.org/10.1180/minmag.1972.038.300.04

Karakas, O., Degruyter, W., Bachmann, O., & Dufek, J. (2017). Lifetime and size of shallow magma bodies controlled by crustal-scale magmatism. *Nature Geoscience*, *10*(6), 446–450. https://doi.org/10.1038/ngeo2959

Kay, R. W., & Kay, S. M. (1993). Delamination and delamination magmatism. *Tectonophysics*, *219*(1), 177–189. https://doi.org/10.1016/0040-1951(93)90295-U

Kelbert, A., Meqbel, N., Egbert, G. D., & Tandon, K. (2014). ModEM: A modular system for inversion of electromagnetic geophysical data. *Computers & Geosciences*, *66*, 40–53. https://doi.org/10.1016/j.cageo.2014.01.010

Kelemen, P. B., Rilling, J. L., Parmentier, E. M., Mehl, L., & Hacker, B. R. (2003). Thermal structure due to solid-state flow in the mantle wedge beneath arcs. In J. Eiler (Ed.), *Geophysical Monograph Series* (Vol. 138, pp. 293–311). American Geophysical Union. https://doi.org/10.1029/138GM13

Kirby, S., Engdahl, R. E., & Denlinger, R. (1996). Intermediate-Depth Intraslab Earthquakes and Arc Volcanism as Physical Expressions of Crustal and Uppermost Mantle Metamorphism in Subducting Slabs. In *Subduction* (pp. 195–214). American Geophysical Union (AGU). https://doi.org/10.1029/GM096p0195

Kistler, R. W., & Peterman, Z. E. (1973). Variations in Sr, Rb, K, Na, and Initial Sr87/Sr86 in Mesozoic Granitic Rocks and Intruded Wall Rocks in Central California. *GSA Bulletin*, *84*(11), 3489–3512. https://doi.org/10.1130/0016-7606(1973)84<3489:VISRKN>2.0.CO;2

Kong, W., Tan, H., Lin, C., Unsworth, M., Lee, B., Peng, M., Wang, M., & Tong, T. (2021). Three-Dimensional Inversion of Magnetotelluric Data for a Resistivity Model With Arbitrary Anisotropy. *Journal of Geophysical Research: Solid Earth*, *126*(8), e2020JB020562. https://doi.org/10.1029/2020JB020562

Kordy, M., Wannamaker, P., Maris, V., Cherkaev, E., & Hill, G. (2016). 3-D magnetotelluric inversion including topography using deformed hexahedral edge finite elements and direct solvers parallelized on SMP computers – Part I: Forward problem and parameter Jacobians. *Geophysical Journal International*, *204*(1), 74–93. https://doi.org/10.1093/gji/ggv410

Kreemer, C., Blewitt, G., & Klein, E. C. (2014). A geodetic plate motion and Global Strain Rate Model. *Geochemistry, Geophysics, Geosystems*, *15*(10), 3849–3889. https://doi.org/10.1002/2014GC005407

Kummerow, J., Raab, S., Schuessler, J. A., & Meyer, R. (2020). Non-reactive and reactive experiments to determine the electrical conductivities of aqueous geothermal solutions up to supercritical conditions. *Journal of Volcanology and Geothermal Research*, *391*, 106388. https://doi.org/10.1016/j.jvolgeores.2018.05.014

Larsen, J. C., Mackie, R. L., Manzella, A., Fiordelisi, A., & Rieven, S. (1996). Robust smooth magnetotelluric transfer functions. *Geophysical Journal International*, *124*(3), 801–819. https://doi.org/10.1111/j.1365-246X.1996.tb05639.x

Laske, G., Ma, Z., Masters, G., & Pasyanos, M. (2013). *CRUST 1.0: A new global crustal model at 1×1 degrees* [Computer software]. https://igppweb.ucsd.edu/~gabi/crust1.html

Laumonier, M., Gaillard, F., Muir, D., Blundy, J., & Unsworth, M. (2017). Giant magmatic water reservoirs at mid-crustal depth inferred from electrical conductivity and the growth of the continental crust. *Earth and Planetary Science Letters*, *457*, 173–180. https://doi.org/10.1016/j.epsl.2016.10.023

Laumonier, M., Gaillard, F., & Sifre, D. (2015). The effect of pressure and water concentration on the electrical conductivity of dacitic melts: Implication for magnetotelluric imaging in subduction areas. *Chemical Geology*, *418*, 66–76. https://doi.org/10.1016/j.chemgeo.2014.09.019

Laumonier, M., Karakas, O., Bachmann, O., Gaillard, F., Lukács, R., Seghedi, I., Menand, T., & Harangi, S. (2019). Evidence for a persistent magma reservoir with large melt content beneath an apparently extinct volcano. *Earth and Planetary Science Letters*, *521*, 79–90. https://doi.org/10.1016/j.epsl.2019.06.004

Le Bas, M. J., Le Maitre, R. W., Streckeisen, A., Zanettin, B., & IUGS Subcommission on the Systematics of Igneous Rocks. (1986). A Chemical Classification of Volcanic Rocks Based on the Total Alkali-Silica Diagram. *Journal of Petrology*, *27*(3), 745–750. https://doi.org/10.1093/petrology/27.3.745

Le Bas, M. J., Le Maitre, R. W., & Woolley, A. R. (1992). The construction of the Total Alkali-Silica chemical classification of volcanic rocks. *Mineralogy and Petrology*, *46*(1), 1–22. https://doi.org/10.1007/BF01160698

Ledo, J., & Jones, A. G. (2001). Regional electrical resistivity structure of the southern Canadian Cordillera and its physical interpretation. *Journal of Geophysical Research: Solid Earth*, *106*(B12), 30755–30769. https://doi.org/10.1029/2001JB000358

Lee, B. (2020). *Improving exploration for geothermal resources with the magnetotelluric method* [PhD]. University of Alberta.

Lee, B., Unsworth, M., Árnason, K., & Cordell, D. (2020). Imaging the magmatic system beneath the Krafla geothermal field, Iceland: A new 3-D electrical resistivity model from inversion of magnetotelluric data. *Geophysical Journal International*, *220*(1), 541–567. https://doi.org/10.1093/gji/ggz427

Lemieux, S. (1999). Seismic Reflection Expression and Tectonic Significance of Late Cretaceous Extensional Faulting of the Western Canada Sedimentary Basin in Southern Alberta. *Bulletin of Canadian Petroleum Geology*, *47*(4), 375–390.

Lewis, J. F., & Jessop, A. M. (1981). Heat flow in the Garibaldi volcanic belt, a possible Canadian geothermal energy resource area. *Canadian Journal of Earth Sciences*, *18*, 366–375. https://doi.org/10.1139/e81-028

Li, B., Zhang, L., Guo, X., Li, W.-C., & Ni, H. (2020). Electrical conductivity of shoshonitic melts with application to magma reservoir beneath the Wudalianchi volcanic field, northeast China. *Physics of the Earth and Planetary Interiors*, *306*, 106545. https://doi.org/10.1016/j.pepi.2020.106545

Light, T. S., Licht, S., Bevilacqua, A. C., & Morash, K. R. (2004). The Fundamental Conductivity and Resistivity of Water. *Electrochemical and Solid-State Letters*, *8*(1), E16. https://doi.org/10.1149/1.1836121

Limberger, J., Boxem, T., Pluymaekers, M., Bruhn, D., Manzella, A., Calcagno, P., Beekman, F., Cloetingh, S., & van Wees, J.-D. (2018). Geothermal energy in deep aquifers: A global assessment of the resource base for direct heat utilization. *Renewable and Sustainable Energy Reviews*, *82*, 961–975. https://doi.org/10.1016/j.rser.2017.09.084

Lorencak, M., Kohn, B. P., Osadetz, K. G., & Gleadow, A. J. W. (2004). Combined apatite fission track and (U–Th)/He thermochronometry in a slowly cooled terrane: Results from a 3440-

m-deep drill hole in the southern Canadian Shield. *Earth and Planetary Science Letters*, *227*(1), 87–104. https://doi.org/10.1016/j.epsl.2004.08.015

Magee, C., Stevenson, C. T. E., Ebmeier, S. K., Keir, D., Hammond, J. O. S., Gottsmann, J. H., Whaler, K. A., Schofield, N., Jackson, C. A.-L., Petronis, M. S., O'Driscoll, B., Morgan, J., Cruden, A., Vollgger, S. A., Dering, G., Micklethwaite, S., & Jackson, M. D. (2018). Magma Plumbing Systems: A Geophysical Perspective. *Journal of Petrology*, *59*(6), 1217–1251. https://doi.org/10.1093/petrology/egy064

Majorowicz, J. A., & Gough, D. I. (1994). A Model of Crustal Conductive Structure In the Canadian Cordillera. *Geophysical Journal International*, *117*(2), 301–312. https://doi.org/10.1111/j.1365-246X.1994.tb03934.x

Majorowicz, J., & Grasby, S. E. (2010a). Heat flow, depth–temperature variations and stored thermal energy for enhanced geothermal systems in Canada. *Journal of Geophysics and Engineering*, *7*(3), 232–241. https://doi.org/10.1088/1742-2132/7/3/002

Majorowicz, J., & Grasby, S. E. (2010b). High Potential Regions for Enhanced Geothermal Systems in Canada. *Natural Resources Research*, *19*(3), 177–188. https://doi.org/10.1007/s11053-010-9119-8

Manley, C. R., Glazner, A. F., & Farmer, G. L. (2000). Timing of volcanism in the Sierra Nevada of California: Evidence for Pliocene delamination of the batholithic root? *Geology*, *28*(9), 811–814. https://doi.org/10.1130/0091-7613(2000)28<811:TOVITS>2.0.CO;2

Manning, C. E. (2018). Fluids of the Lower Crust: Deep Is Different. *Annual Review of Earth and Planetary Sciences*, *46*(1). https://doi.org/10.1146/annurev-earth-060614-105224

Marquis, G., Jones, A. G., & Hyndman, R. D. (1995). Coincident conductive and reflective middle and lower crust in southern British Columbia. *Geophysical Journal International*, *120*(1), 111–131. https://doi.org/10.1111/j.1365-246X.1995.tb05915.x

Massey, F. J. (1951). The Kolmogorov-Smirnov Test for Goodness of Fit. *Journal of the American Statistical Association*, *46*(253), 68–78. https://doi.org/10.1080/01621459.1951.10500769

Maxwell, J. C. (1873). *A Treatise on Electricity and Magnetism* (Vol. 1). Cambridge University Press.

McCrory, P. A., Blair, J. L., Waldhauser, F., & Oppenheimer, D. H. (2012). Juan de Fuca slab geometry and its relation to Wadati-Benioff zone seismicity. *Journal of Geophysical Research: Solid Earth*, *117*(B9). https://doi.org/10.1029/2012JB009407

McCuaig, T. C., Beresford, S., & Hronsky, J. (2010). Translating the mineral systems approach into an effective exploration targeting system. *Ore Geology Reviews*, *38*(3), 128–138. https://doi.org/10.1016/j.oregeorev.2010.05.008

McDonough, M. R., & Simony, P. S. (1988). Structural evolution of basement gneisses and Hadrynian cover, Bulldog Creek area, Rocky Mountains, British Columbia. *Canadian Journal of Earth Sciences*. https://doi.org/10.1139/e88-159

McMechan, M. E. (2012). Deep transverse basement structural control of mineral systems in the southeastern Canadian Cordillera. *Canadian Journal of Earth Sciences*, *49*(5), 693–708. https://doi.org/10.1139/e2012-013

McMechan, M. E., & Thompson, R. I. (1989). Structural Style and History of the Rocky Mountain Fold and Thrust Belt. In *Western Canada Sedimentary Basin: A Case History* (pp. 47–71).

Meqbel, N. M., Egbert, G. D., Wannamaker, P. E., Kelbert, A., & Schultz, A. (2014). Deep electrical resistivity structure of the northwestern U.S. derived from 3-D inversion of USArray magnetotelluric data. *Earth and Planetary Science Letters*, *402*, 290–304. https://doi.org/10.1016/j.epsl.2013.12.026

Moeck, I. S. (2014). Catalog of geothermal play types based on geologic controls. *Renewable and Sustainable Energy Reviews*, *37*, 867–882. https://doi.org/10.1016/j.rser.2014.05.032

Monger, J. W. H., & Price, R. A. (2002). The Canadian Cordillera: Geology and tectonic evolution. *Canadian Society of Exploration Geophysicists Recorder*, *27*, 17–36.

Monger, J. W. H., Price, R. A., & Tempelman-Kluit, D. J. (1982). Tectonic accretion and the origin of the two major metamorphic and plutonic welts in the Canadian Cordillera. *Geology*, *10*(2), 70–75. https://doi.org/10.1130/0091-7613(1982)10<70:TAATOO>2.0.CO;2

Morrison, G. W. (1980). Characteristics and tectonic setting of the shoshonite rock association. *Lithos*, *13*(1), 97–108. https://doi.org/10.1016/0024-4937(80)90067-5

Muhammad, M., Williams-Jones, G., & Barendregt, R. W. (2021). *Applications of structural geology to the exploration of geothermal systems, Mt. Meager, BC* (Report 2021–08; Chapter 8, pp. 177–241). Geoscience BC.

Mullen, E. K., & Weis, D. (2015). Evidence for trench-parallel mantle flow in the northern Cascade Arc from basalt geochemistry. *Earth and Planetary Science Letters*, *414*, 100–107. https://doi.org/10.1016/j.epsl.2015.01.010

Mullen, E. K., Weis, D., Marsh, N. B., & Martindale, M. (2017). Primitive arc magma diversity: New geochemical insights in the Cascade Arc. *Chemical Geology*, *448*, 43–70. https://doi.org/10.1016/j.chemgeo.2016.11.006

Müller, D., Bredemeyer, S., Zorn, E., De Paolo, E., & Walter, T. R. (2021). Surveying fumarole sites and hydrothermal alteration by unoccupied aircraft systems (UAS) at the La Fossa cone, Vulcano Island (Italy). *Journal of Volcanology and Geothermal Research*, *413*, 107208. https://doi.org/10.1016/j.jvolgeores.2021.107208

Munch, F. D., & Grayver, A. (2023). Multi-scale imaging of 3-D electrical conductivity structure under the contiguous US constrains lateral variations in the upper mantle water content. *Earth and Planetary Science Letters*, *602*, 117939. https://doi.org/10.1016/j.epsl.2022.117939

Muñoz, G. (2014). Exploring for Geothermal Resources with Electromagnetic Methods. *Surveys in Geophysics*, *35*(1), 101–122. https://doi.org/10.1007/s10712-013-9236-0

Natural Resources Canada. (2022). *Energy Fact Book 2021-2022*. https://natural-resources.canada.ca/sites/nrcan/files/energy/energy_fact/2021-2022/PDF/2021_Energy-factbook_december23_EN_accessible.pdf

Nesbitt, B. E. (1993). Electrical resistivities of crustal fluids. *Journal of Geophysical Research: Solid Earth*, *98*(B3), 4301–4310. https://doi.org/10.1029/92JB02576

Nesbitt, B. E., & Muehlenbachs, K. (1995). Geochemical studies of the origins and effects of synorogenic crustal fluids in the southern Omineca Belt of British Columbia, Canada. *Bulletin of the Geological Society of America*, *107*(9), 1033–1050. https://doi.org/10.1130/0016-7606(1995)107<1033:GSOTOA>2.3.CO;2

Nevin, A. E., Crandall, J. T., Souther, J. G., & Stauder, J. (1978). Meager Creek geothermal system, British Columbia, Part I: Exploration and Research Program. *Geothermal Resources Council Transactions*, *2*, 491–493.

Ni, H., Keppler, H., & Behrens, H. (2011). Electrical conductivity of hydrous basaltic melts: Implications for partial melting in the upper mantle. *Contributions to Mineralogy and Petrology*, *162*(3), 637–650. https://doi.org/10.1007/s00410-011-0617-4

Nieuwenhuis, G., Unsworth, M. J., Pana, D., Craven, J., & Bertrand, E. (2014). Three-dimensional resistivity structure of Southern Alberta, Canada: Implications for Precambrian tectonics. *Geophysical Journal International*, *197*(2), 838–859. https://doi.org/10.1093/gji/ggu068

Nono, F., Gibert, B., Parat, F., Loggia, D., Cichy, S. B., & Violay, M. (2020). Electrical conductivity of Icelandic deep geothermal reservoirs up to supercritical conditions: Insight from laboratory experiments. *Journal of Volcanology and Geothermal Research*, *391*, 106364. https://doi.org/10.1016/j.jvolgeores.2018.04.021

North, F. K., & Henderson, G. G. L. (1954). The Rocky Mountain Trench. In *Guide Book Fourth Annual Field Conference Banff-Golden-Radium* (pp. 82–100). Canadian Society of Petroleum Geologists.

Olhoeft, G. R. (1981). Electrical properties of granite with implications for the lower crust. *Journal of Geophysical Research: Solid Earth*, *86*(B2), 931–936. https://doi.org/10.1029/JB086iB02p00931

Park, S. K., Hirasuna, B., Jiracek, G. R., & Kinn, C. (1996). Magnetotelluric evidence of lithospheric mantle thinning beneath the southern Sierra Nevada. *Journal of Geophysical Research: Solid Earth*, *101*(B7), 16241–16255. https://doi.org/10.1029/96JB01211

Parker, R. L., & Whaler, K. A. (1981). Numerical methods for establishing solutions to the inverse problem of electromagnetic induction. *Journal of Geophysical Research: Solid Earth*, *86*(B10), 9574–9584. https://doi.org/10.1029/JB086iB10p09574

Parrish, R. R., Carr, S. D., & Parkinson, D. L. (1988). Eocene extensional tectonics and geochronology of the Southern Omineca Belt, British Columbia and Washington. *Tectonics*, *7*(2), 181–212. https://doi.org/10.1029/TC007i002p00181

Patro, P. K., & Egbert, G. D. (2008). Regional conductivity structure of Cascadia: Preliminary results from 3D inversion of USArray transportable array magnetotelluric data. *Geophysical Research Letters*, *35*(20), L20311. https://doi.org/10.1029/2008GL035326

Peacock, J. R., & Siler, D. L. (2021). Bottom-up and top-down control on hydrothermal resources in the Great Basin: An example from Gabbs Valley, Nevada. *Geophysical Research Letters*, *48*(23), 1–10. https://doi.org/10.1029/2021GL095009

Peacock, S. M., & Wang, K. (1999). Seismic Consequences of Warm Versus Cool Subduction Metamorphism: Examples from Southwest and Northeast Japan. *Science*, *286*(5441), 937–939. https://doi.org/10.1126/science.286.5441.937

Pearson, D. G., Scott, J. M., Liu, J., Schaeffer, A., Wang, L. H., van Hunen, J., Szilas, K., Chacko, T., & Kelemen, P. B. (2021). Deep continental roots and cratons. *Nature*, *596*(7871), Article 7871. https://doi.org/10.1038/s41586-021-03600-5

Pellerin, L., Johnston, J. M., & Hohmann, G. W. (1996). A numerical evaluation of electromagnetic methods in geothermal exploration. *Geophysics*, *61*(1), 121–130. https://doi.org/10.1190/1.1443931

Pe-Piper, G., Piper, D. J. W., Koukouvelas, I., Dolansky, L. M., & Kokkalas, S. (2009). Postorogenic shoshonitic rocks and their origin by melting underplated basalts: The Miocene of Limnos, Greece. *Bulletin of the Geological Society of America*, *121*(1–2), 39–54. https://doi.org/10.1130/B26317.1

Pham Van Ngoc. (1977). *Magneto-Telluric Reconnaissance Survey in the Lillooet Valley British Columbia* (Open File 77-20(E); Earth Physics Branch, p. 63). Energy, Mines and Resources Canada.

Pham Van Ngoc. (1978). *Magneto-Telluric Prospecting in the Mount Meager Geothermal Region (British Columbia)* (Open File 78-6(E); Earth Physics Branch, p. 71). Energy, Mines and Resources Canada.

Pham Van Ngoc. (1980). *Magneto-Telluric Survey of the Mount Meager Region of the Squamish Valley (British Columbia)* (Open File 80-8(E); Earth Physics Branch, p. 77). Energy, Mines and Resources Canada.

Pierson, H. O. (1993). *Handbook of Carbon, Graphite, Diamond and Fullerenes* (First Edition). Noyes Publications.

Pilkington, M., Miles, W. F., Ross, G. M., & Roest, W. R. (2000). Potential-field signatures of buried Precambrian basement in the Western Canada Sedimentary Basin. *Canadian Journal of Earth Sciences*, *37*(11), 1453–1471. https://doi.org/10.1139/e00-020

Popa, M., Radulian, M., Szakács, A., Seghedi, I., & Zaharia, B. (2012). New Seismic and Tomography Data in the Southern Part of the Harghita Mountains (Romania, Southeastern Carpathians): Connection with Recent Volcanic Activity. *Pure and Applied Geophysics*, *169*(9), 1557–1573. https://doi.org/10.1007/s00024-011-0428-6

Porter, J. W., Price, R. A., McCrossan, R. G., Kent, P., Bott, M. H. P., McKenzie, D. P., & Williams, C. A. (1982). The Western Canada sedimentary basin. *Philosophical Transactions of the Royal Society of London. Series A, Mathematical and Physical Sciences*, *305*(1489), 169–192. https://doi.org/10.1098/rsta.1982.0032

Prentice, I. C., Farquhar, G. D., Fasham, M. J. R., Goulden, M. L., Heimann, M., Jaramillo, V. J., Kheshgi, H. S., Quéré, C. L., Scholes, R. J., Wallace, D. W. R., Archer, D., Ashmore, M. R., Aumont, O., Baker, D., Battle, M., Bender, M., Bopp, L. P., Bousquet, P., Caldeira, K., … Yool, A. (2001). The carbon cycle and atmospheric carbon dioxide. In *Climate change 2001: The scientific basis*. Intergovernmental panel on climate change. https://hal.science/hal-03333974

Price, R. A. (1986). The southeastern Canadian Cordillera: Thrust faulting, tectonic wedging, and delamination of the lithosphere. *Journal of Structural Geology*, *8*(3–4), 239–254. https://doi.org/10.1016/0191-8141(86)90046-5

Prouteau, G., & Scaillet, B. (2003). Experimental Constraints on the Origin of the 1991 Pinatubo Dacite. *Journal of Petrology*, *44*(12), 2203–2241. https://doi.org/10.1093/petrology/egg075

Read, P. B. (1990). Mount Meager Complex, Garibaldi Belt, Southwestern British Columbia. *Geoscience Canada*. https://journals.lib.unb.ca/index.php/GC/article/view/3672

Reagan, M. K., Sims, K. W. W., Erich, J., Thomas, R. B., Cheng, H., Edwards, R. L., Layne, G., & Ball, L. (2003). Time-scales of Differentiation from Mafic Parents to Rhyolite in North American

Continental Arcs. *Journal of Petrology*, *44*(9), 1703–1726. https://doi.org/10.1093/petrology/egg057

Rikitake, T. (1948). Notes on the Electromagnetic Induction within the Earth. *Bulletin of the Earthquake Research Institute, University of Tokyo*, *24*(1–4), 1–9. https://doi.org/10.15083/0000034291

Rippe, D., Unsworth, M. J., & Currie, C. A. (2013). Magnetotelluric constraints on the fluid content in the upper mantle beneath the southern Canadian Cordillera: Implications for rheology. *Journal of Geophysical Research: Solid Earth*, *118*(10), 5601–5624. https://doi.org/10.1002/jgrb.50255

Roberti, G., Ward, B., van Wyk de Vries, B., Falorni, G., Menounos, B., Friele, P., Williams-Jones, G., Clague, J. J., Perotti, G., Giardino, M., Baldeon, G., & Freschi, S. (2018, June 3). Landslides and glacier retreat at Mt. Meager volcano: Hazard and risk challenges. *Proceedings of Geohazards 7 Conference*. https://cgs.ca/docs/geohazards/canmore2018/GeoHazards2018/pdfs/geohaz149.pdf

Roberti, G., Ward, B., van Wyk de Vries, B., Le Corvec, N., Venugopal, S., Williams-Jones, G., Clague, J. J., Friele, P., Falorni, G., Baldeon, G., Perotti, L., Giardino, M., & Menounos, B. (2021). Could Glacial Retreat-Related Landslides Trigger Volcanic Eruptions? Insights from Mount Meager, British Columbia. In *Catastrophic Landslides and Frontiers of Landslide Science* (Vol. 5, pp. 147–151). Springer Nature. https://doi.org/10.1007/978-3-030-60319-9

Ross, G. M. (1991). Precambrian basement in the Canadian Cordillera: An introduction. *Canadian Journal of Earth Sciences*, *28*(8), 1133–1139. https://doi.org/10.1139/e91-103

Ross, G. M. (2002). Evolution of Precambrian continental lithosphere in Western Canada: Results from Lithoprobe studies in Alberta and beyond. *Canadian Journal of Earth Sciences*, *39*(3), 413–437. https://doi.org/10.1139/e02-012

Ross, G. M., Parrish, R. R., Villeneuve, M. E., & Bowring, S. A. (1991). Geophysics and geochronology of the crystalline basement of the Alberta Basin, western Canada. *Canadian Journal of Earth Sciences*, *28*(4), 512–522. https://doi.org/10.1139/e91-045

Russell, J. K., Stewart, M., Wilson, A., & Williams-Jones, G. (2021). Eruption of Mount Meager, British Columbia, during the early Fraser glaciation. *Canadian Journal of Earth Sciences*, *58*(10), 1146–1154. https://doi.org/10.1139/cjes-2021-0023

Rychert, C. A., Harmon, N., Constable, S., & Wang, S. (2020). The Nature of the Lithosphere-Asthenosphere Boundary. *Journal of Geophysical Research: Solid Earth*, *125*(10), e2018JB016463. https://doi.org/10.1029/2018JB016463

Samrock, F., Grayver, A. V., Bachmann, O., Karakas, Ö., & Saar, M. O. (2021). Integrated magnetotelluric and petrological analysis of felsic magma reservoirs: Insights from Ethiopian rift volcanoes. *Earth and Planetary Science Letters*, *559*, 116765. https://doi.org/10.1016/j.epsl.2021.116765

Savard, G., Bostock, M. G., & Christensen, N. I. (2018). Seismicity, Metamorphism, and Fluid Evolution Across the Northern Cascadia Fore Arc. *Geochemistry, Geophysics, Geosystems*, *19*(6), 1881–1897. https://doi.org/10.1029/2017GC007417

Schaeffer, A. J., & Lebedev, S. (2014). Imaging the North American continent using waveform inversion of global and USArray data. *Earth and Planetary Science Letters*, *402*, 26–41. https://doi.org/10.1016/j.epsl.2014.05.014

Schellart, W. P., & Rawlinson, N. (2013). Global correlations between maximum magnitudes of subduction zone interface thrust earthquakes and physical parameters of subduction zones. *Physics of the Earth and Planetary Interiors*, *225*, 41–67. https://doi.org/10.1016/j.pepi.2013.10.001

Schmandt, B., & Humphreys, E. (2011). Seismically imaged relict slab from the 55 Ma Siletzia accretion to the northwest United States. *Geology*, *39*(2), 175–178. https://doi.org/10.1130/G31558.1

Selway, K. (2014). On the Causes of Electrical Conductivity Anomalies in Tectonically Stable Lithosphere. *Surveys in Geophysics*, *35*(1), 219–257. https://doi.org/10.1007/s10712-013-9235-1

Shore, G. A. (1978). Meager Creek geothermal system, British Columbia, Part III: Resistivity Methods and Results. *Geothermal Resources Council Transactions*, *2*, 593–596.

Simony, P. S., & Carr, S. D. (2011). Cretaceous to Eocene evolution of the southeastern Canadian Cordillera: Continuity of Rocky Mountain thrust systems with zones of “in-sequence” mid-crustal flow. *Journal of Structural Geology*, *33*(9), 1417–1434. https://doi.org/10.1016/j.jsg.2011.06.001

Simpson, F., & Bahr, K. (2005). *Practical Magnetotellurics*. Cambridge University Press.

Sinmyo, R., & Keppler, H. (2017). Electrical conductivity of NaCl-bearing aqueous fluids to 600 °C and 1 GPa. *Contributions to Mineralogy and Petrology*, *172*(1), 4. https://doi.org/10.1007/s00410-016-1323-z

Siripunvaraporn, W. (2012). Three-Dimensional Magnetotelluric Inversion: An Introductory Guide for Developers and Users. *Surveys in Geophysics*, *33*(1), 5–27. https://doi.org/10.1007/s10712-011-9122-6

Siripunvaraporn, W., & Egbert, G. (2009). WSINV3DMT: Vertical magnetic field transfer function inversion and parallel implementation. *Physics of the Earth and Planetary Interiors*, *173*(3), 317–329. https://doi.org/10.1016/j.pepi.2009.01.013

Siripunvaraporn, W., Egbert, G., Lenbury, Y., & Uyeshima, M. (2005). Three-dimensional magnetotelluric inversion: Data-space method. *Physics of the Earth and Planetary Interiors*, *150*(1), 3–14. https://doi.org/10.1016/j.pepi.2004.08.023

Smaï, F., & Wawrzyniak, P. (2020). Razorback, an Open Source Python Library for Robust Processing of Magnetotelluric Data. *Frontiers in Earth Science*, *8*. https://www.frontiersin.org/articles/10.3389/feart.2020.00296

Solomon, S., Plattner, G.-K., Knutti, R., & Friedlingstein, P. (2009). Irreversible climate change due to carbon dioxide emissions. *Proceedings of the National Academy of Sciences*, *106*(6), 1704–1709. https://doi.org/10.1073/pnas.0812721106

Souther, J. G. (1981). Canadian Geothermal Research Program. *American Association of Petroleum Geologists*, *177*, 391–400.

Soyer, W., & Unsworth, M. (2006). Deep electrical structure of the northern Cascadia (British Columbia, Canada) subduction zone: Implications for the distribution of fluids. *Geology*, *34*(1), 53. https://doi.org/10.1130/G21951.1

Srivastava, J. K., Prasad, M., & Wagner, J. B. (1985). Electrical Conductivity of Silicon Dioxide Thermally Grown on Silicon. *Journal of The Electrochemical Society*, *132*(4), 955. https://doi.org/10.1149/1.2113993

Stasiuk, M. V., Russell, J. K., & Hickson, C. J. (1996). Distribution, nature, and origins of the 2400 BP eruption products of Mount Meager, British Columbia: Linkages between magma chemistry and eruption behaviour. *Geological Survey of Canada Bulletin*, *486*, 1–27.

Stern, R. J. (2002). Subduction zones. *Reviews of Geophysics*, *40*(4), 1012. https://doi.org/10.1029/2001RG000108

Syracuse, E. M., van Keken, P. E., & Abers, G. A. (2010). The global range of subduction zone thermal models. *Physics of the Earth and Planetary Interiors*, *183*(1), 73–90. https://doi.org/10.1016/j.pepi.2010.02.004

Thompson, R., Glombick, P., Erdmer, P., Heaman, L., Lemieux, Y., & Daughtry, K. L. (2006). Evolution of the ancestral Pacific margin, southern Canadian Cordillera: Insights from new geologic maps. *Geological Association of Canada Special Paper*, *45*, 433–482.

Tikhonov, A. N. (1950). On determining electric characteristics of the deep layers of the Earth's crust. *Dolk. Acad. Nauk. SSSR*, *73*, 295–297.

Turner, S., Hawkesworth, C., Liu, J., Rogers, N., Kelley, S., & van Calsteren, P. (1993). Timing of Tibetan uplift constrained by analysis of volcanic rocks. *Nature*, *364*(6432), 50–54. https://doi.org/10.1038/364050a0

Tuya Terra Geo Corp. (2016). *Direct-use Geothermal Resources in British Columbia* (Geoscience BC Report 2016–07; Summary of Findings, p. 38). Geoscience BC.

United Nations Development Programme. (2019). *Human Development Report. Beyond income, beyond averages, beyond today: Inequalities in human development in the 21st century.* http://www.hdr.undp.org/en

Unsworth, M. J., Hanneson, C., Williamson, A. R., & Vestrum, Z. E. (2021). *Final report on the 2019-2020 broadband magnetotelluric study at Mount Meager: Implications for structure of the hydrothermal and magmatic system* (Report 2021–08; Chapter 5, pp. 79–146). Geoscience BC.

Ussher, G., Harvey, C., Johnstone, R., & Anderson, E. (2000). *Understanding the resistivities observed in geothermal systems*. 1915–1920.

Usui, Y., Ogawa, Y., Aizawa, K., Kanda, W., Hashimoto, T., Koyama, T., Yamaya, Y., & Kagiyama, T. (2017). Three-dimensional resistivity structure of Asama Volcano revealed by data-space magnetotelluric inversion using unstructured tetrahedral elements. *Geophysical Journal International*, *208*(3), 1359–1372. https://doi.org/10.1093/gji/ggw459

van der Velden, A. J., & Cook, F. A. (1996). Structure and tectonic development of the southern Rocky Mountain trench. *Tectonics*, *15*(3), 517–544. https://doi.org/10.1029/95TC03288

Venugopal, S., Moune, S., Williams-Jones, G., Druitt, T., Vigouroux, N., Wilson, A., & Russell, J. K. (2020). Two distinct mantle sources beneath the Garibaldi Volcanic Belt: Insight from olivine-hosted melt inclusions. *Chemical Geology*, *532*, 119346. https://doi.org/10.1016/j.chemgeo.2019.119346

Wang, E. (2019). *Multidimensional magnetotelluric studies of the Precambrian Alberta basement* [PhD]. University of Alberta.

Wang, E., & Unsworth, M. (2022). Three-dimensional crustal and upper-mantle resistivity structure of Alberta, Canada: Implications for Precambrian tectonics. *Geophysical Journal International*, *230*(3), 1679–1698. https://doi.org/10.1093/gji/ggac128

Warwick, R., Williams-Jones, G., Kelman, M., & Witter, J. (2022). A scenario-based volcanic hazard assessment for the Mount Meager Volcanic Complex, British Columbia. *Journal of Applied Volcanology*, *11*(1), 5. https://doi.org/10.1186/s13617-022-00114-1

Watson, H. C., Roberts, J. J., & Tyburczy, J. A. (2010). Effect of conductive impurities on electrical conductivity in polycrystalline olivine. *Geophysical Research Letters*, *37*(2). https://doi.org/10.1029/2009GL041566

Weisstein, E. W. (2023a). *Hippopede* [Text]. MathWorld--A Wolfram Web Resource; Wolfram Research, Inc. https://mathworld.wolfram.com/Hippopede.html

Weisstein, E. W. (2023b). *Quadrifolium* [Text]. MathWorld--A Wolfram Web Resource; Wolfram Research, Inc. https://mathworld.wolfram.com/Quadrifolium.html

Wiese, H. (1962). Geomagnetische Tiefentellurik Teil II: Die Streichrichtung der untergrundstrukturen des elektrischen Widerstandes, erschlossen aus geomagnetischen

Variationen (Strike direction of underground structures of electric resistivity, inferred from geomagnetic variations). *Geofisica pura e applicata (Pure and applied geophysics)*, *52*(1), 83–103. https://doi.org/10.1007/BF01996002

Wilson, C. R., Spiegelman, M., van Keken, P. E., & Hacker, B. R. (2014). Fluid flow in subduction zones: The role of solid rheology and compaction pressure. *Earth and Planetary Science Letters*, *401*, 261–274. https://doi.org/10.1016/j.epsl.2014.05.052

Wise, T., & Thiel, S. (2020). Proterozoic tectonothermal processes imaged with magnetotellurics and seismic reflection in southern Australia. *Geoscience Frontiers*, *11*(3), 885–893. https://doi.org/10.1016/j.gsf.2019.09.006

Wisian, K. W., & Blackwell, D. D. (2004). Numerical modeling of Basin and Range geothermal systems. *Geothermics*, *33*(6), 713–741. https://doi.org/10.1016/j.geothermics.2004.01.002

Witter, J. (2019). *South Meager Geothermal Project: New Perspectives from Recently Unearthed Data* (2019–07; pp. 1–5). Geoscience BC.

Xi-shuo Wang. (1988). Inversion of magnetovariation event to causative current. III. Test of channelled current model, SABC conductor inverted as chennelled currents and structure evaluation. *Physics of the Earth and Planetary Interiors*, *53*(1), 64–79. https://doi.org/10.1016/0031-9201(88)90137-9

Yang, B., Egbert, G. D., Zhang, H., Meqbel, N., & Hu, X. (2021). Electrical resistivity imaging of continental United States from three-dimensional inversion of EarthScope USArray magnetotelluric data. *Earth and Planetary Science Letters*, *576*, 117244. https://doi.org/10.1016/j.epsl.2021.117244

Yoshino, T., & Noritake, F. (2011). Unstable graphite films on grain boundaries in crustal rocks. *Earth and Planetary Science Letters*, *306*(3), 186–192. https://doi.org/10.1016/j.epsl.2011.04.003

Yu, T.-C., Currie, C. A., Unsworth, M. J., & Chase, B. F. W. (2022). The Structure and Dynamics of the Uppermost Mantle of Southwestern Canada From a Joint Analysis of Geophysical Observations. *Journal of Geophysical Research: Solid Earth*, *127*(10), e2022JB024130. https://doi.org/10.1029/2022JB024130

Zaporozan, T., Frederiksen, A. W., Bryksin, A., & Darbyshire, F. (2018). Surface-wave images of western Canada: Lithospheric variations across the Cordillera–craton boundary. *Canadian Journal of Earth Sciences*, *55*(8), 887–896. https://doi.org/10.1139/cjes-2017-0277

Zhang, B.-H., Guo, X., Yoshino, T., & Xia, Q.-K. (2021). Electrical conductivity of melts: Implications for conductivity anomalies in the Earth's mantle. *National Science Review*, *nwab064*. https://doi.org/10.1093/nsr/nwab064

Zhang, Z., & Duan, Z. (2005). Prediction of the PVT properties of water over wide range of temperatures and pressures from molecular dynamics simulation. *Physics of the Earth and Planetary Interiors*, *149*(3), 335–354. https://doi.org/10.1016/j.pepi.2004.11.003

A. Appendix

Table A.1 lists the computing resources used during the research presented in this thesis. Table A.2 lists the fieldwork undertaken by Cedar Hanneson while a graduate student at the University of Alberta.

***Table A.1**: Digital Research Alliance of Canada (Compute Canada prior to April 1, 2022) computing resources used by Cedar Hanneson while a graduate student at the University of Alberta.*

Accounting Year	Dates	CPU Usage (core years)
2018	2018/04 – 2019/03	2.5
2019	2019/04 – 2020/03	69.8
2020	2020/04 – 2021/03	138.3
2021	2021/04 – 2022/03	157.7
2022	2022/04 – 2023/03	152.8
Total		**521.1**

***Table A.2**: Magnetotelluric fieldwork undertaken by Cedar Hanneson while a graduate student at the University of Alberta.*

Location	Year	Start Date	End Date	Number of Days
Southeastern BC	2018	May 9	May 16	8
Southeastern BC	2018	May 31	June 12	13
Southeastern BC	2018	June 30	July 4	5
Southeastern BC	2018	August 2	August 8	7
Southeastern BC	2018	September 16	September 19	4
Peru	2019	May 16	June 10	26
Mount Meager	2019	June 28	July 30	33
Mount Meager	2020	August 3	August 17	15
Saskatchewan	2021	May 17	May 26	10
Saskatchewan	2021	June 2	June 10	9
Yukon	2021	July 17	August 7	22
Mount Cayley	2021	August 16	August 29	14
Vancouver Island	2021	November 16	November 21	6
Vancouver Island	2022	July 4	July 11	8
Northern Alberta	2022	October 17	October 18	2
Total				**182**

B. Supplementary materials for Chapter 4

B.1. Magnetotelluric data

Table B.1 lists all 66 MT sites that were used in the inversion to create the published model.

Table B.1*: Details of the MT stations that were used in the inversion described in Chapter 4. The 1982 stations were described by Flores-Luna (1986) and the 2001 stations were described by Candy (2001).*

Station Name	Latitude (°N)	Longitude (°W)	Year	Institution / Company	Instrument
MGR101	50.685	123.478	2019	University of Alberta	Phoenix MTU-5A
MGR102	50.623	123.401	2019	University of Alberta	Phoenix MTU-5A
MGR103	50.684	123.493	2019	University of Alberta	Phoenix MTU-5A
MGR104	50.514	123.436	2019	University of Alberta	Phoenix MTU-5A
MGR106	50.510	123.536	2019	University of Alberta	Phoenix MTU-5A
MGR107	50.593	123.354	2019	University of Alberta	Phoenix MTU-5A
MGR108	50.604	123.484	2019	University of Alberta	Phoenix MTU-5A
MGR109	50.547	123.558	2019	University of Alberta	Phoenix MTU-5A
MGR110	50.600	123.671	2019	University of Alberta	Phoenix MTU-5A
MGR111	50.733	123.707	2019	University of Alberta	Phoenix MTU-5A
MGR112	50.580	123.620	2019	University of Alberta	Phoenix MTU-5A
MGR113	50.736	123.470	2019	University of Alberta	Phoenix MTU-5A
MGR114	50.643	123.554	2019	University of Alberta	Phoenix MTU-5A
MGR115	50.734	123.578	2019	University of Alberta	Phoenix MTU-5A
MGR116	50.618	123.572	2019	University of Alberta	Phoenix MTU-5A
MGR117	50.638	123.528	2019	University of Alberta	Phoenix MTU-5A
MGR118	50.625	123.479	2019	University of Alberta	Phoenix MTU-5A
MGR119	50.486	123.498	2019	University of Alberta	Phoenix MTU-5A
MGR120	50.562	123.417	2019	University of Alberta	Phoenix MTU-5A
MGR121	50.697	123.355	2019	University of Alberta	Phoenix MTU-5A
MGR122	50.600	123.434	2019	University of Alberta	Phoenix MTU-5A
MGR123	50.658	123.427	2019	University of Alberta	Phoenix MTU-5A
MGR201	50.679	123.557	2020	University of Alberta	Phoenix MTU-5A
MGR202	50.711	123.610	2020	University of Alberta	Phoenix MTU-5A
MGR203	50.612	123.625	2020	University of Alberta	Phoenix MTU-5A
MGR204	50.602	123.546	2020	University of Alberta	Phoenix MTU-5A
MGR205	50.648	123.606	2020	University of Alberta	Phoenix MTU-5A
MGR206	50.531	123.610	2020	University of Alberta	Phoenix MTU-5A
MGR207	50.640	123.687	2020	University of Alberta	Phoenix MTU-5A
MGR208	50.690	123.679	2020	University of Alberta	Phoenix MTU-5A
MGR209	50.532	123.409	2020	University of Alberta	Phoenix MTU-5A
MGR210	50.602	123.600	2020	University of Alberta	Phoenix MTU-5A
MGR211	50.550	123.593	2020	University of Alberta	Phoenix MTU-5A
MGR212	50.543	123.485	2020	University of Alberta	Phoenix MTU-5A

mt01	50.573	123.561	2001	Frontier Geosciences Inc.	Metronix ADU-06
mt02	50.567	123.558	2001	Frontier Geosciences Inc.	Metronix ADU-06
mt03	50.579	123.550	2001	Frontier Geosciences Inc.	Metronix ADU-06
mt06	50.571	123.553	2001	Frontier Geosciences Inc.	Metronix ADU-06
mt07	50.586	123.555	2001	Frontier Geosciences Inc.	Metronix ADU-06
mt11	50.568	123.536	2001	Frontier Geosciences Inc.	Metronix ADU-06
mt12	50.578	123.531	2001	Frontier Geosciences Inc.	Metronix ADU-06
mt13	50.564	123.528	2001	Frontier Geosciences Inc.	Metronix ADU-06
mt14	50.571	123.526	2001	Frontier Geosciences Inc.	Metronix ADU-06
mt15	50.578	123.519	2001	Frontier Geosciences Inc.	Metronix ADU-06
mt16	50.553	123.506	2001	Frontier Geosciences Inc.	Metronix ADU-06
mt17	50.587	123.524	2001	Frontier Geosciences Inc.	Metronix ADU-06
mt19	50.568	123.515	2001	Frontier Geosciences Inc.	Metronix ADU-06
mt20	50.575	123.513	2001	Frontier Geosciences Inc.	Metronix ADU-06
mt21	50.571	123.505	2001	Frontier Geosciences Inc.	Metronix ADU-06
mt22	50.586	123.516	2001	Frontier Geosciences Inc.	Metronix ADU-06
mt23	50.566	123.503	2001	Frontier Geosciences Inc.	Metronix ADU-06
mt24	50.586	123.509	2001	Frontier Geosciences Inc.	Metronix ADU-06
mt27	50.581	123.488	2001	Frontier Geosciences Inc.	Metronix ADU-06
mt28	50.585	123.492	2001	Frontier Geosciences Inc.	Metronix ADU-06
mt29	50.586	123.499	2001	Frontier Geosciences Inc.	Metronix ADU-06
mt30	50.564	123.486	2001	Frontier Geosciences Inc.	Metronix ADU-06
mt31	50.571	123.489	2001	Frontier Geosciences Inc.	Metronix ADU-06
mt32	50.567	123.549	2001	Frontier Geosciences Inc.	Metronix ADU-06
mt33	50.576	123.490	2001	Frontier Geosciences Inc.	Metronix ADU-06
mt34	50.593	123.501	2001	Frontier Geosciences Inc.	Metronix ADU-06
mt35	50.572	123.520	2001	Frontier Geosciences Inc.	Metronix ADU-06
mt37	50.552	123.483	2001	Frontier Geosciences Inc.	Metronix ADU-06
me4	50.582	123.538	2001	Frontier Geosciences Inc.	Metronix ADU-06
fl03	50.567	123.523	2001	Frontier Geosciences Inc.	Metronix ADU-06
meager82_6	50.579	123.460	1982	Pacific Geoscience Centre	Phoenix MT-1
meager82_7	50.574	123.473	1982	Pacific Geoscience Centre	Phoenix MT-1

Table B.2*: Skin depth in four different half-spaces at the six frequencies shown in Figure 4.4 and Figure* ***4.5****.*

Frequency (Hz)	**Skin Depth (m) at ρ = 1 Ωm**	**Skin Depth (m) at ρ = 10 Ωm**	**Skin Depth (m) at ρ = 100 Ωm**	**Skin Depth (m) at ρ = 1000 Ωm**
100	50	160	500	1,600
10	160	500	1,600	5,000
1	500	1,600	5,000	16,000
0.1	1,600	5,000	16,000	50,000
0.01	5,000	16,000	50,000	160,000
0.001	16,000	50,000	160,000	500,000

B.2. Details of all inversions and sensitivity tests

Table B.3*: Details of inversions that used observed MT data. The preferred model is from iteration 323 of inversion 15 (bold text). Author's note: the preferred model is also referred to as MGR-s66p29r12-C04-v2-run3-iter101.*

Inversion Number	Number of MT Data Sites	Num. of Periods (impedance)	Num. of Periods (tipper)	Horizontal Cell Size (m)	Min. Res. of Alt. Model (Ωm)	Air/Topo. Layer Thickness (m)	Num. of Top Layers Removed	X Covariance Length Scale	Y Covariance Length Scale	Z Covariance Length Scale	Initial Value of λ	Final Value of λ	Initial RMS Misfit	Final RMS Misfit	Total Number of Iterations
Inversions 1-2 were performed before the 2020 data were collected															
1	30	32	0	250	N/A	N/A	N/A	0.3	0.3	0.3	1	10^{-8}	21.8	2.02	309
2	30	32	0	250	N/A	20	0	0.3	0.3	0.3	1	10^{-7}	19.7	1.91	617
Inversions 3-4 used the 2020 data and the tipper data															
3	60	29	29	250	N/A	50	12	0.3	0.3	0.3	1	10^{-4}	11.6	2.21	285
4	66	29	29	250	N/A	50	12	0.3	0.3	0.3	1	10^{-8}	11.7	2.02	670
Inversion 5 started from the inversion 4 model, iteration 670 (for comparison with inversions 6-8)															
5	66	29	29	250	N/A	50	12	0.3	0.3	0.3	1	10^{-8}	2.02	2.00	196
Inversions 6-8 limited the lowest resistivity values (starting from altered versions of the inversion 4 model)															
6	66	29	29	250	1	50	12	0.3	0.3	0.3	1	10^{-8}	2.12	1.86	218
7	66	29	29	250	3	50	12	0.3	0.3	0.3	1	10^{-8}	2.49	1.73	275
8	66	29	29	250	10	50	12	0.3	0.3	0.3	1	10^{-8}	3.47	1.93	146
Inversions 9-17 tested a range of covariance length scales															
9	66	29	29	250	N/A	50	12	0.1	0.1	0.1	10	10^{-8}	11.7	3.77	442
10	66	29	29	250	N/A	50	12	0.1	0.1	0.2	10	10^{-8}	11.7	2.83	469
11	66	29	29	250	N/A	50	12	0.2	0.2	0.2	10	10^{-8}	11.7	2.25	422
12	66	29	29	250	N/A	50	12	0.2	0.2	0.3	10	10^{-8}	11.7	2.42	376
13	66	29	29	250	N/A	50	12	0.3	0.3	0.3	10	10^{-8}	11.7	2.11	329
14	66	29	29	250	N/A	50	12	0.3	0.3	0.4	10	10^{-8}	11.7	1.95	385
15	**66**	**29**	**29**	**250**	**N/A**	**50**	**12**	**0.4**	**0.4**	**0.4**	**10**	$\mathbf{10^{-8}}$	**11.7**	**1.77**	**450**
16	66	29	29	250	N/A	50	12	0.4	0.4	0.5	10	10^{-8}	11.7	2.02	281
17	66	29	29	250	N/A	50	12	0.5	0.5	0.5	10	10^{-8}	11.7	2.05	229
Inversion 18 used impedance data only (i.e., inversion 15 with tipper data removed)															
18	66	29	0	250	N/A	50	12	0.4	0.4	0.4	10	10^{-8}	13.9	1.63	472
Inversion 19 started from the inversion 15 model, iteration 323 (for comparison with inversions 20-23)															
19	66	29	29	250	N/A	50	12	0.4	0.4	0.4	10	10^{-6}	1.92	1.73	186

Inversions 20-23 limited the lowest resistivity values (starting from altered versions of the inversion 15 model)															
20	66	29	29	250	1	50	12	0.4	0.4	0.4	10	10^{-6}	2.03	1.77	163
21	66	29	29	250	2	50	12	0.4	0.4	0.4	10	10^{-6}	2.19	1.75	163
22	66	29	29	250	3	50	12	0.4	0.4	0.4	10	10^{-6}	2.35	1.81	132
23	66	29	29	250	5	50	12	0.4	0.4	0.4	10	10^{-6}	2.67	1.76	102
Inversions 24-27 tested the effect of topography and a reduced dataset (the legacy data were removed)															
24	66	29	29	250	N/A	50	12	0.4	0.4	0.4	10	10^{-8}	10.8	1.73	261
25	66	29	29	250	N/A	50	N/A	0.4	0.4	0.4	10	10^{-8}	12.7	1.84	314
26	34	29	29	250	N/A	50	N/A	0.4	0.4	0.4	10	10^{-8}	14.2	1.45	315
27	34	29	29	250	N/A	50	12	0.4	0.4	0.4	10	10^{-8}	12.6	1.71	399

Table B.4*: Statistics of the responses of inversion models 4, 5, 7, 15, 19, and 21, referred to as i4, i4gt0, i4gt3, i15, i15gt0, and i15gt3, respectively. These models are discussed in Section 6.4.4.2.2.*

Model A Name (#)	Model B Name (#)	Model A R.M.S. Misfit	Model B R.M.S. Misfit	Difference in R.M.S. Misfit	F-test F-value	KS test p-value
i4 (4)	i4gt0 (5)	2.019	2.000	0.019	1.020	0.923
i4 (4)	i4gt3 (7)	2.019	1.734	0.285	1.356	0.000
i4gt0 (5)	i4gt3 (7)	2.000	1.734	0.266	1.330	0.000
i15 (15)	i15gt0 (19)	1.915	1.725	0.190	1.232	0.000
i15 (15)	i15gt2 (21)	1.915	1.751	0.164	1.196	0.000
i15gt0 (19)	i15gt2 (21)	1.725	1.751	0.026	1.030	0.946

Table B.5*: Critical F-value for a variety of confidence levels. The datasets analyzed in Table B.4 all have 20,812 degrees of freedom, so this value was used for the numerator and denominator when calculating the critical F-value.*

Confidence Level	Critical F-value
68%	1.0065
90%	1.0179
91%	1.0188
92%	1.0197
93%	1.0207
94%	1.0218
95%	1.0231
96%	1.0246
97%	1.0264
98%	1.0289
99%	1.0328

The F-test F-value (Table B.4) is the ratio of the squared R.M.S. misfit (i.e., the variance) of the two datasets being compared, with the larger value in the numerator and the smaller value in the denominator, such that the F-value is always greater than 1. The critical F-value (Table B.5) was calculated using 20,812 as both the numerator degrees of freedom and the denominator degrees of freedom, as this is the size of the data vector. Based on chance, we would expect F-values less than 1.0328 to occur 99% of the time and F-values less than 1.0207 to occur 93% of the time, if the variances are from the same distribution. This implies that the change in misfit between i4 and i4gt0, and between i15gt0 and i15gt2, is statistically insignificant. The change in misfit in the other four cases (Table B.4) is statistically significant. In these four cases, the KS test p-value (Table B.4) is 0.000, implying that there is a statistically significant difference between the two resistivity models compared, provided that the residuals are from the same distribution. Similarly, the cases with high p-values (0.923 and 0.946) imply that the models are not statistically significantly different. Based on these results, i15 was chosen as the preferred resistivity model, as discussed in Section 4.4.2.2.

Table B.6*: Results of KS tests when the preferred resistivity model was altered to be very resistive (10,000 Ωm) or very conductive (0.01 Ωm) below a certain depth (left column). The residuals of the preferred model were compared with the residuals of the altered models. These results are discussed in Section 6.4.4.2.3.*

Depth below which the model was altered (km)	10,000 Ωm below the specified depth			0.01 Ωm below the specified depth		
	KS test p-value (impedance and tipper)	KS test p-value (impedance)	KS test p-value (tipper)	KS test p-value (impedance and tipper)	KS test p-value (impedance)	KS test p-value (tipper)
10.7	1.0E-118	4.4E-82	4.5E-43	1.3E-27	3.9E-44	9.9E-06
11.9	3.9E-112	1.8E-76	2.2E-43	5.7E-24	5.3E-39	5.6E-05
13.1	5.1E-108	4.2E-69	1.3E-43	2.3E-22	5.0E-36	2.4E-04
14.6	2.4E-104	1.8E-62	5.0E-44	8.8E-20	4.2E-32	0.0011
16.1	1.7E-95	1.1E-55	3.1E-42	3.6E-18	3.6E-28	0.0043
17.8	6.3E-84	4.1E-47	1.5E-39	3.5E-17	4.5E-27	0.0170
19.7	1.5E-71	2.0E-39	4.8E-35	3.5E-17	2.5E-26	0.0446
21.7	2.6E-60	4.5E-34	7.7E-30	1.8E-17	1.7E-26	0.0619
24.0	1.1E-50	4.8E-32	7.3E-26	4.5E-16	1.9E-24	0.0963
26.5	7.8E-42	2.7E-29	6.0E-22	3.8E-15	8.6E-23	0.0923
29.2	3.5E-35	9.5E-24	2.1E-20	4.1E-15	2.9E-22	0.1700
32.2	2.1E-30	3.2E-22	2.0E-18	3.2E-14	7.7E-21	0.1978
35.5	1.6E-27	1.1E-18	8.9E-19	3.0E-12	1.0E-17	0.2636
39.2	1.5E-24	6.5E-16	2.8E-17	1.1E-09	6.3E-14	0.3783
43.2	4.3E-23	2.6E-15	5.1E-17	4.2E-08	2.1E-11	0.4787
47.6	2.6E-20	1.8E-14	6.4E-16	2.2E-06	4.1E-09	0.5761
52.5	6.0E-19	3.0E-13	3.6E-15	1.2E-05	2.0E-07	0.7500

57.8	1.2E-16	1.9E-11	4.5E-14	4.6E-05	4.5E-06	0.9264
63.7	1.2E-14	9.4E-11	5.1E-13	3.2E-04	7.9E-05	0.9807
70.1	1.0E-11	4.4E-09	3.0E-11	0.0017	2.9E-04	0.9973
77.2	2.6E-09	8.0E-08	1.8E-09	0.0043	8.0E-04	0.9996
85.0	1.6E-06	6.1E-06	1.2E-06	0.0168	0.0038	1.0000
93.6	2.1E-04	1.6E-04	4.3E-04	0.0552	0.0142	1.0000
103.1	0.0076	0.0018	0.0287	0.1137	0.0534	1.0000
113.5	0.1248	0.0314	0.4144	0.2484	0.1717	1.0000
124.9	0.2795	0.1462	0.9346	0.4669	0.3312	1.0000
137.5	0.5364	0.4103	1.0000	0.7488	0.6365	1.0000

B.3. Geochemical data

Table B.7*: A subset of chemical compositional data from rocks of the Mount Meager Volcanic Complex (Hickson et al., 1999; Russell et al., 2021; Stasiuk et al., 1996) and rocks used in laboratory experiments of electrical resistivity (Gaillard 2004, Dai et al. 2014, Laumonier et al. 2015, 2017, 2019, Guo et al. 2016, 2017).* X_A *represents the wt.% ratio of* $Na_2O + K_2O + CaO$ *to* SiO_2 *(Dai et al., 2014).*

Pebble Creek Formation (Hickson et al., 1999) formerly known as Bridge River Assemblage (Stasiuk et al., 1996)							
Rock Type	Pumice	Pumice	Pumice	Pumice	Breccia	Lava	Lava
Sample No.	MM-88-2a	MM-88-2b	KE-90-1	KE-90-3	MM-88-7	MM-88-16	MM-88-32
SiO_2	64.35	67.69	66.90	68.11	68.33	68.64	68.82
CaO	4.17	3.06	3.49	3.17	3.33	3.07	3.07
Na_2O	5.10	5.16	5.32	5.28	5.48	5.32	5.30
K_2O	2.23	2.41	2.22	2.37	2.44	2.46	2.46
Total	99.59	99.39	100.61	100.43	101.22	100.49	100.55
$Na_2O + K_2O$	7.33	7.57	7.54	7.65	7.92	7.78	7.76
X_A	0.18	0.16	0.16	0.16	0.16	0.16	0.16
Plinth Assemblage (Hickson et al., 1999; Stasiuk et al., 1996) * two analyses replicated (Russell et al., 2021)							
Rock Type	Lava	Lava *	Lava	Lava *	Lava	Lava	Lava
Sample No.	MM-88-26	MM-88-26	MM-88-29	MM-88-29	MM-88-30	MM-88-39	MM-88-40
SiO_2	67.10	68.92	68.74	68.34	60.50	68.10	66.94
CaO	3.28	3.03	2.70	3.14	5.06	3.28	3.62
Na_2O	4.99	4.72	5.10	4.59	5.43	5.16	4.90
K_2O	2.83	2.67	3.06	2.49	1.74	2.55	2.44
Total	100.03	100.17	100.44	99.86	99.89	101.01	100.86
$Na_2O + K_2O$	7.82	7.39	8.16	7.08	7.17	7.71	7.34
X_A	0.17	0.15	0.16	0.15	0.20	0.16	0.16
Plinth pyroclastic flow (Russell et al., 2021)			Study measuring the electrical resistivity of granite (Dai et al., 2014)				
Rock Type	Dacite	Dacite	Rock Type	Granite	Granite	Granite	Granite
Sample No.	AW-15-003	AW-15-003r	Sample No.	HBP	XHS7	XHS8	SXW
SiO_2	67.14	67.16	SiO_2	68.26	72.22	74.69	79.29
CaO	3.53	3.52	CaO	3.02	0.84	1.23	0.13
Na_2O	4.50	4.53	Na_2O	5.57	4.63	4.01	3.20
K_2O	2.44	2.45	K_2O	2.41	4.44	4.68	4.97
Total	99.02	99.05	Total	99.82	99.33	100.20	100.76

$Na_2O + K_2O$	6.94	6.98	$Na_2O + K_2O$	7.98	9.07	8.69	8.17
X_A	0.16	0.16	X_A	0.16	0.14	0.13	0.10
Studies measuring the electrical resistivity of silicate melts (Gaillard 2004, Laumonier *et al.* 2015, 2017, 2019, Guo *et al.* 2016, 2017)							
Rock Type	Rhyolite	Rhyolite	Rhyolite	Dacite	Dacite	Andesite	Andesite
Study	Gai-2004	Guo-2016	Guo-2016	Lau-2015	Lau-2019	Lau-2017	Guo-2017
SiO_2	74.51	75.72	75.72	67.93	65.79	60.93	60.79
CaO	0.75	0.16	0.20	3.31	3.83	5.54	10.65
Na_2O	4.15	4.68	4.87	2.09	4.73	2.09	3.22
K_2O	5.64	4.28	4.27	4.69	3.41	3.17	1.39
Total		98.69	98.78	100.00	99.12	98.47	99.31
$Na_2O + K_2O$	9.79	8.96	9.14	6.78	8.14	5.26	4.61
X_A	0.14	0.12	0.12	0.15	0.18	0.18	0.25

B.4. Additional figures

This section contains 23 figures that were mentioned in the CJES publication (Chapter 4) but omitted for brevity.

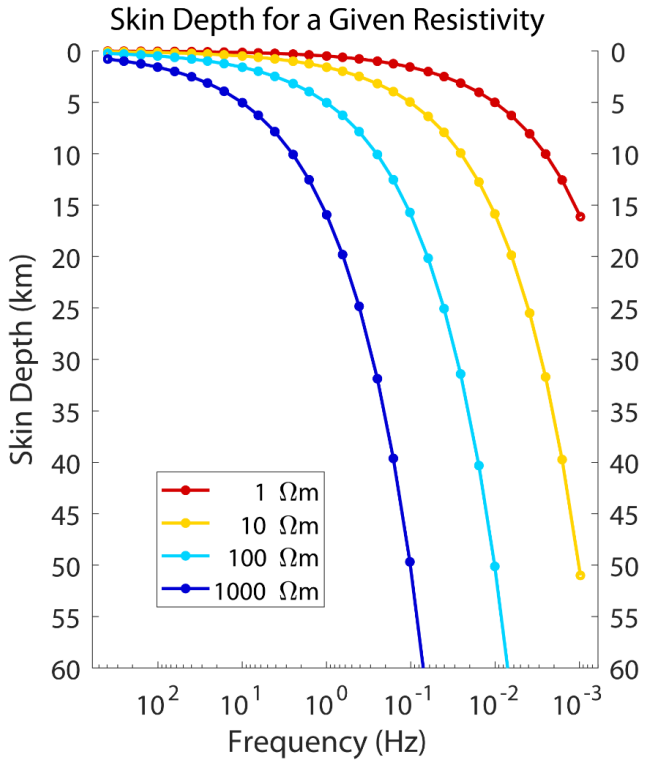

***Figure B.1**: Skin depth for four different half-spaces at the 29 frequencies of the MT dataset.*

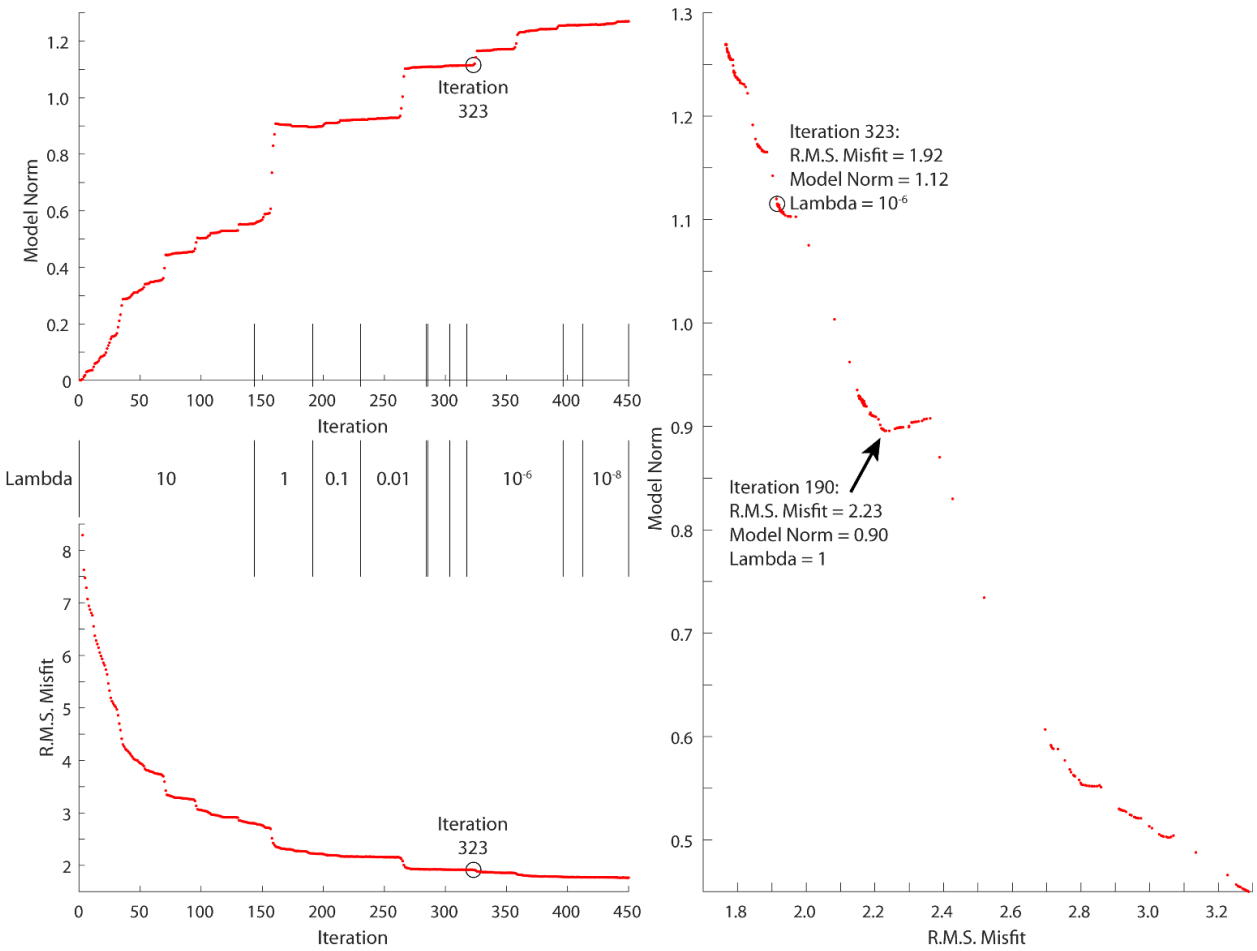

***Figure B.2**: Model norm, lambda, and R.M.S. misfit at each of the 450 inversion iterations (red dots). Model norm increases with iteration number and R.M.S. misfit decreases with iteration number. Lambda was decreased by a factor of 10 each time the change in misfit was less than 10^{-4}, down to and including $\lambda = 10^{-8}$. The preferred model is from iteration 323 (black circle).*

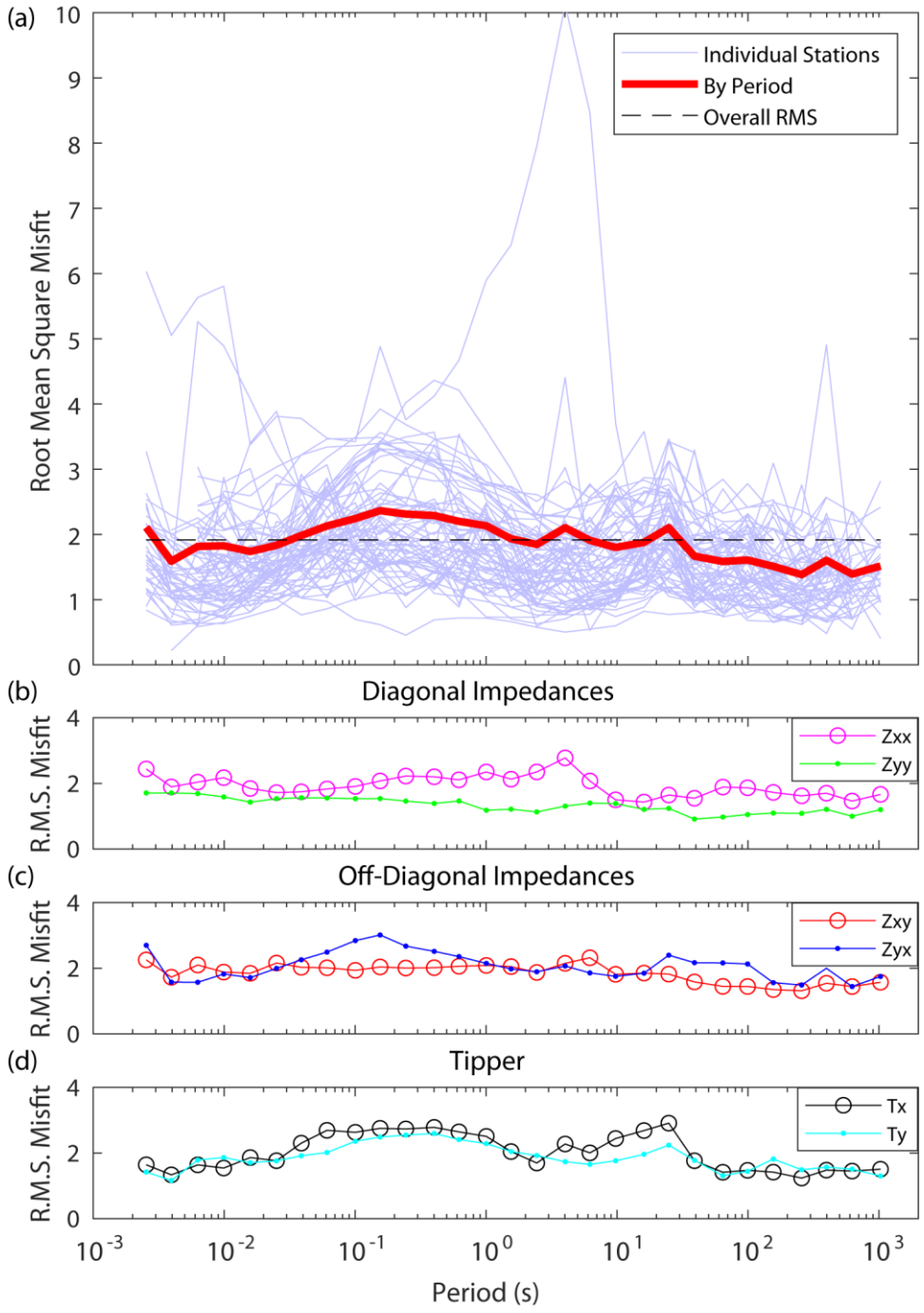

***Figure B.3**: Root-mean-square misfit of observed MT data to predicted MT data from the preferred 3-D resistivity model. (a) Misfit by period and station. (b-d) Misfit by period and data component.*

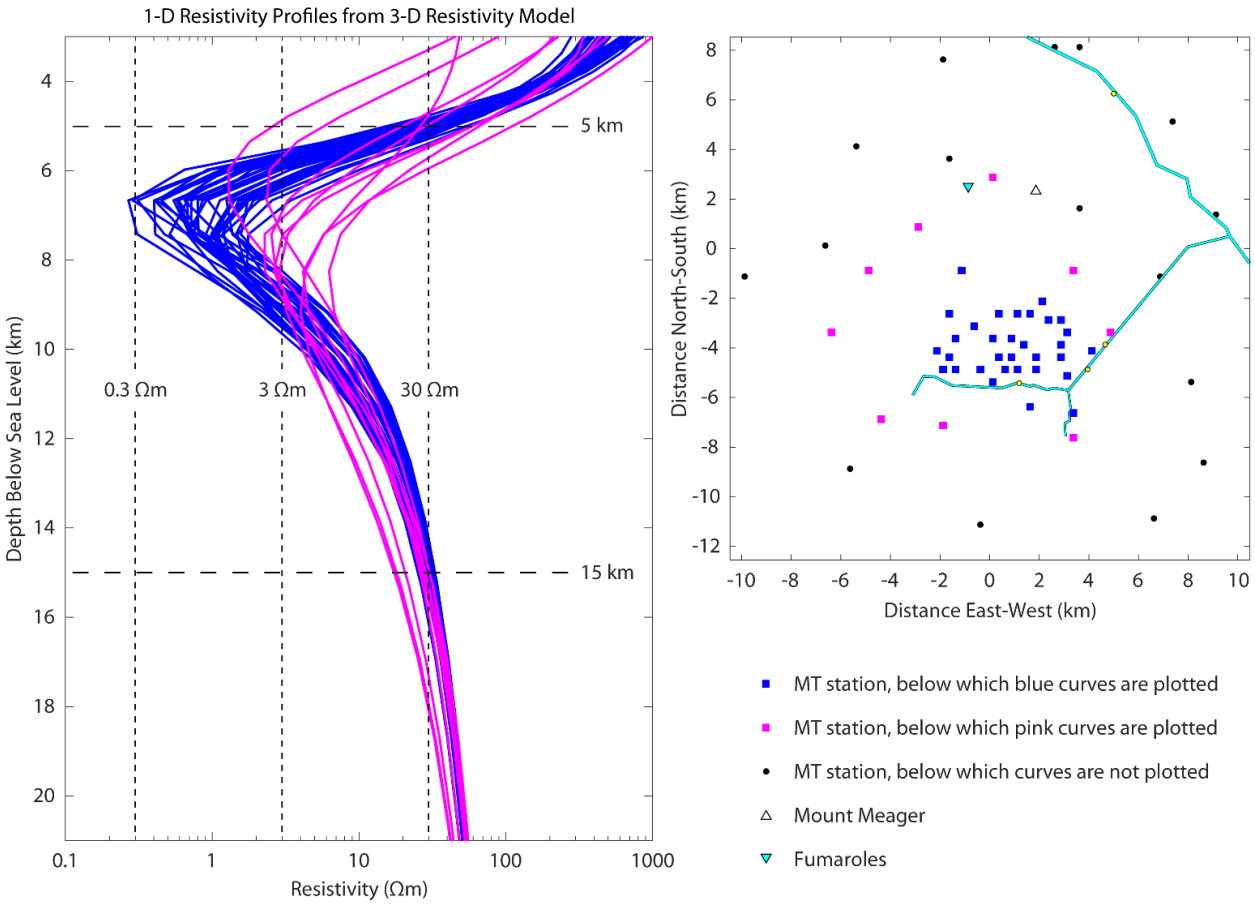

***Figure B.4**: 1-D resistivity profiles from the 3-D resistivity model, plotted beneath MT station locations. The deep conductor (5-15 km below sea level) has a resistivity of 0.3-30 Ωm and an average resistivity around 3 Ωm.*

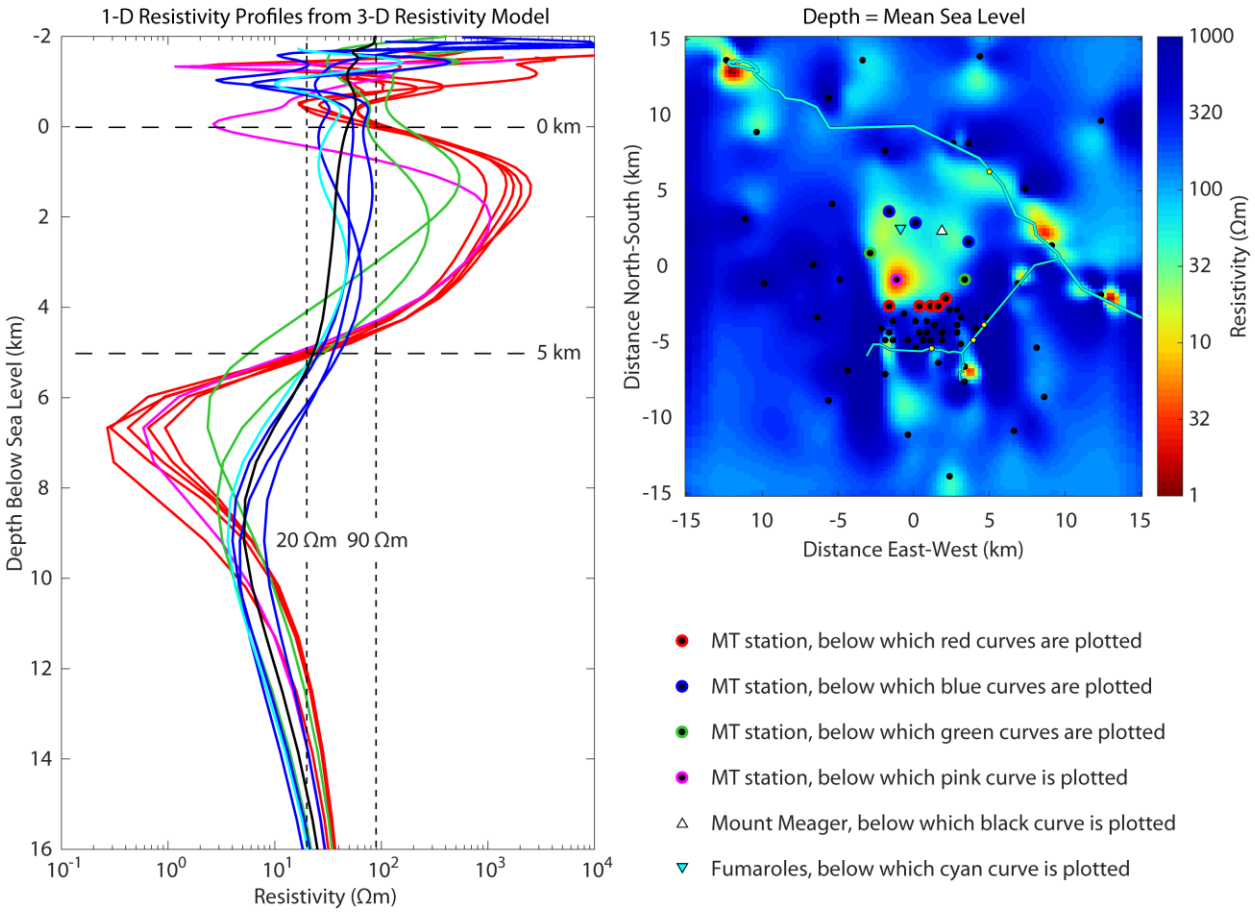

Figure B.5*: 1-D resistivity profiles from the 3-D resistivity model, plotted beneath Mount Meager, the fumaroles, and selected MT station locations. Above the northern part of the deep conductor, there is a conductive pathway up toward Mount Meager and the fumaroles. This conductive zone has a resistivity of 20-90 Ωm.*

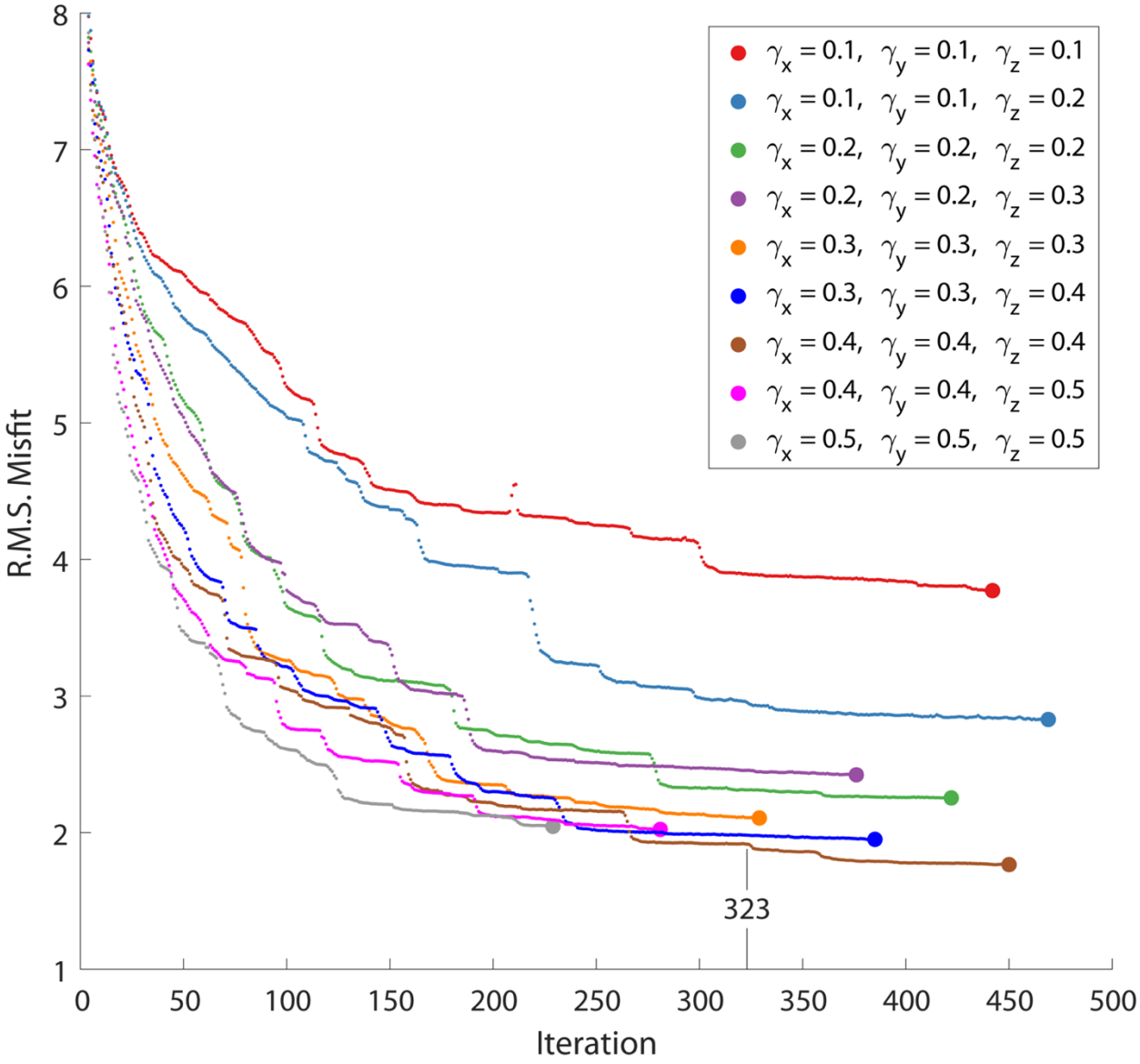

Figure B.6*: R.M.S. misfit, as a function of inversion iteration, for inversions 9-17 (Table S3). These inversions used the same data and starting model, but the model covariance length scale was varied. The preferred resistivity model is from iteration 323 of inversion 15 (brown dots).*

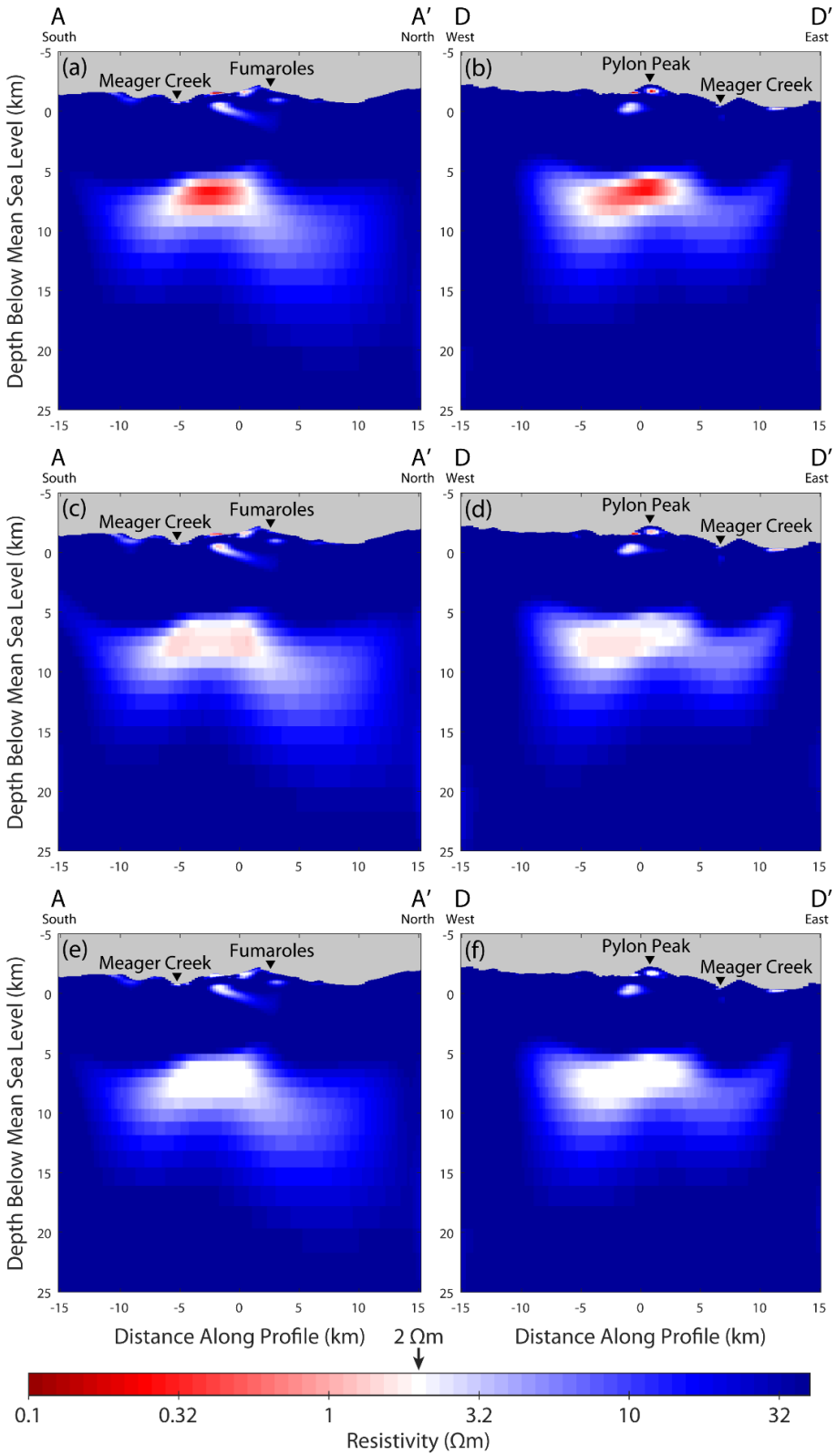

Figure B.7*: (a-b) Cross-sections from the preferred 3-D resistivity model. (c-d) Cross-sections from the 2 Ωm threshold inversion model. (e-f) Cross-sections from the 2 Ωm threshold starting model. Cross-sections A-A′ and D-D′ correspond to Figure 4.9a and 4.9d, respectively. Their locations are shown in Figure 4.9f.*

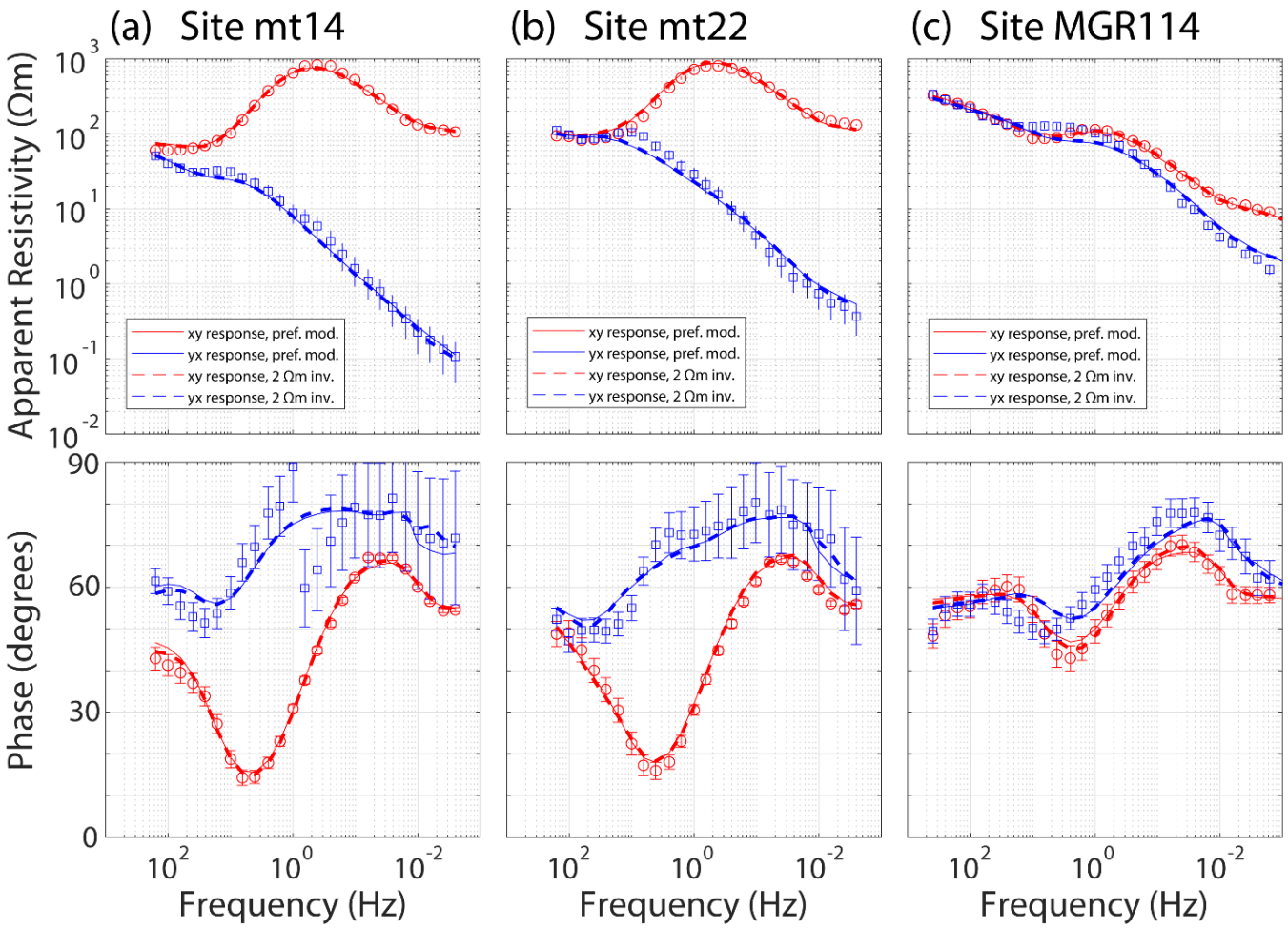

***Figure B.8**: MT responses of the preferred resistivity model (solid lines) and the 2 Ωm threshold inversion model (dashed lines), along with the measured MT data (circles and squares).*

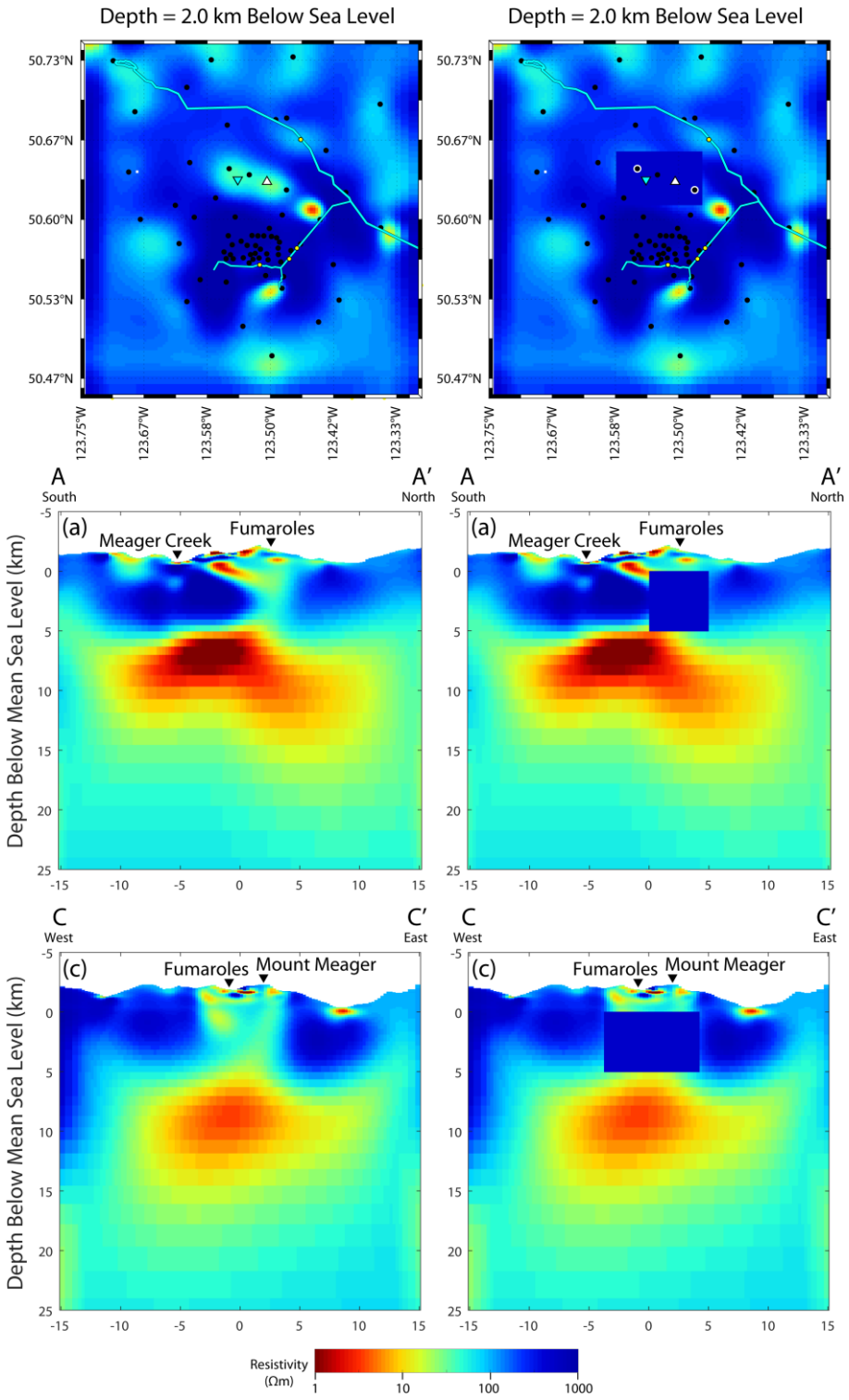

Figure B.9*: Left column: Slices from the preferred resistivity model. Cross-sections A-A′ and C-C′ correspond to Figure 4.9a and 4.9c, respectively. Their locations are shown in Figure 4.9f. Right column: Corresponding model slices where the conductive zone extending upward from the northern part of the deep conductor has been replaced with a 500 Ωm block measuring 5 km (north-south) and 8 km (east-west) at a depth of 0-5 km below sea level. The white circles in the top right figure indicate MGR114 (northwest of the fumaroles) and MGR118 (southeast of Mount Meager). Data from these two sites are shown in Figure B.10.*

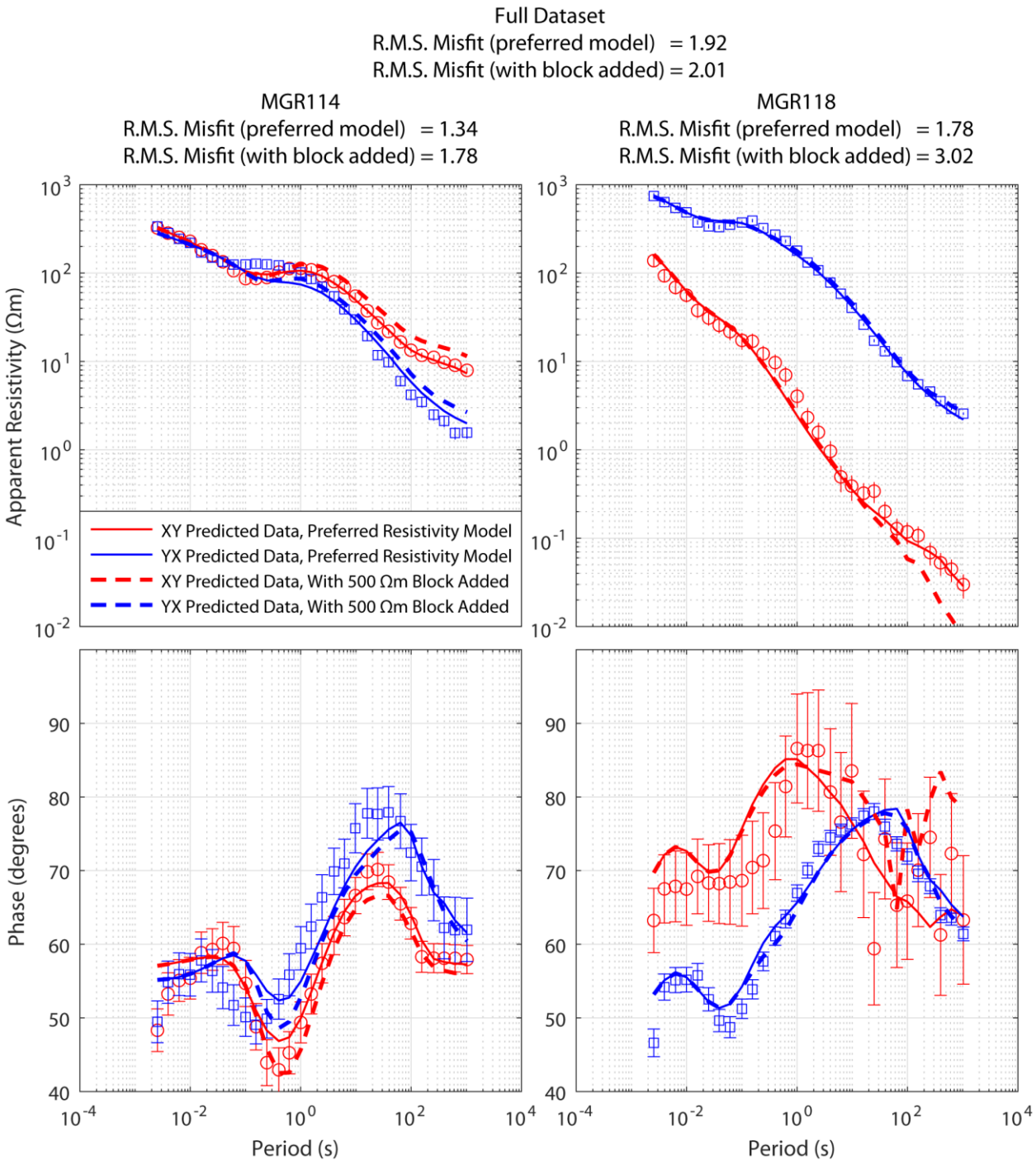

Figure B.10*: Measured MT data (circles and squares) at sites MGR114 and MGR118 (locations shown in Figure B.9). The MT response of the preferred resistivity model is shown by the solid curves and the MT response when a resistive block is added (Figure B.9) is shown by the dashed curves. The root-mean-square misfit is given for each of the two MT sites, as well as the full dataset.*

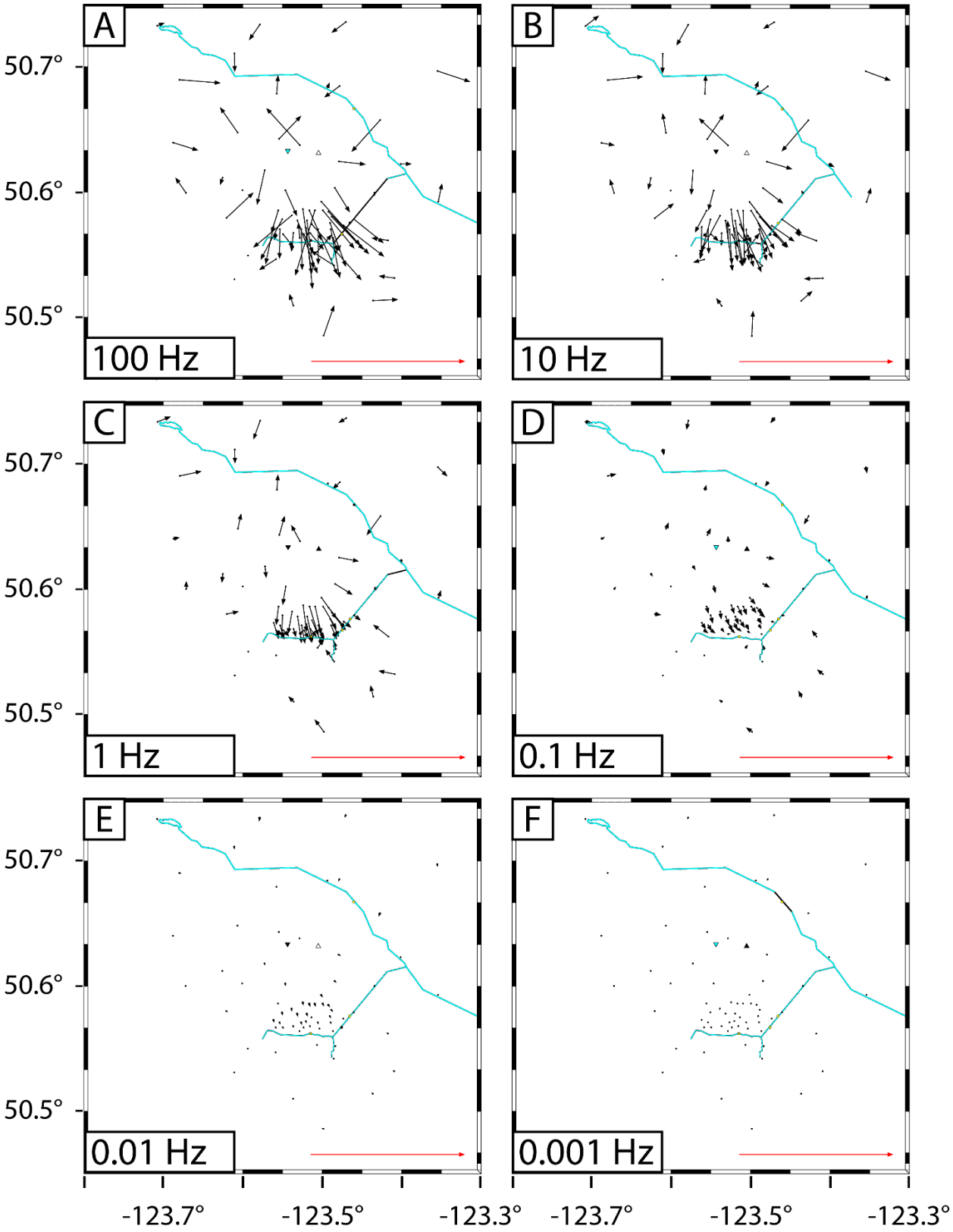

***Figure B.11**: Synthetic induction vectors (real part, using the Wiese convention) from the forward response of a uniform 10 Ωm resistivity model with the same spatial discretization as the preferred resistivity model. Red arrow (bottom right) is a unit vector.*

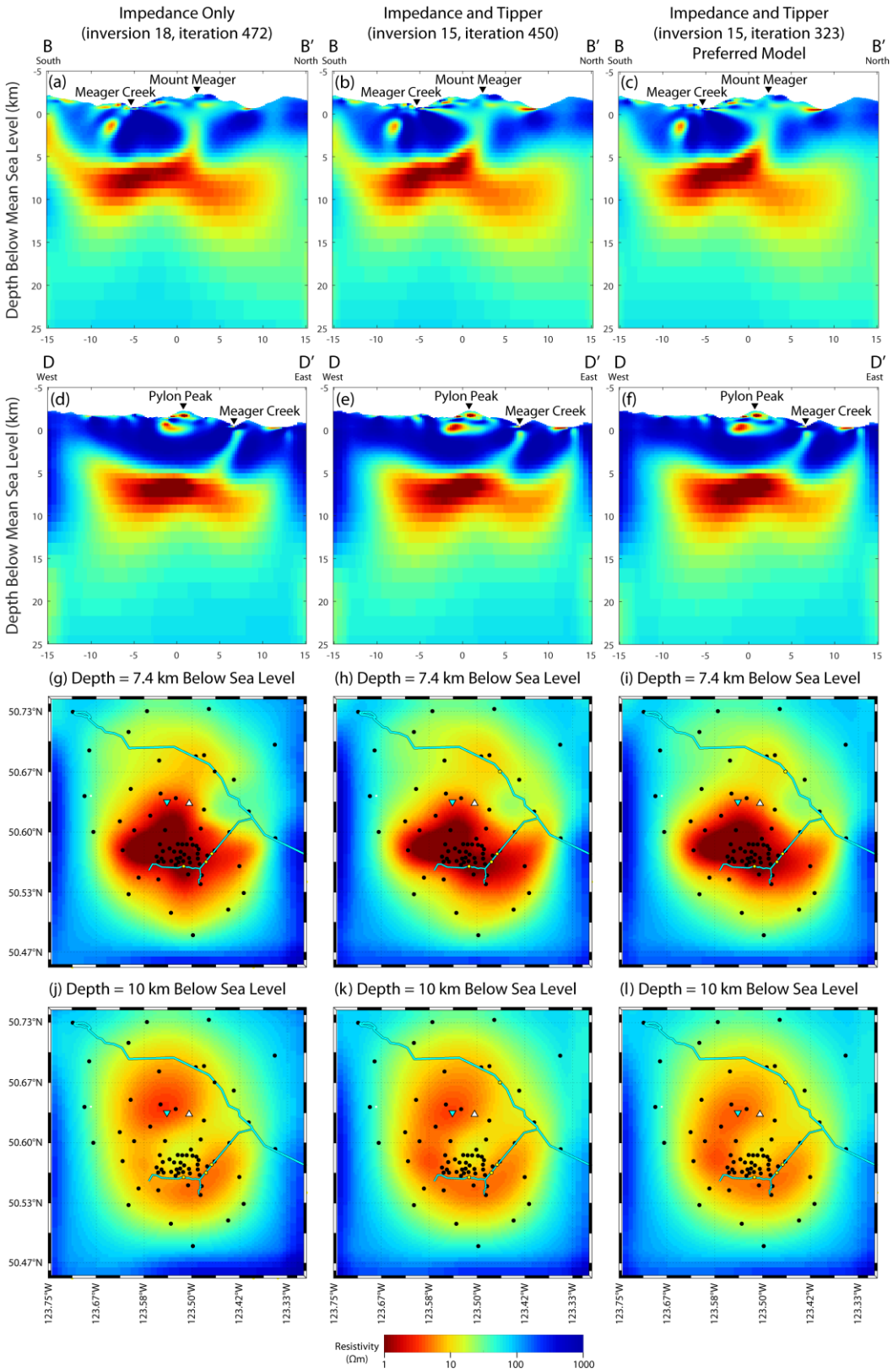

***Figure B.12**: Resistivity model slices from inversions without tipper data (left column) and with tipper data (centre column), along with the preferred resistivity model (right column). (a-f) Cross-sections, as in Figure 4.9. (g-l) Depth slices, as in Figure 4.8.*

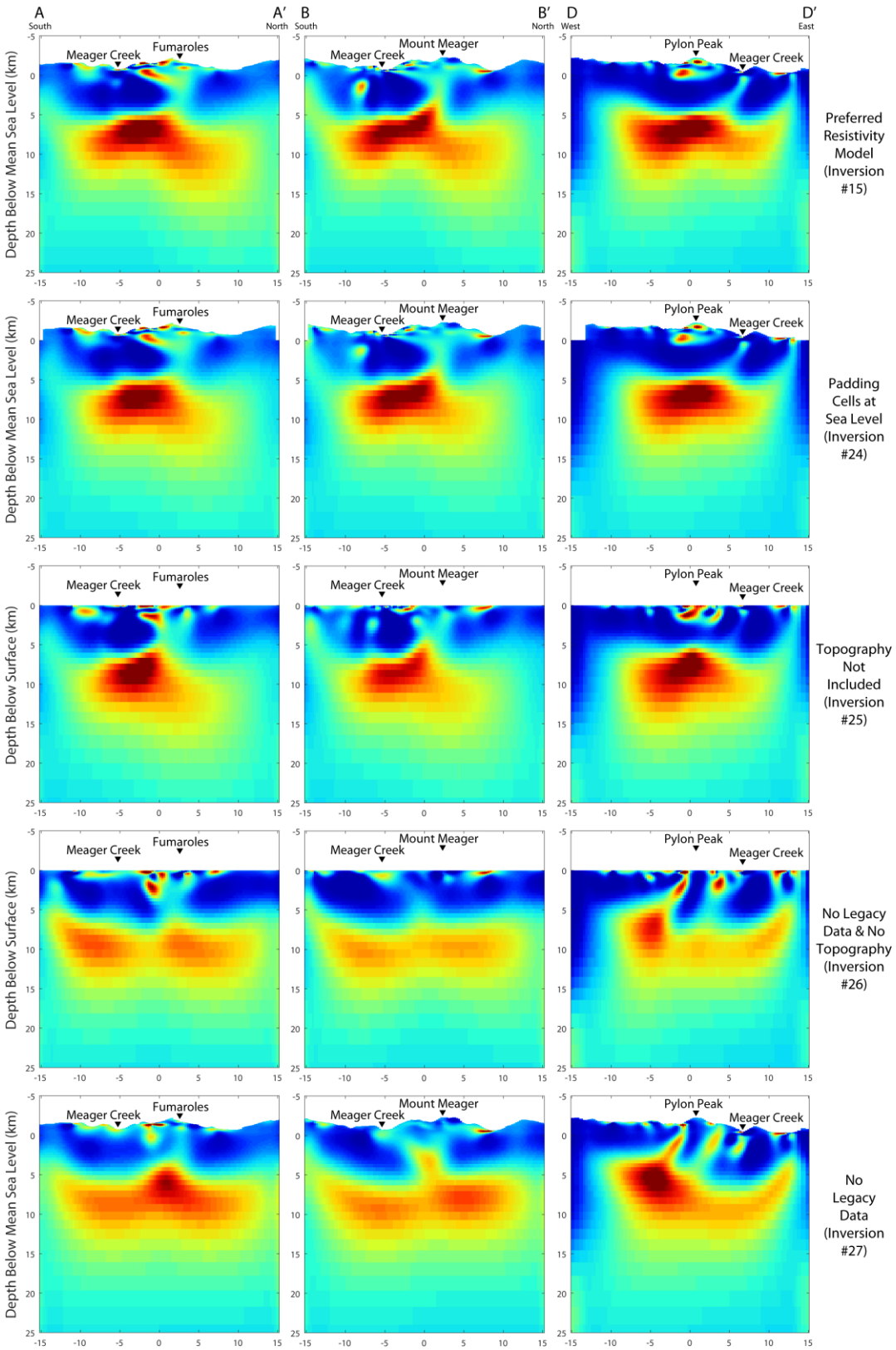

Figure B.13*: Three cross-sections (locations shown in Figure B.14) from five different resistivity models (as stated on the right side of each row). The top three rows used MT data from 66 locations (Figure B.14a) and the bottom two rows used MT data from 34 locations (Figure B.14b).*

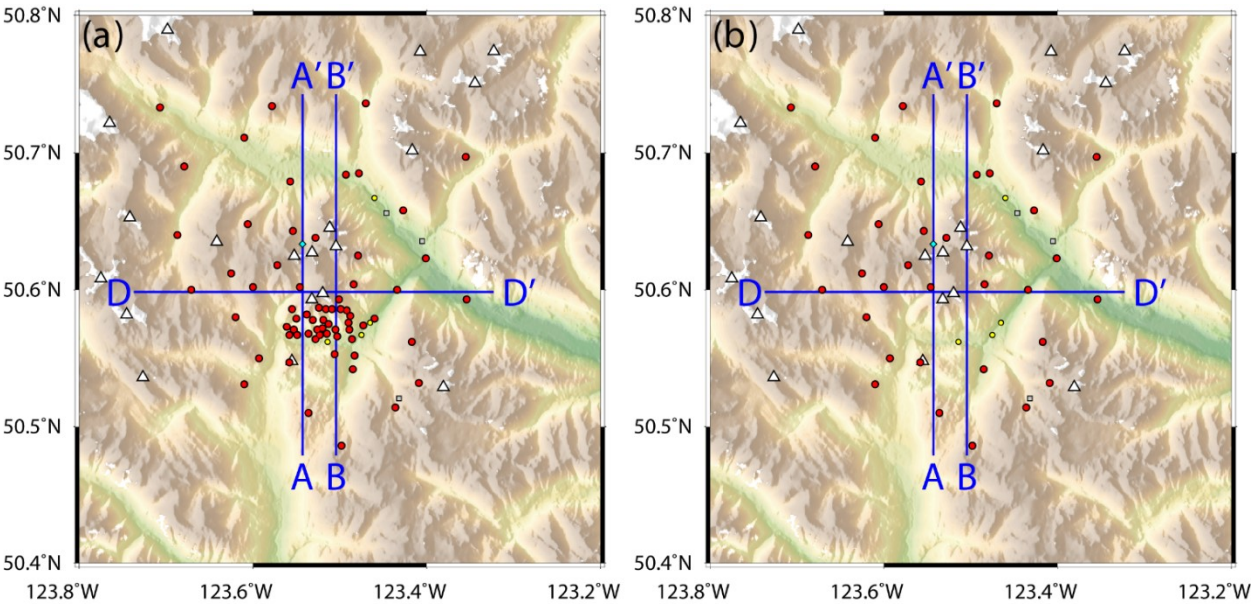

Figure B.14*: (a) Map with 66 MT stations (red dots) corresponding to inversions 15, 24 and 25 in Figure B.13. (b) Map with 34 MT stations (red dots) corresponding to inversions 26 and 27 in Figure B.13. In (a) and (b), the profiles A-A', B-B' and D-D' indicate the locations of the cross-sections shown in Figure B.13.*

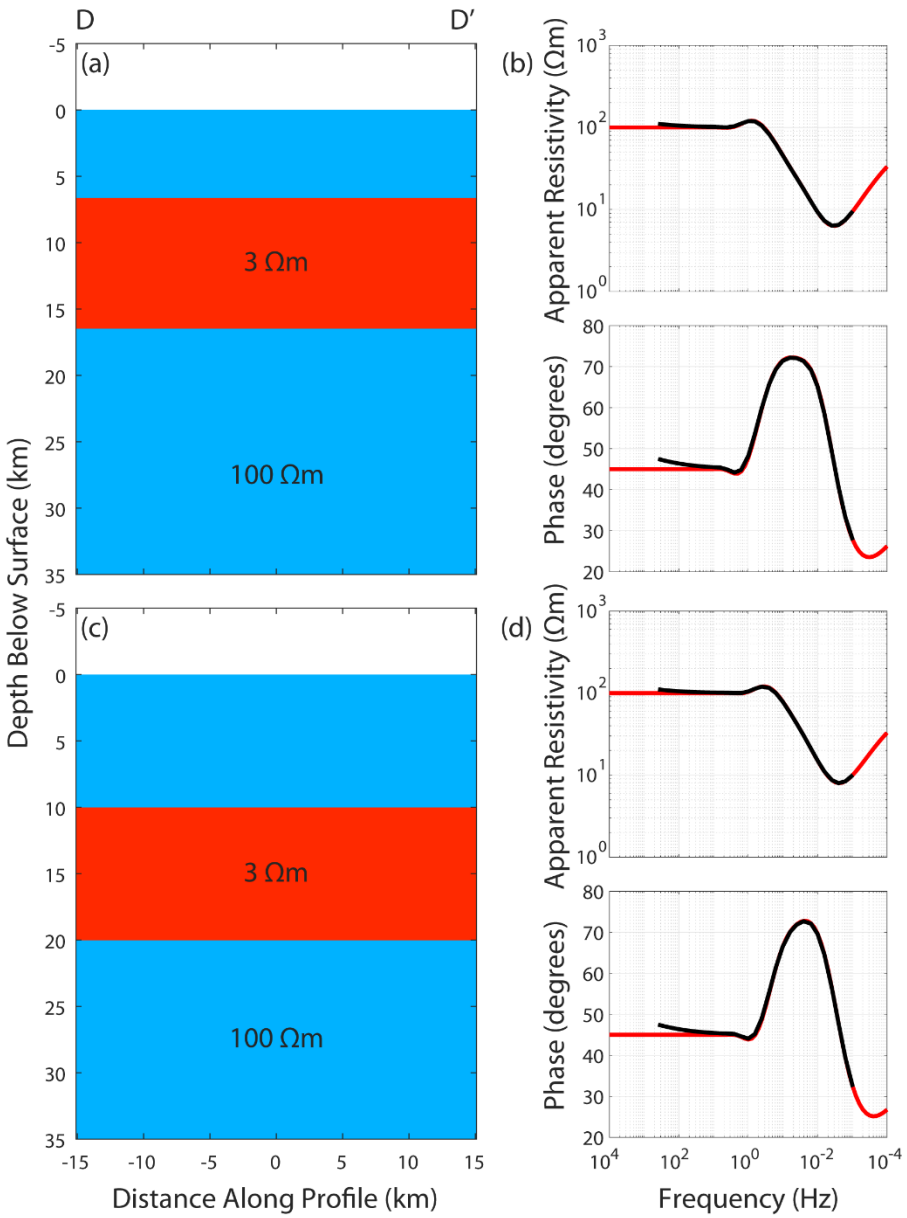

Figure B.15*: (a) A 100 Ωm halfspace with a 3 Ωm layer at 6.7-16.5 km below the surface. (b) The MT response of model (a) using the frequencies and model mesh parameters of the preferred resistivity model (black curves), along with the true 1-D response (red curves). (c) A 100 Ωm halfspace with a 3 Ωm layer at 10.0-20.0 km below the surface. (d) The MT response of model (c) using the frequencies and model mesh parameters of the preferred resistivity model (black curves), along with the true 1-D response (red curves). For the black curves at the highest frequencies, the apparent resistivity is slightly greater than 100 Ωm and the phase is slightly greater than 45°. This is an artifact arising from the model cell size being similar to the skin depth at these frequencies.*

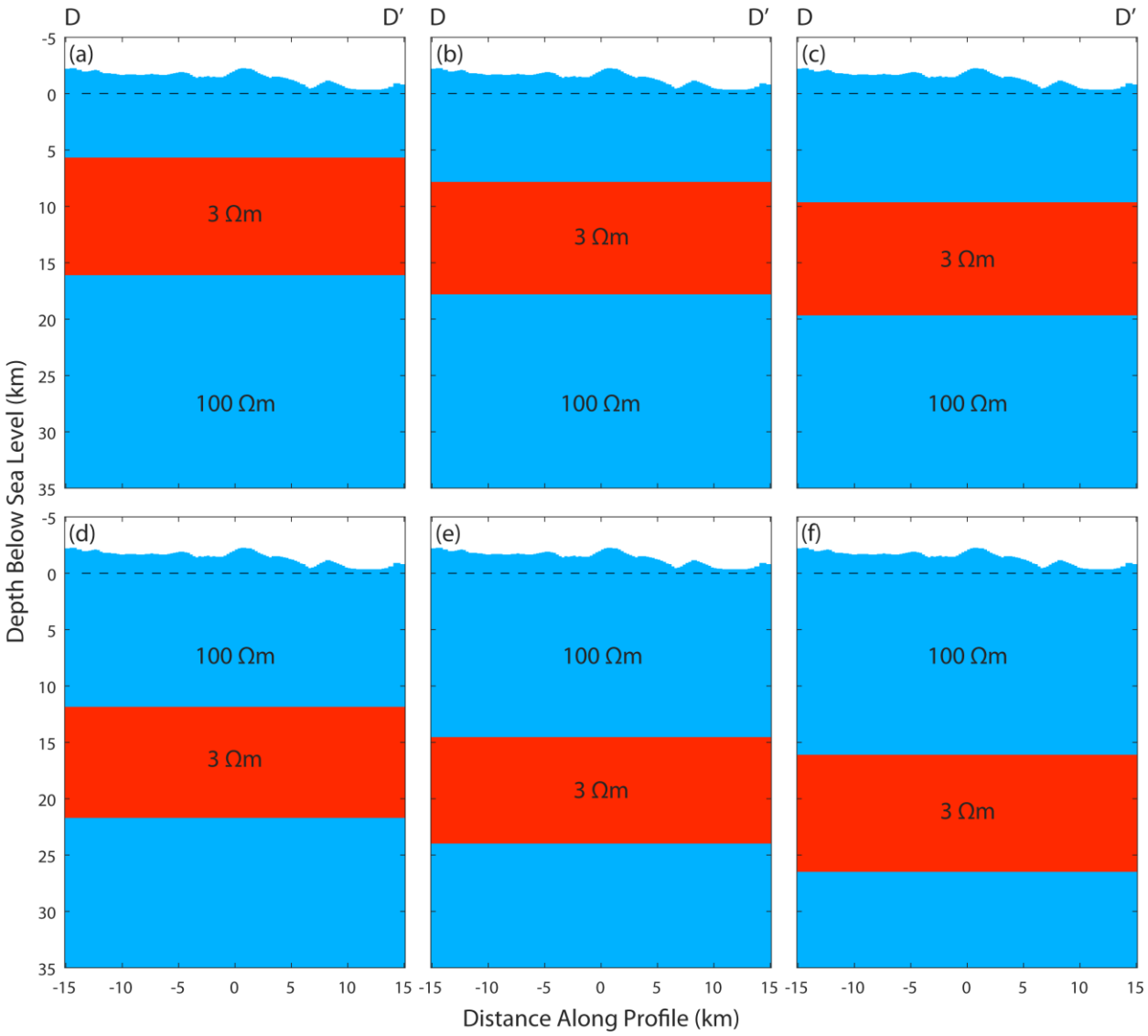

***Figure B.16**: Six 100 Ωm halfspaces, each with a 3 Ωm layer at a different depth, all using the model mesh parameters and topography of the preferred resistivity model. The conductive layer is located at the following depths below sea level: (a) 5.7-16.1 km, (b) 7.8-17.8 km, (c) 9.7-19.7 km, (d) 11.9-21.7 km, (e) 14.6-24.0 km, and (f) 16.1-26.5 km. The MT responses of these models are shown in Figure B.17.*

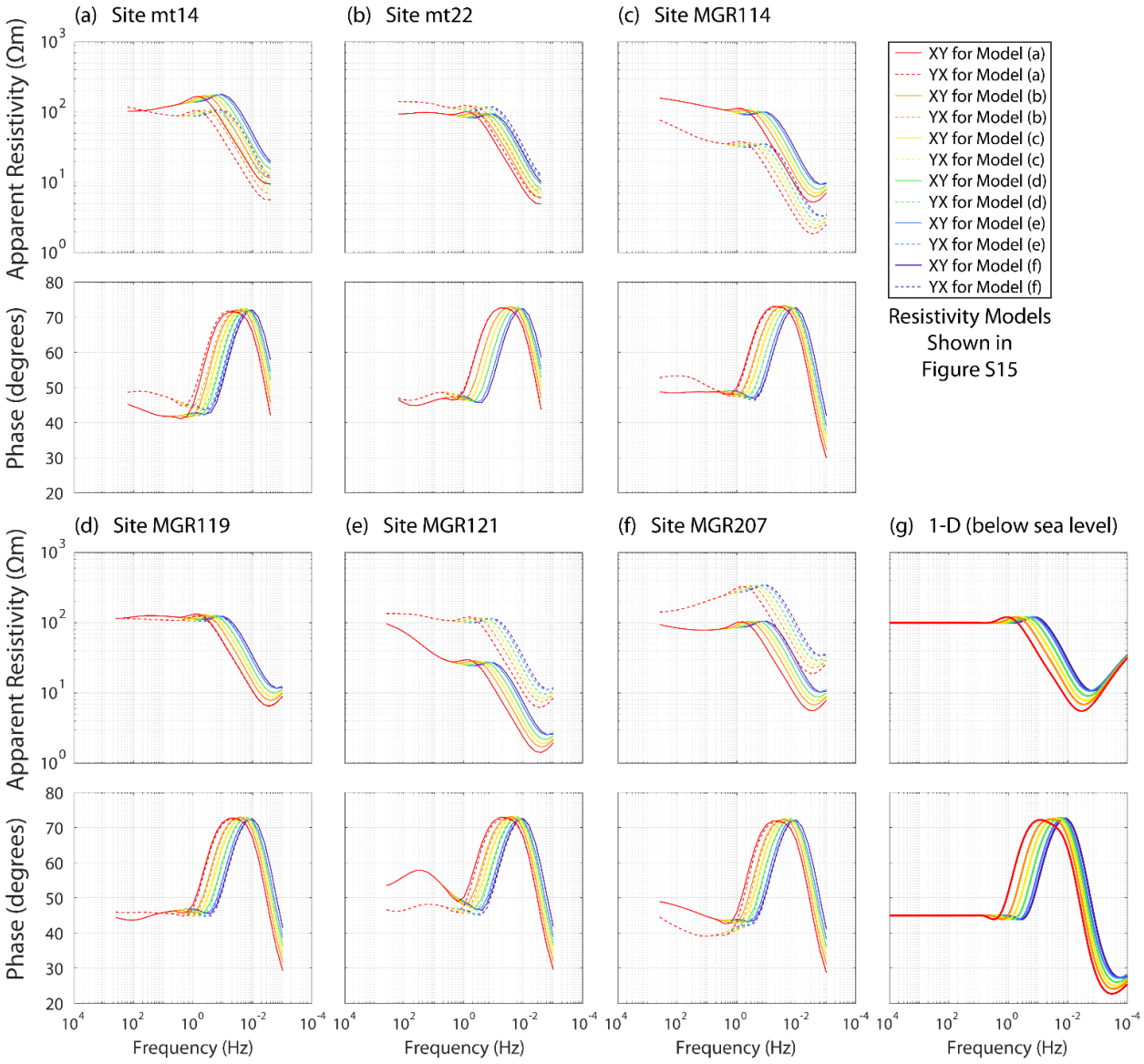

Figure B.17*: (a-f) MT responses of the six models shown in Figure B.16 at the locations of six MT stations. (g) 1-D responses of the six models, calculated below sea level (black dashed lines in Figure B.16).*

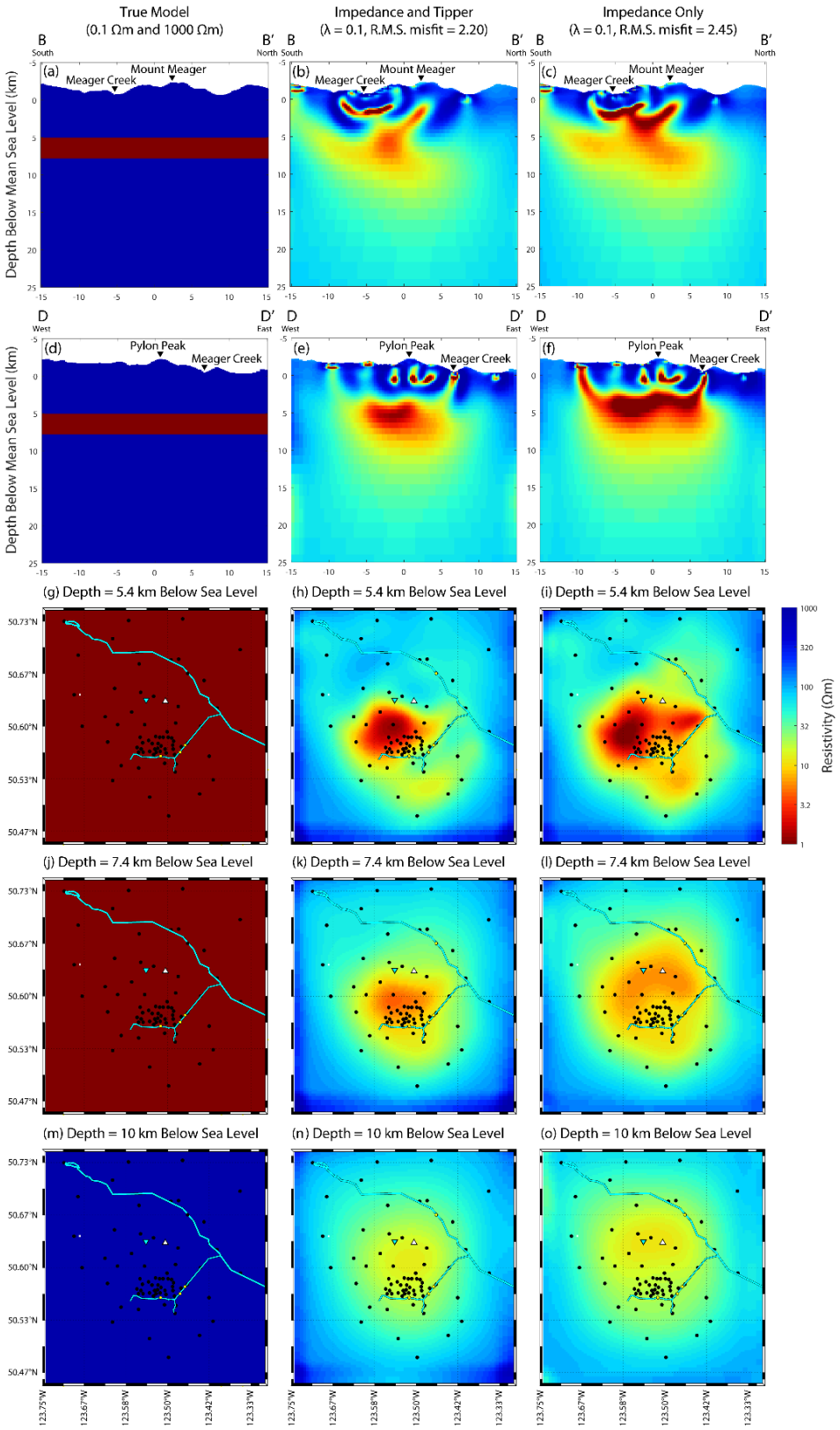

***Figure B.18**: Left column: synthetic resistivity model with a 0.1 Ωm layer in a 1000 Ωm halfspace. Middle column: slices of a resistivity model from inversion of synthetic impedance and tipper data. Right column: slices of a resistivity model from inversion of synthetic impedance data.*

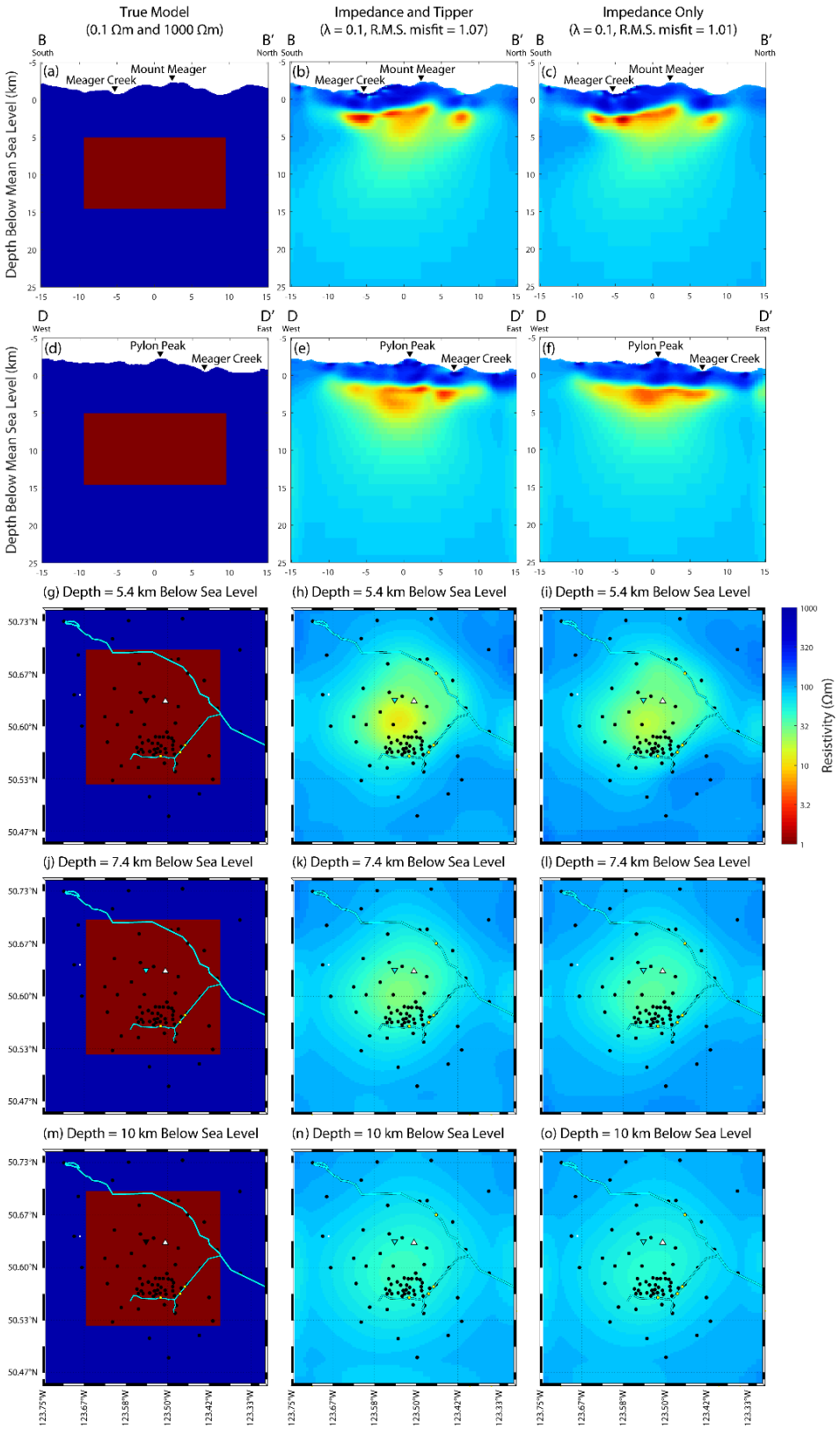

***Figure B.19**: Left column: synthetic resistivity model with a 0.1 Ωm block in a 1000 Ωm halfspace. Middle column: slices of a resistivity model from inversion of synthetic impedance and tipper data. Right column: slices of a resistivity model from inversion of synthetic impedance data.*

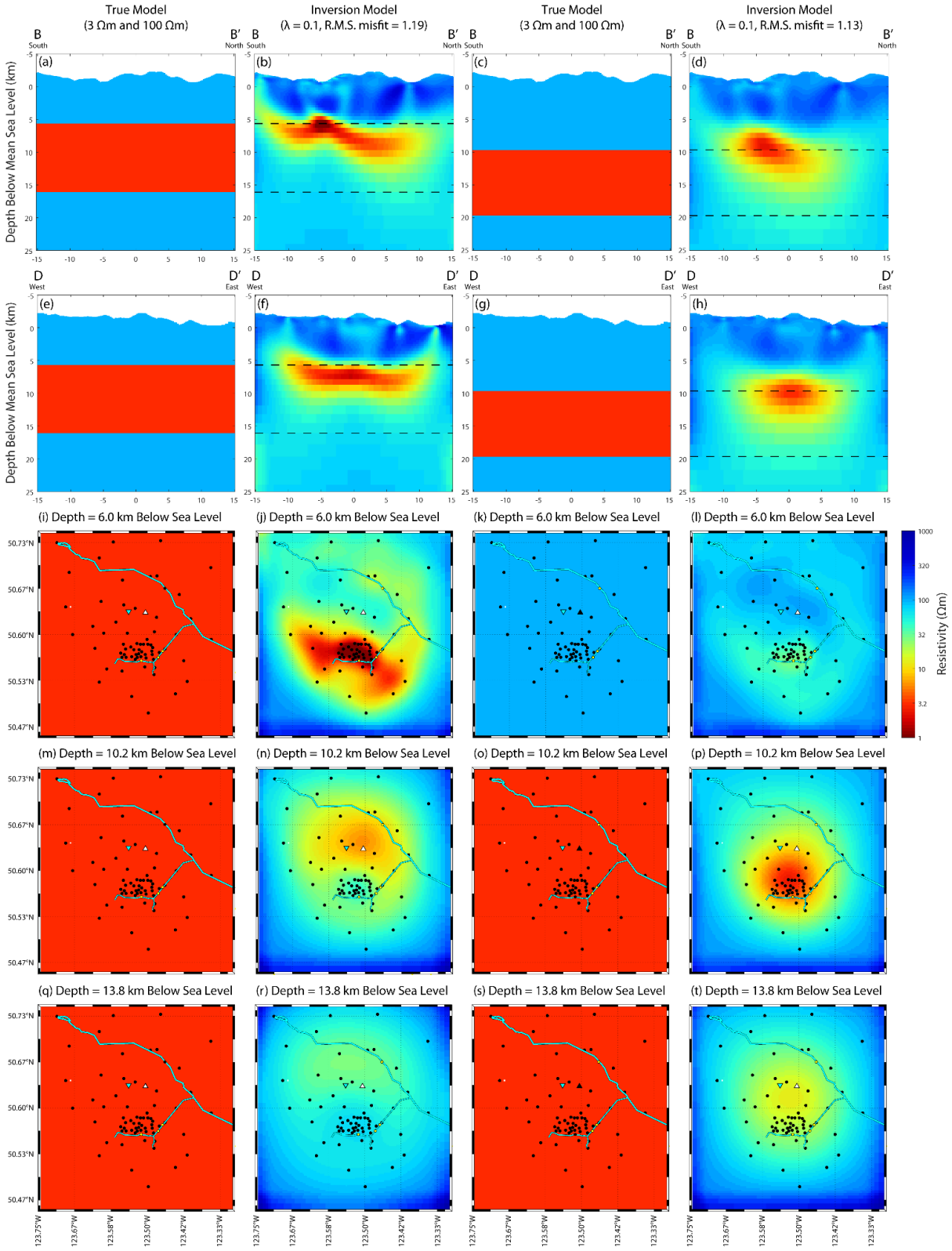

Figure B.20*: Left two columns: a 3 Ωm layer at 5.7-16.1 km below sea level, embedded in a 100 Ωm half-space, and the associated resistivity model from inversion of synthetic data. Right two columns: a 3 Ωm layer at 9.7-19.7 km below sea level, embedded in a 100 Ωm half-space, and the associated resistivity model from inversion of synthetic data.*

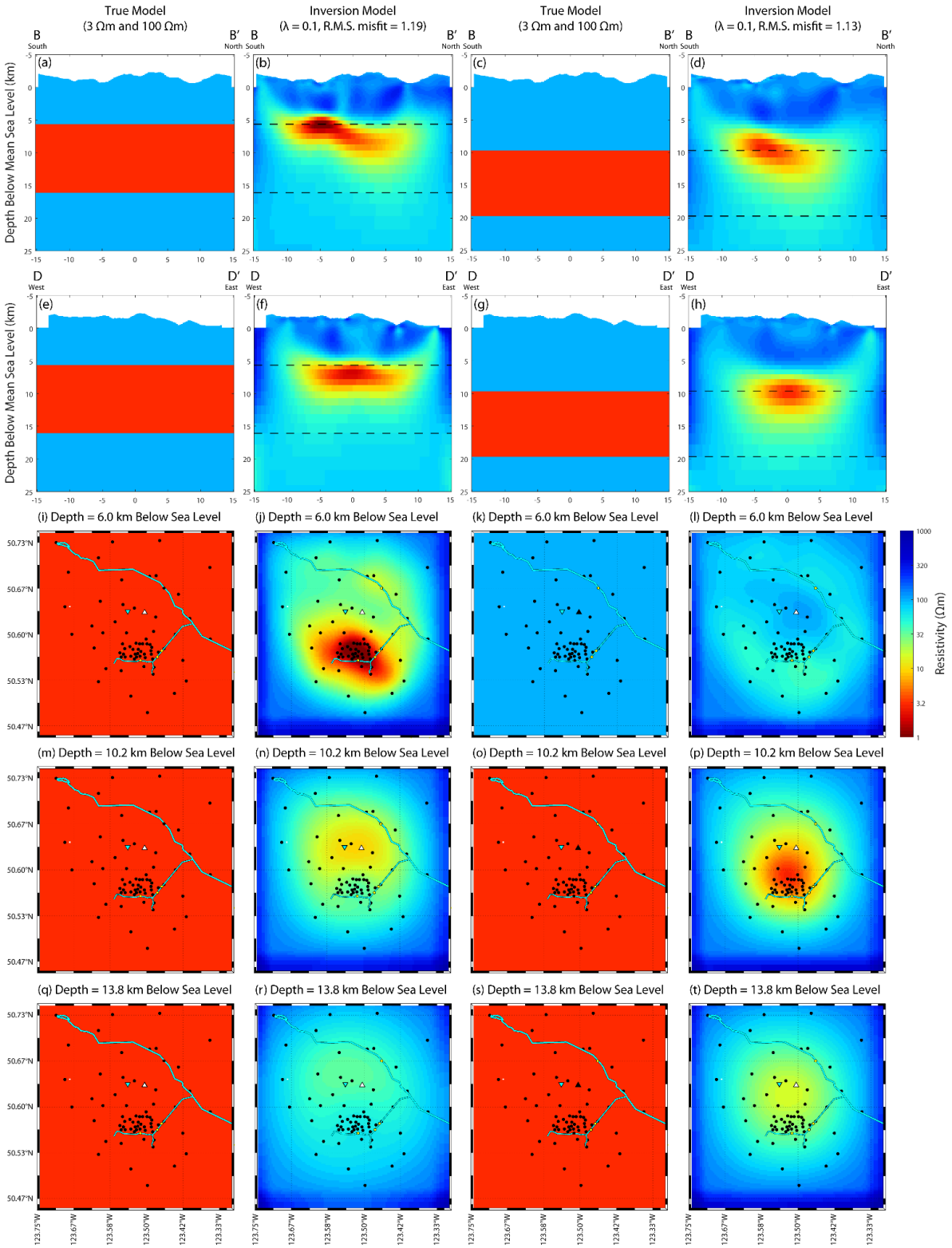

Figure B.21*: Left two columns: a 3 Ωm layer at 5.7-16.1 km below sea level, embedded in a 100 Ωm half-space with padding cell elevation at sea level, and the associated resistivity model from inversion of synthetic data. Right two columns: a 3 Ωm layer at 9.7-19.7 km below sea level, embedded in a 100 Ωm half-space with padding cell elevation at sea level, and the associated resistivity model from inversion of synthetic data.*

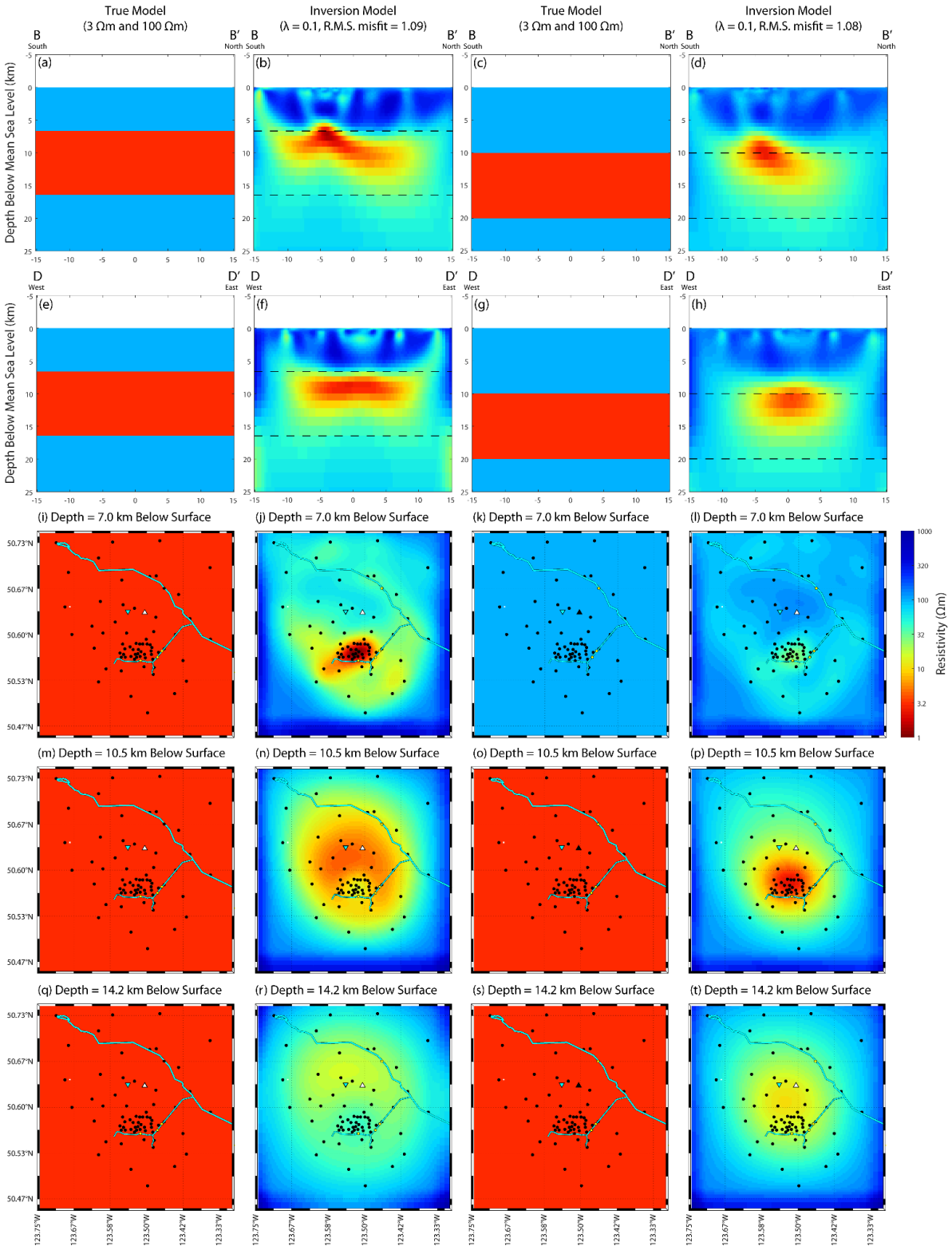

Figure B.22*: Left two columns: a 3 Ωm layer at 6.7-16.5 km below the surface (topography not included), embedded in a 100 Ωm half-space, and the associated resistivity model from inversion of synthetic data. Right two columns: a 3 Ωm layer at 10.0-20.0 km below the surface (topography not included), embedded in a 100 Ωm half-space, and the associated resistivity model from inversion of synthetic data.*

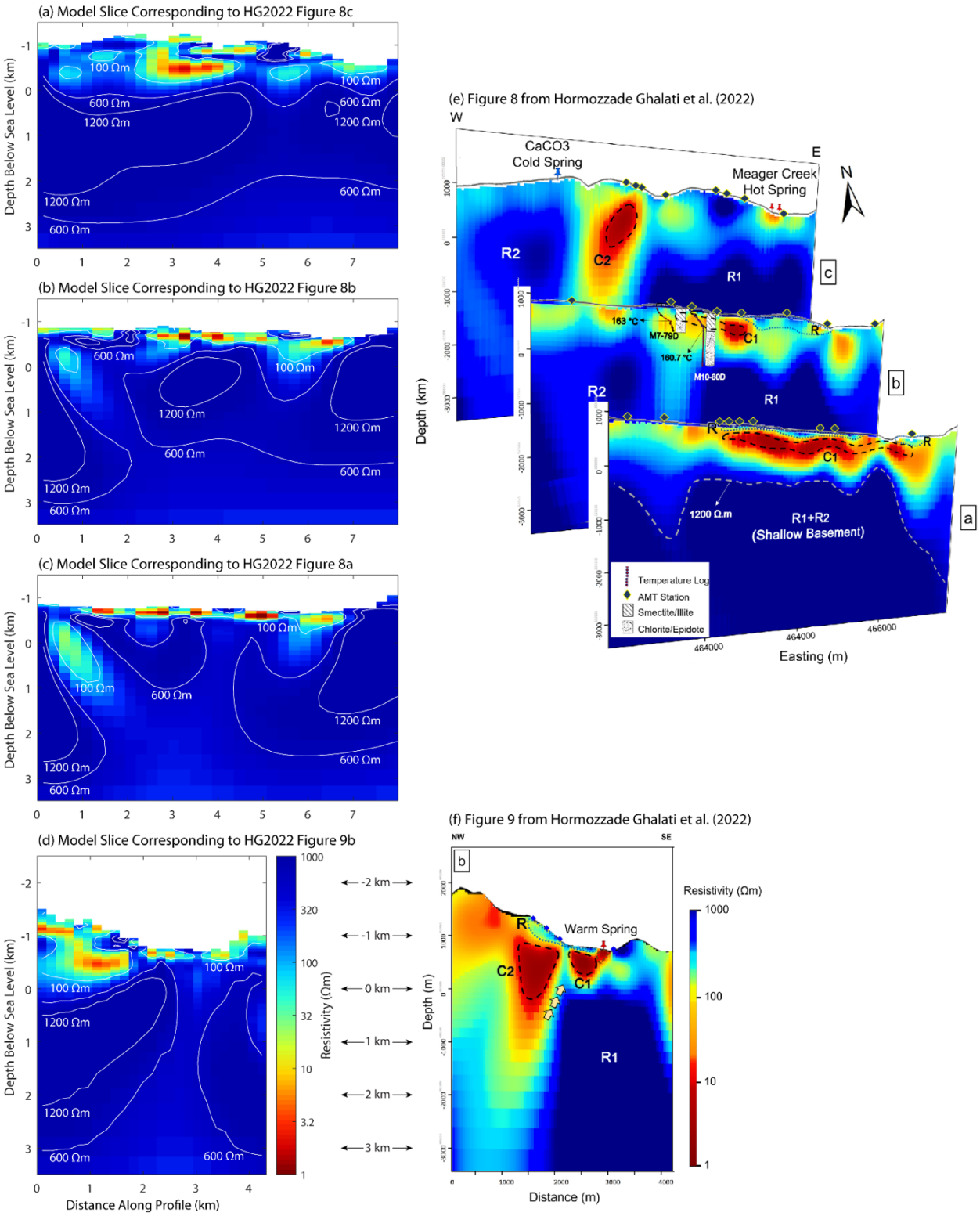

***Figure B.23**: (a-d) Slices from the preferred resistivity model at the locations of the slices on the right. White lines are contours at 100 Ωm, 600 Ωm, and 1200 Ωm. (e-f) Slices from the resistivity model of Hormozzade Ghalati et al. (2022). Note that the colour scales are different, as shown in panels d and f. Each set of figures uses the colour scale from its paper.*

C. Supplementary materials for Chapter 5

C.1. Magnetotelluric theory

This section provides an overview of the magnetotelluric (MT) method which uses natural electromagnetic signals to image the electrical resistivity of the subsurface. The theoretical foundations of the method were developed by Cagniard (1953) and detailed descriptions of the method are given by Simpson & Bahr (2005) and Chave & Jones (2012).

The MT method measures electric field strength (***E***) and magnetic field strength (***H***) time series at the surface of the Earth. These time series data are converted with Fourier analysis to frequency-domain responses which describe the impedance of the Earth. In the general 3-D case, the impedance is a complex-valued full-rank second-order tensor:

$$\boldsymbol{Z}(\omega) = \begin{bmatrix} Z_{xx}(\omega) & Z_{xy}(\omega) \\ Z_{yx}(\omega) & Z_{yy}(\omega) \end{bmatrix} \tag{C.1}$$

where

$$Z_{ij}(\omega) = \frac{E_i(\omega)}{H_j(\omega)} \tag{C.2}$$

for orthogonal horizontal directions *x* and *y*, typically geographic north and east as in this study. We have assumed an $e^{i\omega t}$ temporal variation of the electromagnetic signals, which are assumed to be plane waves, and ω is the angular frequency. A second transfer function, the vertical magnetic transfer function, can be computed using only the magnetic field components:

$$\boldsymbol{T}(\omega) = \begin{bmatrix} T_{zx}(\omega) & T_{zy}(\omega) \end{bmatrix} = \begin{bmatrix} \dfrac{H_z(\omega)}{H_x(\omega)} & \dfrac{H_z(\omega)}{H_y(\omega)} \end{bmatrix} \tag{C.3}$$

where *z* is the vertical direction, pointing downwards in a conventional right-handed coordinate system. The vertical magnetic transfer function is often called the tipper and is referred to as such throughout the main manuscript.

These transfer functions are used to estimate the electrical resistivity at depth, where the frequency of the electromagnetic signals controls the depth of exploration, in metres, according to the skin depth equation:

$$\delta = 503\sqrt{\rho T} \tag{C.4}$$

where ρ is the bulk resistivity in Ωm, and $T = 2\pi/\omega$ is the period of the signal in seconds. Therefore, longer periods give information about deeper resistivity structures. The apparent resistivity and phase, respectively, are calculated from the impedance as:

$$\rho_{a\,ij}(\omega) = \frac{1}{\omega\mu_0}\left|Z_{ij}(\omega)\right|^2 \tag{C.5}$$

where the magnetic permeability of the Earth is assumed to be μ_0, the permeability of free space, and

$$\phi_{ij}(\omega) = Arg[Z_{ij}(\omega)] = \tan^{-1}\left[\frac{Im\left[Z_{ij}(\omega)\right]}{Re\left[Z_{ij}(\omega)\right]}\right] \tag{C.6}$$

which is usually between 0 and 90 degrees. For 1-D Earth structure, the phase is less than 45° when the resistivity is increasing with depth and it is greater than 45° when the resistivity is decreasing with depth.

Once the electromagnetic time series are processed, MT data are generally viewed as apparent resistivity, phase, and tipper curves in the frequency domain. MT data may also be viewed as determinant apparent resistivity and determinant phase, where the impedance in equations C.5 and C.6 is replaced with the square root of the determinant of the impedance tensor:

$$Z_{det}(\omega) = det\begin{bmatrix} Z_{xx}(\omega) & Z_{xy}(\omega) \\ Z_{yx}(\omega) & Z_{yy}(\omega) \end{bmatrix}^{1/2} = \left[Z_{xx}(\omega) * Z_{yy}(\omega) - Z_{xy}(\omega) * Z_{yx}(\omega)\right]^{1/2} \tag{C.7}$$

which is a single complex number. Tipper data are often viewed in map view as induction vectors:

$$\boldsymbol{I}(\omega) = T_{zx}(\omega)\,\hat{x} + T_{zy}(\omega)\,\hat{y} \tag{C.8}$$

which point away from conductive regions, known as the Wiese convention, when the real part is plotted. If equation C.8 is multiplied by -1, the induction vectors point toward conductive regions, known as the Parkinson convention. Some examples of these quantities are shown and discussed in Section 5.3.2.

C.2. Sensitivity tests

C.2.1. Depth range of data sensitivity

To determine the maximum depth at which the MT data were sensitive to resistivity variations, the preferred resistivity model was altered to be 1 Ωm below specified depths (Table C.3). The MT response of the preferred model was compared to the response of these edited models by using the Kolmogorov-Smirnov (KS) test (Massey, 1951) to determine if the residuals of the forward responses were statistically significantly different, as described by Lee *et al.* (2020). If the asymptotic significance (*p*-value) is less than the specified significance level (0.02), then the residuals are from statistically different distributions at a specified confidence level (98%). This indicates that the models are different in a statistical sense and that the MT data are sensitive to resistivity variations at the depth of the 1 Ωm layer. The exact resistivity value is not important; it just needs to be significantly lower than the starting resistivity of 100 Ωm.

When the conductive layer was shallower than 415 km depth, the *p*-value was less than 0.02 for the full dataset as well as for the impedance and tipper data separately (Table C.3). The MT data are therefore sensitive to resistivity variations in the upper 415 km. This study interprets upper mantle structure to a depth of 100 km and this test shows that this part of the resistivity model is well resolved by the MT data.

The minimum depth at which the MT data were sensitive to resistivity variations was investigated using the skin depth (equation C.4). The mean resistivity of the upper 15 km of the model, excluding padding cells, was 870 Ωm, which corresponds to a skin depth of 15 km at the shortest period of 1 s (Figure C.15). A lower resistivity would give a shallower skin depth. Taking these factors into account, it was decided to reduce interpretation of structure in the upper 10 km of the model.

C.2.2. Inversion of synthetic MT data

Synthetic inversions were then used to investigate model resolution. Test models were generated with features representing the CCRC, RDC, SABC, and asthenosphere. Various resistivity values and configurations were used (Figure C.16-Figure C**.26**).

Synthetic MT data were generated for 17 resistivity models, then Gaussian noise was added (5% for impedance data and 0.03 for tipper data). The error floors defined in Section 5.3.3 were applied, then the synthetic MT data were inverted using a range of model covariance length scales (Table C.4 and Table C.**5**).

The effect of horizontal smoothing was investigated by using $\gamma = 0.4$ in the vertical direction and $\gamma = \{0.3, 0.4, 0.5, 0.6\}$ in the horizontal directions (Figure C.16-Figure C.**20**). With low γ, the CCRC polygon was recovered as a mottled swath of low resistivity, and it was too shallow when the background resistivity was high. With high γ, the resistivity was more uniform but too low in some places. It was decided that $\gamma = 0.5$ was the best choice for the horizontal directions for the inversion to reliably recover the structure.

The effect of vertical smoothing was investigated by using $\gamma = 0.5$ in the horizontal directions and $\gamma = \{0.3, 0.4, 0.5\}$ in the vertical direction (Figure C.16-Figure C.**20**). With high γ, many of the recovered conductors were too thick, so it was decided that $\gamma = 0.3$ was the best choice for the vertical direction. The observed MT data were inverted using $\gamma(x,y,z) = (0.5,0.5,0.3)$ as mentioned in Section 5.3.4.

The ability to resolve the CCRC as multiple discrete conductors was investigated with resistivity models consisting of regions with sets of parallel conductors (Table C.5 and Figure C.21-Figure C.**26**). Synthetic MT data from 12 synthetic resistivity models were inverted using $\gamma(x,y,z) = (0.5,0.5,0.3)$. The conductors were 22 km thick in all configurations, and located in the depth range 16-38 km. The gaps between conductors were always the same width as the conductors. When the conductors were 10 km, 20 km, or 0.2° latitude (~22 km) wide, the inversions did not recover the true resistivity patterns. It should be recalled that the model cells were 5 km wide, and the median interstation distance was 22 km. When the conductors were 30 km or 40 km wide, the inversions recovered the true resistivity patterns very well when the background resistivity was 100 Ωm and moderately well when the background resistivity was 1,000 Ωm.

For the scenario with 10 km wide conductors and a background resistivity of 100 Ωm, the synthetic MT data are shown in Figure C.27, and the data predicted by the inversion model are shown in Figure C.28. For the scenario with 40 km wide conductors and a background resistivity of 100 Ωm, the synthetic MT data are shown in Figure C.29, and the data predicted

by the inversion model are shown in Figure C.30. In both cases, the data were fit well by the inversion.

These synthetic inversions illustrated some key properties inherent to magnetotelluric imaging that should be considered when interpreting the preferred resistivity model. MT cannot always accurately image a conductor located beneath another conductor, especially when the upper one is less resistive than the lower one. This was seen by the fact that the asthenosphere (30 Ωm) was not always well-resolved below the CCRC (3 Ωm). Also, it is very important to consider MT station locations. Some of the synthetic results show a clear correlation between low resistivity and locations of MT stations. Caution must be employed when interpreting a resistivity model in an area with spatially sparse MT data. Finally, anomalies should not be considered robust unless they are at least 30 km (six model cells) wide.

C.3. Calculations of temperature and pressure

Geotherms in the southern Omineca belt and adjacent craton were taken from previous studies that used heat flow data, seismic velocities, mantle xenoliths, and other observations (Currie & Hyndman, 2006; Hyndman, 2010; Hyndman et al., 2009). The geotherms are based on heat flow values of 80-100 mW/m^2 in the southern Omineca belt, 50-60 mW/m^2 in the southern Foreland belt, and 40-45 mW/m^2 in the adjacent craton (Hyndman & Lewis 1999).

The brittle-ductile transition (BDT) occurs at a temperature of ~400 °C ± 50 °C (Nesbitt & Muehlenbachs, 1995) corresponding to ~14-17 km depth in the backarc region of the southern Canadian Cordillera and ~29-42 km depth in the adjacent craton. There is an increase in crustal thickness from ~35 km in the southern Omineca belt to more than 40 km in the adjacent craton, and the geotherms predict Moho temperatures > 800 °C in the southern Omineca belt and > 400 °C in the craton.

There is considerable uncertainty about the mantle temperature beneath the southern Canadian Cordillera (Canil et al., 2021; Currie & Hyndman, 2006; Hyndman, 2010; Hyndman et al., 2009). The geotherm in panel (a) of Figure 5.10 is equal to the mantle adiabat below the LAB, assumed to be at a depth of 56 km, and the mantle adiabat is based on a potential temperature of 1,300 °C and an adiabatic gradient of 0.4 °C/km (Currie & Hyndman, 2006).

This results in temperatures of 1,325 °C at a depth of 62 km and 1,340 °C at a depth of 100 km. Hyndman *et al.* (2009) used shear wave velocity data to estimate temperatures of ~1,100 °C at a depth of 62 km and ~1,200 °C at a depth of 100 km. Canil *et al.* (2021) used mantle xenolith data from Canadian Cordilleran lavas to calculate depths of equilibration of 45-100 km and temperatures of origin of 1,300-1,475 °C. The mean depth of origin of the lavas from southern BC was 62 km.

Pressure-depth profiles were derived as follows. Fluid pressure is expected to be approximately hydrostatic in the brittle regime and approximately lithostatic in the ductile regime (Nesbitt & Muehlenbachs, 1995). Assuming this, Figure 5.10 shows approximate fluid pressure given uniform densities of 0.9 g/cm^3 for water and 3.1 g/cm^3 for rock. The density of water increases with increasing pressure and decreases with increasing temperature (Anderson et al., 1991). Since temperature and pressure both increase with depth, the density of water is ~0.9 g/cm^3 at temperatures of ~200-500 °C and corresponding pressures of ~0.1-0.5 GPa (Figure C.39). Lithostatic pressure was also calculated using a three-layer model and the difference was negligible, so the uniform-density calculation was shown.

C.4. Magnetotelluric data

Table C.1 lists all 331 MT sites that were used in the inversion to create the published resistivity model.

Table C.1*: Details of the MT sites that were used in the inversion described in Chapter 5.*

Station Name	Latitude	Longitude	Year	Institution or Project	Instrument
aba114	49.082	-113.308	2008	U of A	NIMS
aba115	49.082	-112.369	2008	U of A	NIMS
aba314	50.295	-113.322	2008	U of A	NIMS
aba315	50.318	-112.399	2008	U of A	NIMS
aba415	50.932	-112.730	2008	U of A	NIMS
aba513	51.589	-114.085	2008	U of A	NIMS
aba613	52.218	-114.023	2008	U of A	NIMS
aba614	52.346	-113.273	2008	U of A	NIMS
aba713	52.909	-113.861	2008	U of A	NIMS
aba714	52.909	-113.088	2008	U of A	NIMS
aba715	53.220	-112.528	2010	U of A	NIMS
aba716	52.858	-112.435	2010	U of A	NIMS
aba730	52.934	-113.475	2014	U of A	NIMS

aba735	53.119	-113.979	2014	U of A	NIMS
aba740	53.294	-113.668	2014	U of A	NIMS
aba745	53.295	-114.419	2014	U of A	NIMS
aba750	53.650	-114.340	2014	U of A	NIMS
aba813	53.435	-114.089	2008	U of A	NIMS
aba814	53.130	-113.358	2010	U of A	NIMS
aba840	53.843	-112.881	2014	U of A	NIMS
aba915	53.718	-112.443	2010	U of A	NIMS
abc122	49.247	-121.926	2003	U of A	LIMS
abc125	49.319	-121.614	2003	U of A	NIMS
abc132	49.492	-121.279	2003	U of A	LIMS
abc134	49.601	-121.005	2003	U of A	LIMS
abc136	49.742	-120.898	2003	U of A	LIMS
abc140	49.879	-120.639	2003	U of A	LIMS
abc146	50.201	-120.158	2003	U of A	LIMS
abc150	50.463	-119.878	2003	U of A	LIMS
abc154	50.603	-119.532	2003	U of A	LIMS
abc158	50.746	-119.138	2003	U of A	LIMS
abc162	50.892	-118.679	2003	U of A	LIMS
abc166	50.941	-118.229	2004	U of A	NIMS
abc172	51.232	-117.674	2004	U of A	NIMS
abc176	51.362	-117.434	2004	U of A	NIMS
abc184	51.575	-116.788	2004	U of A	NIMS
abc188	51.803	-116.587	2004	U of A	NIMS
abc190	52.012	-116.569	2004	U of A	NIMS
abc192	52.166	-116.481	2004	U of A	NIMS
abc194	52.336	-116.358	2004	U of A	NIMS
abc198	52.516	-116.190	2004	U of A	NIMS
abc202	52.709	-115.735	2004	U of A	NIMS
abc204	52.838	-115.510	2004	U of A	NIMS
abc206	52.988	-115.340	2004	U of A	NIMS
abc208	53.088	-115.191	2004	U of A	NIMS
abc260	48.899	-121.892	2003	U of A	NIMS
abc285	51.500	-121.126	2009	U of A	NIMS
abc295	51.504	-120.496	2009	U of A	NIMS
abc300	51.491	-120.252	2004	U of A	NIMS
abc310	51.792	-119.692	2006	U of A	NIMS
abc325	52.136	-119.354	2006	U of A	NIMS
abc345	52.560	-119.048	2006	U of A	NIMS
abc365	52.868	-118.556	2006	U of A	NIMS
abc375	52.996	-118.082	2006	U of A	NIMS
abc380	53.136	-118.020	2006	U of A	NIMS
abc384	53.370	-117.765	2006	U of A	NIMS
abc386	53.519	-117.418	2006	U of A	NIMS
abc388	53.569	-116.971	2006	U of A	NIMS
abc390	53.726	-116.533	2006	U of A	NIMS

abt012	52.682	-112.003		Lithoprobe	LIMS
abt013	52.533	-112.289		Lithoprobe	LIMS
abt016	52.467	-112.700		Lithoprobe	LIMS
abt018	52.654	-113.128		Lithoprobe	LIMS
abt022	52.712	-114.052		Lithoprobe	LIMS
abt023	52.809	-114.236		Lithoprobe	LIMS
abt025	52.977	-114.243		Lithoprobe	LIMS
abt026	53.066	-114.634		Lithoprobe	LIMS
abt030	53.426	-114.823		Lithoprobe	LIMS
abt031	52.147	-113.481		Lithoprobe	LIMS
abt032	52.703	-114.418		Lithoprobe	LIMS
abt033	51.950	-112.883		Lithoprobe	LIMS
abt034	51.880	-112.508		Lithoprobe	LIMS
abt035	51.910	-112.138		Lithoprobe	LIMS
abt036	51.995	-113.337		Lithoprobe	LIMS
abt037	52.263	-114.607		Lithoprobe	LIMS
abt040	51.235	-112.702		Lithoprobe	LIMS
abt042	51.128	-112.374		Lithoprobe	LIMS
abt043	51.393	-112.945		Lithoprobe	LIMS
abt044	51.553	-113.026		Lithoprobe	LIMS
abt048	51.061	-112.013		Lithoprobe	LIMS
abt062	50.842	-112.049		Lithoprobe	LIMS
abt064	50.616	-112.081		Lithoprobe	LIMS
abt068	51.713	-113.158		Lithoprobe	LIMS
abt070	51.693	-113.648		Lithoprobe	LIMS
abt072	51.809	-113.783		Lithoprobe	LIMS
abt074	51.955	-113.926		Lithoprobe	LIMS
abt076	52.020	-114.215		Lithoprobe	LIMS
abt078	52.131	-114.435		Lithoprobe	LIMS
abt081	52.330	-115.017		Lithoprobe	LIMS
abt083	52.543	-113.757		Lithoprobe	LIMS
abt089	53.731	-114.921		Lithoprobe	LIMS
abt092	53.873	-115.453		Lithoprobe	LIMS
abt109	53.924	-112.104		Lithoprobe	LIMS
abt201	49.428	-113.734		Lithoprobe	LIMS
abt202	49.431	-113.444		Lithoprobe	LIMS
abt203	49.453	-112.960		Lithoprobe	LIMS
abt205	49.544	-112.664		Lithoprobe	LIMS
abt207	49.689	-112.237		Lithoprobe	LIMS
abt233	49.617	-113.483		Lithoprobe	LIMS
abt234	49.778	-113.448		Lithoprobe	LIMS
abt236	49.948	-113.711		Lithoprobe	LIMS
abt237	50.113	-113.684		Lithoprobe	LIMS
abt238	50.247	-113.812		Lithoprobe	LIMS
abt239	50.378	-113.888		Lithoprobe	LIMS
abt240	50.462	-114.097		Lithoprobe	LIMS

abt241	50.580	-114.161		Lithoprobe	LIMS
abt242	50.681	-114.402		Lithoprobe	LIMS
abt244	50.837	-114.506		Lithoprobe	LIMS
abt245	51.077	-114.501		Lithoprobe	LIMS
abt246	51.142	-114.666		Lithoprobe	LIMS
abt247	51.259	-114.446		Lithoprobe	LIMS
abt248	51.366	-114.601		Lithoprobe	LIMS
abt249	50.968	-114.611		Lithoprobe	LIMS
abt250	51.570	-114.455		Lithoprobe	LIMS
abt251	50.549	-113.038		Lithoprobe	LIMS
abt252	50.794	-113.362		Lithoprobe	LIMS
abt253	50.246	-112.878		Lithoprobe	LIMS
abt256	50.963	-113.388		Lithoprobe	LIMS
abt314	53.987	-115.029		Lithoprobe	LIMS
aet88_10	49.741	-117.058	1988	Lithoprobe	EMAP
bca009	49.288	-117.674	2009	U of A	NIMS
bca010	49.166	-116.651	2009	U of A	NIMS
bca109	49.739	-117.493	2009	U of A	NIMS
bca310	50.370	-117.015	2009	U of A	NIMS
bhn001	51.633	-114.753	2016	U of A	NIMS
bhn002	51.559	-115.056	2016	U of A	NIMS
bhn003	51.276	-115.055	2016	U of A	NIMS
BNP001	51.665	-116.437	2015	U of A	NIMS
BNP003	51.399	-116.124	2015	U of A	NIMS
BNP004	51.276	-115.912	2015	U of A	NIMS
BNP005	51.164	-115.624	2015	U of A	NIMS
CLW001	52.831	-114.849	2015	U of A	NIMS
CLW002	52.629	-115.167	2015	U of A	NIMS
CLW003	52.743	-116.151	2015	U of A	NIMS
CLW004	52.619	-116.432	2015	U of A	NIMS
CLW006	52.150	-115.933	2015	U of A	NIMS
CLW008	52.463	-115.538	2015	U of A	NIMS
clw012	51.915	-114.548	2016	U of A	NIMS
dun-86_5	49.406	-115.809	1986	Duncan	
duncan_23	49.146	-115.565		Duncan	
duncan_38	49.233	-114.229		Duncan	
emr87_16	49.601	-116.662	1987	Lithoprobe	
emr87_20	49.676	-116.338	1987	Lithoprobe	
emr87_23	49.634	-116.145	1987	Lithoprobe	
emr87_24	49.761	-115.663	1987	Lithoprobe	
emr87_26	49.508	-117.702	1987	Lithoprobe	
emr87_5	49.622	-117.130	1987	Lithoprobe	
emr87_9	49.742	-116.676	1987	Lithoprobe	
FH1	52.189	-115.317	2002	U of A	V5-2000
FH2	52.042	-115.541	2002	U of A	V5-2000
flat_4	49.104	-114.490	1985	Shell	

IDA11	48.935	-116.444	2007	EarthScope / USArray	
IDC11	47.839	-116.273	2008	EarthScope / USArray	
JNP001	52.732	-117.639	2015	U of A	NIMS
JNP002	52.740	-117.955	2015	U of A	NIMS
JNP004	52.550	-117.665	2015	U of A	NIMS
JNP006	52.307	-117.329	2015	U of A	NIMS
JNP008	52.070	-116.908	2015	U of A	NIMS
KNP001	50.682	-115.864	2018	U of A	NIMS
KNP002	50.825	-116.013	2018	U of A	NIMS
KNP004	51.168	-116.147	2018	U of A	NIMS
kooc1_1	48.994	-114.959		Phoenix / GSC	
kooc1_14	48.930	-115.322		Phoenix / GSC	
kooc9_14	48.221	-115.974		Phoenix / GSC	
kooc9_15	48.238	-114.990		Phoenix / GSC	
line10_5	50.232	-119.807	1989	Lithoprobe	
line100e_11	49.616	-119.550	1990	Lithoprobe	
line100e_2	49.616	-118.315	1990	Lithoprobe	
line100e_4	49.421	-118.730	1990	Lithoprobe	
line100e_5	49.596	-118.920	1990	Lithoprobe	
line100w_12	49.638	-121.545	1990	Lithoprobe	
line100w_2	49.807	-120.181	1990	Lithoprobe	
line100w_3	49.770	-120.327	1990	Lithoprobe	
line100w_4	49.793	-119.505	1990	Lithoprobe	
line100w_6	49.623	-120.629	1990	Lithoprobe	
line10s_1	49.776	-118.784	1989	Lithoprobe	
line10s_10	49.529	-119.783	1989	Lithoprobe	
line10s_13	49.563	-120.153	1989	Lithoprobe	
line10s_15	49.405	-120.409	1989	Lithoprobe	
line10s_5	49.707	-119.211	1989	Lithoprobe	
line11-12_4	50.322	-121.987	1989	Lithoprobe	
line11-12_5	50.467	-120.759	1989	Lithoprobe	
line13_4	50.673	-121.934	1989	Lithoprobe	
line200_2	49.843	-119.778	1990	Lithoprobe	
line200_4	50.059	-119.808	1990	Lithoprobe	
line300_1	49.539	-121.966	1990	Lithoprobe	
line400_12	51.468	-121.904	1990	Lithoprobe	
line5_4	49.726	-117.983	1989	Lithoprobe	
line500_3	50.353	-119.544	1990	Lithoprobe	
line500_6	50.391	-119.143	1990	Lithoprobe	
line6_1	49.965	-118.083	1989	Lithoprobe	
line6_9	50.407	-118.056	1989	Lithoprobe	
line600_2	49.995	-121.647	1990	Lithoprobe	
line600_3	49.768	-121.775	1990	Lithoprobe	
line600_6	50.044	-121.390	1990	Lithoprobe	
line700_4	50.365	-117.514	1990	Lithoprobe	
line7-9_10	50.191	-118.759	1989	Lithoprobe	

line7-9_13	50.135	-119.074	1989	Lithoprobe	
line7-9_6	50.283	-118.448	1989	Lithoprobe	
line800_1	49.658	-115.879	1990	Lithoprobe	
line800_10	49.604	-114.466	1990	Lithoprobe	
line800_11	49.608	-114.223	1990	Lithoprobe	
line800_12	49.588	-114.002	1990	Lithoprobe	
line800_13	49.630	-113.830	1990	Lithoprobe	
line800_5	49.661	-115.397	1990	Lithoprobe	
line800_7	49.636	-115.072	1990	Lithoprobe	
line800_9	49.636	-114.695	1990	Lithoprobe	
MTB12	48.448	-115.563	2008	EarthScope / USArray	
MTB13	48.373	-114.454	2008	EarthScope / USArray	
MTB14	48.311	-113.325	2008	EarthScope / USArray	
MTB15	48.313	-112.447	2008	EarthScope / USArray	
MTC12	47.889	-115.454	2008	EarthScope / USArray	
MTC13	47.842	-114.559	2008	EarthScope / USArray	
MTC14	47.840	-113.429	2008	EarthScope / USArray	
MTC15	47.745	-112.507	2008	EarthScope / USArray	
rdc010	53.953	-114.289	2008	U of A	NIMS
rdc020	53.830	-113.887	2008	U of A	NIMS
rdc030	53.723	-113.552	2008	U of A	NIMS
rdc040	53.636	-113.130	2008	U of A	NIMS
rdc050	53.542	-112.749	2008	U of A	NIMS
rdc060	53.426	-112.419	2008	U of A	NIMS
rdc070	53.313	-112.039	2008	U of A	NIMS
RMN003	51.105	-116.464	2017	U of A	NIMS
RMN004	50.887	-116.462	2017	U of A	NIMS
RMN005	50.992	-116.216	2017	U of A	NIMS
RMN006	50.548	-116.156	2017	U of A	NIMS
RMN007	50.561	-115.732	2017	U of A	NIMS
RMN008	50.356	-115.581	2017	U of A	NIMS
RMN009	50.221	-116.047	2017	U of A	NIMS
RMN012	49.930	-114.858	2017	U of A	NIMS
RMN013	50.207	-114.992	2017	U of A	NIMS
RMN014	49.257	-116.344	2018	U of A	NIMS
RMN015	50.704	-116.336	2018	U of A	NIMS
RMN016	50.730	-115.658	2018	U of A	NIMS
RMN017	50.363	-116.364	2018	U of A	NIMS
RMN018	49.447	-116.690	2018	U of A	NIMS
RMN019	49.970	-115.820	2018	U of A	NIMS
RMN020	50.150	-115.425	2018	U of A	NIMS
RMN021	49.304	-114.925	2018	U of A	NIMS
RMN022	49.133	-115.132	2018	U of A	NIMS
RMN025	49.054	-116.122	2018	U of A	NIMS
RMN026	50.757	-116.699	2018	U of A	NIMS
RMN028	50.088	-116.118	2018	U of A	NIMS

RMN031	50.677	-117.076	2018	U of A	NIMS
RMN032	50.061	-117.383	2018	U of A	NIMS
RMN036	49.012	-117.178	2018	U of A	NIMS
RMN038	49.372	-116.100	2018	U of A	NIMS
sab001	49.117	-114.000	2009	U of A	NIMS
sab005	49.447	-114.086	2009	U of A	NIMS
sab010	49.817	-114.164	2009	U of A	NIMS
sab015	50.222	-114.182	2009	U of A	NIMS
sab020	49.944	-113.064	2009	U of A	NIMS
sab030	51.246	-113.928	2009	U of A	NIMS
sab035	51.424	-113.540	2009	U of A	NIMS
sab040	49.982	-112.677	2009	U of A	NIMS
sab045	49.978	-112.255	2009	U of A	NIMS
sab055	50.914	-114.221	2009	U of A	NIMS
sab060	51.366	-114.171	2009	U of A	NIMS
sab065	51.792	-114.312	2009	U of A	NIMS
sab070	51.543	-113.518	2009	U of A	NIMS
sab075	50.608	-113.804	2009	U of A	NIMS
sab080	50.895	-113.637	2009	U of A	NIMS
sab085	51.056	-113.731	2009	U of A	NIMS
sab090	51.438	-113.791	2009	U of A	NIMS
sab095	50.440	-112.929	2009	U of A	NIMS
sab100	50.674	-113.120	2009	U of A	NIMS
sab105	51.253	-113.233	2009	U of A	NIMS
sab110	51.846	-113.446	2009	U of A	NIMS
sab115	50.509	-112.590	2009	U of A	NIMS
sab117	50.649	-112.758	2009	U of A	NIMS
sab120	51.061	-112.910	2009	U of A	NIMS
sab125	51.808	-113.058	2009	U of A	NIMS
sab130	50.809	-112.313	2009	U of A	NIMS
sab140	51.460	-112.572	2009	U of A	NIMS
sab145	51.722	-112.509	2009	U of A	NIMS
sab155	51.318	-112.188	2009	U of A	NIMS
sab200	52.171	-112.903	2009	U of A	NIMS
sab204	52.259	-112.374	2010	U of A	NIMS
sab210	51.990	-112.385	2009	U of A	NIMS
SLK001	51.553	-117.297	2017	U of A	NIMS
SLK002	51.708	-117.539	2017	U of A	NIMS
SLK003	51.806	-117.324	2017	U of A	NIMS
SLK004	51.848	-117.808	2017	U of A	NIMS
SLK005	52.099	-118.462	2017	U of A	NIMS
SLK006	51.828	-118.514	2017	U of A	NIMS
SLK007	51.671	-118.550	2017	U of A	NIMS
SLK008	51.418	-118.406	2017	U of A	NIMS
SLK009	51.214	-118.201	2017	U of A	NIMS
SLK010	51.454	-118.155	2017	U of A	NIMS

SLK011	51.014	-116.671	2017	U of A	NIMS
SLK012	51.119	-116.989	2017	U of A	NIMS
SSK001	50.015	-114.422	2018	U of A	NIMS
SSK002	50.276	-114.575	2018	U of A	NIMS
SSK003	50.518	-114.836	2018	U of A	NIMS
SSK004	50.825	-114.868	2018	U of A	NIMS
ten015	51.133	-121.433		Gough	
ten023	53.160	-121.843		Gough	
ten601	53.468	-119.895		Gough	
ten609	53.478	-120.633		Gough	
ten706	53.243	-120.388		Gough	
ten709	53.311	-119.398		Gough	
ten712	53.015	-119.726		Gough	
ten808	50.308	-121.121		Gough	
ten809	50.488	-121.514		Gough	
ten814	50.263	-120.699		Gough	
ten902	53.353	-121.123		Gough	
WAA10	48.927	-117.597	2007	EarthScope / USArray	
WAB05	48.192	-122.040	2007	EarthScope / USArray	
WAB06	48.521	-121.387	2007	EarthScope / USArray	
WAB07	48.507	-120.264	2007	EarthScope / USArray	
WAB08	48.567	-119.430	2007	EarthScope / USArray	
WAB10	48.264	-117.329	2007	EarthScope / USArray	
WAC05	47.899	-121.721	2007	EarthScope / USArray	
WAC06	47.881	-120.666	2007	EarthScope / USArray	
WAC07	47.804	-119.912	2007	EarthScope / USArray	
WAC08	47.770	-119.174	2007	EarthScope / USArray	
WAC09	47.821	-118.200	2007	EarthScope / USArray	
WAC10	47.812	-117.284	2007	EarthScope / USArray	
YHD001	53.533	-115.490	2015	U of A	NIMS
YHD002	53.563	-116.263	2015	U of A	NIMS
YHD003	53.365	-115.801	2015	U of A	NIMS
YHD004	53.367	-116.609	2015	U of A	NIMS
YHD005	53.276	-116.322	2015	U of A	NIMS
YHD006	53.125	-115.924	2015	U of A	NIMS
YHD008	53.354	-117.198	2015	U of A	NIMS
YHD009	53.175	-116.811	2015	U of A	NIMS
YHD010	53.073	-116.532	2015	U of A	NIMS
YHD011	52.931	-116.369	2015	U of A	NIMS
YHD012	53.203	-117.542	2015	U of A	NIMS
YHD013	53.044	-117.101	2015	U of A	NIMS
YHD014	52.813	-116.900	2015	U of A	NIMS

C.5. Details of all inversions and sensitivity tests

Table C.2*: Details of the inversions that used observed MT data. The preferred model is from iteration 313 of inversion 20. Author's note: the preferred model is also referred to as SEBC-s331p18r12-run2-iter170.*

Inversion Number	Number of MT Data Locations	Num. of Periods (impedance)	Num. of Periods (tipper)	Horizontal Cell Size (km)	Half-space Resistivity (Ωm)	Tear (N = no, Y = yes, H = half)	Resistivity Above Tear (Ωm)	X Covariance Length Scale	Y Covariance Length Scale	Z Covariance Length Scale	Initial Value of λ	Final Value of λ	Initial RMS Misfit	Final RMS Misfit	Total Number of Iterations
Inversions 1-7 explored different datasets with a constant value of λ															
1	213	19	0	6	100	N	N/A	0.3	0.3	0.3	1	1	10.0	2.66	52
2	213	19	0	6	100	N	N/A	0.4	0.4	0.4	1	1	10.0	2.08	123
3	264	19	19	5	100	N	N/A	0.3	0.3	0.4	1	1	18.6	4.07	92
4	263	19	19	5	100	N	N/A	0.3	0.3	0.4	1	1	18.4	3.38	101
5	263	19	0	5	100	N	N/A	0.3	0.3	0.4	1	1	22.0	3.81	53
6	344	18	0	5	100	N	N/A	0.3	0.3	0.4	1	1	21.1	3.58	97
7	339	18	18	5	100	N	N/A	0.3	0.3	0.4	1	1	77.4	5.96	22
Inversions 8-11 explored different values of λ with the same dataset															
8	338	18	18	5	100	N	N/A	0.3	0.3	0.4	1	10^{-8}	77.6	2.76	322
9	338	18	18	5	100	N	N/A	0.3	0.3	0.4	100	1	77.6	3.09	344
10	338	18	18	5	100	N	N/A	0.4	0.4	0.4	100	100	77.6	6.45	24
11	338	18	18	5	100	N	N/A	0.4	0.4	0.4	1	0.1	77.6	2.98	194
Inversions 12-15 explored different initial model configurations (see Section 3.4)															
12	336	18	18	5	100	N	N/A	0.3	0.3	0.4	1	10^{-8}	17.5	2.35	310
13	336	18	18	5	100	Y	100	0.3	0.3	0.4	1	10^{-8}	17.5	2.81	321
14	336	18	18	5	100	Y	10	0.3	0.3	0.4	1	10^{-8}	15.7	2.70	296
15	336	18	18	5	100	H	10	0.3	0.3	0.4	1	10^{-8}	15.9	2.42	348
Inversions 16 and 17 used less tipper data (see Section 3.3)															
16	336	18	0	5	100	N	N/A	0.3	0.3	0.4	1	10^{-8}	20.9	1.93	447
17	336	18	16	5	100	H	10	0.3	0.3	0.4	1	10^{-8}	16.0	2.23	297
Inversions 18 and 19 used different covariance length scales															
18	336	18	16	5	100	H	10	0.5	0.5	0.5	1	10^{-8}	16.0	2.10	342
19	336	18	16	5	100	H	10	0.5	0.5	0.3	1	10^{-8}	16.0	2.17	329
Inversion 20 used 331 data locations instead of 336															
20	331	18	16	5	100	H	10	0.5	0.5	0.3	1	10^{-8}	15.8	1.94	382

***Table C.3**: Results of Kolmogorov-Smirnov (KS) tests between the residuals of the responses of the preferred model and altered models. The altered models labeled "Yes" had residuals that were from the same distribution as the preferred model, with 98% confidence. The model layers listed in the second column were changed to 1 Ωm, then forward calculations were performed. The misfit of the altered models is shown in the last two columns.*

Edited Models		Impedance and Tipper		Impedance Only		Tipper Only		RMS Misfit (Unaltered = 2.08)	
1 Ωm Depth	**Layers**	***p*-value**	**Same?**	***p*-value**	**Same?**	***p*-value**	**Same?**	**Altered**	**Increase**
51 km	37-58	0.0000	No	0.0000	No	0.0000	No	5.40	3.31
102 km	42-58	0.0000	No	0.0000	No	0.0000	No	4.18	2.10
206 km	47-58	0.0000	No	0.0000	No	0.0000	No	2.89	0.81
273 km	49-58	0.0000	No	0.0000	No	0.0000	No	2.48	0.39
314 km	50-58	0.0000	No	0.0000	No	0.0002	No	2.33	0.24
361 km	51-58	0.0010	No	0.0168	No	0.0101	No	2.22	0.14
415 km	52-58	0.1179	Yes	0.6653	Yes	0.1047	Yes	2.16	0.07
477 km	53-58	0.6759	Yes	0.9759	Yes	0.6132	Yes	2.12	0.04

***Table C.4**: Details of inversions that used synthetic data from simplified models. Model slices are shown in Figures C.7-C.11.*

Inversion Name	Background Resistivity (Ωm)	CCRC Resistivity (Ωm)	SABC and RDC Resistivity (Ωm)	Astheno-sphere Resistivity (Ωm)	γ_x	γ_y	γ_z	Initial RMS Misfit ($\lambda = 1$)	Final RMS Misfit ($\lambda = 10^{-8}$)
Synthetic Model 1									
syn1-inv1	100	30	N/A	N/A	0.3	0.3	0.4	1.07	0.82
syn1-inv2	100	30	N/A	N/A	0.4	0.4	0.4	1.07	0.81
syn1-inv3	100	30	N/A	N/A	0.5	0.5	0.4	1.07	0.81
syn1-inv4	100	30	N/A	N/A	0.6	0.6	0.4	1.07	0.81
syn1-inv5	100	30	N/A	N/A	0.5	0.5	0.5	1.07	0.82
syn1-inv6	100	30	N/A	N/A	0.5	0.5	0.3	1.07	0.81
Synthetic Model 2									
syn2-inv1	100	10	N/A	N/A	0.3	0.3	0.4	1.98	0.82
syn2-inv2	100	10	N/A	N/A	0.4	0.4	0.4	1.98	0.82
syn2-inv3	100	10	N/A	N/A	0.5	0.5	0.4	1.98	0.82
syn2-inv4	100	10	N/A	N/A	0.6	0.6	0.4	1.98	0.81
syn2-inv5	100	10	N/A	N/A	0.5	0.5	0.5	1.98	0.82
syn2-inv6	100	10	N/A	N/A	0.5	0.5	0.3	1.98	0.82
Synthetic Model 3									
syn3-inv1	100	3	N/A	N/A	0.3	0.3	0.4	3.93	0.82
syn3-inv2	100	3	N/A	N/A	0.4	0.4	0.4	3.93	0.82
syn3-inv3	100	3	N/A	N/A	0.5	0.5	0.4	3.93	0.82
syn3-inv4	100	3	N/A	N/A	0.6	0.6	0.4	3.93	0.82
syn3-inv5	100	3	N/A	N/A	0.5	0.5	0.5	3.93	0.82
syn3-inv6	100	3	N/A	N/A	0.5	0.5	0.3	3.93	0.82

Synthetic Model 4									
syn4-inv1	100	3	3	30	0.3	0.3	0.4	4.82	0.82
syn4-inv2	100	3	3	30	0.4	0.4	0.4	4.82	0.82
syn4-inv3	100	3	3	30	0.5	0.5	0.4	4.82	0.82
syn4-inv4	100	3	3	30	0.6	0.6	0.4	4.82	0.83
syn4-inv5	100	3	3	30	0.5	0.5	0.5	4.82	0.83
syn4-inv6	100	3	3	30	0.5	0.5	0.3	4.82	0.82
Synthetic Model 5									
syn5-inv1	1000	3	3	30	0.3	0.3	0.4	6.79	0.84
syn5-inv2	1000	3	3	30	0.4	0.4	0.4	6.79	0.86
syn5-inv3	1000	3	3	30	0.5	0.5	0.4	6.79	0.85
syn5-inv4	1000	3	3	30	0.6	0.6	0.4	6.79	0.85
syn5-inv5	1000	3	3	30	0.5	0.5	0.5	6.79	0.86
syn5-inv6	1000	3	3	30	0.5	0.5	0.3	6.79	0.85

Table C.5*: Details of inversions that used synthetic data from simplified models. All conductive prisms are 22 km thick, at 16-38 km depth. Model slices are shown in Figures C.12-C.17.*

Inversion Name	**Background Resistivity (Ωm)**	**Conductor Resistivity (Ωm)**	**Width of Prisms**	**Shape of Prisms**	γ_x	γ_y	γ_z	**Initial RMS Misfit ($\lambda = 1$)**	**Final RMS Misfit ($\lambda = 10^{-8}$)**
Synthetic Models 6 and 7 (with 17 Conductive Prisms)									
syn6-inv1	100	3	10 km	Rectangle	0.5	0.5	0.3	2.28	0.83
syn7-inv1	1000	3	10 km	Rectangle	0.5	0.5	0.3	5.54	0.89
Synthetic Models 8 and 9 (with 9 Conductive Prisms)									
syn8-inv1	100	3	20 km	Rectangle	0.5	0.5	0.3	2.35	0.83
syn9-inv1	1000	3	20 km	Rectangle	0.5	0.5	0.3	5.51	0.91
Synthetic Models 10 and 11 (with 6 Conductive Prisms)									
syn10-inv1	100	3	30 km	Rectangle	0.5	0.5	0.3	2.53	0.81
syn11-inv1	1000	3	30 km	Rectangle	0.5	0.5	0.3	5.40	0.88
Synthetic Models 12 and 13 (with 5 Conductive Prisms)									
syn12-inv1	100	3	40 km	Rectangle	0.5	0.5	0.3	2.65	0.82
syn13-inv1	1000	3	40 km	Rectangle	0.5	0.5	0.3	5.49	0.82
Synthetic Models 14-17 (with 8 Conductive Prisms)									
syn14-inv1	100	3	0.2° lat.	Polygon	0.5	0.5	0.3	1.80	0.82
syn15-inv1	1000	3	0.2° lat.	Polygon	0.5	0.5	0.3	5.37	0.88
syn16-inv1	100	3	0.2° lat.	Diagonal	0.5	0.5	0.3	2.35	0.82
syn17-inv1	1000	3	0.2° lat.	Diagonal	0.5	0.5	0.3	5.28	0.89

***Table C.6**: Skin depth in three different half-spaces at the four periods shown in Figure 5.4.*

Period (s)	δ(10 Ωm) in km	δ(100 Ωm) in km	δ(1000 Ωm) in km
5.82	4	12	38
31.2	9	28	89
177	21	67	211
3,150	89	282	893

C.6. Additional figures

This section contains 39 figures that were mentioned in the GJI publication (Chapter 5) but omitted for brevity.

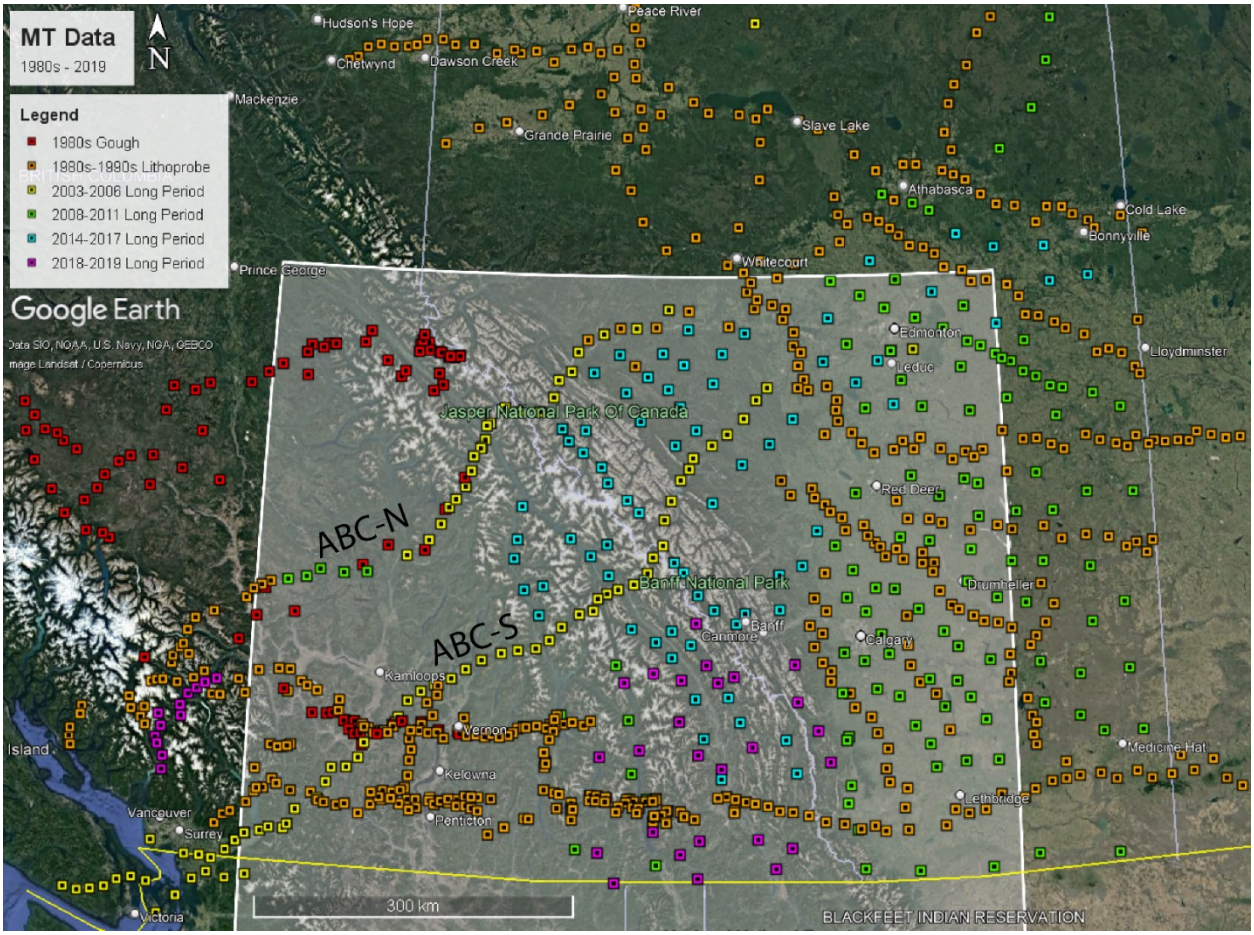

***Figure C.1**: Locations of MT data in southwestern Canada, collected over four decades from the 1980s through the 2010s. The white polygon is the area covered by the inversion dataset. ABC-N and ABC-S are the profiles of Rippe et al. (2013) as shown in Figure C.14. Image source: Google Earth / Landsat / Copernicus.*

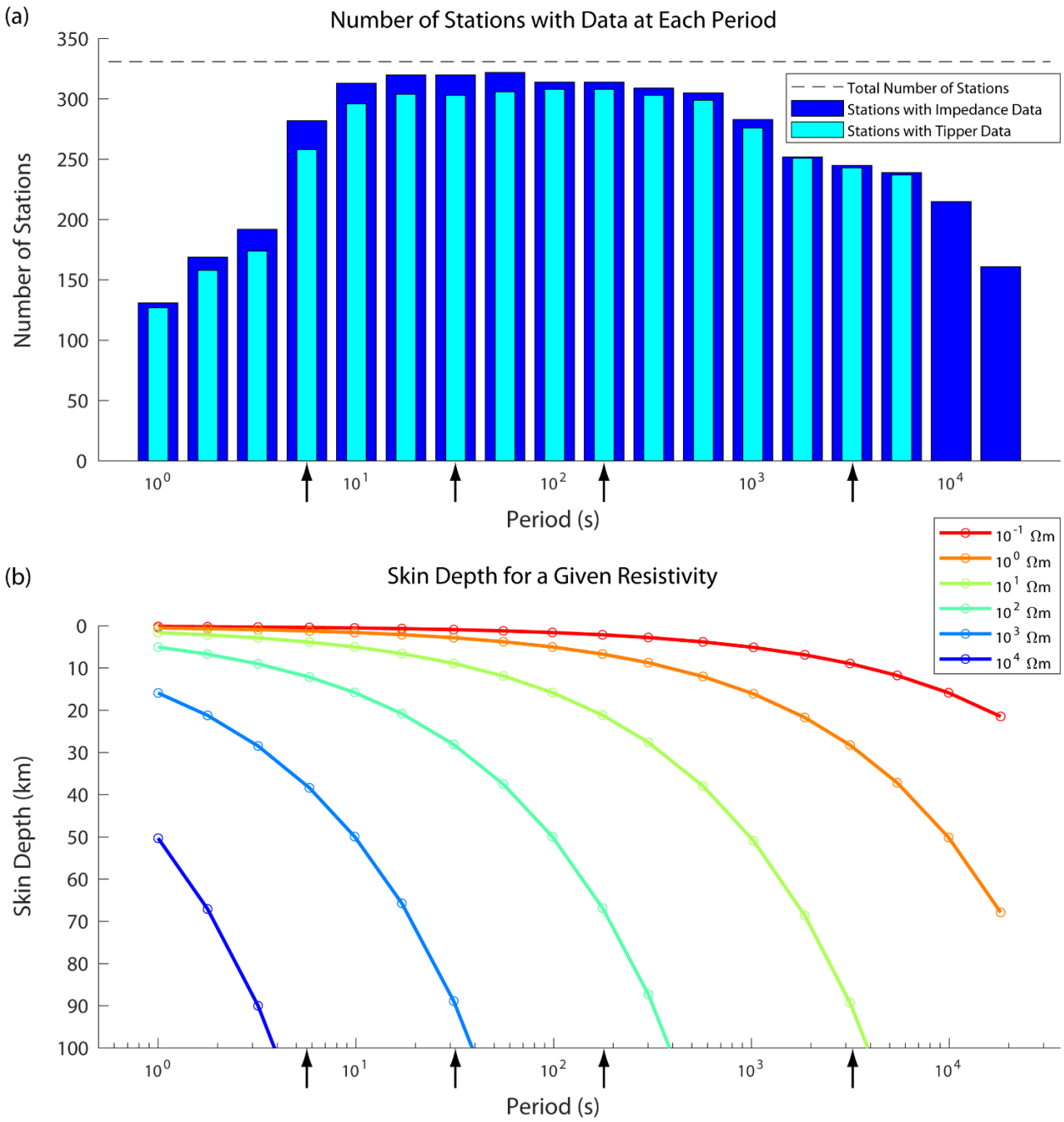

***Figure C.2**: (a) Periods used in the inversion and the number of MT stations with data at each period. (b) Skin depth evaluated at the periods above and six resistivity values between 0.1 and 10,000 Ωm. Black arrows indicate the periods shown in Figures 5.4 and 5.5.*

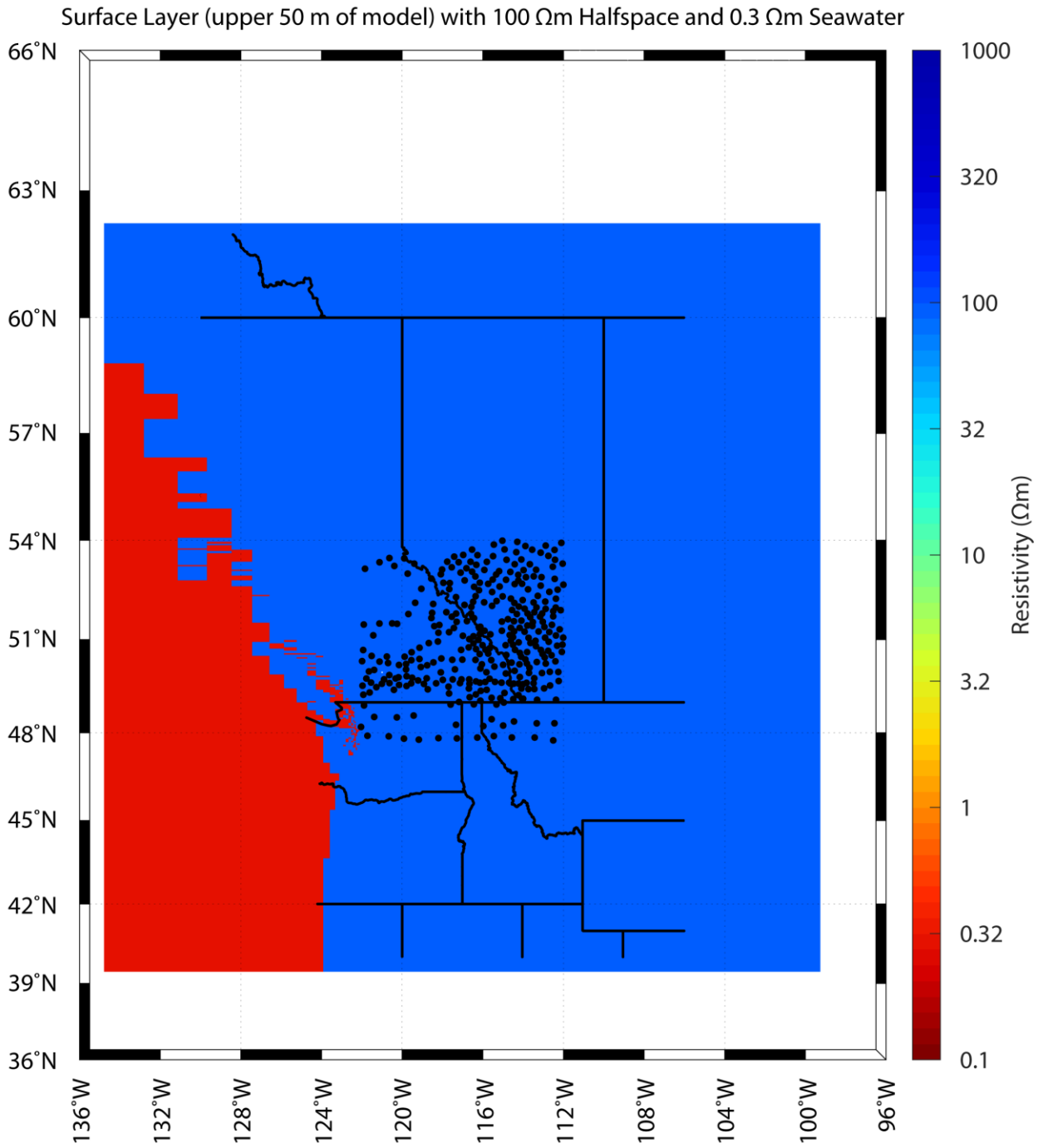

***Figure C.3**: The top layer of a model with 0.3 Ωm seawater in a 100 Ωm halfspace. In the central part of the model, where MT data are defined (black dots), the model cells are 5x5 km horizontally. There are 20 padding cells in each horizontal direction, increasing geometrically by a factor of 1.19. The top layer is 50 m thick and layer thickness increases geometrically by a factor of 1.15. The model is 2698 km, 2728 km, and 1105 km in the N-S, E-W, and vertical directions, respectively (186x192x58 model cells). The MT response of this model is shown in Figures C.4-C.7.*

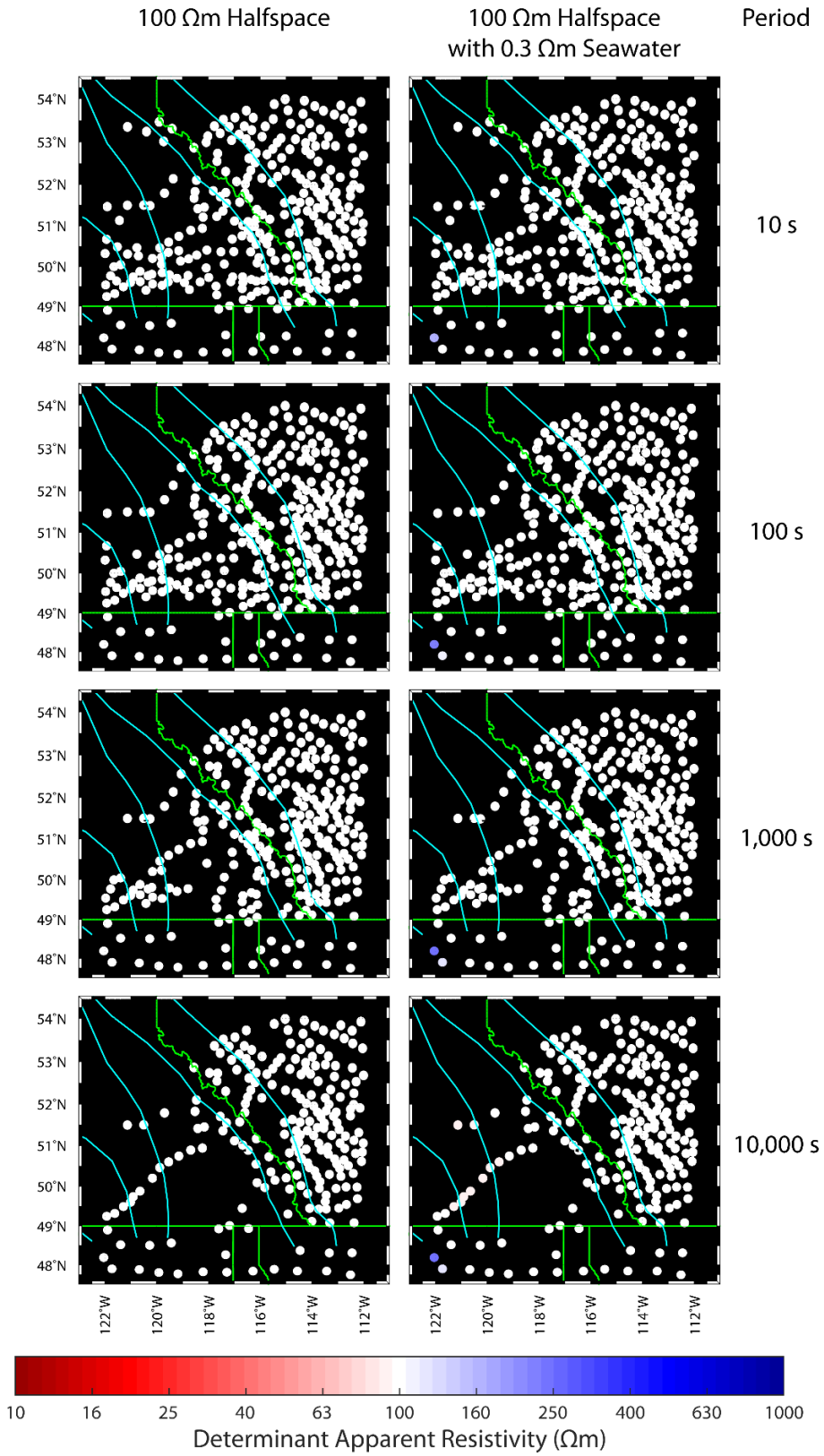

***Figure C.4**: Determinant apparent resistivity calculated from a 100 Ωm halfspace (left column) and the resistivity model shown in Figure C.3 (right column) at four periods. The apparent resistivity is near 100 Ωm in the right column, implying that the 0.3 Ωm seawater does not significantly affect the MT response.*

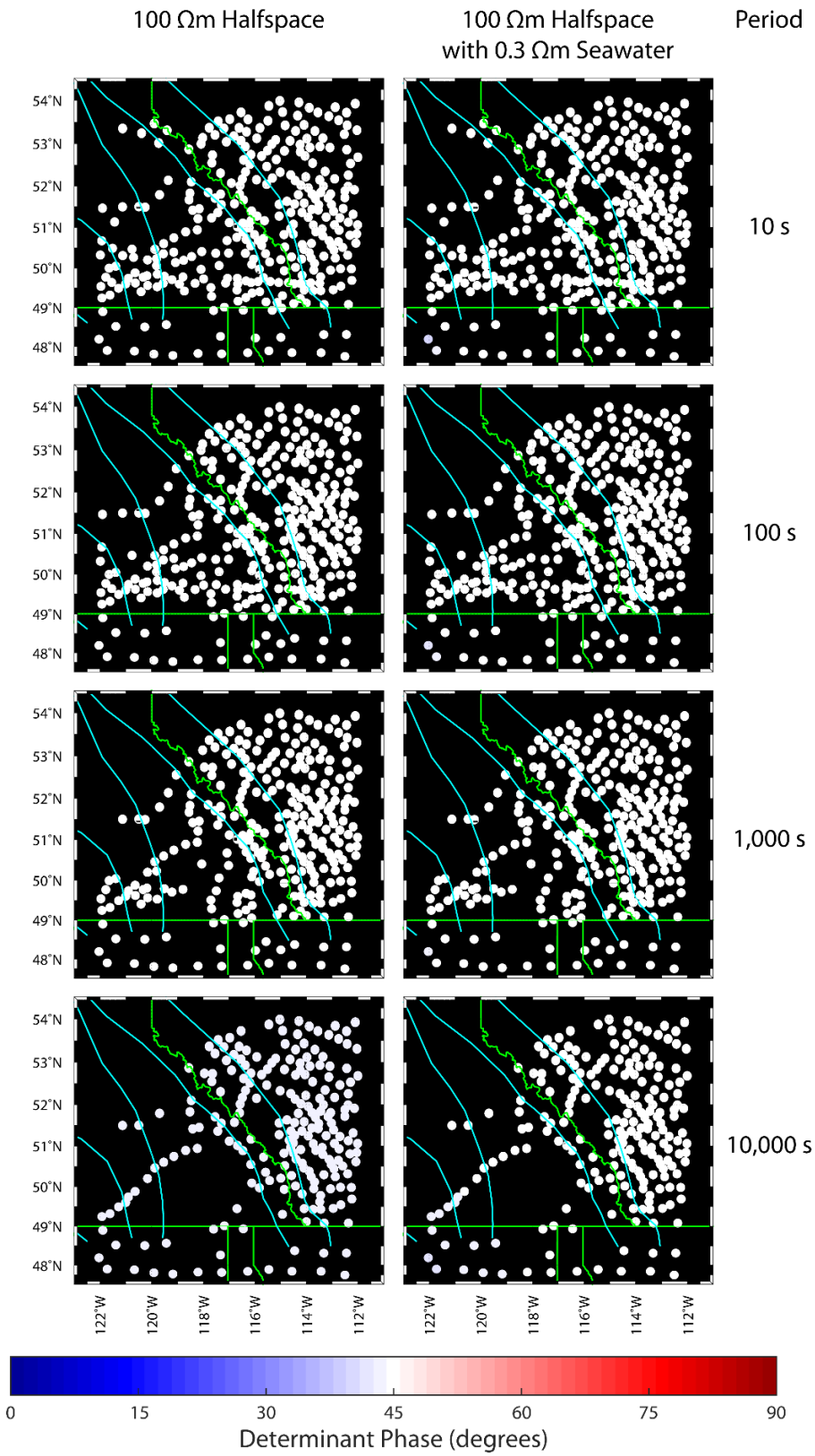

***Figure C.5**: Determinant phase calculated from a 100 Ωm halfspace (left column) and the resistivity model shown in Figure C.3 (right column) at four periods. The phase is near 45° in the right column, implying that the 0.3 Ωm seawater does not significantly affect the MT response.*

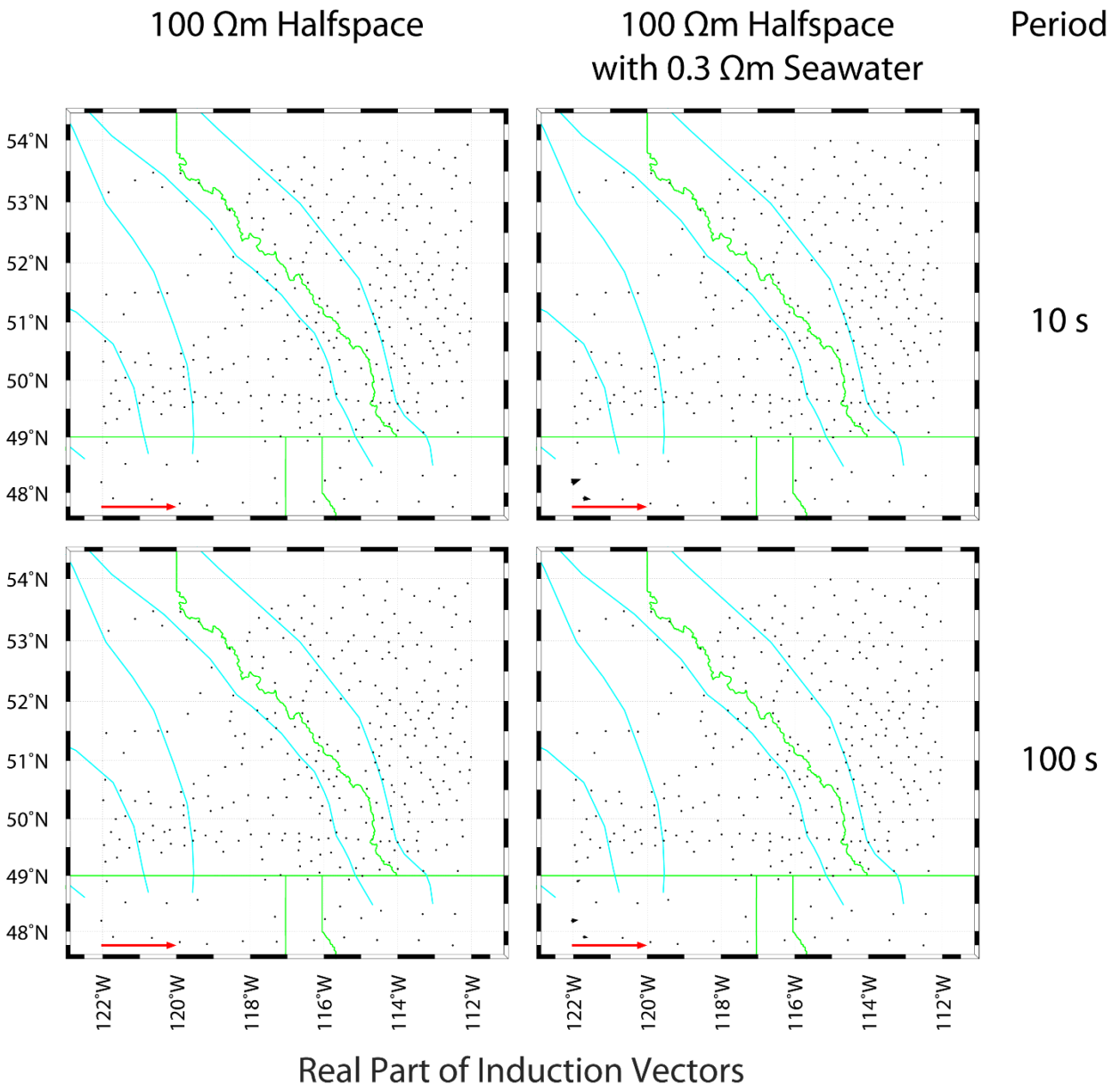

***Figure C.6**: Real part of induction vectors calculated from a 100 Ωm halfspace (left column) and the resistivity model shown in Figure C.3 (right column) at two periods. The induction vector magnitudes in the right column are near zero, implying that the 0.3 Ωm seawater does not significantly affect the tipper response.*

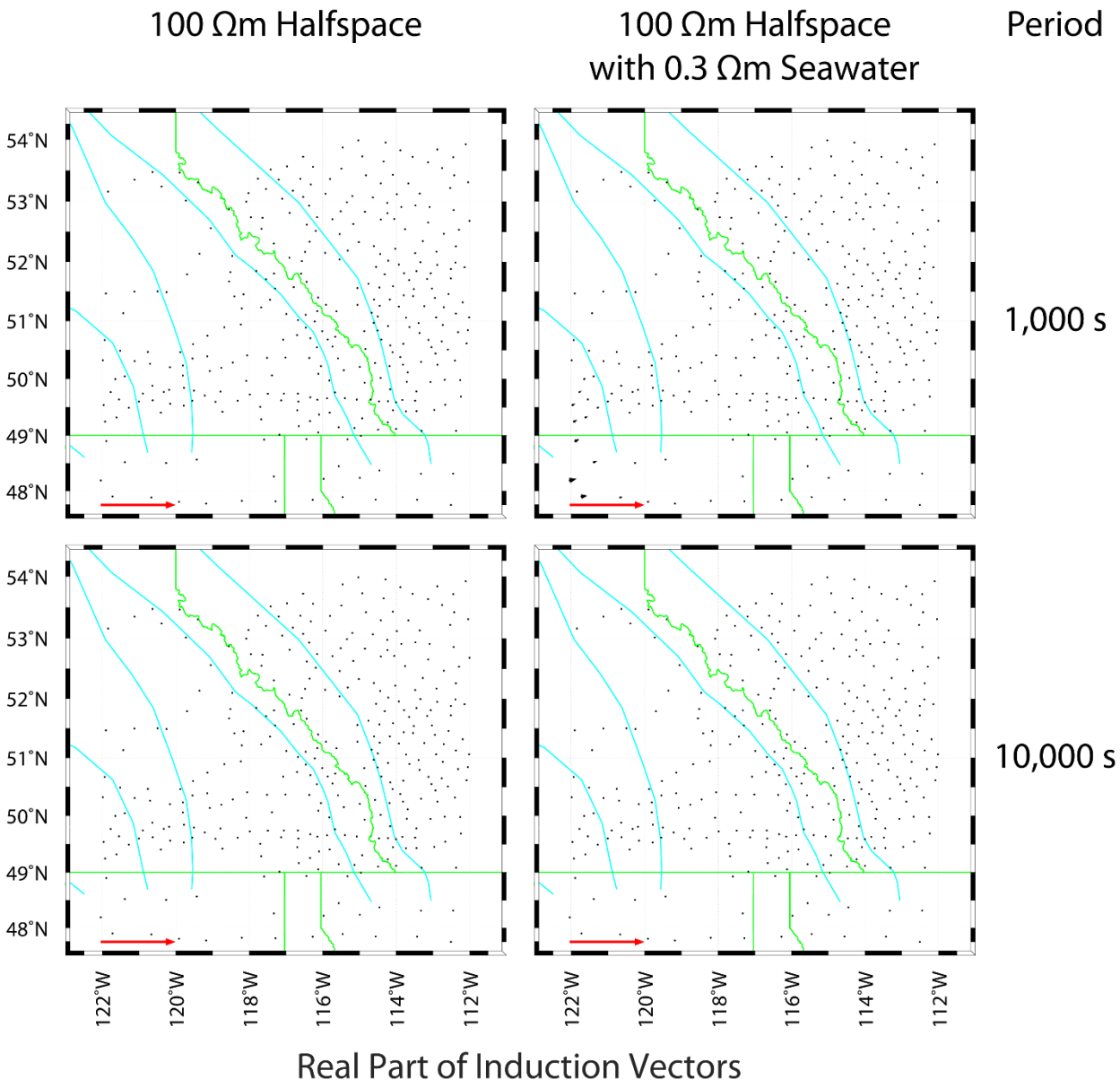

***Figure C.7**: Real part of induction vectors calculated from a 100 Ωm halfspace (left column) and the resistivity model shown in Figure C.3 (right column) at two periods. The induction vector magnitudes in the right column are near zero, implying that the 0.3 Ωm seawater does not significantly affect the tipper response.*

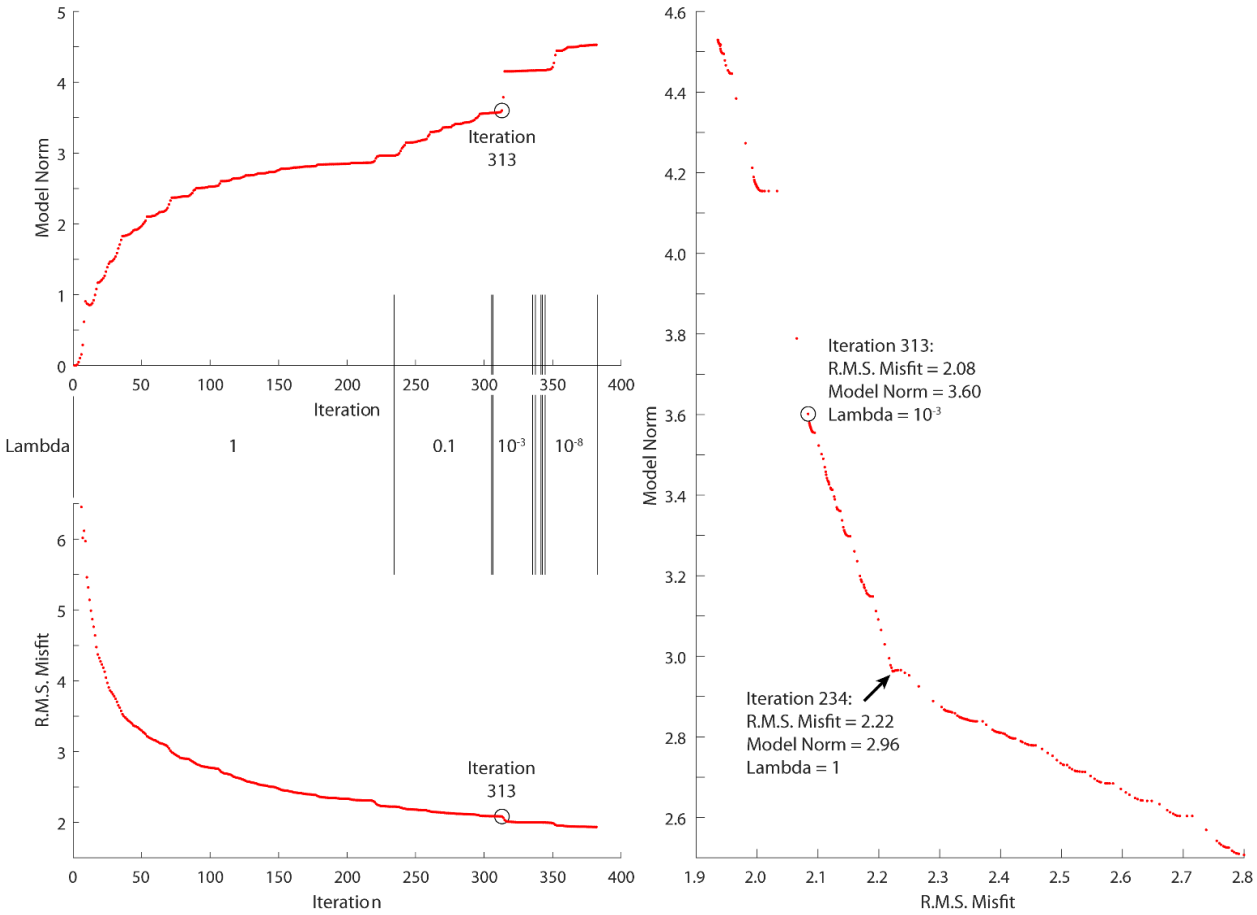

***Figure C.8**: Model norm, lambda, and R.M.S. misfit at each of the 382 inversion iterations (red dots). Model norm increases with iteration number and R.M.S. misfit decreases with iteration number. Lambda was decreased by a factor of 10 each time the change in misfit was less than 10^{-4}, down to and including $\lambda = 10^{-8}$. The preferred model is from iteration 313 (black circle).*

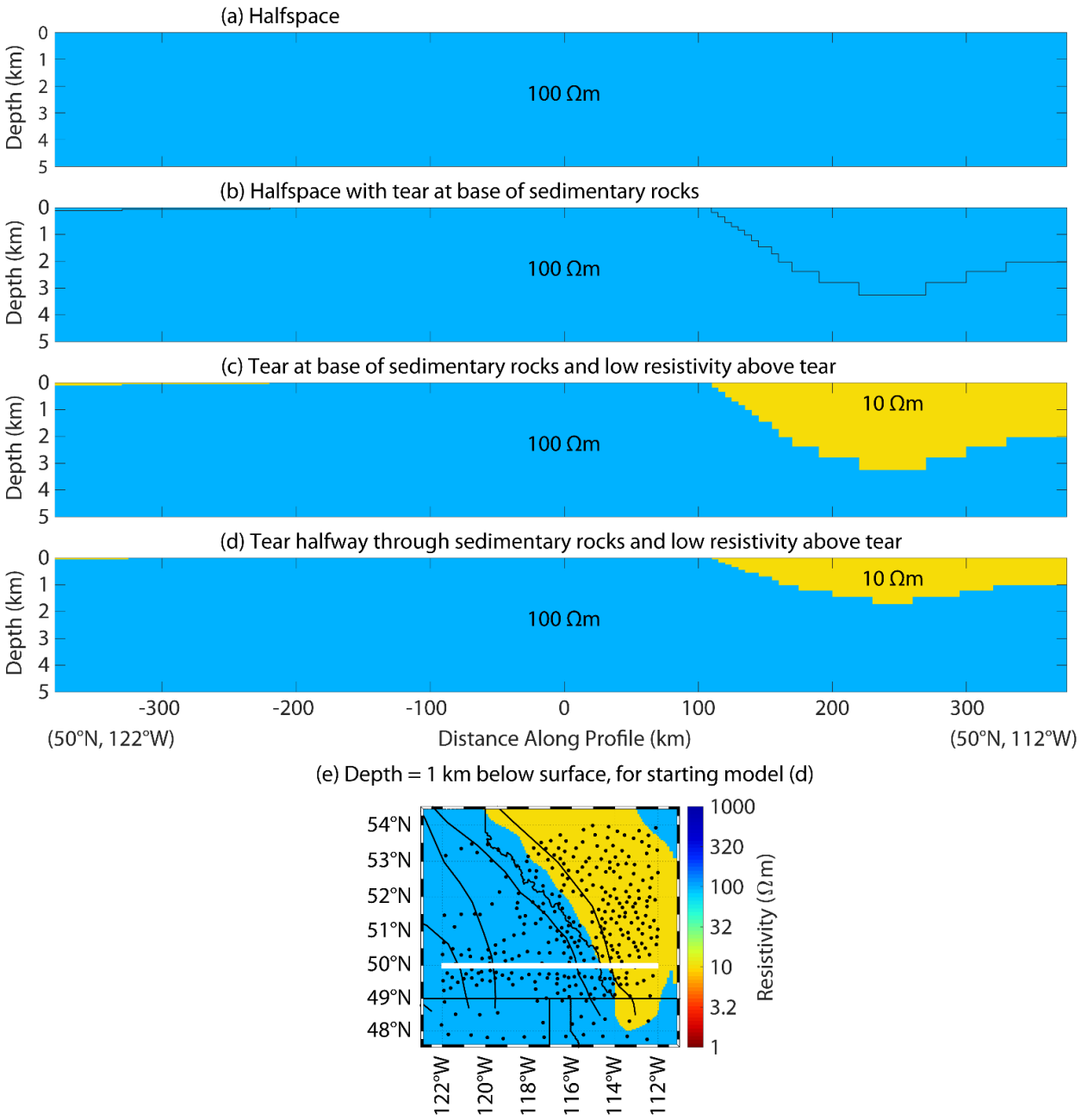

***Figure C.9**: (a-d) The four starting models used in inversions 12-15 (Table C.2) and described in Section 5.3.4. The upper 5 km of the models are shown, vertically exaggerated by a factor of 20. (e) Starting model d at a depth of 1 km. The white line indicates the location of the cross-sections shown above.*

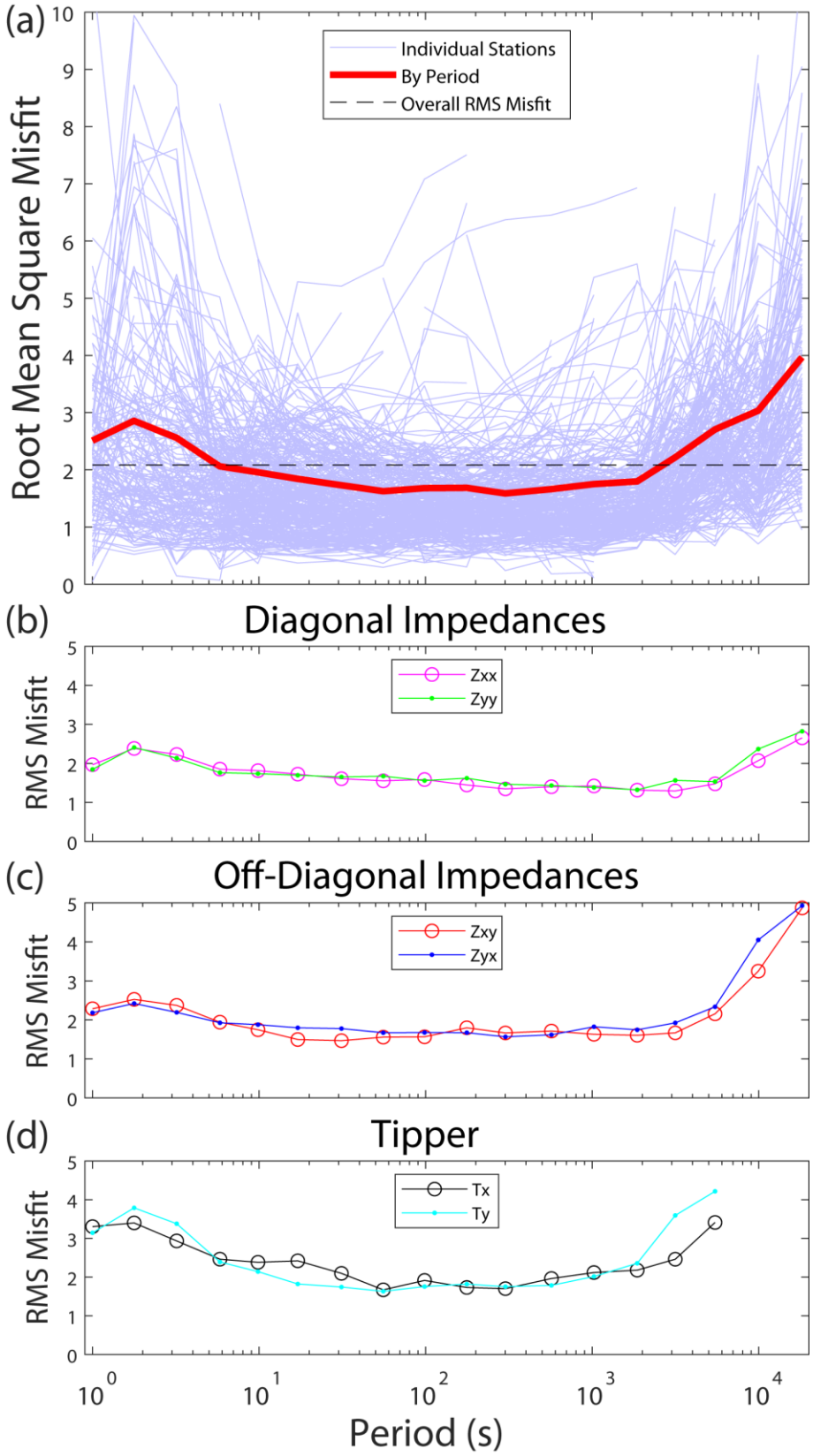

***Figure C.10**: Root-mean-square misfit of observed MT data to predicted MT data from the preferred 3-D resistivity model. (a) Misfit by period and station. (b-d) Misfit by period and data component.*

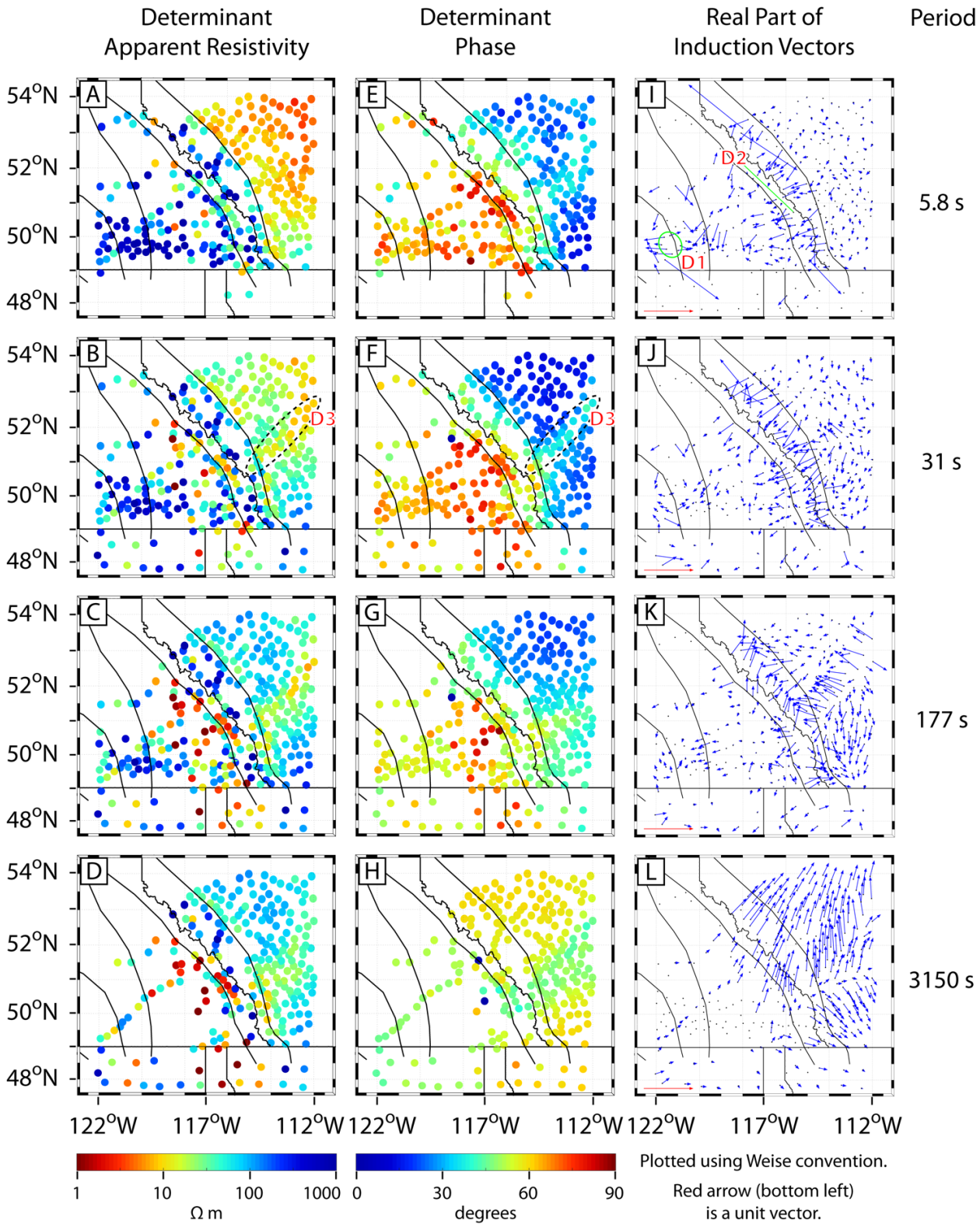

***Figure C.11a**: Determinant apparent resistivity (A-D), determinant phase (E-H), and real part of induction vectors using the Wiese convention (I-L) at four representative periods as predicted by the preferred resistivity model (inversion 20 in Table C.2) which was shown in Figures 5.6-5.8 of the main manuscript.*

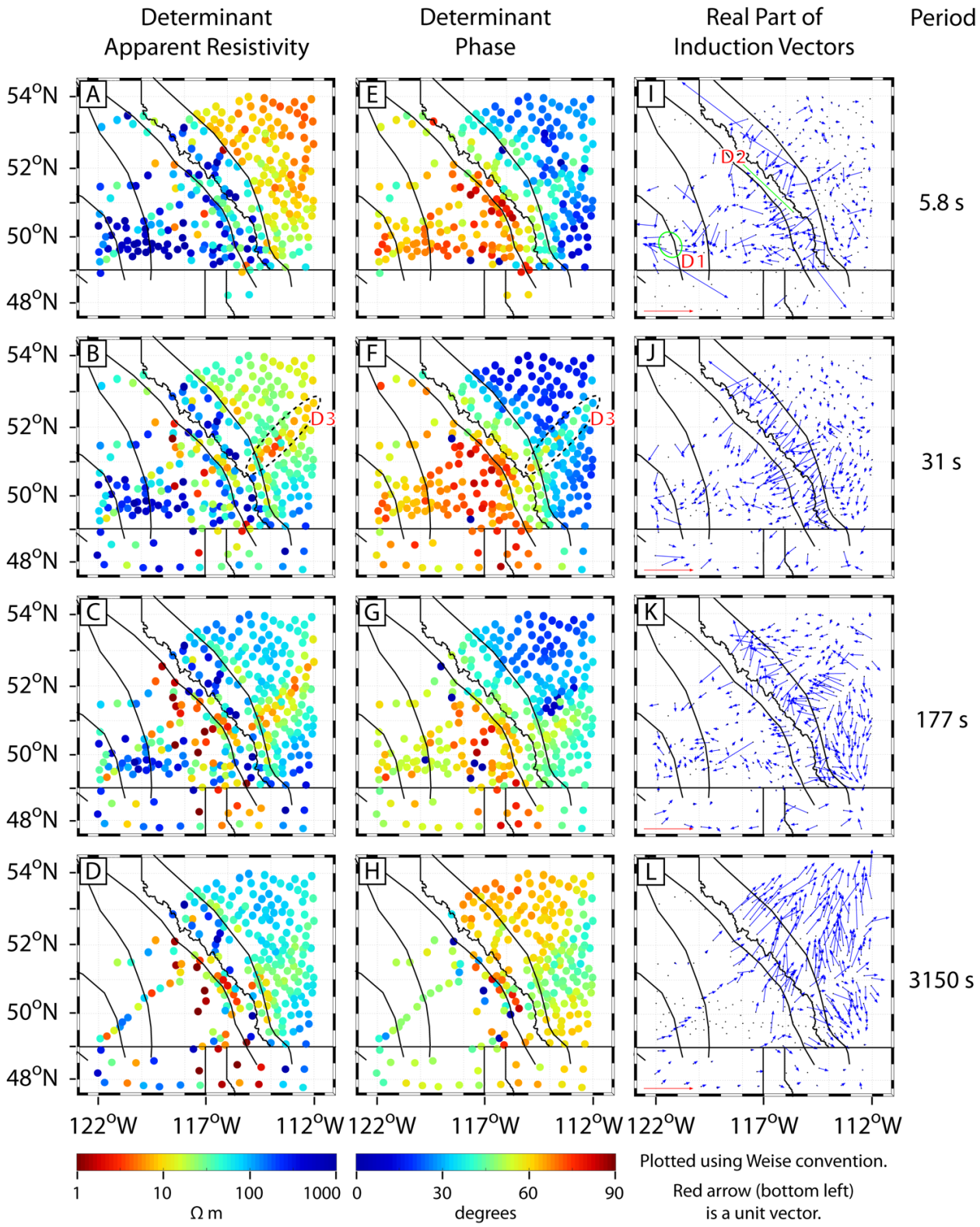

***Figure C.11b**: Determinant apparent resistivity (A-D), determinant phase (E-H), and real part of induction vectors using the Wiese convention (I-L) at four representative periods of the observed data. This shows the same data as Figures 5.4 and 5.5.*

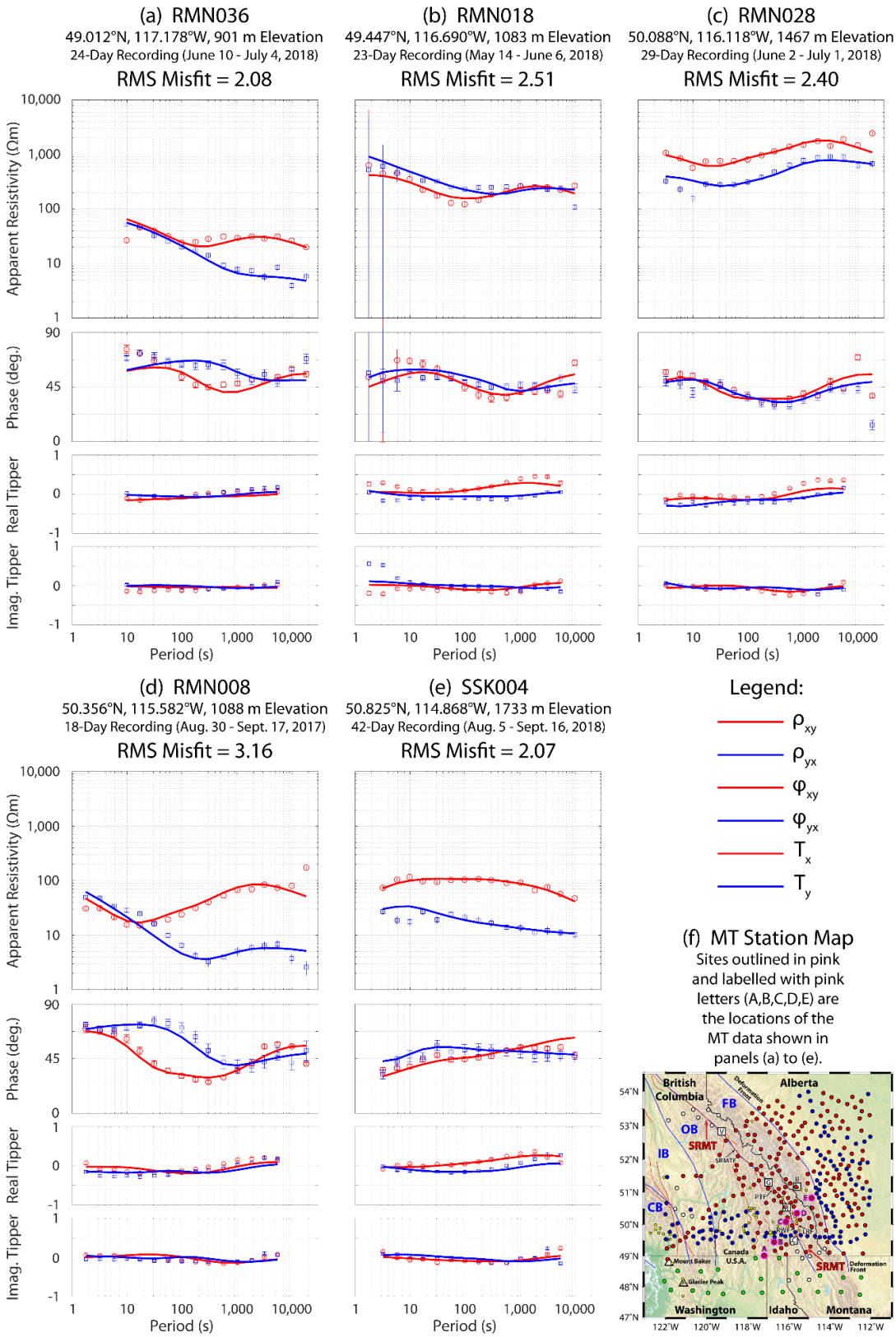

***Figure C.12**: (a-e) Apparent resistivity (ρ), phase (φ), and tipper (T) data at five MT sites. Curves are model responses and circles are measured data. The diagonal components of ρ and φ have been omitted to simplify the figure. (f) Map showing MT station locations.*

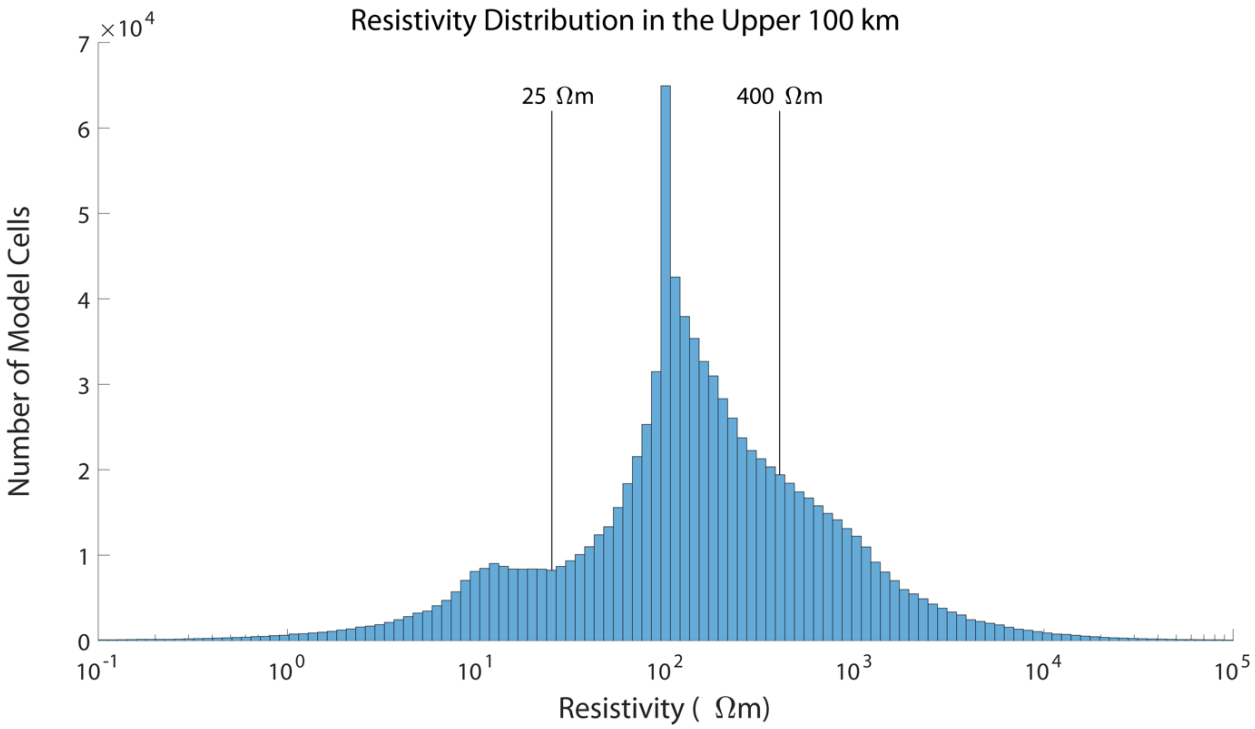

***Figure C.13**: Histogram of model cell resistivity in the upper 100 km of the preferred model, excluding padding cells. Model slices were plotted with 25 m and 400 Ωm resistivity contours, which are equidistant from the initial resistivity of 100 Ωm.*

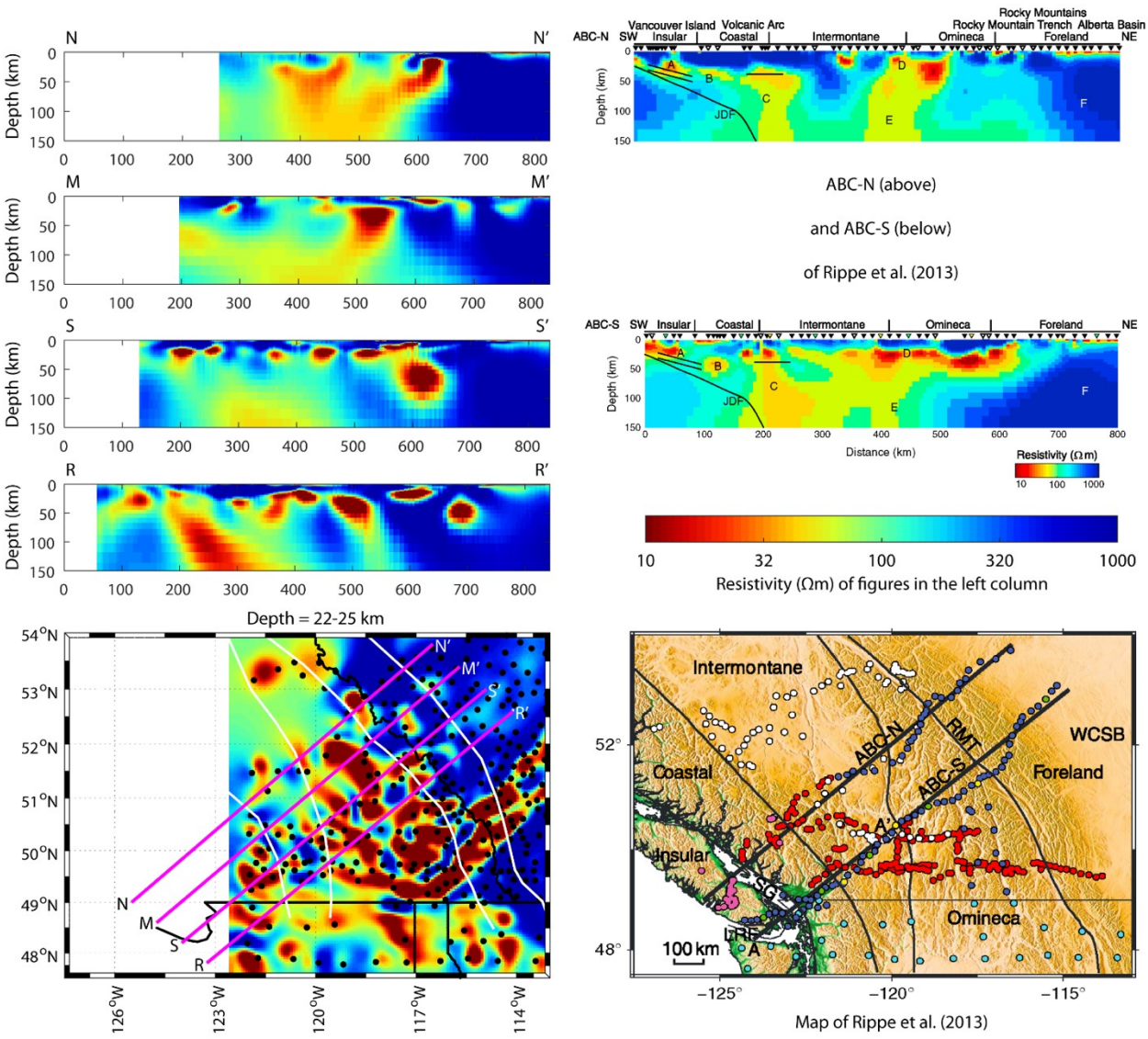

Figure C.14*: Cross-sections from the preferred 3-D resistivity model at the locations indicated by the pink lines. Cross-sections N-N′ and S-S′ correspond to cross-sections ABC-N and ABC-S of Rippe et al. (2013). Note that the resistivity colour range is 10-1,000 Ωm, instead of 1-1,000 Ωm as in the other figures. This was done to be consistent with Rippe et al. (2013) to facilitate a better comparison.*

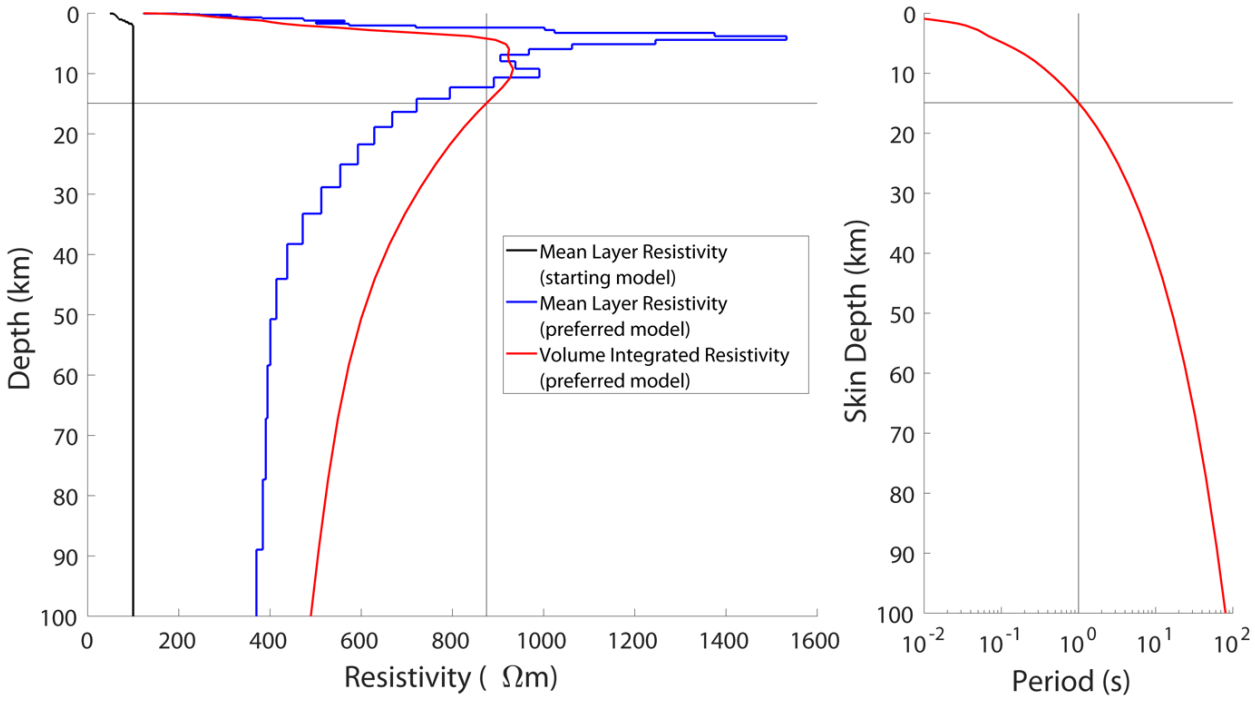

***Figure C.15**: (a) Mean resistivity of individual layers of the starting model (black), mean resistivity of individual layers of the preferred model (blue), and mean resistivity of the volume above a given depth (red), where the padding cells were excluded in all cases. (b) Skin depth as a function of period where the resistivity was determined by the volume average above each depth. The mean resistivity, by volume, of the upper 15 km of the preferred model, excluding padding cells, was 870 Ωm. The skin depth at a period of 1 s in an 870 Ωm half-space is 15 km.*

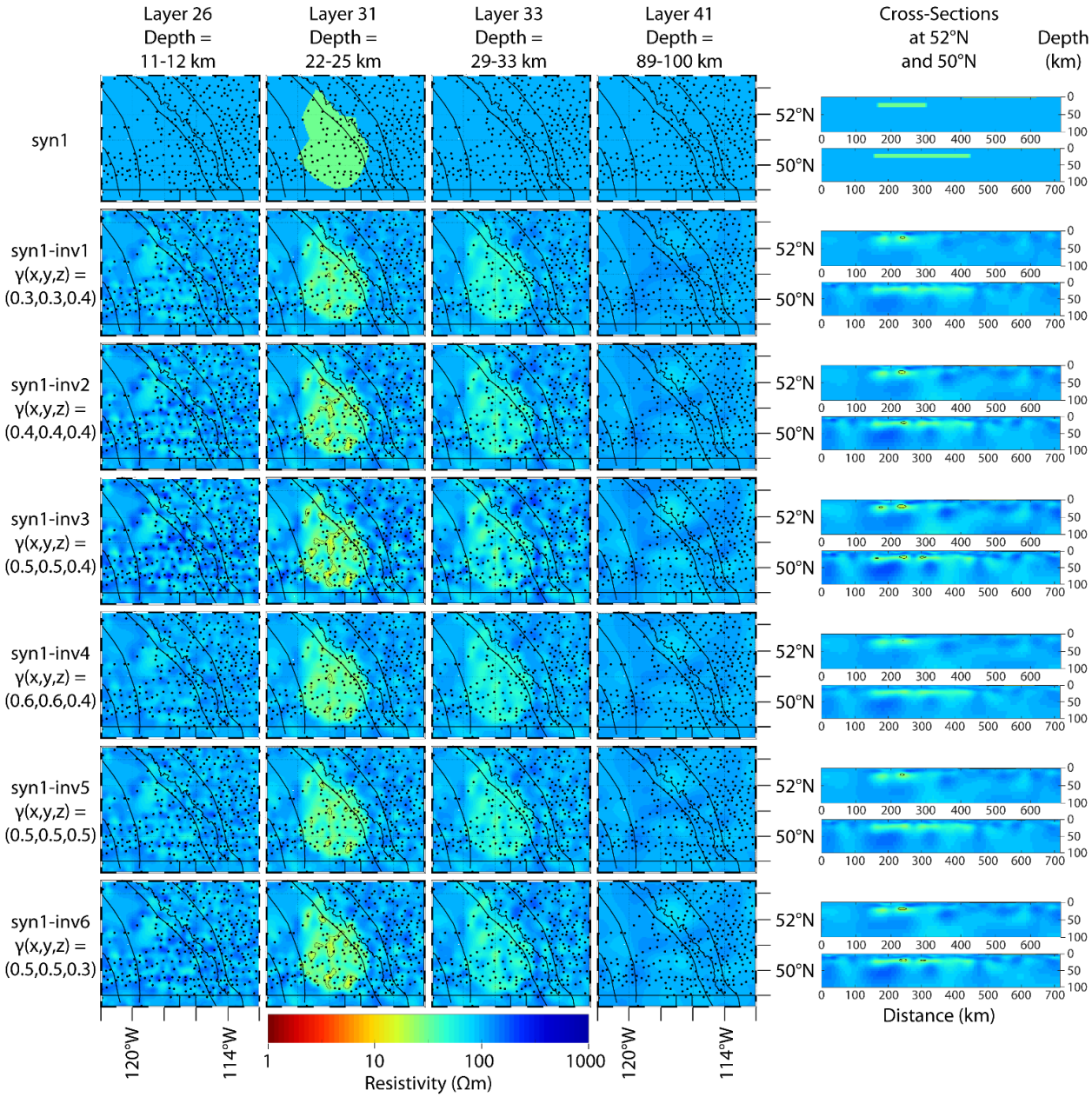

***Figure C.16**: Inversion of synthetic MT data from resistivity model syn1, as described in Section 5.4.2. In this model, the CCRC was approximated by a polygon of 30 Ωm in the depth range 16-29 km, the upper half of the sedimentary basins were assigned a resistivity of 10 Ωm, and the remainder of the model was 100 Ωm. Six inversions (covariance schemes) are listed in Table C.4. The initial R.M.S. misfit was 1.07 and the final R.M.S. misfits were 0.82, 0.81, 0.81, 0.81, 0.82 and 0.81, respectively.*

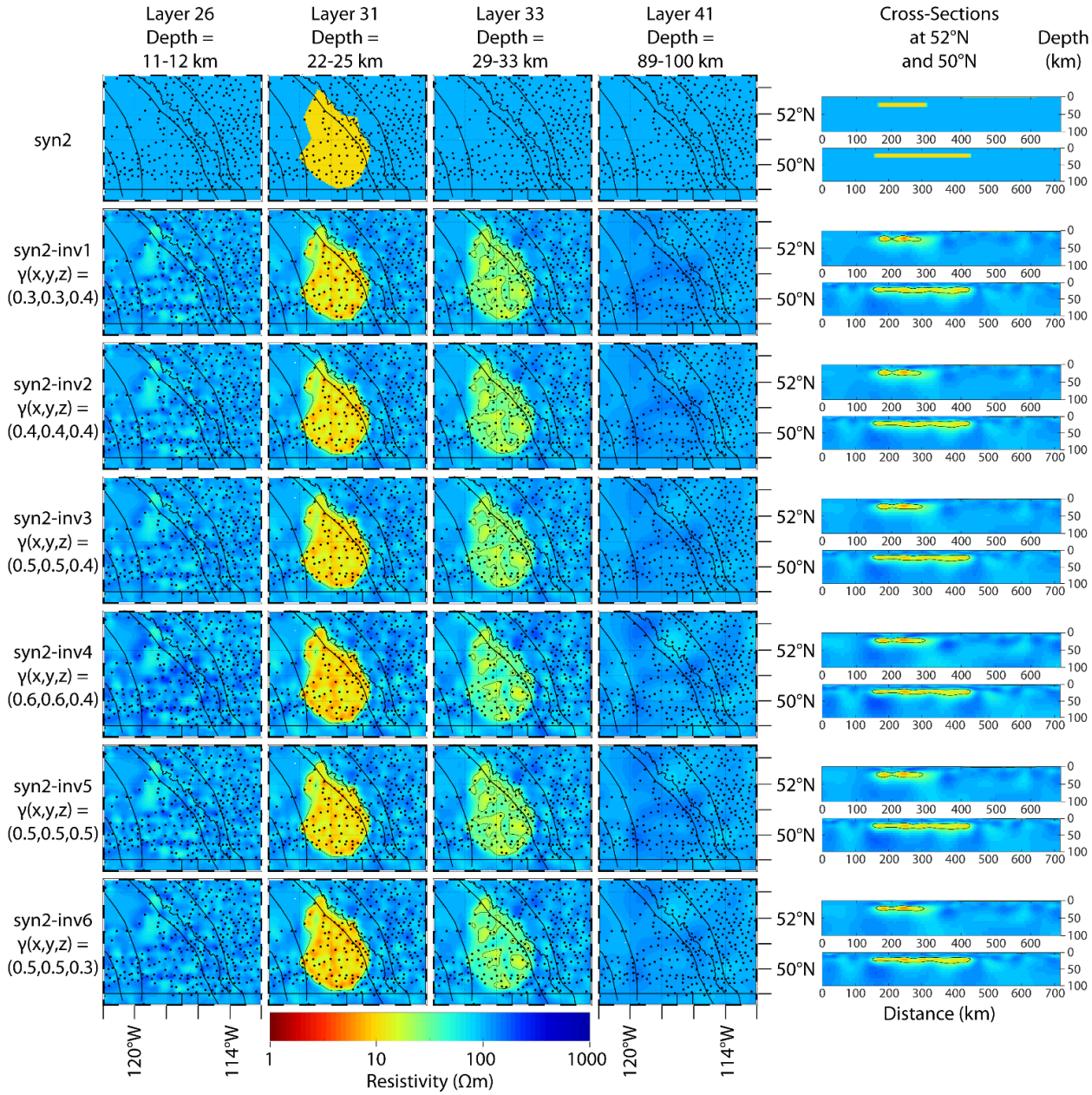

***Figure C.17**: Inversion of synthetic MT data from resistivity model syn2, as described in Section 5.4.2. In this model, the CCRC was approximated by a polygon of 10 Ωm in the depth range 16-29 km, the upper half of the sedimentary basins were assigned a resistivity of 10 Ωm, and the remainder of the model was 100 Ωm. Six inversions (covariance schemes) are listed in Table C.4. The initial R.M.S. misfit was 1.98 and the final R.M.S. misfits were 0.82, 0.82, 0.82, 0.81, 0.82 and 0.82, respectively.*

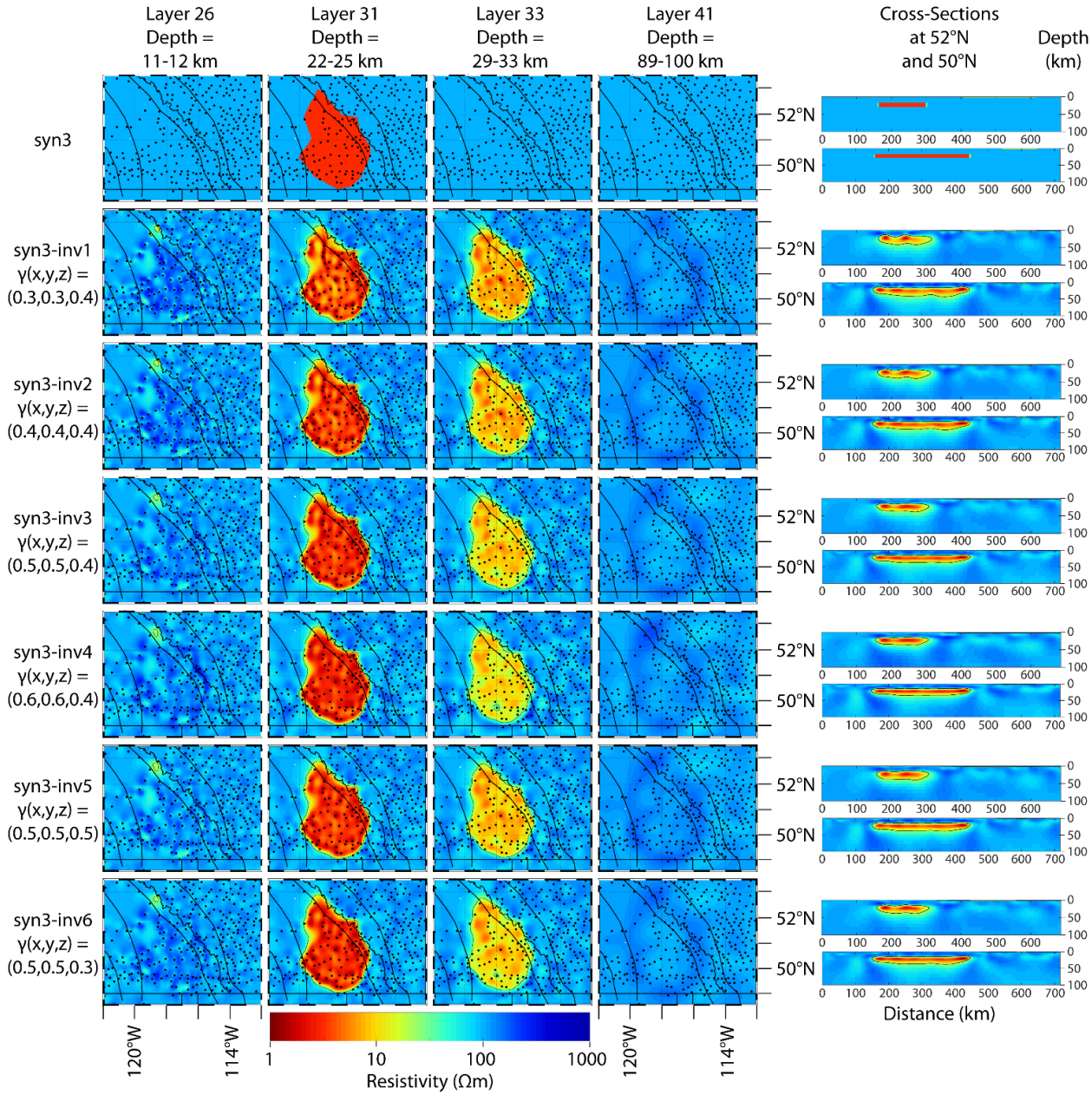

***Figure C.18**: Inversion of synthetic MT data from resistivity model syn3, as described in Section 5.4.2. In this model, the CCRC was approximated by a polygon of 3 Ωm in the depth range 16-29 km, the upper half of the sedimentary basins were assigned a resistivity of 10 Ωm, and the remainder of the model was 100 Ωm. Six inversions (covariance schemes) are listed in Table C.4. The initial R.M.S. misfit was 3.93 and the final R.M.S. misfit was 0.82 in all six cases.*

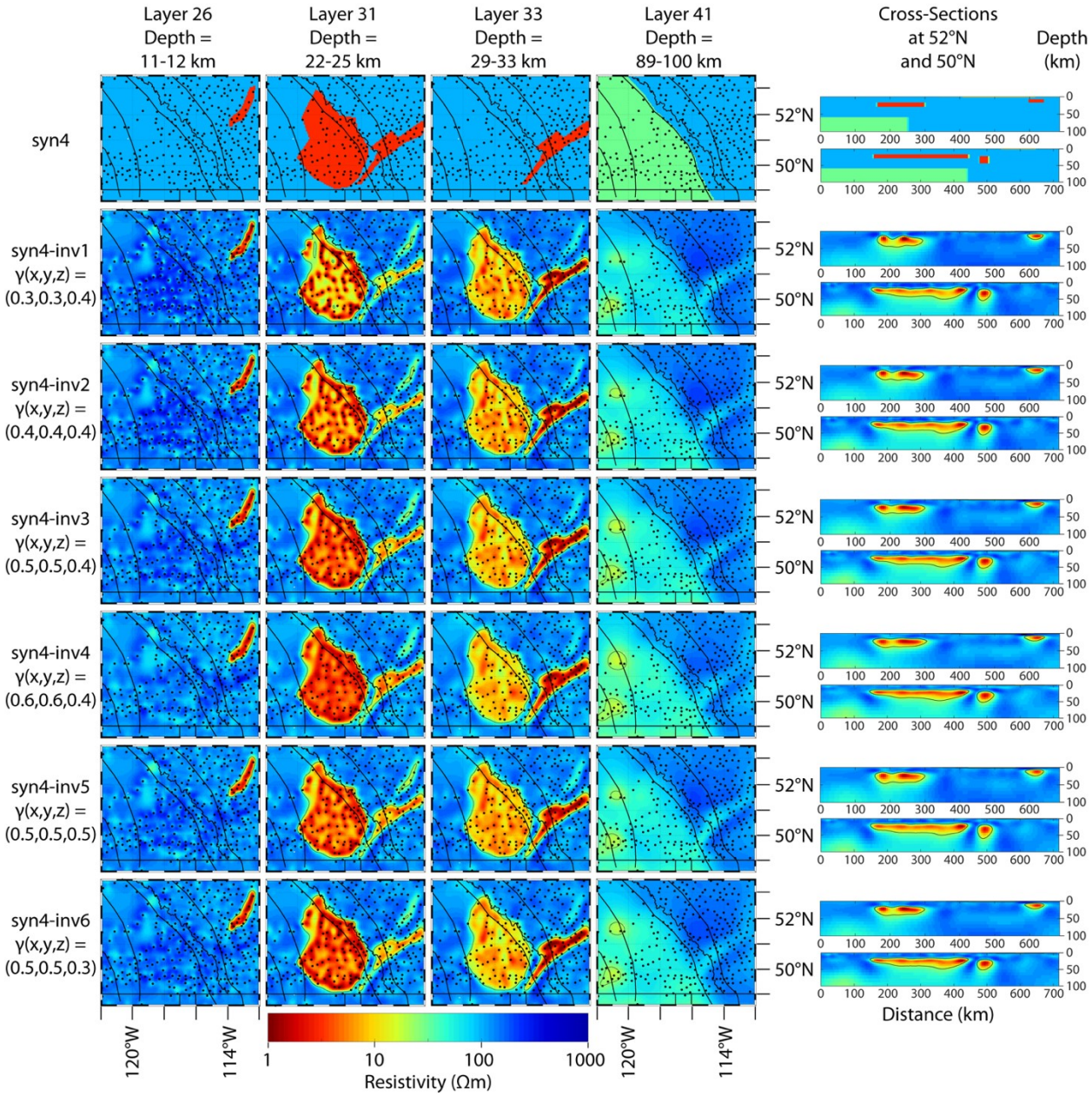

Figure C.19*: Inversion of synthetic MT data from resistivity model syn4, as described in Section 5.4.2. In this model, the RDC was approximated by a polygon of 3 Ωm in the depth range 7-16 km, the SABC conductor was approximated by a polygon of 3 Ωm in the depth range 22-44 km, the CCRC was approximated by a polygon of 3 Ωm in the depth range 16-29 km, and the upper half of the sedimentary basins were assigned a resistivity of 10 Ωm. West of the Omineca-Foreland boundary, depths greater than 58 km were assigned a resistivity of 30 Ωm, and east of the Omineca-Foreland boundary, depths greater than 180 km were assigned a resistivity of 30 Ωm, to represent the asthenosphere. The remainder of the model was 100 Ωm. Six inversions (covariance schemes) are listed in Table C.4. The initial R.M.S. misfit was 4.82 and the final R.M.S. misfits were 0.82, 0.82, 0.82, 0.83, 0.83 and 0.82, respectively.*

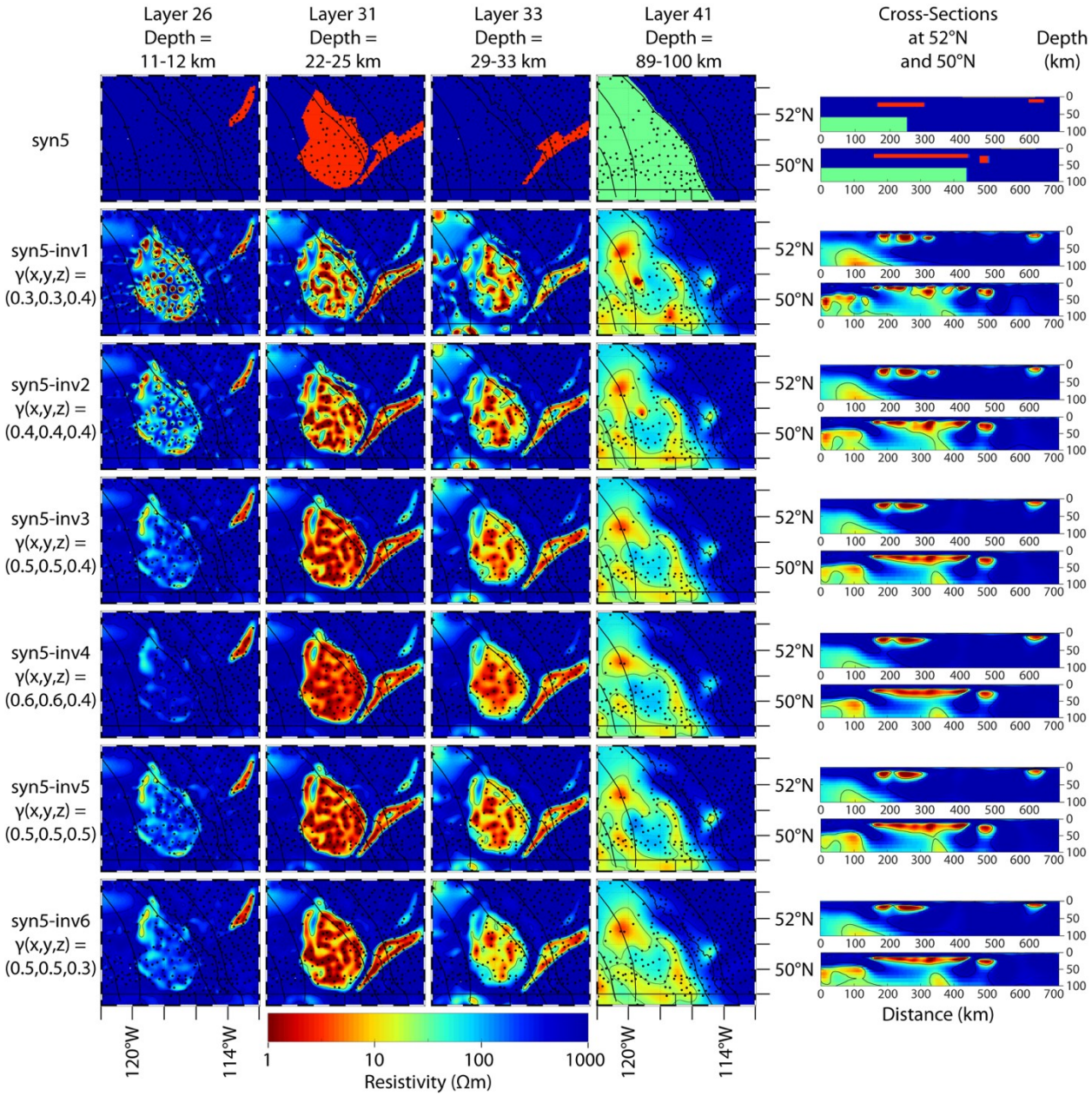

Figure C.20*: Inversion of synthetic MT data from resistivity model syn5, as described in Section 5.4.2. In this model, the RDC was approximated by a polygon of 3 Ωm in the depth range 7-16 km, the SABC conductor was approximated by a polygon of 3 Ωm in the depth range 22-44 km, the CCRC was approximated by a polygon of 3 Ωm in the depth range 16-29 km, and the upper half of the sedimentary basins were assigned a resistivity of 10 Ωm. West of the Omineca-Foreland boundary, depths greater than 58 km were assigned a resistivity of 30 Ωm, and east of the Omineca-Foreland boundary, depths greater than 180 km were assigned a resistivity of 30 Ωm, to represent the asthenosphere. The remainder of the model was 1000 Ωm. Six inversions (covariance schemes) are listed in Table C.4. The initial R.M.S. misfit was 6.79 and the final R.M.S. misfits were 0.84, 0.86, 0.85, 0.85, 0.86 and 0.85, respectively.*

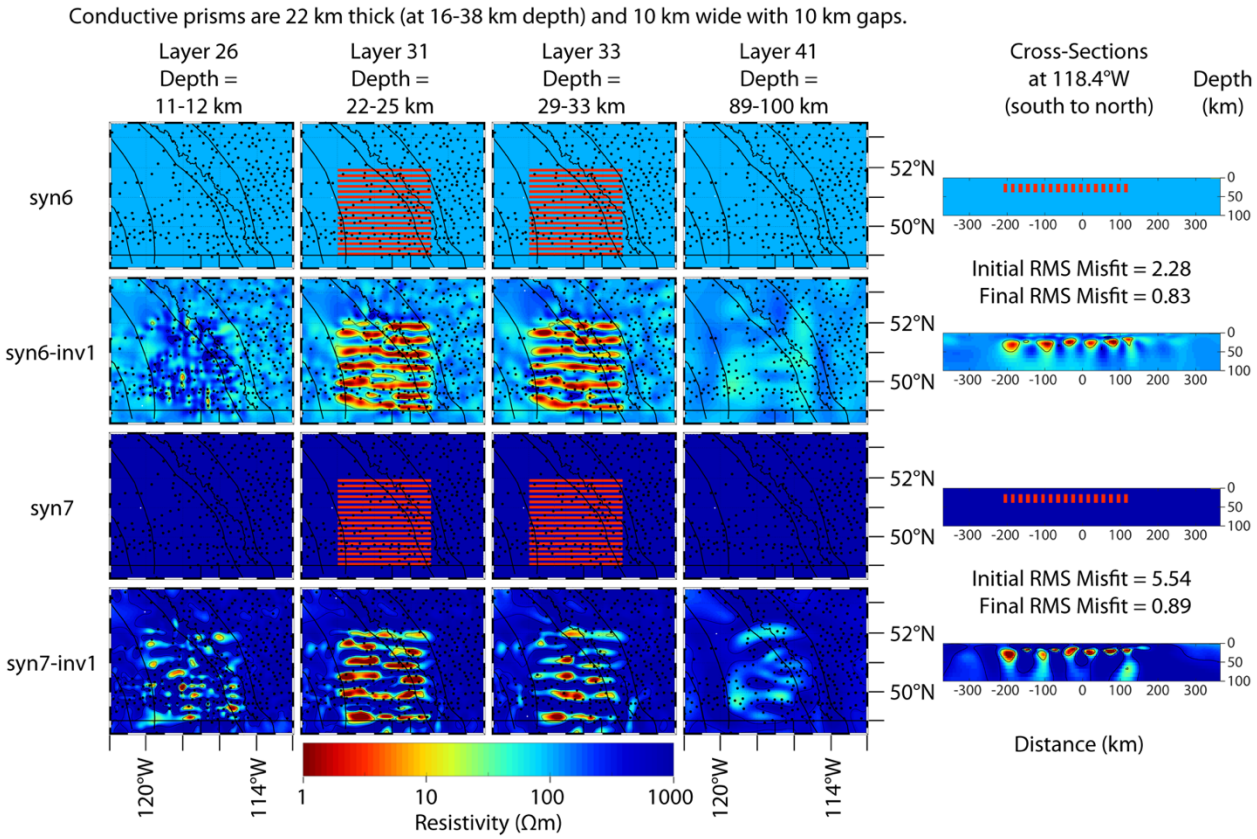

Figure C.21*: Inversion of synthetic MT data from resistivity models syn6 and syn7, as described in Section 5.4.2. Details are given in Table C.5. In these models, the upper half of the sedimentary basins were assigned a resistivity of 10 Ωm and the conductive prisms were assigned a resistivity of 3 Ωm.*

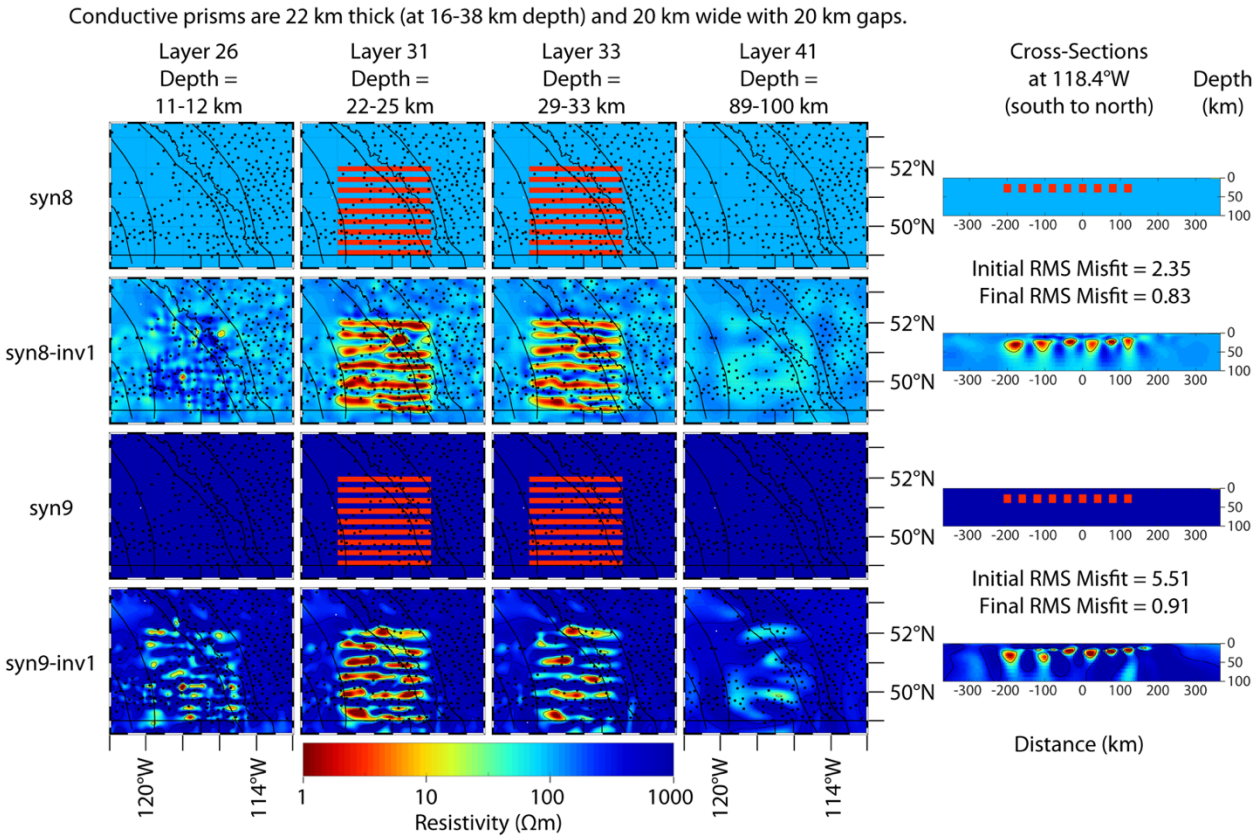

***Figure C.22**: Inversion of synthetic MT data from resistivity models syn8 and syn9, as described in Section 5.4.2. Details are given in Table C.5. In these models, the upper half of the sedimentary basins were assigned a resistivity of 10 Ωm and the conductive prisms were assigned a resistivity of 3 Ωm.*

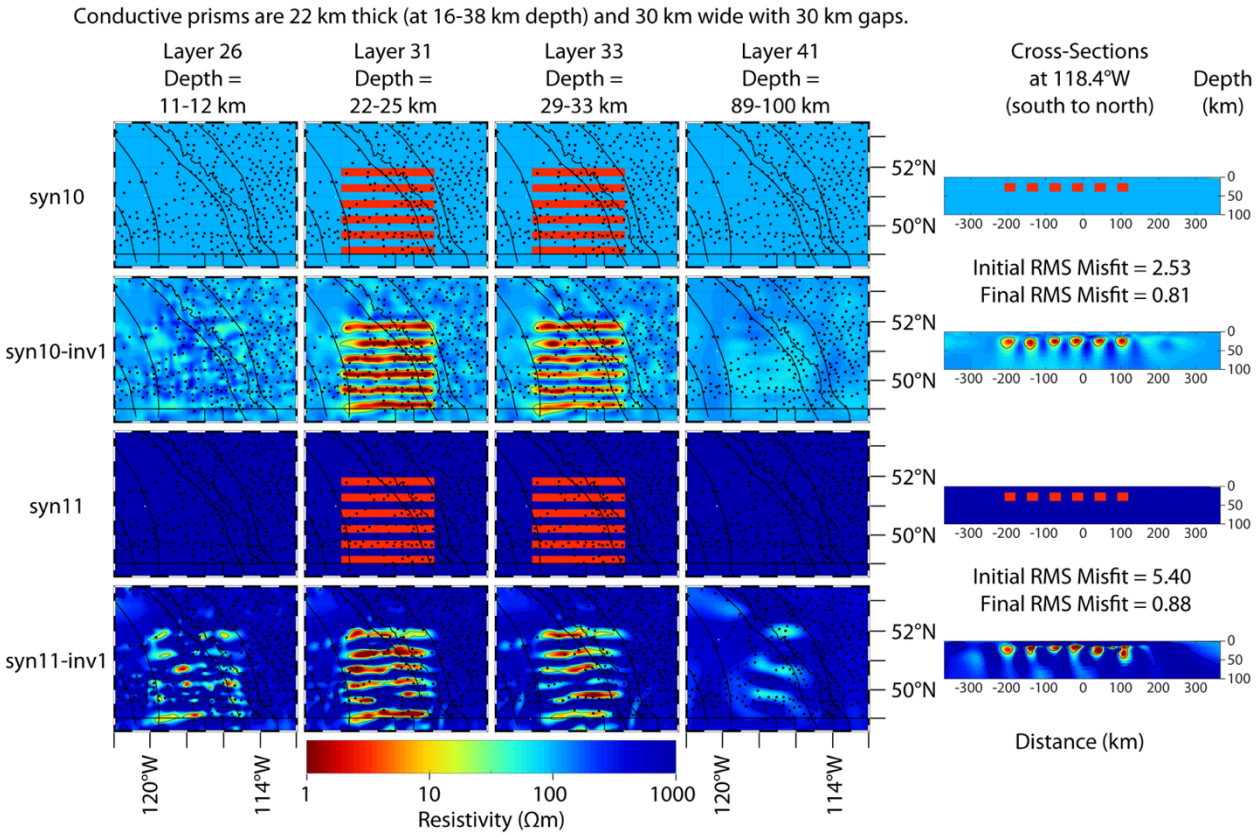

Figure C.23*: Inversion of synthetic MT data from resistivity models syn10 and syn11, as described in Section 5.4.2. Details are given in Table C.5. In these models, the upper half of the sedimentary basins were assigned a resistivity of 10 Ωm and the conductive prisms were assigned a resistivity of 3 Ωm.*

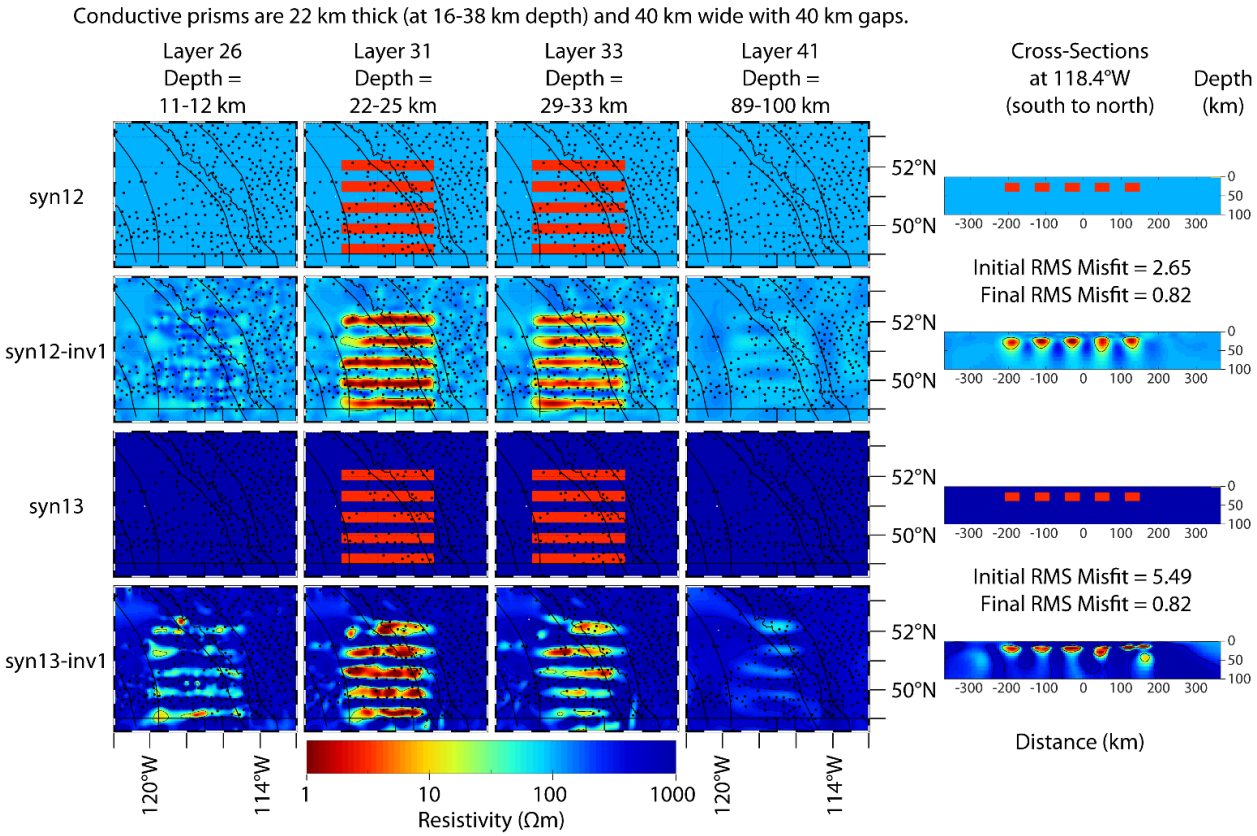

***Figure C.24**: Inversion of synthetic MT data from resistivity models syn12 and syn13, as described in Section 5.4.2. Details are given in Table C.5. In these models, the upper half of the sedimentary basins were assigned a resistivity of 10 Ωm and the conductive prisms were assigned a resistivity of 3 Ωm.*

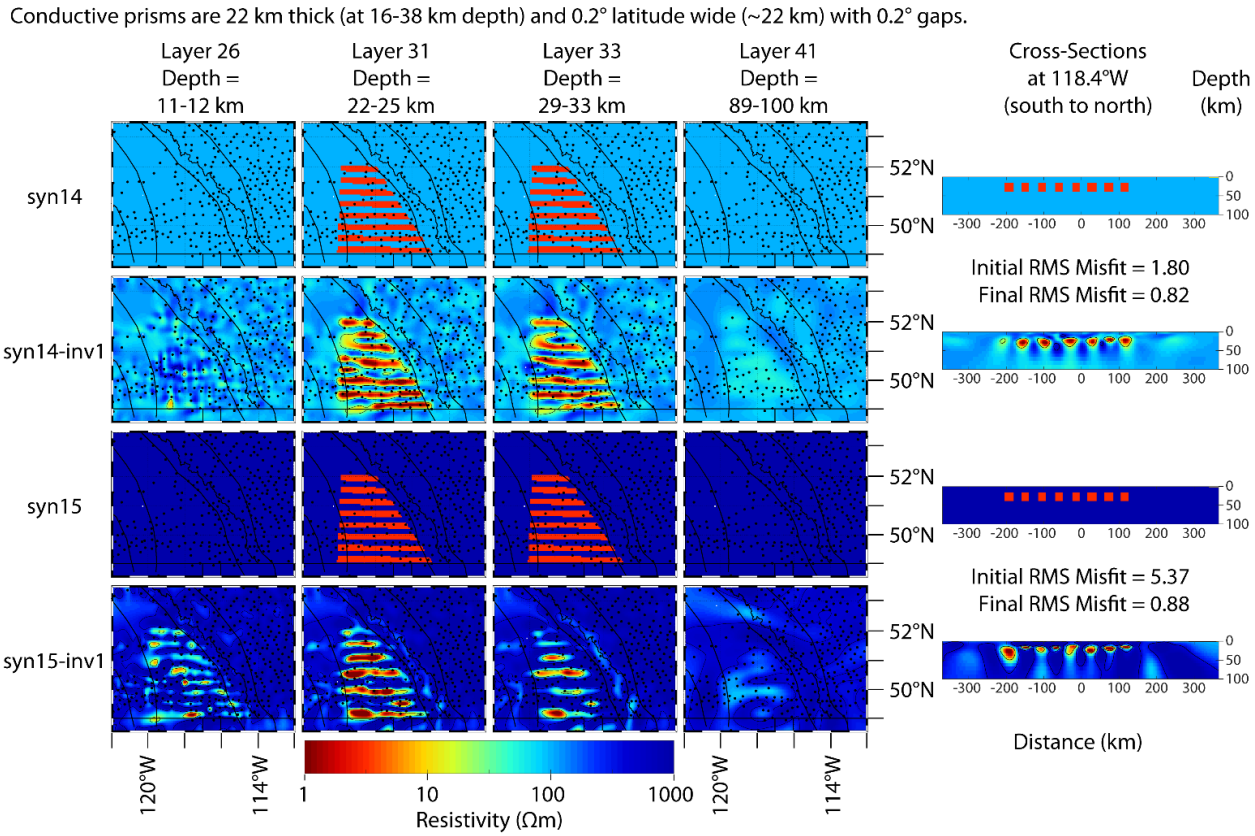

***Figure C.25**: Inversion of synthetic MT data from resistivity models syn14 and syn14, as described in Section 5.4.2. Details are given in Table C.5. In these models, the upper half of the sedimentary basins were assigned a resistivity of 10 Ωm and the conductive prisms were assigned a resistivity of 3 Ωm.*

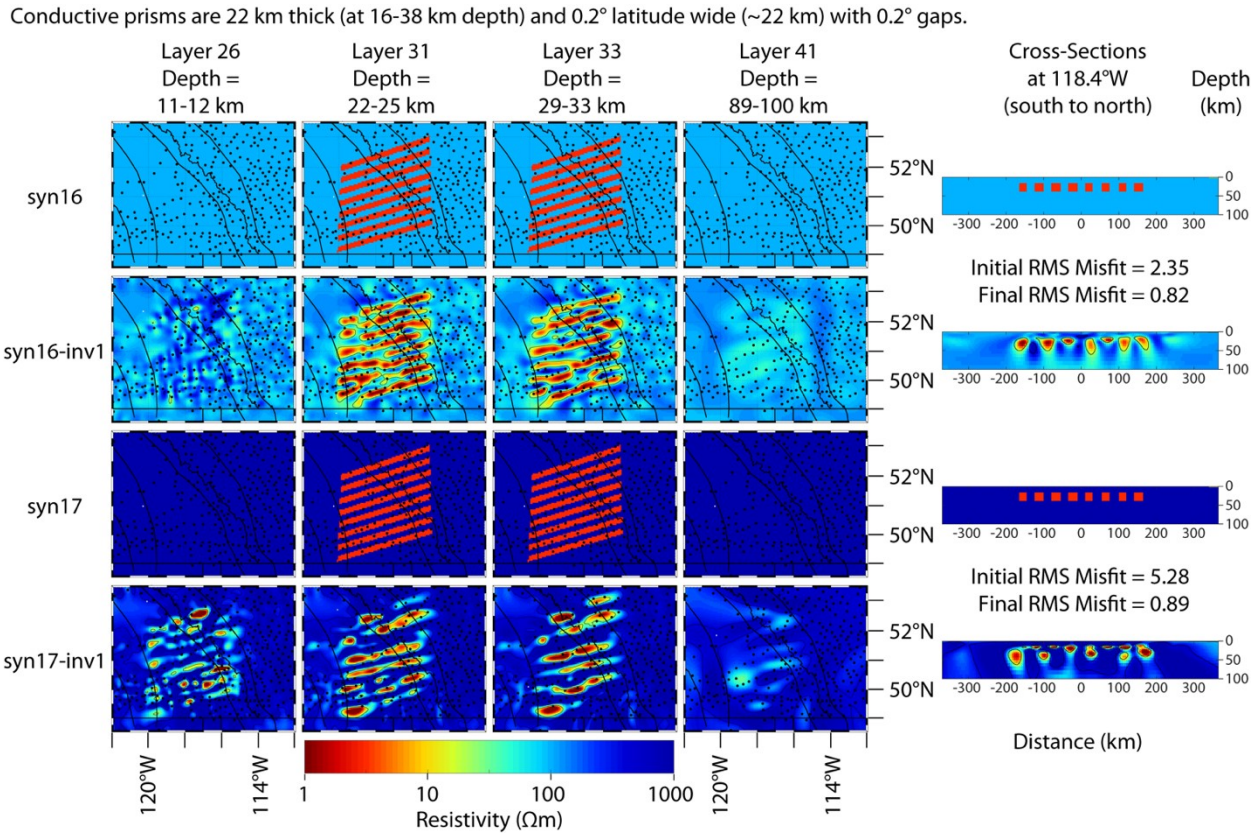

Figure C.26*: Inversion of synthetic MT data from resistivity models syn16 and syn17, as described in Section 5.4.2. Details are given in Table C.5. In these models, the upper half of the sedimentary basins were assigned a resistivity of 10 Ωm and the conductive prisms were assigned a resistivity of 3 Ωm.*

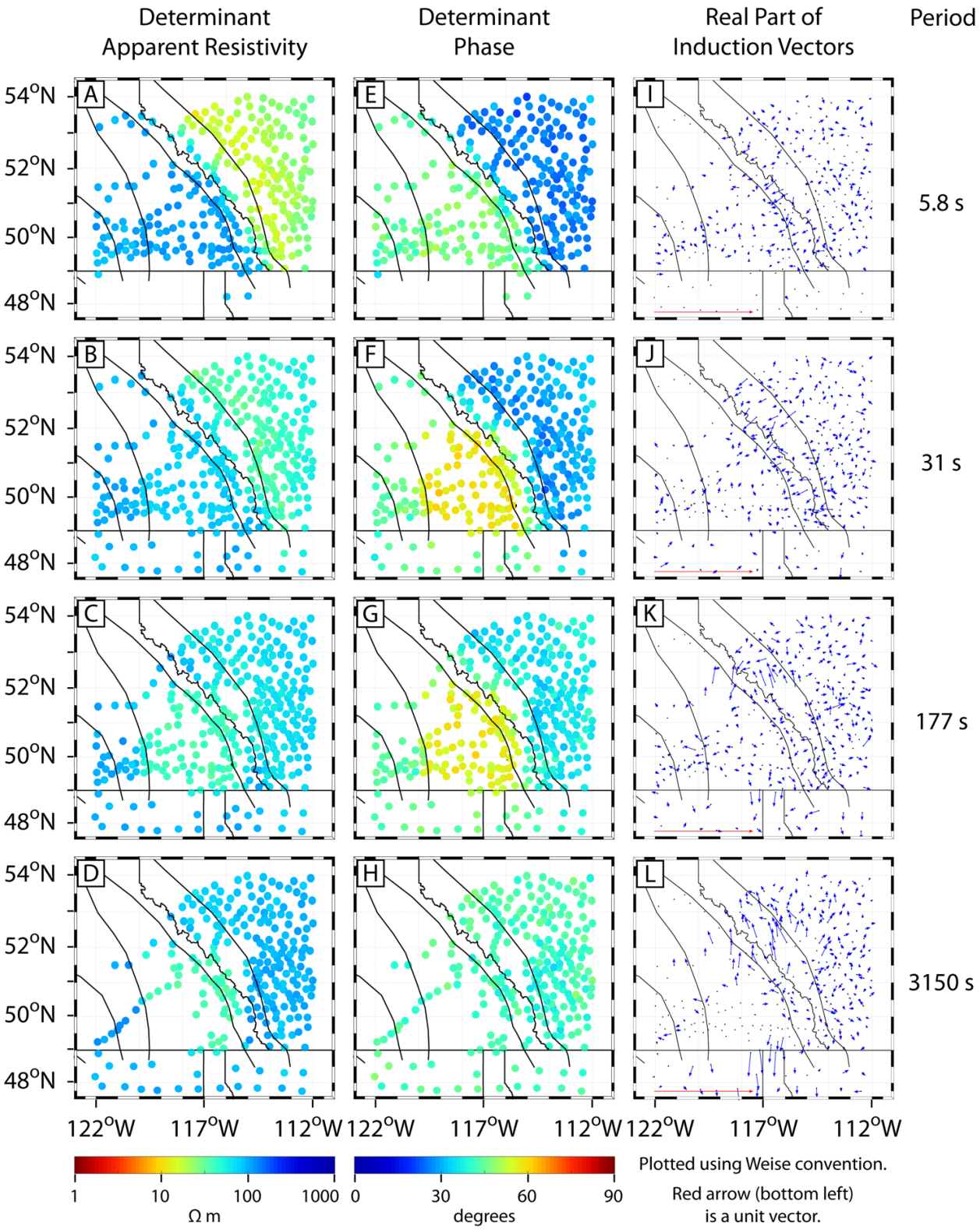

***Figure C.27**: Synthetic MT data from resistivity model syn6, as described in Section 5.4.2.*

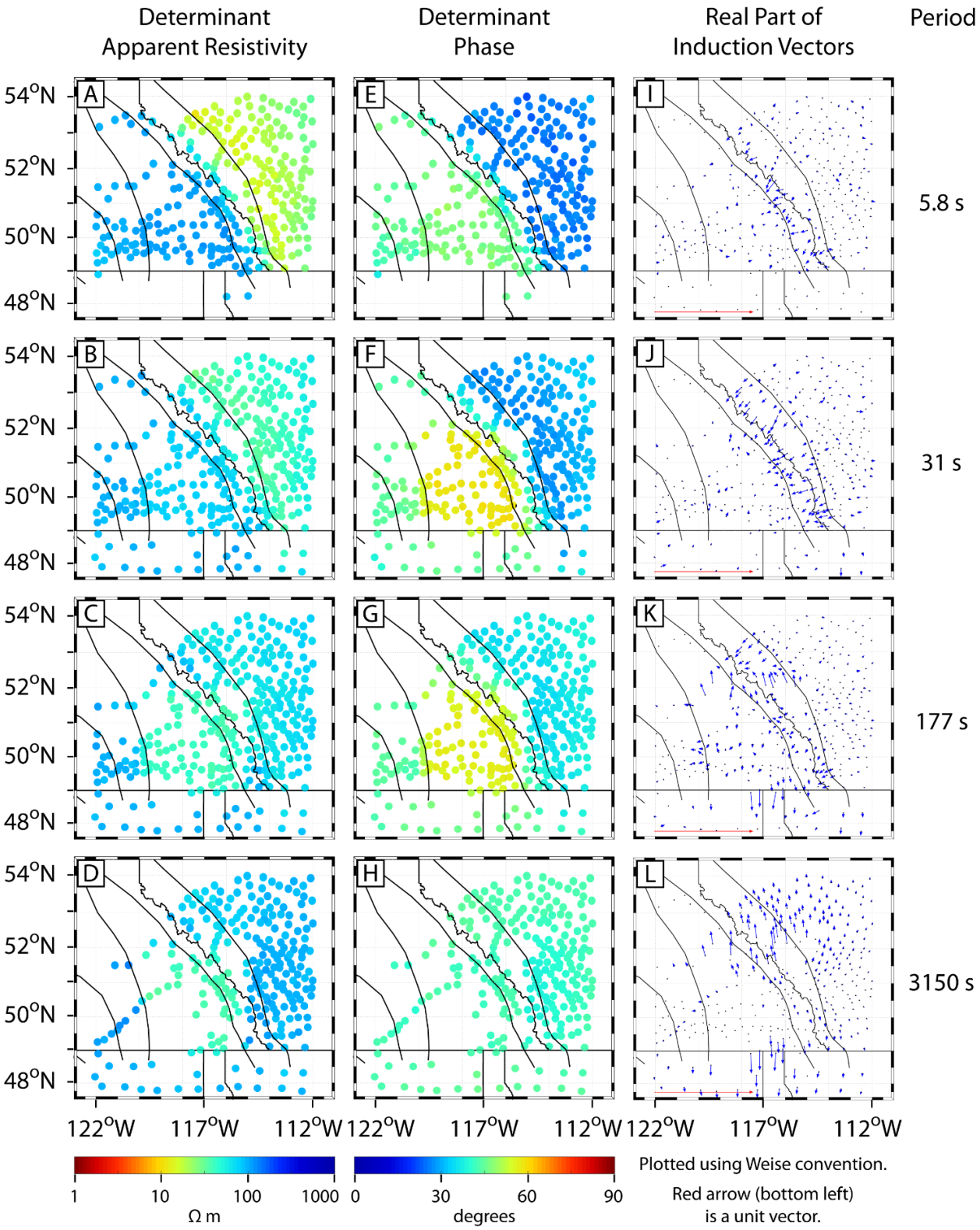

***Figure C.28**: MT data predicted by resistivity model syn6-inv1, as described in Section 5.4.2.*

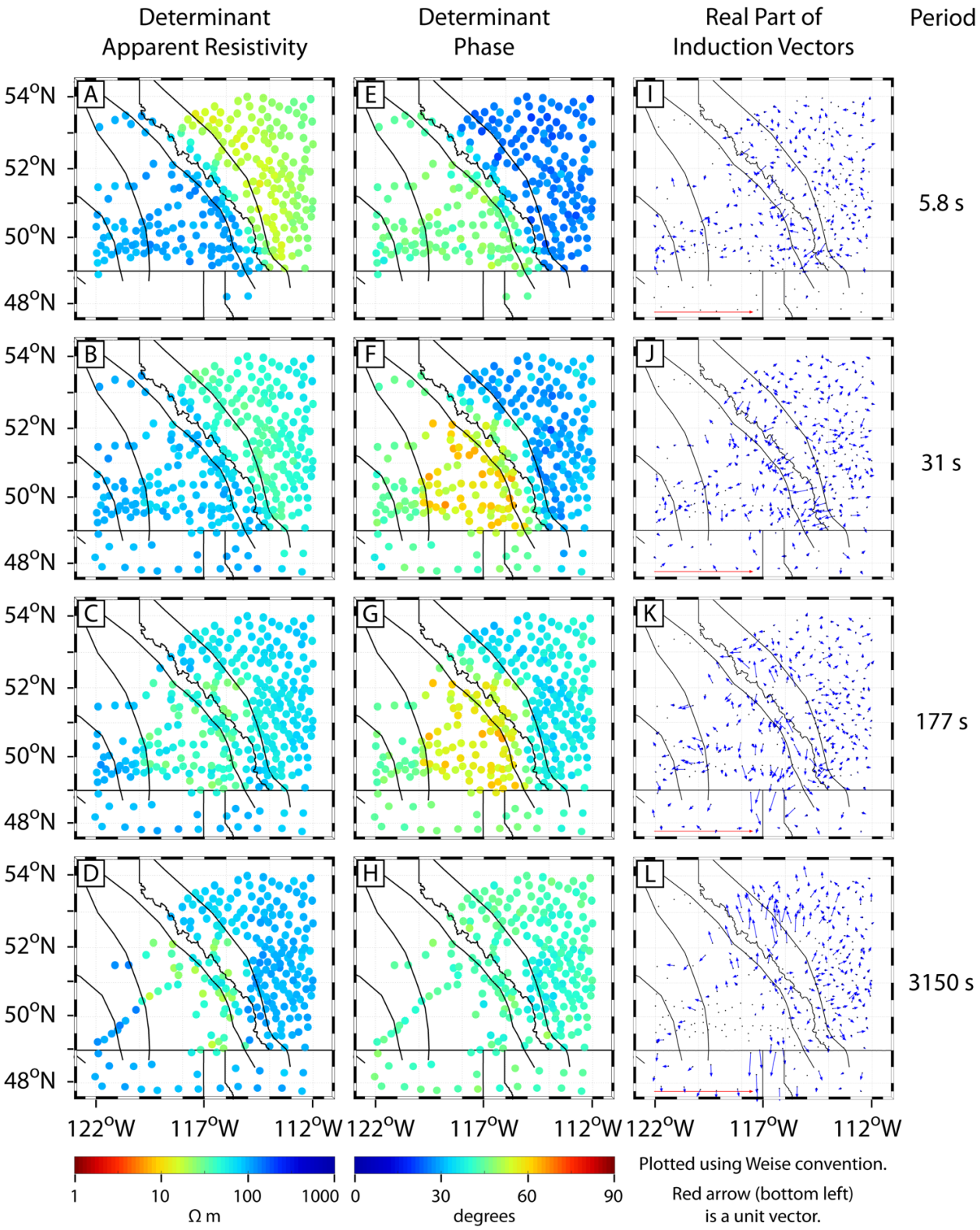

***Figure C.29**: Synthetic MT data from resistivity model syn12, as described in Section 5.4.2.*

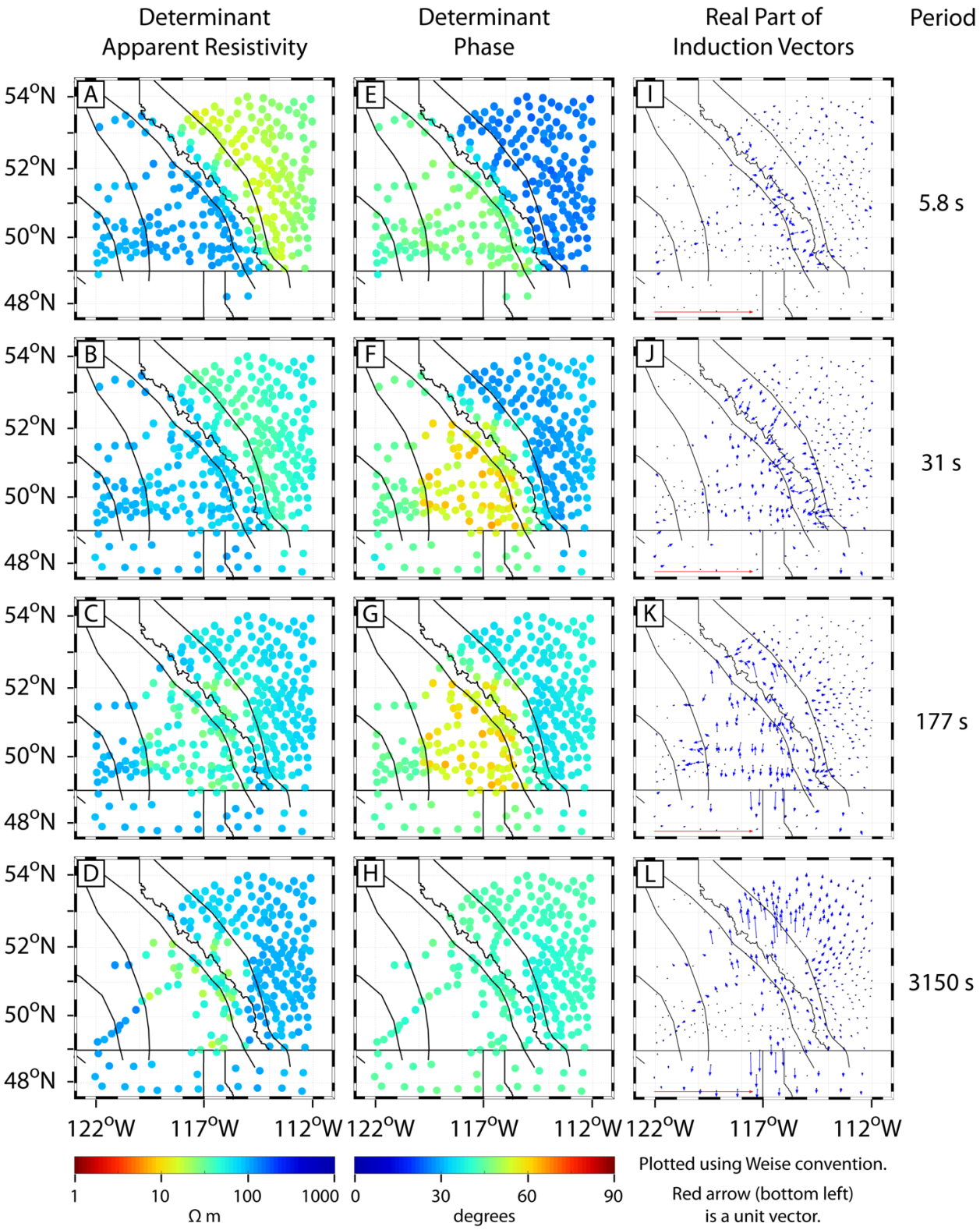

***Figure C.30**: MT data predicted by resistivity model syn12-inv1, as described in Section 5.4.2.*

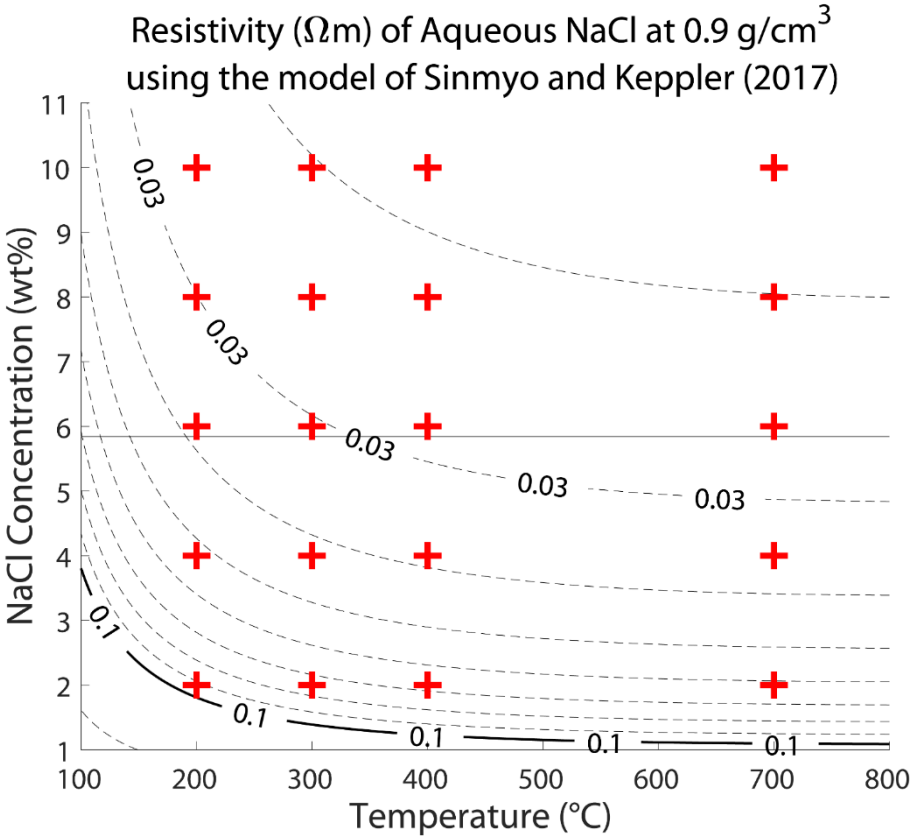

***Figure C.31**: Resistivity (contours) of NaCl-bearing aqueous fluids at 100-800 °C (Sinmyo & Keppler, 2017). The horizontal grey line is the maximum concentration at which the equation was calibrated. However, Sinmyo and Keppler note that the equation "is not purely empirical, but theoretically justified." Red crosses indicate the temperatures and NaCl concentrations used in Figure C.32. The higher concentrations required extrapolation of the equation of Sinmyo and Keppler (2017).*

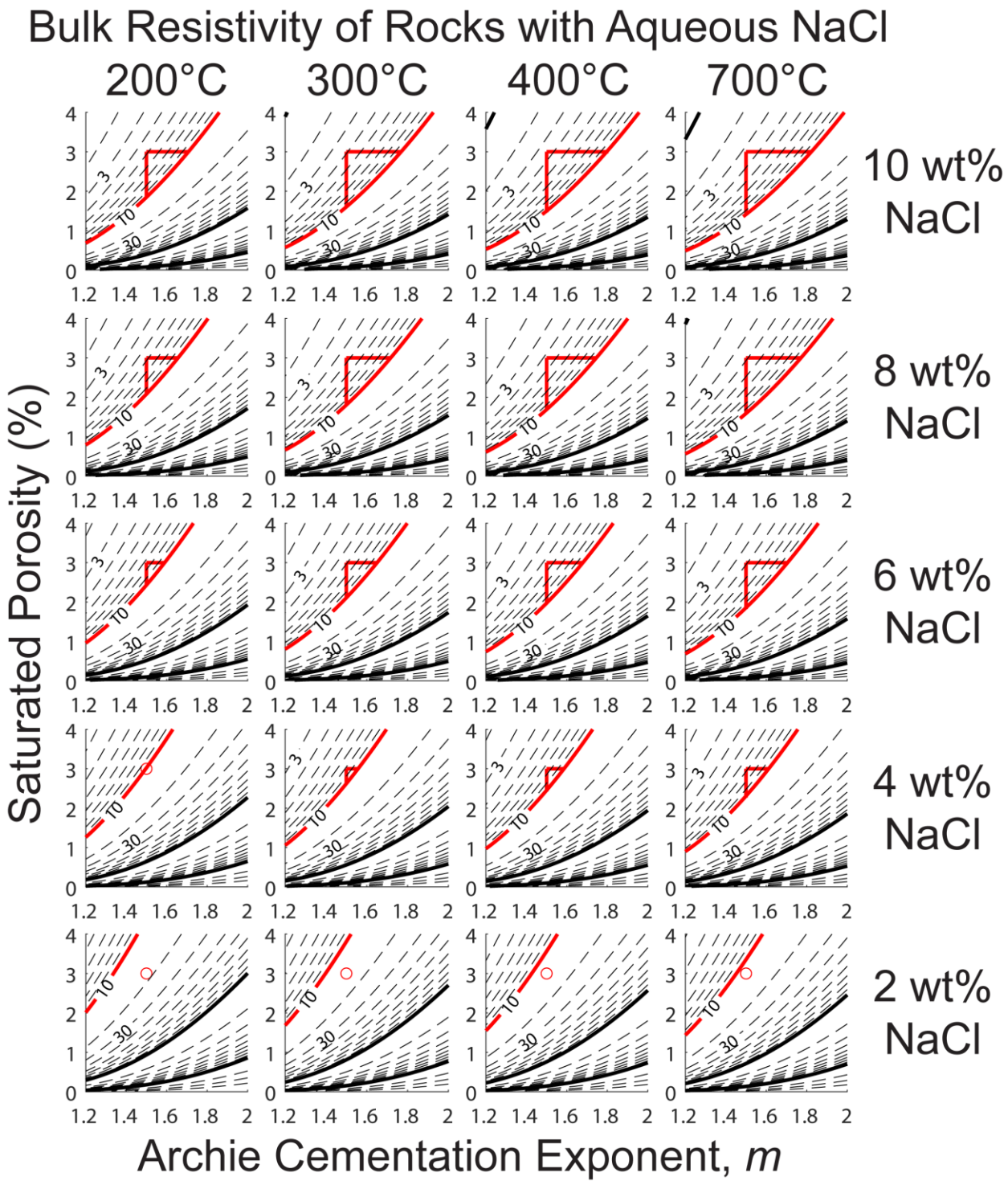

***Figure C.32**: Bulk resistivity (contours) of rocks containing aqueous NaCl, calculated using the modified Archie's Law of Glover et al. (2000), as a function of porosity (saturated) and fluid connectivity. A range of temperatures and salinities are shown, as indicated by the red crosses in Figure C.31. A resistivity of 5,000 Ωm was used for the solid phase (rock matrix). Other values (1,000 Ωm, 10,000 Ωm and 100,000 Ωm) were tested and the difference was negligible except at low porosity (<0.5%). Red lines show bulk resistivity < 10 Ωm when porosity < 3% and m > 1.5. Red circles show porosity = 3% and m = 1.5 when bulk resistivity > 10 Ωm.*

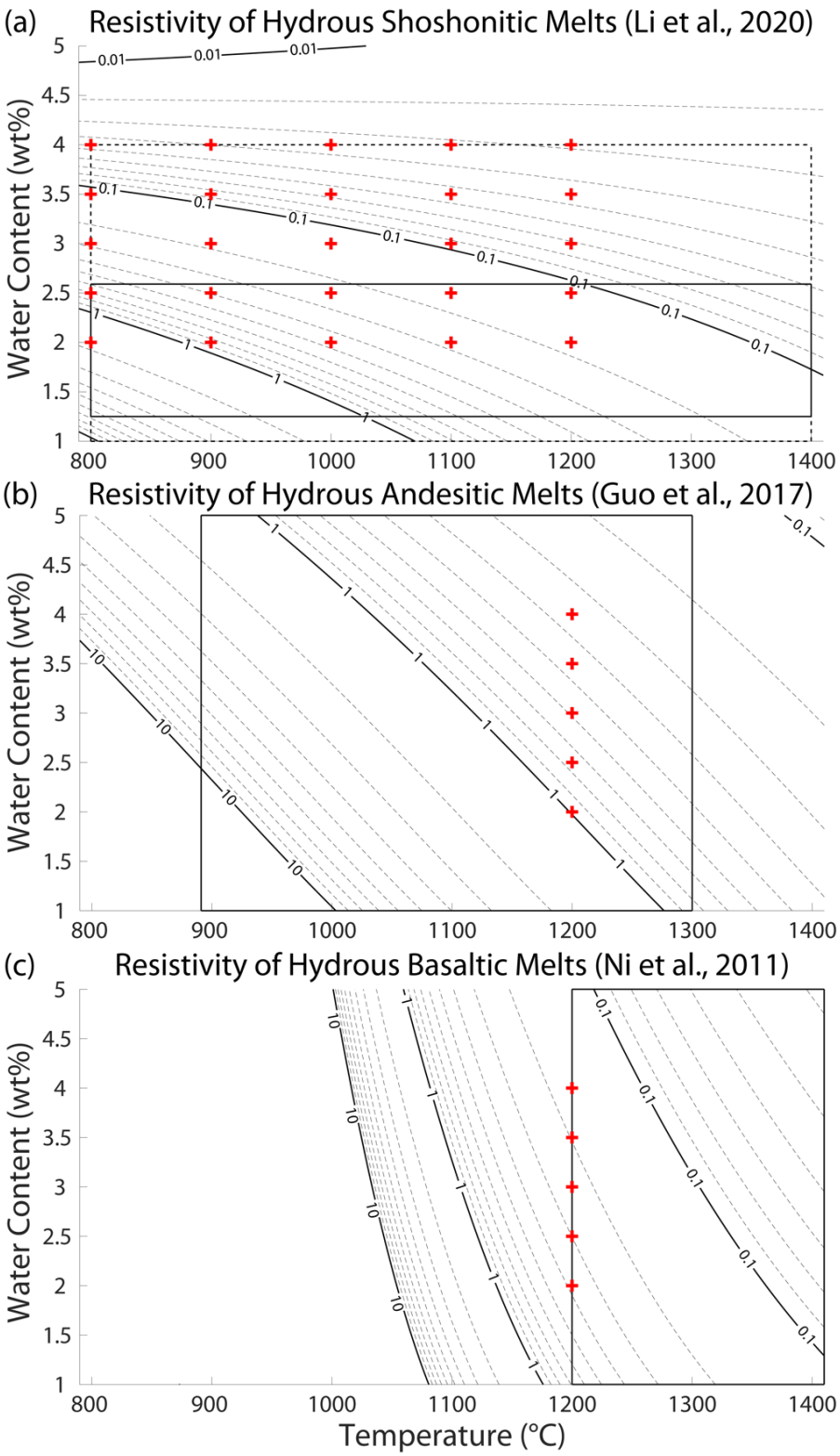

Figure C.33*: Resistivity of hydrous melts with different compositions: (a) shoshonitic (Li et al., 2020), (b) andesitic (X. Guo et al., 2017), and (c) basaltic (Ni et al., 2011). Resistivity contours from 0.01 Ωm to 10 Ωm are shown. Red crosses indicate the compositions, temperatures, and water contents used in Figure C.34. Black rectangles enclose the experimental conditions and the dashed line in (a) encloses the stated range of applicability.*

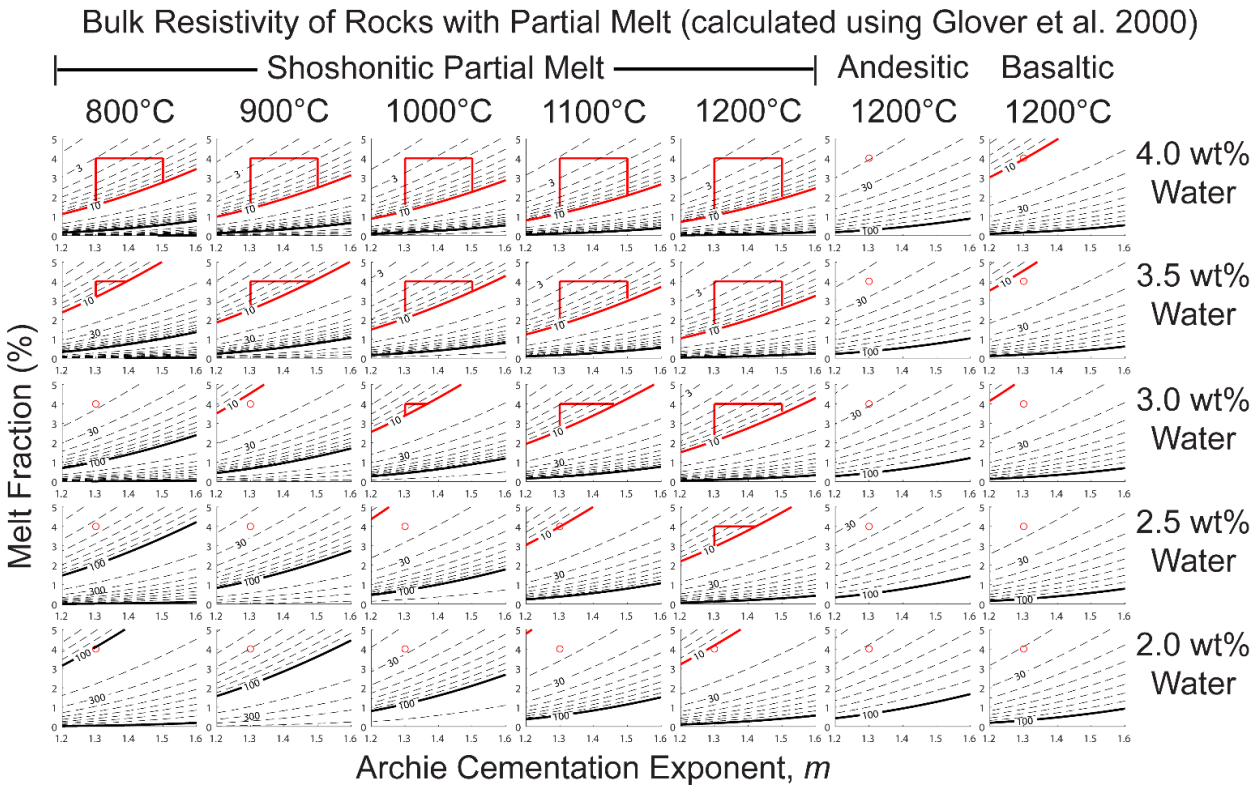

***Figure C.34**: Bulk resistivity (contours) of rocks containing partial melt, calculated using the modified Archie's Law of Glover et al. (2000), as a function of melt fraction and melt connectivity. A range of temperatures and water contents are shown, as indicated by the red crosses in Figure C.33. The resistivity of the solid phase was calculated using an empirical model (Hashim et al., 2013) but its variation has negligible effect when the melt fraction is greater than 0.5%. Red polygons enclose the conditions for which: (1) melt fraction < 4%, (2) 1.3 < m < 1.5 and (3) bulk resistivity < 10 Ωm. Red circles indicate that melt fraction < 4% and m > 1.3 cannot explain bulk resistivity < 10 Ωm.*

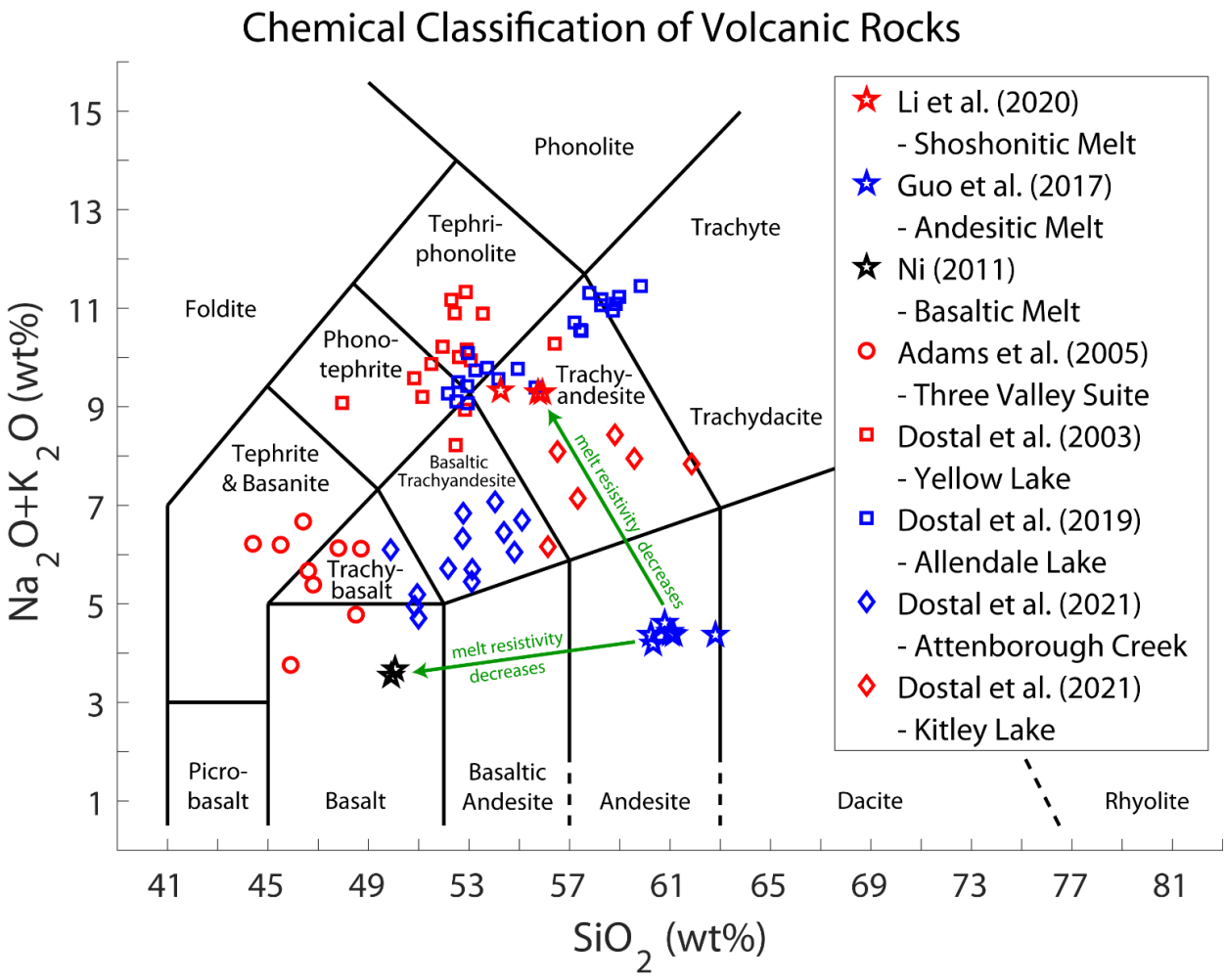

***Figure C.35**: Total alkali-silica (TAS) diagram with the chemical classification of Le Bas et al. (1986, 1992). Chemical composition of rocks from melt conductivity experiments (X. Guo et al., 2017; Li et al., 2020; Ni et al., 2011) and Eocene volcanic rocks in the southern Canadian Cordillera (Dostal et al. 2003, 2019, 2021, Adams et al. 2005) are shown. Melt resistivity decreases with decreasing silica content and with increasing alkali content.*

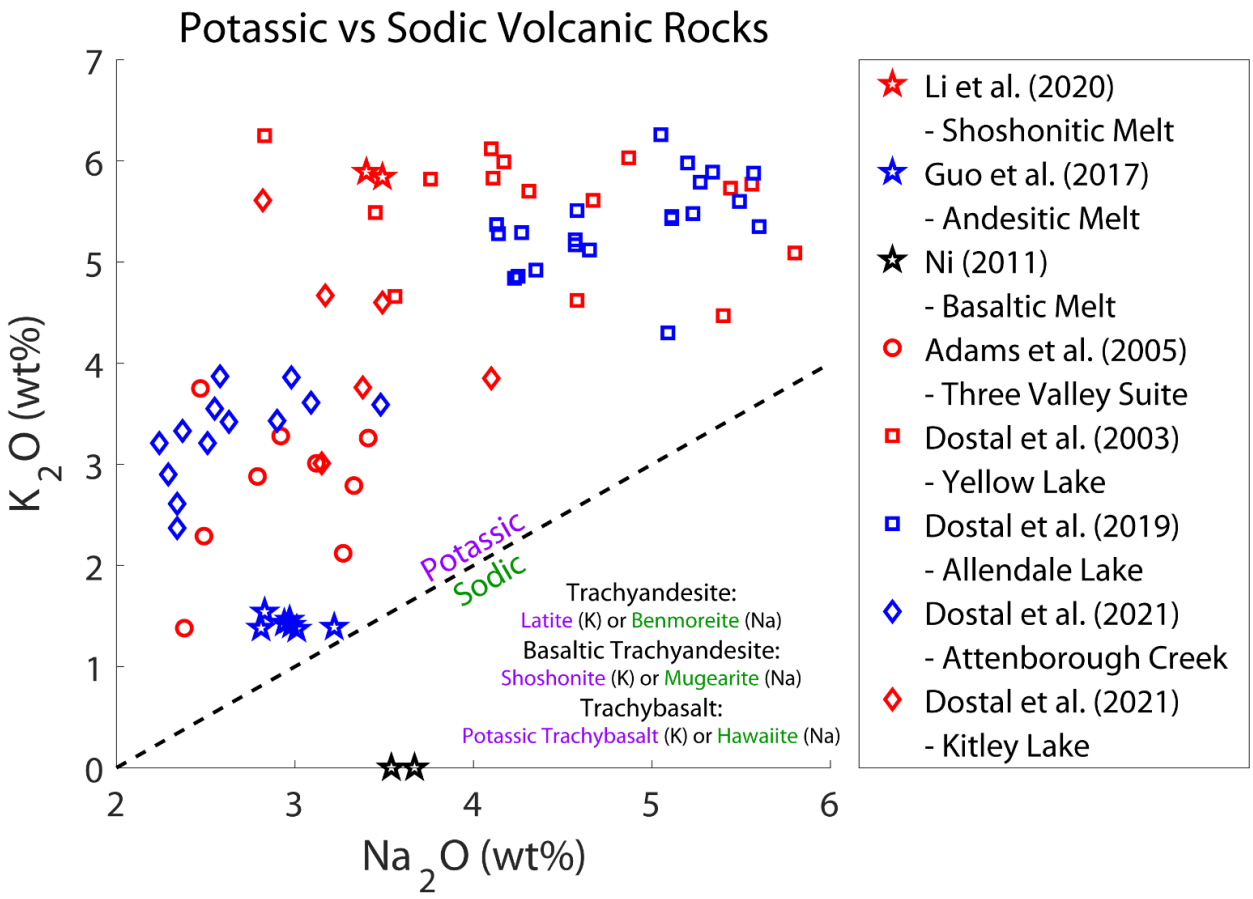

***Figure C.36**: Plot of potassium oxide as a function of sodium oxide, along with the chemical classification of Le Bas et al. (1986, 1992) in purple and green. Chemical composition of rocks from melt conductivity experiments (X. Guo et al., 2017; Li et al., 2020; Ni et al., 2011) and Eocene volcanic rocks in the southern Canadian Cordillera (Dostal et al. 2003, 2019, 2021, Adams et al. 2005) are shown.*

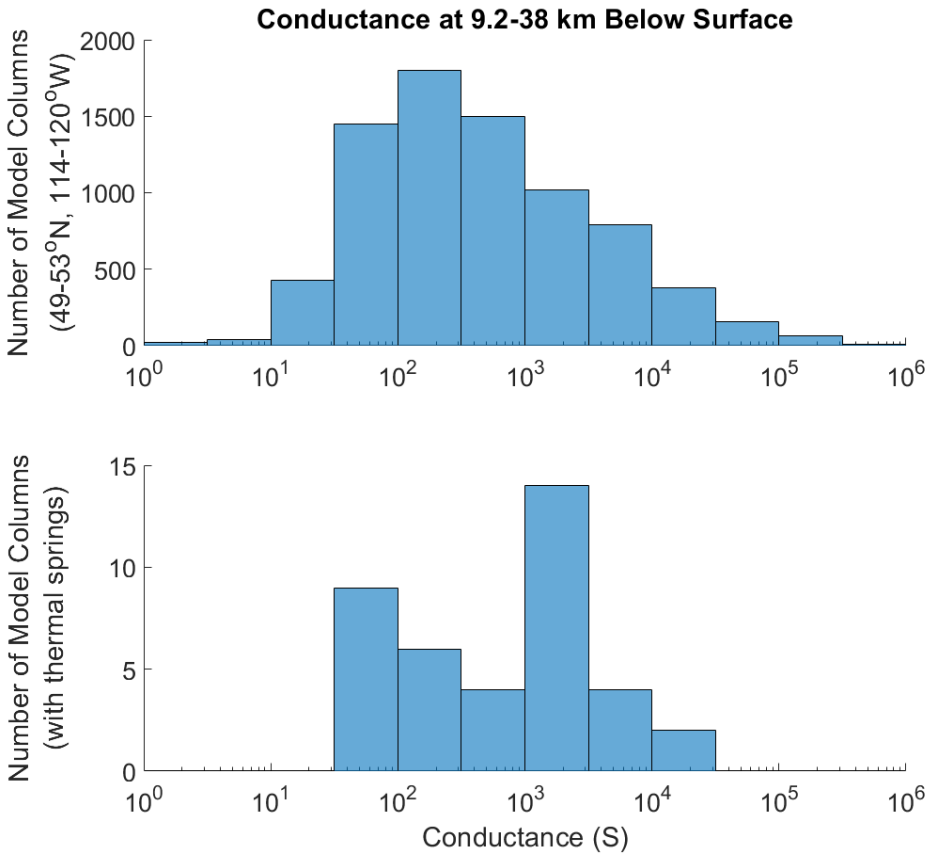

Figure C.37*: Histograms of conductance of model columns of the preferred 3-D resistivity model (inversion 20 in Table C.2) within the area 49-53 °N and 114-120 °W in the depth range 9.2-38 km. The top panel shows the distribution of all model columns, and the bottom panel shows the distribution of the columns associated with the 39 thermal springs within the area.*

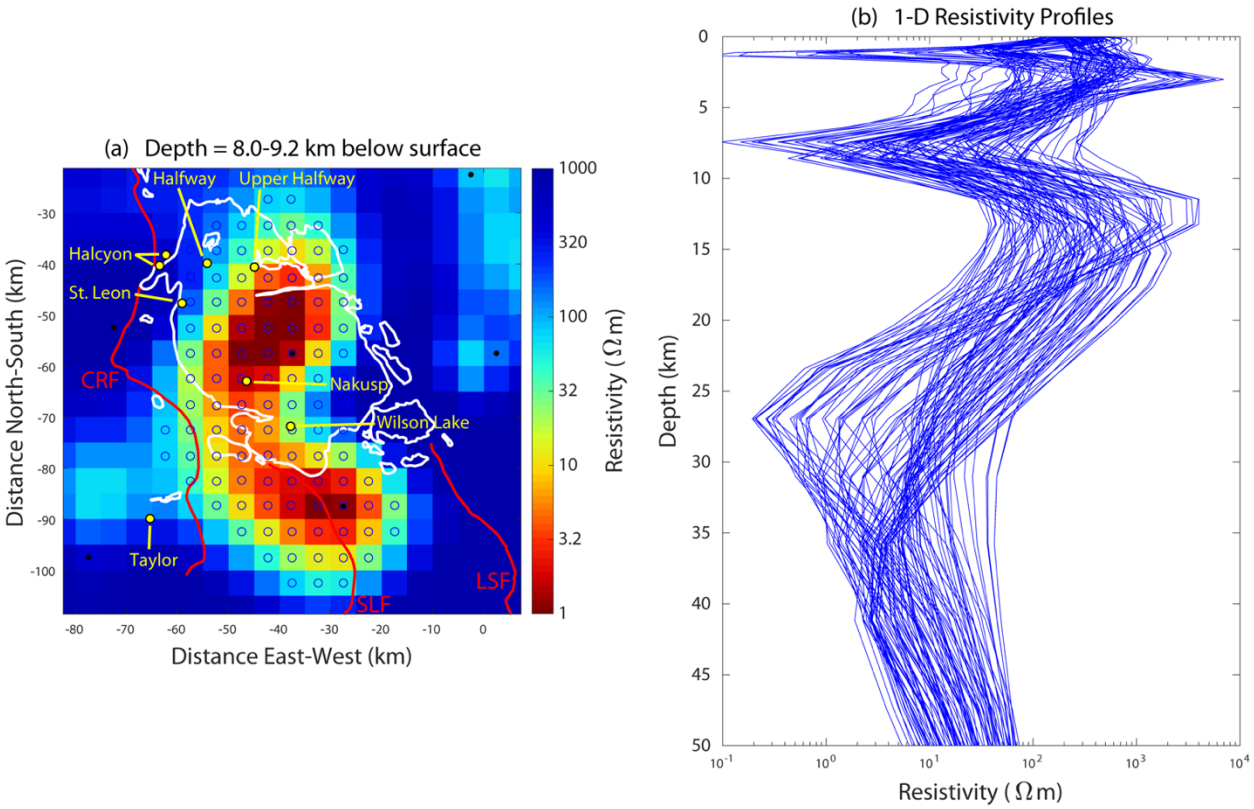

***Figure C.38**: (a) Resistivity model at 8.0-9.2 km depth in an area containing the surface trace of the Kuskanax batholith (white lines). Thermal springs (yellow dots) are identified with yellow lines and names. Surface traces of major faults (red lines) are: CRF = Columbia River fault, SLF = Slocan Lake fault, and LSF = Lakeshore fault. (b) Modelled resistivity as a function of depth in each of the model columns indicated by the blue circles in panel a.*

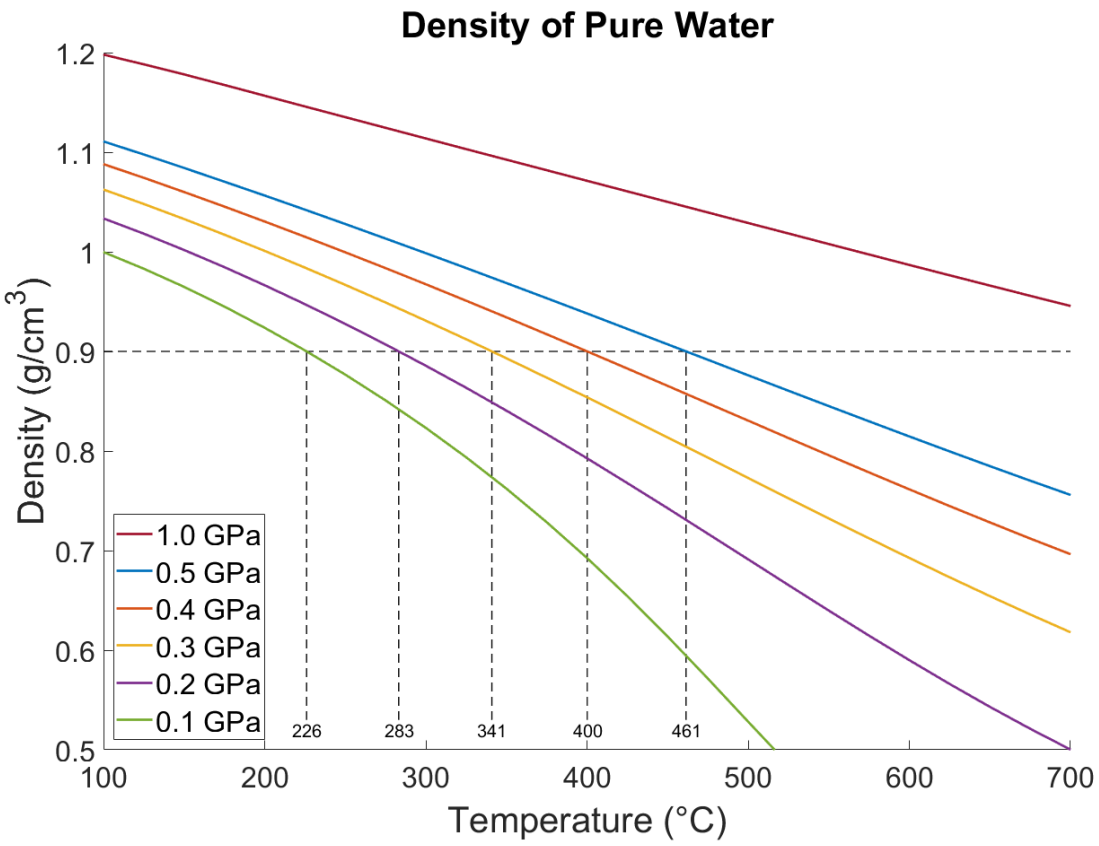

***Figure C.39**: Density of pure water as a function of temperature at six pressures (Anderson et al., 1991) showing that a density of 0.9 g/cm^3 (dashed lines) is a reasonable approximation at the temperatures and pressures of the middle crust of the southern Canadian Cordillera.*

D. Supplementary materials for Chapter 6

D.1. Magnetotelluric data and previous magnetotelluric studies

Table D.1 lists all 331 MT sites that were used in the inversion to create the published resistivity model. Table D.2 summarizes previous 3-D MT studies that overlap spatially with this study.

Table D.1*: Details of the MT sites that were used in the inversion described in Chapter 6. The sites are sorted into eight groups, colour coded in Figure 6.3. The station number column has a group number, as well as the authors' reference number in parentheses.*

Number	Name	Latitude	Longitude	Year	Institution or Project	Instrument
Group 1 (red) = Coast Belt at 49-52 °N						
G1-01 (118)	abc122	49.247	-121.926	2003	University of Alberta	LIMS
G1-02 (119)	abc125	49.319	-121.614	2003	University of Alberta	NIMS
G1-03 (120)	abc132	49.492	-121.279	2003	University of Alberta	LIMS
G1-04 (244)	line100w_12	49.638	-121.545	1990	Lithoprobe	
G1-05 (255)	line11-12_4	50.322	-121.987	1989	Lithoprobe	
G1-06 (257)	line13_4	50.673	-121.934	1989	Lithoprobe	
G1-07 (260)	line300_1	49.539	-121.966	1990	Lithoprobe	
G1-08 (265)	line600_2	49.995	-121.647	1990	Lithoprobe	
G1-09 (266)	line600_3	49.768	-121.775	1990	Lithoprobe	
G1-10 (267)	line600_6	50.044	-121.390	1990	Lithoprobe	
Group 2 (orange) = Intermontane Belt at 49-52 °N						
G2-01 (121)	abc134	49.601	-121.005	2003	University of Alberta	LIMS
G2-02 (122)	abc136	49.742	-120.898	2003	University of Alberta	LIMS
G2-03 (123)	abc140	49.879	-120.639	2003	University of Alberta	LIMS
G2-04 (124)	abc146	50.201	-120.158	2003	University of Alberta	LIMS
G2-05 (125)	abc150	50.463	-119.878	2003	University of Alberta	LIMS
G2-06 (143)	abc285	51.500	-121.126	2009	University of Alberta	NIMS
G2-07 (144)	abc295	51.504	-120.496	2009	University of Alberta	NIMS
G2-08 (245)	line100w_2	49.807	-120.181	1990	Lithoprobe	
G2-09 (246)	line100w_3	49.770	-120.327	1990	Lithoprobe	
G2-10 (248)	line100w_6	49.623	-120.629	1990	Lithoprobe	
G2-11 (249)	line10_5	50.232	-119.807	1989	Lithoprobe	
G2-12 (251)	line10s_10	49.529	-119.783	1989	Lithoprobe	
G2-13 (252)	line10s_13	49.563	-120.153	1989	Lithoprobe	
G2-14 (253)	line10s_15	49.405	-120.409	1989	Lithoprobe	

G2-15 (256)	line11-12_5	50.467	-120.759	1989	Lithoprobe	
G2-16 (258)	line200_2	49.843	-119.778	1990	Lithoprobe	
G2-17 (259)	line200_4	50.059	-119.808	1990	Lithoprobe	
G2-18 (261)	line400_12	51.468	-121.904	1990	Lithoprobe	
G2-19 (321)	ten015	51.133	-121.433		Gough	
G2-20 (328)	ten808	50.308	-121.121		Gough	
G2-21 (329)	ten809	50.488	-121.514		Gough	
G2-22 (330)	ten814	50.263	-120.699		Gough	
Group 3 (yellow) = Omineca Belt at 49-52 °N, west of strontium isopleth						
G3-01 (126)	abc154	50.603	-119.532	2003	University of Alberta	LIMS
G3-02 (127)	abc158	50.746	-119.138	2003	University of Alberta	LIMS
G3-03 (145)	abc300	51.491	-120.252	2004	University of Alberta	NIMS
G3-04 (146)	abc310	51.792	-119.692	2006	University of Alberta	NIMS
G3-05 (240)	line100e_11	49.616	-119.550	1990	Lithoprobe	
G3-06 (247)	line100w_4	49.793	-119.505	1990	Lithoprobe	
G3-07 (254)	line10s_5	49.707	-119.211	1989	Lithoprobe	
G3-08 (262)	line500_3	50.353	-119.544	1990	Lithoprobe	
G3-09 (263)	line500_6	50.391	-119.143	1990	Lithoprobe	
G3-10 (271)	line7-9_13	50.135	-119.074	1989	Lithoprobe	
Group 4 (green) = Omineca Belt at 49-52 °N, east of strontium isopleth and west of Kootenay Arc						
G4-01 (053)	RMN032	50.061	-117.383	2018	University of Alberta	NIMS
G4-02 (061)	SLK006	51.828	-118.514	2017	University of Alberta	NIMS
G4-03 (062)	SLK007	51.671	-118.550	2017	University of Alberta	NIMS
G4-04 (063)	SLK008	51.418	-118.406	2017	University of Alberta	NIMS
G4-05 (064)	SLK009	51.214	-118.201	2017	University of Alberta	NIMS
G4-06 (128)	abc162	50.892	-118.679	2003	University of Alberta	LIMS
G4-07 (129)	abc166	50.941	-118.229	2004	University of Alberta	NIMS
G4-08 (216)	aet88_10	49.741	-117.058	1988	Lithoprobe	EMAP
G4-09 (217)	bca009	49.288	-117.674	2009	University of Alberta	NIMS
G4-10 (219)	bca109	49.739	-117.493	2009	University of Alberta	NIMS
G4-11 (232)	emr87_26	49.508	-117.702	1987	Lithoprobe	
G4-12 (233)	emr87_5	49.622	-117.130	1987	Lithoprobe	
G4-13 (241)	line100e_2	49.616	-118.315	1990	Lithoprobe	
G4-14 (242)	line100e_4	49.421	-118.730	1990	Lithoprobe	
G4-15 (243)	line100e_5	49.596	-118.920	1990	Lithoprobe	
G4-16 (250)	line10s_1	49.776	-118.784	1989	Lithoprobe	
G4-17 (264)	line5_4	49.726	-117.983	1989	Lithoprobe	
G4-18 (268)	line6_1	49.965	-118.083	1989	Lithoprobe	
G4-19 (269)	line6_9	50.407	-118.056	1989	Lithoprobe	
G4-20 (270)	line7-9_10	50.191	-118.759	1989	Lithoprobe	
G4-21 (272)	line7-9_6	50.283	-118.448	1989	Lithoprobe	
G4-22 (273)	line700_4	50.365	-117.514	1990	Lithoprobe	

Group 5 (cyan) = Omineca Belt at 49-52°N, east of western boundary of Kootenay Arc						
G5-01 (032)	RMN004	50.887	-116.462	2017	University of Alberta	NIMS
G5-02 (034)	RMN006	50.548	-116.156	2017	University of Alberta	NIMS
G5-03 (037)	RMN009	50.221	-116.047	2017	University of Alberta	NIMS
G5-04 (040)	RMN014	49.257	-116.344	2018	University of Alberta	NIMS
G5-05 (041)	RMN015	50.704	-116.336	2018	University of Alberta	NIMS
G5-06 (043)	RMN017	50.363	-116.364	2018	University of Alberta	NIMS
G5-07 (044)	RMN018	49.447	-116.690	2018	University of Alberta	NIMS
G5-08 (045)	RMN019	49.970	-115.820	2018	University of Alberta	NIMS
G5-09 (049)	RMN025	49.054	-116.122	2018	University of Alberta	NIMS
G5-10 (050)	RMN026	50.757	-116.699	2018	University of Alberta	NIMS
G5-11 (051)	RMN028	50.088	-116.118	2018	University of Alberta	NIMS
G5-12 (052)	RMN031	50.677	-117.076	2018	University of Alberta	NIMS
G5-13 (054)	RMN036	49.012	-117.178	2018	University of Alberta	NIMS
G5-14 (055)	RMN038	49.372	-116.100	2018	University of Alberta	NIMS
G5-15 (065)	SLK010	51.454	-118.155	2017	University of Alberta	NIMS
G5-16 (066)	SLK011	51.014	-116.671	2017	University of Alberta	NIMS
G5-17 (067)	SLK012	51.119	-116.989	2017	University of Alberta	NIMS
G5-18 (130)	abc172	51.232	-117.674	2004	University of Alberta	NIMS
G5-19 (131)	abc176	51.362	-117.434	2004	University of Alberta	NIMS
G5-20 (218)	bca010	49.166	-116.651	2009	University of Alberta	NIMS
G5-21 (220)	bca310	50.370	-117.015	2009	University of Alberta	NIMS
G5-22 (225)	dun-86_5	49.406	-115.809	1986	Duncan	
G5-23 (226)	duncan_23	49.146	-115.565		Duncan	
G5-24 (228)	emr87_16	49.601	-116.662	1987	Lithoprobe	
G5-25 (229)	emr87_20	49.676	-116.338	1987	Lithoprobe	
G5-26 (230)	emr87_23	49.634	-116.145	1987	Lithoprobe	
G5-27 (234)	emr87_9	49.742	-116.676	1987	Lithoprobe	
G5-28 (274)	line800_1	49.658	-115.879	1990	Lithoprobe	
Group 6 (blue) = Foreland Belt at 49-52 °N						
G6-01 (001)	BNP001	51.665	-116.437	2015	University of Alberta	NIMS
G6-02 (002)	BNP003	51.399	-116.124	2015	University of Alberta	NIMS
G6-03 (003)	BNP004	51.276	-115.912	2015	University of Alberta	NIMS
G6-04 (004)	BNP005	51.164	-115.624	2015	University of Alberta	NIMS
G6-05 (020)	KNP001	50.682	-115.864	2018	University of Alberta	NIMS
G6-06 (021)	KNP002	50.825	-116.013	2018	University of Alberta	NIMS
G6-07 (022)	KNP004	51.168	-116.147	2018	University of Alberta	NIMS
G6-08 (031)	RMN003	51.105	-116.464	2017	University of Alberta	NIMS
G6-09 (033)	RMN005	50.992	-116.216	2017	University of Alberta	NIMS
G6-10 (035)	RMN007	50.561	-115.732	2017	University of Alberta	NIMS
G6-11 (036)	RMN008	50.356	-115.581	2017	University of Alberta	NIMS
G6-12 (038)	RMN012	49.930	-114.858	2017	University of Alberta	NIMS

G6-13 (039)	RMN013	50.207	-114.992	2017	University of Alberta	NIMS
G6-14 (042)	RMN016	50.730	-115.658	2018	University of Alberta	NIMS
G6-15 (046)	RMN020	50.150	-115.425	2018	University of Alberta	NIMS
G6-16 (047)	RMN021	49.304	-114.925	2018	University of Alberta	NIMS
G6-17 (048)	RMN022	49.133	-115.132	2018	University of Alberta	NIMS
G6-18 (056)	SLK001	51.553	-117.297	2017	University of Alberta	NIMS
G6-19 (057)	SLK002	51.708	-117.539	2017	University of Alberta	NIMS
G6-20 (058)	SLK003	51.806	-117.324	2017	University of Alberta	NIMS
G6-21 (059)	SLK004	51.848	-117.808	2017	University of Alberta	NIMS
G6-22 (068)	SSK001	50.015	-114.422	2018	University of Alberta	NIMS
G6-23 (069)	SSK002	50.276	-114.575	2018	University of Alberta	NIMS
G6-24 (070)	SSK003	50.518	-114.836	2018	University of Alberta	NIMS
G6-25 (071)	SSK004	50.825	-114.868	2018	University of Alberta	NIMS
G6-26 (132)	abc184	51.575	-116.788	2004	University of Alberta	NIMS
G6-27 (133)	abc188	51.803	-116.587	2004	University of Alberta	NIMS
G6-28 (209)	abt249	50.968	-114.611		Lithoprobe	LIMS
G6-29 (222)	bhn002	51.559	-115.056	2016	University of Alberta	NIMS
G6-30 (223)	bhn003	51.276	-115.055	2016	University of Alberta	NIMS
G6-31 (227)	duncan_38	49.233	-114.229		Duncan	
G6-32 (231)	emr87_24	49.761	-115.663	1987	Lithoprobe	
G6-33 (235)	flat_4	49.104	-114.490	1985	Shell	
G6-34 (275)	line800_10	49.604	-114.466	1990	Lithoprobe	
G6-35 (276)	line800_11	49.608	-114.223	1990	Lithoprobe	
G6-36 (279)	line800_5	49.661	-115.397	1990	Lithoprobe	
G6-37 (280)	line800_7	49.636	-115.072	1990	Lithoprobe	
G6-38 (281)	line800_9	49.636	-114.695	1990	Lithoprobe	
G6-39 (289)	sab001	49.117	-114.000	2009	University of Alberta	NIMS
G6-40 (290)	sab005	49.447	-114.086	2009	University of Alberta	NIMS
G6-41 (291)	sab010	49.817	-114.164	2009	University of Alberta	NIMS
Group 7 (purple) = 49-52 °N, east of Foreland Belt						
G7-01 (097)	aba114	49.082	-113.308	2008	University of Alberta	NIMS
G7-02 (098)	aba115	49.082	-112.369	2008	University of Alberta	NIMS
G7-03 (099)	aba314	50.295	-113.322	2008	University of Alberta	NIMS
G7-04 (100)	aba315	50.318	-112.399	2008	University of Alberta	NIMS
G7-05 (101)	aba415	50.932	-112.730	2008	University of Alberta	NIMS
G7-06 (102)	aba513	51.589	-114.085	2008	University of Alberta	NIMS
G7-07 (167)	abt033	51.950	-112.883		Lithoprobe	LIMS
G7-08 (168)	abt034	51.880	-112.508		Lithoprobe	LIMS
G7-09 (169)	abt035	51.910	-112.138		Lithoprobe	LIMS
G7-10 (170)	abt036	51.995	-113.337		Lithoprobe	LIMS
G7-11 (172)	abt040	51.235	-112.702		Lithoprobe	LIMS
G7-12 (173)	abt042	51.128	-112.374		Lithoprobe	LIMS
G7-13 (174)	abt043	51.393	-112.945		Lithoprobe	LIMS
G7-14 (175)	abt044	51.553	-113.026		Lithoprobe	LIMS

G7-15 (176)	abt048	51.061	-112.013		Lithoprobe	LIMS
G7-16 (177)	abt062	50.842	-112.049		Lithoprobe	LIMS
G7-17 (178)	abt064	50.616	-112.081		Lithoprobe	LIMS
G7-18 (179)	abt068	51.713	-113.158		Lithoprobe	LIMS
G7-19 (180)	abt070	51.693	-113.648		Lithoprobe	LIMS
G7-20 (181)	abt072	51.809	-113.783		Lithoprobe	LIMS
G7-21 (182)	abt074	51.955	-113.926		Lithoprobe	LIMS
G7-22 (190)	abt201	49.428	-113.734		Lithoprobe	LIMS
G7-23 (191)	abt202	49.431	-113.444		Lithoprobe	LIMS
G7-24 (192)	abt203	49.453	-112.960		Lithoprobe	LIMS
G7-25 (193)	abt205	49.544	-112.664		Lithoprobe	LIMS
G7-26 (194)	abt207	49.689	-112.237		Lithoprobe	LIMS
G7-27 (195)	abt233	49.617	-113.483		Lithoprobe	LIMS
G7-28 (196)	abt234	49.778	-113.448		Lithoprobe	LIMS
G7-29 (197)	abt236	49.948	-113.711		Lithoprobe	LIMS
G7-30 (198)	abt237	50.113	-113.684		Lithoprobe	LIMS
G7-31 (199)	abt238	50.247	-113.812		Lithoprobe	LIMS
G7-32 (200)	abt239	50.378	-113.888		Lithoprobe	LIMS
G7-33 (201)	abt240	50.462	-114.097		Lithoprobe	LIMS
G7-34 (202)	abt241	50.580	-114.161		Lithoprobe	LIMS
G7-35 (203)	abt242	50.681	-114.402		Lithoprobe	LIMS
G7-36 (204)	abt244	50.837	-114.506		Lithoprobe	LIMS
G7-37 (205)	abt245	51.077	-114.501		Lithoprobe	LIMS
G7-38 (206)	abt246	51.142	-114.666		Lithoprobe	LIMS
G7-39 (207)	abt247	51.259	-114.446		Lithoprobe	LIMS
G7-40 (208)	abt248	51.366	-114.601		Lithoprobe	LIMS
G7-41 (210)	abt250	51.570	-114.455		Lithoprobe	LIMS
G7-42 (211)	abt251	50.549	-113.038		Lithoprobe	LIMS
G7-43 (212)	abt252	50.794	-113.362		Lithoprobe	LIMS
G7-44 (213)	abt253	50.246	-112.878		Lithoprobe	LIMS
G7-45 (214)	abt256	50.963	-113.388		Lithoprobe	LIMS
G7-46 (221)	bhn001	51.633	-114.753	2016	University of Alberta	NIMS
G7-47 (224)	clw012	51.915	-114.548	2016	University of Alberta	NIMS
G7-48 (277)	line800_12	49.588	-114.002	1990	Lithoprobe	
G7-49 (278)	line800_13	49.630	-113.830	1990	Lithoprobe	
G7-50 (292)	sab015	50.222	-114.182	2009	University of Alberta	NIMS
G7-51 (293)	sab020	49.944	-113.064	2009	University of Alberta	NIMS
G7-52 (294)	sab030	51.246	-113.928	2009	University of Alberta	NIMS
G7-53 (295)	sab035	51.424	-113.540	2009	University of Alberta	NIMS
G7-54 (296)	sab040	49.982	-112.677	2009	University of Alberta	NIMS
G7-55 (297)	sab045	49.978	-112.255	2009	University of Alberta	NIMS
G7-56 (298)	sab055	50.914	-114.221	2009	University of Alberta	NIMS
G7-57 (299)	sab060	51.366	-114.171	2009	University of Alberta	NIMS
G7-58 (300)	sab065	51.792	-114.312	2009	University of Alberta	NIMS
G7-59 (301)	sab070	51.543	-113.518	2009	University of Alberta	NIMS
G7-60 (302)	sab075	50.608	-113.804	2009	University of Alberta	NIMS

G7-61 (303)	sab080	50.895	-113.637	2009	University of Alberta	NIMS
G7-62 (304)	sab085	51.056	-113.731	2009	University of Alberta	NIMS
G7-63 (305)	sab090	51.438	-113.791	2009	University of Alberta	NIMS
G7-64 (306)	sab095	50.440	-112.929	2009	University of Alberta	NIMS
G7-65 (307)	sab100	50.674	-113.120	2009	University of Alberta	NIMS
G7-66 (308)	sab105	51.253	-113.233	2009	University of Alberta	NIMS
G7-67 (309)	sab110	51.846	-113.446	2009	University of Alberta	NIMS
G7-68 (310)	sab115	50.509	-112.590	2009	University of Alberta	NIMS
G7-69 (311)	sab117	50.649	-112.758	2009	University of Alberta	NIMS
G7-70 (312)	sab120	51.061	-112.910	2009	University of Alberta	NIMS
G7-71 (313)	sab125	51.808	-113.058	2009	University of Alberta	NIMS
G7-72 (314)	sab130	50.809	-112.313	2009	University of Alberta	NIMS
G7-73 (315)	sab140	51.460	-112.572	2009	University of Alberta	NIMS
G7-74 (316)	sab145	51.722	-112.509	2009	University of Alberta	NIMS
G7-75 (317)	sab155	51.318	-112.188	2009	University of Alberta	NIMS
G7-76 (320)	sab210	51.990	-112.385	2009	University of Alberta	NIMS
Group 8 (white) = south of 49 °N or north of 52 °N						
G8-001 (005)	CLW001	52.831	-114.849	2015	University of Alberta	NIMS
G8-002 (006)	CLW002	52.629	-115.167	2015	University of Alberta	NIMS
G8-003 (007)	CLW003	52.743	-116.151	2015	University of Alberta	NIMS
G8-004 (008)	CLW004	52.619	-116.432	2015	University of Alberta	NIMS
G8-005 (009)	CLW006	52.150	-115.933	2015	University of Alberta	NIMS
G8-006 (010)	CLW008	52.463	-115.538	2015	University of Alberta	NIMS
G8-007 (011)	FH1	52.189	-115.317	2002	University of Alberta	V5-2000
G8-008 (012)	FH2	52.042	-115.541	2002	University of Alberta	V5-2000
G8-009 (013)	IDA11	48.935	-116.444	2007	EarthScope / USArray	
G8-010 (014)	IDC11	47.839	-116.273	2008	EarthScope / USArray	
G8-011 (015)	JNP001	52.732	-117.639	2015	University of Alberta	NIMS
G8-012 (016)	JNP002	52.740	-117.955	2015	University of Alberta	NIMS
G8-013 (017)	JNP004	52.550	-117.665	2015	University of Alberta	NIMS
G8-014 (018)	JNP006	52.307	-117.329	2015	University of Alberta	NIMS
G8-015 (019)	JNP008	52.070	-116.908	2015	University of Alberta	NIMS
G8-016 (023)	MTB12	48.448	-115.563	2008	EarthScope / USArray	
G8-017 (024)	MTB13	48.373	-114.454	2008	EarthScope / USArray	
G8-018 (025)	MTB14	48.311	-113.325	2008	EarthScope / USArray	
G8-019 (026)	MTB15	48.313	-112.447	2008	EarthScope / USArray	
G8-020 (027)	MTC12	47.889	-115.454	2008	EarthScope / USArray	
G8-021 (028)	MTC13	47.842	-114.559	2008	EarthScope / USArray	
G8-022 (029)	MTC14	47.840	-113.429	2008	EarthScope / USArray	
G8-023 (030)	MTC15	47.745	-112.507	2008	EarthScope / USArray	
G8-024 (060)	SLK005	52.099	-118.462	2017	University of Alberta	NIMS
G8-025 (072)	WAA10	48.927	-117.597	2007	EarthScope / USArray	
G8-026 (073)	WAB05	48.192	-122.040	2007	EarthScope / USArray	
G8-027 (074)	WAB06	48.521	-121.387	2007	EarthScope / USArray	

G8-028 (075)	WAB07	48.507	-120.264	2007	EarthScope / USArray	
G8-029 (076)	WAB08	48.567	-119.430	2007	EarthScope / USArray	
G8-030 (077)	WAB10	48.264	-117.329	2007	EarthScope / USArray	
G8-031 (078)	WAC05	47.899	-121.721	2007	EarthScope / USArray	
G8-032 (079)	WAC06	47.881	-120.666	2007	EarthScope / USArray	
G8-033 (080)	WAC07	47.804	-119.912	2007	EarthScope / USArray	
G8-034 (081)	WAC08	47.770	-119.174	2007	EarthScope / USArray	
G8-035 (082)	WAC09	47.821	-118.200	2007	EarthScope / USArray	
G8-036 (083)	WAC10	47.812	-117.284	2007	EarthScope / USArray	
G8-037 (084)	YHD001	53.533	-115.490	2015	University of Alberta	NIMS
G8-038 (085)	YHD002	53.563	-116.263	2015	University of Alberta	NIMS
G8-039 (086)	YHD003	53.365	-115.801	2015	University of Alberta	NIMS
G8-040 (087)	YHD004	53.367	-116.609	2015	University of Alberta	NIMS
G8-041 (088)	YHD005	53.276	-116.322	2015	University of Alberta	NIMS
G8-042 (089)	YHD006	53.125	-115.924	2015	University of Alberta	NIMS
G8-043 (090)	YHD008	53.354	-117.198	2015	University of Alberta	NIMS
G8-044 (091)	YHD009	53.175	-116.811	2015	University of Alberta	NIMS
G8-045 (092)	YHD010	53.073	-116.532	2015	University of Alberta	NIMS
G8-046 (093)	YHD011	52.931	-116.369	2015	University of Alberta	NIMS
G8-047 (094)	YHD012	53.203	-117.542	2015	University of Alberta	NIMS
G8-048 (095)	YHD013	53.044	-117.101	2015	University of Alberta	NIMS
G8-049 (096)	YHD014	52.813	-116.900	2015	University of Alberta	NIMS
G8-050 (103)	aba613	52.218	-114.023	2008	University of Alberta	NIMS
G8-051 (104)	aba614	52.346	-113.273	2008	University of Alberta	NIMS
G8-052 (105)	aba713	52.909	-113.861	2008	University of Alberta	NIMS
G8-053 (106)	aba714	52.909	-113.088	2008	University of Alberta	NIMS
G8-054 (107)	aba715	53.220	-112.528	2010	University of Alberta	NIMS
G8-055 (108)	aba716	52.858	-112.435	2010	University of Alberta	NIMS
G8-056 (109)	aba730	52.934	-113.475	2014	University of Alberta	NIMS
G8-057 (110)	aba735	53.119	-113.979	2014	University of Alberta	NIMS
G8-058 (111)	aba740	53.294	-113.668	2014	University of Alberta	NIMS
G8-059 (112)	aba745	53.295	-114.419	2014	University of Alberta	NIMS
G8-060 (113)	aba750	53.650	-114.340	2014	University of Alberta	NIMS
G8-061 (114)	aba813	53.435	-114.089	2008	University of Alberta	NIMS
G8-062 (115)	aba814	53.130	-113.358	2010	University of Alberta	NIMS
G8-063 (116)	aba840	53.843	-112.881	2014	University of Alberta	NIMS
G8-064 (117)	aba915	53.718	-112.443	2010	University of Alberta	NIMS
G8-065 (134)	abc190	52.012	-116.569	2004	University of Alberta	NIMS
G8-066 (135)	abc192	52.166	-116.481	2004	University of Alberta	NIMS
G8-067 (136)	abc194	52.336	-116.358	2004	University of Alberta	NIMS
G8-068 (137)	abc198	52.516	-116.190	2004	University of Alberta	NIMS
G8-069 (138)	abc202	52.709	-115.735	2004	University of Alberta	NIMS
G8-070 (139)	abc204	52.838	-115.510	2004	University of Alberta	NIMS
G8-071 (140)	abc206	52.988	-115.340	2004	University of Alberta	NIMS
G8-072 (141)	abc208	53.088	-115.191	2004	University of Alberta	NIMS
G8-073 (142)	abc260	48.899	-121.892	2003	University of Alberta	NIMS

G8-074 (147)	abc325	52.136	-119.354	2006	University of Alberta	NIMS
G8-075 (148)	abc345	52.560	-119.048	2006	University of Alberta	NIMS
G8-076 (149)	abc365	52.868	-118.556	2006	University of Alberta	NIMS
G8-077 (150)	abc375	52.996	-118.082	2006	University of Alberta	NIMS
G8-078 (151)	abc380	53.136	-118.020	2006	University of Alberta	NIMS
G8-079 (152)	abc384	53.370	-117.765	2006	University of Alberta	NIMS
G8-080 (153)	abc386	53.519	-117.418	2006	University of Alberta	NIMS
G8-081 (154)	abc388	53.569	-116.971	2006	University of Alberta	NIMS
G8-082 (155)	abc390	53.726	-116.533	2006	University of Alberta	NIMS
G8-083 (156)	abt012	52.682	-112.003		Lithoprobe	LIMS
G8-084 (157)	abt013	52.533	-112.289		Lithoprobe	LIMS
G8-085 (158)	abt016	52.467	-112.700		Lithoprobe	LIMS
G8-086 (159)	abt018	52.654	-113.128		Lithoprobe	LIMS
G8-087 (160)	abt022	52.712	-114.052		Lithoprobe	LIMS
G8-088 (161)	abt023	52.809	-114.236		Lithoprobe	LIMS
G8-089 (162)	abt025	52.977	-114.243		Lithoprobe	LIMS
G8-090 (163)	abt026	53.066	-114.634		Lithoprobe	LIMS
G8-091 (164)	abt030	53.426	-114.823		Lithoprobe	LIMS
G8-092 (165)	abt031	52.147	-113.481		Lithoprobe	LIMS
G8-093 (166)	abt032	52.703	-114.418		Lithoprobe	LIMS
G8-094 (171)	abt037	52.263	-114.607		Lithoprobe	LIMS
G8-095 (183)	abt076	52.020	-114.215		Lithoprobe	LIMS
G8-096 (184)	abt078	52.131	-114.435		Lithoprobe	LIMS
G8-097 (185)	abt081	52.330	-115.017		Lithoprobe	LIMS
G8-098 (186)	abt083	52.543	-113.757		Lithoprobe	LIMS
G8-099 (187)	abt089	53.731	-114.921		Lithoprobe	LIMS
G8-100 (188)	abt092	53.873	-115.453		Lithoprobe	LIMS
G8-101 (189)	abt109	53.924	-112.104		Lithoprobe	LIMS
G8-102 (215)	abt314	53.987	-115.029		Lithoprobe	LIMS
G8-103 (236)	kooc1_1	48.994	-114.959		Phoenix / GSC	
G8-104 (237)	kooc1_14	48.930	-115.322		Phoenix / GSC	
G8-105 (238)	kooc9_14	48.221	-115.974		Phoenix / GSC	
G8-106 (239)	kooc9_15	48.238	-114.990		Phoenix / GSC	
G8-107 (282)	rdc010	53.953	-114.289	2008	University of Alberta	NIMS
G8-108 (283)	rdc020	53.830	-113.887	2008	University of Alberta	NIMS
G8-109 (284)	rdc030	53.723	-113.552	2008	University of Alberta	NIMS
G8-110 (285)	rdc040	53.636	-113.130	2008	University of Alberta	NIMS
G8-111 (286)	rdc050	53.542	-112.749	2008	University of Alberta	NIMS
G8-112 (287)	rdc060	53.426	-112.419	2008	University of Alberta	NIMS
G8-113 (288)	rdc070	53.313	-112.039	2008	University of Alberta	NIMS
G8-114 (318)	sab200	52.171	-112.903	2009	University of Alberta	NIMS
G8-115 (319)	sab204	52.259	-112.374	2010	University of Alberta	NIMS
G8-116 (322)	ten023	53.160	-121.843		Gough	
G8-117 (323)	ten601	53.468	-119.895		Gough	
G8-118 (324)	ten609	53.478	-120.633		Gough	
G8-119 (325)	ten706	53.243	-120.388		Gough	

G8-120 (326)	ten709	53.311	-119.398		Gough	
G8-121 (327)	ten712	53.015	-119.726		Gough	
G8-122 (331)	ten902	53.353	-121.123		Gough	

***Table D.2**: Previous 3-D MT studies that overlap spatially with this study. They used the inversion programs WSINV3DMT (Siripunvaraporn et al., 2005; Siripunvaraporn & Egbert, 2009), ModEM (Kelbert et al., 2014), and GoFEM (Grayver, 2015; Grayver et al., 2019; Grayver & Kolev, 2015). Latitude and longitude ranges are rounded to the nearest degree, and they represent the areal extent of the MT data used in each study. The maximum depth for each study is given, as presented in the figures of their respective publications.*

Authors (Year)	Inversion Program	Latitude Range (°N)	Longitude Range (°W)	Horizontal Cell Size (km)	Number of MT Sites	Number of Periods	Period Range (s)	Max. Depth (km)
University of Alberta Studies (Section 6.2.4.2.1)								
Nieuwenhuis et al. (2014)	WSINV 3DMT	49 – 53	110 – 115	10	87	?	1 – 10,000	300
Wang & Unsworth (2022)	ModEM	49 – 60	110 – 120	8	396	31	2 – 13,000	400
Hanneson & Unsworth (2023b)	ModEM	48 – 54	112 – 122	5	331	18	1 – 18,000	100
Hanneson & Unsworth (this study)	ModEM	48 – 54	112 – 122	5	331	18	1 – 18,000	400
EarthScope USArray Studies (Section 6.2.4.2.2)								
Patro & Egbert (2008)	WSINV 3DMT	42 – 49	115 – 124	12	109	8	100 – 8,000	100
Bedrosian & Feucht (2014)	WSINV 3DMT	39 – 49	107 – 124	15	241	10	10 – 10,000	150
Meqbel et al. (2014)	ModEM	39 – 49	107 – 124	12.5	325	22	10 – 20,000	400
Yang et al. (2021)	ModEM	31 – 49	68 – 124	30	423	30	10 – 20,000	400
Munch & Grayver (2023)	GoFEM	25 – 50	65 – 125	Variable	1,291	?	10 – 30,000	400

D.2. Sensitivity tests

Table D.3*: Results of Kolmogorov-Smirnov (KS) tests between the residuals of the responses of the preferred model and altered models. The altered models labeled "Yes" had residuals that were from the same distribution as the preferred model, with 98% confidence. The model layers listed in the second column were changed to 1 Ωm, then forward calculations were performed. The misfit of the altered models is shown in the last two columns.*

Edited Models		Impedance and Tipper		Impedance Only		Tipper Only		R.M.S. Misfit (Unedited = 2.08)	
1 Ωm Depth	**Layers**	***p*-value**	**Same?**	***p*-value**	**Same?**	***p*-value**	**Same?**	**Edited**	**Increase**
51 km	37-58	0.0000	No	0.0000	No	0.0000	No	5.40	3.31
102 km	42-58	0.0000	No	0.0000	No	0.0000	No	4.18	2.10
206 km	47-58	0.0000	No	0.0000	No	0.0000	No	2.89	0.81
273 km	49-58	0.0000	No	0.0000	No	0.0000	No	2.48	0.39
314 km	50-58	0.0000	No	0.0000	No	0.0002	No	2.33	0.24
361 km	51-58	0.0010	No	0.0168	No	0.0101	No	2.22	0.14
415 km	52-58	0.1179	Yes	0.6653	Yes	0.1047	Yes	2.16	0.07
477 km	53-58	0.6759	Yes	0.9759	Yes	0.6132	Yes	2.12	0.04

Table D.4*: Details of resistivity models used to generate synthetic MT data for testing the resolvability of the lithosphere-asthenosphere boundary (LAB). The modelled LAB depth is listed in the third and fourth columns. The LAB is modelled as being vertical at the backarc-craton lithosphere step at one of three locations: (1) a constant longitude of 119 °W, near the $^{87}Sr/^{86}Sr$ = 0.706 isopleth (Sr.706) in southern BC, (2) near the western boundary of the Kootenay Arc (WKA) approximated after Archibald et al. (1983) and a constant longitude of 118.1 °W to the north and south of the WKA, and (3) near the boundary between the Omineca belt and Foreland belt (SRMT). In all cases, the LAB is modelled as a sharp boundary with 1,000 Ωm above and 30 Ωm below. This is physically unrealistic, but serves the purpose of these resolution tests. All of the resistivity models include the conductive sedimentary basins of the preferred starting model. The upper 50 km are 1,000 Ωm elsewhere (Simple) but they include conductive polygons in some cases (Polygons). In other cases, the upper 50 km were replaced by the upper 50 km of the published resistivity model (Complex). These 14 resistivity models are shown in Figures D.3-D.16. Model 4 used a different error floor, which is why the R.M.S. misfit is lower.*

Model Number	Authors' Identifier	Cordillera LAB (km)	Craton LAB (km)	Vertical Step Near	Upper 50 km	Figure Number	R.M.S. Misfit
1	CCB-Syn2	58	179	Sr.706	Simple	D.3	0.978
2	CCB-Syn10	58	179	WKA	Simple	D.4	0.986
3	CCB-Syn1	58	179	SRMT	Simple	D.5	0.973
4	SEBC-Syn7	58	179	SRMT	Polygons	D.6	0.850
5	CCB-Syn4	58	273	Sr.706	Simple	D.7	0.986
6	CCB-Syn11	58	273	WKA	Simple	D.8	0.978
7	CCB-Syn3	58	273	SRMT	Simple	D.9	0.985
8	CCB-Syn5	58	156-314 (north dipping)	Sr.706	Simple	D.10	0.986
9	CCB-Syn6	58	156-314 (north dipping)	Sr.706	Polygons	D.11	0.978

10	CCB-Syn7	58	156-314 (north dipping)	Sr.706	Complex	D.12	1.237
11	CCB-Syn8	67	179-361 (north dipping)	Sr.706	Polygons	D.13	0.966
12	CCB-Syn9	67	179-361 (north dipping)	Sr.706	Complex	D.14	1.202
13	CCB-Syn12	67	179-361 (north dipping)	WKA	Complex	D.15	1.196
14	CCB-Syn13	67	179-361 (north dipping)	SRMT	Complex	D.16	1.211

D.3. Analysis

Table D.5*: Means, minima and maxima of the 28 sets of resistivity values (Ωm) discussed in Section 6.5.1 and shown in Figures 6.8 and 6.9.*

Group	G1	G2	G3	G4	G5	G6	G7
0–75 km							
Mean	35	91	15	5	4	10	8
(min–max)	(9–220)	(42–232)	(2–109)	(0.5–149)	(0.3–997)	(0.4–806)	(0.5–431)
75–150 km							
Mean	85	50	78	127	96	131	117
(min–max)	(59–162)	(22–78)	(43–139)	(49–499)	(14–1012)	(32–1736)	(16–949)
150–250 km							
Mean	105	44	44	50	32	41	51
(min–max)	(79–155)	(32–76)	(34–55)	(30–105)	(18–139)	(19–239)	(15–215)
250–400 km							
Mean	82	54	41	38	32	31	37
(min–max)	(72–94)	(42–72)	(38–45)	(34–43)	(27–43)	(24–42)	(24–66)

D.4. Additional figures

This section contains 21 figures that were mentioned in the paper but omitted to satisfy the length limit.

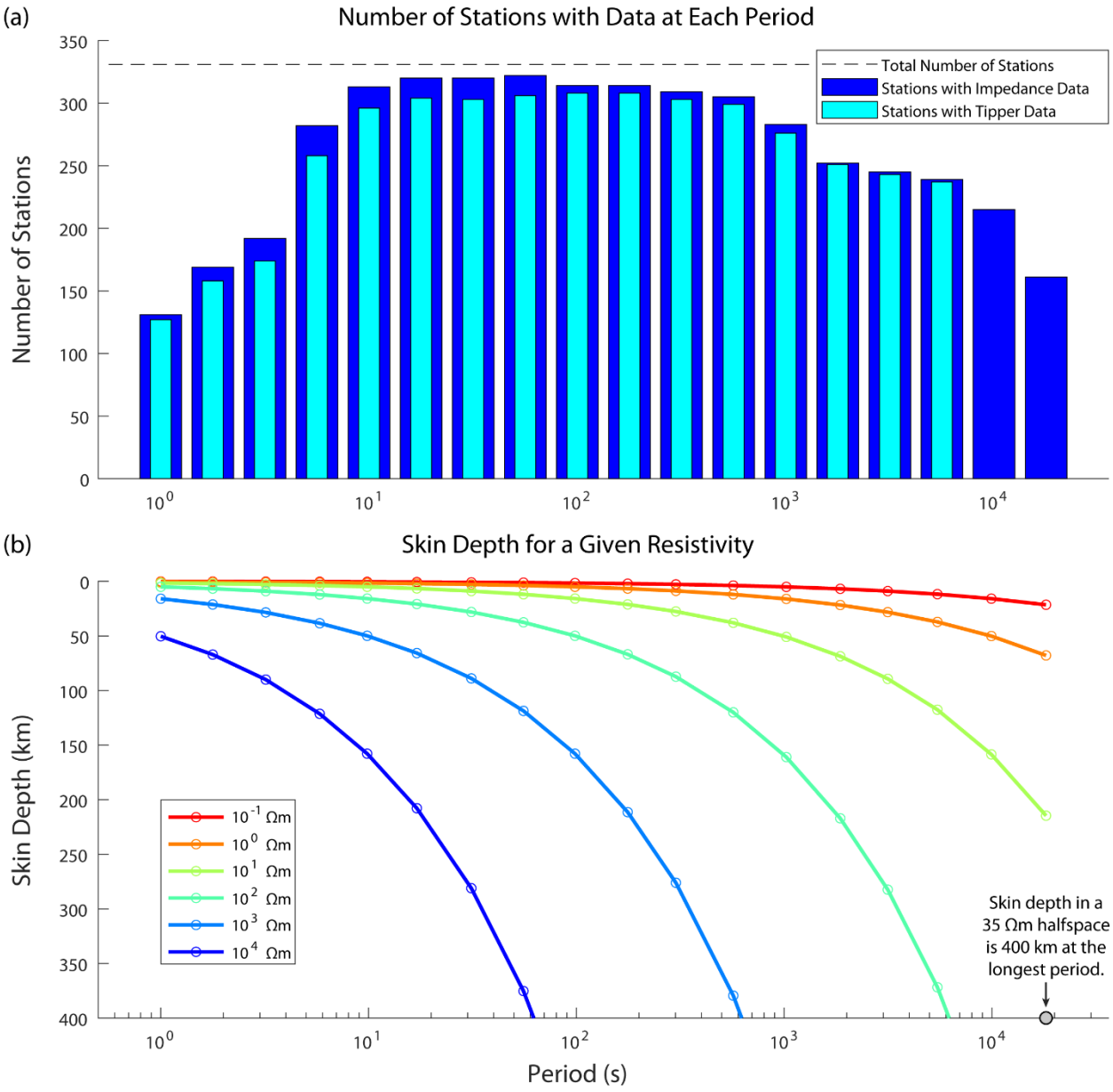

***Figure D.1**: (a) Periods used in the inversion and the number of MT stations with data at each period. (b) Skin depth evaluated at the periods above and six resistivity values between 0.1 and 10,000 Ωm.*

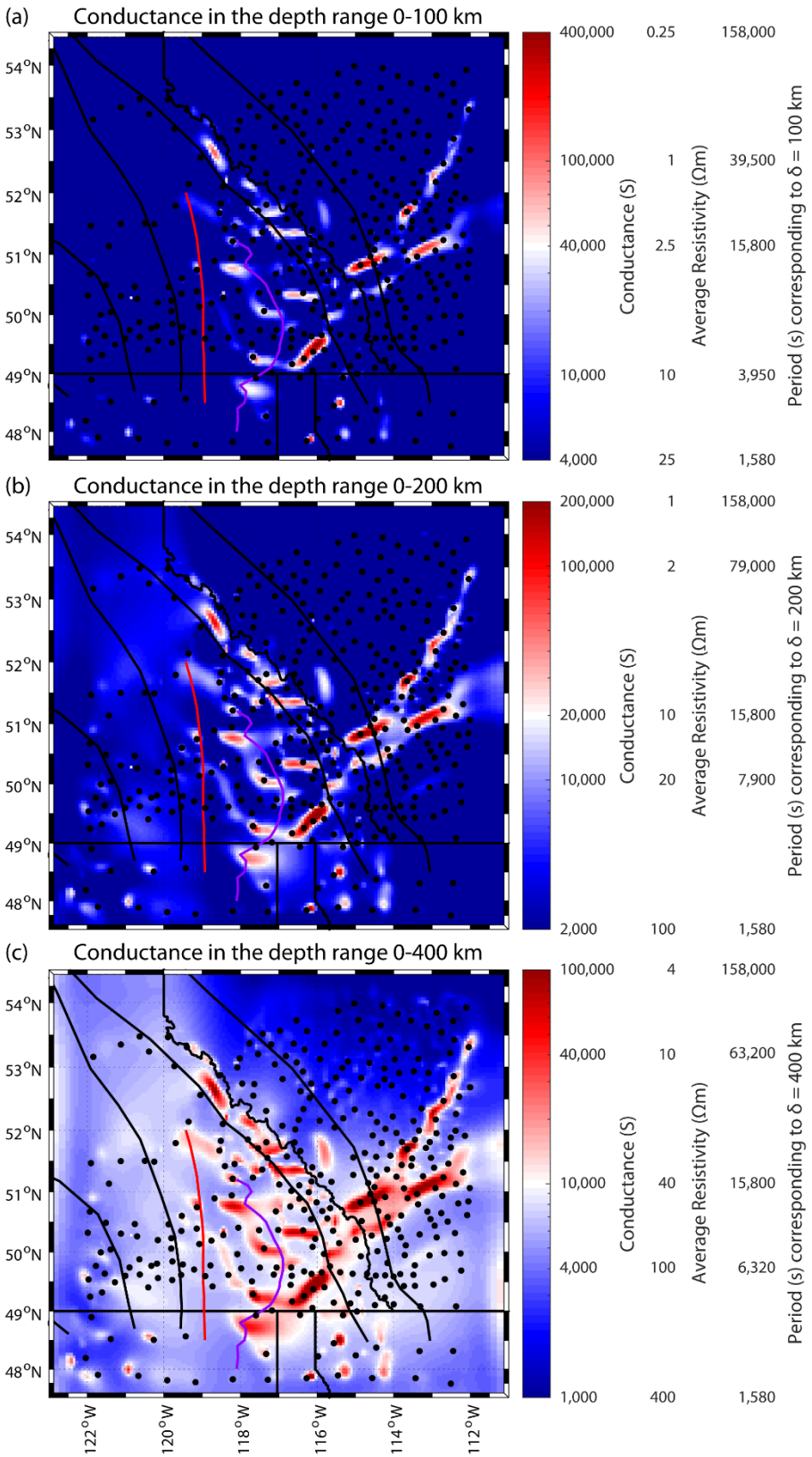

***Figure D.2**: Conductance of the preferred resistivity model, calculated over three depth ranges: (a) 0-100 km, (b) 0-200 km, and (c) 0-400 km. The average resistivity is thickness divided by conductance, and δ is the skin depth.*

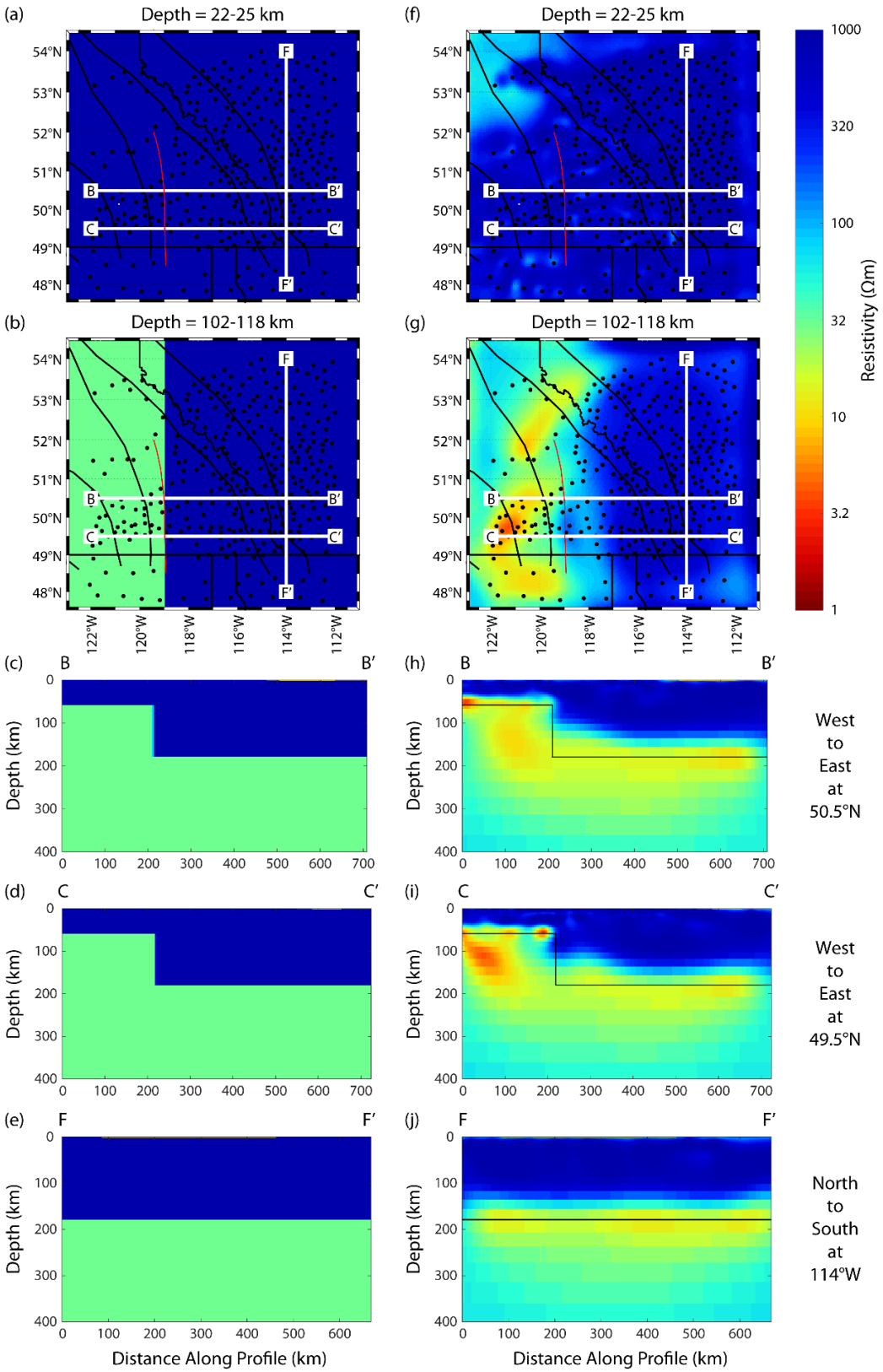

***Figure D.3**: (a-e) Resistivity model 1 (Table D.3) representing the LAB with 1,000 Ωm above it and 30 Ωm below it. (f-j) Resistivity model from inversion of synthetic MT data generated using the resistivity model on the left.*

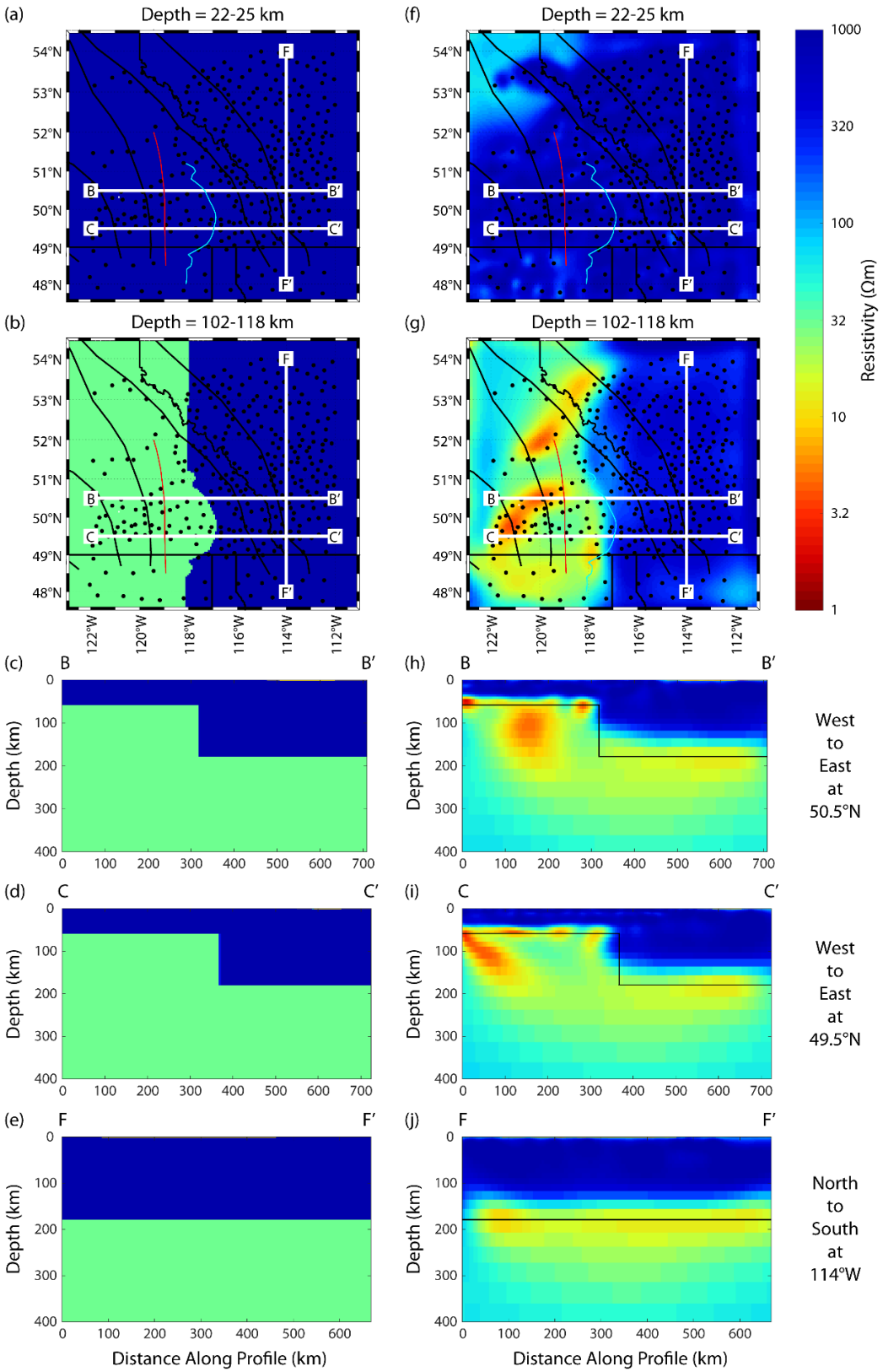

***Figure D.4**: (a-e) Resistivity model 2 (Table D.3) representing the LAB with 1,000 Ωm above it and 30 Ωm below it. (f-j) Resistivity model from inversion of synthetic MT data generated using the resistivity model on the left.*

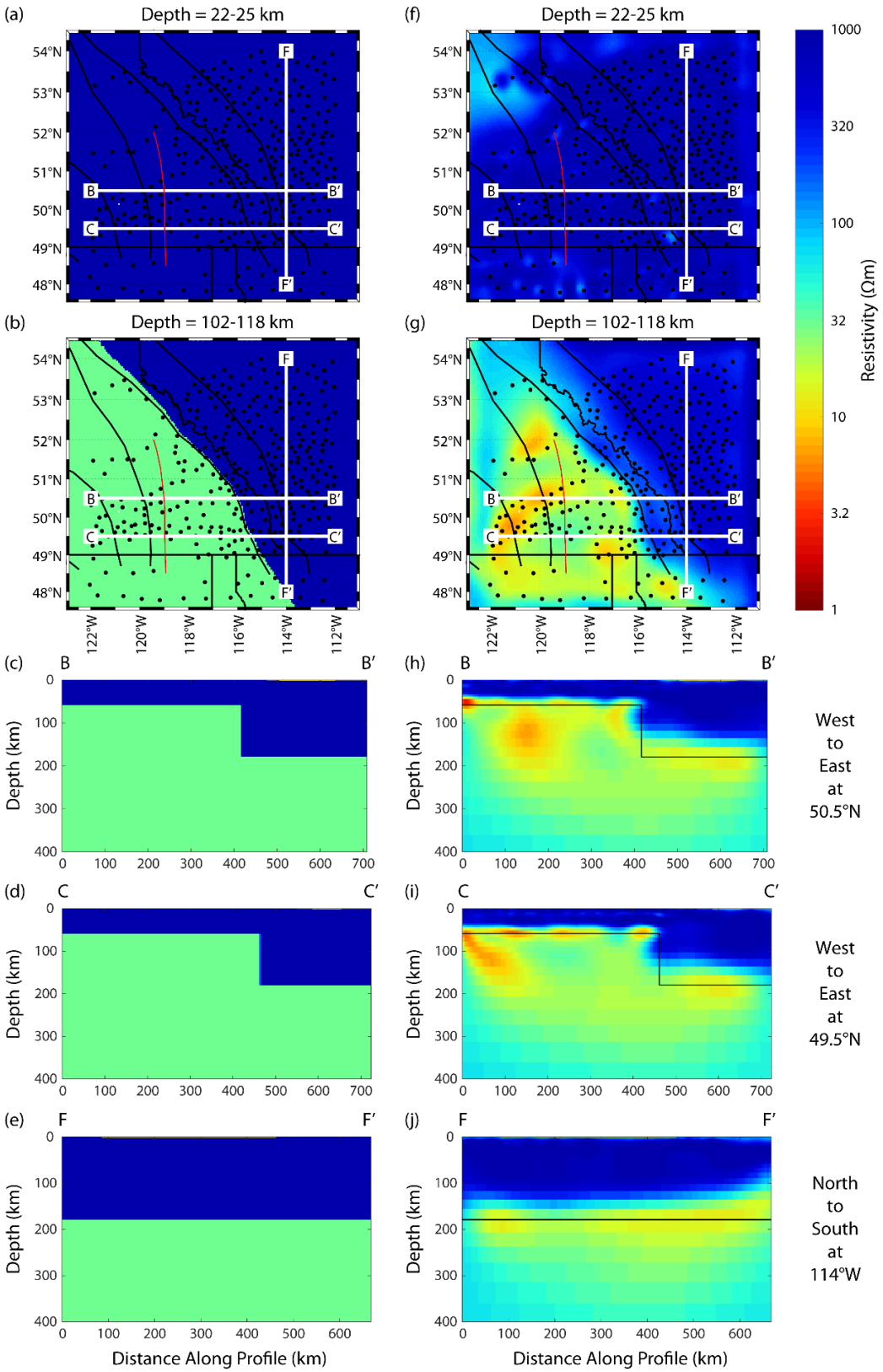

Figure D.5*: (a-e) Resistivity model 3 (Table D.3) representing the LAB with 1,000 Ωm above it and 30 Ωm below it. (f-j) Resistivity model from inversion of synthetic MT data generated using the resistivity model on the left.*

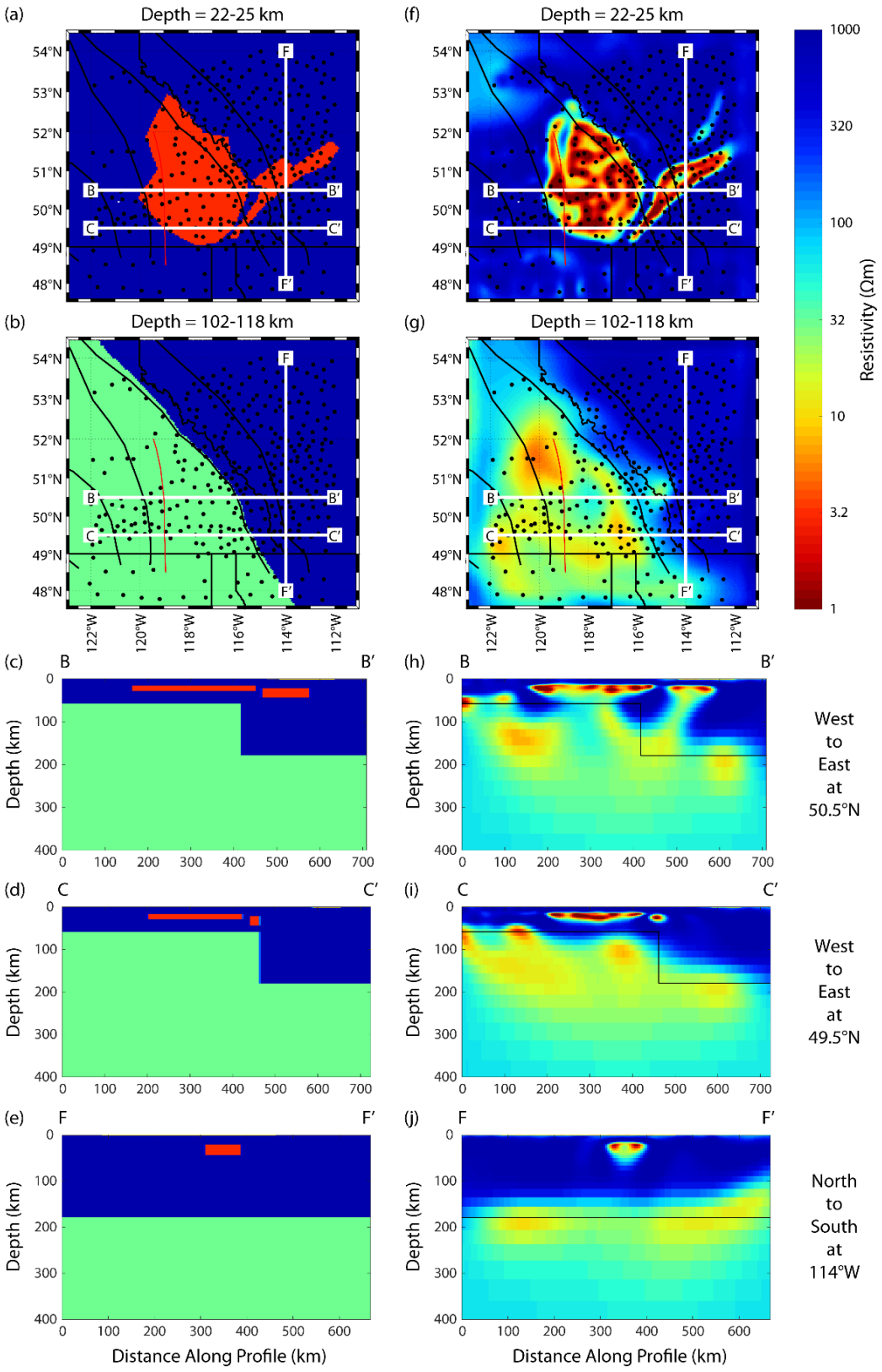

Figure D.6*: (a-e) Resistivity model 4 (Table D.3) representing the LAB with 1,000 Ωm above it and 30 Ωm below it. Conductive polygons in the upper 50 km are 3 Ωm. (f-j) Resistivity model from inversion of synthetic MT data generated using the resistivity model on the left.*

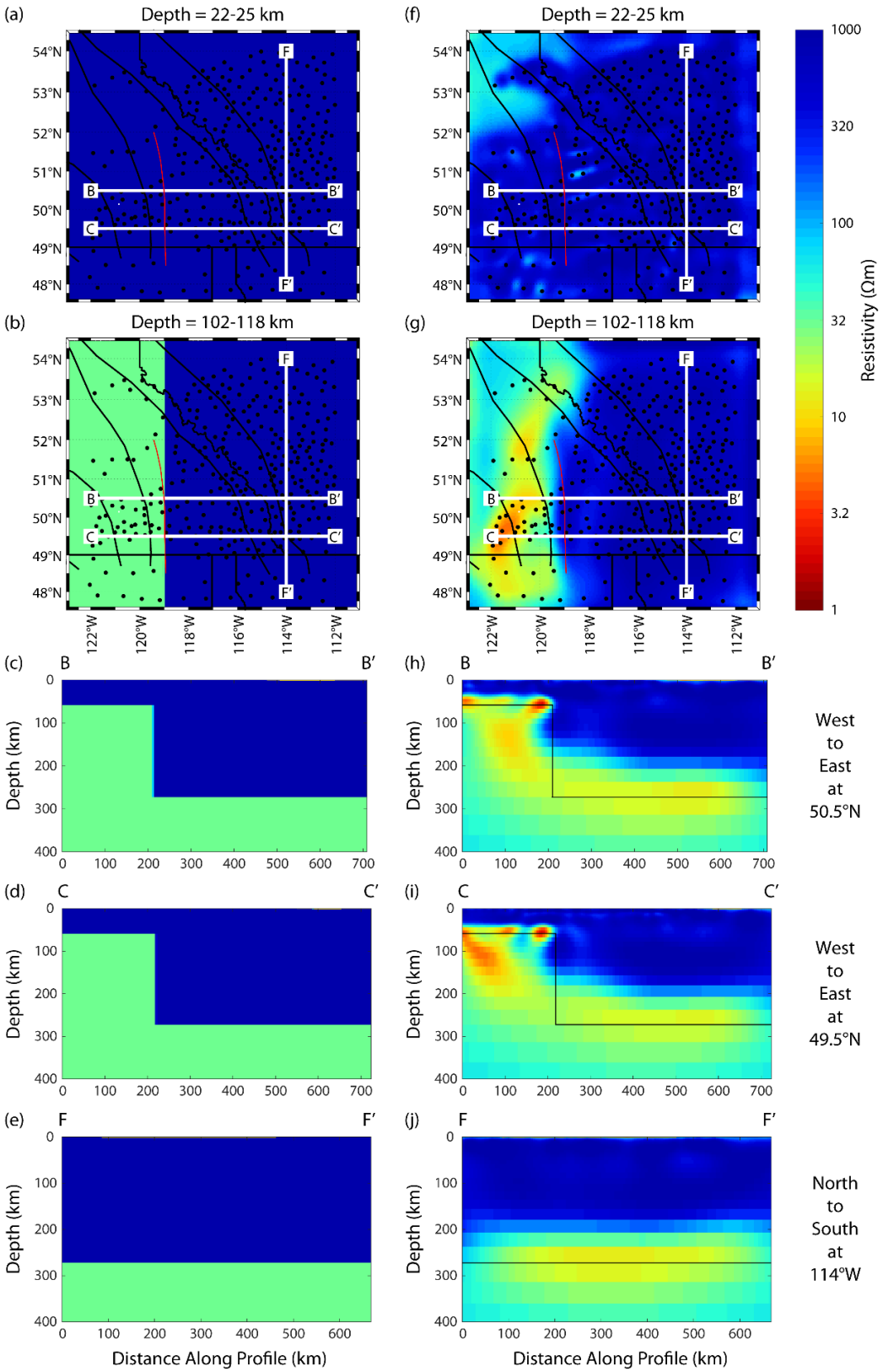

***Figure D.7**: (a-e) Resistivity model 5 (Table D.3) representing the LAB with 1,000 Ωm above it and 30 Ωm below it. (f-j) Resistivity model from inversion of synthetic MT data generated using the resistivity model on the left.*

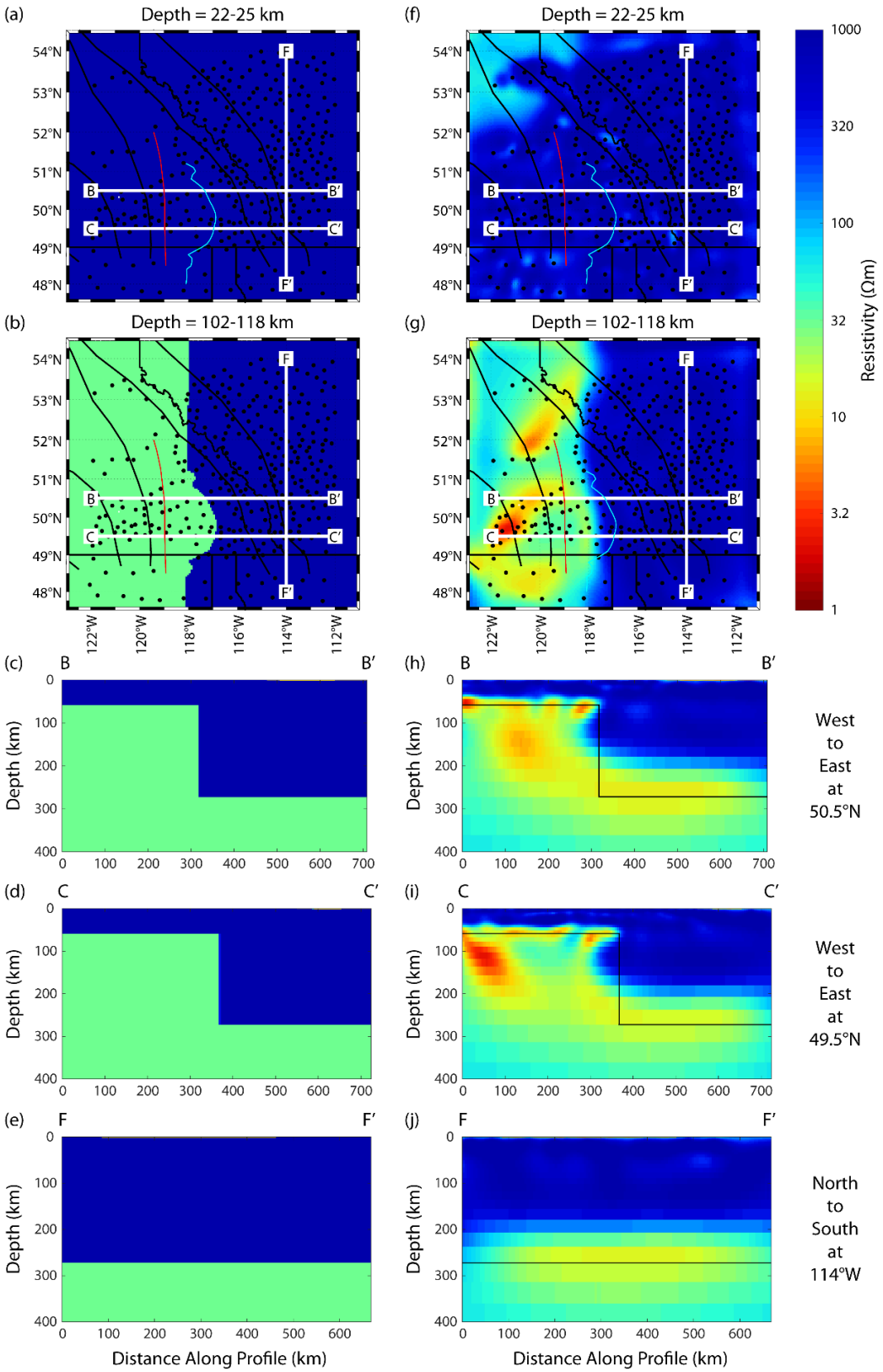

***Figure D.8**: (a-e) Resistivity model 6 (Table D.3) representing the LAB with 1,000 Ωm above it and 30 Ωm below it. (f-j) Resistivity model from inversion of synthetic MT data generated using the resistivity model on the left.*

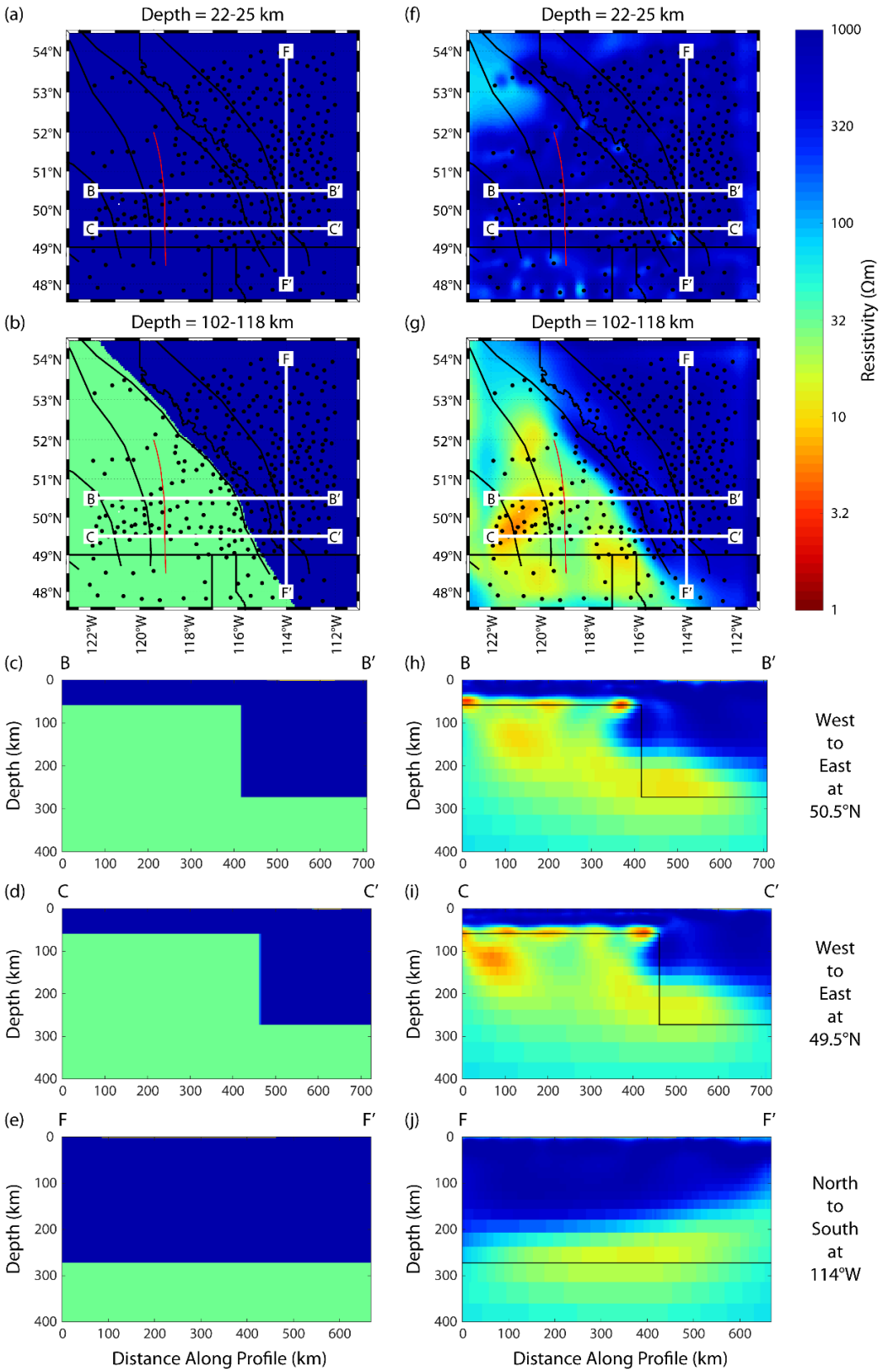

***Figure D.9**: (a-e) Resistivity model 7 (Table D.3) representing the LAB with 1,000 Ωm above it and 30 Ωm below it. (f-j) Resistivity model from inversion of synthetic MT data generated using the resistivity model on the left.*

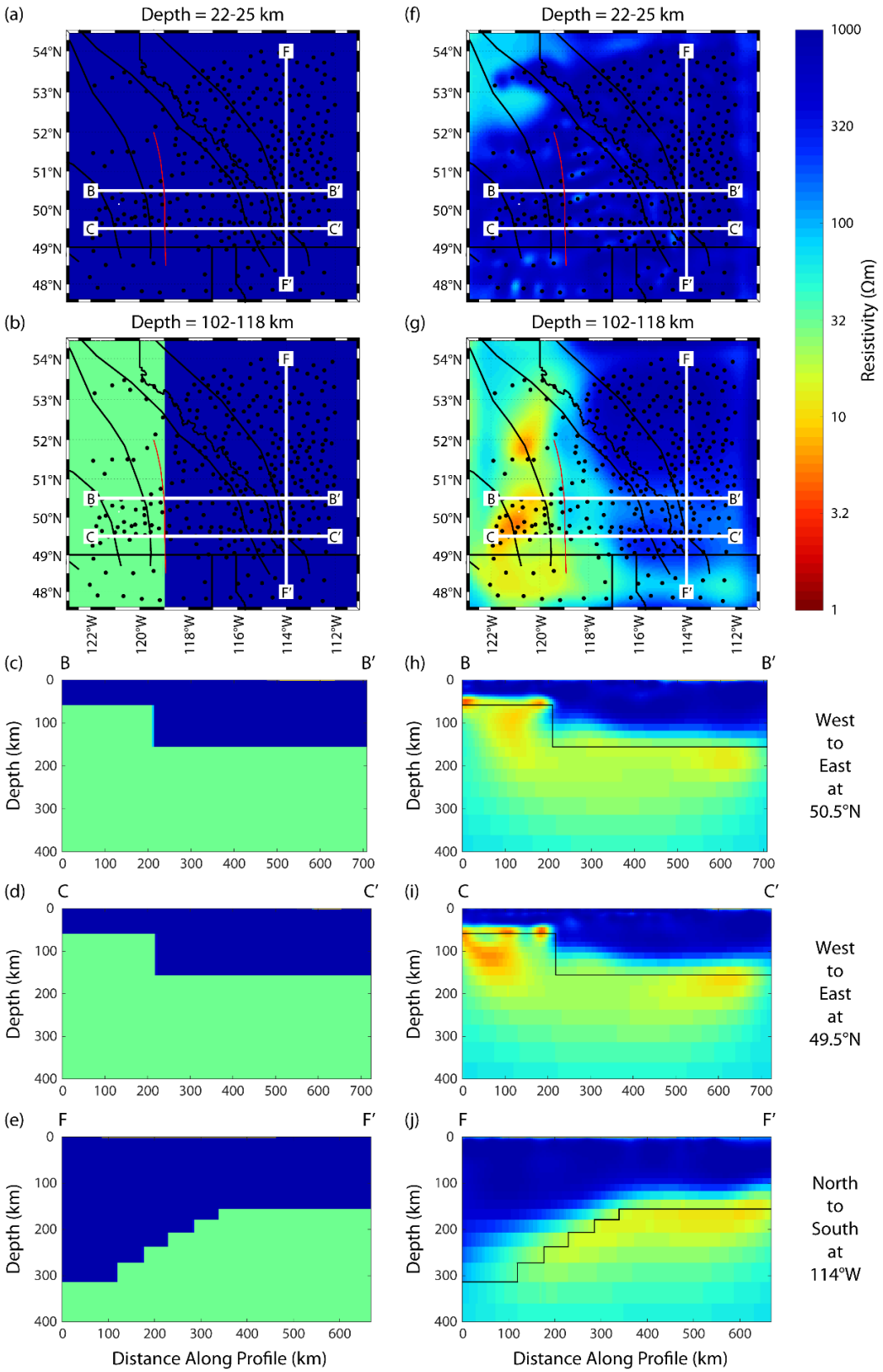

***Figure D.10**: (a-e) Resistivity model 8 (Table D.3) representing the LAB with 1,000 Ωm above it and 30 Ωm below it. (f-j) Resistivity model from inversion of synthetic MT data generated using the resistivity model on the left.*

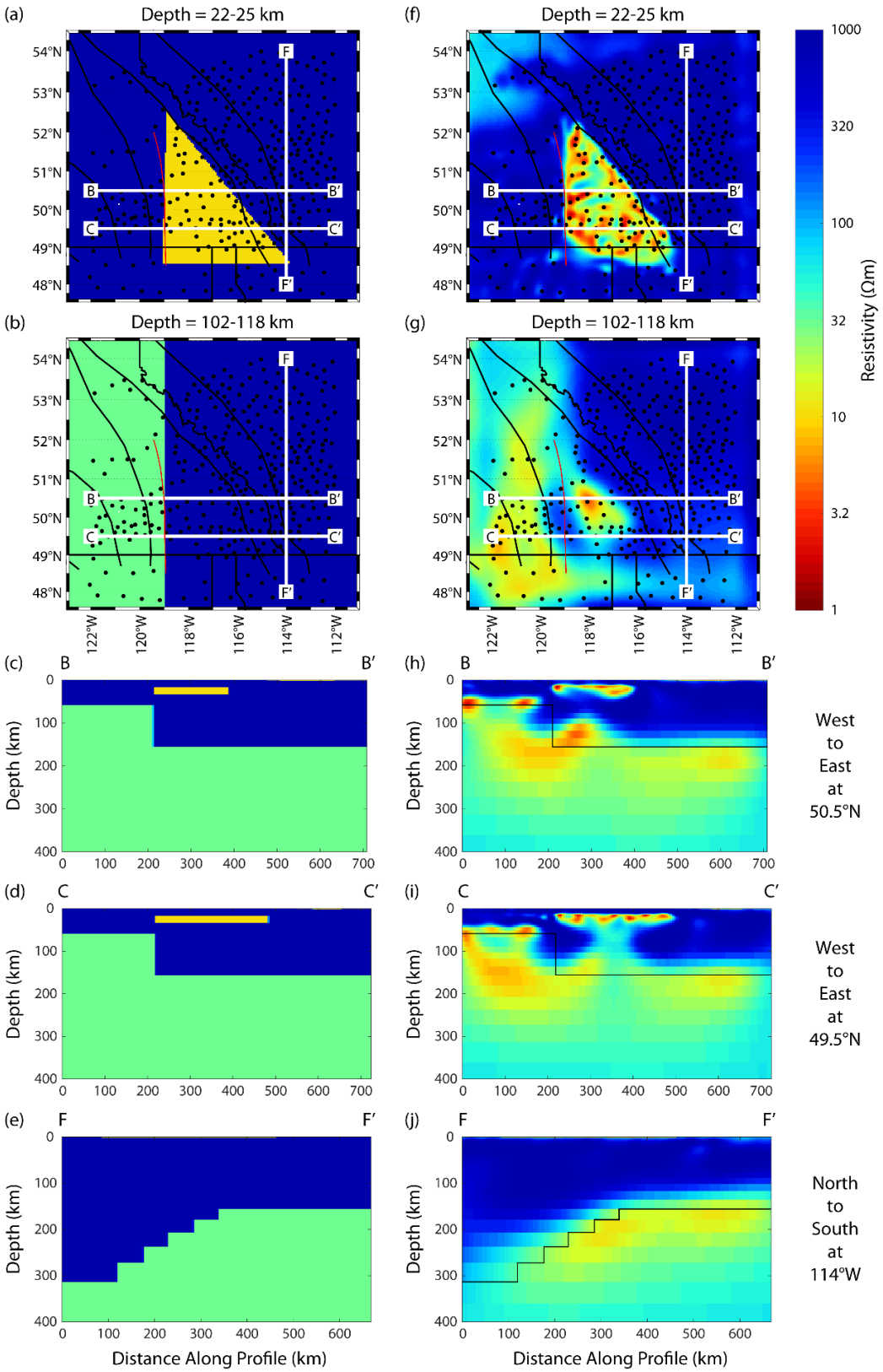

***Figure D.11**: (a-e) Resistivity model 9 (Table D.3) representing the LAB with 1,000 Ωm above it and 30 Ωm below it. The conductive polygon in the upper 50 km is 10 Ωm. (f-j) Resistivity model from inversion of synthetic MT data generated using the resistivity model on the left.*

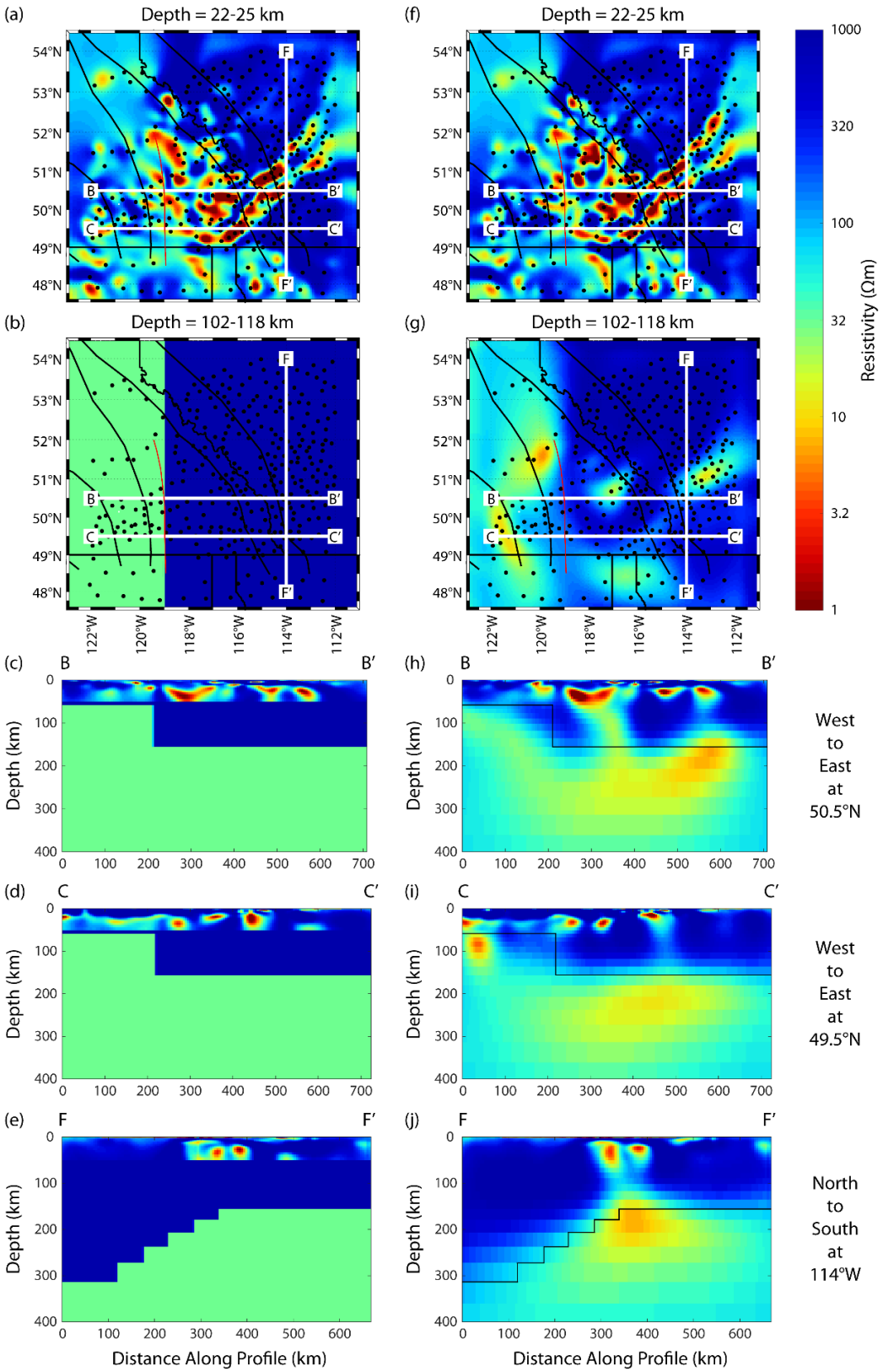

***Figure D.12**: (a-e) Resistivity model 10 (Table D.3) representing the LAB with 1,000 Ωm above it and 30 Ωm below it. The upper 50 km are identical to the preferred resistivity model. (f-j) Resistivity model from inversion of synthetic MT data generated using the resistivity model on the left.*

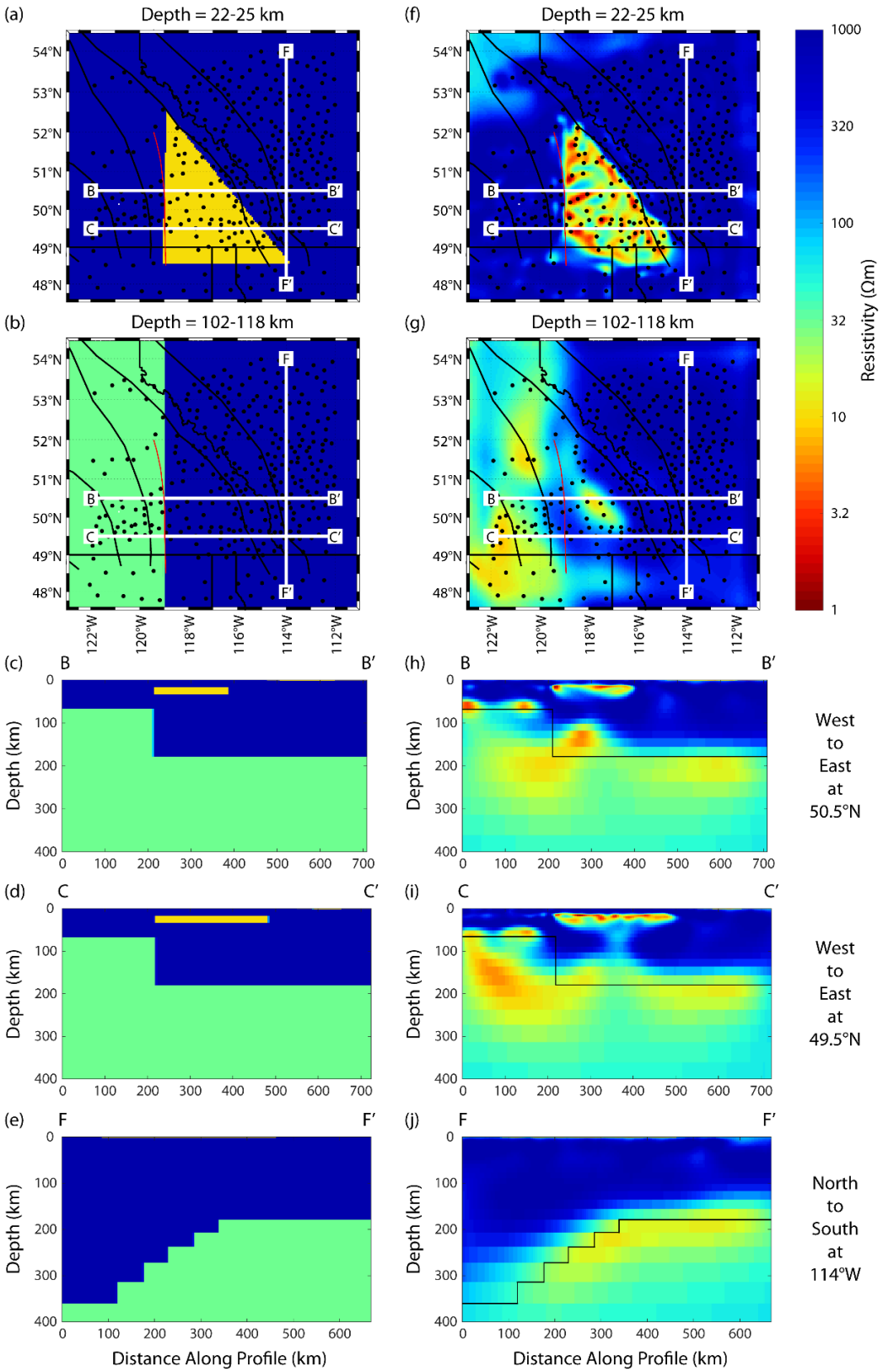

***Figure D.13**: (a-e) Resistivity model 11 (Table D.3) representing the LAB with 1,000 Ωm above it and 30 Ωm below it. The conductive polygon in the upper 50 km is 10 Ωm. (f-j) Resistivity model from inversion of synthetic MT data generated using the resistivity model on the left.*

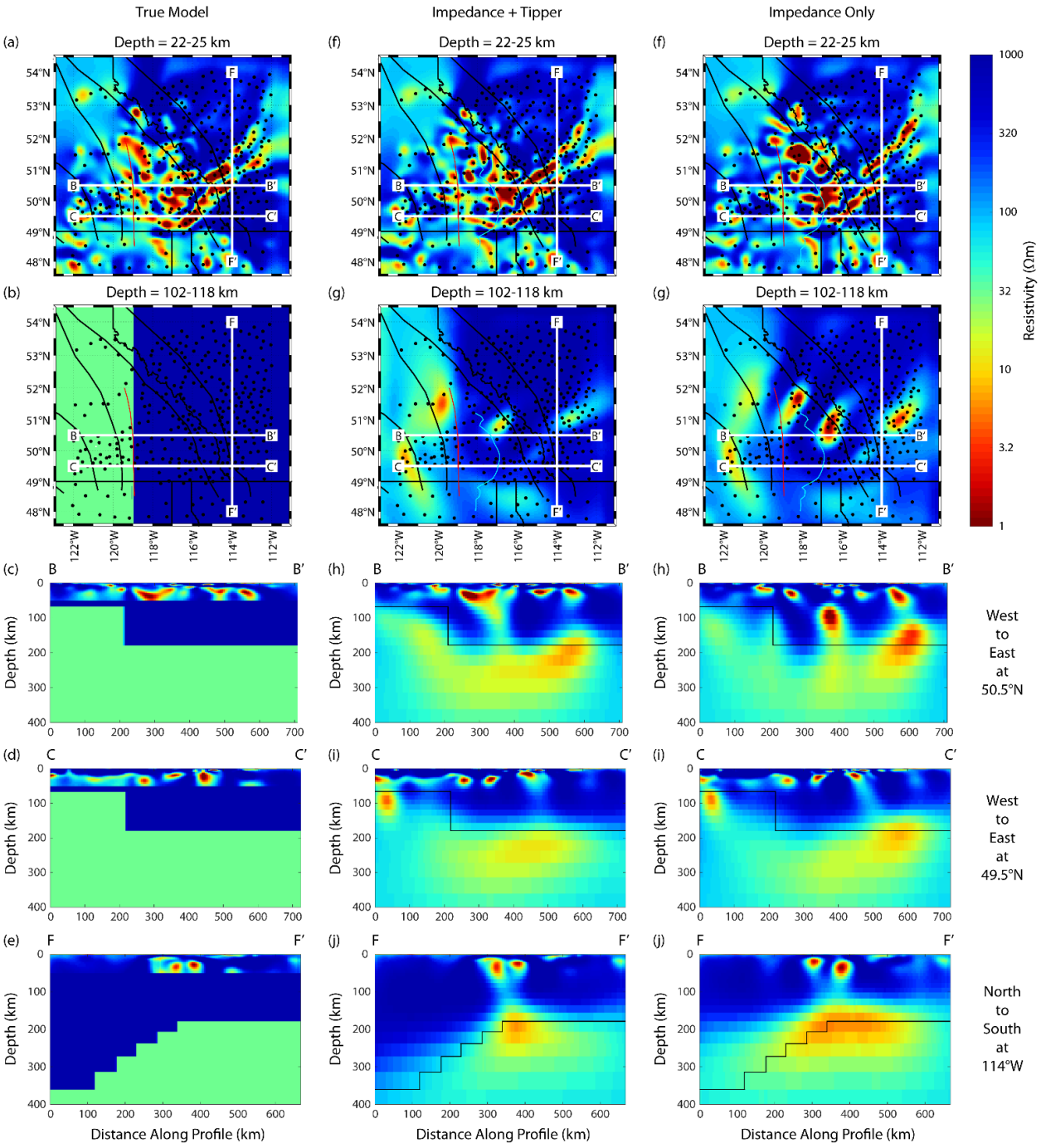

***Figure D.14**: (a-e) Resistivity model 12 (Table D.3) representing the LAB with 1,000 Ωm above it and 30 Ωm below it. The upper 50 km are identical to the preferred resistivity model. (f-j) Resistivity model from inversion of synthetic MT data (impedance and tipper) generated using the resistivity model on the left. (k-o) Resistivity model from inversion of synthetic MT data (impedance only) generated using the resistivity model on the left.*

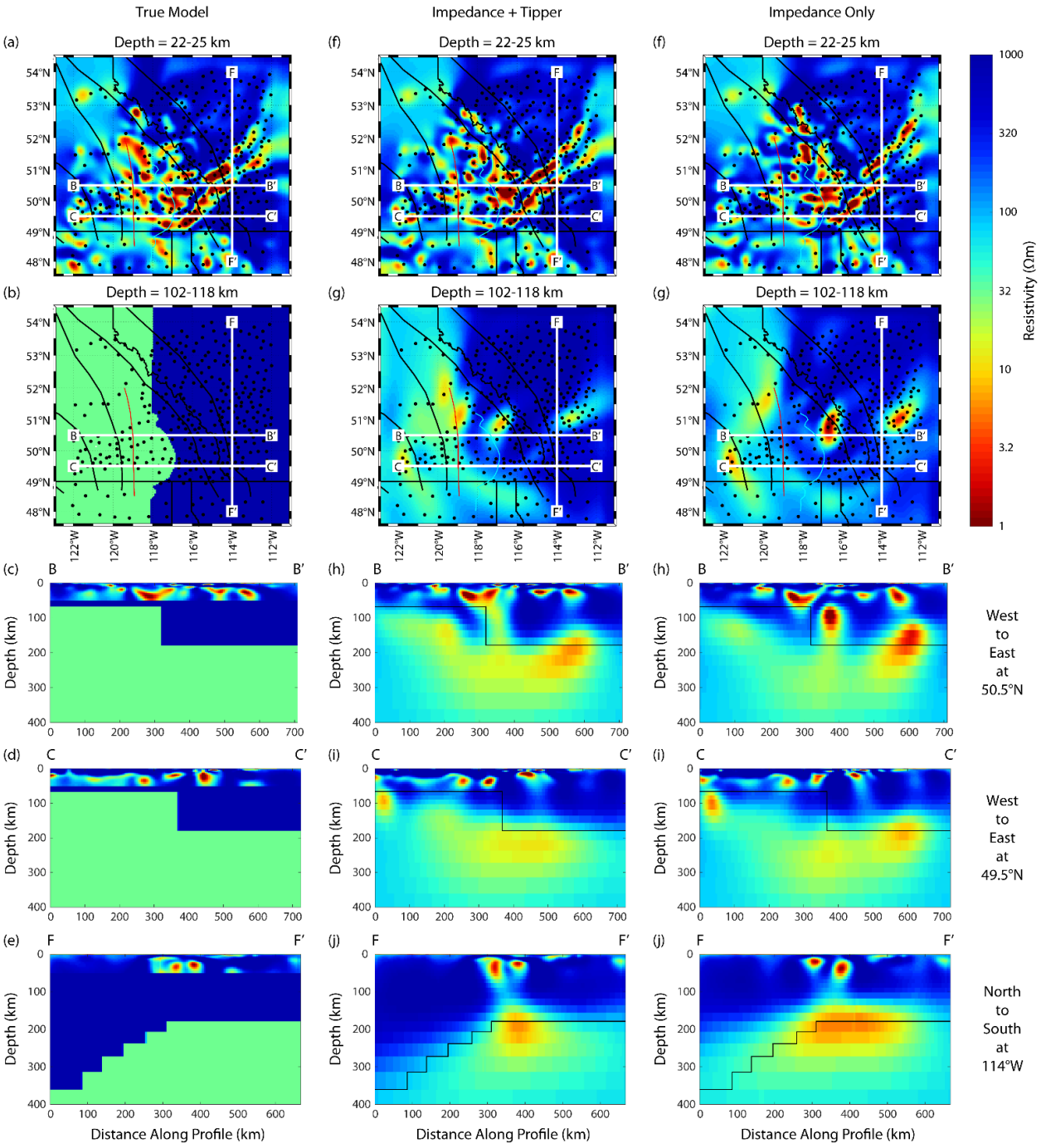

***Figure D.15**: (a-e) Resistivity model 13 (Table D.3) representing the LAB with 1,000 Ωm above it and 30 Ωm below it. The upper 50 km are identical to the preferred resistivity model. (f-j) Resistivity model from inversion of synthetic MT data (impedance and tipper) generated using the resistivity model on the left. (k-o) Resistivity model from inversion of synthetic MT data (impedance only) generated using the resistivity model on the left.*

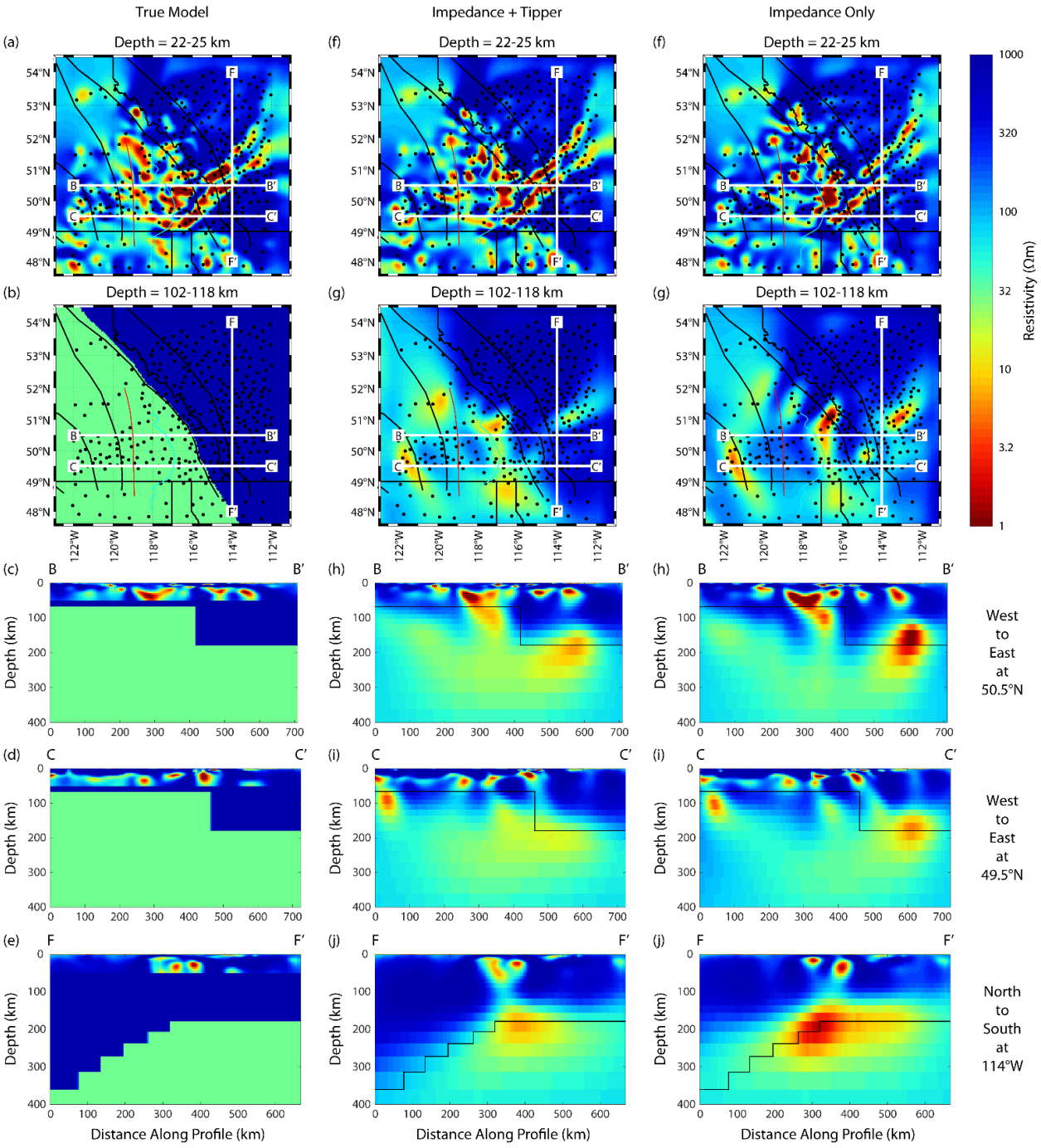

***Figure D.16**: (a-e) Resistivity model 14 (Table D.3) representing the LAB with 1,000 Ωm above it and 30 Ωm below it. The upper 50 km are identical to the preferred resistivity model. (f-j) Resistivity model from inversion of synthetic MT data (impedance and tipper) generated using the resistivity model on the left. (k-o) Resistivity model from inversion of synthetic MT data (impedance only) generated using the resistivity model on the left.*

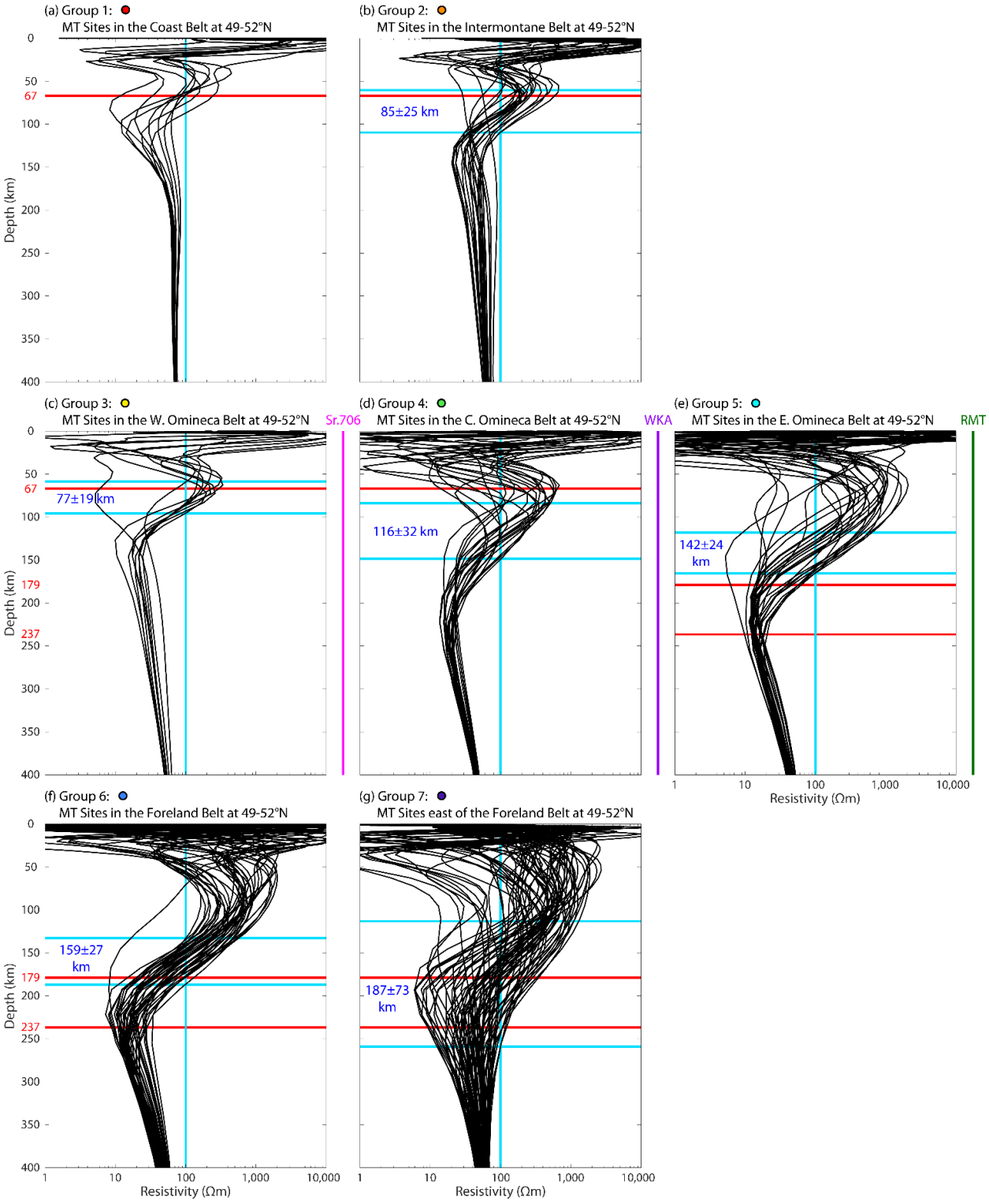

Figure D.17*: Resistivity-depth profiles for synthetic inversion 13 (Figure 6.7) beneath the MT stations in groups G1-G7. Blue lines indicate the depths at which the resistivity is 100 Ωm. These depth ranges (blue numbers) provide estimates of LAB depth. Red lines and red numbers indicate the true LAB depth.*

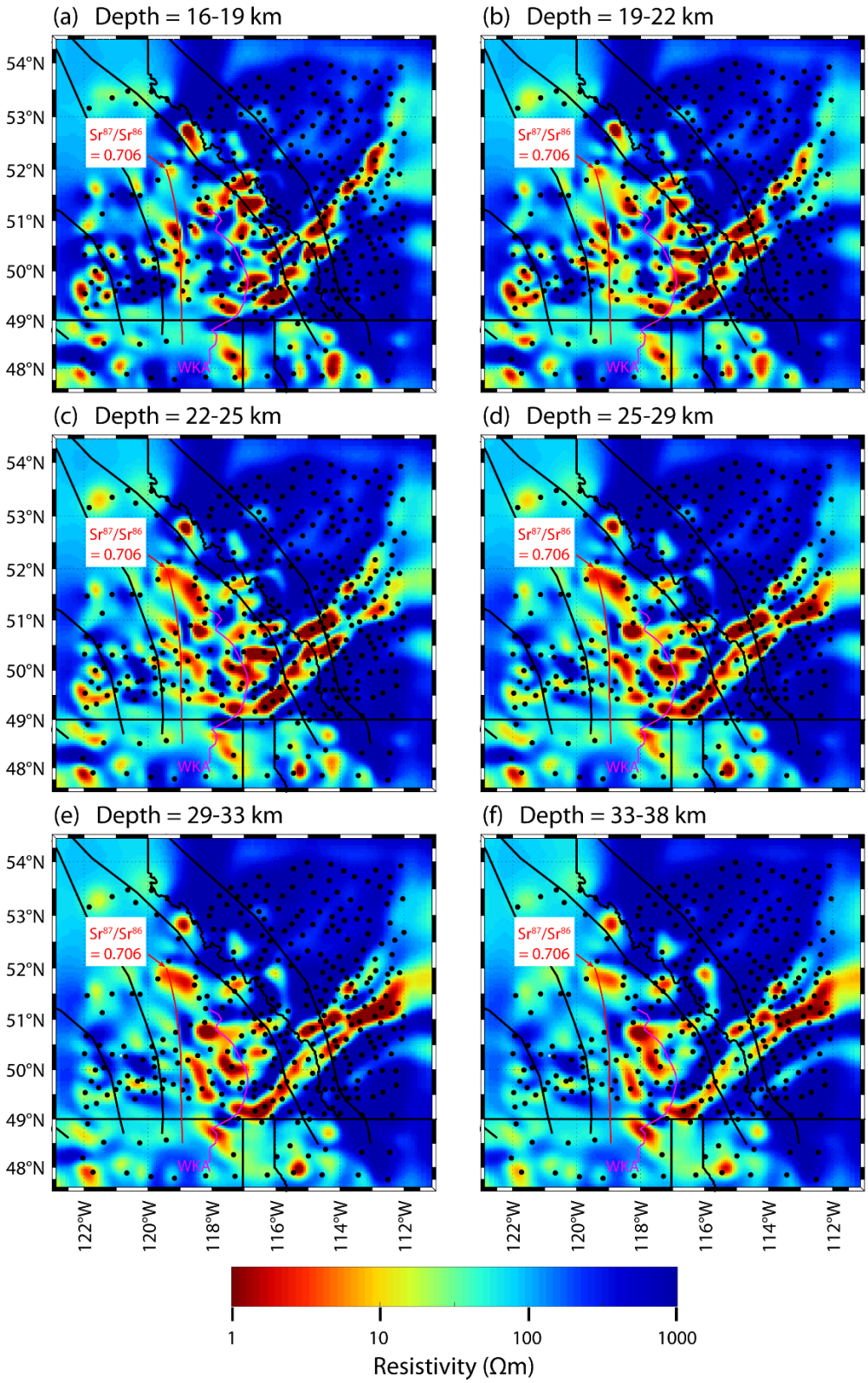

***Figure D.18**: Six horizontal layers of the preferred 3-D resistivity model. Black lines are political and morphogeological boundaries. The red line is the approximate location of the $^{87}Sr/^{86}Sr = 0.706$ isopleth. The purple line is the western boundary of the Kootenay Arc. Black dots are MT data locations. The combined conductance of these six layers is shown in Figure D.19.*

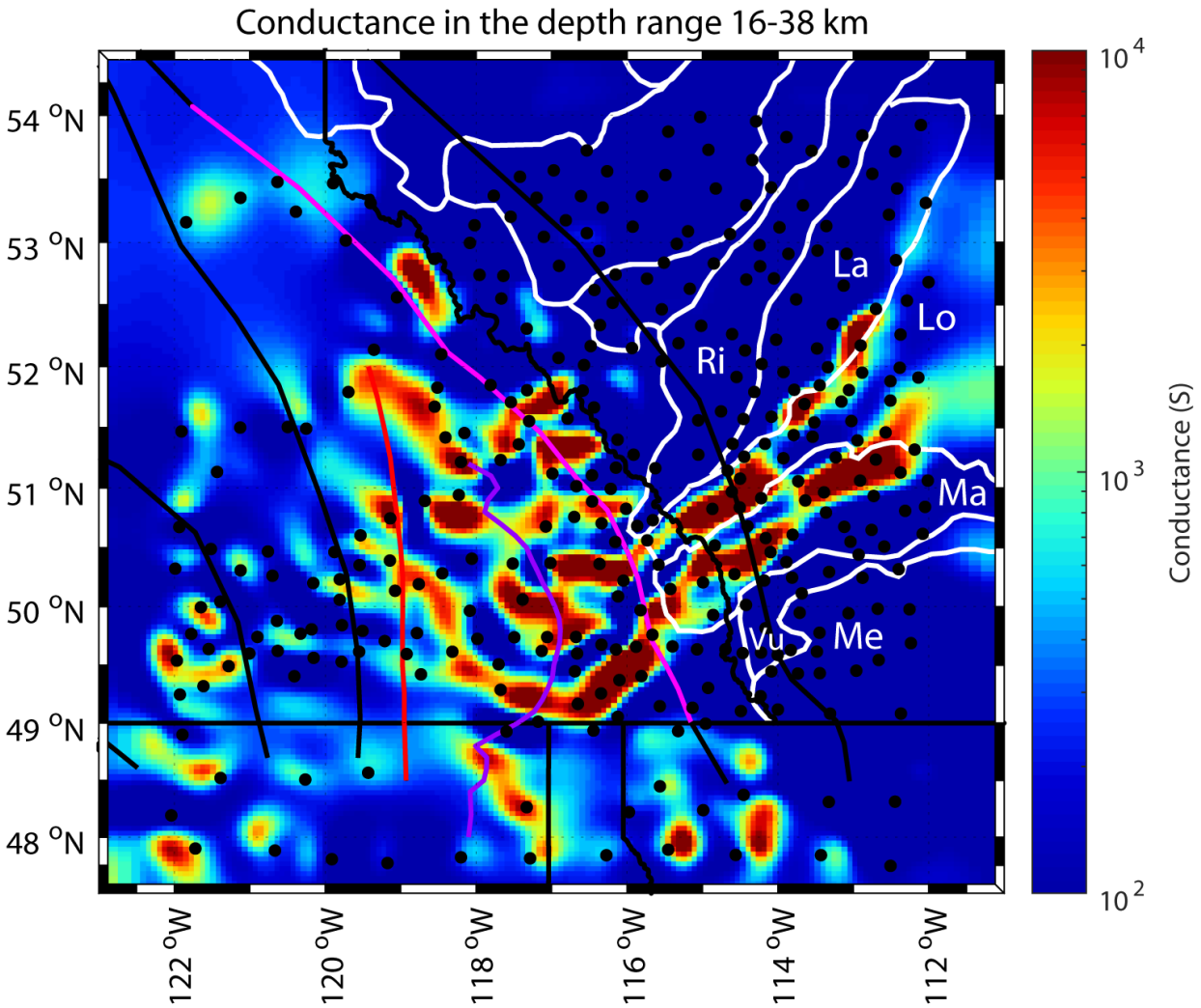

***Figure D.19**: Conductance of the preferred 3-D resistivity model in the depth range 16-38 km. The six model layers in this depth range are shown in Figure D.18. Black dots are MT data locations. Black lines are political and morphogeological boundaries. The red line is the approximate location of the $^{87}Sr/^{86}Sr$ = 0.706 isopleth. The purple line is the western boundary of the Kootenay Arc. The pink line is the SRMT. Pink lines delineate Precambrian basement domains (Pilkington et al., 2000). Ri = Rimbey High, La = Lacombe Domain, Lo = Loverna Block, Ma = Matzhiwin High, Vu = Vulcan Low, and Me = Medicine Hat Block.*

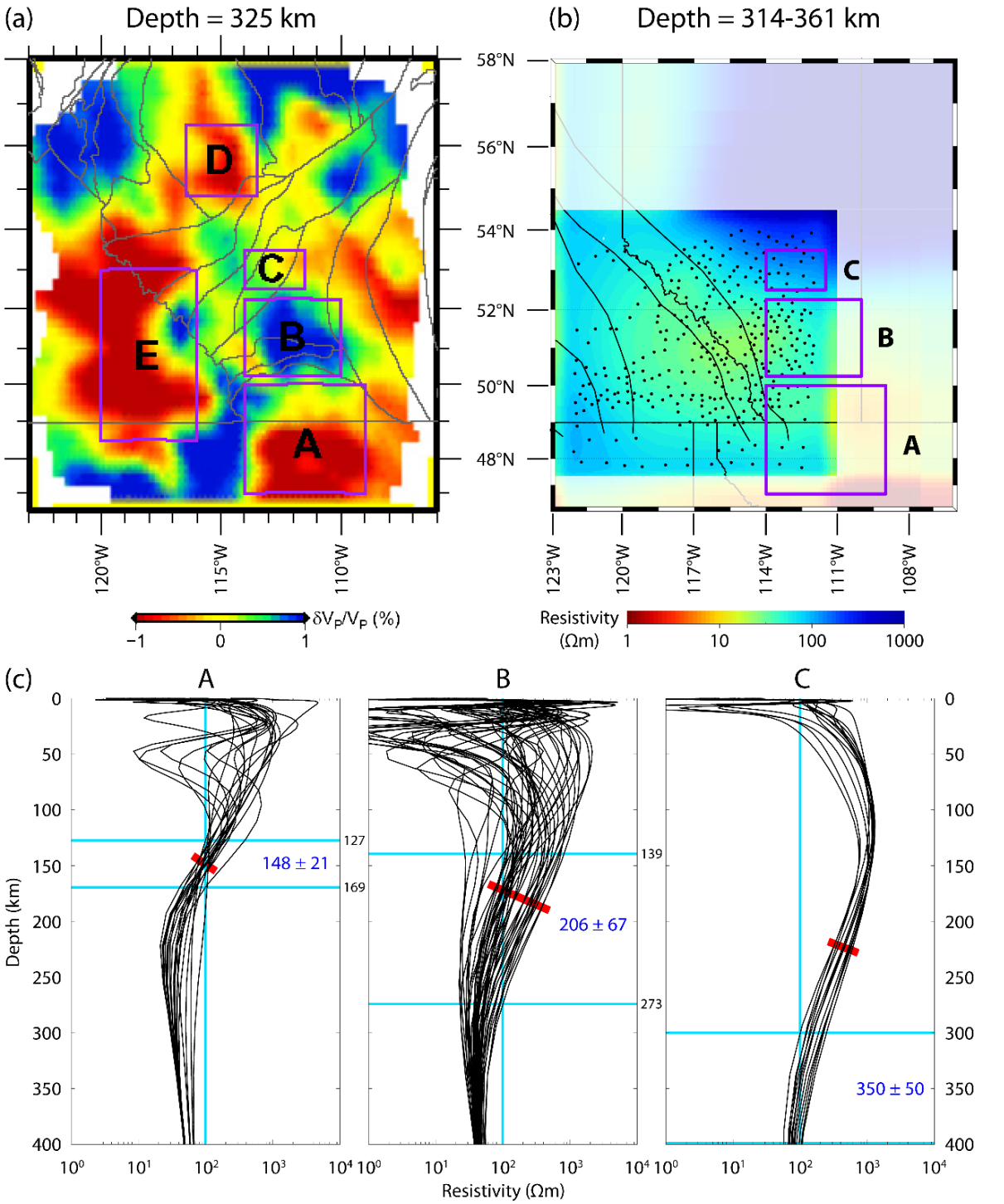

***Figure D.20**: (a) P-wave velocity perturbations at a depth of 325 km, modified from Chen et al. (2017). Region A represents the Medicine Hat Block, region B represents the southern Hearne province, and region C represents the Lacombe domain. (b) A depth slice of the preferred resistivity model, corresponding to panel (a), shaded white outside the study area. (c) Resistivity-depth profiles beneath the MT stations (black dots) located in regions A, B, and C. Blue lines indicate the depths at which the resistivity is 100 Ωm. These depth ranges (blue numbers) provide estimates of LAB depth (e.g., Nieuwenhuis et al. 2014; Wang & Unsworth 2022). Red lines indicate the approximate locations of the inflection points, determined visually. Resistivity inflection points have been used to estimate LAB locations (Bettac et al., 2023).*

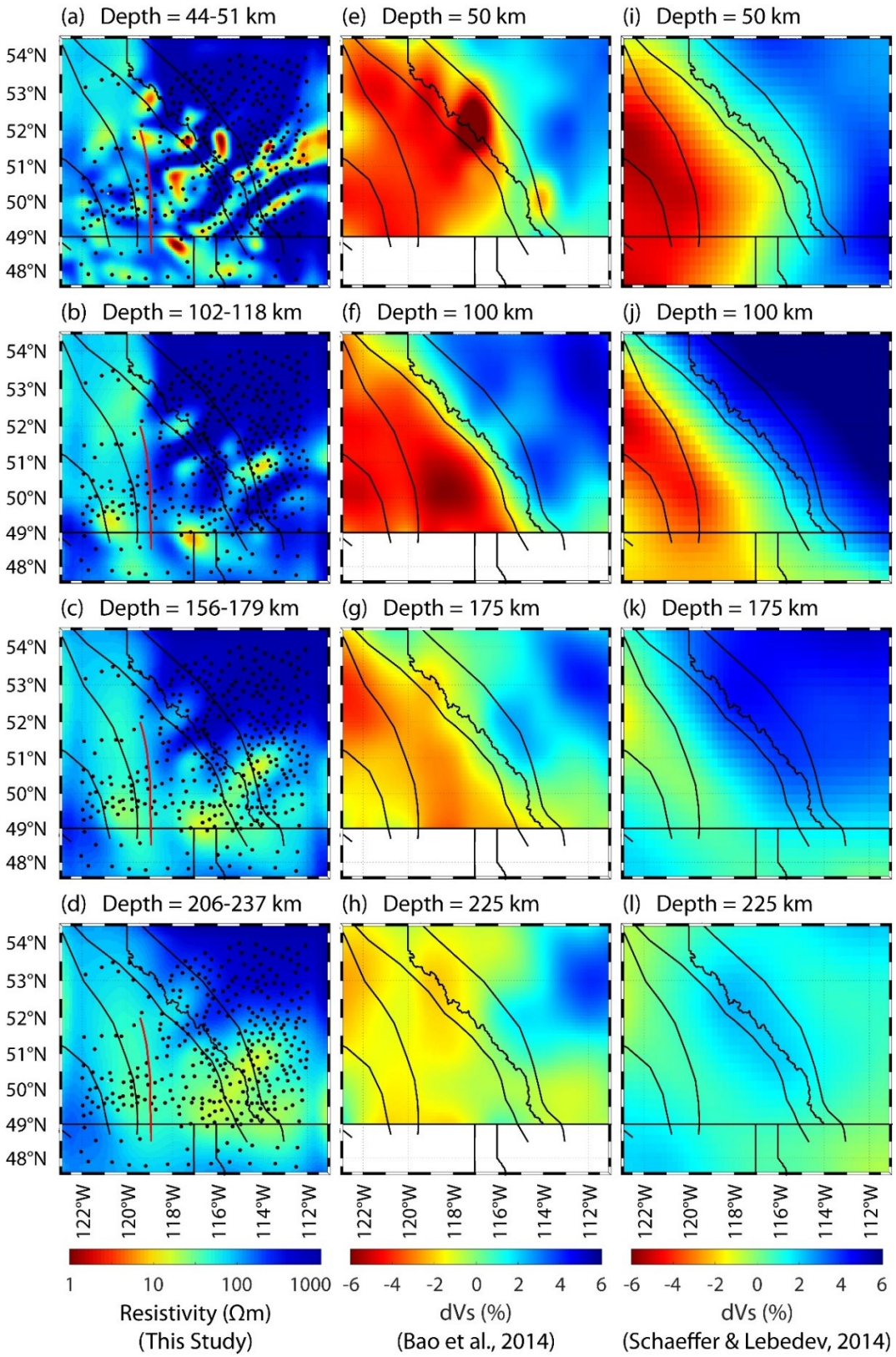

***Figure D.21**: (a-d) Depth slices of the preferred resistivity model. (e-h) S-wave velocity perturbations, based on the model of Bao et al. (2014). (i-l) S-wave velocity perturbations, based on the model of Schaeffer and Lebedev (2014).*